UNIVERSITÀ DEGLI STUDI DI MILANO

Dottorato di Ricerca in Scienze della Terra
Ciclo XXXI

Geochemistry of Amphibole from Archean and Early Proterozoic Ultramafic Rocks: Implications for the Secular Evolution of the Earth's Mantle

Ph.D. Thesis

Gianluca Sessa
Matricola R11208

Tutor	**Academic Year**	*Coordinator*
Prof. Massimo Tiepolo	**2017-2018**	**Prof. ssa Elisabetta Erba**

Abstract

Since its formation at 4.5 Ga, the Earth underwent a complex evolution that progressively differentiated its original composition into the reservoirs that we presently know. Our knowledge on the composition and differentiation mechanisms active in the Early and Ancient Earth are still fragmentary for the paucity of suitable preserved rock records. The poor knowledge on the Archean mantle composition arises a series of problems spanning from the effective chondritic composition of the Earth to how volatile elements (hydrogen, oxygen, chlorine and fluorine) were added to the Earth. For the unavailability of mantle sectors preserving the Archean geochemical signature, valuable information on the Archean mantle composition can be exclusively extracted from Archean mantle-derived igneous rocks. In the Archean greenstone belts, different products of mantle melting are found as lavas and sills spanning in composition from tholeiites through Fe-picrites to komatiites. All these rocks are generally affected by extensive alteration which prevent the bulk rocks to be fully informative on the primary mantle melt composition and particularly on its volatile element contents. However, in some of these rocks primary igneous mineral phases such as amphibole are preserved that may be useful to constrain the primary melt composition including its volatile budgets.

In this thesis amphibole-bearing ultramafic rocks of late Archean and Early Proterozoic age (Stone et al., 2003; Fiorentini et al., 2004; Fiorentini et al., 2008) were selected. For comparison amphibole-bearing ultramafic rocks from different tectonic settings of the Phanerozoic were also considered. The Archean and Early Proterozoic rocks share many petrographic and textural similarities with hornblendites and amphibole-bearing pyroxenites from Phanerozoic orogenic settings. In all studied rocks the crystallisation of amphibole follows that of the early crystallising minerals: olivine + spinel ± orthopyroxene + clinopyroxene. The chemical composition of Archean and Early Proterozoic amphiboles is more similar to that of amphibole from alkaline lavas than that of amphibole in orogenic settings. The geobarometric calculations on Archean and Early Proterozoic rocks yield large uncertainty on the pressure of crystallisation with values between 0 and >3 Kbar, which are not conclusive about the deep or shallow origin of amphibole. In the Archean and Early Proterozoic rocks amphibole is in clear disequilibrium with the early crystallizing clinopyroxene. Modelling of melt differentiation suggests that amphibole crystallized from a melt percolating the cumulate pile. Such melt evolved by crystallization of olivine and pyroxene and subsequently modified its composition in response to olivine assimilation.

A major problem in the studied Archean and Early Proterozoic rocks is about the origin of the H_2O necessary to stabilize amphibole. The H_2O concentrations in the Archean and early Proterozoic

amphiboles are comparable to those of either subduction-related or amphibole megacrysts from alkaline lavas, thus suggesting that melts in equilibrium with amphiboles possessed almost the same water contents irrespective of age. According to the composition of amphibole in fluid-mobile elements (e.g., F, Cl, B and Sr) a contribution of seawater-derived fluid in the Archean and Early Proterozoic rocks is unlikely. The range of δD values of the Archean and Paleoproterozoic amphiboles is between -99.5 ‰ and -129.8 ‰, that is slightly lower than the mantle range but still consistent with a magmatic origin for water. The hypothesis of a crustal contribution in the origin of the amphiboles (and in turn a crustal origin of water) contrasts with the oxygen isotope signature of amphibole showing $\delta^{18}O$ values lighter than those of the mantle. Because the involvement of recycled crustal materials, able to provide the required seawater-like geochemical anomalies, is unlikely for the genesis of the studied amphiboles, the light $\delta^{18}O$ signature is interpreted as a primary feature of the mantle source.

In order to monitor possible changes marked by amphibole in the secular evolution of the Earth's mantle, the trace element composition of the melt in equilibrium with amphibole from Archean and Early Proterozoic rocks was calculated and compared with that of melts produced nowadays at the different geodynamic settings. Equilibrium melts show increasing Nb/Y ratios from komatiites through tholeiites to Fe-picrites that are in agreement with the increased alkalinity of the parental melt as inferred from the literature. All calculated melts share an incompatible trace element pattern paralleling that of present-day OIB. The comparison of the water content in primary melts calculated from Archean-early Proterozoic amphiboles and present-day primary mantle melts reveals that the mantle source of the Archean komatiites had a much higher water content than that characterizing present day OIB. The highly variable water contents in Fe-picrites however suggest a large heterogeneity in the composition of the mantle source. The comparison between the Archean-early Proterozoic amphiboles and those from the Phanerozoic has also revealed heterogeneities in the Nb/Ta ratios of the mantle through the Earth's history. Some of the calculated melts (since early Proterozoic) show an enriched Nb/Ta signature that is independent from space (geological setting) and time and that was interpreted as a primary feature of the different mantle sources. The observed heterogeneous Nb/Ta signature of the Earth's mantle was interpreted as related to the addition of extra-terrestrial material after the mantle-core equilibration prior to 4.4 Ga and to an incomplete equilibration of these domains during the Earth's evolution.

In conclusion, the data of this thesis suggest that the Earth's mantle is much more heterogeneous than commonly assumed. The occurrence in the Archean and Early Proterozoic of mantle domains enriched in volatile elements but unrelated to subduction processes has been documented. An extra-terrestrial signature for some mantle domains was also reported and I do not exclude that the light oxygen

isotope signature of the Archean and Early Proterozoic rocks is also a reminiscence of extra-terrestrial inputs possibly related to the meteoritic Late Veneer.

Introduction

Since its formation at 4.5 Ga, the Earth underwent a complex evolution that progressively differentiated its original composition into the reservoirs that we presently know: core, mantle, crust, atmosphere and hydrosphere. Our knowledge on the composition and differentiation mechanisms active in the Early and Ancient Earth are still fragmentary for the paucity of suitable preserved records. During the Hadean eon, the entire planet was thought to be covered by a magma ocean (e.g., Elkins-Tanton, 2008). After the moon-forming impact, the Hadean experienced ongoing meteoritic bombardment, culminating with the late heavy bombardment in the Eoarchaean (Bottke et al., 2012) that may have facilitated early tectonics (Hansen, 2007). During the freezing of the magma ocean Earth lost much of its early atmosphere (e.g. Pepin & Porcelli, 2006) and, at some point, a steam-rich atmosphere rained liquid water, forever changing the geochemistry of the surface and somehow giving birth to primordial life either during, or shortly after the Eoarchaean (e.g. Buick et al., 1981). From Archean to the present systematic changes in crustal composition and magma chemistry have been observed by means of geochemical and petrological studies. Differences between Archean and post-Archean crusts have led to much discussion about the style and rate of Archean tectonics, for which the preponderance of granite–greenstone terranes, the high-Na Trondhjemite–Tonalite–Granodiorite (TTG) plutons, and the peculiar nature of the ultramafic komatiite lavas have to be taken into account (e.g., Condie & Kröner, 2008; Greber et al., 2017). In spite of the paucity of Archean rocks, it is proven that the early differentiation events must have left an indelible mark on the mantle.

The poor knowledge on the Archean mantle composition arises a series of problems spanning from the effective chondritic composition of the Earth (Campbell & O'Neill, 2012) to how volatile elements (hydrogen, oxygen, chlorine and fluorine) were added to the Earth and how their deep cycle evolved giving origin to life and to the present atmosphere. The imbalance in Lithophile elements between the chemical composition of the silicate Earth and that of chondrites has arisen, for example, several geochemical "paradoxes" that led to question the chondritic Earth composition (Campbell & O'Neill, 2012) or were used to model planetary accretion and better understand how Earth formed and evolved through time. In this context, in order to account for the Nb-Ta imbalance between the composition of the silicate Earth and the chondrites, the involvements of reduced asteroidal building blocks with subchondritic Nb/Ta ratios in the Earth's accretion process has been recently supposed (Münker et al., 2017). However, this and other models are based on the assumption that the Earth's mantle is homogeneously subchondritic in the Nb-Ta composition, assumption that is supported by an

extremely limited and questionable dataset (Münker et al., 2003). Another key aspect of mantle evolution since Archean is the secular variability of oxygen fugacity which is a crucial thermodynamic parameter that controls fundamental processes as planetary differentiation, mantle melting, and possible core-mantle exchange. Although most studies, that largely concentrated on the rocks derived from the upper mantle, have concluded that the mantle fO_2 has remained constant within approximately 1.0 log unit since at least the early Archean (Canil, 1997; Canil & Fedortchouk, 2001; Delano, 2001; Li & Lee, 2004; Berry et al., 2008), some researchers have argued for an increase in modern upper mantle fO_2 since the early Archean by as much as 1.5 log units (e.g., Aulbach & Stagno, 2016). Constraining the evolution of the redox state of the mantle is thus of paramount importance for understanding the chemical evolution of major terrestrial reservoirs, including core and atmosphere.

Even more uncertain are the Archean mantle volatile composition and its secular variation. The mantle composition in atmophile elements (carbon, water) and its evolution are, indeed, of particular importance. Volatile elements have large impact on mantle dynamics and are the building blocks of the molecules at the base of life. Atmophiles are key elements in the structure of amino acids, proteins, nucleic acids, and other molecules vital to life. The general atmophile behaviour of these elements, namely their high volatility and general low solubility in mantle minerals, caused them to be primarily partitioned into the atmosphere during Earth differentiation leaving extremely low concentrations in the Earth's mantle. However, at present, mantle is the only proxy we have to decipher the proto atmosphere and how the conditions became favourable for life. Sometime in the mid- to late Archean (e.g., Farquhar et al., 2011), microbial life developed the ability to perform oxygenic photosynthesis, which uses energy from the sun and raw materials extracted from the geosphere (CO_2 + H_2O) to generate energy and eventually releases oxygen in a gas phase (O_2) as a waste product. Over time these biological processes cumulatively oxygenated the Earth's surface.

The Archean mantle is poorly represented on the present-day Earth. Fragments of the Archean crust (greenstone belts) and mantle are found enclosed in Precambrian cratons and Proterozoic basements. An example of Archean mantle is represented by mantle-derived peridotite bodies enclosed in the gneisses of the Western Gneiss Region, Norway (Brueckner et al., 2002). However, the metamorphic reworking of these rocks almost erased the primary geochemical signature of most elements. Valuable information on the Archean mantle have thus to be extracted from mantle-derived igneous rocks generated by partial melting of Archean mantle sources. In the Archean greenstone belts, different products of mantle melting are found as lavas and sills spanning in composition from tholeiites through Fe-picrites to komatiites.

Chapter 1

1.1 Komatiites

Komatiites are believed to provide the most reliable information on bulk mantle compositions because formed through high degrees of partial melting (e.g., Campbell & Griffiths, 1992). Mafic melts and komatiites represent a unique window into the Archean mantle composition. However, these mafic rocks were often affected by metamorphic overprint that, in many cases, altered the original bulk rock chemical composition. Additional processes, such as degassing or the seafloor hydrothermal alteration, also contributed to change the original composition of these Archean volcanics and have to be deciphered and taken into account. Komatiite can therefore be defined as a rock whose field relations or textures provide evidence of a volcanic or subvolcanic origin and whose mineral assemblages or major-element contents indicate an ultramafic composition. Features that can be used to indicate a volcanic setting include a fine-grained, chilled upper margin or, more conclusively, the presence of breccia or hyaloclastite. Fine grain size throughout the unit, spinifex textures, amygdales, complete conformity with surrounding units (lack of intrusive contacts) are consistent with, but do not prove, a volcanic origin. The chemical limit between komatiite and other less magnesian volcanic rocks was set, rather arbitrarily, at 18% MgO, a value that corresponds to a minimum in the relative abundances of komatiitic rocks in many, though not all, greenstone belts. Implicit to the definition of komatiite is the notion – difficult to prove – that komatiites crystallize from liquids that contained more than about 18% MgO. To distinguish komatiite from other types of highly magnesian volcanic rocks, it is useful to include spinifex texture in the definition of the rock type. Spinifex, a texture characterized by the presence of large skeletal or dendritic crystals of olivine or pyroxene, is present in many, but not all komatiite flows. Many komatiite flows comprise an upper spinifex-textured layer and a lower olivine-cumulate layer; and other flows grade along strike from layered spinifex-textured portions to massive olivine–phyric units. Komatiitic basalts display similar textures with pyroxene rather than olivine as the dominant mineral (Arndt et al., 2008). Compositional differences of komatiites have led to their classification as either Aluminum-Depleted Komatiites (ADKs) or Aluminum-Undepleted Komatiites (AUKs) (Nesbitt & Sun, 1979). A third, less common type, Aluminum- Enriched Komatiites (AEK), has also been defined (Jahn et al., 1982). ADKs are typified by subchondritic Al/Ti ratios (10) and superchondritic Gd_N/Yb_N ratios (13–16) and are interpreted to reflect partial melting in the presence of residual (majoritic) garnet (Nesbitt & Sun, 1979; Nesbitt et al., 1982), which sequesters Al and the heavy rare earth elements (HREE) with respect to Ti and the middle REE (MREE). As pressure increases, garnet becomes increasingly stable in peridotitic compositions (Ringwood & Major, 1971; Zhang & Herzberg, 1994), and, accordingly, ADKs

are considered to have been sourced from high pressures (between 8 and 13 GPa; Herzberg, 1995; Walter, 1998; Robin-Popieul et al., 2012) at moderate degrees of partial melting (~30%) so as not to exhaust garnet. Conversely, AUKs have chondritic Al/Ti ratios (20) and unfractionated Gd/YbN ratios, and are therefore thought to have formed by larger degrees of partial melting (~50%) at lower, garnet-absent pressures (Arndt, 2003; Sossi et al., 2016). High temperature is the defining feature of the komatiite source. Unless the effect of high temperature was counterbalanced by its composition – an elevated content of Fe or garnet, for example – the source would be less dense than surrounding mantle and would have ascended at a rate depending on its shape and size and on the rheology of the surrounding mantle. Numerous studies have been done about komatiite source and a mantle plume might be an adequate option. The source could have been a mantle plume of the type thought (by most authors) to be feeding Hawaii and other chains of oceanic islands – a cylinder of hot, buoyant material rising from deeper in the mantle – or it could have been a 'starting mantle plume' – a huge, roughly mushroom-shaped structure that probably rose from the core–mantle boundary. The composition of the source of komatiite magmas is also uncertain. Several lines of argument show, however, that this source may not have had the normal pyrolite composition commonly used as a starting point in the discussions of the origin of basaltic magmas. For example, Hanson and Langmuir (1978) and Francis (1995) argued, on the basis of the major element compositions of komatiites and picrites, that the source of most komatiites had a higher Mg–Fe ratio, and probably a higher FeO content, than the source of most modern basalts. Don Francis, in his model, argued for secular variation in the composition of the source of komatiites and picrites, the Archean source being richer in FeO than the modern source. Sobolev et al. (2005, 2007) proposed that the sources of some komatiites contained a significant proportion of eclogite, up to 40% in the case of Proterozoic komatiitic basalts from Gilmour Island. For most Archean komatiites, as well as for the Cretaceous Gorgona komatiites, the proportion of the eclogite component was far less, averaging around 20%. The trace-element composition of the komatiite source is poorly constrained. The depletion of incompatible trace elements that characterizes AUKs indicates that the material from which they formed was similarly depleted in these elements. However, if, as is likely, these magmas formed through fractional melting, it is possible that the pre-melting source was less depleted or even enriched in incompatible elements and that the depletion recorded by the trace elements resulted from the separation of earlier melts. On the other hand, the ubiquitous high initial $^{143}Nd/^{144}Nd$ and low $^{87}Sr/^{86}Sr$ of AUKs suggest that the source had undergone long-term depletion of incompatible elements. ADKs may be a rare example of a mantle-derived magma that formed by batch melting. Under normal conditions, the silicate melt has a lower density than the solid from which it forms. For normal mafic magma, the density difference is sufficient to cause the magma to escape from its source as soon as the

degree of melting exceeds a low threshold, probably 1–3%. Fractional melting of the source then produces more magma. This magma may either pond or mix with the products of low-degree melting, or else it may, under exceptional circumstances, escape to the surface (Kerr et al., 1995). At high pressures the situation is different. Silicate liquids are more compressible than solid silicate minerals, which means that as pressure increases, the difference in density between magma and solid residue decreases (Ohtani, 1984; Rigden et al., 1984; Miller et al., 1991). The experiments of Ohtani et al. (1998) have shown that at pressures of about 13–17 GPa, the density of an ultramafic liquid may be slightly greater than that of olivine. The peculiar Al depletion and the low levels of HREE of Barberton-type komatiites are attributed to melting in the presence of garnet (Green, 1981; Sun, 1984). At low pressure, garnet melts near the solidus and is eliminated from the residue before the melt acquires an ultramafic composition. For garnet to be retained in the residue of an ultramafic magma, the pressure must be high (Sossi et al., 2016).

With this preamble we can define the komatiite source as broadly peridotitic, perhaps slightly richer in Fe than the source of modern oceanic basalts and picrites, and in most cases moderately depleted in the more incompatible trace elements. The komatiite source was most probably heterogeneous, but, because the degree of melting required to produce komatiite is generally high, and particularly if the source fractionally melted, the removal of early-formed melts would have preferentially extracted the more enriched components, which generally melt at relatively low temperatures. The immediate source of most komatiite therefore was the relatively refractory material left after extraction of early-formed melts (Arndt et al., 2008). As komatiites represent the hottest magmas erupted on Earth, they present a unique window into the dynamics of the Archean mantle.

1.2 Fe-picrites

Other products of the Archean mantle are the ferropicritic magmas. Although terrestrial picritic magmas with $FeO_{TOT} \geq 13$ wt.% are rare in the geological record, they were relatively common about 2.7 Ga during the Neoarchean episode of enhanced global growth of continental crust (Milidragovic et al., 2016). Neoarchean ferropicrites form two distinct groups in terms of their trace element geochemistry. Alkaline ferropicrites have fractionated REE profiles and show no systematic HFSE anomalies, broadly resembling the trace element character of modern-day ocean island basalt (OIB) magmas. Magmas parental to ca. 2.7 Ga alkaline ferropicrites also had high Nb/Y_{PM} (>2), low $Al2O_3/TiO_2$ (<8) and Sc/Fe ratios, and were enriched in Ni relative to primary pyrolite mantle-derived melts. The high Ni contents of the alkaline ferropicrites coupled with the low Sc/Fe ratios are consistent with derivation from olivine-free garnet-pyroxenite sources. The second ferropicrite group is characterized by decisively nonalkaline primary trace element profiles that range from flat to LREE-

depleted, resembling Archean tholeiitic basalts and komatiites. In contrast to the alkaline ferropicrites, the magmas parental to the subalkaline ferropicrites had flat HREE, lower Nb/Y_{PM} (<2), higher Al_2O_3/TiO_2 (8–25) ratio, and were depleted in Ni relative to melts of pyrolitic peridotite; suggesting they were derived from garnet-free peridotite sources (Milidragovic et al., 2016).

Some of the earliest reported ferropicrite occurrences on Earth (e.g. Rajamani et al., 1985; Hanski and Smolkin, 1995) are from Neoarchean localities in the Superior Province, Canada. These include the ferropicrites of the Newton Lake Formation in the Vermillion district (Green and Schulz, 1977; Schulz, 1982) and the Boston Creek Flow ferropicrites (Stone et al., 1987, 1995a,b) from the Abitibi subprovince. Since then, ferropicrites of Neoarchean age have been identified in the Wawa and Wabigoon subprovinces of the western Superior Province (Goldstein and Francis, 2008; Kitayama and Francis, 2014) and the Ungava craton of the Northeastern Superior Province (Milidragovic et al., 2014). Neoarchean ferropicrites from other cratonic blocks of North America, such as the Slave Province, have also been studied in detail (Francis et al., 1999). Many ferropicrites, such as the Fe-rich ultramafic lavas of the Meredale Member (FeO_{TOT} = 12–23 wt.%; McIver et al., 1982; Schweitzer and Kröner, 1985; Van der Westhuizen et al., 1991), the lowermost unit of the ca. 2.71 Ga (Armstrong et al., 1991) Vestendorp Supergroup in South Africa's Kaapvaal Craton, had been previously classified as enriched komatiites, Al-depleted komatiites or transitional to alkaline basalts (Goldstein and Francis, 2008). Uranium–Pb zircon dating of the Boston Creek Flow (2720 ± 2 Ma; Corfu and Noble, 1992), and the tightly constrained emplacement age of the Fe-rich high-Mg basalts from the Western Churchill Province (2691–2711 Ma; Sandeman et al., 2004), suggest that Neoarchean ferropicrites were emplaced during the ca. 2.7 Ga peak in global igneous activity and continental crust production (see van Kranendonk et al., 2012 for recent review). Furthermore, ferropicritic magmatism has produced a variety of volcanic and subvolcanic formations in the upper part of the early Proterozoic Pechenga Group, including sills, tufts, pillowed and massive lavas, and thick, differentiated lava flows that possess spinifex-textured upper parts-and lower cumulate parts enriched in olivine (Hanski and Smolkin, 1995). Various olivine and pyroxene spinifex types can be distinguished. The occurrence of the spinifex texture in the Pechenga ferropicrites demonstrates that this texture is not restricted to rocks of komatiitic affinity. The existence of kaersutitic amphibole in spinifex-textured ferropicrites is discussed as a paleodepth indicator of the volcanism. The parental ferropicritic magma contained about 15 wt.% MgO. Other geochemical characteristics include high FeOtot and TiO_2 and low Al_2O_3 contents and high abundances of LREE and HFSE. Many incompatible element ratios correspond to those found in modern ocean island basalts (Hanski and Smolkin, 1995).

1.3 Tholeiitic basalts

Another product of the Archean mantle are tholeiitic basalts. These rocks have moderately evolved compositions with low MgO contents between 5 and 8%, flat mantle-normalized trace-element patterns, and isotopic compositions that indicate derivation from a moderately depleted mantle source (Condie, 1990; Laflèche et al., 1992; Arndt, 2008). In many respects, their petrological and geochemical characteristics resemble those of tholeiitic basalts in oceanic plateaus and, if the effects of crustal contamination are ignored, continental flood basaltic provinces. Only slightly elevated Fe and Ni contents and lower levels of moderately incompatible trace elements, such as the HREE, distinguish the Archean tholeiites (Arndt, 1991; Condie, 1994). These differences may indicate either secular variation in the composition of the mantle source, as advocated by Condie (1984, 1994) and Francis et al. (1999), or, alternatively, changes in the conditions of partial melting. Arndt et al. (1997a) suggested that the combination of high Fe–Ni and low HREE indicated that the melting that produced Archean tholeiites took place at greater depths and from a hotter source than the melting that produced basalts in modern volcanic plateaus. The exact relationship between tholeiites and komatiites remains unclear. The two types of magma occur together – komatiite is always associated with tholeiite, even though tholeiites need not be accompanied by komatiite – and the two magmas alternate in many Archean greenstone belts, hence indicating that they formed simultaneously, presumably by melting in different parts of the mantle (Arndt, 2008).

The relicts of the primary igneous assemblage are the only present record of the composition of the melt derived from the Archean mantle. The mineral structure of the major constituents of komatiites, i.e. olivine, orthopyroxene and clinopyroxene, however operates a significant filter in the uptake of trace elements. These minerals cannot give information about the signatures of the mantle source in terms of Nb-Ta or the large ion lithophile elements (LILE), fundamental tracers of mantle fertility. Furthermore, none of these minerals can incorporate and fix significant amounts of volatile elements in their structure, thus hampering robust inferences on the volatile content of the mantle source. Ultramafic rocks having amphiboles with textures and compositions of proven igneous origin (Stone et al., 1997) are reported in the late Archean greenstone belts (Stone et al., 2003; Fiorentini et al., 2004) as well as in Proterozoic belts (Fiorentini et al., 2008).

1.4 Amphibole in the Archean and Early Proterozoic rocks

Stone and co-authors (2003) have studied Archean hydromagmatic amphiboles from the Al-depleted tholeiites and ferropicrites of the Abitibi greenstone belt, Canada. The amphiboles are observed in peridotite layers and basal chill zone of thick differentiated basic and ultrabasic sills and flows, and are titanian pargasite in composition. The authors divided the amphiboles in two petrographic types:

amphiboles in the groundmass and amphibole-bearing melt inclusions. The former are oikocrysts hosting / enclosing cumulus olivines (Fo_{83}) that are rounded in shape, embayed and smaller in size. The amphibole-bearing melt inclusions are spherical to ovoid in shape and are hosted in cumulus olivines (Fo_{79} in tholeiitic rocks). In-situ analysis ion probe of the amphiboles reveal enrichment in Nb, LREE and Zr and depletion in Sr and HREE relative to primitive mantle. The water contents are in the range of 1-3 wt. % and overall display δD values from 50 ‰ to -140 ‰, mainly in the range of -60 ‰ and -90 ‰ (Stone et al., 2003). The authors suggest that amphibole formation was driven by subsolidus reaction of residual hydrous silicate melt with primitive assemblage of olivine and clinopyroxene. Bulk composition of the melt inclusions and presence of magmatic water suggest amphibole crystallization from olivine and pyroxene residual melts with at least 2-3 wt. % of water during rapid solidification of the host units. For the authors, adjustment for the anhydrous phase crystallization suggests the initial melts contained 1-2 wt. % H_2O. In the study by Stone et al. (2005), in-situ H isotope analysis of igneous amphibole from the Boston Creek ferropicrite, a 100-m-thick layered mafic-ultramafic unit, provides understandings into the evolution of Archean mantle-derived hydrous melts in the crust. Ion microprobe analyses of the ultramafic-rock-hosted interstitial igneous Mg-hastingsite indicate a wide range of δD values, from –47 ‰ to +54 ‰ and 2–3 wt% H_2O at the 100–1000 μm intragrain scale (Stone et al., 2005). The authors also have observed that amphiboles show relatively uniform major-element and incompatible trace-element compositions. This wide range includes values significantly higher than the δD values of –50 ‰ for whole-rock samples, <+10 ‰ for igneous amphiboles from ultramafic sills, –80 ‰ to –30 ‰ values for hydrothermal-metamorphic fluids in the area, and –90 ‰ to –60 ‰ values for mantle materials. For Stone and co-authors, the anomalously high δD values cannot be attributed completely to H loss from amphibole during secondary processes. The contrast with the relatively uniform Mg-hastingsite composition and H_2O and trace-element contents of the amphibole excludes the possibility that the δD values reflect variable fluid/mineral fractionation. Stone et al. (2005) suggest that the anomalously high δD values most plausibly record the composition of the ferropicritic melt from which the amphibole formed.

Fiorentini et al. (2010, 2012) also described Archean hydromagmatic amphiboles in the komatiites of Mount Keith and Mount Clifford in the Agnew-Wiluna greenstone belt, Australia. Komatiite sills up to 500 m thick contain widespread occurrence of hydromagmatic amphibole in orthocumulate- and mesocumulate-textured rocks, which contain ca. 40–50 wt% MgO and 3 wt% TiO_2. Conversely, komatiite flows do not contain any volatile-bearing mineral phases: about 150-m-thick flows only contain vesicles, amygdales and segregation structures, whereas 5–10-m thick flows lack any textural and petrographic evidence of primary volatile contents (Fiorentini et al., 2012). The authors

suggest that komatiites from the Agnew-Wiluna greenstone belt, irrespective of their initial water content, have degassed upon emplacement, flow and crystallization. More importantly, data show that komatiite flows most likely degassed more water than komatiite intrusions. Komatiite degassing may have indirectly influenced numerous physical and chemical parameters of the water from the primordial oceans and hence indirectly contributed to the creation of a complex zonation at the interface between water and seafloor.

Fiorentini et al. (2008) have studied the Paleoproterozoic Pechenga complex (Russia) and provide insights into the controversial source of volatiles that are implicated in Precambrian ultramafic magmatism. The intrusions mainly contain oikocrystic kaersutites and pargasites, whereas lava flows generally include idiomorphic Fe-kaersutites and Fe-pargasites. All orthomagmatic amphiboles display slightly LREE-enriched chondrite-normalised patterns. Primitive mantle-normalised patterns of amphiboles from the intrusions display positive Nb–Ta, moderate negative Th–U and distinctive negative Sr–Li anomalies. Conversely, Fe-kaersutites and Fe-pargasites from the lava flows display undepleted Th, U, Sr and Li signatures. Boron and Cl enrichment is primarily observed in secondary edenites, which locally rim orthomagmatic kaersutites. In-situ δD measurements of hydromagmatic amphiboles from the gabbro–wehrlite intrusions display values ranging between −70‰ and −170‰, and total water contents between 1 and 3 wt. %. Conversely, primary hydromagmatic amphiboles from the Pechenga flows display lighter δD compositions ranging between −100‰ and −270‰, and lower (>2 wt.%) total water contents. The Ti– and Nb–Ta-enriched nature of hydromagmatic amphiboles from the intrusions and lava flows indicates that the source of volatiles in the Pechenga ferropicrites could be either a metasomatised subcontinental mantle or a volatile-bearing plume. Positive Nb–Ta/La anomalies in amphiboles from the intrusions rule out crustal contamination with granitoid crust during petrogenesis and emplacement as the main source of the volatiles. Local B–Cl enrichment suggests that some samples may have interacted with hydrothermal fluids. The range of in-situ δD values in hydromagmatic amphiboles is consistent with the presence of magmatic water. The lighter hydrogen isotopic composition and lower water contents of the primary igneous amphiboles from the lava flows compared to amphiboles from the intrusions indicate that the lava flows degassed upon emplacement.

1.5 Aim of this work

The goal of this study is to propose a novel approach in deciphering the Archean mantle geochemical signature by deriving the trace element composition of the mantle from that of the melt in equilibrium with accessory minerals of Archean ultramafic rocks such as primary amphibole. Some Archean and Paleoproterozoic ultramafic sequences comprise layers with cumulate texture preserving amphibole as primary igneous minerals. Among mafic minerals, amphibole is efficient in preserving

information on the equilibrium melt for its capability to incorporate almost all the petrologically relevant elements. These include fO_2 sensitive elements (e.g., V), Nb-Ta, LILE and volatiles (H_2O, Cl and F). A detailed geochemical study on Archean amphibole is fundamental to constrain the relations between this mineral and primary mantle melts in order to evaluate the volatiles budget of Archean mantle. Thus, the information about chemical composition of the Archean mantle may answer to the actual debates on the wet or dry nature of the Archean mantle sources as well as the Nb "paradox" on sub-chondritic signature of the mantle.

Chapter 2

Geological setting and petrography of selected samples

The geological setting and the petrography of the samples considered for this study are reported in this Chapter which is divided according to age and localities. Phanerozoic amphibole-bearing samples are reported for a comparison with the Precambrian amphiboles in order to evaluate secular variations in the mantle compositions of the volatiles elements. Phanerozoic samples are from subduction-related setting and from alkaline lavas.

The reader should consider that the samples of Archean and Paleoproterozoic age studied in this thesis were made available through the collaboration with Prof. Marco Fiorentini, Centre for Exploration Targeting, University of Western Australia (Perth, Western Australia). Furthermore, several of these Archean and Paleoproterozoic samples were also objects of previous studies (Fiorentini et al., 2008, 2010, 2012). The samples of Phanerozoic age were also objects of previous studies related to ongoing international scientific collaborations involving Prof. Massimo Tiepolo (Esna-Ashari et al., 2016; Ma et al., 2013a,b; Tiepolo et al., 2008, 2011, 2012).

The following sections provide the geological setting of the different sample localities and about the essential petrographic features of the selected samples. The Precambrian samples were accurately selected by a collection of 131 samples by considering the presence of hydromagmatic amphibole and the best possible preservation of the primary textural features.

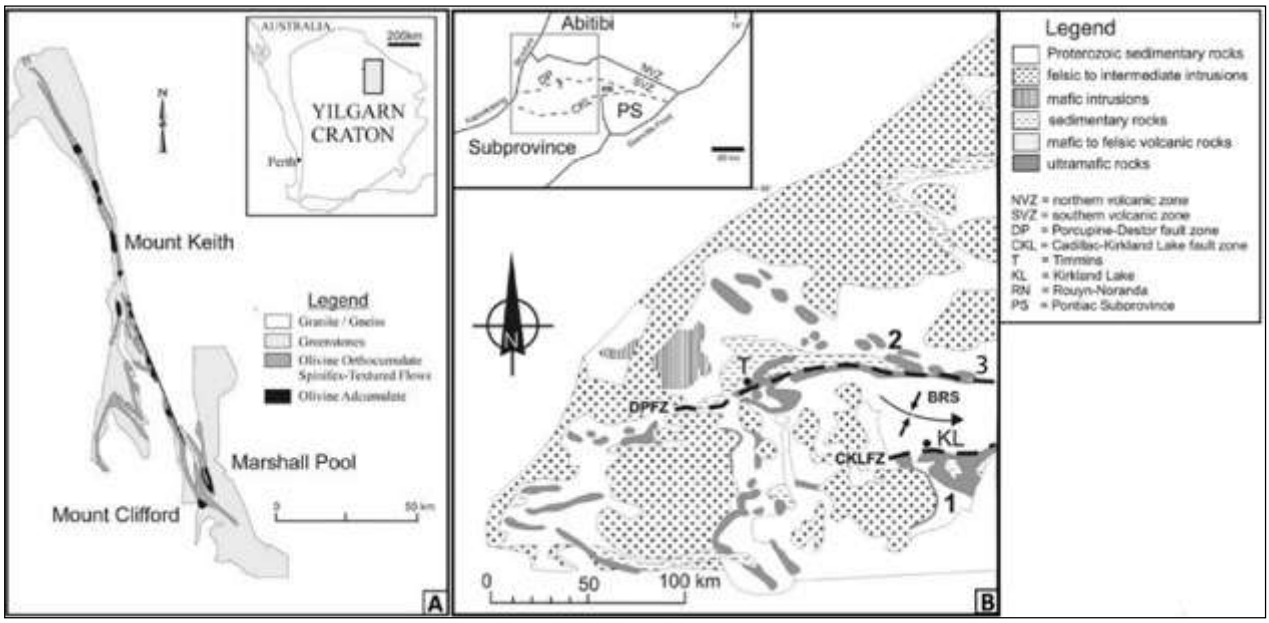

Figure 1 - Neoarchean samples locations and simplified geological setting. (A) samples from Mount Keith and Mount Clifford, Agnew-Wiluna greenstone belt, Western Australia (modified from Fiorentini et al., 2012); (B) samples from (1) Boston Creek flow, (2) Theo's Flow and (3) Ghost Range, Abitibi greenstone belt, Canada (modified from Stone et al., 2005).

2.1 Agnew-Wiluna greenstone belt (Western Australia)

The Agnew-Wiluna belt is located within the northern part of the Kalgoorlie terrane, the most westerly of the three terranes (the others are Kurnalpi and Burtville) that collectively make up the Eastern Goldfields superterrane of the Yilgarn craton, Western Australia (Myers, 1997; Cassidy et al., 2006). The Kalgoorlie terrane is bounded by the Youanmi terrane to the west and the Kurnalpi terrane to the east. Terrane boundaries are marked by major NNW-trending fault zones; the Ida fault forms the western boundary of the Kalgoorlie terrane and seismic traverses reveal that it extends to the base of the crust (Drummond et al., 2000; Mole et al., 2013, 2014; Zibra et al., 2013). Supracrustal sequences in the Kalgoorlie terrane are dominated by a variety of volcanic rocks with lesser volumes of volcaniclastic and epiclastic lithologies, dated to between 2720 and 2660 Ma (Nelson, 1997; Swager, 1997; Kositcin et al., 2008; Czarnota et al., 2010). These locally rest on older supracrustal sequences, such as the 2930 ± 4 Ma Penneshaw Formation at Norseman (Nelson, 1997), the > 2749 ± 7 Ma eastern basaltic sequence at Wiluna (Kent and Hagemann, 1996), the 2736 ± 3 Ma Kathleen Valley Gabbro southwest of Yakabindie (Liu et al., 2002), and the ca. 2730 Ma intermediate to felsic volcanic footwall sequence at Cosmos (De Joux et al., 2013). The 2720 to 2660 Ma episode of greenstone formation comprises three major sequences, which can be correlated across most of the strike extent of the Kalgoorlie terrane. The 2720 to 2690 Ma Kambalda sequence consists of intercalated basaltic and komatiitic volcanic rocks,

with a component of felsic to intermediate calc-alkaline volcanic and volcaniclastic rocks that becomes increasingly voluminous to the north of Kambalda. The geochemistry of the upper parts of the komatiitic sequence at Kambalda and of the overlying basalt, and the presence of >2900 Ma xenocrystic zircons, indicate that a component of crustal assimilation was important in the petrogenesis of these mafic and ultramafic volcanic rocks. These rocks were probably erupted onto older continental crust (Arndt and Jenner, 1986; Compston et al., 1986; Morris, 1993; Lesher and Arndt, 1995; Nelson, 1997; Bateman et al., 2001).

The presence of pillow basalts and of hemipelagic sedimentary rocks intercalated with the mafic to ultramafic stratigraphy has led to the interpretation of the Kambalda sequence as being deposited in a back-arc setting (Barley et al., 1989; Krapež, 1997). This interpretation is further supported by the recognition that the Kurnalpi terrane to the east comprises a sequence of ~2715 to 2704 Ma calc-alkaline andesitic volcanic complexes (Morris and Witt, 1997; Barley et al., 2008). However, more recent analysis of the geochemical composition of basaltic and andesitic rocks from the Eastern Goldfields superterrane reveals subtle departures from distinctive island arc signatures (Barnes et al., 2012b; Barnes and Van Kranendonk, 2014). These authors argue that the geochemical data are more consistent with magma derivation from a plume head (low-Th basalt) or during plume-crust interaction (high-Th siliceous basalts and andesites).

The Kambalda sequence is overlain unconformably by the 2690 to 2665 Ma Kalgoorlie sequence, comprising andesitic, dacitic, and rhyolitic volcaniclastic and epiclastic rocks with subordinate volcanic rocks (Barley et al., 2002; Kositcin et al., 2008; Krapež and Hand, 2008). These rocks typically display tonalite-trondhjemite-granodiorite geochemical characteristics, consistent with an origin via slab melting in a convergent margin setting (Czarnota et al., 2010), although derivation through melting of underplated basaltic material is also considered as an alternative (Barnes and Van Kranendonk, 2014). Rocks of the Kalgoorlie sequence are coeval with the main phase of high-Ca granitoid magmatism (Champion and Sheraton, 1997; Champion and Cassidy, 2007) and almost certainly represent the volcanic and volcaniclastic equivalents of these granitoids. The coincidence of the cessation of volcanism in the Eastern Goldfields superterrane at ~2670 Ma with the onset of regional D2 contraction (Blewett and Czarnota, 2007a, b) and with a coarsening-upward trend in the uppermost parts of the Kalgoorlie sequence (Squire et al., 2007) suggests that this sequence records the switch from regional extension and volcanism to basin closure and orogenesis (Czarnota et al., 2010).

Siliciclastic sedimentation in late basins occurred at about 2660 Ma in the Kalgoorlie terrane (Krapež et al., 2000) and marks the final stage of greenstone formation (Krapež et al., 2000, 2008; Kositicin et al., 2008). Facies analysis indicates a change from fluviatile to deep-water marine deposition over time in the Kalgoorlie terrane. These basins record the first exhumation of granite domes, since

they contain granitic detritus and occur in the hanging wall of the extensional shear zones that mark the contact between large granitic domes and the margins of greenstone belts (Blewett et al., 2010a). The late basins and extensional shear zones share similar P-T-t paths (Goscombe et al., 2007), suggesting that the two are genetically linked. There is also a spatial link with syenites, which tend to be emplaced during tectonic extension (Smithies and Champion, 1999). Czarnota et al. (2010) suggested that these basins formed as a result of far-field extension, rather than in response to strike-slip movement on major NNW-trending faults as proposed by Krapež and Barley (2008).

A comprehensive review of the structural history of the Eastern Goldfields superterrane is presented by Blewett et al. (2010a) and a geodynamic model is presented by Czarnota et al. (2010). These authors recognize five main deformation events. D1 relates to the period of pericratonic, ensialic extension that accompanied submarine volcanism and sedimentation in the Kalgoorlie terrane. The strong NNW-trending structural grain evident in the Eastern Goldfields superterrane was probably established at least as early as the ~2810 Ma phase of rifting and greenstone formation and would have controlled the location and orientation of the 2720 to 2670 Ma rift. All terranes of the Eastern Goldfields superterrane display a common structural history post-2670 Ma, although the timing of each event is diachronous, occurring earlier in the east than in the west. East-northeast contraction marks the D2 event which produced regional-scale NNW-striking upright folds. This event occurred at ~2665 Ma in the Kalgoorlie terrane.

Mid-orogenic E-NE extension (D3) occurred in response to magmatic and tectonic crustal thickening and/or slab roll-back, possibly associated with lower crustal delamination. The majority of major crustal-penetrating shear zones were reactivated during D3, which occurred at ~2660 Ma in the Kalgoorlie terrane and coincided with formation of the late basins. The D4 event is subdivided into a period of E-NE contraction (D4a: ~2655 Ma) followed by a period of east-southeast contraction (D4b: ~2650 Ma in the Kalgoorlie terrane). The inherited extensional architecture controlled the localization of D4 structures and the late basins were folded and faulted at this time. The change in orientation of the principal stress from east-northeast to east-southeast resulted in principally strike-slip movement on the previously established NNW-trending fault systems. Sinistral transpressional shear zones developed during D4b are overprinted by N- to NE-striking D5 faults as the principal compression direction shifted to the NE at ~2650 Ma in the Kalgoorlie terrane. Two further events with uncertain relative timing affected the Eastern Goldfields superterrane: a phase of vertical shortening which produced extensional faults with no preferred orientation, and a further event which produced brittle E-Wstriking sinistral faults, possibly related to Proterozoic dike emplacement.

The geodynamic model of Czarnota et al. (2010) favors a plate tectonic reconstruction of the Eastern Goldfields superterrane with the initiation of a westward-dipping subduction zone to the east producing a back-arc basin and volcanic arc in which the 2720 to 2670 Ma volcanic stratigraphy of the Kalgoorlie and Kurnalpi terranes was deposited. However, as noted by Barnes and Fiorentini (2012), one of the unique features of the Kalgoorlie terrane is the great abundance of komatiitic rocks (and particularly of olivine adcumulates), many of which crystallized from komatiitic magmas that were unusually primitive. The high MgO content of komatiitic lavas led to early models for the development of the Agnew-Wiluna belt development based on a mantle plume impinging on the Archean crust (Campbell and Hill, 1988; Campbell et al., 1989). Blewett et al. (2010b) presented magneto-telluric data for the SE margin of the Yilgarn craton that support the observation of Begg et al. (2010). The terranes, such as the Kalgoorlie and Kurnalpi terranes, are typically underlain by thinner subcontinental lithospheric mantle relative to older, more evolved terranes like the Youanmi. Mole (2012) proposes a model for the formation of the Kalgoorlie terrane in which cratonic margin extension and crustal thinning caused the impinging plume head to be diverted to shallower crustal levels where high degrees of melting took place in response to drop in pressure (Mole et al., 2013, 2014). This model predicts extremely high-flux komatiitic eruptions with minimal ponding and fractionation of magma during ascent. Both processes would have been facilitated by the thinned lithosphere and the presence of mantle-tapping structures in an extensional cratonic margin setting (Begg et al., 2010).

2.1.1 Mount Clifford

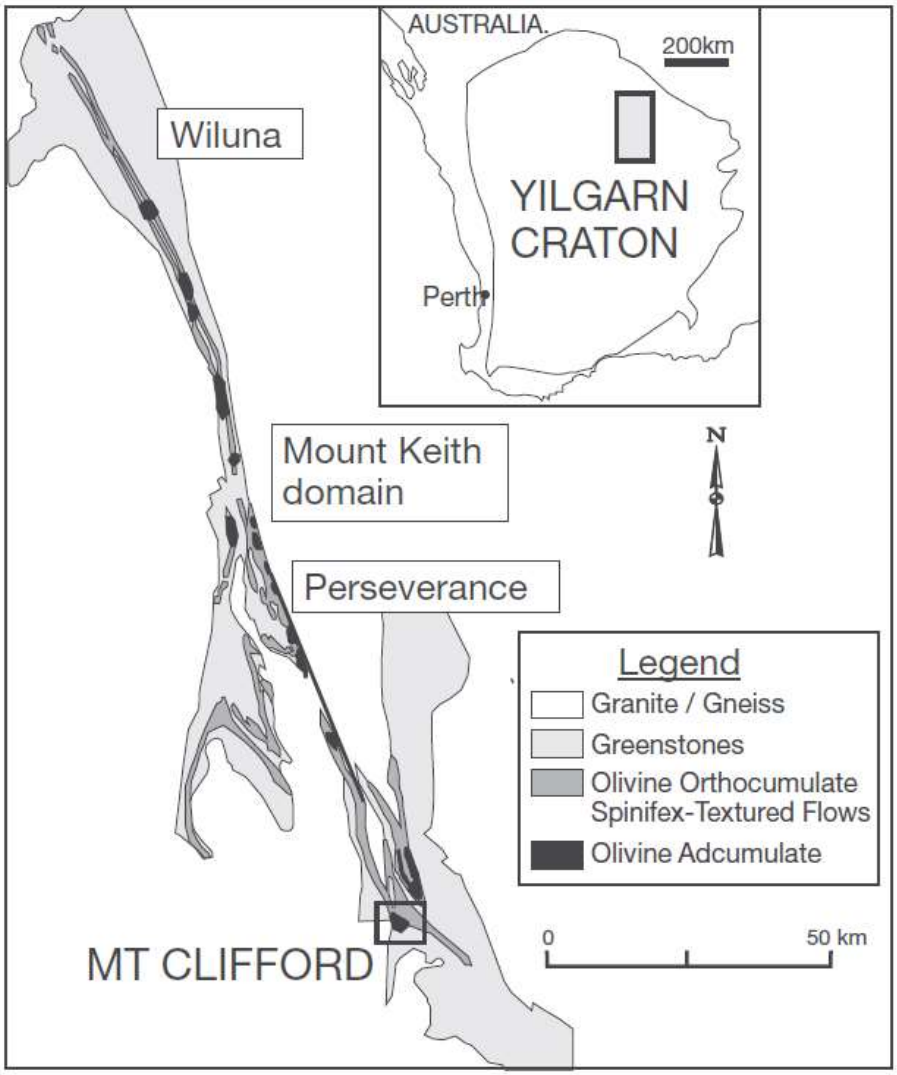

Figure 2 - Map of Agnew-Wiluna belt (Western Australia), showing location of Mount Clifford dunite (from Locmelis et al., 2009)

The Mount Clifford dunite body is located in the southern part of the Agnew-Wiluna greenstone belt (Fig. 2), in Western Australia.

The stratigraphy of the Mount Clifford dunite body (Fig. 3) is well described by Donaldson (1982), Donaldson et al. (1986), and Hill et al. (1990). The base of the dunite body is defined by an altered, chilled margin in contact with a metasedimentary rock that overlies the tholeiitic footwall. The chilled margin is overlain by an approximately 70 m-thick layer of olivine orthocumulates and olivine-clinopyroxene cumulates. This layer is overlain by a 1,000 m-thick olivine adcumulate unit, which is intersected by a thin, magnesian-augite pyroxenite layer. Above the olivine adcumulate body, a thin sequence exists that contains coarse grained olivine characterized by the development of harrisitic textures. The sequence is overlain by a thin olivine orthocumulate layer and another thin pyroxenite

layer. On top of the pyroxenite layer, an approximately 100 m-thick layered gabbro occurs, with a fine-grained and locally clinopyroxene spinifex–textured upper chilled zone. The gabbroic unit is overlain by a komatiite sequence that contains a laterally restricted, 150 m-thick unit composed of chevron-textured olivine orthocumulates with irregular intervals of harrisite and olivine spinifex. This unit is interpreted as a compound komatiite flow and hosts a zone of nickel sulfide mineralization called the Marriott's nickel prospect (Hudson and Travis, 1981). The Marriott's flow is overlain by a sequence of spinifex-textured flows and intercalated shales (Locmelis et al., 2009).

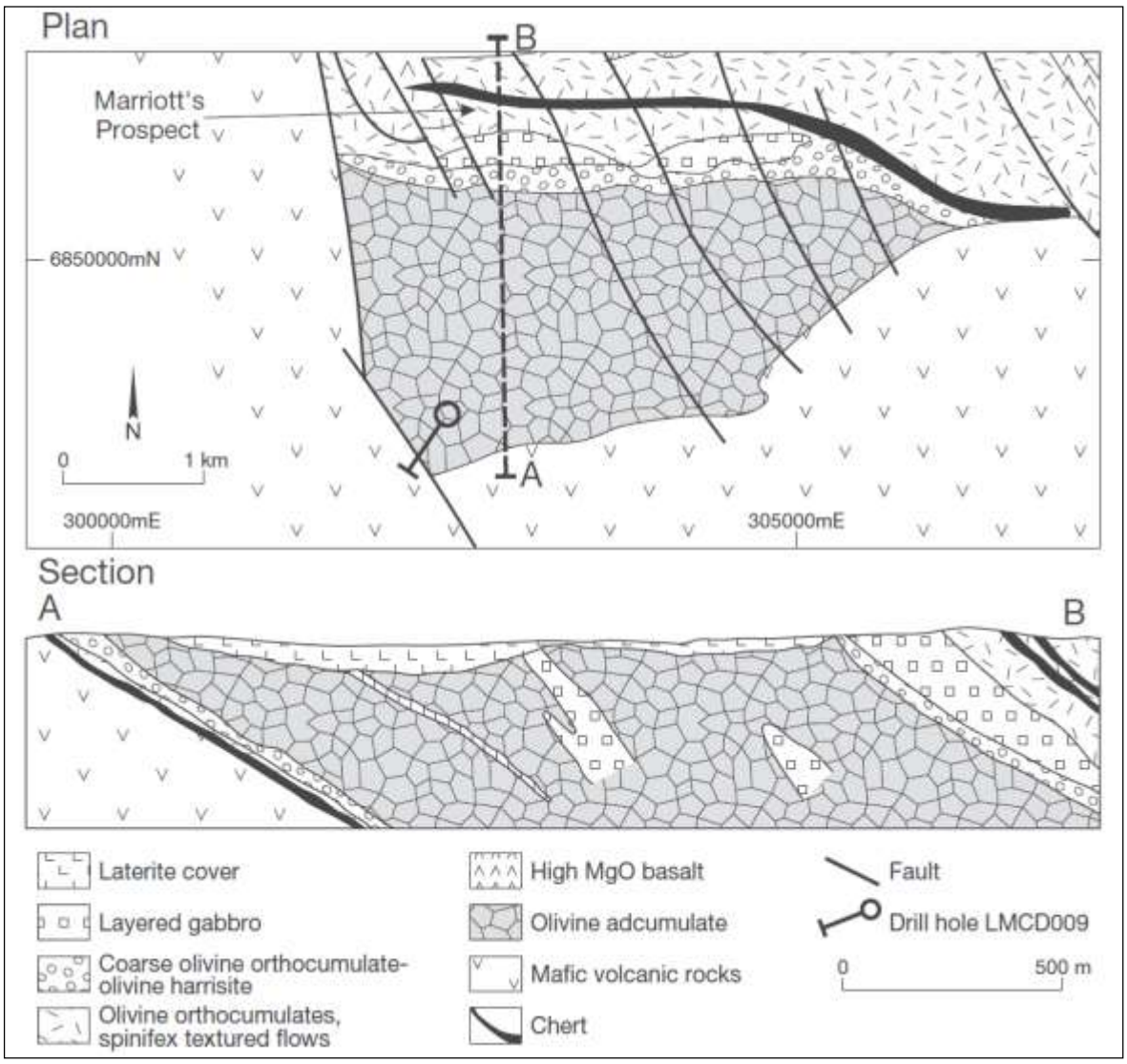

Figure 3 - Detailed map and idealized section of the Mount Clifford Dunite (from Locmelis et al., 2009)

At Mount Clifford ca. 5–10% modal primary oikocrystic amphiboles are concentrated in the stratigraphically lower part of the dunite body (olivine-clinopyroxene cumulates). Pargasite, Mg-hastingsite and kaersutite amphiboles are generally contained in mesocumulate- and adcumulate-textured rocks (Fiorentini et al., 2012).

In sample 85437 primary phases are deeply substituted by secondary minerals as serpentine, chlorite and tremolite-actinolite. The brown amphibole (20-25 vol.%) has poikilitic texture, with inclusions of primary minerals completely substituted by secondary minerals. Locally, amphibole changes from brown to colourless. Clinopyroxene (50-60 vol.%) is present as relict oikocrysts (≤2 mm) rimmed by brown amphibole. Pyroxene shows rounded inclusions of other phases (completely substituted by alteration products) and round spinels. Along the crystallographic planes of amphibole exolution lamellae of Fe-oxides are found. Accessories phases are Cr spinel, secondary magnetite along the rim of the spinel or in the fracture of altered silicates, and pyrite (disseminated among silicates).

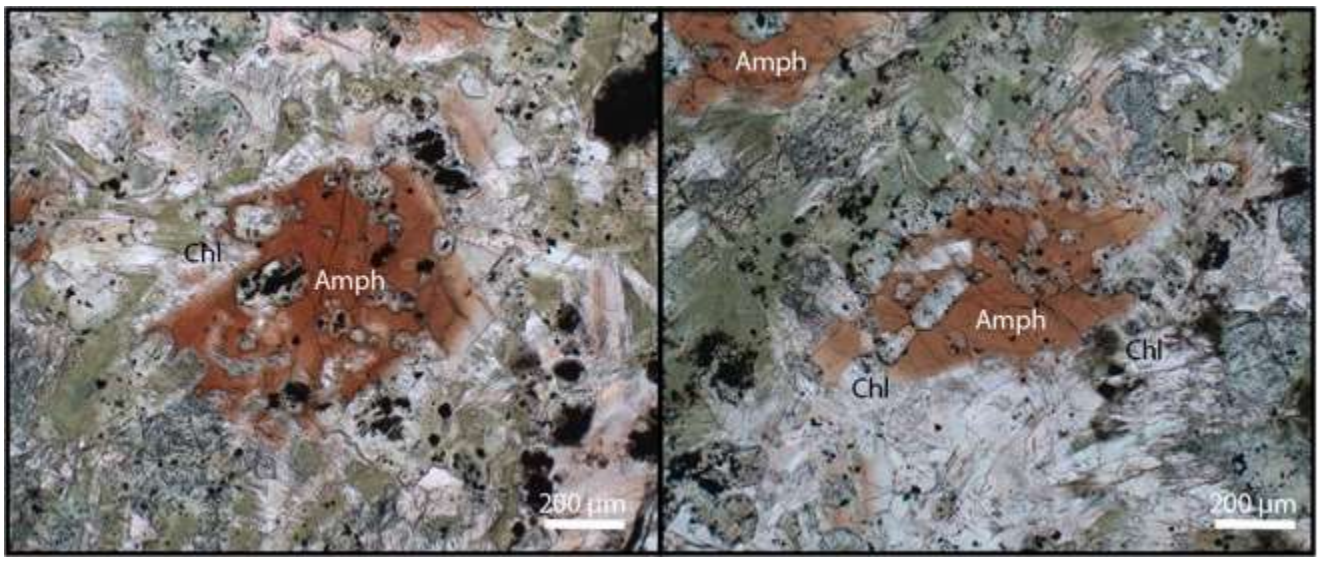

Figure 4 - Photomicrographs of polished thin section (85437) displaying varying textures between primary hydromagmatic amphiboles (Amph) and secondary alteration phases (Chl).

2.1.2 Mount Keith

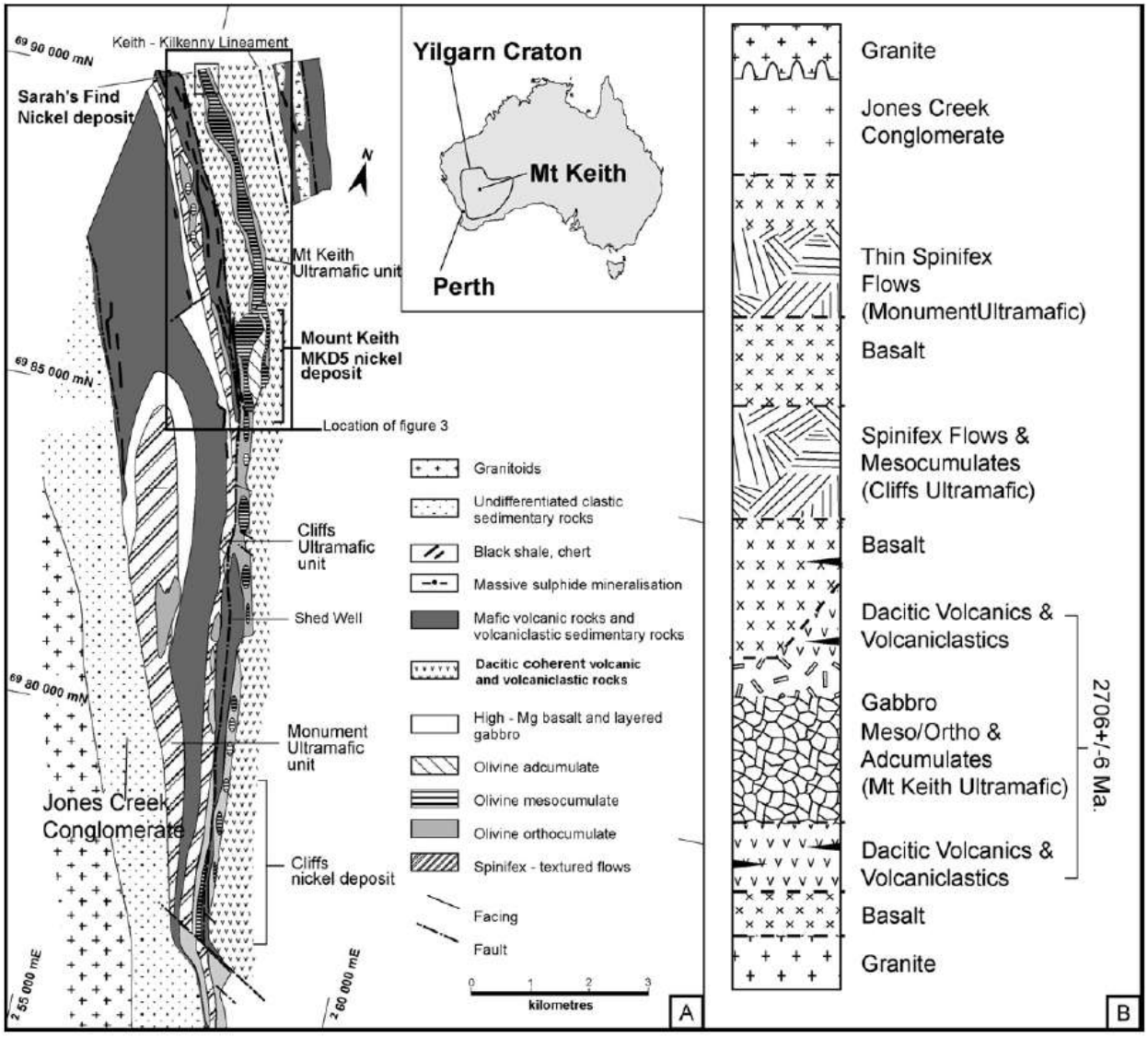

Figure 5 A, B – In Fig. (A) is illustrated the regional geology of the Mt Keith region and the distribution of felsic, mafic and ultramafic units (from Rosengren et al., 2008). (B) Stratigraphy of the Agnew-Wiluna Belt in the Mt Keith Region. Sedimentary units such as black shale and chert are indicated by black wedges within dacite and basalt sequence (from Rosengren et al., 2008).

Many of the komatiite units in the Mount Keith area consist almost of a variety of cumulate lithologies and are hence termed cumulate units. Although the Mount Keith region has undergone greenschist facies metamorphism, igneous textures are commonly preserved. Elongate cord-shaped zones of thickening within cumulate units are common and these thickened portions are characterized by more magnesian rocks (olivine meso- to adcumulate rocks) than the flanking sequences (dominated by olivine orthocumulate rocks). These thickened portions are interpreted as positions of focused fluid flow (Hill et al., 1990, 1995; Barnes, 2006), either as lava in a tube-fed flow complex or as magma in a subvolcanic sill, and are referred to as “pathways” (Barnes, 2006). In portions of a typical komatiite flow

unit spinifex textures may be either well preserved or else converted to alternating bands of tremolite-chlorite and serpentine-tremolite-chlorite rocks (Gole et al., 1989; Hill et al., 1990). Variably sulfidic shale-like and cherty metasedimentary horizons may be intercalated with these magmatic units. Together they are described as sequences of thin komatiite flow units, whether or not spinifex textures are preserved. The frequently sheared contacts between komatiite and country rocks, the metasomatized nature of the latter and the paucity of outcrops make it almost impossible to determine whether or not the contacts of cumulate units are intrusive or extrusive (e.g., Trofimovs, 2003).

Mount Keith ultramafic unit

The Mount Keith ultramafic unit (MKU; Fig. 5 A) extends over a strike length of more than 36 km, extending south into the Yakabindie area and possibly north to Albion Downs and beyond. The Mount Keith ultramafic unit faces and dips steeply to the west and wraps around a synclinal fold closure (hinge plunging gently south) in the Palm Well area. It is hosted by Mount Keith Dacite (Fig. 5 A and B) and lies east of the Hanging Wall shear zone. The Mount Keith ultramafic unit is dominated by highly magnesian, olivine-cumulate lithologies. It is made up of a series of lenticular tectonic slices, separated from one another by apparent sinistral displacement on N-trending, steeply W-dipping faults. From north to south these are the Mount Keith, Golgotha, Cerberus, Spinifex Park, Fortuna, and Betheno slices. The Mount Keith unit as a whole has been described previously by Dowling and Hill (1990, 1993) and Hill et al. (1990, 1995), while Burt and Sheppy (1975), Fiorentini et al. (2007), and Rosengren et al. (2007) described the internal stratigraphy of the unit in the immediate vicinity of the MKD5 mine area, exploiting a world-class nickel deposit in the Mount Keith slice. Lenticular pods of olivine adcumulate rock are mantled and linked by thinner sequences of olivine meso- to orthocumulate rock. Fractionated sequences of interlayered gabbro and pyroxenite occur at the top of the Mount Keith ultramafic unit in the Mount Keith, Spinifex Park, Fortuna, and Betheno slices but not in the Cerberus or Golgotha slices. Profiles through portions of the Mount Keith ultramafic unit that are capped by fractionated sequences show marked similarities with Fred's Flow at Munro Township (Arndt et al., 1977) but with the addition of an adcumulate core to the olivine orthocumulate basal portion. Forsterite contents, estimated from fresh, unmineralized olivine adcumulate rocks from all slices, typically range from 92 to 94%, in keeping with the estimates of Dowling and Hill (1990) and Barnes et al. (2011, 2012a) and similar to those reported from Fred's Flow (Arndt et al., 1977). The chilled upper margin of the Mount Keith ultramafic unit varies in composition in a predictable way, depending upon the internal stratigraphy of the unit: fractionated sequences are overlain by basaltic to basaltic-andesite chilled margins, whereas olivine orthocumulate rocks are overlain by ultramafic chilled margins, as observed by Gole et al. (2013, at the Mount Keith MKD5 mine area) and by Perring (2015b). Furthermore, pyroxene and olivine spinifex-

textured rocks are reported from the upper margin of the Mount Keith slice near the northwest wall of the Mount Keith pit (Gole et al., 2013). Spinifex textures are rarely preserved at the upper contact of the Spinifex Park slice, above the fractionated zone (Duggan et al., 2008). For Perring (2015b), these observations support an extrusive rather than an intrusive origin for the Mount Keith ultramafic unit, although the interpretation is still open to debate. Work undertaken as part of the study by Rosengren et al. (2005) has revealed previously undocumented contact relationships between the MKU and the stratigraphic dacitic hangingwall. The relationships displayed at the upper contacts are indicative of an intrusive relationship between the MKU and the enclosing dacite. These relationships, coupled with the lack of definitive extrusive features such as spinifex and flow-top breccias (Rosengren 2004), indicate that the MKU has an intrusive origin (Rosengren et al., 2008).

Although the Mount Keith ultramafic unit as a whole dips steeply to the west, the attitude of the igneous layering within the unit is quite variable and may be discordant to one or both contacts; most contacts are areas of high ductile strain, but some portions are clearly faulted.

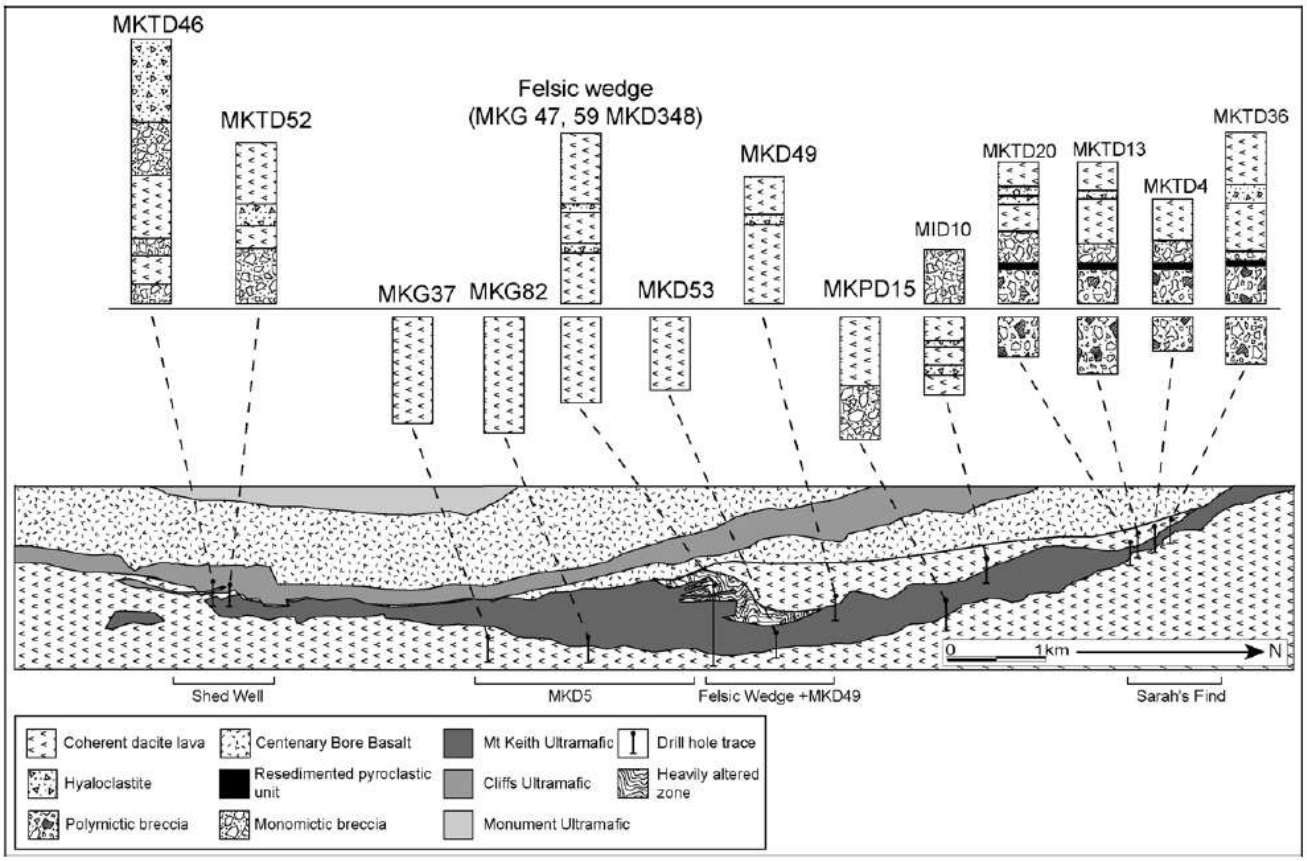

Figure 6 - Local geology in the Mt Keith region illustrating simplified geology and distribution of drill holes (from Rasengren et al., 2008).

As shown in Fig. 6, the MT Keith area were interested by extended drilling by the WMC Resources Ltd that had provided facies information within the felsic succession (Rosengren et al., 2008).

A thin (<5 m) metasedimentary unit (made of sulfidic chert and shale) separates the lower cumulate unit from an overlying sequence of three to four texturally differentiated and occasionally fractionated komatiite flow units at Spinifex Park, while a thin dacitic horizon is developed in the same stratigraphic position at Fortuna. Low MgO komatiitic rocks also occur immediately above the Mount Keith slice at Palm Well. The drilling density is low, but the stratigraphic relationship appears similar to the cumulate unit–thin-flow unit pairings seen at Leinster (Perring, 2015a) and the thin-flow units could be interpreted as sequences of break-out flows originating from ruptured pathways in the underlying cumulate unit at times of high lava flux (Dann, 2001; Houlé et al., 2009). However, as with the intrusive versus extrusive debate on the origin of the cumulate-rich komatiite units, the degree of structural and metamorphic overprinting in the Mount Keith region precludes an unequivocal interpretation.

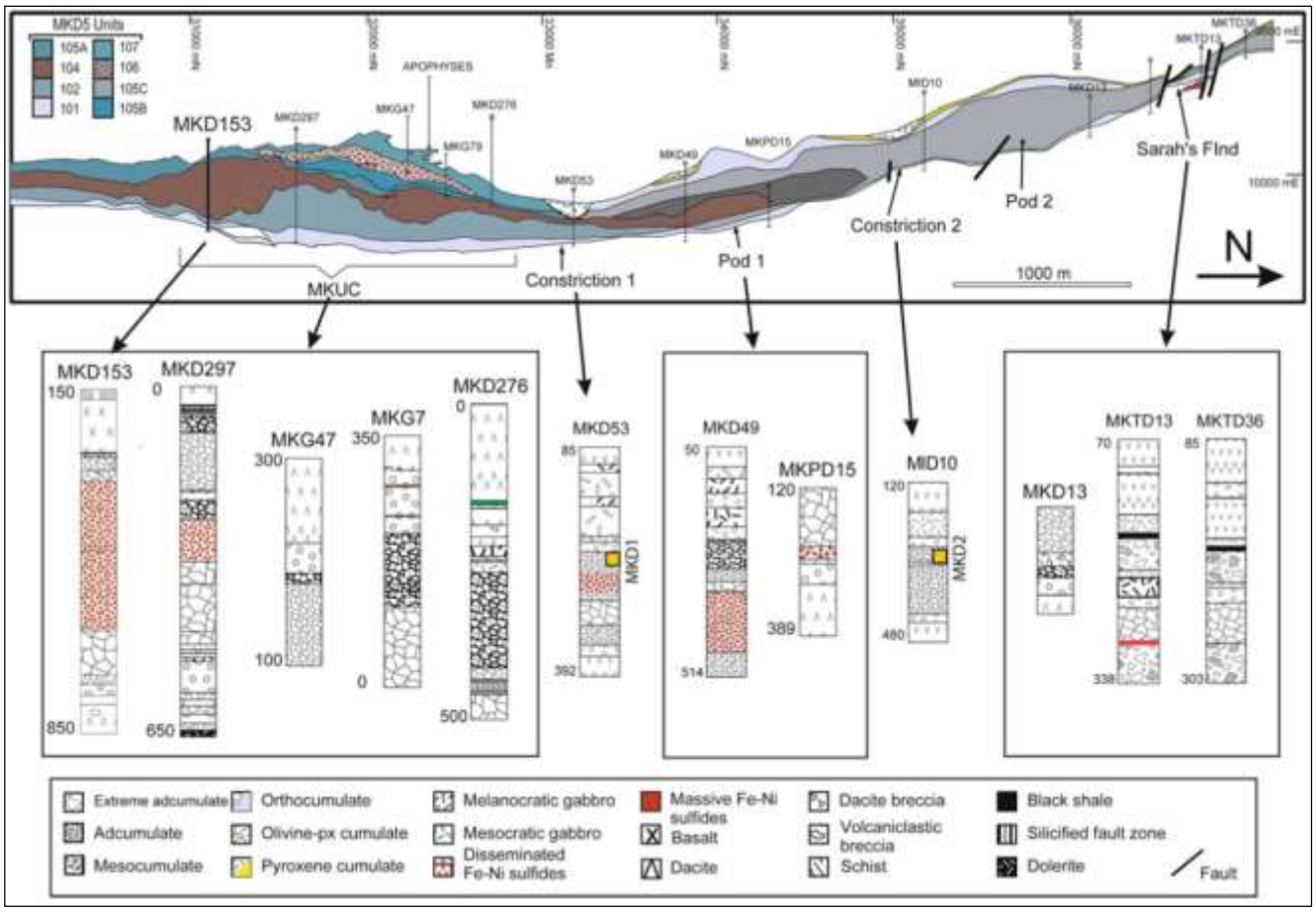

Figure 7 – Stratigraphy of the Mount Keith units and location of sample MKD1 in Unit 104 is shown (from Fiorentini et al., 2012).

The sequence at the Mount Keith MKD5 deposit is better known because of the exploitation of the nickel mineralization. The MKD5 deposit probably formed more proximal to an intrarift spreading center; several authors have interpreted the association of thick, olivine adcumulate-rich komatiitic sequences, dacitic volcanic and volcaniclastic rocks and exhalative iron sulfide horizons as indicative of

the rift axis position (Barnes et al., 2007; Beresford et al., 2009; Barnes and Fiorentini, 2012; Fiorentini et al., 2012). In the case of MKD5, the vent may have been located where the spreading center was intersected by a transform fault with lava flowing downslope, away from the spreading center and parallel to the transform fault, before cascading into a half graben and flowing parallel to the spreading center (Perring, 2015b).

As described by Fiorentini et al. (2012), at Mount Keith ca. 5–10% modal primary oikocrystic amphiboles are concentrated in the stratigraphically lower MKU cumulates associated with the thinnest parts of the belt (according to Fiorentini et al., 2007a), which are located to the north of the MKD5 nickel deposit (Fig. 7). Hydromagmatic amphibole grains of Mg-hastingsite, pargasite and kaersutite are generally contained in mesocumulate- and adcumulate-textured rocks of Units 101, 102 and 104 (Fig. 7; Rosengren et al., 2007; Fiorentini et al., 2012). At Mount Keith, volatile-bearing phases are also contained in differentiated gabbroic and pyroxenitic units (Units 105A and 105B, Rosengren et al., 2007; Fiorentini et al., 2012). Specifically, the amphibole-bearing sample (MKD1) was collected by Fiorentini et al. (2012) from drill core MKD49, in the 104 Unit (Fig. 7). The Unit is a part of the komatiite sequence of the MKU emplaced into dacite.

In the sample MKD1, the primary phases are mostly replaced by alteration minerals as serpentine, tremolite-actinolite and secondary magnetite. Olivine (30 vol.%) and pyroxene (40 vol.%) constitute the primary assemblage. The brown amphibole is present as poikilitic crystals (10-15 vol.%) and shows inclusions of the primary assemblage completely replaced by alteration phases. Amphibole is common associated with altered and colourless pyroxene oikocrysts. The latter shows typical texture with sub-parallel crystallographic planes with amphibole at the margin of the oikocryst. The volume of clinopyroxene is approximately 30-40%. The inclusions (20-25 vol.%) into the brown amphibole and pyroxene have elongated-rounded texture, completely substituted by alteration phases as serpentine, chlorite, tremolite-actinolite. The mica is present, associated to brown amphibole, as brown-pleochroic lamellae (~3 vol.%). The other phases are Cr spinel (<1 vol.%) and secondary magnetite (≤2 vol.%). The latter is present as rounded aggregates interstitial to the silicates.

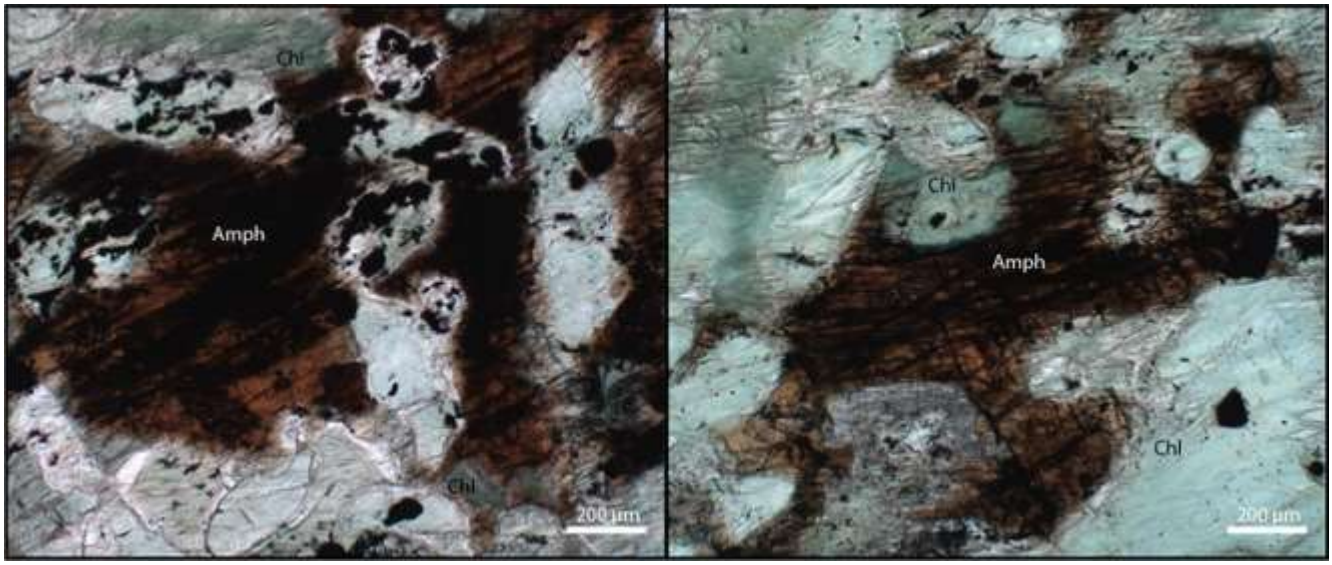

Figure 8 - Photomicrographs of polished thin section (MKD 1) displaying different textures between primary hydromagmatic amphiboles (Amph) and secondary alteration phases (Chl).

2.2 Abitibi greenstone belt (Ontario - Canada)

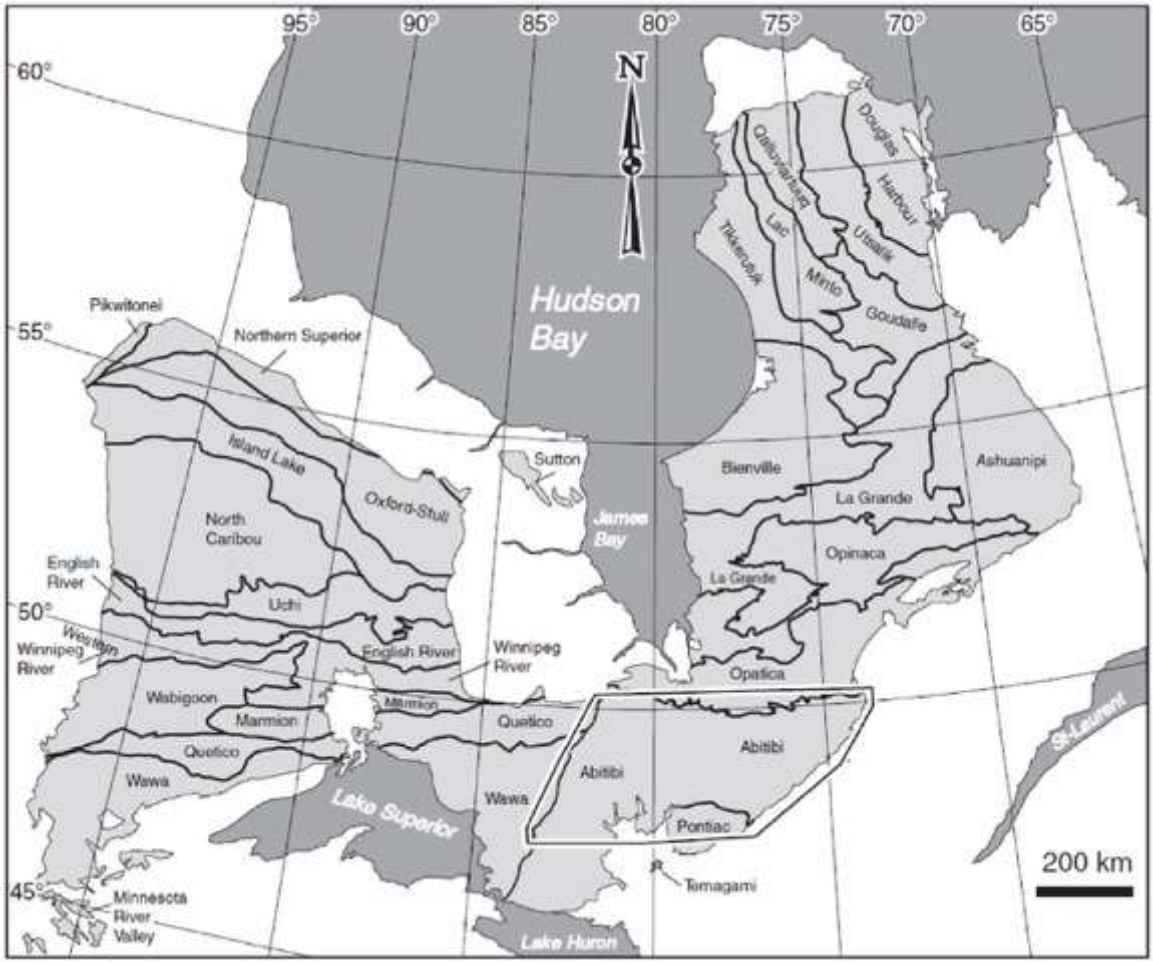

Figure 9 - Location of the Abitibi greenstone belt within the Superior province (from Thurston et al., 2008).

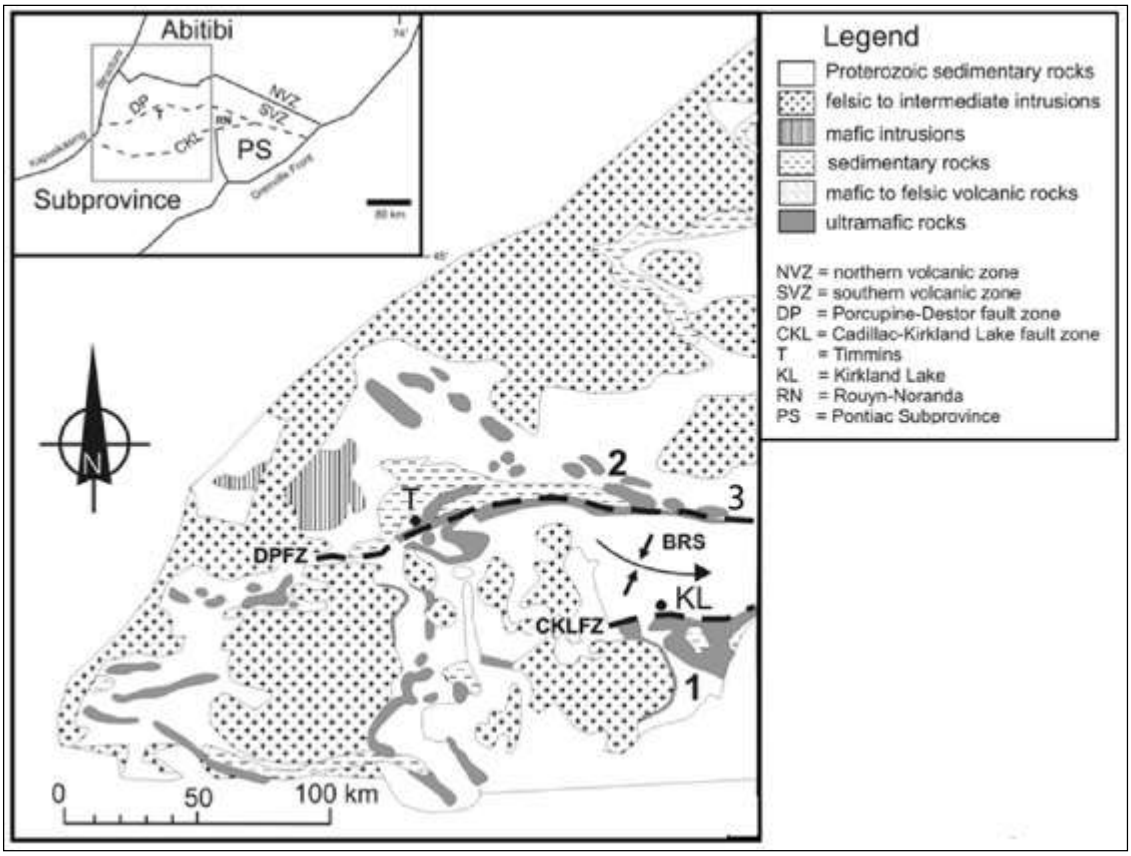

Figure 10 – Geological map of the Abitibi greenstone belt within the Ontario, Canada (modified from Stone et al., 2005).

The Abitibi greenstone belt is located in Ontario, Eastern Canada (Fig. 9), and is part of the Superior craton. It is approximately 800 km long and 240 km wide and is made up by a sequence of volcanic, sedimentary and intrusive rocks (Fig. 10). The belt is cut by swarms of Matachewan dikes. In the southern part of the Kirkland Lake area, the Archean rocks are overlain by Proterozoic sedimentary rocks of the Cobalt Group. In the Kirkland Lake area, the Archean rocks are preserved in a synclinal structure located between the Lake Abititbi Batholith and the Round Lake Batholith. The axis of the synclinal occurs midway between the two batholiths and sinks to the east (Jensen and Langford, 1985). The northern and southern limbs of the synclinal structure are cut by two fault zones developed to the E: the Destor-Porcupine Fault Zone and the Kirkland Lake-Larder Lake Fault Zone, respectively. The Archean rocks of the area have been affected by greenschist regional metamorphism. The volcanic rocks of the Abitibi greenstone belt were formed during cycles of volcanism associated with sedimentation and plutonism. Each cycle consisting of komatiitic volcanism followed by tholeiitic, calc-alkalic and alkali volcanism (Jensen et al., 1979). The older volcanic cycle rocks are confined in the outer part of the synclinal structure, near the Lake Abitibi and Round Lake batholiths. These rocks are referred to the Lower Supergroup whereas the rocks of younger volcanic cycle form most of the synclinal structure and are assigned to the Upper Supergroup. The Lower Supergroup contains a cycle of komatiitic, tholeiitic and calc-alkalic volcanics rocks: another stock of calc-alkalic volcanic rocks is present below this cycle,

suggesting that an even older volcanic cycle was developed in the area (Jensen and Langford, 1985). As the Lower Supergroup, the Upper Supergroup is made up by a cycle of komatiitic, tholeiitic and calc-alkalic volcanic rocks (Jensen and Langford, 1985).

2.2.1 Boston Creek

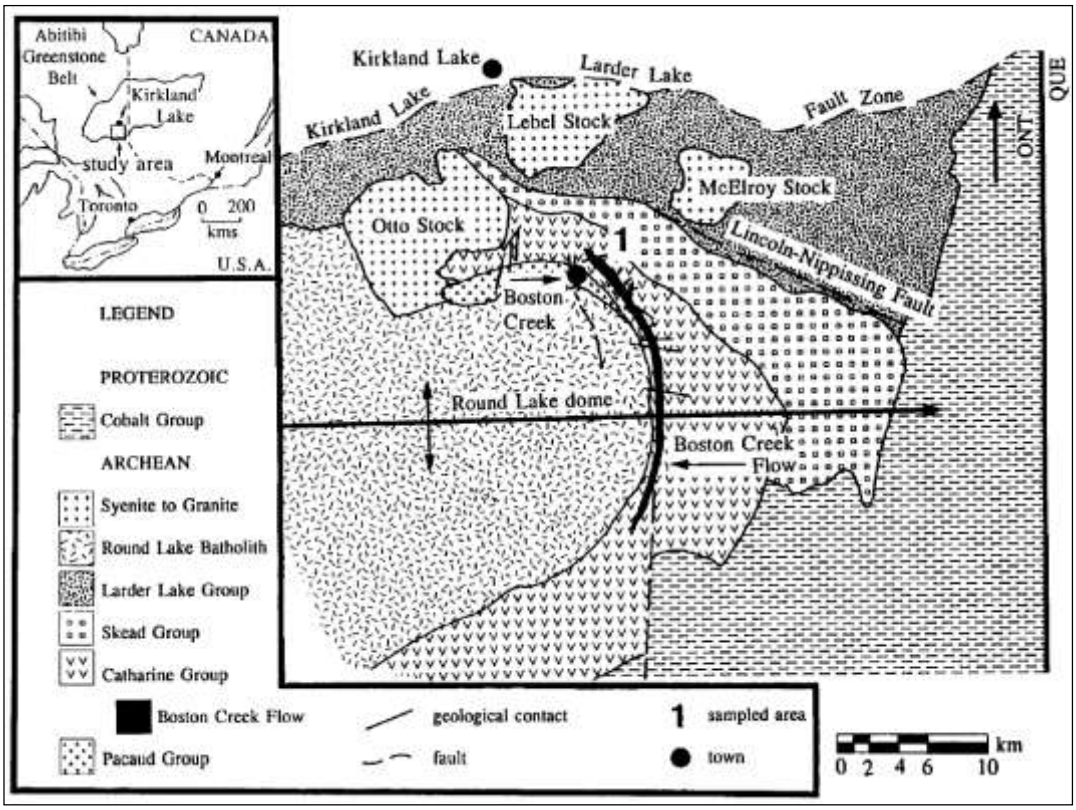

Figure 11 - Regional-scale map of the Round Lake dome area, Abitibi greenstone belt, Ontario, showing the geologic setting of the Boston Creek flow (from Stone et at., 1995) and the sample location.

The Boston Creek flow (2720±2 Ma; Corfu and Noble, 1992) crops out in the SE part of the Abitibi greenstone belt, 16 km south of Kirkland Lake, Ontario and is part of the Lower Supergroup of the Abitibi greenstone belt. The geologic section (16 km thick) in this area consists of mafic volcanic flows, felsic pyroclastic rocks, ultramafic flows and intrusions, magnetite iron-formation, clastic sedimentary rocks, and granitoid batholiths (Jensen, 1985; Jackson and Harrap, 1989). The Boston Creek Flow occurs S of the Kirkland Lake – Larder Lake - Cadillac “Break”. The flow crops out near the base of the geologic section, in a sequence of pillowed and massive basalts (Stone et al., 1987), and is regionally metamorphosed to prehnite–pumpellyite facies and deformed and contact metamorphosed to greenschist facies during granitoid intrusion (Jolly, 1980). Despite the superimposed effects of the metamorphism and deformation, primary igneous minerals (clino-pyroxene, magnetite–ilmenite, and amphibole) and particularly textures (cumulate and spinifex) are preserved in the flow. The Boston Creek flow is up to 100-m thick, subvertically dipping, and traceable as a positive magnetic high on

aeromagnetic maps for 15 km (Larson et al., 1998). The flow has thin chill margins and is layered internally in the upward sequence olivine cumulate, clinopyroxene cumulate, gabbrodiorite, and spinifex-textured clinopyroxenite (Stone et al., 1995b). For Stone et al. (1995b) the Boston Creek Flow can be divided into five layers: basal pyroxenite, peridotite, pyroxenite, gabbro and spinifex-textured lava.

The basal pyroxenite, the lowermost layer of the sequence, is ~3.5 m thick. The 5-10 cm at the bottom of the unit consist of a dark-grey-weathering rock composed of 25% acicular amphibole crystals in a matrix of fine-grained chlorite, actinolite and opaques. The upper part of the unit is formed of a brown-weathering rock containing actinolite pseudomorphs after clinopyroxene and smaller brown Mg-hastingsite and hornblende in a very fine-grained matrix of opaques, actinolite and chlorite (Stone et al., 1987).

The peridotite layer is 31 m thick maximum; olivine grains are completely serpentinized with formation of secondary magnetite. The latter minerals form round, polyhedral, granular, tabular, or elongate pseudomorphs after olivine. The proportion of olivine decreases upwards within the peridotite unit, but the size of the grain increases from 1 mm to 3 mm in diameter (Stone et al., 1987). Well-preserved clinopyroxene is present throughout most of the peridotite layer as intercumulus grains of diopside, except for the basal part of the peridotite where they are completely replaced by tremolite and chlorite. Brown pleochroic pargasite occurs only within the upper part of the peridotite (Stone et al., 1987; 2003). Pargasite occurs as 1 mm-sized intercumulus grains, variably altered to tremolite, in places associated with small euhedral grains of titano-magnetite. Cr-spinel grains up to 1 mm in diameter occur as anhedral to euhedral opaque grains within or interstitial to olivine. The primary Cr spinels are completely altered to ferri-chromite and have rims of secondary magnetite. Matrix material of the peridotite has been altered to an assemblage of serpentine, magnetite, chlorite, carbonate, and tremolite.

The following detailed description concerns the state of art of the sequence of the Boston Creek flow (Stone et al., 1995, 2003, 2005). The peridotite-pyroxenite contact is not exposed, but it is easily delineated because the intensity of the magnetic signature of the pyroxenite is weaker. The pyroxenite (9.5 m thick) is an equigranular, fine- to medium-grained rock. A 20 cm-wide shear zone parallel to contacts of the pyroxenite is present within its basal part. The shear zone occupies the centre of an approximately 3 m-wide zone of intense amphibolitization affecting the uppermost part of the peridotite and the lower and middle part of the pyroxenite. The average grain size in the pyroxenite increases upwards. Clinopyroxene is preserved in the normative-clinopyroxene-enriched upper part of the pyroxenite unit. Hornblende (Mg-hastingsite), occurring as brown pleochroic subhedral to euhedral grains 0.5 - 1 mm in diameter, is commonly mantled or extensively replaced by actinolite, characteristically containing concentrations of microscopic rutile along cleavage planes (Stone et al.,

2003). The proportion of hornblende gradually decreases upwards through the layer such that it is present only in trace amounts in the uppermost pyroxenite. Cr-spinel altered to ferri-chromite is found only in the basal part of the layer, whereas Ti-bearing oxides are present in the basal part. However, the relative abundance of titanite aggregates in the basal part of the pyroxenite indicates that titano-magnetite was originally present with chromite in the basal pyroxenite or that the spinel was a titaniferous chromium-bearing spinel. Up section, the magnetite grains increase in size, and they are found in symplectitic intergrowths with clinopyroxene. Titaniferous blebs are in some places present in the magnetite. The interstitial groundmass of the pyroxenite consists of plagioclase, chlorite, acintolite, and opaques. Plagioclase grains, which represent only a small proportion of the rock, are fine-grained, untwinned, and composed of albite.

The contact between the pyroxenite and gabbro layers is marked by a sudden increase in proportion of plagioclase, an abrupt change in weathering colour from brown to dark green, and a prominent increase in both grain size and magnetic intensity. Two kinds of gabbro are recognized. The more abundant is melanocratic, clinopyroxene rich, equigranular to slightly pyroxene porphyritic, and medium to coarse-grained. The other is a mesocratic, relatively plagioclase-rich, medium-grained rock that occurs in the melanogabbro as metre-scale patches. The thickness of the gabbro is approximately 15 m. The gabbro is the least-altered rock layer of the Boston Creek Flow, and clinopyroxene grains 1-10 mm in diameter are commonly well preserved, although grain margins are invariably amphibolitized. The clinopyroxene grains are subhedral to euhedral and sometimes twinned, although only rarely zoned, and have compositions generally in the salite field and less commonly in the augite field. Clinopyroxene grains in the mesogabbro, which is in general more altered than the melanogabbro, are largely replaced by actinolite and sometimes also by fan-shaped aggregates of stilpnomelane. Plagioclase occurs as subhedral and commonly twinned cumulate, intercumulate, and fine-grained groundmass material. Grain size ranges from <0.5 to >3 mm across. The proportion of plagioclase, like that of clinopyroxene, is variable throughout the gabbro. Titanomagnetite is a common and prominent mineral phase in the gabbro, particularly in the melanogabbro, 0.5-1 mm across and as tree- and bug-shaped forms, symplectically intergrown with clinopyroxene grains. Some titanomagnetite grains contain ilmenite lamellae or blebs in the form of trellis texture. The rims and cores of titanomagnetite grains are commonly corroded and apparently replaced by actinolite, epidote, carbonate, and titanite. Small subhedral to euhedral elongate grains of ilmenite are commonly present in association with this alteration assemblage. A mixed assemblage of fine-grained chlorite, actinolite, subhedral plagioclase, yellow pleochroic epidote, and sometimes calcite represents interstitial material. The contact between the gabbro and spinifex-textured layers is marked by the abrupt appearance of rod-shaped clinopyroxene.

Compared with the gabbro, the spinifex layer is more altered, is less magnetic, and weathers to a paler green colour. Most of the approximately 33 m thick spinifex layer consists of optically continuous amphibole pseudomorphs after sheaves of spinifex clinopyroxene 10- 100 mm long and 0.5 - 1 mm wide oriented subperpendicular to the flow top. Many grains are curved and bent. The basal 2 m of the spinifex-textured layer consists, however, of short, stubby, roughly parallel, and sometimes curved spinifex clinopyroxene grains in a plagioclase-bearing matrix, whereas the uppermost 3 m of the spinifex-textured layer consists of individual, randomly oriented, fine- to medium-grained amphibole pseudomorphs after spinifex clinopyroxene within a matrix of chlorite and amphibole. Neither olivine nor pseudomorphs after olivine are recognized in the spinifex layer. Relict clinopyroxenes are present only in the basal 10 m of the spinifex layer. They are the most strongly zoned pyroxenes of the Boston Creek Flow. Most grains and all grain margins are pseudomorphed by actinolite. Primary hornblende occurs in the basal spinifex-textured layer as rare, small, anhedral to subhedral, extensively altered grains of Mg-hastingsitic hornblende. The pseudomorphs of spinifex clinopyroxene in the uppermost 3 m of the spinifex-textured layer are stubbier and much smaller than those of the rest of the layer, and the rock appears to have a higher proportion of altered glass (now metamorphosed to chlorite) and solid pyroxene grains (now amphibole) than the bulk of the spinifex-textured layer. A few have cores of chlorite, perhaps after glass rather than pigeonite, because the chlorite of the cores is compositionally indistinguishable from chlorite in the matrix. Cr spinel within the spinifex-textured layer is also restricted to the uppermost 3 m in the form of small anhedral to subhedral grains of ferri-chromite rimmed by magnetite. Magnetite and Ti-bearing oxides occur throughout the spinifex-textured layer but are most common in the basal few metres of the layer. Many of the grains have tree- and bug-like shapes, and some display trellis-textured ilmenite lamellae. The matrix consists of variable assemblage of plagioclase, amphibole, hornblende, chlorite, epidote, carbonate, titanite, and opaques. Plagioclase occurs throughout all but the uppermost 3 m of the spinifex-textured layer. It occurs as fine-grained, rounded grains and subhedral, commonly twinned laths, variably altered to albite, epidote and amphibole. Grain size ranges from 0.1 to 1 mm and gradually decreases upwards. Patches of fine-grained chlorite intergrown with amphibole needles are possibly replacements of volcanic glass. Calcite is present throughout the spinifex-textured layer, both in the matrix and in association with clinopyroxene grains and their pseudomorphs. Calcite seems to have replaced clinopyroxene.

The rocks of the flow are enriched in iron (15–25% FeO), light-rare earth elements (LREE) and Nb–Ta relative to alumina, heavy-rare earths and Zr–Hf, and show heterogeneous magnesian contents (<2–30% MgO) (Stone et al., 1995b). Despite the fact the rocks composing the flow are LREE-enriched, the source of the flow had experienced long-term LREE depletion prior to eruption, as is evidenced by an average initial εNd of +2.6 (Stone et al., 1995a). This composition is very similar to the value of εNd

+2.2 that is the composition of De Paolo's (1981) model upper mantle at 2.7 Ga. The iron enrichment in the flow is manifested mineralogically as major amounts of magnetite (Stone et al., 1995a). Magnetite is present as two principal petrographic types: (1) lamellae intergrown with ilmenite in coarse (up to 10 mm in size), relict igneous grains (up to 20 modal%) in the interstitial areas between clinopyroxene grains within the clinopyroxene cumulate layer, spinifex-textured layer, and particularly the gabbro-diorite layer; and (2) net-, mesh- and mat-like alteration aggregates (up to 15 modal%) in and about serpentine pseudomorphs of olivine, formed as a product of olivine hydration during serpentinization (e.g., Stone et al., 1987). Magnetite intergrown with ilmenite hosts disseminated chalcopyrite and pyrite grains (≤ 1%) which, in turn, host platinum-group minerals (PGM) (Stone et al., 1992, 1993).

The Fe-picrite in sample B-5 was collected by the geologist W.E. Stone in the peridotite unit and shows cumulate texture and the cumulus phase (likely olivine, 60 vol.%) is completely serpentinized. The intercumulus phases are clinopyroxene and brown amphibole. Clinopyroxene (20 vol.%) has poikilitic texture and is well preserved in some portions of the sample, whereas in other parts is partially to completely altered. Locally, euhedral Cr spinel included into the pyroxene is observed. The brown amphibole (7 vol.%) occurs (a) as an intercumulus phase, (b) at the margin of deeply altered clinopyroxene crystals and (c) as poikilitic crystals. The contacts between clinopyroxene and brown amphibole are not well defined because the altered rims of clinopyroxene. Accessory phases are euhedral spinel (included in olivine, clinopyroxene and brown amphibole) and secondary magnetite and serpentinization-related silicates (e.g. talc, chlorite, tremolite).

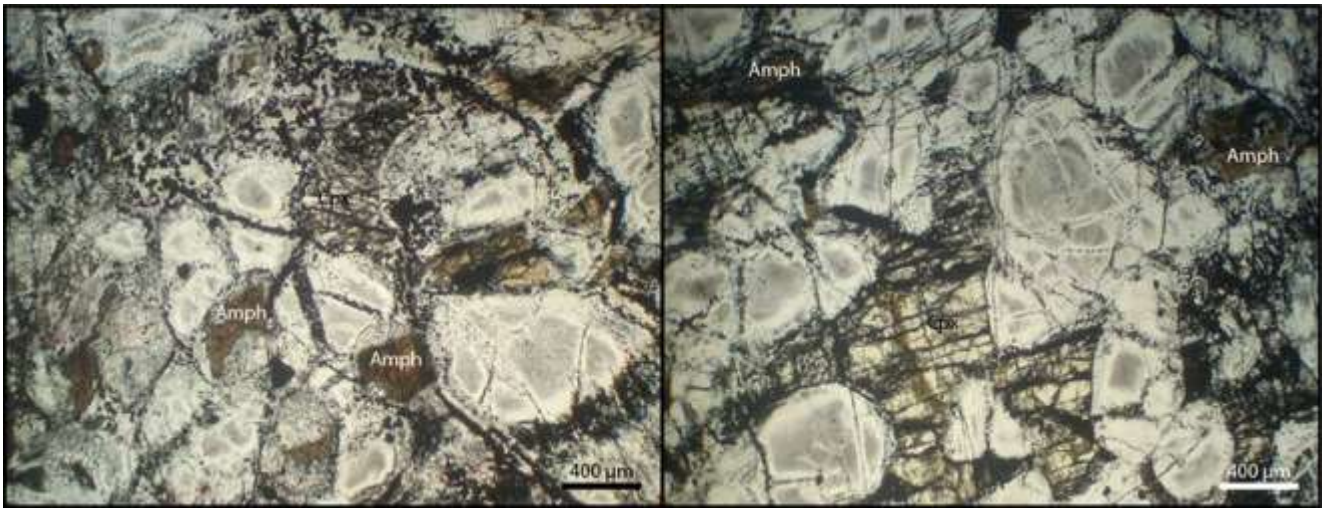

Figure 12 - Photomicrographs of polished thin section (B5) displaying different textures between primary hydromagmatic amphiboles (Amph) and clinopyroxene oikocrysts (Cpx).

2.2.2 Theo's Flow

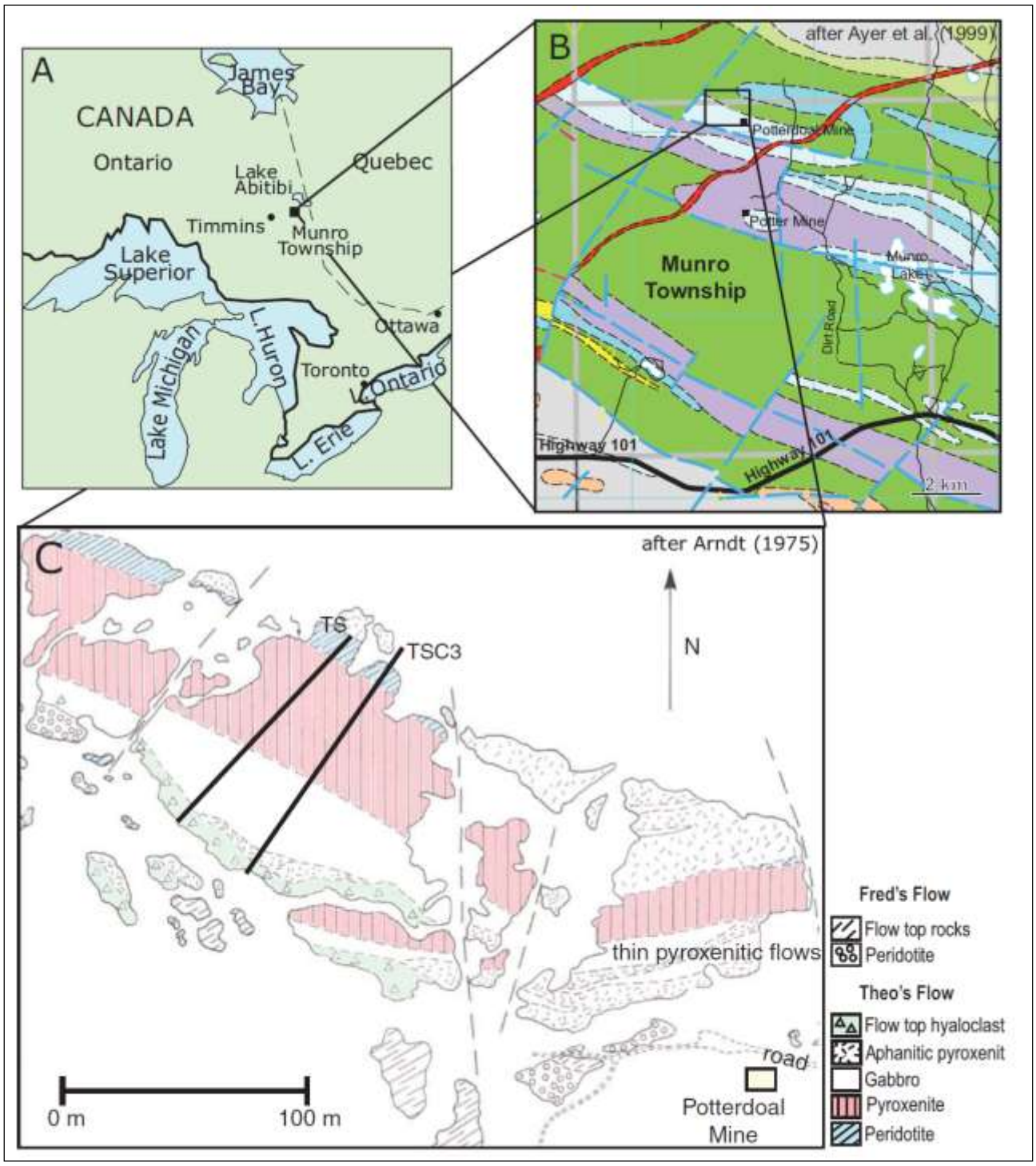

Figure 13 – In Figure are illustrate (A) the location of Munro Township in eastern Ontario, (B) the location of the Theo's Flow area within Munro Township, and (C) the generalized outcrop geology of the main Theo's Flow exposure (from Lentz et al., 2011).

Theo's Flow is part of the Archean Abitibi greenstone belt, Ontario (Figure 13 A, B; Arndt, 1975). Although the age of Theo's Flow has not been determined, nearby komatiites date from ca. 2.7 Ga (Shirey, 1997), and this is a reasonable approximation for the age of Theo's Flow. Pyroclastics,

hyaloclastics, and pillow basalts (Condie, 1981) suggest both subaerial and shallow submarine settings for the volcanics in the area (Lentz et al., 2011).

Metamorphic alteration is predominantly greenschist facies, with amphibolite facies limited to areas near felsic plutons. Theo's Flow lies in the N-central portion of Munro Township (Fig. 13 B), an area first mapped by Satterly (1951). It is part of the Lower Supergroup of the Abitibi greenstone belt.

This area is characterized by intrusive and extrusive mafic to ultramafic formations (Arndt, 1975; Johnstone, 1987), including world-famous komatiite exposures (e.g., Arndt et al., 1977; Arndt, 1977, 2008). One of these, Fred's Flow, is geographically adjacent to, and stratigraphically above Theo's Flow. Another, Pyke's Hill, is well known for spectacular examples of spinifex-textured komatiite. The type locality, and best outcrop, of Theo's Flow is an upturned (~70°) section stretching east-west for ~500 m that is bounded stratigraphically underneath by an unrelated gabbro, above by the basaltic komatiite Fred's Flow, to the east by a complex of thinner (5–25 m) pyroxenitic flows, and to the west by a fault. The relationships of the east and west boundaries make the orientation of the exposed cross section unclear, although Arndt (1975) reported that regional fabrics and flow features suggest that flow was east to west, implying the outcrop is along-flow. Metamorphic alteration was chlorite to prehnite-pumpellyite grade (Arndt, 1975; Condie, 1981), causing serpentinization of olivine, chloritization of orthopyroxene, and alteration (e.g., pseudomorphic replacement) of plagioclase and minor phases. Augites are largely unaltered, and textural relationships are well preserved throughout the unit. Theo's Flow can be divided into four distinct lithologic units: a thin basal peridotite (0–9 m), a thick pyroxenite unit (50–60 m), gabbro (35–40 m), and a hyaloclastic, brecciated top (8–10 m). Stone et al. (1995; 2003) described and analysed hydromagmatic amphibole from samples deriving from the upper part of the peridotitic unit at Munro Township.

The following sections are a detailed description of the Theo's Flow sequence described in the studies of Arndt (1977), Stone et al. (1995; 2003) and Lentz et al. (2011).

Peridotite (0–9 m Thick)

The true basal unit of Theo's Flow is a serpentinized peridotite. In the field, the basal contact is not obvious, marked only by a subtle change in weathering color. The peridotite contains pseudomorphically replaced olivines (equant serpentine outlined by magnetite), large (up to 2 mm-wide) poikilitic pyroxenes enclosing replaced olivine, and minor amounts (1–2 vol%) of spinel with euhedral cores and Ti-rich rims. The abundance of olivine phenocrysts is low (~30 vol%) for a peridotite, although much of the groundmass serpentine and chlorite (55 vol%) may be replaced olivine. Pyroxene in the peridotite grades from orthopyroxene in the lower half (~14 vol%, pseudomorphically chloritized) to clinopyroxene (~10 vol%) in the upper portion of the peridotite. Brown amphibole is also present as

accessory phase (~5 vol%). The transition from peridotite to pyroxenite is characterized by alternating bands of orange (olivine-rich pyroxenite) and dark-gray (olivine-poor pyroxenite) weathering on the outcrop. Petrographically, the change is marked by a switch from intergrown augite and olivine to smaller augites with interstitial olivine. For several meters above the banded contact, ghostly subhedral pseudomorphs after olivine are present as a minor phase.

Pyroxenite (50–60 m Thick)

The pyroxenite layer is remarkably consistent texturally. Clinopyroxene occurs as euhedral to subhedral twinned grains. Interstitial plagioclase has been largely replaced by prehnite, epidote, and chlorite, pseudomorphing the plagioclase. The original plagioclase grains are inferred, thus, to be long and thin in habit, arranged in radiating sprays (as is common in nakhlites; Treiman, 2005). There are also sporadic occurrences of spinel and sulfides (pyrite and chalcopyrite). Augite abundance varies but decreases on average up section, whereas plagioclase gradually increases in abundance. In the pyroxenites, abundances of interstitial groundmass vary widely, and without obvious trend, from 16 to 30 vol%. Within the Theo's Flow pyroxenite, average grain sizes are essentially uniform (on the order of ±50 μm), although maximum grain sizes increase systematically with stratigraphic height. The augite grains of the transitional gabbro show average grain size similar to the pyroxenite. As discussed by Lentz et al. (2011), the pyroxenite also exhibits significant grain clustering, suggesting settling of grains in clumps or chains, rather than as individuals. Plagioclase grain size is also fairly constant throughout the pyroxenite, averaging 50–100 μm in width. Spinel tends to be a fine-grained matrix phase in the pyroxenite, no longer euhedral, and its abundance varies from <1 vol.% to nearly 3 vol.%.

Gabbro (35–40 m Thick)

The transition from pyroxenite to gabbro is difficult to recognize in the field because the transition is gradual and because plagioclase, the key marker of the gabbro, is extensively altered. The lower 15 m of the gabbro, the transitional gabbro, are petrographically distinct from the underlying pyroxenite and overlying gabbro proper. The change from pyroxenite to gabbro is marked by changes in size, shape, and abundance of plagioclase (i.e., its pseudomorphs). At the transition, the average width of plagioclase crystals increases sharply from around 50 μm in the uppermost pyroxenite to >150 μm in the transitional gabbro, which is larger than the cumulus augite grains. Plagioclase in the pyroxenite occurred as sprays of thin tablets, though in the gabbro, plagioclase formed tabular, equant (idiomorphic) grains. Likewise, the abundance of plagioclase increases from ~15–20 vol.% in the pyroxenite to 27 vol% in the transitional gabbro. Augite remains euhedral in the transitional gabbro, and it is basically indistinguishable from augite in the pyroxenite.

The change from transitional gabbro to typical-texture gabbro is also abrupt and marked by a sharp increase in the proportion of plagioclase and then a discontinuous increase to 38 vol.%, marking

the start of a true gabbro. The gabbro has a typical subophitic texture, marked by intergrown euhedra of plagioclase and augite. Moving upward in the section, the abundance of plagioclase increases to 52 vol.%, whereas that of augite decreases to 28 vol%. The uppermost portion of the gabbro has an ophitic texture, with plagioclase euhedra partially or completely enclosed by anhedral augite grains. Minor (<6 vol%) iron oxides occur throughout, with a skeletal cuniform texture. The oxide grains are altered, so original compositions are unknown, but X-ray elemental maps show a correlated abundance of Fe and Ti. In some occurrences, the original titanomagnetite is adorned by a lattice of ilmenite exsolved from the magnetite.

The uppermost gabbro was capped by a very coarse, nearly pegmatitic, lithology, ~3 m in thickness, that modally is a pyroxenite: 45–55 vol% clinopyroxene, 24–26 vol% plagioclase. This is likely one of several small pegmatitic lenses that Arndt (1975) noted in the area.

Hyaloclastite (8–10 m Thick)

The top layer of the flow is a rubbly, knobby breccia. Arndt (1975) described it in detail and called it a hyaloclastite, thereby implying an extrusive, submarine origin for Theo's Flow. The preponderance of altered glass and the fragmental material suggest the material was indeed the product of lava-water interactions, consistent with the theory that much of the region was covered by a shallow sea at the time of Theo's Flow formation (Condie, 1981; Lentz et al., 2011). Lentz et al. (2011) described samples that have both altered glass and crystalline fragments, sometimes juxtaposed, though the textures gradually become more crystalline with depth. However, even the crystalline areas exhibit quench textures from fine sprays to vermicular and fishbone growths of pyroxene. In the more glass-rich samples, there are small phenocrysts (0.2–0.3 mm) of pyroxene and serpentinized olivine in minor amounts (~7 vol% total), some displaying skeletal structures with axial cavities. The authors did not find a layer beneath the hyaloclastic top of similar bulk composition to the breccia but of medium grain size from more gradual cooling, as described by Arndt (1975). Such a "roof layer" would be expected to form as heat radiated from the flow's surface if a solidification front were advancing downward (Mangan and Marsh, 1992). Arndt (1975, 1977) mapped an "aphanitic pyroxenite" described as being immediately beneath the hyaloclastite, but of variable thickness. This layer could be the missing roof crust.

Samples T-2 and T-3 were collected by the geologist W.E. Stone into the peridotite layer, at 23 m upsection of flow base and 25 m upsection of basal contact, respectively.

Sample T-2 shows partially preserved cumulus texture even if the major cumulus phase, olivine, is completely serpentinized, with formation of typical secondary magnetite. Clinopyroxene is the most abundant phase,~30 vol.%, with dimension of crystals ≤ 2 mm. The textural characteristics of pyroxene

as well as its relations with the other phases are not well preserved. Locally, the original poikilitic texture can be recognised. Brown amphibole (2 vol.%) occurs in the intercumulus domain inbetween the rounded serpentinized portions of the sample. It is usually altered and weakly pleochroic. The dimensions of the amphibole crystals are < 1 mm. Accessory phases are biotite (< 1 vol.%), associated to relict phases and to opaque minerals (magnetite and pyrrhotite). Magnetite is found in sub-millimetric aggregates as product of alteration or associated to biotite. Pyrrhotite occurs as blebs at the margin of relict pyroxenes, in the "intercumulus" portion of the sample.

Sample T-3 shows cumulate texture and moderate serpentinization of the primary phases. The cumulus "phase" (40-50 vol.%) is made up by rounded aggregates of alteration-related minerals (serpentine, chlorite, tremolite-actinolite and secondary magnetite). Clinopyroxene (30-40 vol.%) is present as relict crystals with dissolved boundary or as oikocrysts with rounded inclusions of olivine. Brown amphibole (3 vol.%) occurs at the rim of clinopyroxene in sub-millimetric crystals with exolution lamellae along the crystallographic planes and locally deeply altered. The accessory phases are magnetite, zoned Cr spinel (opaque with magnetite at the rim) and sulfides. The latter are presents in fine grained string between the serpentinized minerals and in the alteration product "groundmass".

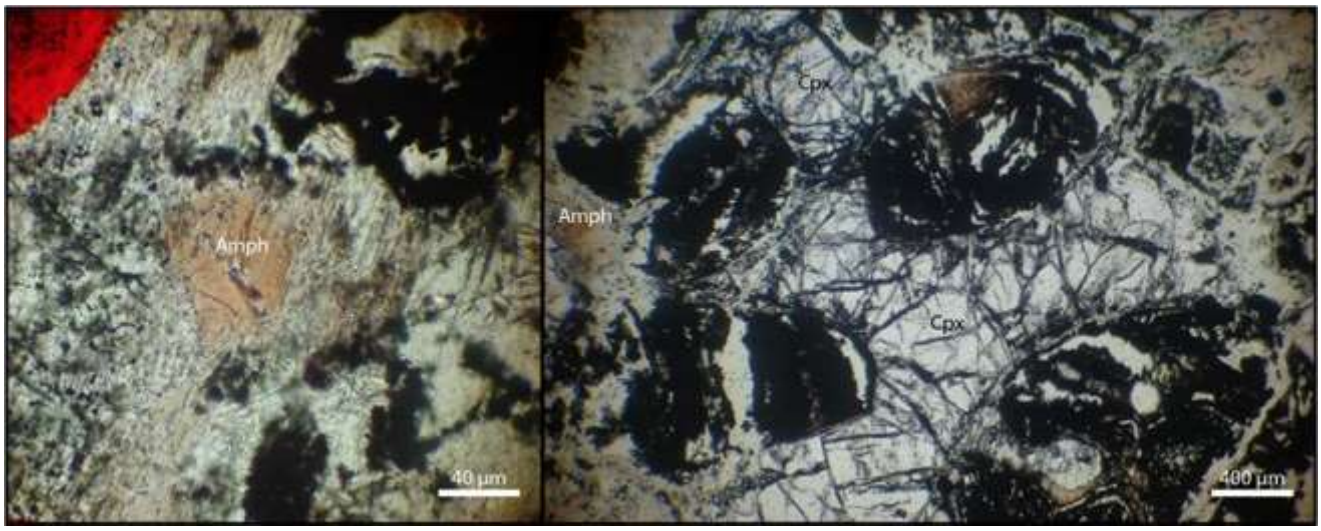

Figure 14 – Thin section view (samples T2 and T3) of the relations between amphibole (Amph) and oikocrysts of clinopyroxene (Cpx). In T2 the primary cumulus phase is completely substituted by aggregates of secondary minerals (serpentine, chlorite, tremolite-actinolite and magnetite).

2.2.3 Ghost Range

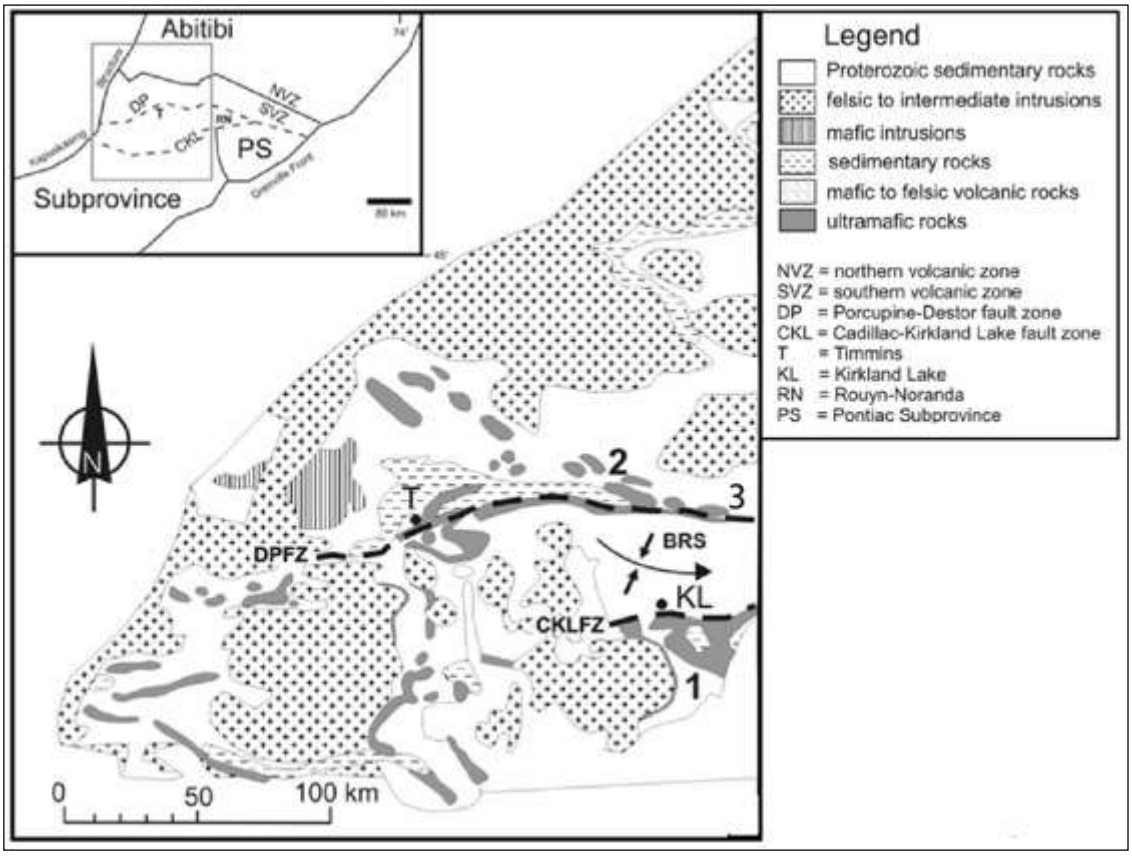

Figure 15 – Simplified geological setting of the Abitibi greenstone belt and (3) Ghost Range location (modified after Stone et al., 2005).

The Ghost Range occurs in the eastern part of the Abitibi, Ontario (Fig. 15), close to the Porcupine-Destor fault zone (Jensen and Langford, 1985). The Ghost Range was first mapped (Satterly, 1952b, 1954; MacRae, 1969) as a 760 m thick layered ultramafic to mafic sill, made up by peridotite, clinopyroxenite and gabbro, which was subsequently folded into doubly plunging syncline. Jensen and Langford (1985) interpreted the Ghost Range as the basal sequence of the Stoughton – Roquemaure Group, part of the Lower Supergroup of the Abitibi greenstone belt, and as a complex composed of thick, flat-lying lava flows resting unconformably on folded calc-alkalic volcanic rocks of the Hunter Mine Group. The Ghost Range is a 10 km long ridge and the calc-alkalic rocks of the Hunter Mine Group are exposed on all sides of the ridge.

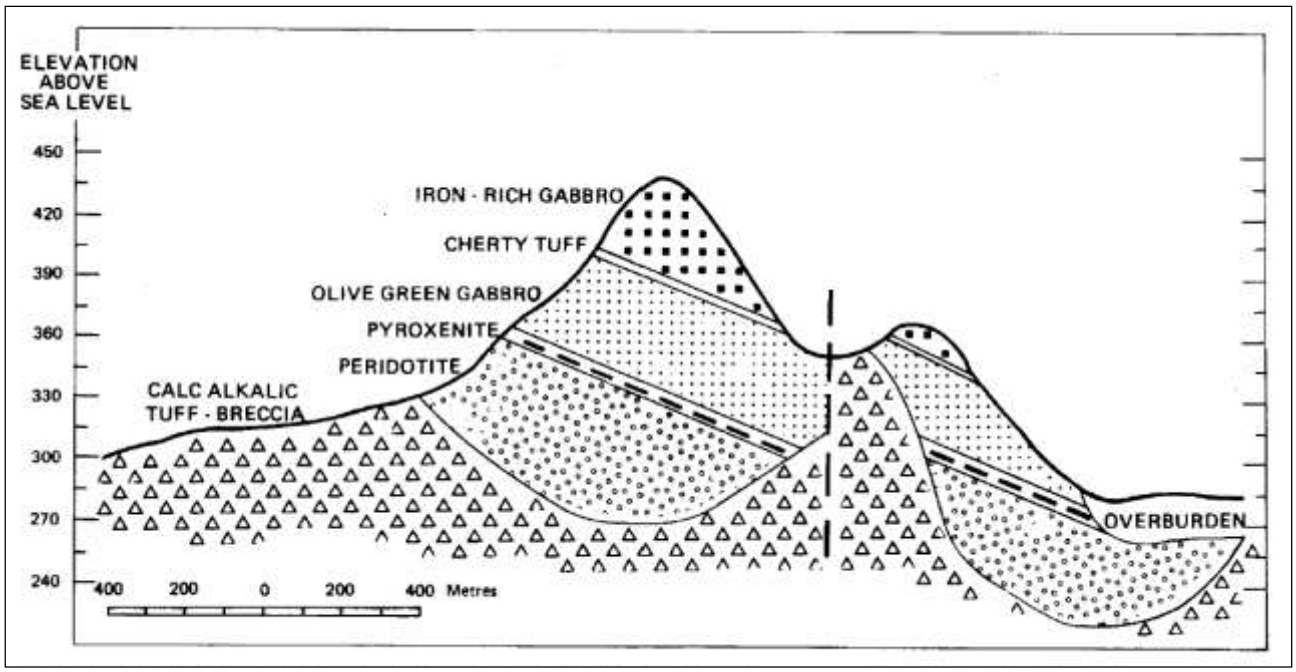

Figure 16 – Cross-section of the Ghost Range sequence (from Jensen and Langfron, 1985)

The sequence in the Ghost Range (Fig. 16), in ascending order / from bottom to top, are peridotite, clinopyroxenite, olive-green gabbro, a thin layer of cherty tuff and a dark green to black iron-rich gabbro (Jensen and Langford, 1985). For the authors, peridotites have geochemical affinity with komatiitic peridotites, whereas the clinopyroxenites and olive-green gabbros have geochemical affinity with basaltic komatiites, Mg-rich tholeiites and calc-alkalic basalts. The upper dark green to black gabbros show geochemistry affinity with iron-rich tholeiitic basalt and tholeiitic andesite. MacRae (1969) interpreted the peridotite and pyroxenite to have resulted from olivine and pyroxene crystals settling in a magma chamber.

The peridotite is up to 140 m thick and its contact with lower calc-alkalic volcanic rocks is considered to be a vertical fault contact. Sheared peridotite rests against pillowed lavas of calc-alkalic basalts (Jensen and Langford, 1985).

The clinopyroxenite is described as 2 to 6 m thick intensely sheared over a width of few cm at its lower contact with the peridotite and as having a sharp contact with the overlying gabbro (MacRae, 1969). For Jensen and Langford (1985), the lower contact does not show any sign of shearing but a gradational contact about 10 cm thick is observed. The upper contact between the pyroxenite and the gabbro is described with a slight decrease in grain size in the gabbro.

The gabbro above the pyroxenite is about 120 m-thick and shows geochemical composition from basaltic komatiite to Mg-rich tholeiitic basalt and, where the plagioclase is abundant, to calc-alkalic basalt (Jensen and Langford, 1985). The gabbro has a grain size of 2 to 3 mm and is composed of 40-60% clinopyroxene, 40-60% plagioclase and accessory serpentine and magnetite pseudomorphic after

olivine. The calc-alkalic tuff is 10 cm to 3 m-thick and separates the olive-green gabbro from the dark green to black gabbros.

The gabbroic rocks which form the upper unit above the tuff are dark green to black iron-rich rocks, with diabasic textures. These rocks are described to contain 40-50& pyroxene, 30-40% plagioclase, 2-10% quartz and 4-8% titanium-rich magnetite (Jensen and Langford, 1985). The iron-rich parts form 20 to 50 m-thick layers and comprise numerous irregular zones of pegmatitic granophyre. Fine-grained 3 to 10 m-thick layers separate the iron-rich layers. These fine-grained rocks grade upward into coarse-grained rocks and some extend for 1.5 to 3 km which indicates that they may represent either flow or intrusive contacts (Jensen and Langford, 1985). The authors did not detect chilled margins and interpreted the iron-rich gabbros as massive tabular flows of iron-rich tholeiitic basalt.

The fine-grained layers were not observed in the gabbros below the tuffs. The peridotite and the pyroxenite, as well as the olive-green gabbro, were possibly derived from the same magma: this may have represented a komatiitic lava flow in which olivine and pyroxene crystals settled. After solidification the flow was overlain by tuff and additional flows of iron-rich tholeiitic basalt (Jensen and Langford, 1985). MacRae (1969) suggested that the gabbros at Ghost Range were derived from fractionation of olivine and clinopyroxene, as illustrated by Arndt (1975) for Theo's Flow in which iron-rich gabbro can form by olivine and clinopyroxene fractionation from tholeiitic picritic magma. For Jensen and Langford (1985), the different geochemical affinity of the lower units (peridotite, clinopyroxenite and olive-green gabbro) with respect to the upper gabbroic rocks suggests a different parental magma. If the lower rocks were derived from a komatiitic magma, the flow would have had to be about 400 m thick.

The sample GR 1 was collected by the geologist W.E. Stone from the basal zone of the peridotite unit and has poikilitic/cumulate texture with its main assemblage made up by olivine, clinopyroxene and orthopyroxene. Accessory phases are brown amphibole and phlogopite. Olivine (35 vol.%) occurs as rounded crystals included into oikocrystic clinopyroxene (27 vol.%), as intercumulus crystals of ≤1 mm in diameter with exolution lamellae of ilmenite, rounded spinel and inclusions of secondary magnetite. Only local domains of olivine cores are preserved from alteration. Round spinels and brown amphibole are locally present at the margin of the clinopyroxene. Orthopyroxene is well preserved and forms oikocrysts of 2-3 mm in diameter, with inclusions of spinel. The olivine included into the orthopyroxene results appears to be more preserved and the contacts between the two phases are sharp. Brown amphibole crystallizes at the margin of clinopyroxene or as oikocrysts with diameter < 1 mm. Locally amphibole shows inclusions of spinel. When in contact with clinopyroxene, brown amphibole shows well-defined margins or, locally, a smooth transition to pyroxene.

Sample GR 2 is analogous to sample GR 1. It shows the same cumulate/poikilitic texture and the phases have the same characteristics of the sample GR 1. The only difference is a slight increase in the modal percentage of brown amphibole (7 vol.%) and decrease in that of clinopyroxene (25 vol.%).

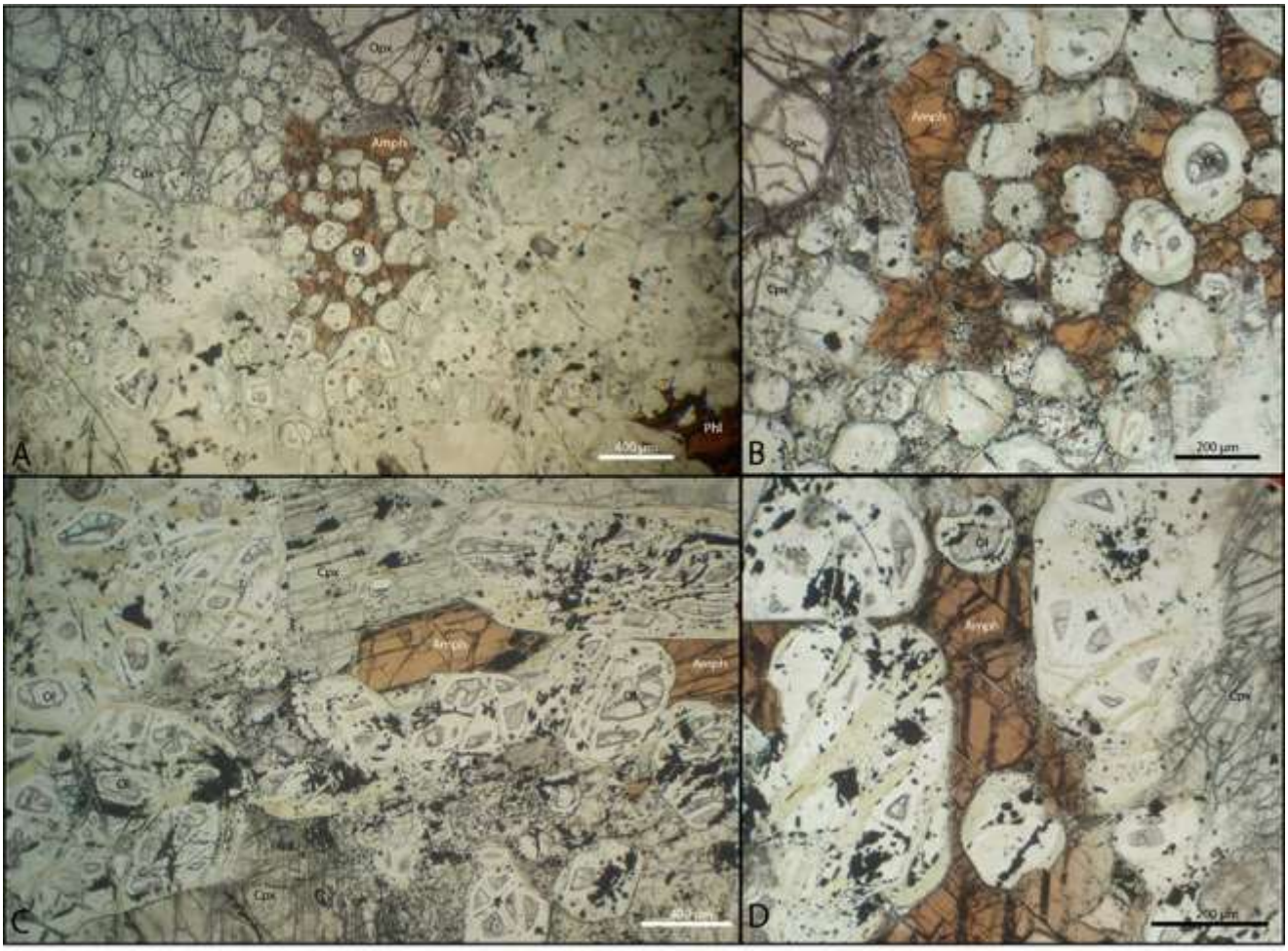

Figure 17 – Photomicrographs of polished thin sections (GR1, GR2) displaying varying textures between primary hydromagmatic amphiboles (Amph), relict olivine (Ol), clinopyroxene oikocrysts (Cpx), orthopyroxene (Opx) and brown mica (Phl). Thin sections (A) and (B) are from the sample GR1 whereas (C) and (D) show the textures of sample GR2.

2.3 Paleoproterozoic samples

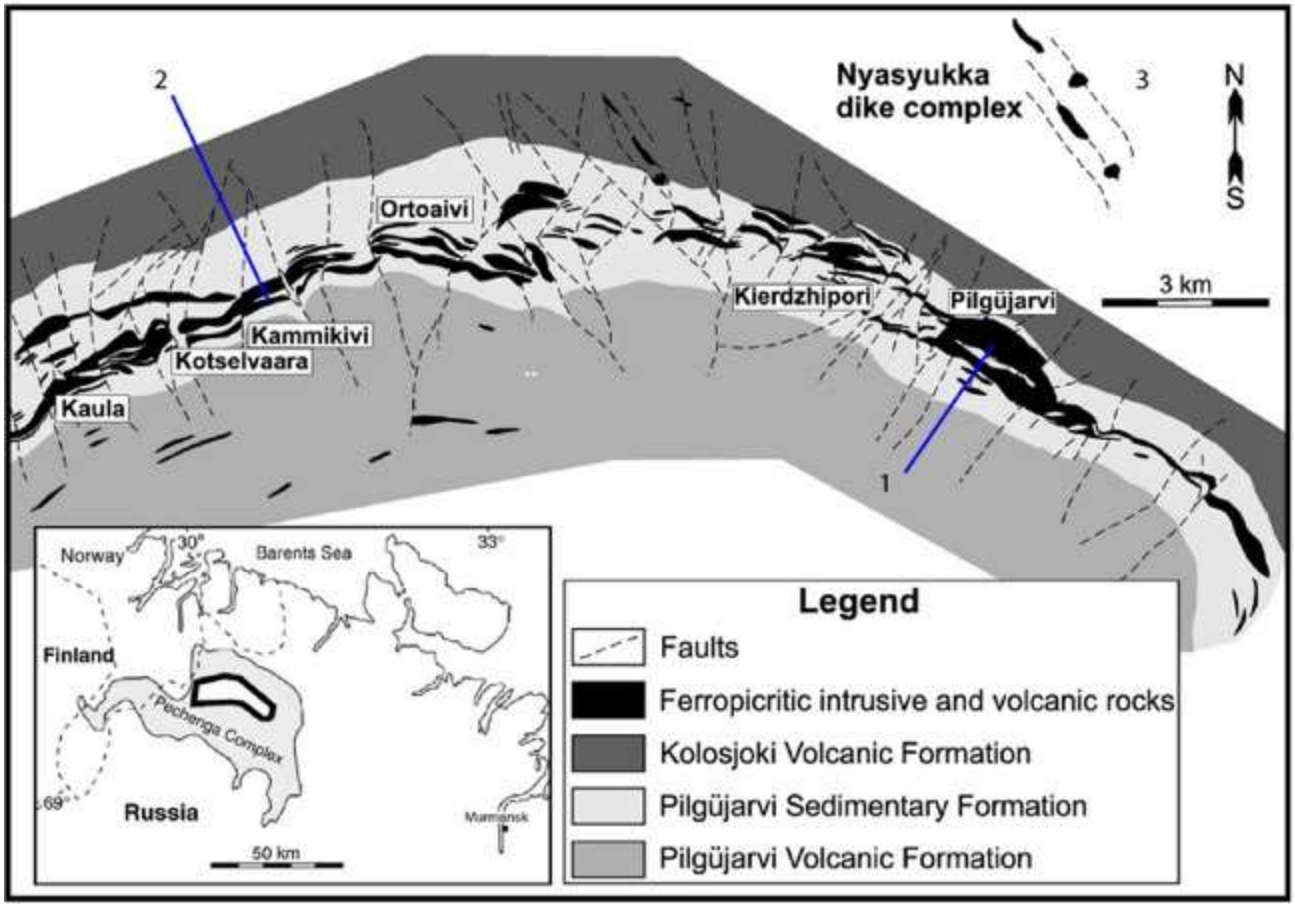

Figure 18 – Paleoproterozoic samples location and simplified geological setting of the Pechenga Complex and Nyasyukka dike complex. Samples locations (1) from Pilgüjarvi sill, (2) from Kammikivi sill and (3) from Nyasyukka dike complex (modified from Fiorentini et al., 2008).

2.3.1 Pechenga Complex (Russia)

The Pechenga Complex is part of the Pechenga – Imandra/Varzuga – Ust'Ponoy supracrustal belt, which runs in the NW–SE direction across the north-eastern part of the Fennoscandian Shield. The Paleoproterozoic volcano-sedimentary succession in the so-called Pechenga Greenstone Belt is assigned to the Petsamo Supergroup, which is divided into the North Pechenga and South Pechenga Groups (Fiorentini et al., 2008). The North Pechenga Group (more than 10 km in thickness) comprises four cycles with each having a sedimentary lower and volcanic upper part. The group is divided into eight lithostratigraphic formations of which the two uppermost are called the Pilgüjarvi Sedimentary and Volcanic Formations. The Pilgüjarvi Sedimentary Formation is a tuffaceous sedimentary unit, which comprises sulfide- and graphite-rich greywackes and shales. The unit hosts numerous nickel sulfide ores of economic interest associated with differentiated gabbro–wehrlite intrusions and sills in its central,

thickest portion. The overlying Pilgüjarvi Volcanic Formation is made up of a thick pile of tholeiitic and ferropicritic lava flows. Ten kilometers NE of the margin of the Pechenga supracrustal belt, peridotites and olivine gabbros of the Nyasyukka dyke complex form a rather heterogeneous, but geochemically consistent, NNW-trending and steeply dipping dyke swarm in the Archaean granite–gneiss basement. For Pechenga, Sm–Nd isotope data gave an age of 1980±40 Ma with an initial εNd value of +1.4±0.4. Pb–Pb isotopic analyses yielded an age of 1988±39 Ma, with an estimated μ of 7.91 (μ=238U/204Pb), consistent with derivation from mantle with little ancient upper crustal contamination (Fiorentini et al., 2008). Smolkin et al. (2003) were obtained a baddeleyite age of 1941±3 Ma for the Nyasyukka dyke complex, that is consistent with the Sm-Nd isochron age of 1956±20 and an initial εNd value of +1.4±0.4 reported by Hanski et al. (2014) report a Sm–Nd isochron age.

The magma type of these igneous bodies was termed ferropicrite because of its exceptionally high FeO content, which usually exceeds 14 wt.% (FeOtot), and high MgO content close to 15 wt.% in liquid composition (Hanski, 1992). Ferropicrites are also characterised by low Al_2O_3 and Al_2O_3/TiO_2 and relatively high TiO_2, Zr and other incompatible elements. Ferropicrites are strongly enriched in the light rare-earth elements relative to heavy rare-earth elements (HREE) and have immobile trace element characteristics similar to those of within-plate transitional or alkali basalts (Hanski and Smolkin, 1995).

Pilgujärvi Sedimentary Formation and age relationships

The Pilgujärvi Sedimentary Formation is the thickest sedimentary succession in the Pechenga Belt. It is the host unit to mafic-ultramafic intrusions containing the Pechenga sulphide Ni-Cu deposits. The formation is dominated by S- and C_{org}-bearing turbiditic greywacke-shale, ferropicritic and mafic tuffs intruded by numerous mafic and ultramafic sills. Skuf'in and Bayanova (2006) reported zircon and baddeleyite U/Pb ages of 1987 ± 5 Ma and 1980 ± 10 Ma, respectively, for the ore-bearing Pilgujärvi intrusion. On the basis of geochemistry and other isotopic signatures (Sm-Nd, Pb-Pb, Re-Os), this and other related intrusions can be regarded as co-genetic with the ferropicritic volcanism of the Pilgujärvi Sedimentary and Volcanic Formations (Hanski, 1992). This age range can also be considered as the depositional age of the Pilgujärvi Sedimentary Formation because the ferropicritic volcanism was pene-contemporaneous with these sedimentary rocks. The Pilgujärvi Sedimentary Formation is intruded by a ferropicritic vent, named the Kaula Eruptive Centre (Melezhik et al.,1994b). In the Kotselvaara open pit, the eruption centre crops out as a ca. 100 × 50 m body comprising a fragment-supported breccia with a matrix of ferropicritic lapilli tuff, which passes gradually upwards through graded lapilli tuff into ferropicritic black shale. Among the breccia fragments there are angular clasts and blocks of C-rich, phosphorus-bearing, laminated limestone (4.3 wt% P_2O_5; Melezhik et al., 1994b). All limestone fragments are characterized by low $^{13}C_{carb}$ (from −8.7 to −7.7‰; Melezhik and Fallick, 1996). The phosphatic, low-$^{13}C_{carb}$ limestones are known neither in the underlying formations of the North Pechenga

Group nor within the Pilgujärvi Sedimentary Formation hosting the eruptive breccia (Melezhik and Hanski, 2012).

Pilgujärvi Volcanic Formation

The Pilgujärvi Volcanic Formation is the thickest volcanic unit of the North Pechenga Group. It is ~3 km thick and is mafic in composition, containing pillowed and massive lava flows, hyaloclastites and pillow breccias deposited in a submarine setting. Minor rock types include ferropicritic flows and sills, felsic tuffs and fragmental deposits, and thin black shale and chert intercalations. The mafic rocks have a tholeiitic (T-)MORB-like affinity with flat chondrite-normalised REE patterns (Hanski et al., 2014). Among the tholeiitic basalts, only the uppermost (southernmost) lavas (the Suppvara Formation of Skuf'in and Theart, 2005) are more enriched in incompatible trace elements and akin to E-MORBs. The felsic tuffs, occurring as thin intercalations in the thick mafic lava pile, form a distinct marker horizon at a level of 800–1000 m from the base of the Pilgujärvi Volcanic Formation (Zagorodny et al., 1964; Predovskyet al., 1974). They were dated at ~1970 Ma by the bulk U-Pb zircon method by Hanski et al. (1990). The felsic tuffs occur in doublets and triplets separated by tholeiitic basalts within a stratigraphic interval of several tens of metres and extend several tens of kilometres along strike. Individual felsic units range in thickness from a few centimetres up to 13 metres and vary in lithology (Fiorentini et al., 2008). Most units show cyclic coarsening- or fining-upward development, with bases of massive lapilli tuff containing volcanic bombs. These gradually pass upwards through medium-grained crystalloclastic tuffs to either thinly bedded and laminated or massive, obsidian-like deposits. Individual sequences are distinguished by erosional surfaces between the cycles, intense soft-sediment deformation, well-developed current bedding, and the presence of sedimentary dykes (Melezhik et al., 1994). Geochemically, the felsic tuffs correspond to relatively iron-rich, A-type, peralkaline dacites to high-silica rhyolites (Hanski, 1992). The fragmental felsic rocks contain crystal clasts of resorbed quartz, plagioclase and K-feldspar, and rock fragments composed of vesicular, glassy shards, fine-grained, porphyritic felsic lava, holocrystalline basaltic lava, granophyre and importantly, granite and tonalitic gneiss. The gneiss fragments have undergone amphibolite facies metamorphism before incorporation into the felsic magma. The genesis of the rocks has been controversial with the proposed magmatic models including fractional crystallization (Hanski, 1992), silicate liquid immiscibility (Skuf'in, 1993), or a meteorite impact (Jones et al., 2003). Even though the bulk of the material seems to be of volcanic origin, as, for example, indicated by resorbed quartz phenocrysts, Negrutsa (1995) suggested a long-distance transport by a submarine mass-flow and deposition of clastic material on a continental slope. The same conclusion was also drawn recently by Smolkin et al. (2011) based on their discovery of Archaean zircon grains in the felsic rocks. Melezhik et al. (1994b) suggested in situ eruption with major

eruption centre located in the Lake Luotna area where they documented a remnant of probable eruption centre. The inferred centre is represented by a ca. 13-m-thick succession of fel-sic tuffs containing abundant xenolithic fragments and blocks (up to1 m) of basaltic ferropicrites, ferro-basalts, ferroandesite, tholeiitic basalts, limestones, calcareous sandstones, and several 1–10-m-sized blocks of flow-folded rhyolite and soft-sediment deformed, thinly bedded rhyolitic tuffs. The rock assemblage was interpreted to represent hot and cold-lahar deposits (Melezhik et al., 1994). The zircon age of ca. 1970 Ma that was reported by Hanski et al. (1990) for the felsic volcanic rocks of the Pilgujärvi Volcanic Formation (sampled in the Lake Ostrovnoe area) was based on conventional bulk TIMS analysis, but there was a limited amount of material available, permitting only one zircon fraction to be analysed without sufficient error estimation. Re-examination is warranted because the studied felsic volcanic rocks are known to contain exotic felsic gneiss xenoliths. Earlier Smolkin et al. (1993) reported the presence of two zircon populations in the felsic rocks in the Lake Ostrovnoe area, with one having a rounded morphology and an Archaean (ca. 2700 Ma) age, though actual isotopic data for this population were not documented. Recently, Smolkin et al. (2011) sampled another outcrop near Lake Ilya Souker and analysed separated zircon grains by SHRIMP. Most surprisingly, they obtained dates that are mostly Archaean, 2655 ± 10 Ma, and even the youngest grains gave dates not younger than 2311 ± 37 Ma. Given the deviating age results published in the three mentioned articles, it is important to ascertain the age of zircon in the felsic rocks of the Pilgujärvi Volcanic Formation.

Pilgüjarvi layered intrusion

The thickness of the gabbro–wehrlite intrusion ranges between 5 and 250 m and locally attains 540 m (Smolkin, 1977). The intrusion is generally concordant with respect to the primary bedding of the enclosing sedimentary rocks (Zak et al., 1982). Ultramafic rocks generally occupy the lower third of the intrusion stratigraphy, whereas gabbroic rocks form the upper part. Smolkin (1977) sub-divided the intrusion into seven zones, which are, from the base upwards: 1) the lower marginal zone (3–5m-thick), 2) the wehrlite olivinite zone (60–190 m-thick), 3) the intermediate zone (10–30 m-thick), 4) the gabbro–pyroxenite zone (110–175 m-thick), 5) the gabbro zone (40–110 m-thick), 6) the fine gabbro zone (25–125 m-thick), and 7) the upper marginal zone (1–8 m-thick). The wehrlite–olivinite zone is not internally homogeneous: the lower and upper parts comprise pyroxenite–wehrlites with a 25–50 vol.%of olivine, whereas the middle horizon is made up of intercalated pyroxene olivinites (75–90 vol.% olivine) and wehrlites (50–75 vol.% olivine). The cumulus minerals in Zone 2 are olivine and chrome spinel, whereas intercumulus phases comprise clinopyroxene, amphibole, brown mica, plagioclase and ilmenite. Intercumulus phases generally form poikilitic crystals enclosing olivine grains. The olivine cumulates at the base of the Pilgüjarvi layered intrusion locally contain massive and disseminated nickel sulfide mineralization.

The peridotite (sample Pilg 8 – 38) was collected by Fiorentini et al. (2008) from the wehrlite olivinite zone of the Pilgüjarvi layered intrusion. The sample shows poikilitic texture and the main assemblage is made up by olivine, clinopyroxene and brown amphibole. The major phase (60 vol%) is olivine that forms rounded relict crystals, ≤ 1.5 mm in diameter, serpentinized at the rims. The relict olivine shows inclusion of spinel whereas along the fractures are present secondary fine-grained magnetites. The contacts between olivine and the others main phases are not preserved, however the primary cumulus texture is recognisable. Clinopyroxene forms the intercumulus phase (18 vol%) with poikilitic texture and inclusions of spinel. Brown amphibole (10 vol%) is crystallised as intercumulus phase with poikilitic texture or at the margin of the clinopyroxene, with not evidences of substitution of this latter by amphibole. Amphibole is associated to sulphides and magnetite. Accessory phases are biotite (3-4 vol%), associated to the intercumulus phases, spinel (rounded crystals included into olivine and clinopyroxene), secondary magnetite (4 vol%), around relict olivine and in the fractures of the silicates, and sulphides. These are made up by pyrrhotite (2 vol%) with exolution of pentlandite (<1 vol%).

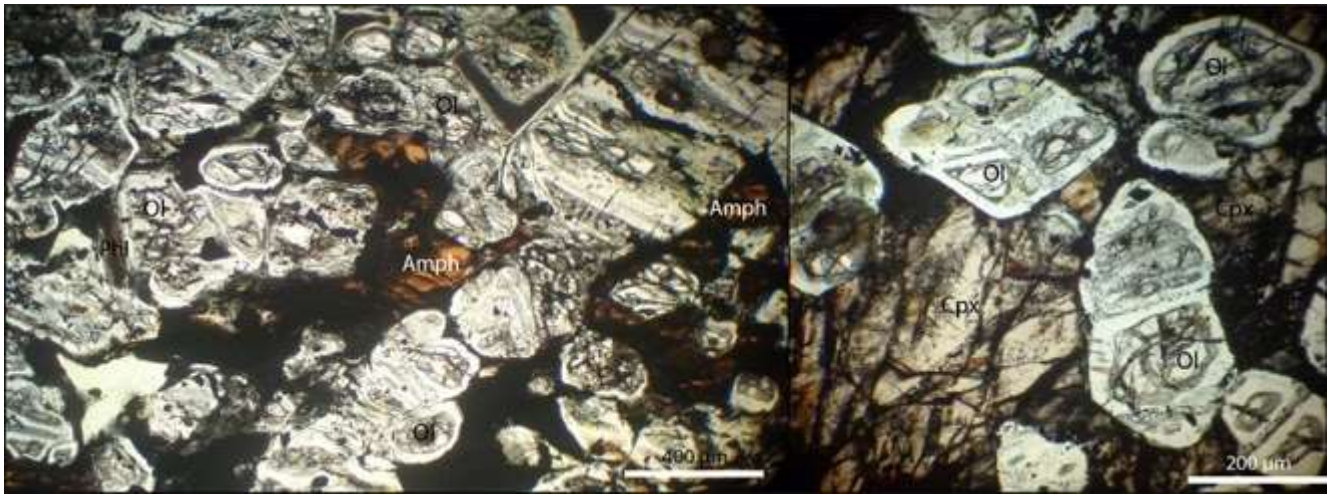

Figure 19 - Photomicrographs **of polished thin sections (Pilg 8 - 38) illustrate the different textures between primary hydromagmatic amphiboles (Amph), relict olivine (Ol), clinopyroxene (Cpx) and brown mica (Phl).**

The olivine-magnetite peridotite (sample 116-6) was collected by the geologist Earo Hanski from the (stratigraphically and geographically) middle part of the Pilgujärvi intrusion (a zone between the ultramafic and gabbroic parts of the intrusion). The peridotite shows cumulate texture, coarse-grained cumulus oxides (ilmenite) and olivine, the latter completely serpentinized. Olivine (50 vol%) is completely serpentinized but is recognisable the original texture of coarse-grained cumulus crystals. Clinopyroxene forms the intercumulus phase between the altered olivine and the ilmenite, associated to brown amphibole (3 vol.%). The latter crystallized in the peripheral portions of the clinopyroxene and only in one spot as intercumulus mono-phase. The contact between amphibole and pyroxene are sharp

where there are no evidences of alteration, otherwise the transition between the two phases is not clear. The other cumulus phase is made up by rounded ilmenite (40 vol.%). At the margin of ilmenite crystals fine-grained aggregates of pyrrhotite may be present. The accessory phases are biotite, associated to clinopyroxene and brown amphibole, and magnetite, as a product of serpentinization, along the fracture of silicates.

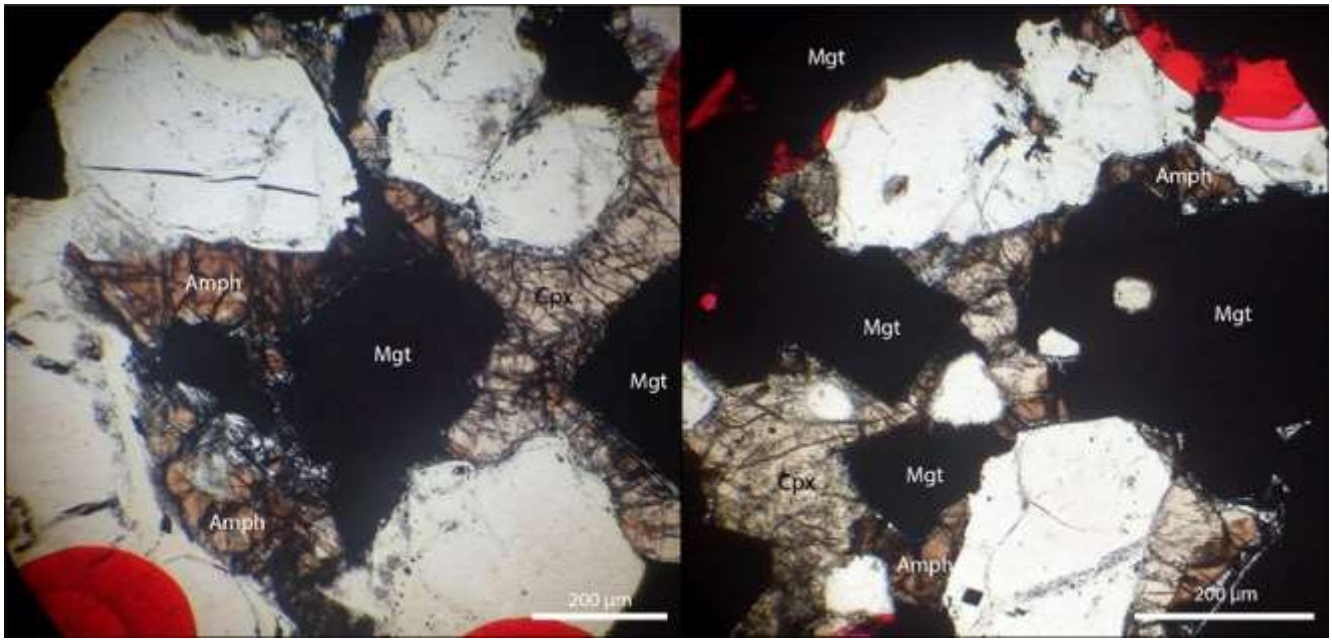

Figure 20 - Photomicrographs of polished thin sections (116-6) displaying varying textural relationship between primary hydromagmatic amphiboles (Amph) and clinopyroxene (Cpx). The sample is constituted by cumulitic magnetite (Mgt) with ilmenite intergrowth. The olivine is completely substituted by alteration minerals (e.g. chlorite).

The olivine cumulate (sample 106-44) was collected by the geologist Earo Hanski from the ultramafic part of the Pilgujärvi intrusion. Olivine cumulate has poikilitic/cumulate texture and main assemblage of olivine, clinopyroxene and brown amphibole. Olivine is the most abundant phase (70 vol%) and is present as rounded and "corroded" crystals (≤ 1 mm in diameter). In some spots olivine shows inclusions of spinel. Clinopyroxene (15 vol%) forms oikocrysts, associated to brown amphibole and phlogopite, and enveloping the relict olivine. Brown amphibole (10 vol%) makes up oikocrysts or aggregates at the margin of clinopyroxene. It is associated to phlogopite and sulphides and shows sharp contacts with pyroxene and frequent altered boundaries with olivine. The textural relations between clinopyroxene and amphibole suggest that the crystallization of amphibole is coeval or just follows the crystallization of pyroxene. Accessories phases are phlogopite (2 vol%), as sub-millimetric intercumulus lamellae, spinel, as inclusions into the relict olivine, sulphides (pyrrhotite, pentlandite and chalcopyrite), with networking texture, and secondary magnetite.

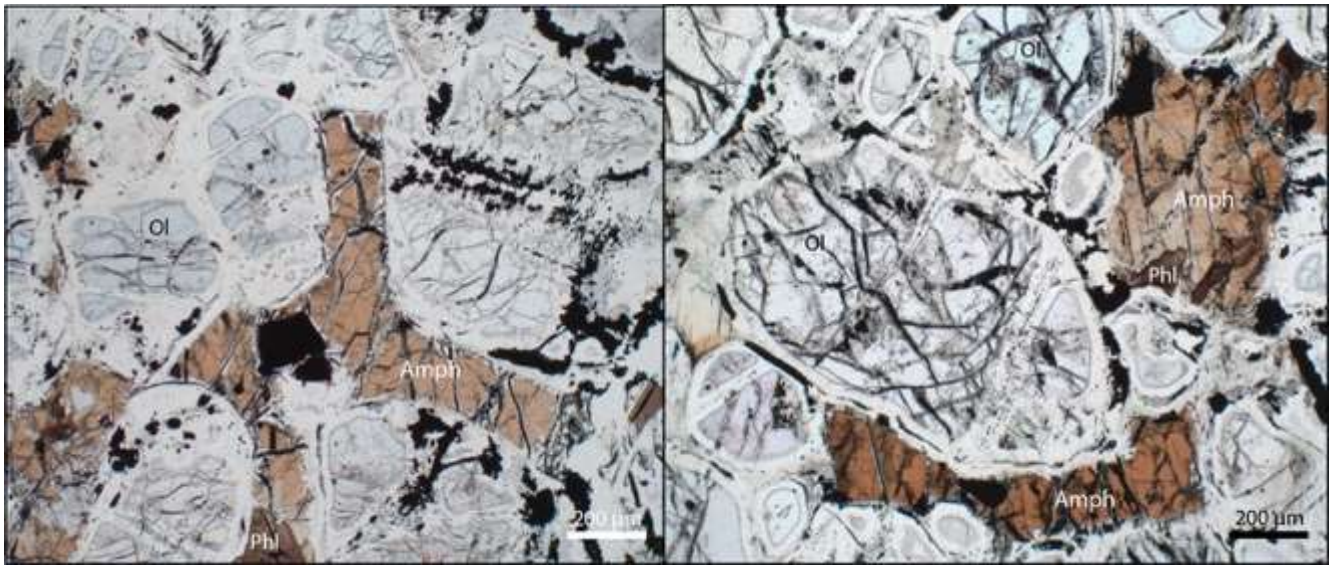

Figure 21 - Photomicrographs of polished thin sections (106-44) displaying varying textural relationship between primary hydromagmatic amphiboles (Amph), relict olivine (Ol) and brown mica (Phl).

Kammikivi, Ortoaivi and Kotselvaara sills

The layered sills are generally 100 m-thick and hosted in sulfur-poor phyllites (Hanski, 1992). The lower portion of the sills generally comprises olivine–chrome spinel cumulate. The most abundant silicate intercumulus phases are clinopyroxene, amphibole and brown mica. Pyroxene and amphibole may occur as poikilitic grains but are generally prismatic or needle-like. Locally, densely disseminated sulfide mineralization occurs in a 3–5 m-thick horizon at the base of this interval. A 2.5 m-thick pyroxenite overlies the basal olivine–chrome spinel cumulate. The upper part of the pyroxenite is fine-grained, with grain size varying between 0.05 and 0.6 mm. The grain size increases downwards to a typical range of 0.5–1.5 mm. With respect to its mineralogy and texture, the unit comprises clinopyroxene grains locally with skeletal interiors and brown amphibole fringes and less abundant euhedral olivines altered to serpentine. The chloritic groundmass contains dark brown amphibole needles and skeletal sphene pseudomorphs after magnetite (Hanski, 1992). The uppermost portions of the sills generally comprise gabbroic rocks, which generally display textures indicative of rapid cooling, including skeletal magnetite, needle-like dark brown amphiboles and cryptocrystalline groundmass material, probably after original glass.

The samples from Kammikivi sill (57a-HV-28 and 57b-HV-28) were collected by geologist Heikki Väyrynen in 1928. They come from the same location from the basal part of the Kammikivi sill and display cumulate/poikilitic texture and the main assemblage made up by olivine (65 vol%) and clinopyroxene (20 vol%). Olivine is partially resorbed and only the cores of the crystals are preserved. Clinopyroxene forms oikocrysts (5 mm to 1 cm in diameter) that envelop olivine and is associated to brown amphibole (5 vol%), phlogopite (< 1 vol%) and spinel. The latter is present as inclusions into

pyroxene and amphibole. Brown amphibole forms oikocrysts or aggregates at the margins of clinopyroxene. As described before, amphibole contains inclusions of spinel and is associated to phlogopite. When amphibole is at the margin of clinopyroxene, the contacts between the two phases are generally sharp but locally with lobes, suggesting a substitution of pyroxene by amphibole. Accessory phases are phlogopite, and Cr spinel, ilmenite and magnetite. Phlogopite occurs as lamellae in the intercumulus domain, while spinel as inclusions into clinopyroxene and brown amphibole. Ilmenite forms aggregates in the portions of intercumulus of the sample, in some spots in the serpentinized portions of the olivine, while magnetite is present along the fractures of the silicates and in the serpentinized portions as well.

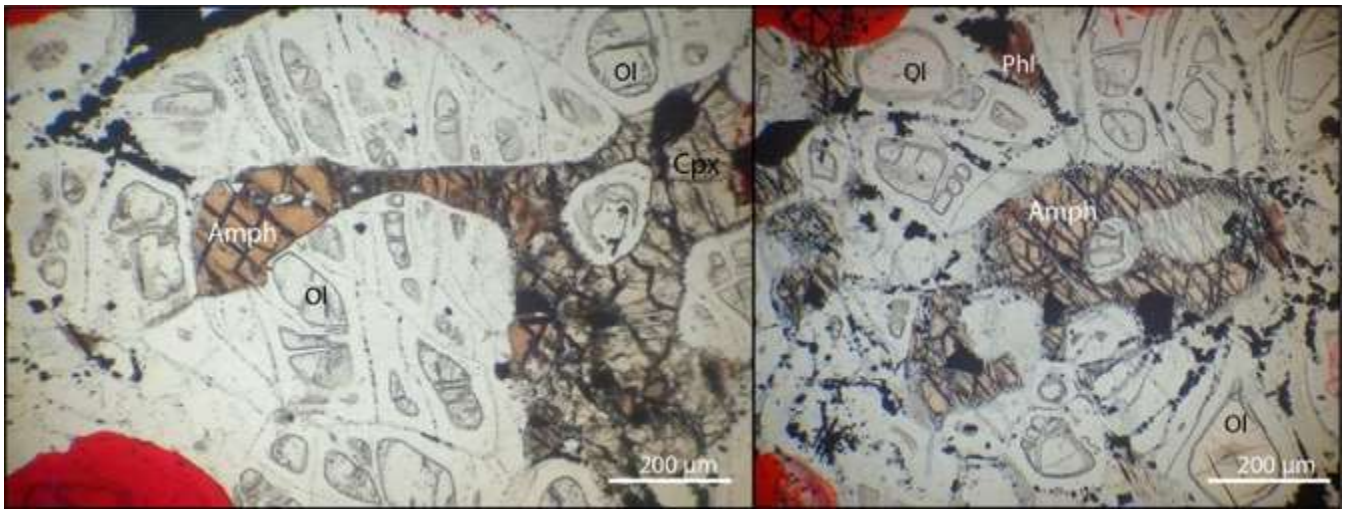

Figure 22 - Photomicrographs of polished thin sections (57HV28) show different textures between primary hydromagmatic amphiboles (Amph), relict olivine (Ol), clinopyroxene oikocrysts (Cpx) and brown mica (Phl).

Nyasyukka dyke complex

On the NE side of the Paleoproterozoic Pechenga Complex, there is a group of mafic to ultramafic dikes, geochemically correlative to the Pechenga Complex, which have been assigned to the Nyasyukka dike complex. Currently the number of known dikes exceeds 40. They form a NNW-trending and steeply dipping swarm occurring within an area of 30 x 40 km^2 and extending from the Luostari railway station to the coast of the Barents Sea (Smolkin et al., 2015).

There is also another dike swarm in the area, which is NNE oriented, thus forming an angle of 45° with the Nyasyukka dike complex. These dikes are more evolved and composed of gabbro diabases and quartz gabbros (Smolkin, Borisova, 1995). The dike-forming process was affected by deep magma differentiation, which resulted in the concentration of dikes of different composition in different subswarms. Three parallel series are distinguished. The dikes of the western and eastern series are composed predominantly of olivine gabbro and vary in thickness from 30 to 130 meters and in length from 1 to 8 kilometers. The central series comprises dikes swarms that are 40–150, sometimes up to 200

meters thick and up to 22 km long, and are composed of plagioclase- and kaersutite-bearing peridotites. In addition to these dike systems, a plagioclase-bearing olivine pyroxenite stock is located at the southern termination of the eastern series. Peridotites of the Nyasyukka dyke complex are olivine cumulates with oikocrystic dark brown amphibole, plagioclase, and clinopyroxene. Peridotites are medium to coarse-grained rocks with a massive or porphyritic-looking texture, the latter being caused by large poikilitic amphibole crystals. Locally, peridotites display a pegmatoid texture. The minor minerals include bronzite, biotite, magnetite, ilmenite, and apatite. Olivine gabbros are medium-grained, massive rocks having a wide variation in the relative proportions of the major minerals. Fiorentini et al. (2008) had collected four amphibole-bearing peridotites from the 150 m-thick central ultramafic dyke in the Nyasyukka area: one sample was collected from a pegmatoid pocket, whereas three samples were collected from the cumulate portions.In the cumulate portions of the intrusions, the rounded shapes, smaller size and embayed contacts of the olivine inclusions within poikilitic amphibole indicate olivine resorption to be important in amphibole formation. Decreasing temperature facilitated reaction of hydrous residual melt with olivine and pyroxene and production of the amphibole in the late magmatic stage. Olivine had crystallized before pyroxene, and plagioclase is xenomorphic with respect to the main mafic minerals. There is often an orthopyroxene-amphibole corona at the contact between olivine and plagioclase. Orthopyroxene is present in the Nyasyukka dikes but has not been found in the Pechenga rocks, suggesting a higher silica activity in the magma parental to the former rocks. Olivine and plagioclase typically coexist in the olivine gabbros of the Nyasyukka complex whereas the gabbroic rocks of the Pechenga intrusions commonly lack olivine or contain only a small amount of olivine.
Volatiles were implicated in the petrogenesis and evolution of the Pechenga ferropicrites. On the basis of the Ti– and Nb–Ta-enriched nature of hydromagmatic amphiboles from the intrusions and lava flows, Fiorentini et al. (2008) argue that the source of volatiles in the Pechenga ferropicrites could be either a metasomatised subcontinental mantle or a volatile-bearing plume. Positive Nb–Ta/La anomalies in amphiboles from the intrusions rule out crustal contamination with granitoid crust as the main source of the volatiles. Local B–Cl enrichment suggests that some samples may have interacted with hydrothermal fluids. The range of in-situ δD values in hydromagmatic amphiboles is consistent with the presence of magmatic water. The lighter hydrogen isotopic composition and lower water contents of the primary igneous amphiboles from the lava flows compared to amphiboles from the intrusions indicate that the lava flows degassed upon emplacement. This is the first documentation of significant degassing in ultramafic magmas.

The samples N 2 and N 3 from the Nyasyukka dike complex derive from amphibole-bearing peridotites of the central dike series, emplaced into Archean granite. These samples were described in

the study by Fiorentini et al. (2008) and were made available by the collaboration with Centre for Exploration Targeting.

The peridotite in sample N 2 and N 3 is made up principally by olivine (25 to 30 vol.%) cumulate with brown amphibole (30-32 vol.%) oikocrysts and clinopyroxene (20-25 vol.%). Olivine occurs as rounded sub-euhedral crystals, locally with ameboid texture, included into oikocrystic amphibole. Locally, olivine shows inclusions of ilmenite and magnetite. Brown amphibole oikocrysts have intense pleochroism and show exolution lamellae of ilmenite along the crystallographic planes. Brown amphibole has inclusions of granular ilmenite and magnetite. Clinopyroxene occurs as small (>30 μm) relict crystals and, where preserved, the contacts with brown amphibole are sharp. Locally, clinopyroxene is enveloped by the amphibole oikocrysts. Biotite occurs as large crystals associated to brown amphibole. Only interstitial plagioclase (2 vol.%) is observed. The other accessory phases are ilmenite (3 vol.%), magnetite (5 vol.%) and sulphides (pyrrhotite and pentlandite, 5 vol.%).

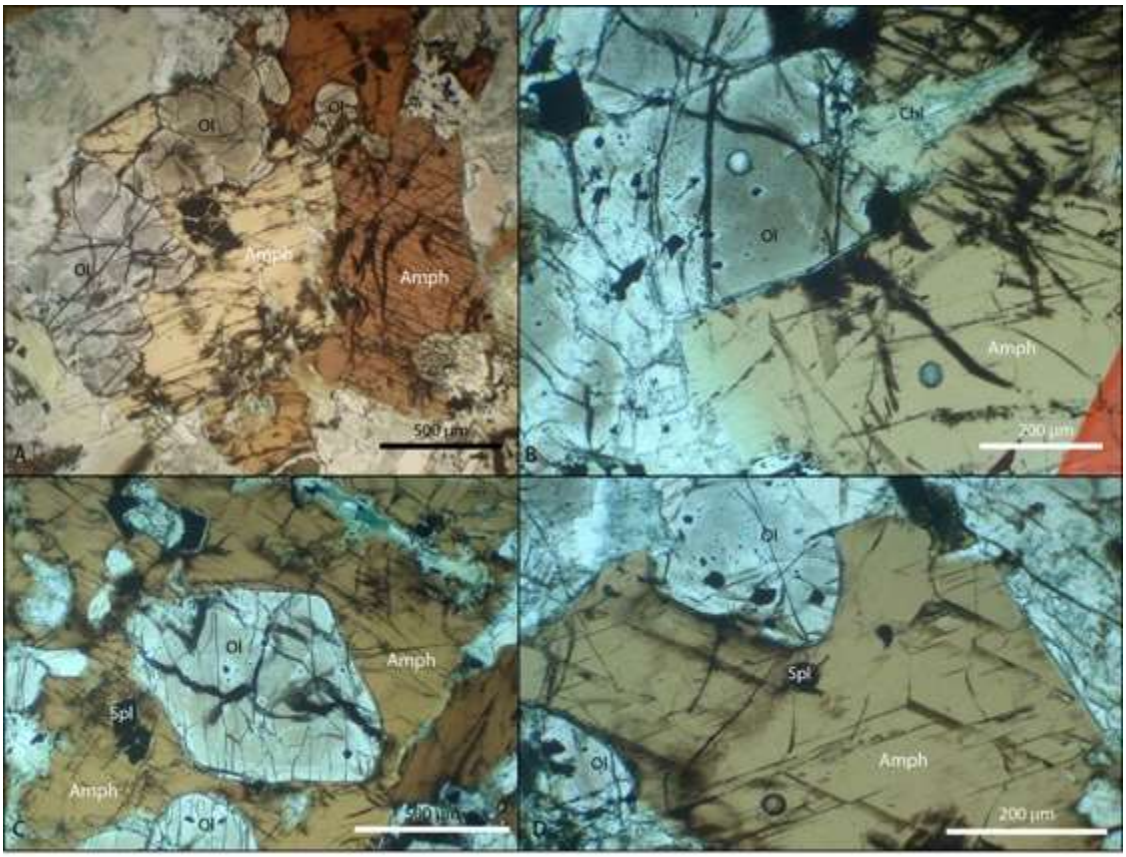

Figure 23 - Photomicrographs of polished thin sections (N2, N3) displaying varying textures between primary hydromagmatic amphiboles (Amph), olivine (Ol), and accessory spinel (spl). Thin sections (A) and (B) are from the sample N2 whereas (C) and (D) illustrate sample N3.

2.4 Phanerozoic samples

2.4.1 Ross Orogen (Husky Ridge), Antarctica

The Ross-Delamerian Orogen, located in the Northern Victoria Land, Antarctica, is the result of the subduction of the Palaeo-Pacific oceanic plate beneath the continental margin of Gondwana during the Early Palaeozoic (e.g. Cooper & Tulloch, 1992; Münker & Crawford, 2000; Boger & Miller, 2004; Foster et al., 2005 – in Tiepolo & Tribuzio, 2008). The orogen is represented by a belt extending from southeastern Australia to the margin of the East Antarctic craton (e.g. Borg & DePaolo, 1991; Stump, 1995; Rocchi et al., 1998). The Transantarctic Mountains, which extend across the entire Antarctic continent, represent the uplifted basement of the Ross Orogen (Stump, 1995). The oldest magmatic products with calc-alkaline affinity (found in southern Victoria Land) mark the onset of the subduction at about 540 Ma (Allibone & Wysoczanski, 2002). In northern Victoria Land (NVL), three major fault-bounded tectonostratigraphic terranes of debated origin are identified from west to east: the Wilson, Bowers and Robertson Bay terranes. In particular, the Wilson terrane is considered as representing the active continental margin of Gondwana at the beginning of the Palaeozoic subduction. The subduction-related magmatic products along this continental margin are known as the Granite Harbour Intrusive series (Gunn & Warren, 1962). The majority of magmatic products in NVL have ages clustering around 500 Ma and are mostly granitoids with calcalkaline affinity (granites, granodiorites, tonalites and minor gabbro-diorites) and variable K_2O enrichment (Di Vincenzo et al., 1997; Rocchi et al., 1998; Dallai et al., 2003). The magmatic products related to the early Cambrian stages of subduction are limited to sporadic deformed granitoids with rare mafic to ultramafic enclaves dating between 544 and 520 Ma (Black & Sheraton, 1990; Rocchi et al., 2004; Giacomini et al., 2007). Peraluminous leucogranites and basic melts with shoshonitic affinity were intruded during a late orogenic phase, which probably post-dated the subduction event, at about 480 Ma (Rocchi et al., 1998; Di Vincenzo & Rocchi, 1999). The rare mafic-ultramafic intrusive rocks of the orogeny are mostly scattered along the suture zone between the Wilson and Bowers terranes. Three main gabbroic sequences preserve their original intrusive features; namely, Niagara Icefall, Husky Ridge and Tiger Gabbro sequences. Only the Niagara Icefall has been dated (514 Ma) and characterized in its geochemical and petrological features which are compatible with a boninitic affinity (Tribuzio et al., 2007). The Husky Ridge is located in the middle of the Meander Glacier, c. 10 km north of Mt Murchison (Fig. 24). In the eastern sector of the ridge, a 50-100 m-wide body of undeformed to weakly deformed amphibole-rich mafic intrusive rocks made of quartz diorites.

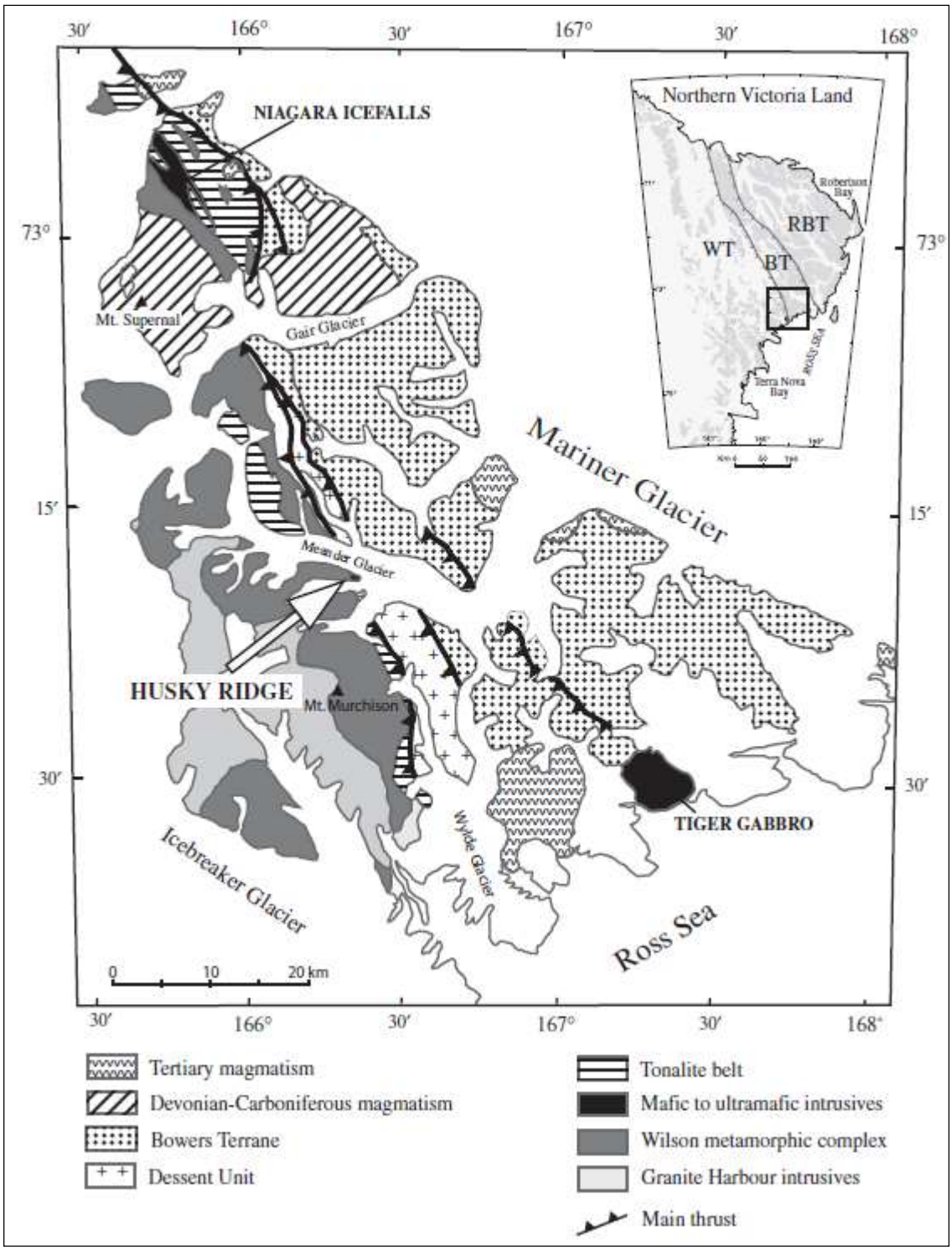

Figure 24 – Simplified geological map of the southern portion of the tectonic boundary between Wilson and Bowers Terranes, northern Victoria Land, showing the location of the Husky Ridge gabbroic sequences (from Tiepolo & Tribuzio, 2008).

Quartz diorites were emplaced in the mid-crust at about 516 Ma (Tiepolo & Tribuzio, 2008), in amphibolite-facies migmatitic gneisses, with overall features comparable with what observed in the Bregaglia intrusion in the Central Alps (Tiepolo et al., 2002 – see below). The Husky Ridge quartz-

diorites display two assemblages including high Mg-number mafic phases, involving clinopyroxene and magmatic brown and green amphibole, yet with markedly different trace element signatures. Such differences, involving REE, LILE and HFSE element fractionation, suggest equilibrium with two different parental magmas, one affine with sanukitic melts and the other derived from sanukite-like melts but crystallizing amphibole in deeper magma chambers (Tiepolo & Tribuzio, 2008).

The sample (TT329) from Husky Ridge is part of the collection by Tiepolo & Tribuzio (2008). In the quartz-diorite the main assemblage consists of brown amphibole (50-60 vol.%), green amphibole (20-25 vol.%), plagioclase (15 vol.%) and clinopyroxene (3-5 vol.%). The amphibole grains are characterized by brown core and greenish rims. The green amphibole is observed also as single crystals inbetween the plagioclase pockets. Clinopyroxene and biotite are included into brown amphibole. The accessory minerals are biotite, quartz, titanite and opaque phases (pyrite and ilmenite).

2.4.2 Alpine Orogen (Adamello batholith and Valmasino-Bregaglia/Bergell pluton), Italy

Tiepolo et al. (2014) debated about the existing uncertainties regarding the origin of the Periadriatic magmatism, developed during the Alpine Orogeny from c. 44 to c. 31 Ma, and its relationships with tectonic evolution of the Alps.

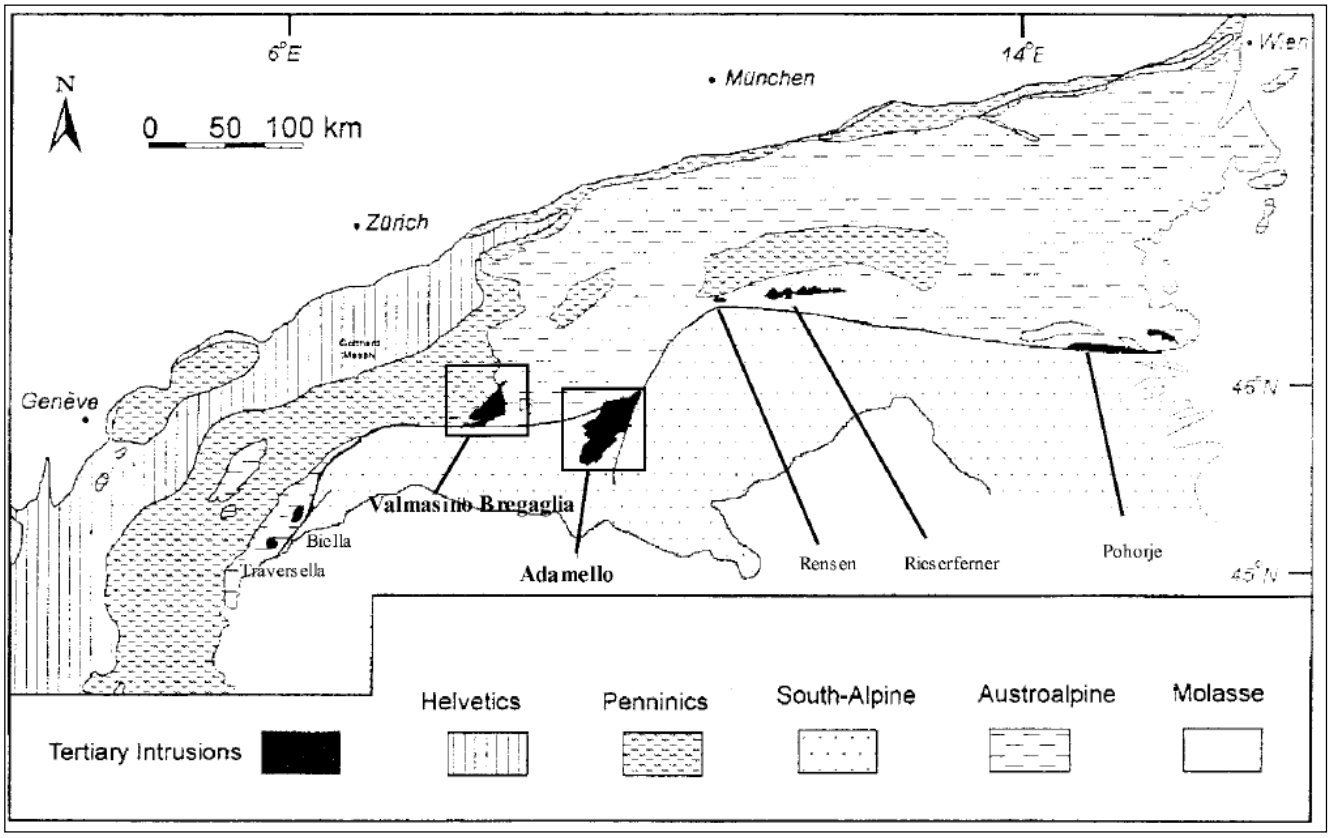

Figure 25 – Geological sketch of the Alpine belt with the location of Valmasino and Adamello intrusions (from Tiepolo et al., 2002).

Particularly the tectonic processes responsible for mantle melting along the Alpine belt are still not well defined. Geochemical data indicate an origin from a suprasubduction mantle wedge (Kagami et al. 1991; Tiepolo et al. 2002, 2011), while the melting triggering mechanism could be a post-collision lithospheric extension (Laubsher 1983, 2010) or a slab break-off process (Davies & von Blanckenburg, 1995). In analogy with what observed in other orogenic belts and because of negligible crustal contributions, the rare mafic-ultramafic rocks associated with the subduction-relaetd granitoid bodies may provide useful information about mantle sources and related petrogenetic processes.

The Adamello batholith and the Bregaglia pluton are not only the two largest Palaeogene intrusive bodies of the Alpine belt, but also the only two Periadriatic intrusions including mafic–ultramafic rock sequences containing magmatic amphibole. U–Pb geochronology and Hf isotopic ratios on zircon from amphibole-rich mafic and ultramafic facies from both plutons by Tiepolo et al. (2014) contributed to build up a magmatic-tectonic framework in which the Adamello emplacement (characterized by a major crystallization event at c. 41 Ma and older age peaks at c. 50 and c. 45 Ma) predates the one of the Bregaglia pluton, taking place 10–15 Ma later. Moreover, the two intrusions appear to be related to different sources linked to the evolution of the subduction process. The geochemical imprints of the Adamello batholith suggest a depleted mantle source activated by the subduction of the Ligurian–Piedmontese Basin, while the signatures of mafic-ultramafic rock facies in the younger Bregaglia pluton are compatible with melts derived from the activation of a different mantle sector which was metasomatized by the subduction of the Valais Basin.

The Adamello batholith is exposed over an area of about 700 km^2 at the intersection of the Periadriatic Lineament with the Giudicarie Line and consists of multiple intrusive units ranging in age from about 42 Ma to about 29 Ma (Del Moro et al., 1983; Callegari & Brack, 2002; Tiepolo et al., 2011). The batholith is intruded into the upper continental crust of the Southern Alps and principally consists of tonalites, trondjhemites and granodiorites; mafic and ultramafic bodies are found locally, especially in the southernmost Re di Castello unit (Callegari & Dal Piaz, 1973; Ulmer et al., 1983; Blundy & Sparks, 1992). The mafic bodies are best exposed in the Val Fredda and Cornone di Blumone areas. The Val Fredda Complex consists of granodiorites, tonalites and quartz-diorites intruded by several mafic sheets of metre to decametre thickness (Blundy & Sparks, 1992). Two types of mafic sheet have been recognized in the Val Fredda Complex, specifically in the Mt. Cadino and Mt. Mattoni sequences. The Mt. Cadino mafic rocks range from hornblende gabbros to quartz-diorites and the Mt. Mattoni mafic rocks consist of hornblende-phyric, pyroxene-bearing gabbros (hereafter amph-gabbros) with subordinate hornblendite blocks or bands (Tiepolo et al., 2011).

The Valmasino Bregaglia calc-alkaline intrusion is located in the south-eastern part of the central Alps and was dated at 31.3–31.9 Ma (Hansmann 1996). Hornblende-bearing tonalite and granodiorite are the main lithologies in the southern and northern areas respectively (Montrasio and Tromsdorff 1983). The mafic rocks (hornblendites, amphibole-gabbros and diorites) crop out at the eastern border of the pluton (Tiepolo et al., 2002 and references therein).

The samples from Mt. Mattoni (MAT1, MAT2, MAT15) were collected by Tiepolo et al. (2002) and are hornblendites and the main assemblages consist of poikilitic amphiboles (75-80 vol.%) (Fig. 26), olivine (15-20 vol. %) and clinopyroxene (5 vol.%). The amphibole grains are characterized by brown core and greenish rims. Green amphibole is observed also as single crystals interstitial to / inbetween the zoned poikilitic amphiboles. Olivine occurs as rounded inclusions into the poikilitic amphibole. Clinopyroxene occurs as partially replaced crystals at the core of the zoned amphiboles. The sample (VS9) from the Bregaglia intrusion was collected by Tiepolo et al. (2002) and is a hornblendite consisting of poikilitic amphibole (70 vol.%) (Fig. 27), clinopyroxene (15 vol.%) and olivine (7-10 vol.%). Amphibole shows brown core and greenish rim. Clinopyroxene is resorbed and included into the zoned amphibole. Like clinopyroxene, olivine as well is enveloped into amphibole and partially resorbed.

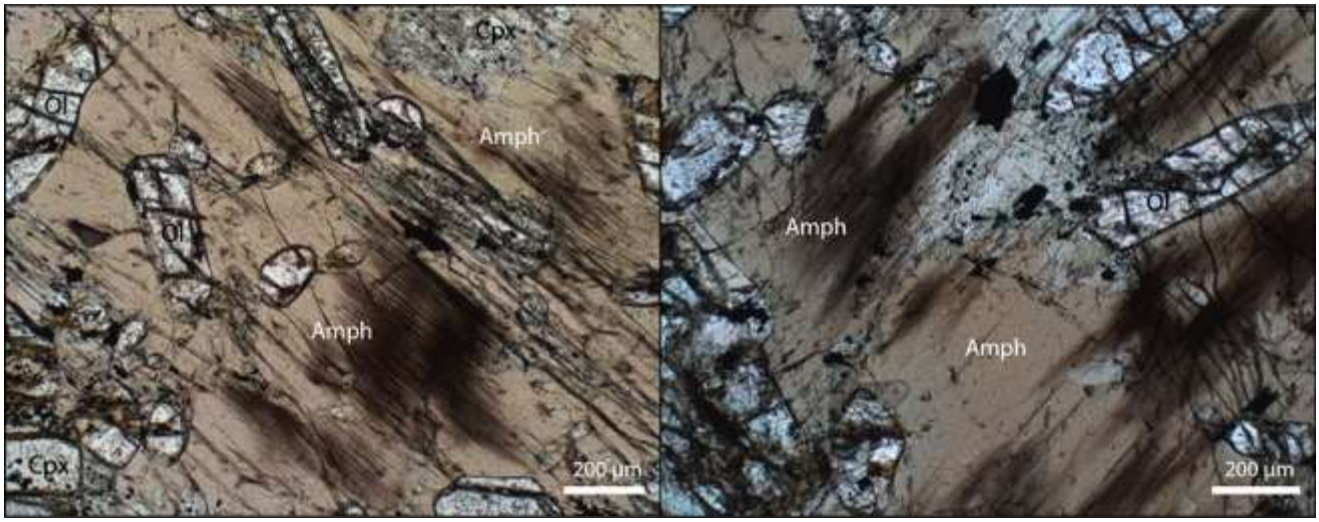

Figure 26 - Photomicrographs of polished thin section (MAT15) displaying varying textures between amphiboles (Amph), olivine (Ol) and clinopyroxene (Cpx).

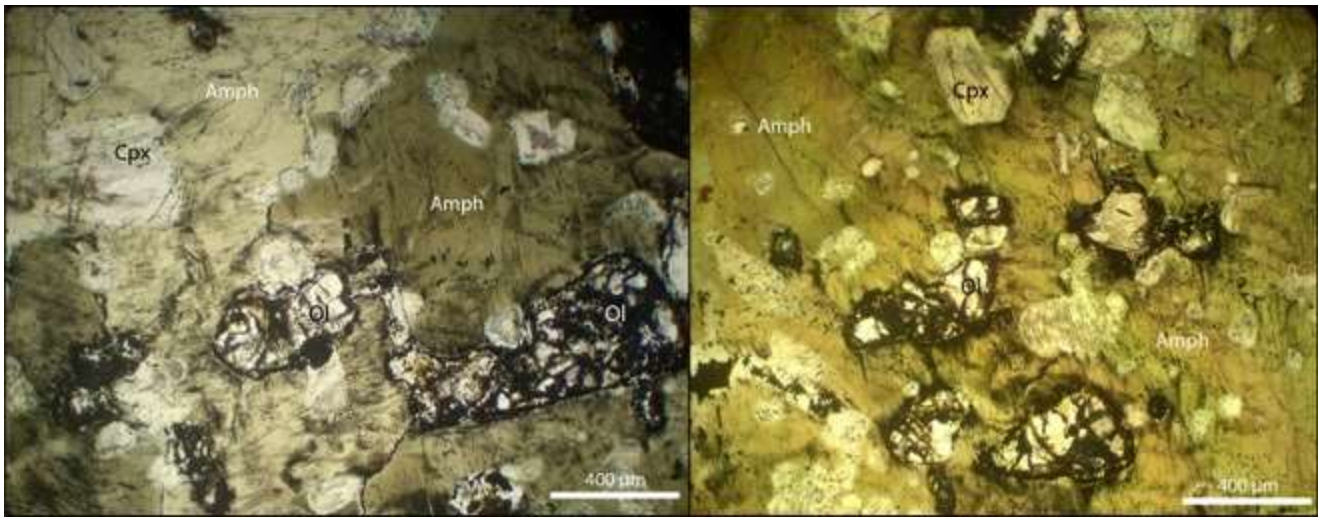

Figure 27 - Photomicrographs of polished thin section (VS9) displaying varying textures between amphiboles (Amph), olivine (Ol) and clinopyroxene (Cpx).

2.4.3 Continental arc, Japan

Cretaceous igneous rocks are widespread throughout the Inner Zone of southwest Japan (Sato et al., 2016). This zone represents a huge igneous belt that developed along the continental margin of East Asia before the Miocene opening of the Japan Sea (Takahashi, 1983) (Fig. 28). Early Cretaceous magmatism in southwest Japan is characterized by the intrusion of small volumes of high-Mg and adakitic magmas, and I-type granite magmas (Kamei et al., 2004). Throughout the Cretaceous granitic rocks, ultramafic to intermediate magmatism is recorded as small-scale hornblenditic, gabbroic and dioritic intrusions (Langone et al., 2009) which are found in three locations: Taku (Kunisaki Peninsula and Shikanoshima Island, Kyushu) in the southern part of Japan (Fig. 29), Ina Mountain / Zenifudo and Hitachi / Hase no Yatzu (central and northern Honshu – Fig. 28).

In all localities mafic and ultramafic rocks are closely associated with granitoids rocks, but only in the Shikanoshima island the relations between the two litologies are exposed.

Mineral chemistry (major and trace elements) and U/Pb geochronology data determined by Tiepolo et al. (2012) on the amphibole-rich porphyritic gabbrodiorite from Taku outcrops outlined a complex picture involving disequilibrium between the large brown amphiboles (and related clinopyroxene inclusions) and the assemblage in the fine-grained matrix. The coarse-grained brown amphibole and related clinopyroxene inclusions would represent xenocrysts inherited from hornblendites crystallized from a melt affine to continental arc basalts. The fine-grained amphibole-bearing matrix crystallized from a parental liquid similar to sanukite-type, High Mg andesite (HMA) magmas derived from mantle melts affected by crustal processes and contaminated by crustal material. Analogies exist with amphibole-rich mafic intrusive rocks in other orogenic settings worldwide and specifically those occurring in the Alpine chain and in the Ross Orogen (Antarctica) described above.

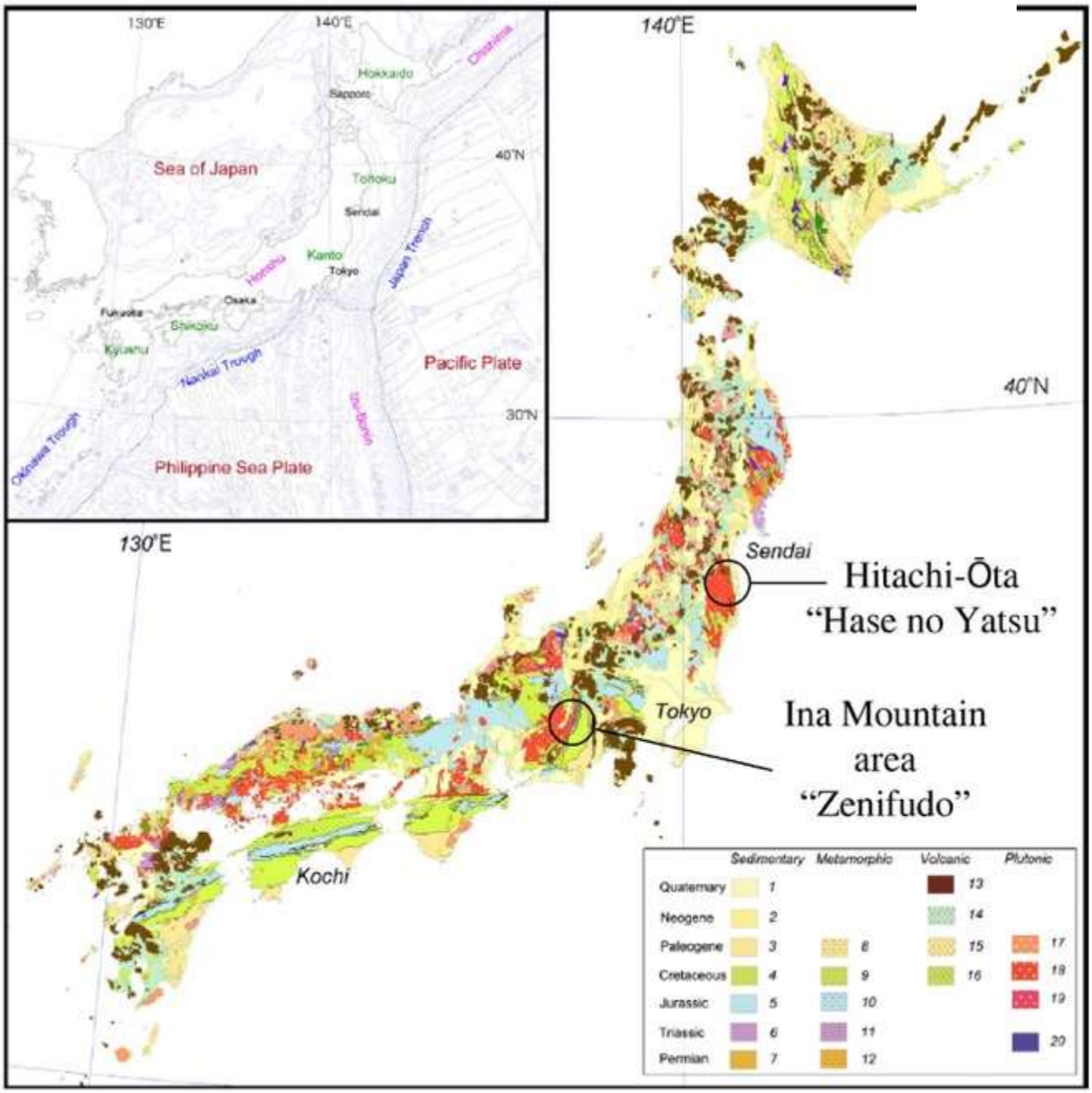

Figure 28 - Geological Map of the Japanese Islands. Japanese part of the International Geological Map of Asia at a scale of 1:5,000,000 (IGMA5000) is based on this geological map data. 1: Quaternary sediments, 2: Neogene sedimentary rocks, 3: Paleogene sedimentary rocks and accretionary complex, 4: Cretaceous sedimentary rocks and accretionary complex, 5: Jurassic sedimentary rocks and accretionary complex, 6: Triassic sedimentary rocks, 7: Permian sedimentary rocks and accretionary complex, 8: Paleogene metamorphic rocks, 9: Cretaceous metamorphic rocks, 10: Jurassic metamorphic rocks, 11: Triassic metamorphic rocks, 12: Permian metamorphic rocks, 13: Quaternary volcanic rocks, 14: Neogene volcanic rocks, 15: Paleogene volcanic rocks, 16: Cretaceous volcanic rocks, 17: Paleogene plutonic rocks, 18: Cretaceous plutonic rocks, 19: Jurassic plutonic rocks, 20: ultramafic rocks. (from Wakita, 2013).

The mafic-ultramafic rock types located at Hase no Yatzu are represented by both porphyritic gabbrodiorite and hornblendite, whereas at Zenifudo hornblendites only are found (Langone et al, 2009). Like previously noted, the mafic rocks across the continental arc reveal a complicated geochronologic history with petrological features providing evidence of multiple components. According to the preliminary investigations by Langone et al. (2009), the clinopyroxene inclusions hosted in amphiboles are relics of pre-existing ultramafic rocks (pyroxenites?) assimilated by the evolved melt crystallizing olivine/orthopyroxene/amphibole. Geochronology provides a younger age for the mafic rocks from Taku (c.a. 100 Ma) than for those from Hase No Yatsu (117 Ma), but the former contain inherited zircons from 110 up to 123 Ma. Given the clear interaction of the Taku mafic rocks with granitoids at 100 Ma, the authors supposed that all mafic rocks from the three areas might have been emplaced between 110-120 Ma. On the other side, a significantly younger age at 70 Ma obtained for Zenifudo could be not related to emplacement of the ultramafic rock but related to a late stage injection of melt.

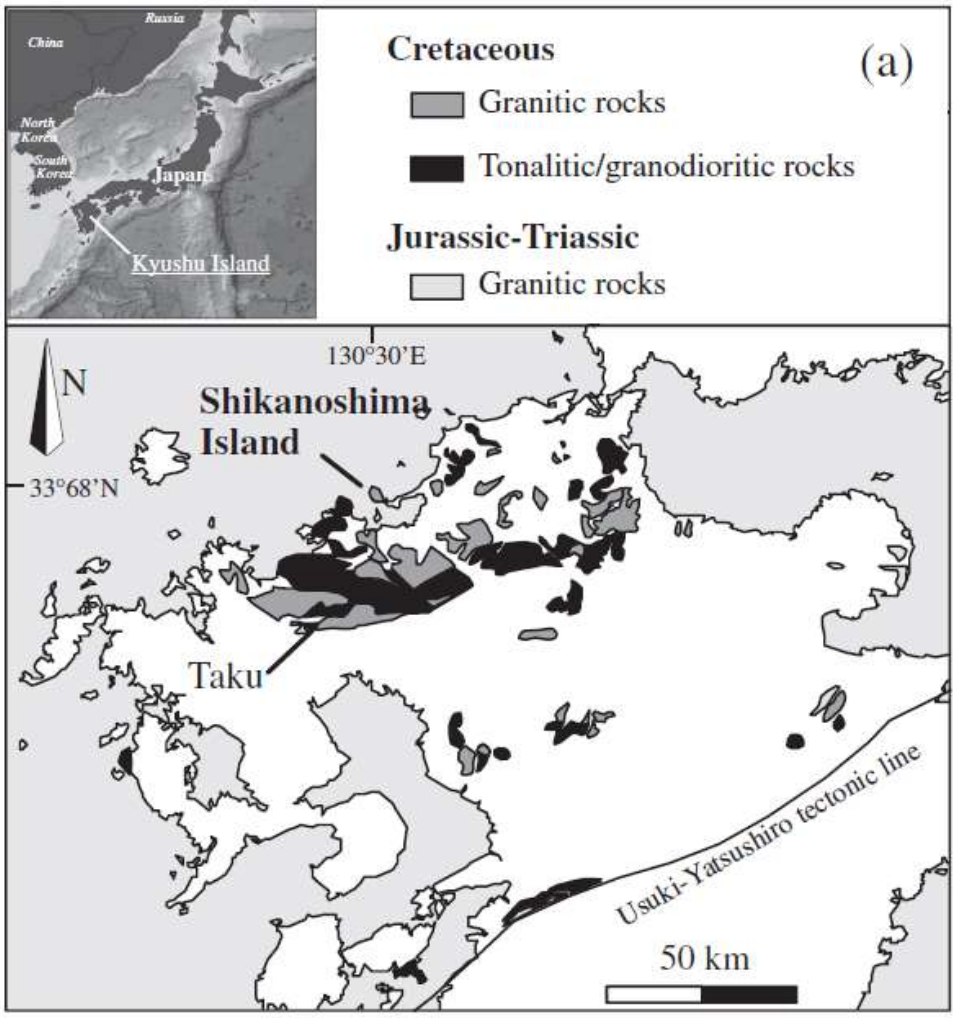

Figure 29 – Simplified geological map of northern Kyushu showing the location of Taku area (from Tiepolo et al., 2012).

The sample (TK1B – Fig. 30a) from Taku Island (Kyushu Island) is selected from the collection by Tiepolo et al. (2012) and is a gabbrodiorite (whose main assemblage consists of brown amphibole (35 vol.%), green amphibole (20 vol.%), orthopyroxene (20 vol.%), clinopyroxene (10 vol.%), olivine (10 vol.%), plagioclase (4 vol.%) and accessory sulphides and Fe-oxides. Poikilitic amphibole typically displays brown core, with exolution lamellae of Fe-oxides, and green rim. Pyroxenes are partially resorbed: clinopyroxene has rounded habitus and is included into amphibole whereas orthopyroxene is associated to amphibole with sharp contacts and displays exolutions of Fe-oxides. Olivine occurs as rounded grains included into amphibole. Olivine is also observed at the rims of interstitial pockets of plagioclase.

The hornblendite (ZN5 – Fig. 30b) from Zenifudo (Honshu Island) was collected by Massimo Tiepolo and is characterized by a main assemblage comprising brown amphibole (25 vol.%), clinopyroxene (20 vol.%), olivine (18 vol.%), orthopyroxene (15 vol.%), green amphibole (15 vol.%) and plagioclase (10 vol.%). Accessories are biotite and Fe-oxides. Similarily to what observed in the samples from Taku Island, the poikilitic amphibole grains are characterized by brown cores and greenish rims, and amphibole shows exolution lamellae of Fe-oxides and inclusions of round olivine grains. Two types of clinopyroxene grains are observed: (1) rounded grains included within amphibole (<1 mm) and (2) grains partially resorbed or completely altered in serpentine. Orthopyroxene is observed as rounded grains that may include olivine. Plagioclase is present in the matrix enveloping the amphibole-pyroxenes-olivine aggregates.

The main assemblage of the hornblendite (HSY3B), collected by Massimo Tiepolo, from Hase no Yatsu (Honshu Island) includes brown amphibole (35 vol.%), clinopyroxene (20 vol.%), olivine (10 vol.%), orthopyroxene (10 vol.%), green amphibole (10 vol.%) and accessory biotite (7 vol.%) and Fe-oxides (8 vol.%). Brown amphibole has poikilitic texture with exolution lamellae of Fe-oxides. Rounded olivine and pyroxenes grains occur as inclusions within the brown amphibole.

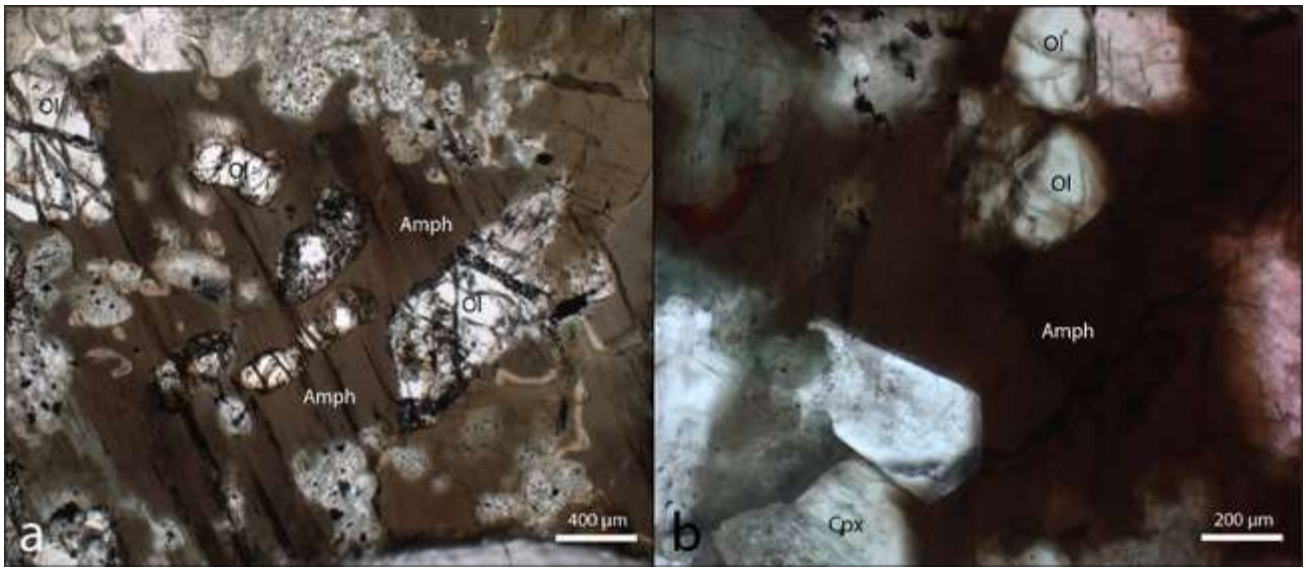

Figure 30 - Photomicrographs of polished thin sections (TK1B, ZN5) with amphiboles (Amph), olivine (Ol), and clinopyroxene (Cpx) forming differet textures. (a) Sample TK1B; (b) sample ZN5.

2.4.4 Himalayan Orogen (Gangdese batholith), China

Ongoing research about Gangdese granitic magmatism (Tibetan sector of Himalayan orogen) is summarized in Ma et al., 2013a). These studies have been contributing to unravel mechanisms of crustal growth and the extent of mantle contribution along convergent margins.

The Gangdese batholith (also named as "Trans-Himalaian Batholith"; Wen et al., 2008) was emplaced within the Lhasa Block, in southern Tibet, from the Cretaceous to Eocene (Fig. 31a-b). The batholith has been regarded as a major constituent of the Andean-type convergent margin resulting from northward subduction of the Neo-Tethyan oceanic lithosphere under Asia. Late Cretaceous mafic–felsic magmatic rocks are widely distributed along the southern margin of the Gangdese region, in the southern part of the Lhasa Block (Ma et al., 2013a,b; Wen et al., 2008a,b; Zhang et al., 2010). The Gangdese batholith consists predominantly of granodiorites, granites and minor intermediate-mafic facies (diorites, gabbros), and was mainly generated between 198 and 43 Ma (Chu et al., 2006; Chung et al., 2003; Ji et al., 2009; Wen et al., 2008a,b). Minor mafic-ultramafic intrusions occur in the Milin County, on the eastern side of the Gangdese batholith (Ma et al., 2013b). The mafic magma intruded the Bala Formation metamorphic rocks (gneisses, amphibolite, marble and schist) as stocks or dykes, with no obvious chilled margins.

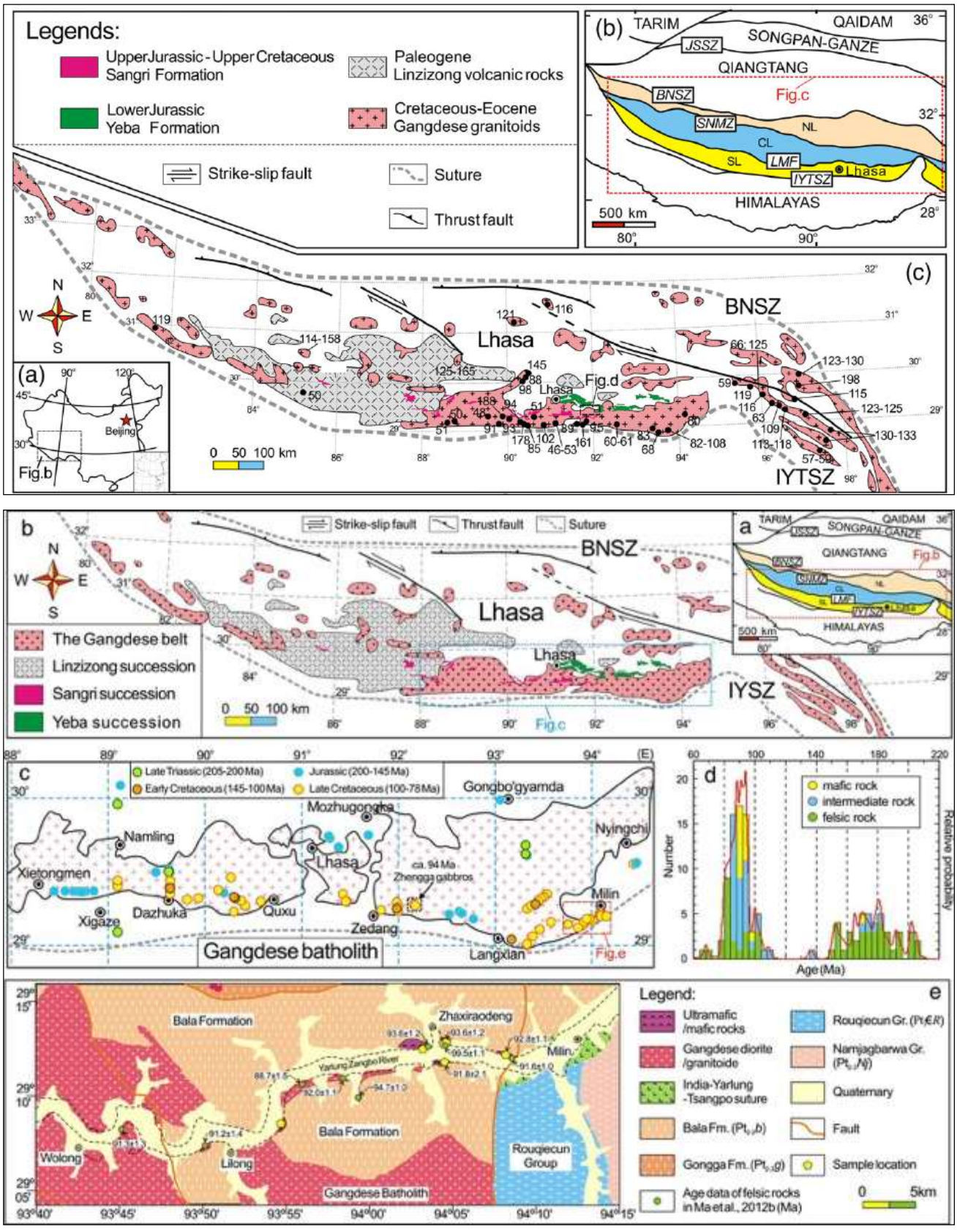

Figure 31 - Sketch maps of the Tibetan Plateau, the Lhasa Block (from Ma et al., 2013). (a) Inset with the outline of the Lhasa Block in the context of the Tibetan Plateau. (b) Sketch of the Lhasa Block; (c) and (d) geographic and age distribution of felsic, intermediate and mafic intrusions within the Gangdese batholith; (e) geological sketchmap of the Milin county with the localization of norites and hornblendites.

The mafic intrusive rocks consist of massive norites and hornblendites with heterogeneous granular texture (Ma et al., 2013a,b). Trace element and Sr-Nd-Hf isotope signatures determined by Ma and coworkers for the Milin norites and hornblendites are compatible with mineral fractionation and accumulation fom a common parental magma during the early and late stages of the magma evolution. The parental magma may have generated by the interaction of upwelling asthenospheric and metasomatized lithospheric mantle. The samples (14JT50, 14JT51) from the Milin area were collected by geologist Lin Ma and are hornblendites generally composed of brown amphibole (50-60 vol.%), clinopyroxene (30 vol.%) and accessory brown mica and Fe-oxides. The amphibole grains show cores enriched in exolution lamellae of Fe-oxides. Clinopyroxene is a relict phase observed within or interstitial to the amphibole grains.

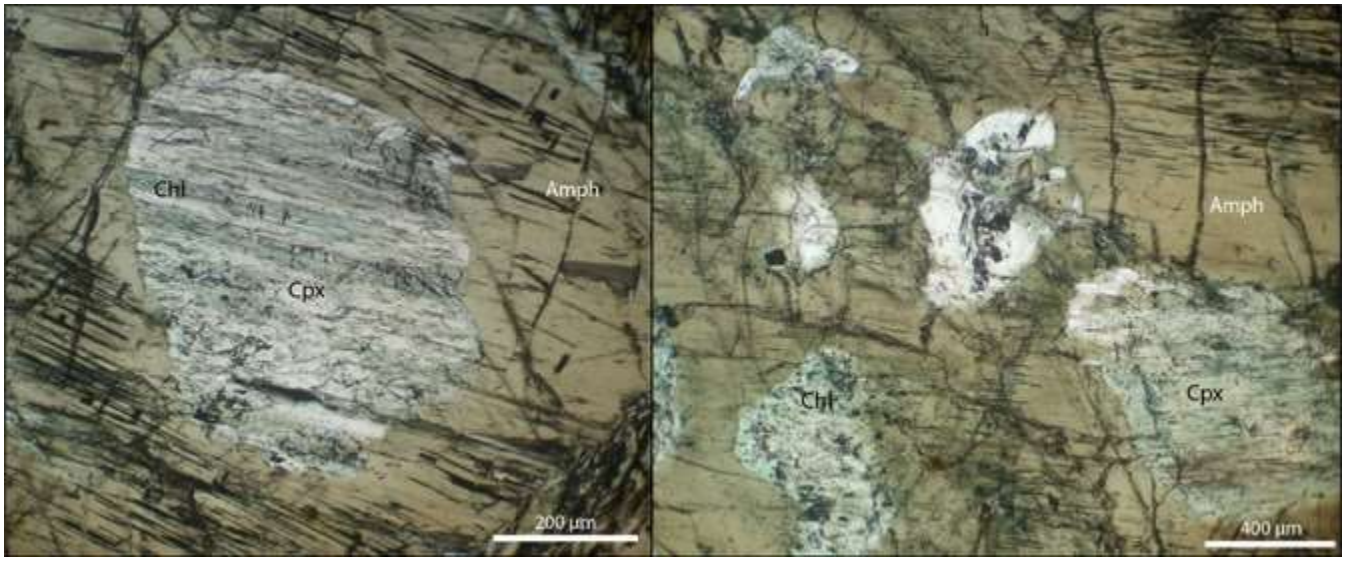

Figure 32 - Photomicrographs of polished thin section (14JT50) with amphiboles (Amph), clinopyroxene (Cpx) and chlorite (Chl) defining different textures.

2.4.5 Zagros Orogen (Sanandaj–Sirjan Zone; Aligoodarz pluton), Iran

The Zagros orogenic belt extends from the Turkish–Iranian border in the NW, to the Makran area in the SE. The orogenic belt is related to the long-standing convergence between Eurasia and Gondwana-derived continental fragments, and, in particular, it results from the collision between the Arabian and the Central Iranian microplates after the northeast-dipping subduction of the Neo Tethys oceanic lithosphere below Central Iran (e.g., Dewey et al., 1973; Sengör, 1984). From northeast to southwest, three parallel tectonic zones are distinguished (Agard et al., 2011; Alavi, 2004): (1) the Urumieh–Dokhtar magmatic arc (UDMA), (2) the Sanandaj–Sirjan Zone (SSZ), and (3) the Zagros folded-thrust belt (ZFTB) (Fig. 33a). The SSZ is of particular interest for this study. During the Mesozoic the SSZ acted as an active Andean-like margin in response to the subduction of the Neo Tethys ocean. The central sector of the SSZ is characterized by the presence of a series of arc-related calc-alkaline

granitoid complexes emplaced during the middle Jurassic. But Esna-Ashari et al. (2016) reported about the first evidence of ultramafic rocks related to such granitoid complexes, specifically in the Aligoodarz intrusive complex (Fig. 33b-c).

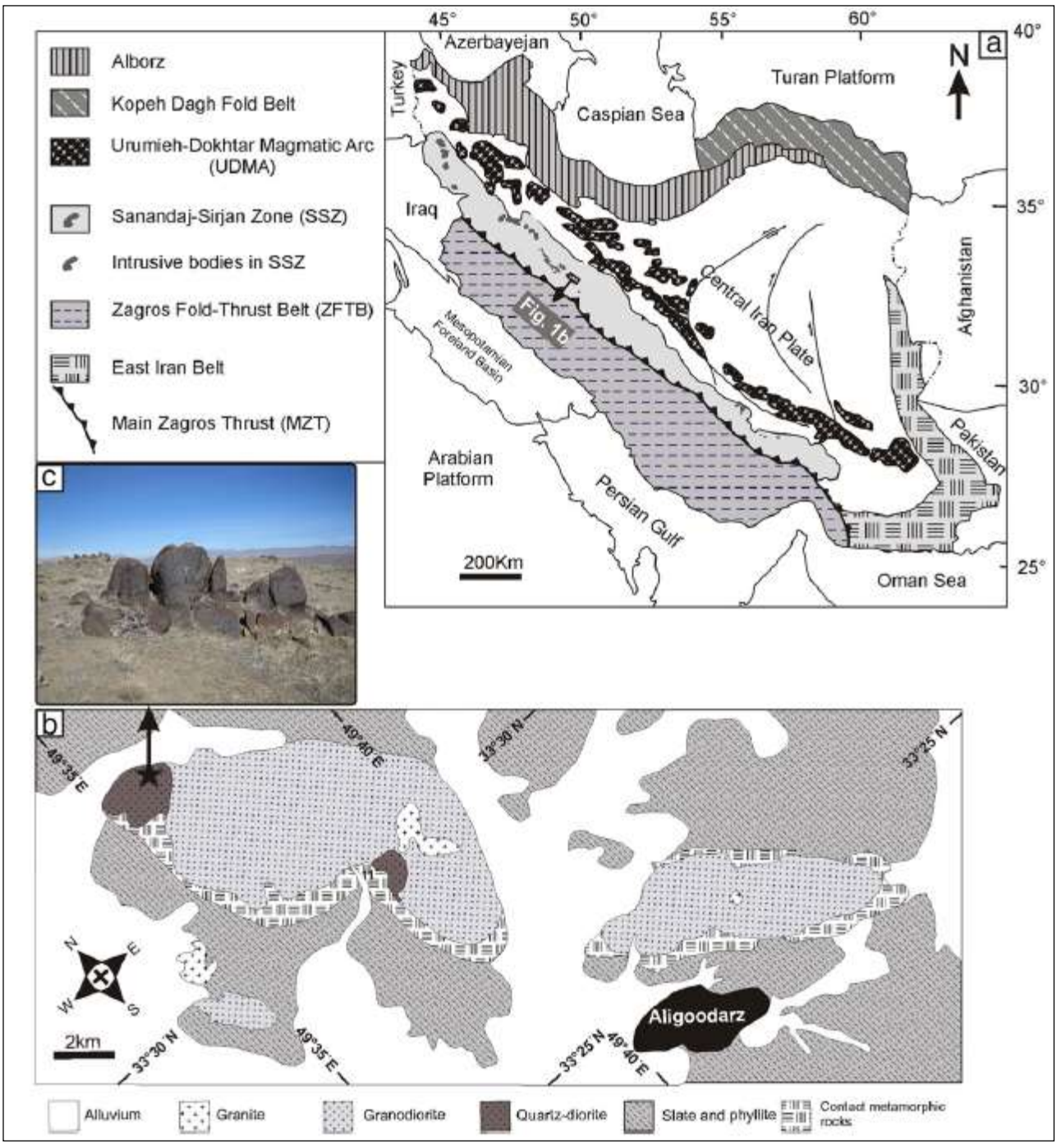

Figure 33 - (a) simplified geological map of Iran with the location of the major intrusive and volcanic rocks in the Sanandaj–Sirjan Zone. (b) Simplified lithological map of the Aligoodarz intrusive complex. The star locates the ultramafic rocks. (c) Typical outcrop of the ultramafic rocks (from Esna-Ashari et al., 2016).

The complex consists of dominant granodiorite, quartz-diorite and granite. The amphibole-bearing ultramafic rock facies are represented by medium to coarse-grained pyroxenites and hornblendites, which occur in association with the northernmost lobe made of quartz-diorite. According to the authors, amphibole, although magmatic, is late and in disequilibrium with earlier boninite-related cumulate phases olivine, clino- and orthopyroxenes. The geochemical signatures of amphibole suggest its derivation from a liquid undergoing differentiation via a melt-rock reaction process. In the model by Esna-Ashari et al. (2016) the interaction between the ultramafic cumulates and the infiltrated melt might have generated a new liquid of calc-alkaline affinity and compositionally similar to high-Mg andesites and to the quartz-diorites hosting the ultramafic cumulates. The early, boninitic magma, highly depleted in incompatible elements, would be related to partial melting of a depleted mantle wedge in response to the onset of NeoTethys subduction, while the infiltrating calc-alkaline melt would represent the mature stage of arc magmatism postdating boninite.

The sample from the SSZ (AL89) was collected by Esna-Ashari et al. (2016) and represents the olivine-hornblende pyroxenite. This rock facies consists of brown amphibole (20-30 vol.%), orthopyroxene (15-20 vol.%), olivine (10-15 vol.%) and clinopyroxene (10 vol.%) with subordinated biotite (3-5 vol.%), spinel (3-5 vol.%) and sulphides (2-3 vol.%). Brown amphibole has poikilitic texture with abundant exolution lamellae of Fe-oxides close to inclusions of relict olivine and clinopyroxene. Orthopyroxene is observed as intergranular phase and shows reaction rims with amphibole.

2.4.6 Sunda arc (Batu Hijau district, Sumbawa), Indonesia

The youngest (late Miocene) amphibole-bearing magmatic rock considered for this study comes from Batu Hijau, Sumbawa island, Indonesia, and is provided by Steve Garwin and Marco Fiorentini, University of Western Australia. Within the Sunda arc the Sumbawa island is in a pivotal position because it is located at a major structural discontinuity inducing variations in the tectonic and magmatic regimes across the volcanic arc (Fig. 34). As described by Fiorentini & Garwin (2010) and references therein, Sumbawa hosts an early Miocene-Holocene volcanic arc succession built up on oceanic crust near a continental margin (Sunda shelf) and recording a progressive change from calc-alkaline to shoshonitic character with time. Located in the SW part of the island, Batu Hijau is a mining district exploiting several Cu-Au porphyry deposits centered on diorite to tonalite/granodiorite stocks and dikes of late Miocene to Pliocene age (5.9-3.7 Ma; U-Pb zircon ages; in Garwin, 2002). The sequence is developed within a major arc-transverse oblique-slip fault zone which appears to have controlled magmatism, tectonics and sedimentation since Miocene. The Miocene low-K calc-alkaline magmatic suite is of particular interest as it is marked by a juvenile Nd signature ($^{143}Nd/^{144}Nd = 0.5130$) and by

whole-rock trace element and lead isotopic features suggestive of minimal involvement of sediment component in arc petrogenesis.

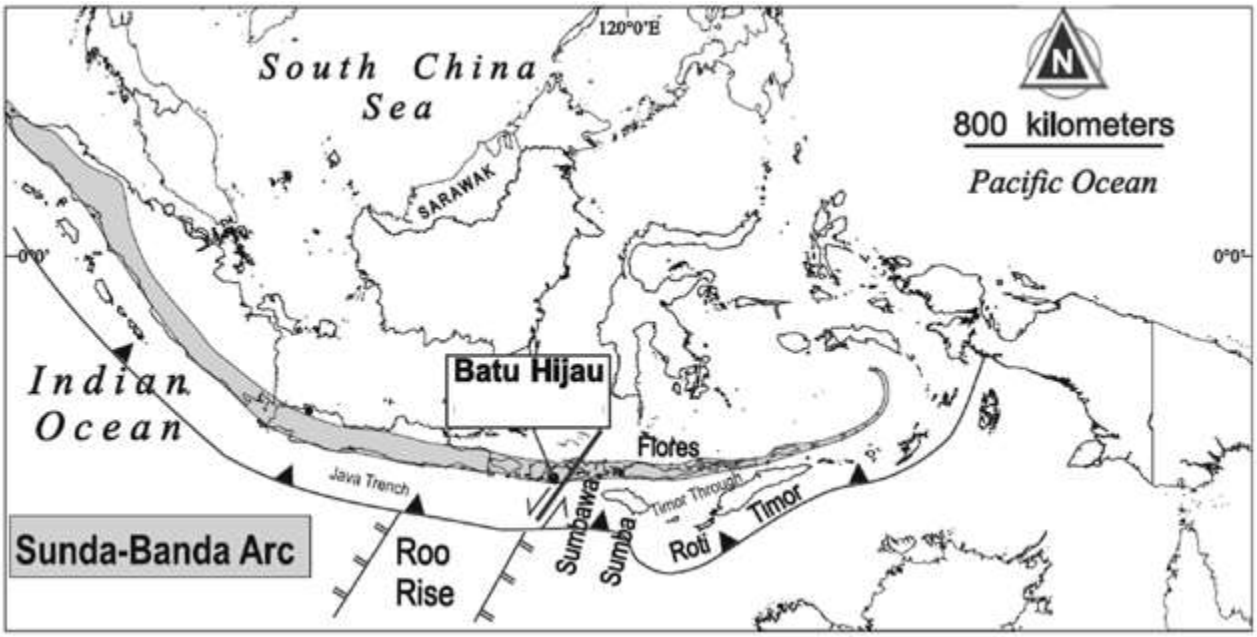

Figure 34 - Simplified map showing the Indonesian archipelago, the Roo Rise, an oceanic plateau on the subducting Indian Ocean Plate, and the location of the Batu Hijau district on the island of Sumbawa (from Fiorentini & Garwin, 2010).

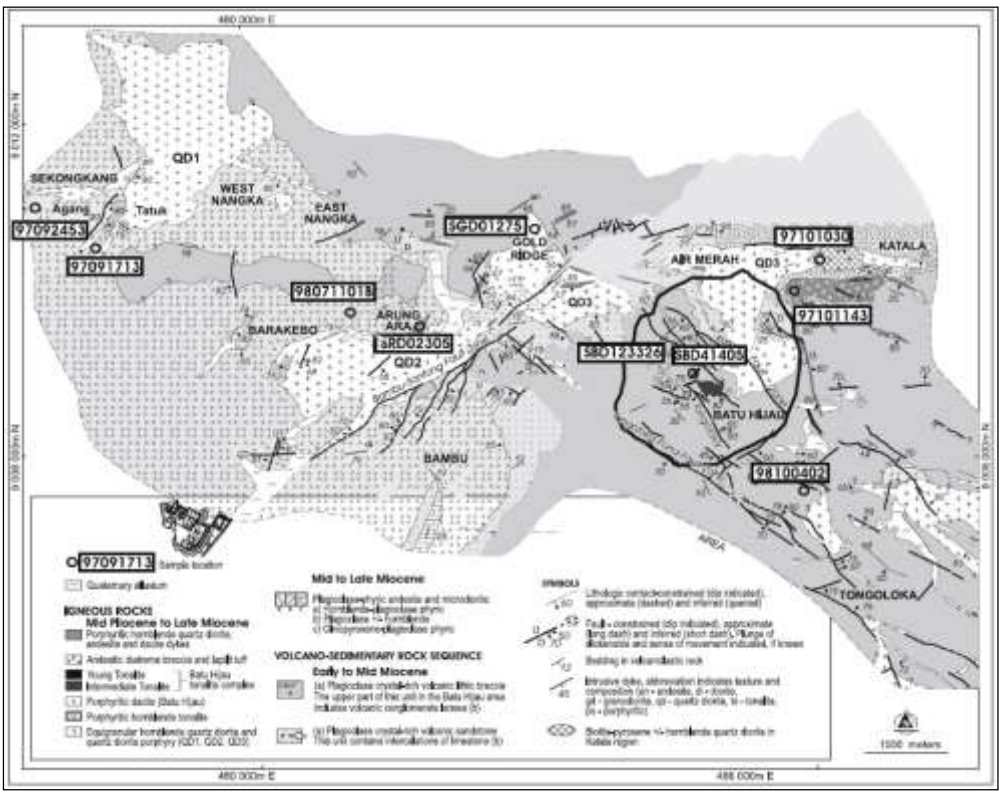

Figure 35 - Simplified geological sketch of the Batu Hijau area indicating sample (SRD02305) location (Fiorentini & Garwin, 2010).

Preliminary geochemical characterization done by Fiorentini and Garwin (2010) on primary magmatic amphiboles revealed very low B and Li concentrations and hydrogen isotope signatures consistent with an original mantle origin. Such features would reflect involvement of fluids not entirely derived from dehydration of a subducting slab during the petrogenesis of the calc-alkaline melts. According to the authors, the B- and Li-poor fluids might at least be partially derived from dehydration of uprising asthenospheric mantle. Fig. 35 shows the position of the sampling sets by Fiorentini and Garwin (2010) in relation to a simplified geological scheme of the Batu Hijau mining area.

For the present study, the sample (SRD02305) was collected by Steve Garwin (2002) and is representative of the porphyritic hornblende tonalite facies consisting of plagioclase (60-50 vol.%), amphibole phenocrysts (15 vol.%) and quartz (15 vol.%) (Fig. 36). The sample was selected from one 4.99 Ma old porphyritic tonalitic stock (Fig. 36).

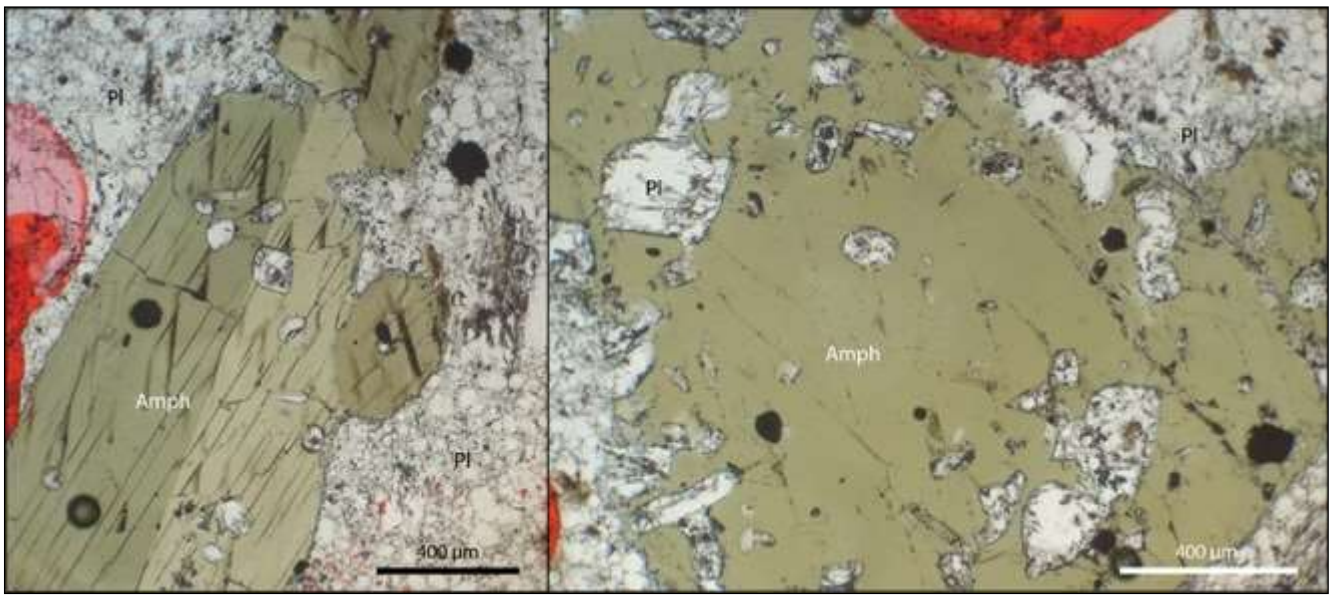

Figure 36 - Photomicrographs of polished thin section (SRD02305) displaying different textures between green amphibole (Amph) and plagioclase (Pl).

2.4.7 Alkali amphibole megacrysts, USA

In alkalic basalts mantle-derived amphiboles of kaersutitic to pargasitic composition may be present as poikilitic grains, veins in peridotites and pyroxenites, and interstitial grains within inclusions of chromium-spinel peridotites, and as megacrysts. Occurrences of the vein and megacryst types have been reported from several sites in USA. These US amphibole types attracted attention since the 50s (e.g., Campbell & Schenk, 1950) and were studied to some depth between the 70s and 90s (e.g., Garcia et al., 1980 and references therein; Wilshire et al., 1980; Bell & Hoering, 1994). In particular, the past authors considered the origin of amphibole megacrysts as problematic: interpretations ranged from amphibole megacrysts as being either cogenetic with the host magma or completely unrelated, especially

on the basis of different isotopic signatures. Sr isotope signatures of the megacrysts are affine to MORB, while preliminary results of bulk hydrogen isotope and H_2O content analyses by Bell and Hoering (1994) showed high potential for detecting preserved primary H and D/H signatures in such amphiboles. Therefore, amphibole megacrysts collected by Massimo Tiepolo were included in the sample batch for this study. The amphibole megacrysts come from two localities in the southwest USA considered in the works quoted above (see locations in Fig. 37).

Figure 37 - Location of the amphibole megacrysts from Dish Hill, California, and Hoover Dam, Arizona. (Modified after Righter & Carmichael, 1993).

The first sample is from alkali olivine basalt dikes which crop out along the U.S. Highway 93 at Hoover Dam, northwest Arizona. The dikes were emplaced in fanglomerate deposits of Quaternary age (Campbell and Schenk, 1950) (Fig. 38). The dikes show conspicuous concentrations of kaersutite megacrysts (up to 10 cm long), as shown in the samples of Fig. 39.

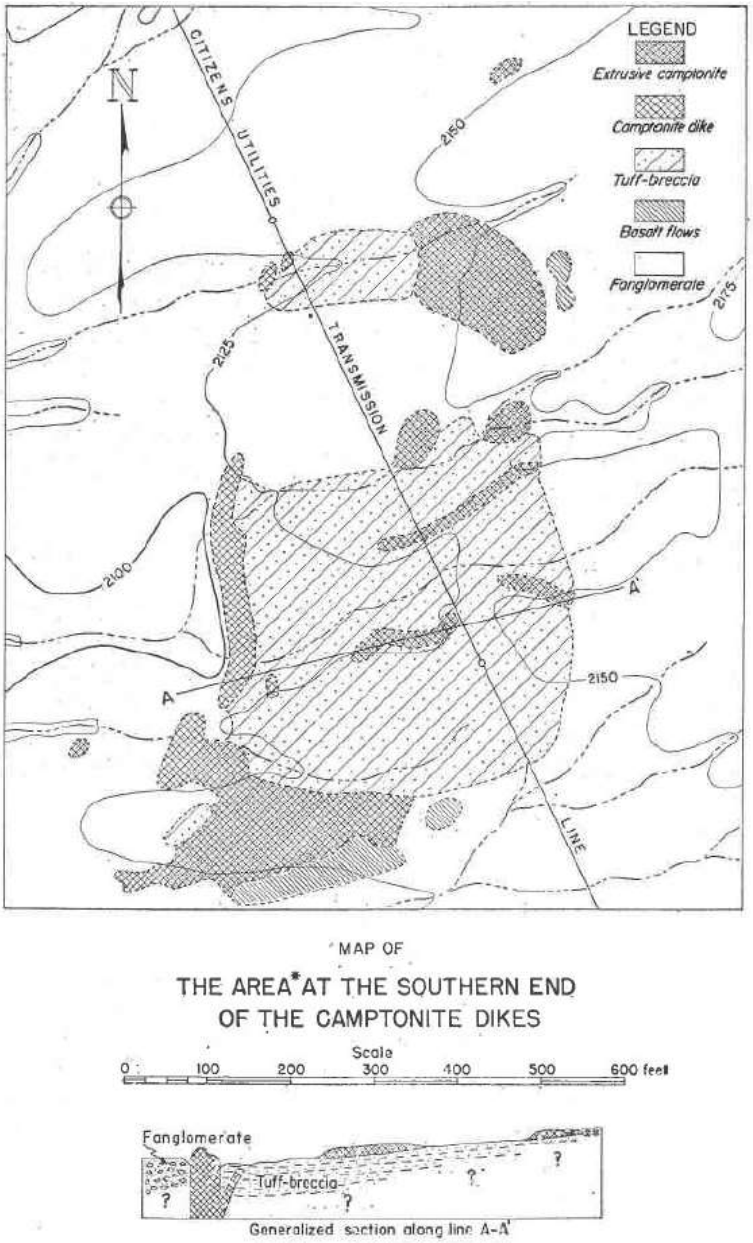

Figure 38 – Simplified geological sketch of the camptonite dike of Hoover Dam, Arizona (USA). (From Campbell and Schenk, 1950).

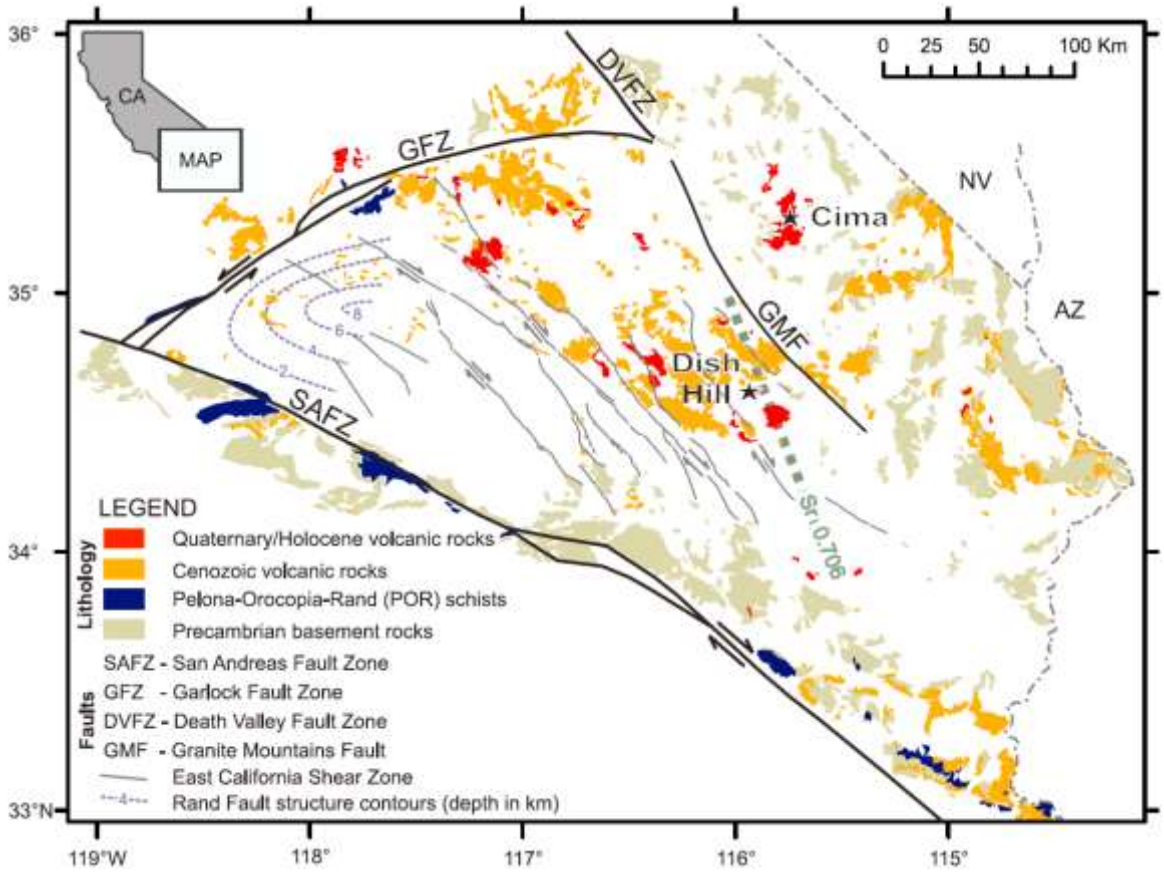

Figure 39 - Map showing the locations of mantle xenoliths from Dish Hill, California (from Luffi et al., 2009).

The second sample is from the Dish Hill complex (Mojave Desert, California – see Fig. 40 for location and schematic geology). The complex consists of two volcanic cones, Dish Hill Crater and Siberia Crater, and is well known because of the abundance of mantle-derived xenoliths and megacrysts in the lavas.

Figure 40 – Samples of alkali olivine basalt with amphibole megacrysts from Hoover Dam, Arizona.

Such xenoliths were considered in a recent work, Luffi et al. (2009), for constraining a model of lithospheric mantle duplex beneath the central Mojave Desert by means of whole-rock chemistry, clinopyroxene trace element and Nd isotope data. The imbricated nature of the sub-Mojave lithosphere would be consequent to the low-angle subduction (underthrusting) of the Farallon plate beneath North America during the Laramide orogeny.

Xenoliths consist of spinel lherzolites, dunites and pyroxenites and may contain megacrysts of amphibole (with variable composition) and phlogopite, and phenocrysts of clinopyroxene, olivine, spinel, magnetite and apatite (Wilshire et al., 1971, 1972).

Table 2.1 - Summary of the petrography and ages of the selected samples.

	Locality Sample name	Rock type	Main assemblage	Accessory minerals	Age
Australia Agnew- Wiluna GB	Mt. Keith MKD1	Pyroxenite	pyroxene - brown amph	olivine - sulphides spinel	2.7 Ga
	Mt. Clifford 85437	Pyroxenite	olivine - pyroxene	brown amph - Cr-spinel brown mica -magnetite	2.7 Ga
Canada Abitibi GB	Theo's Flow T-2	Peridotite	clinopyroxene	brown amph - Cr-spinel magnetite - sulphides	2.7 Ga
	Boston Creek B5	Peridotite	olivine - clinopyroxene	brown amph - Cr-spinel magnetite - talc chlorite - tremolite	2.7 Ga
	Ghost Range GR1-GR2	Peridotites	olivine - clinopyroxene orthopyroxene	brown amph - brown mica Cr-spinel	2.7 Ga
Russia Pechenga Complex	Pilgüjarvi sill Pilg8-38; 106-44;	Peridotites	olivine - clinopyroxene	brown amph - brown mica magnetite - sulphides	1.98 Ga
	116-6	Magnetite-peridotite	magnetite - ilmenite olivine	clinopyroxene -sulphides brown amph - brown mica	1.98 Ga
	Kammikivi sill 57HV28	Peridotite	olivine - clinopyroxene	brown amph - brown mica Cr-spinel - magnetite	1.98 Ga
	Nyasyukka dike complex N2; N3	Peridotites	olivine - brown amph clinopyroxene	brown mica - plagioclase magnetite - sulphides ilmenite	1.96 Ga

Continued Table 2.1

Antarctica Ross Orogen	Husky Ridge TT329	Qtz-diorite	brown amph - green amph plagioclase	clinopyroxene brown mica - qtz titanite - sulphides	512 Ma
Italy Alps Orogen	Mt. Mattoni MAT1; MAT2; MAT15	Hornblendites	brown amph - olivine	clinopyroxene green amph - magnetite sulphides	40 Ma
Alps Orogen	Val Masino VS9	Hornblendite	brown amph- clinopyroxene olivine	green amph - magnetite sulphides	30 Ma
Japan Japan Arc	Taku TK1b	Gabbrodiorite	brown amph - green amph clinopyroxene - orthopyroxene olivine	plagioclase - sulphides Fe-oxides	120 Ma
	Zenifudo ZN5	Hornblendite	brown amph - clinopyroxene orthopyroxene - olivine green amph - plagioclase	brown mica - Fe-oxides	76 Ma
	Hase no Yatsu HSY3B	Hornblendite	brown amph - clinopyroxene orthopyroxene - olivine green amph	brown mica - Fe-oxides	117 Ma
Tibet Himalayan Orogen	Gangdese batholith 14JT50; 14JT51	Hornblendites	brown amph - green amph clinopyroxene	brown mica - Fe-oxides	82 Ma
Iran Zagros Orogen	Sanandaj-Sirjan Zone; Aligoodarz pluton AL89	Olivine-hornblende Pyroxenite	brown amph - clinopyroxene orthopyroxene - olivine	brown mica - spinel sulphides	165 Ma
Indonesia Sunda arc	Batu Hijau district Sumbawa	Porphyritic hornblende Tonalite	plagioclase - brown amph qtz	Fe-oxides	4.9 Ma
USA	Hoover Dam	Alkali amphibole megacrysts	brown amphibole		2-3 Ma
	Dish Hill	Alkali amphibole megacrysts	brown amphibole		2-3 Ma

Table 2.2 - Modal proportions of the minerals of the selected samples.

Samples	Location	Olivine	Clinopyroxene	Orthopyroxene	Brown Amphibole	Green Amphibole	Fe-oxides	Sulphide minerals	Brown Mica	Plagioclase	Quartz
MKD 1	Australia	20%	30%		15%	20%	10%	2%	3%		
85437	Australia	15%	40%		15%	20%	7%	1%	2%		
B-5	Canada	60%	20%		10%		7%	2%	1%		
T 2	Canada	60%	30%		3%		4%	2%	1%		
T 3	Canada	55%	35%		3%		5%	2%			
GR-1	Canada	33%	27%	20%	7%		8%	3%	2%		
GR-2	Canada	35%	25%	20%	7%		8%	3%	2%		
PILG 8-38	Russia	62%	18%		10%		5%	2%	3%		
106 44	Russia	70%	10%		10%		4%	3%	3%		
116-6	Russia	45%	15%		3%		35%	1%	1%		
57A-HV-28	Russia	70%	20%		5%		3%	1%	1%		
57B-HV-28	Russia	70%	25%		5%		3%	1%	1%		
N-2	Russia	30%	15%		35%		8%	5%	7%		
N-3	Russia	30%	15%		35%		8%	5%	7%		
TT329	Antarctica		5%		50%	22%	3%	1%	3%	15%	1%
Mat 15	Italy	20%			35%	40%	4%	1%			
VS-9	Italy	10%	15%		55%	15%	3%	2%			
TK1B	Japan	10%	18%	8%	37%	20%	1%	1%		5%	
ZN5	Japan	10%	14%	10%	34%	15%	1%	1%		15%	
HSY3B	Japan		40%		40%	10%	9%	1%			
14JT50	Tibet		27%	1%	70%		1%	1%			
AL 89	Iran	15%	10%	15%	20%	30%	5%	2%	3%		
SRD	Indonesia				15%		5%		5%	60%	15%

Chapter 3

Geochemical characterization of amphibole

3.1 Methods

Major elements analysis

In-situ major element concentrations in olivine, clinopyroxene and amphibole grains were analysed with a Jeol JXA - 8200 electron Super probe at Università degli Studi di Milano, Milan (Italy). The microprobe is equipped with WDS-wavelength-dispersive spectrometers, electron-dispersive spectrometer and a cathodoluminescence detector. Operating conditions included a beam size of 5 μm and current of 20 nA, with an accelerating voltage of 15 kV. All data were obtained using wavelength-dispersive spectrometers and counting times of 20 s on peak and 20 s on background.

Trace elements analysis

In-situ trace element concentrations of olivine, clinopyroxene and amphibole grains were determined by laser ablation Inductively Coupled Plasma-Mass Spectrometry (LA-ICP-MS) at the Istituto di Geoscienze e Georisorse – Consiglio Nazionale delle Ricerche (IGG-CNR), Pavia (Italy). The instrument couples a 266 nm Nd:YAG laser microprobe (Brilliant, Quantel) to a quadrupole ICP-MS system (DRCe from PerkinElmer). NIST-SRM612 was used as an external standard, whereas 43Ca or 29Si were adopted as internal standards, depending on the analysed mineral. In each analytical run the USGS reference sample BCR2 was analysed together with the unknowns for quality control. Precision and accuracy are better than 5% and 10%, respectively.

Sample preparation for Secondary ion Mass Spectrometry analysis

The samples were prepared for in-situ secondary ions mass spectrometry (SIMS) analysis at the Università degli Studi di Milano and at the IGG-CNR of Pavia. The Precambrian amphibole grains most suitable for the analysis were selected on the polished thin sections and then drilled out in the form of a core of 2 mm-diameter. The cores were cleaned with acetone and embedded in indium mount. For the In mount preparation the procedure described by the SIMS laboratory of the University of Edinburgh was followed. The indium was placed in an Al-well in the middle of an Al-disk. Successively, the Al-

holder was transferred to the hot plate set at ~180 °C and the indium allowed to melt. The indium was pressed into the Al-well and was applied a sheet of Melinex to protect the indium surface by the steel block of the hydraulic press. This ensures that the steel block does not bond to the surface of the indium and produces a clean scratch free surface. The cores with selected amphiboles were gently pushed into the indium with the hydraulic press, using again the Melinex sheet to protect the samples into the indium.

Secondary Ion Mass Spectrometry

The ion probe employs a focused primary ion beam, generated by an ion gun, which bombards the sample surface and sputters material of the domain to be analysed. While many of the matrix atoms are sputtered away as neutral particles, some are released as ions and ionized molecules. The secondary ion beam is extracted by using an accelerating voltage and an ion optical system followed by energy filtering which leads to a mass spectrometer for nominal mass (mass-to charge ratio) separation and finally to an ion counting unit. The SIMS primary beam produces ions from solid samples without prior vaporization. A basic SIMS instrument will, therefore, consist of a primary beam source (usually O^{2+}, O^-, Cs^+, Ar^+, Ga^+ or neutrals) to supply the bombarding species, a mass analyser to isolate the ion of interest (quadrupole, magnetic sector, double focusing magnetic sector or time of flight) and an ion detection system to record the magnitude of the secondary ion signal (photographic plate, Faraday cup, electron multiplier or a CCD camera and image plate).

Hydrogen and oxygen isotopic analytical method

Igneous amphiboles were analysed in-situ for δD and $\delta^{18}O$ ratio with a CAMECA IMS 1270 E7 ion microprobe at the Centre de Recherche Pétrographiques et Géochimiques-Centre National de la Recherche Scientifique CRPG-CNRS of Nancy (France). The stable isotopic compositions of low-mass (light) elements such as oxygen and hydrogen are normally reported as "delta" (δ) values in parts per thousand (denoted as ‰) enrichments or depletions relative to a standard of known composition. The δ values are calculated by:

$(\text{in } ‰) = (R_{sample}/R_{standard} - 1) \times 1000$

where "R" is the ratio of the heavy to light isotope in the sample or standard. For the element oxygen, the average terrestrial abundance ratio of the heavy to the light isotope is 1:500 (oxygen) and the ratio 2H:1H is 1:6410. A positive d value means that the sample contains more of the heavy isotope than the standard; a negative d value means that the sample contains less of the heavy isotope than the standard. The spots for SIMS analysis were carried out on fresh amphibole grain surface, far from scratches. The following procedure is described in Deloule et al. (1991a). The D/H ratio of amphibole can thus be

measured in situ with a precision of ± 10‰. The samples were goldcoated. The negative primary oxygen beam, with intensity ranging from 2 to 5 nA, is focused to produce a beam 10 μm wide rastered over 25 μm. Mass resolution at 1300 is sufficient for separating deuterium from hydrogen ions. No energy filtering is applied and the energy slit is kept wide open. Moisture is removed by baking the sample and ion probe at 120°C, and using a liquid nitrogen trap. The electron multiplier is used in the counting mode. The counting rates on the H peak range from 30,000 to 60,000 cps. Counting times of 3, 2 and 15 seconds are used for H, H2 and D, respectively, and waiting time is 1.5 s.

Oxygen isotopes were analysed using the CRPG-CNRS Cameca 1270 at Nancy (France) as O^- ions produced with a $^{133}Cs^+$ primary beam at 10 kV and at 5 nA intensity. The spot size varied from 30 to 50 μm with a depth of about 2 μm. The normal incidence electron flood gun was used to compensate for sample charging during analysis. Secondary negative ions were accelerated to 10 kV and analysed without energy filtering at a mass resolution (M/ΔM) of 5000. Oxygen isotopes were measured in multicollection mode on two off-axis Faraday cups (L'2 and H1). Secondary ion intensities ranged from 3 to 8 x 10^6 cps on ^{18}O and the typical acquisition time was 60 s per analysis. The standard use are the amphiboles Bamble, Kipawa, Seljas, Illimaussac and Bipa (Deloule et al., 1991b)

Hydrogen, Fl and Cl concentrations analytical method

The H, F and Cl concentration were measured with the ion probe Cameca IMS 4f, at the CNR-Istituto di Geoscienze e Georisorse (IGG)-Unità di Pavia, following the method described in Gentili et al. (2015). Analyses were carried out with a primary $^{16}O^-$ ion beam characterized by an acceleration voltage of -12.5kV and a current intensity of 5 nA. Spot diameter is 8-10 μm. Prior the analysis the sample and the standard for H were cleaned, platinum-coated (about 40 nm) and placed in the sample chamber of the ion microprobe to be degassed for a few days to a vacuum of $2*10^{-9}$ torr. The analyses consisted in the acquisition of the signals of masses: $^1H^+$, $^{19}F^+$, $^{35}Cl^+$, $^{37}Cl^+$ and $^{30}Si^+$.The reference samples used for the calibration of the instrument and for the conversion of ionic signals in concentration (ppm wt) were for H, the amphiboles: DL-5 (Ottolini et al., 1995) and LC, belonging to the laboratory-working curve for H in silicates (Ottolini et al., 1994). The standards used for F and Cl were kearsutites Soda Spring (KSS), belonging to the laboratory-working curve for F in silicates (Ottolini et al., 1994), and scapolite USNM R66001 (Ottolini and Le Févre, 2008), respectively. Analytical accuracy is estimated to be better than 10% for the concentration of H (conventionally quantified as H_2O wt.%), 15% for F (ppm) and 20% for Cl (ppm).

3.2 Major, trace elements and isotope compositions of Archean and Early Proterozoic samples

The major and trace element compositions of the samples are reported in Appendix A and B, respectively.

3.2.1 Agnew-Wiluna greenstone belt (Australia)

Mount Keith (sample MKD1)

Amphibole has pargasitic composition, with Mg-number [Mg/(Mg+Fe_{TOT})] about 0.80 mol (Fig. 41). The TiO_2 mean content is 2.60 ± 0.95 wt.% and alumina shows homogenous values (10.71 ± 0.19 wt.%). Titanium has variable contents in comparison with Mg-number whereas Al_2O_3 does not show correlation with Mg-number. Calcium and FeO_{tot} show average contents of 11.98 ± 0.27 wt.% and 7.41 ± 0.16 wt.%, respectively. The Na_2O average value is 2.5 ± 0.07 wt.%, whereas the K_2O values vary in the range 0.71–0.91 wt.% (Fig. 41; Tab. 1 Appendix A).

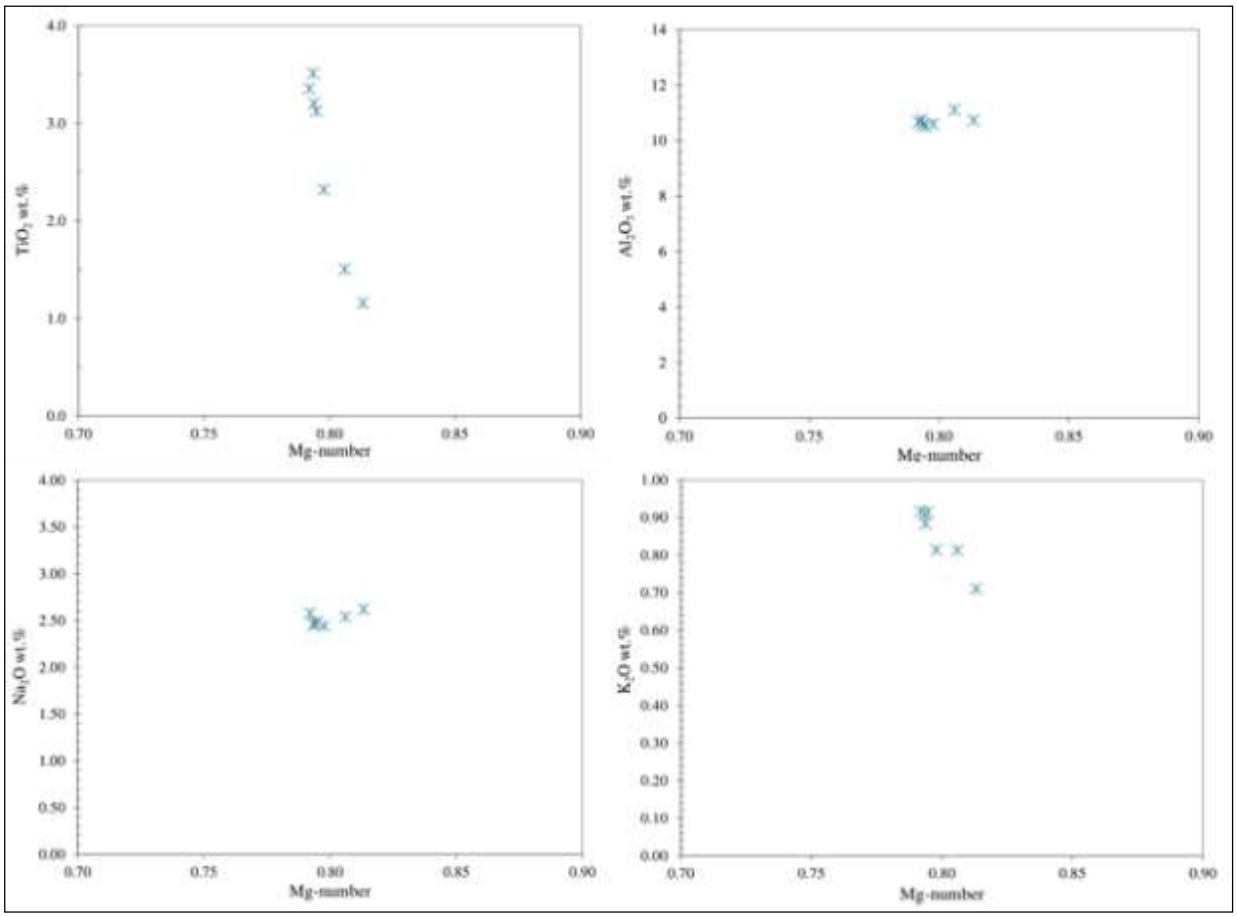

Figure 41 – Mg-number vs TiO_2, Al_2O_3, Na_2O and K_2O contents of amphibole from Mt Keith, Agnew-Wiluna GB, Australia.

The chondrite-normalized REE patterns are hump-shaped and show slight depletion in LREE (La_N/Sm_N = 0.68 ± 0.21; La_N/Yb_N = 1.39 ± 0.39), with almost flat HREE (Gd_N/Yb_N = 1.83 ± 0.2) which are approximately 90 times the CI chondrite values (Fig. 42; Tab. 1 Appendix B). The Europium is depleted into amphiboles, with Eu/Eu* ratio around 0.55. The chondrite-normalized patterns of incompatible elements exhibit peculiar negative Li, Rb, B, Sr and Pb, and moderate negative Eu and Zr anomalies (Fig. 43). Conversely, the patterns show a marked positive anomaly for Ba. The Nb/Ta and Zr/Hf mean ratios are 17.43 and 24.75, respectively. About the LILE, as mentioned before Ba has positive anomaly (Rb/Ba = 0.02) and is 66 times the chondrite value. The Sr (49.11 ppm) and Rb (3.22 ppm) mean values are 6.73 and 1.40 times the CI chondrite, respectively. The Cr contents are variable in the range 4566-8703 ppm, whereas Ni, Sc and V average values are 873 ± 38 ppm, 90 ± 11 ppm and 681 ± 45 ppm, respectively (Tab. 1 Appendix B).

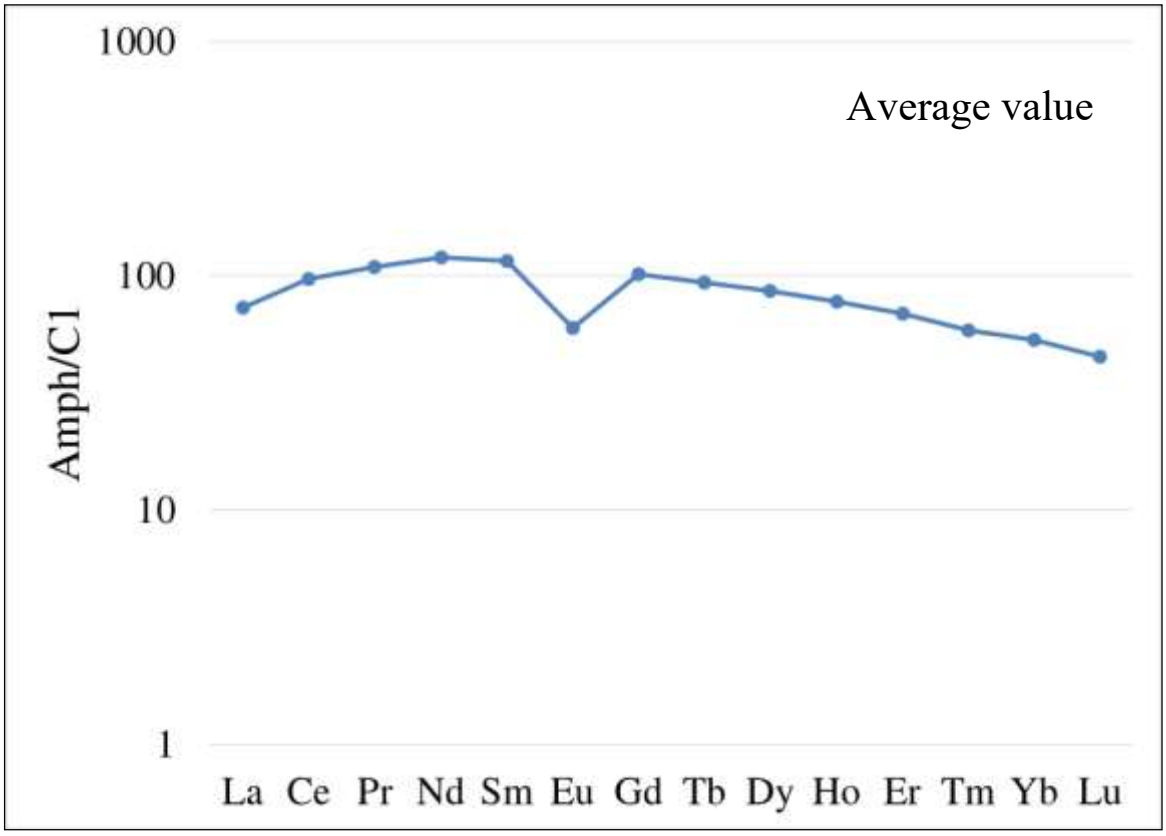

Figure 42 – Chondrite-normalized REE pattern of amphibole from Mt. Keith, Agnew-Wiluna greenstone belt (C1 chondrite from McDonough & Sun, 1995).

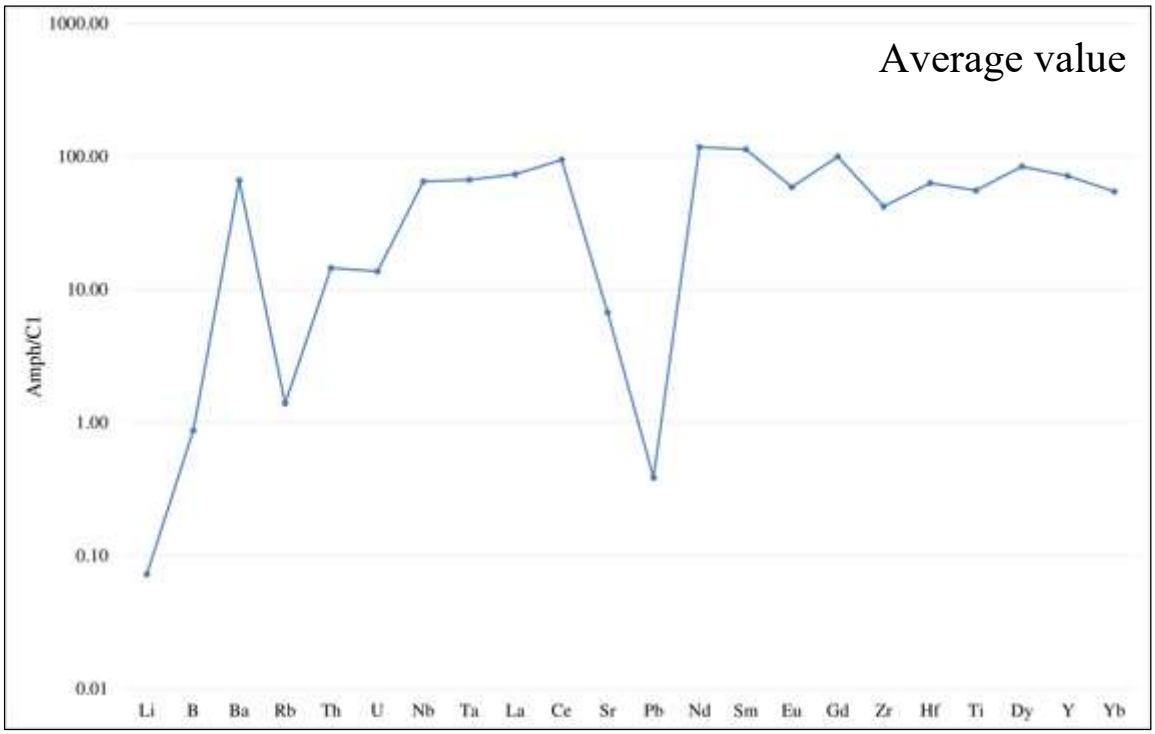

Figure 43 - Chondrite-normalized incompatible pattern of amphibole from Mt. Keith, Agnew-Wiluna greenstone belt (C1 chondrite from McDonough & Sun, 1995).

In-situ ion probe measurements reveal an average H_2O contents of 0.81 ± 0.03 wt.% (Tab. 43 Appendix B). The average contents of fluorine and chlorine are 333 ppm and 3926 ppm, respectively. Li and B mean values are 0.11 ± 0.04 ppm and 2.12 ppm, respectively (Tab. 43 Appendix B). The isotopes in-situ analyses by ion probe reveal for the δD and $\delta^{18}O$ ratios mean values of -115.6 ± 6.7 ‰ and 5.0 ± 0.3 ‰, respectively (Tab. 47 Appendix B).

Spinel from Mt. Keith pyroxenite has homogeneous composition. Spinel is Cr-rich (Cr_2O_3 = 32.5-33.2 wt.%), with variable titanium content (TiO_2 = 0.77-1.34 wt.%). MgO contents differ from 2.9 to 3.7 wt.%, whereas iron (FeO_T) mean value is 49.7 wt.%. Al_2O_3 and MnO contents are in the range 10.7-11.1 and 0.6-0.9 wt.%, respectively.

Mount Clifford (sample 85437)

Amphibole has pargasitic composition and has Mg-number values in the range 0.75-0.78 mol. The TiO_2 contents are variable in the range between 2.69 and 4.06 wt.%. Alumina values differ between 8.45 and 11.1 wt.%. Titanium and Al2O3 do not show correlation with Mg-number. CaO and FeO_{tot} have average values of 11.66 ± 0.28 wt.% and 8.79 ± 0.34 wt.%, respectively. The Na_2O content is homogeneous in the range 2.6-3 wt.%, as well as the K_2O which average value is 0.45 ± 0.07 wt.%. Sodium and potassium have moderate positive correlation with Mg-number (Fig. 44; Tab. 2 Appendix A).

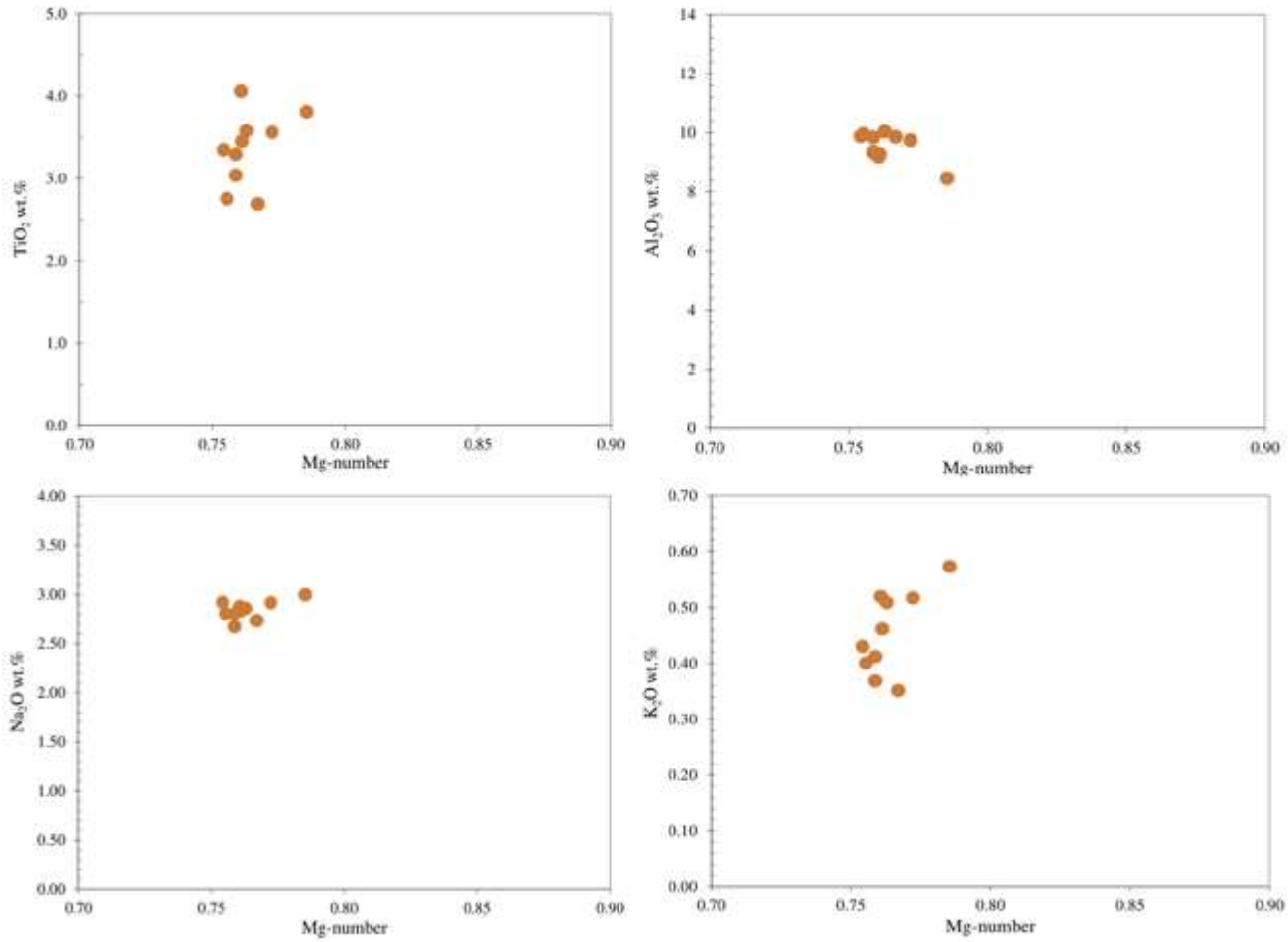

Figure 44 - Mg-number vs TiO_2, Al_2O_3, Na_2O and K_2O contents of amphibole.

The chondrite-normalized REE patterns are hump-shaped and show slight enrichment in LREE compared to HREE (La_N/Sm_N = 0.79 ± 0.25; La_N/Yb_N = 1.31 ± 0.12) that are almost flat (Gd_N/Yb_N = 1.53 ± 0.57) which are approximately 130-170 times the CI chondrite values (Fig. 45; Tab. 2 Appendix B). The europium value is characterized by a marked negative anomaly (Eu/Eu* = 0.42). The chondrite-normalized incompatible patterns of amphibole exhibit peculiar negative Rb, B, Sr, Pb, Eu and Ti relative to the neighbouring elements (Fig. 46). The Nb/Ta and Zr/Hf ratios are 21.70 and 38.55, respectively. Barium has value roughly 32 times the CI chondritic and Rb/Ba ratio of 0.03. The Ni and V contents are homogeneous which mean values are 569 ± 29 ppm and 810 ± 39 ppm, respectively. However, Cr and Sc values are variable in the ranges 3686-5947 ppm and 31.38-81.79 ppm, respectively (Tab. 2 Appendix B).

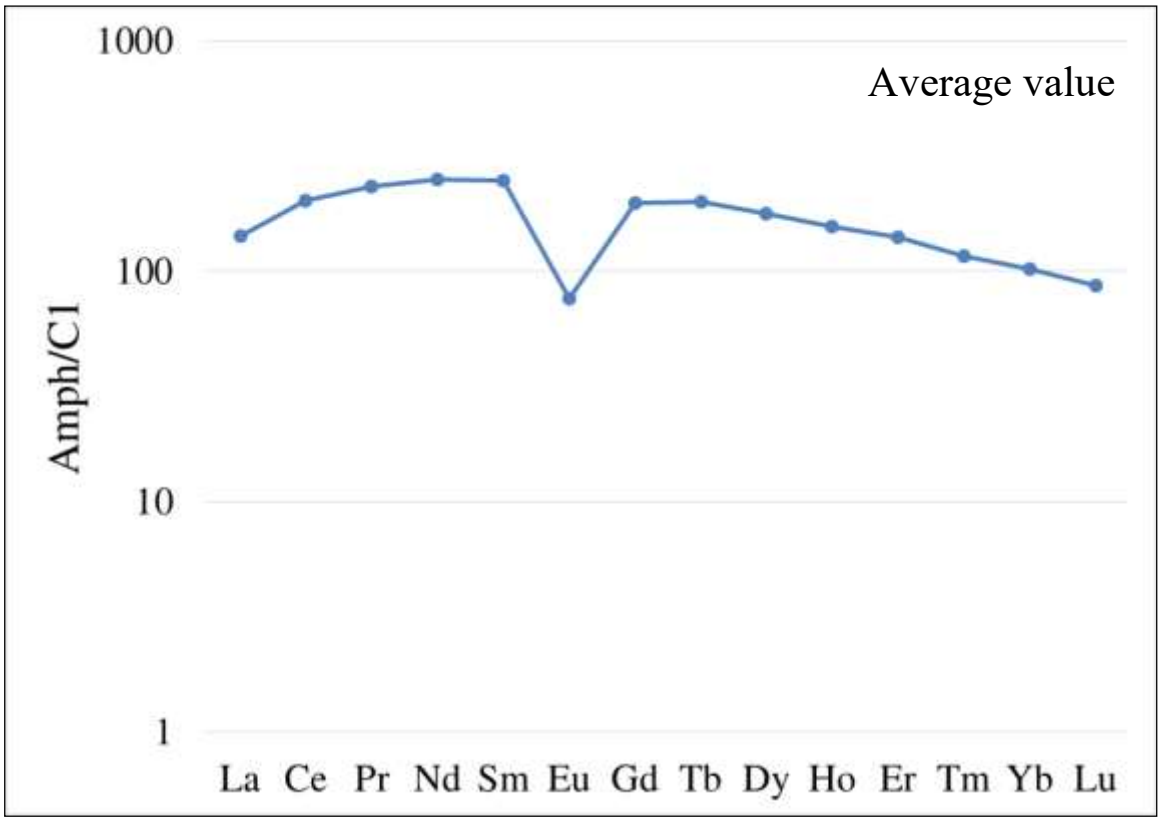

Figure 45 - Chondrite-normalized REE pattern of amphibole from Mt. Clifford, Agnew-Wiluna greenstone belt (C1 chondrite from McDonough & Sun, 1995).

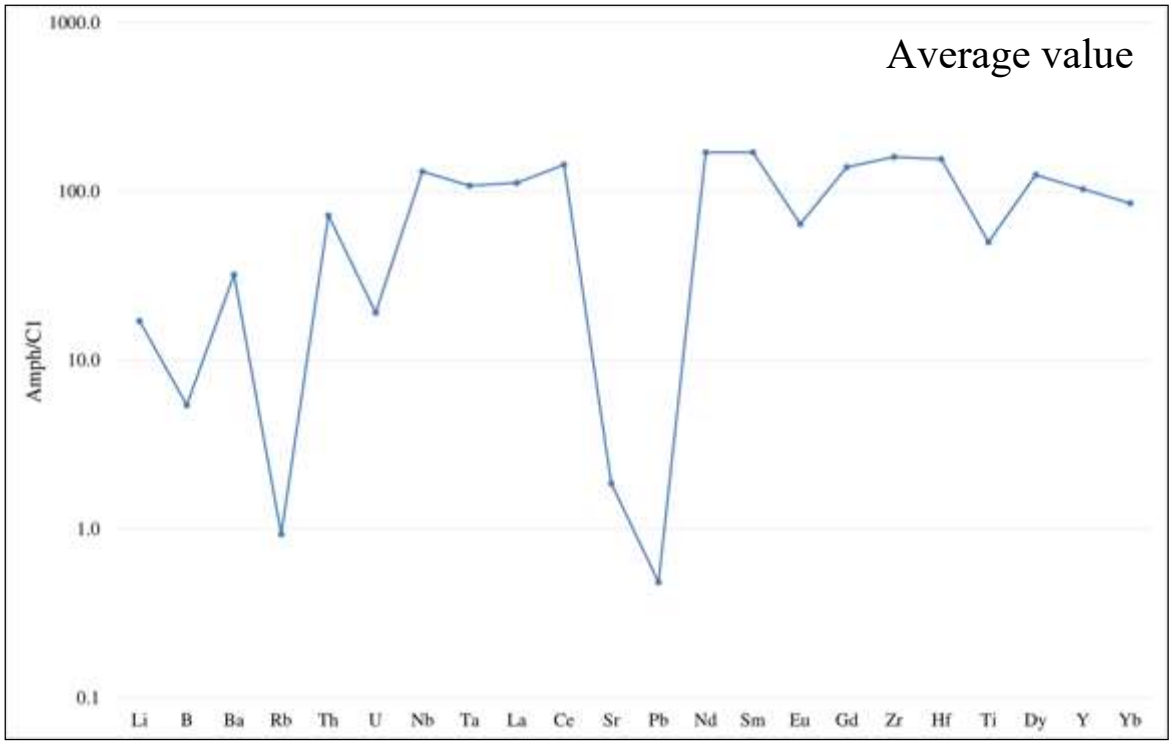

Figure 46 - Chondrite-normalized incompatible pattern of amphibole from Mt. Clifford, Agnew-Wiluna greenstone belt (C1 chondrite from McDonough & Sun, 1995).

In-situ ion probe measurements reveal an average value for water of 0.73 ± 0.09 wt.% (Tab. 43 Appendix B). The contents of fluorine and chlorine are 347 ± 80 ppm and 4421 ± 339 ppm, respectively. Li and B mean contents are 2.14 ± 0.40 ppm and 4.96 ± 1.08 ppm, respectively (Tab. 43 Appendix B). The ion probe isotopes analyses show a δD average value of -129.6 ± 11 ‰ and low $\delta^{18}O$ average value of 2.5 ± 0.42 ‰ (Tab. 47 Appendix B).

3.2.2 Abitibi greenstone belt (Canada)

Theo's Flow (sample T2)

Clinopyroxene shows moderate variability in its Mg-number values (0.8-0.85 mol), which is negatively correlated with TiO_2 (0.27-0.47 wt.%) and Al_2O_3 (1.56-2.23 wt.%). The Cr_2O_3 contents (0.47-1.12 wt.%) are positively correlated with Mg-number, whereas the Na_2O content (0.29 wt.%) does not show correlation with Mg# (Fig. 47; Tab. 3 Appendix A).

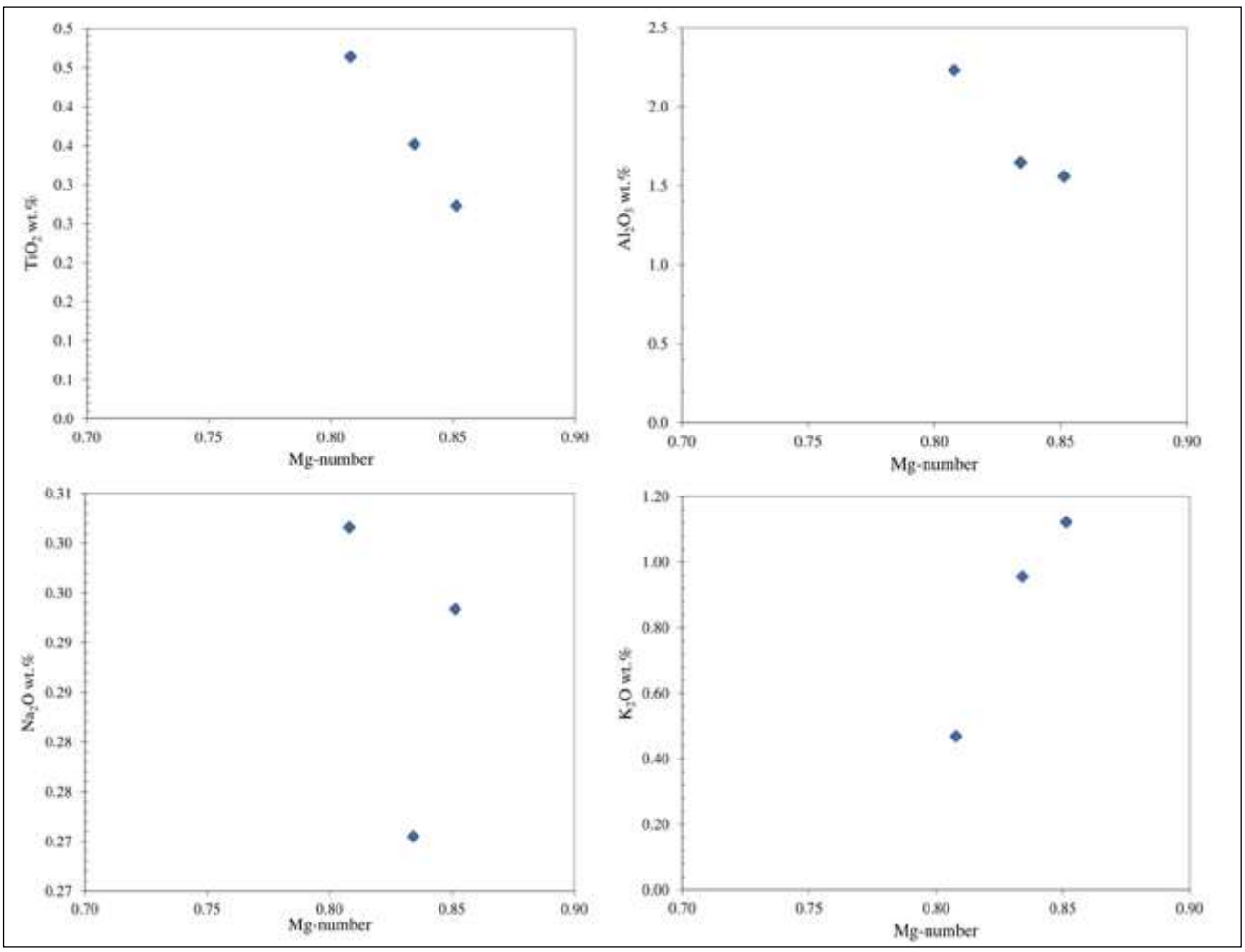

Figure 47 - Mg-number vs TiO_2, Al_2O_3, Na_2O and K_2O contents of clinopyroxene from Theo's Flow, Abitibi greenstone belt.

The chondrite-normalized REE patterns of clinopyroxene are characterized by a depletion in light REE (LREE) (La_N/Sm_N = 0.15; La_N/Yb_N = 0.28) relative to heavy REE (HREE) values that are almost flat (Gd_N/Yb_N = 1.38) at about 6-8 times C1 chondrite (Fig. 48; Tab. 3 Appendix B). The Eu/Eu* ratio has value of 0.95. The chondrite-normalized patterns of incompatibles exhibit depletion in Th, Nb, Pb and Zr (Fig. 49). The Ni and Cr values are in the range 325-381 ppm and 4658-6672 ppm, respectively. The Sc and V contents are 64.79 ppm and 192.72 ppm, respectively (Tab. 3 Appendix B).

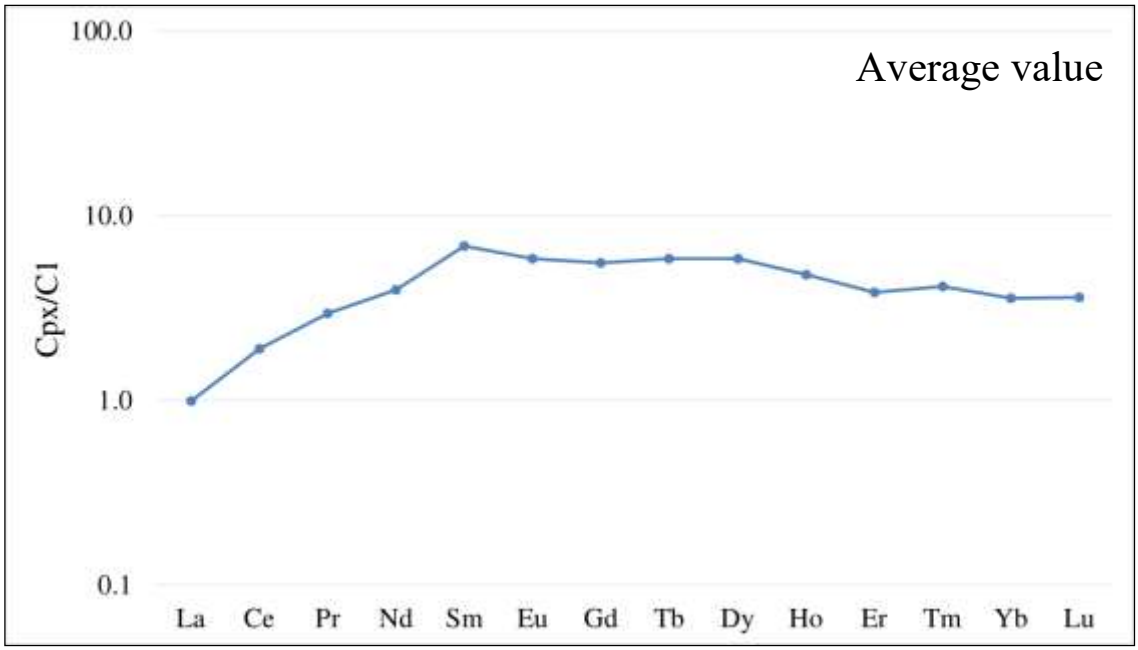

Figure 48 - Chondrite-normalized REE pattern of clinopyroxene from Theo's Flow, Abitibi greenstone belt (C1 chondrite from McDonough & Sun, 1995).

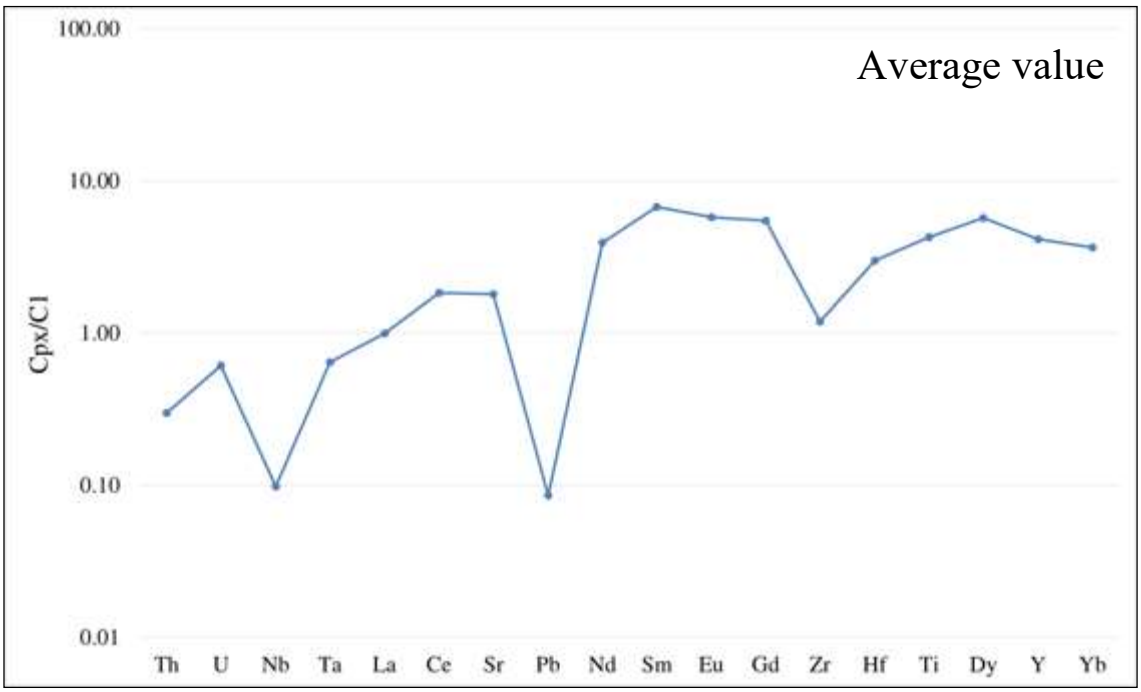

Figure 49 - Chondrite-normalized incompatible pattern of clinopyroxene from Theo's Flow, Abitibi greenstone belt (C1 chondrite from McDonough & Sun, 1995).

Amphibole has pargasitic composition, with an average Mg-number of 0.77 mol. The TiO_2 contents are in the range between 2.75 and 3.15 wt.%, and alumina shows homogenous values (7-7.61 wt.%). The Na_2O content is generally between 1.32 and 3.05 wt.%, whereas the K_2O values vary in the range 0.16–0.57 wt.% (Fig. 50; Tab. 4 Appendix A).

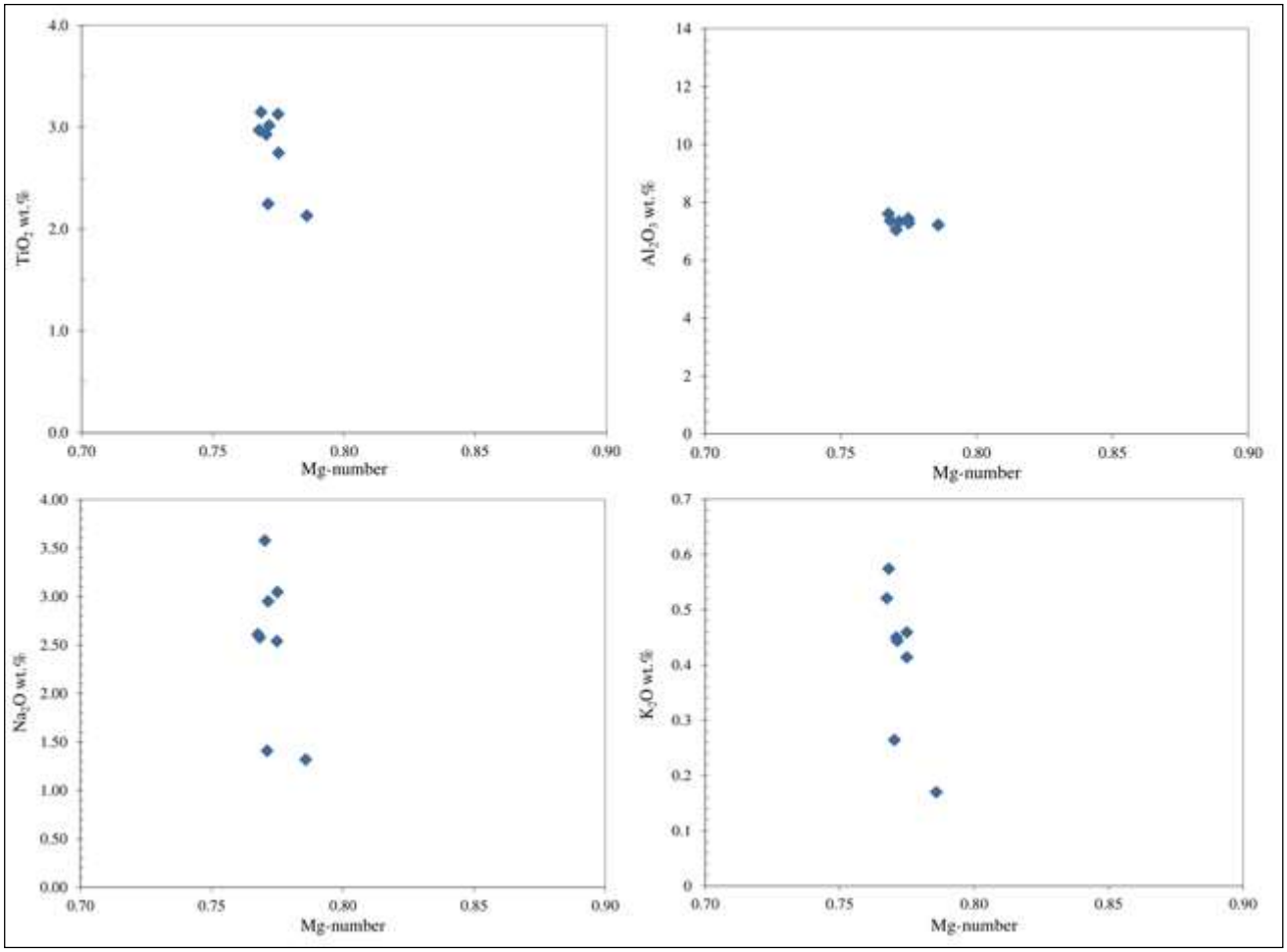

Figure 50 - Mg-number vs TiO_2, Al_2O_3, Na_2O and K_2O contents of amphibole from Theo's Flow, Abitibi greenstone belt.

The chondrite-normalized REE patterns are hump-shaped and show slight depletion in LREE (La_N/Sm_N = 0.54; La_N/Yb_N = 1.03), with almost flat HREE (Gd_N/Yb_N = 1.2-1.6) which are 50 times the CI chondrite values (Fig. 51; Tab. 4 Appendix B). The Eu/Eu* ratio has value of 0.76 at about 50 times CI chondrite. Chondrite-normalized patterns of incompatible elements of amphibole display positively Nb-Ta and negative Eu, Ba (Rb/Ba = 0.12) and Sr anomalies. The Zr/Hf and Nb/Ta ratios are 47.37 and 24.15, respectively (Fig. 52; Tab. 4 Appendix B). Titanium shows a slight depletion with value 26 times the chondrite value. About large ion lithophile elements (LILE), Cs, Rb and Sr have average contents of 0.13 ppm, 0.45 ppm and 14.47 ppm, respectively. As previously mentioned, amphiboles is depleted in Ba with mean value of 3.68 ppm. Sc and V show positive anomalies with values around 7 times the CI

chondrite value. The average contents for Cr, Ni, Sc and V are 1202 ppm, 713 ppm, 40.14 ppm and 403 ppm, respectively. The Co and Zn mean values are 68.91 ppm and 59.84 ppm, respectively (Tab. 4 Appendix B).

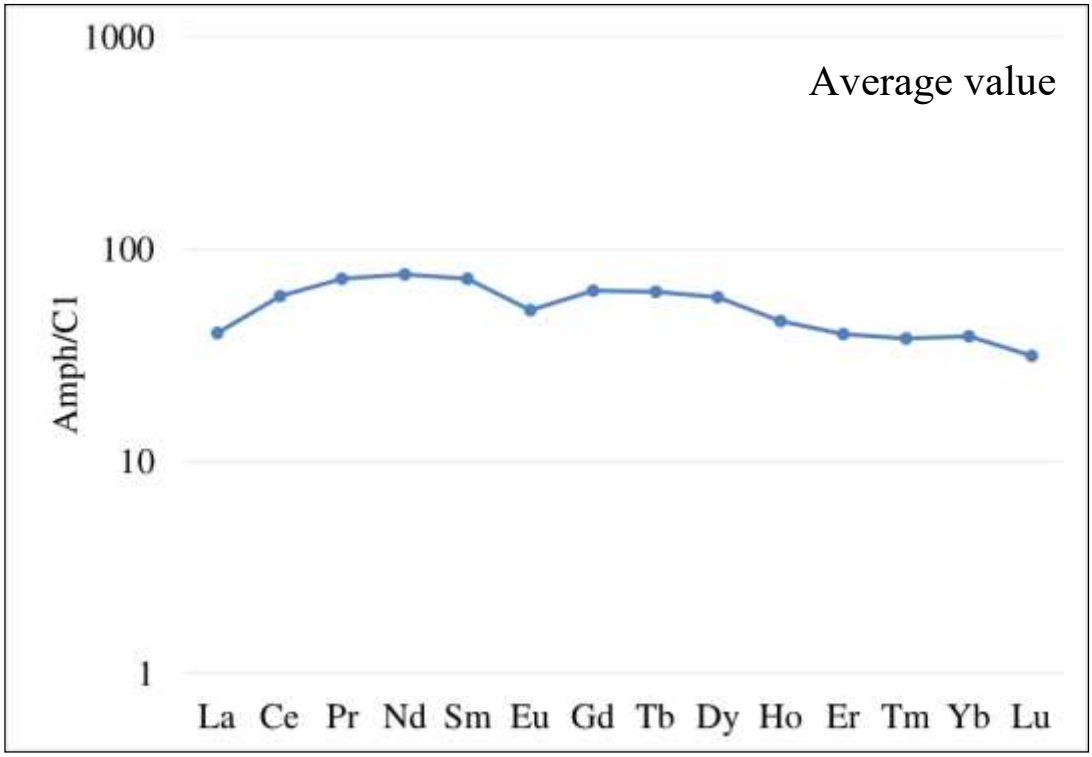

Figure 51 - Chondrite-normalized REE pattern of amphibole from Theo's Flow, Abitibi greenstone belt (C1 chondrite from McDonough & Sun, 1995).

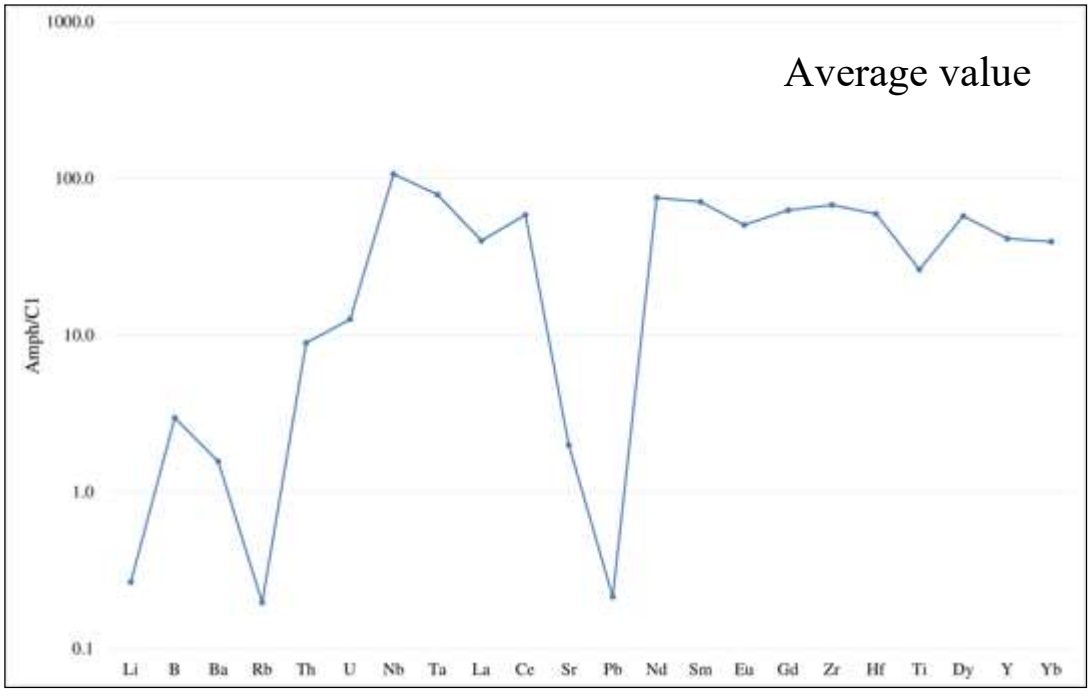

Figure 52 - Chondrite-normalized incompatible pattern of amphibole from Theo's Flow, Abitibi greenstone belt (C1 chondrite from McDonough & Sun, 1995).

Li and B contents are measured by ion probe (Tab. 44 Appendix B) and show mean values of 0.4 ppm and 4.81 ppm, respectively. In-situ ion probe measurements of the amphibole reveal an average H_2O content of 1.06 ±0.08 wt.% (Tab. 44 Appendix B). The mean contents of fluorine and chlorine are 10321 ppm and 2435 ppm, respectively (Tab. 44 Appendix B). The δD ratio of amphibole shows an average value of -101,5 ±10 ‰ (Tab. 48 Appendix B). Oxygen isotope analysis were not performed due to the lack of good spot positions on amphibole grains (Tab. 48 Appendix B).

Spinel has a wide compositional variation. At the core, spinel has chromite composition (Cr_2O_3 = 49.5 wt.%; MgO = 6.1 wt.%), and exibits alumina and iron (FeO_T) mean values of 8.1 wt.% and 34.6 wt.%, respectively. TiO_2 and MnO contents are in the range 1.12-1.43 and 0.19-0.26 wt.%, respectively. At the rims of chromite, spinels are enriched in titanium and manganese (TiO_2 = 3.9-10.4 wt.%; MnO = 1.6-2.9 wt.%), and are depleted in Cr_2O_3 (12.8-15.9 wt.%) and MgO (0.08 wt.%). The content of Al_2O_3 is remarkably variable, ranging from 2.18 to 7.63 wt.%, whereas the FeO_T mean value is 67.5 wt.%.

Boston Creek flow (sample B-5)

Clinopyroxene has Mg-number values ranging between 0.81 and 0.83 mol. Mg-number shows negatively correlation with alumina (0.91-1.75 wt.%) and TiO_2 contents (0.27-0.54 wt.%). Clinopyroxene exhibits a range of Cr_2O_3 (0.7-0.9 wt.%) without correlation with Mg-number (Fig. 53; Tab. 5 Appendix A). The clinopyroxene exhibits Ni and Cr contents in the range 461-490 ppm and 4372-5775 ppm, respectively (Tab. 5 Appendix B).

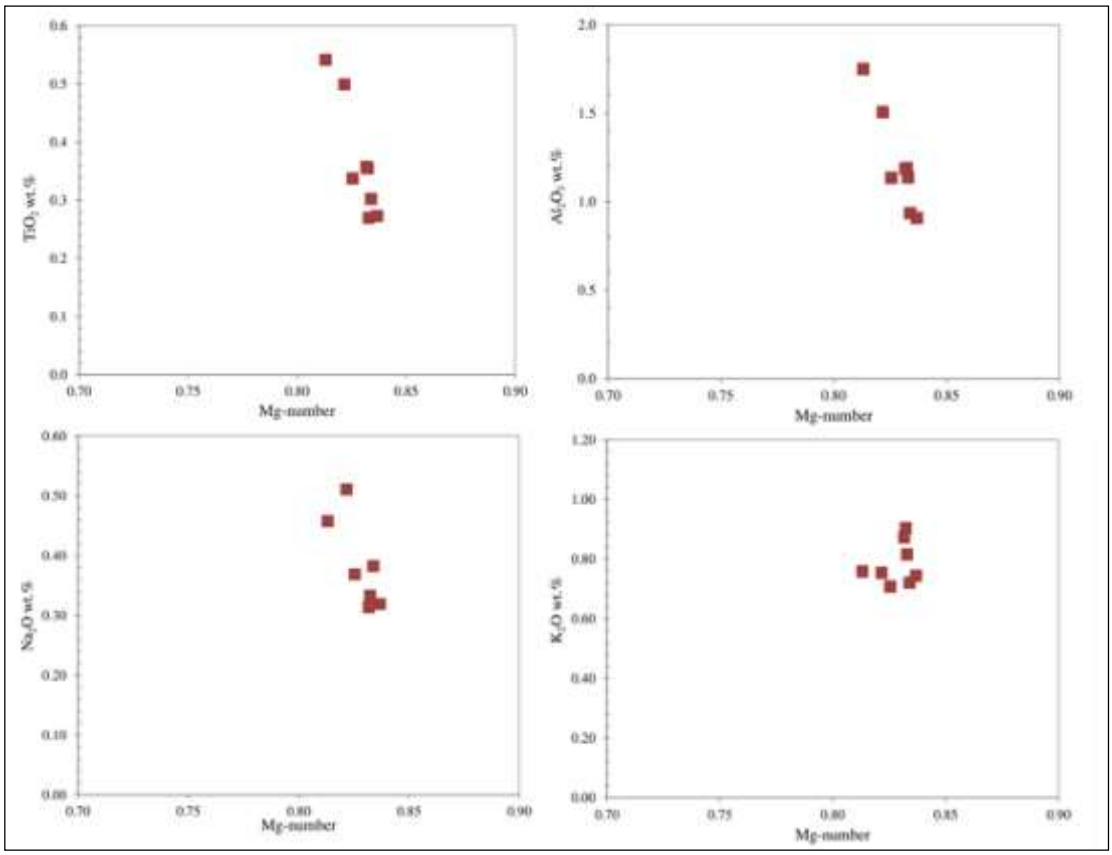

Figure 53 - Mg-number vs TiO_2, Al_2O_3, Na_2O and K_2O contents of clinopyroxene from Boston Creek, Abitibi greenstone belt.

The chondrite-normalized REE patterns of clinopyroxene are hump-shaped and characterized by LREE slight enrichment (La_N/Sm_N = 0.41-0.76; La_N/Yb_N = 1.03) relative to HREE values that are almost flat (Gd_N/Yb_N = 1.48-8.87) (Fig. 54; Tab. 5 Appendix B). The chondrite-normalized patterns of incompatibles exhibit depletion in Nb, Ta, Pb and Zr (Fig. 55; Tab. 5 Appendix B).

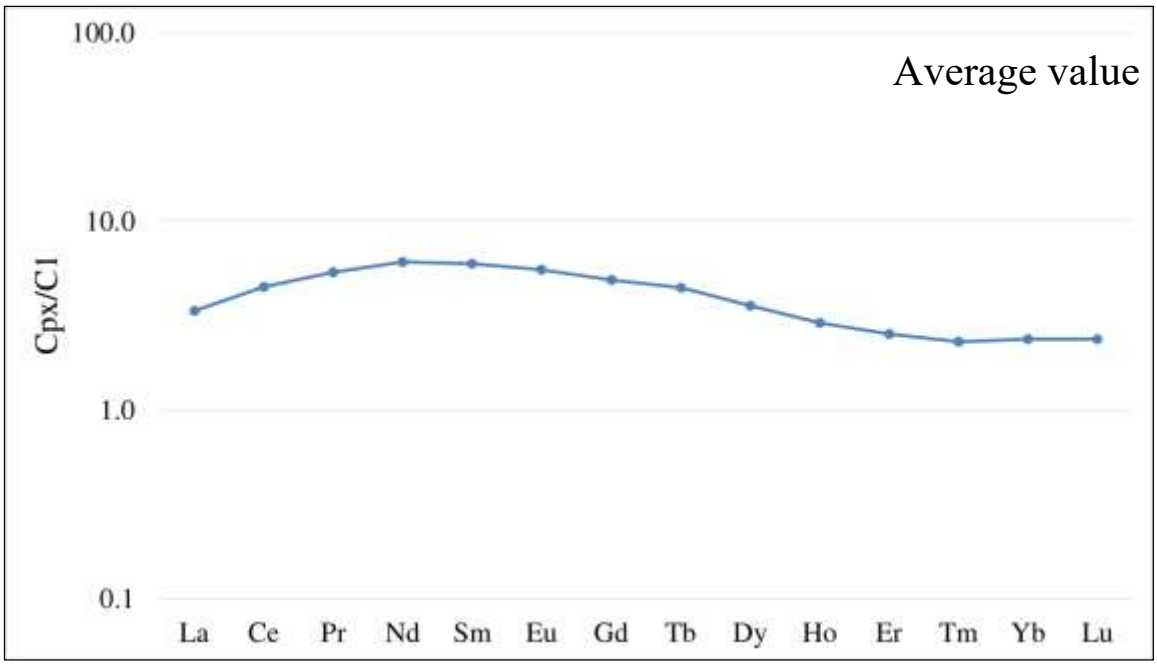

Figure 54 - Chondrite-normalized REE pattern of clinopyroxene from Boston Creek, Abitibi greenstone belt (C1 chondrite from McDonough & Sun, 1995).

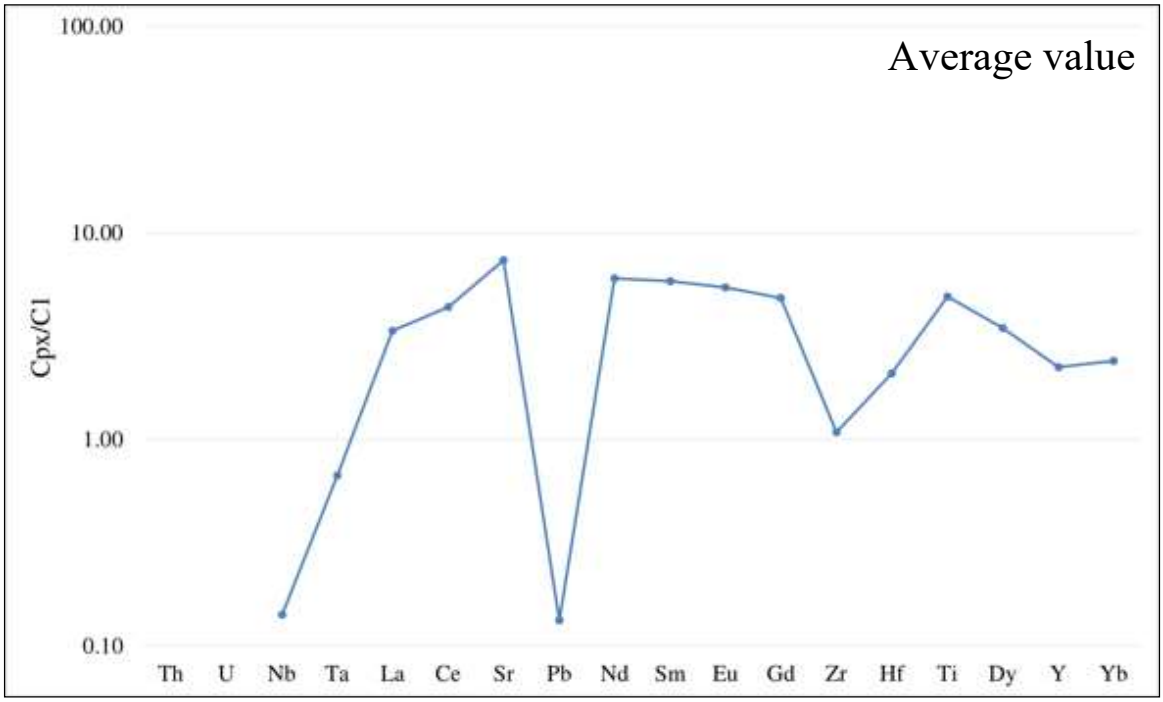

Figure 55 - Chondrite-normalized incompatible pattern of clinopyroxene from Boston Creek, Abitibi greenstone belt (C1 chondrite from McDonough & Sun, 1995).

Brown amphibole is Ti-pargasite in composition with Mg-number ranging between 0.63 and 0.67 mol. No significant intra-grain zoning was observed. Amphibole is enriched in TiO_2 (3.13-4.59 wt.%) and Al_2O_3 contents vary from 11.47 to 12.86 wt.%. The Na_2O mean content is 3.31 wt.%, whereas the K_2O values vary in the range 0.36–0.44 wt.% (Fig. 56; Tab. 6 Appendix A).

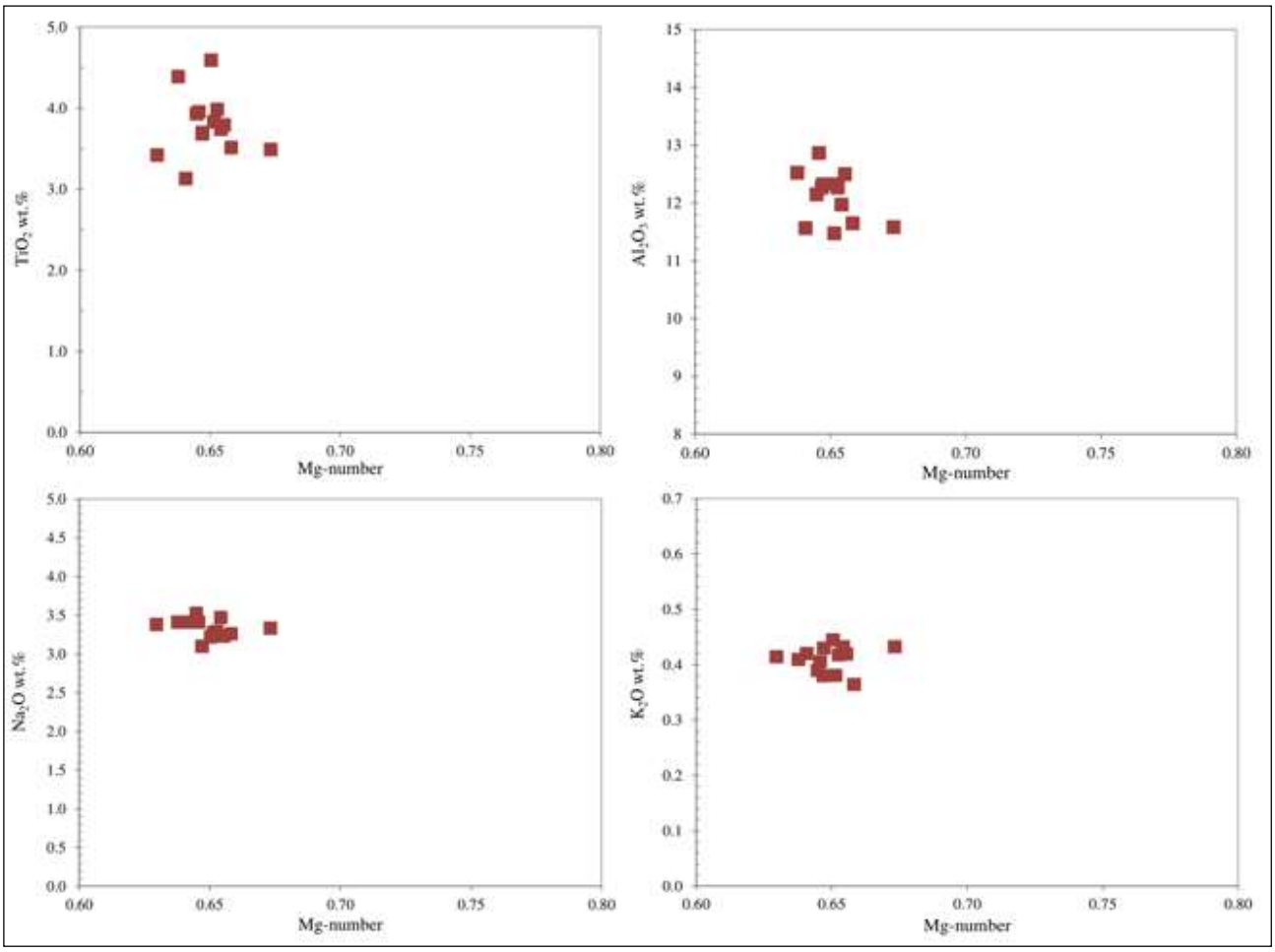

Figure 56 - Mg-number vs TiO_2, Al_2O_3, Na_2O and K_2O contents of amphibole from Boston Creek, Abitibi greenstone belt.

The chondrite-normalized REE patterns are characterized by a steady decrease from LREE to HREE (La_N/Yb_N = 0.9-1.7; Gd_N/Yb_N = 1.5-2.7) which are 4 times the CI chondrite values (Fig. 57; Tab. 6 Appendix B). The incompatible element pattern reveals a depletion in Li, Rb (Rb/Ba = 0.01), U, B and Pb and enrichment in Nb-Ta (Fig. 58; Tab. 6 Appendix B). Amphibole exhibits slightly negative anomalies for Zr and Ti. Nb/Ta and Zr/Hf ratios are 18.41 and 32.81, respectively. Cs and Ba contents are 0.06 ppm and 265 ppm, respectively. Ni content is 558 ± 44 ppm and the average values for Cr, Sc and V are 25 ppm, 6.6 ppm and 232 ppm, respectively (Tab. 6 Appendix B).

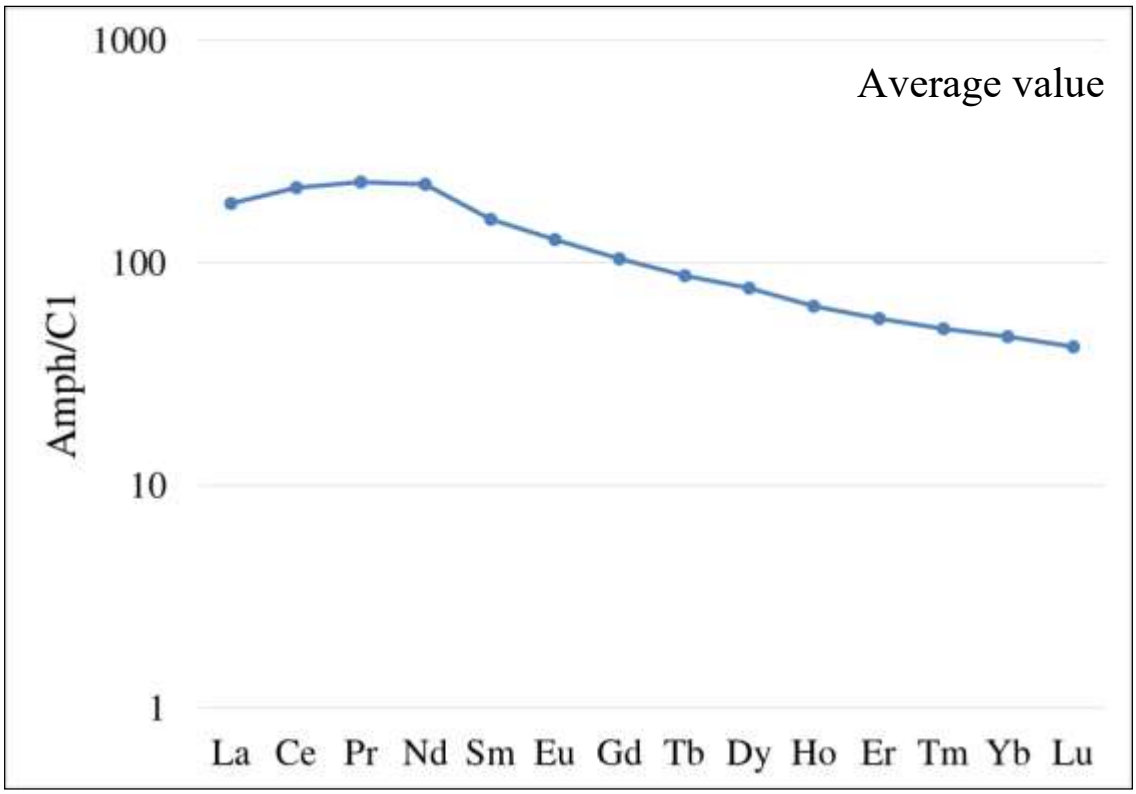

Figure 57 - Chondrite-normalized REE pattern of amphibole from Boston Creek, Abitibi greenstone belt (C1 chondrite from McDonough & Sun, 1995).

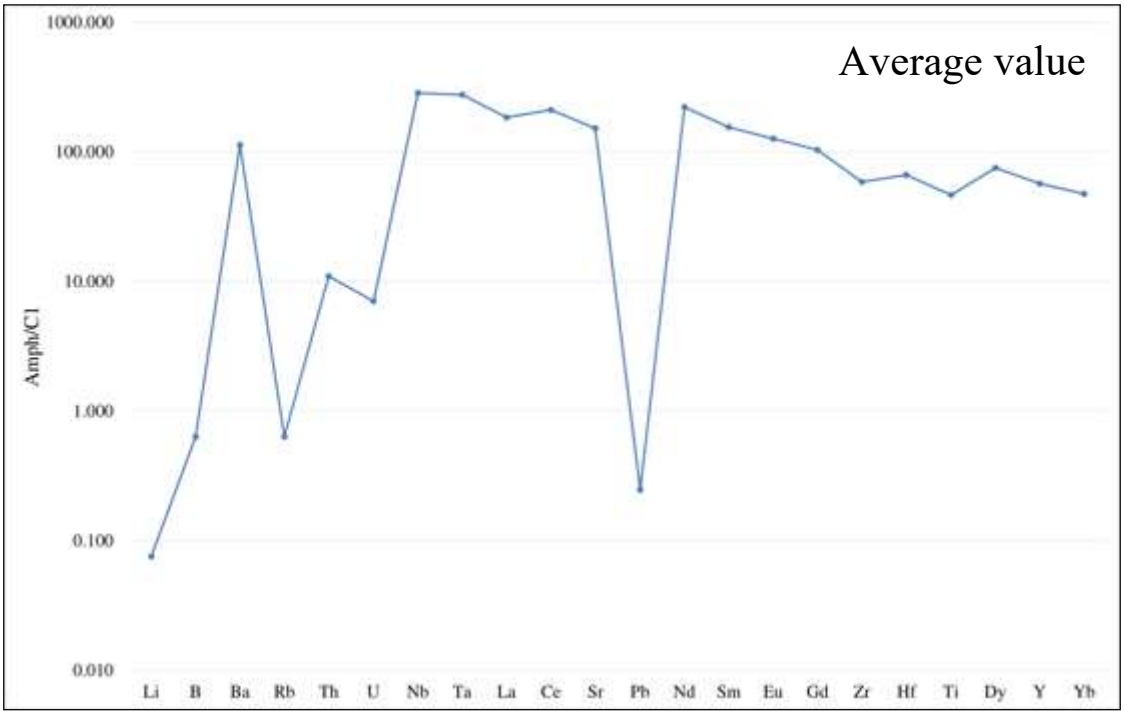

Figure 58 - Chondrite-normalized incompatible pattern of amphibole from Boston Creek, Abitibi greenstone belt (C1 chondrite from McDonough & Sun, 1995).

Li and B mean contents are 0.11 ppm and 3.21 ppm, respectively (Tab. 44 Appendix B). The H_2O contents ranging between 1.02 and 1.35 wt.%. The average contents of fluorine and chlorine are

229 ppm and 1434 ppm, respectively. The δD ratio of amphibole shows an average value of -115.8 ± 11.4 ‰, whereas the $\delta^{18}O$ mean value is 3.7 ± 0.75 ‰ (Tab. 44 Appendix B).

Spinel has a wide compositional variation. At the core, spinel shows chromite composition (Cr_2O_3 = 38.8-43.5 wt.%) and has variable contents of magnesium (MgO = 0.4-3.8 wt.%). Chromite exhibits Al_2O_3 and FeO_T mean values of 5.4 wt.% and 45.4 wt.%, respectively. TiO_2 and MnO contents are in the range 1.9-2.6 and 1.2-4.3 wt.%, respectively. At the rims of chromite, spinels have magnetite composition, with FeO_T contents between 86.5 and 91.2 wt.%. Titanium contents are in the range 0.4-1 wt.% of TiO_2 and MgO values are less than or equal to 0.06 wt.%. Cr_2O_3 and Al_2O_3 contents is remarkably variable in the ranges 0.03-0.3 and 7.63 wt.%, respectively.

Ghost Range (samples GR-1 and GR-2)

Olivine has Fo contents of 83 mol, in both samples (GR-1 and GR-2). Olivine has contents of Cr between 71 and 126 ppm, and Ni values ranging between 1845 and 2060 ppm (Tab. 7-8 Appendix A and Tab. 7-8 Appendix B).

Clinopyroxene associated to brown amphibole is augitic in composition with a Mg-number of 0.87 mol (Fig. 59; Tab. 9 Appendix A). The Al_2O_3 contents are variable and range from 1.01 to 2.52 wt.%, the TiO_2 contents are nearly 0.26 wt.%. The Na_2O contents are homogeneous with mean value of 0.37 wt.%.

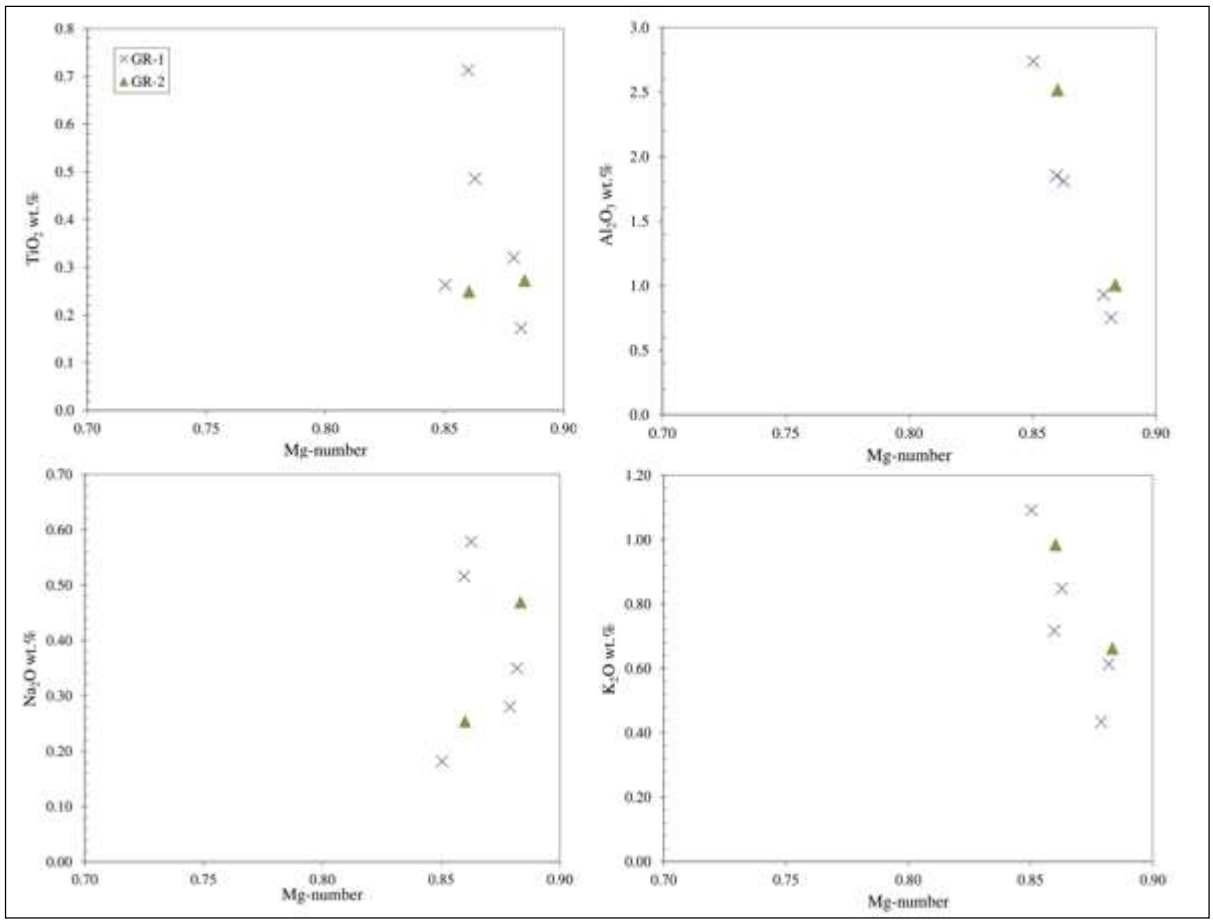

Figure 59 - Mg-number vs TiO_2, Al_2O_3, Na_2O and K_2O contents of clinopyroxene Ghost Range, Abitibi greenstone belt.

The chondrite-normalized REE patterns are characterized by a slight depletion in LREE (La_N/Sm_N = 0.22-0.31; La_N/Yb_N = 0.23-0.33) relative to HREE (Gd_N/Yb_N = 1.17-1.74), which is nearly flat at about 5 times CI chondrite (Fig. 60; Tab. 9 Appendix B). The incompatible element patterns reveal positive anomalies in U, Ta, Eu (Eu/Eu* = 0.96) and Gd and depletion in Nb, Pb and Zr relative to the neighbouring elements (Fig. 61; Tab. 9 Appendix B). Cr contents are in the range 5539-8265 ppm whereas Ni values are homogeneous with average of 382 ppm.

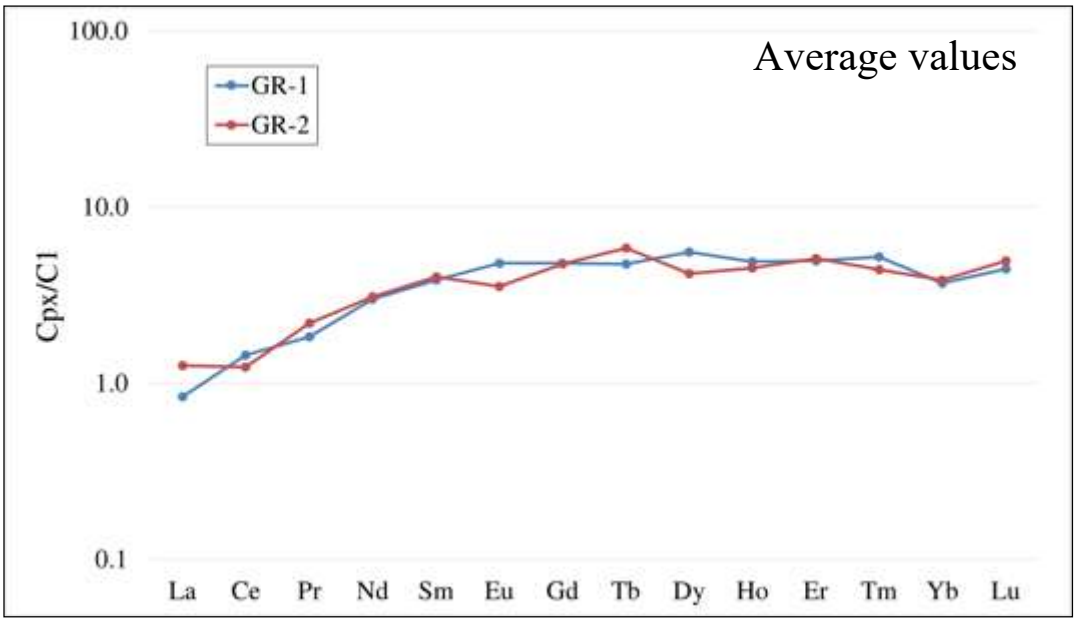

Figure 60 - Chondrite-normalized REE pattern of clinopyroxene Ghost Range, Abitibi greenstone belt (C1 chondrite from McDonough & Sun, 1995).

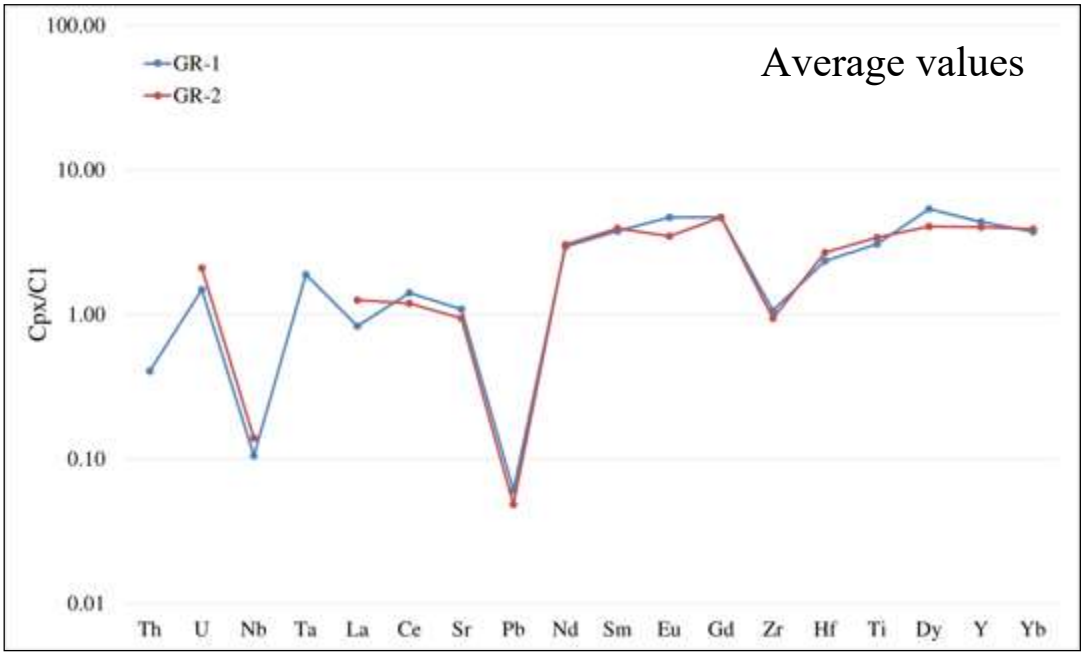

Figure 61 - Chondrite-normalized incompatible pattern of clinopyroxene Ghost Range, Abitibi greenstone belt (C1 chondrite from McDonough & Sun, 1995).

Brown amphibole is pargasite in composition and has Mg-numbers of 0.80 mol. The amphibole has significantly variable TiO_2 (2.67-5.1 wt.%) and Al_2O_3 (8-12.33 wt.%) contents. The Na_2O and K_2O contents ranging between 2.67-3.06 wt.% and 0.5–0.8 wt.%, respectively (Fig. 62; Tab. 10-11 Appendix A).

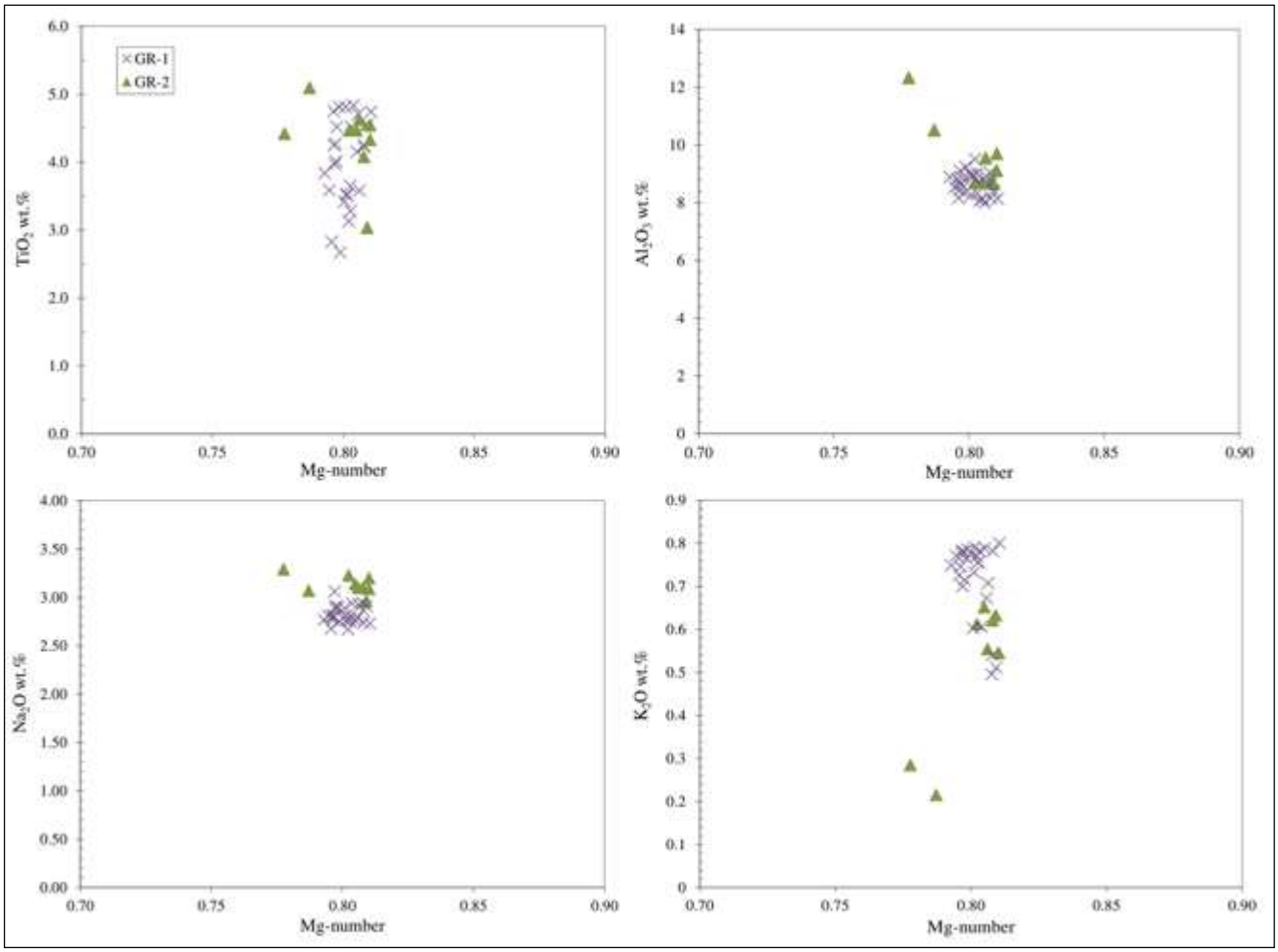

Figure 62 - Mg-number vs TiO_2, Al_2O_3, Na_2O and K_2O contents of amphibole Ghost Range, Abitibi greenstone belt.

The chondrite-normalized REE patterns of amphibole are hump-shaped and characterized by LREE enrichment (La_N/Sm_N = 0.97; La_N/Yb_N = 1.52-2.15) over HREE (Gd_N/Yb_N = 1.46) which are 60-100 times CI chondrite values (Fig. 63; Tab. 10-11 Appendix B). The REE-patterns also show a slightly depletion of Eu (Eu/Eu* = 0.70). Chondrite-normalized patterns of trace elements display distinctive negative Li, Rb (Rb/Ba = 0.04), Sr and Pb anomalies and positive Ba, Th, Nb-Ta (Nb/Ta = 16.78) and Zr-Hf (Zr/Hf = 31.71) anomalies (Fig. 64; Tab. 10-11 Appendix B). About the LILE, Ba has variables contents between 44.51 ppm and 122 ppm. The Cs mean value is 0.04 ppm. Brown amphibole shows high concentrations in Cr (8858-9568 ppm), Sc (84.55 ppm) and V (777 ppm) wich are 14 times the CI chondrite. The Ni contents are in the range 583-611 ppm. In-situ ion probe analyses (Tab. 44 Appendix B) reveal H_2O contents ranging between 0.71 and 1.32 wt.%.

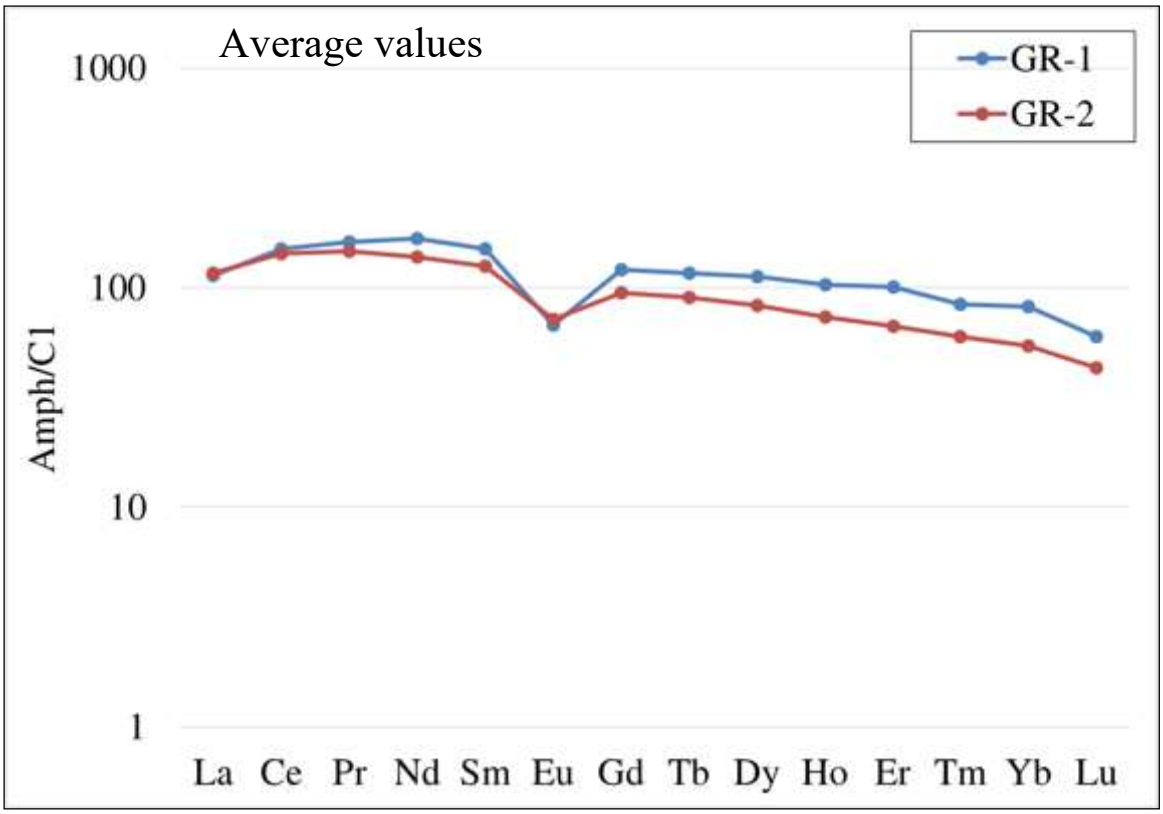

Figure 63 - Chondrite-normalized REE pattern of amphibole Ghost Range, Abitibi greenstone belt (C1 chondrite from McDonough & Sun, 1995).

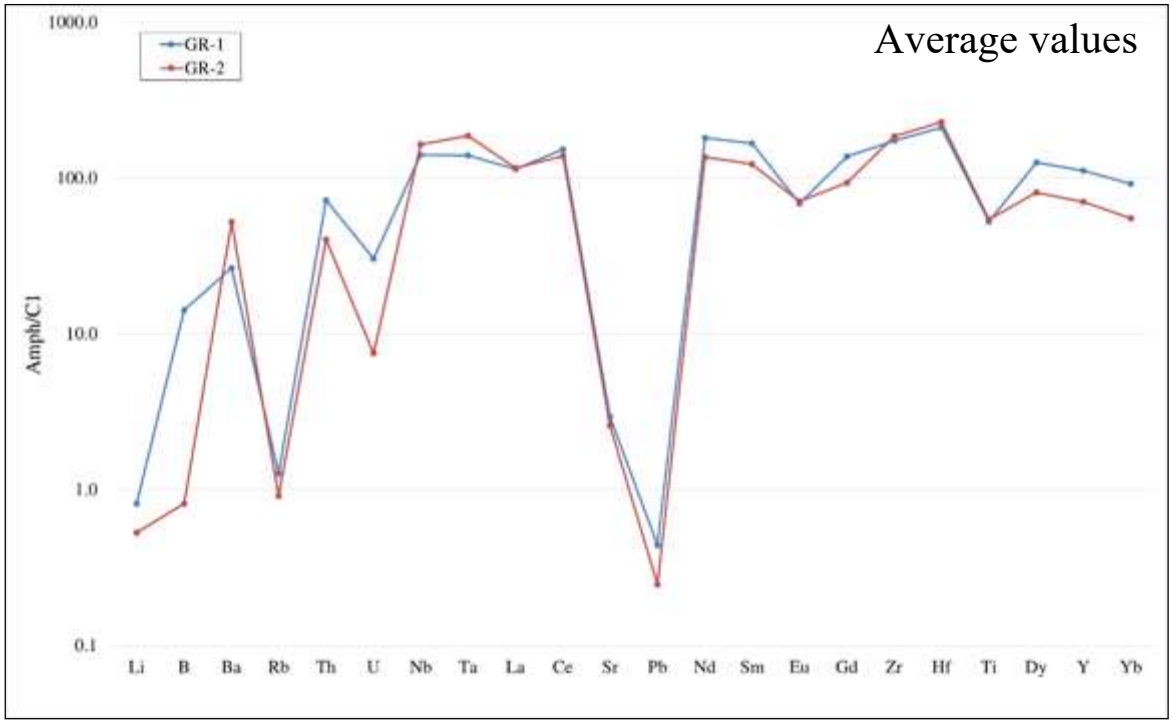

Figure 64 - Chondrite-normalized pattern of incompatible elements of amphibole Ghost Range, Abitibi greenstone belt (C1 chondrite from McDonough & Sun, 1995).

In amphibole of samples GR-1 and GR-2, Li contents are 1.22 ppm and 0.79 ppm, respectively (Tab. 44 Appendix B). Sample GR-1 is enriched in B (average value of 12.73 ppm), whereas in GR-2

the mean content is 1.81 ppm (Tab. 44 Appendix B). Samples from Ghost Range peridotite show high enrichment in fluorine (1930-4024 ppm) and chlorine (3650-4021 ppm) (Tab. 44 Appendix B). The δ D ratio of amphibole shows an average value of -197,6 ‰, for sample GR-1, and -236.3 ‰, for sample GR-2 (Tab. 48 Appendix B). The $\delta^{18}O$ ratio is in the range 3.8-4.2 ‰ (Tab. 48 Appendix B).

Spinel from Ghost Range has Cr_2O_3 contents in the range 29-39.9 wt.%, whereas the MgO contents are remarkably variable (4.45-8.8 wt.%). Spinel shows heterogeneous Al_2O_3 contents (6-14 wt.%), that are negatively correlated with the TiO_2 contents (1.2-5.7 wt.%). Spinel of sample GR-2 has Cr_2O_3 contents ranging between 30.5 and 36.3 wt.%, whereas Al_2O_3 values differ from 6.4 to 13 wt.%. The MgO and TiO_2 contents are 5.78-8.13 wt.% and 3.7-8.1 wt.%. Spinel is Mn-poor (MnO = 0.22-0.35 wt.%), and has variable FeO_T contents (37.4-47.9 wt.%).

3.2.3 Pechenga Complex (Russia)

Pilgüjarvi sill (sample Pilg 8 38)

Olivine has Fo contents of 77 mol and has average values of Ni of 1257 ± 12.33 ppm, whereas Cr content is variable between 65 and 88 ppm (Tab. 12 Appendix A and Tab. 12 Appendix B).

Clinopyroxene is augite and has Mg-number value 0.83 mol (Fig. 65; Tab. 13 Appendix A). Mg-number shows slightly negative correlation with alumina (2.24-3.54 wt.%) and TiO_2 contents (0.93-1.57 wt.%). Clinopyroxene exhibits a range of Cr_2O_3 (0.52-0.86 wt.%) with positive correlation with Mg-number. The Na_2O value is homogeneous (0.41 ± 0.09 wt.%) and does not show correlation with Mg-number (Fig. 65; Tab. 13 Appendix A).

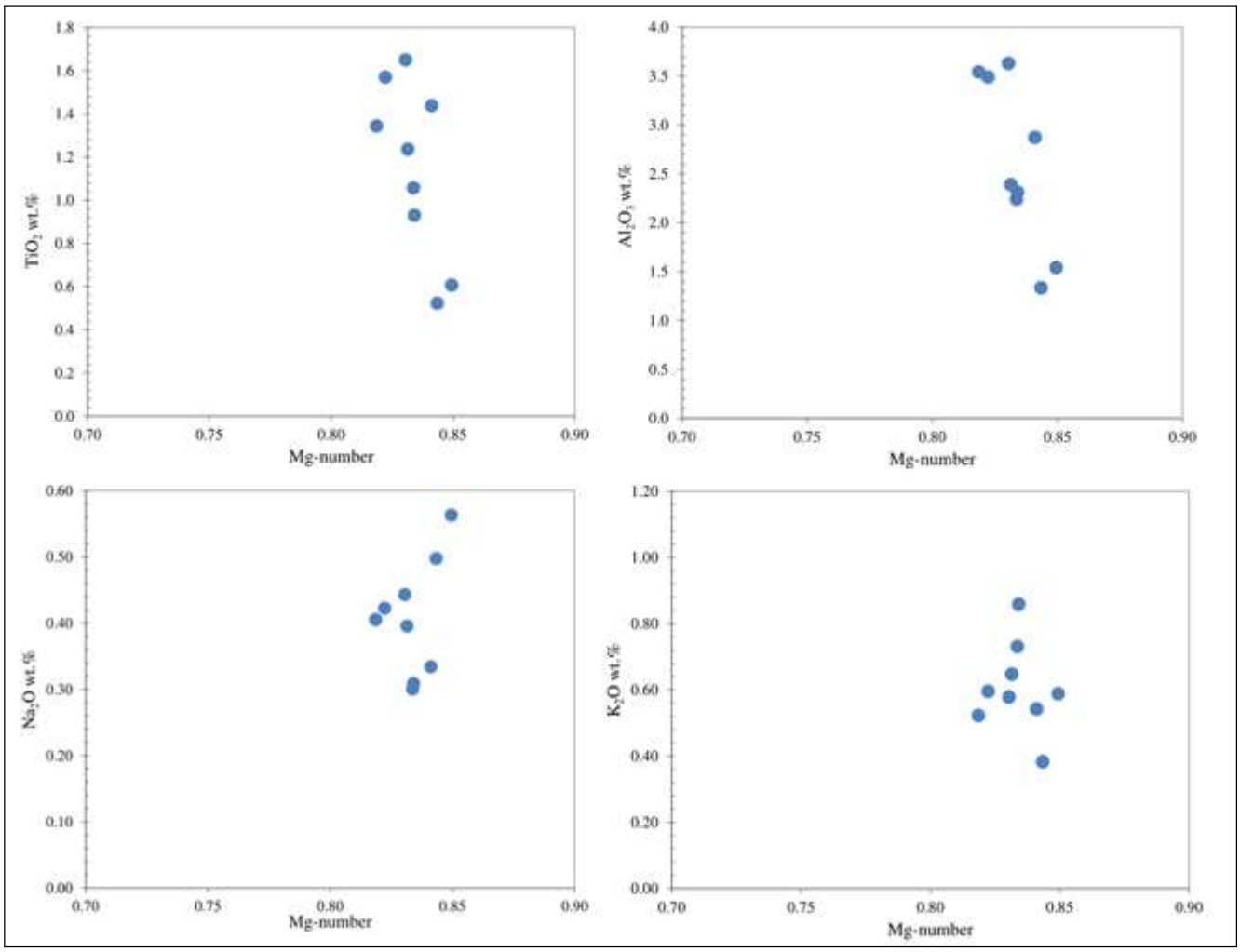

Figure 65 - Mg-number vs TiO_2, Al_2O_3, Na_2O and K_2O contents of clinopyroxene from Pilgüjarvi sill, Pechenga Complex.

The chondrite-normalized REE patterns of clinopyroxene are hump-shaped and characterized by LREE (La_N/Sm_N = 0.38) and to HREE (Gd_N/Yb_N = 4.46) depletion relative to MREE (La_N/Yb_N = 2.20) that are roughly 95 times the CI chondrite values (Fig. 66; Tab. 13 Appendix B). The chondrite-normalized patterns of the incompatible elements display negative anomalies in U, Sr, Pb, Zr and Ti relative to the neighbouring elements. The Ni and Cr contents are 176 ppm and 3506 ppm, respectively (Fig. 67; Tab. 13 Appendix B).

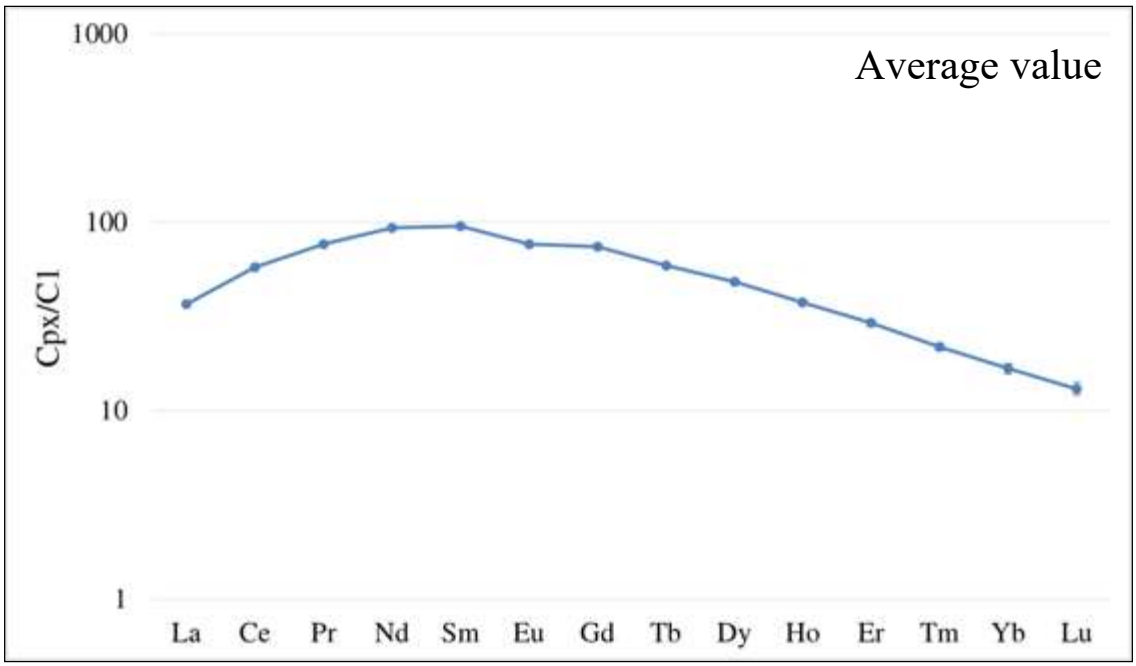

Figure 66 - Chondrite-normalized REE pattern of clinopyroxene from Pilgüjarvi sill, Pechenga Complex (C1 chondrite from McDonough & Sun, 1995).

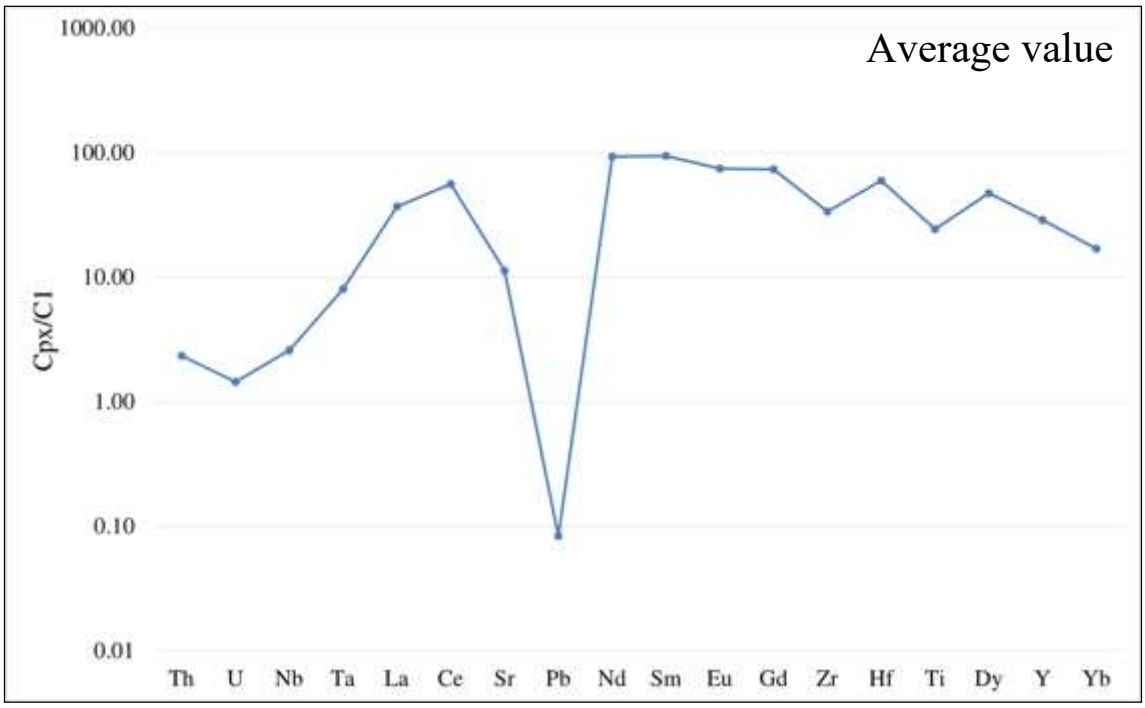

Figure 67 - Chondrite-normalized incompatible pattern of clinopyroxene from Pilgüjarvi sill, Pechenga Complex (C1 chondrite from McDonough & Sun, 1995).

Brown amphibole is Ti-pargasite with Mg-number of 0.77 mol (Fig. 68; Tab. 14 Appendix A). No significant intra-grain zoning was observed. Amphibole is enriched in TiO_2 (4.43-5.41 wt.%) and Al_2O_3 contents vary from 9.33 to 10.38 wt.%. The iron (FeO_{tot}) has homogeneous content approximately 7.73 ± 0.10 wt.%. The Na_2O and K_2O mean contents are 3.09 ± 0.06 wt.% and 0.77 ± 0.03 wt.%, respectively, and both show a positive correlation with Mg-number (Fig. 68; Tab. 14 Appendix A).

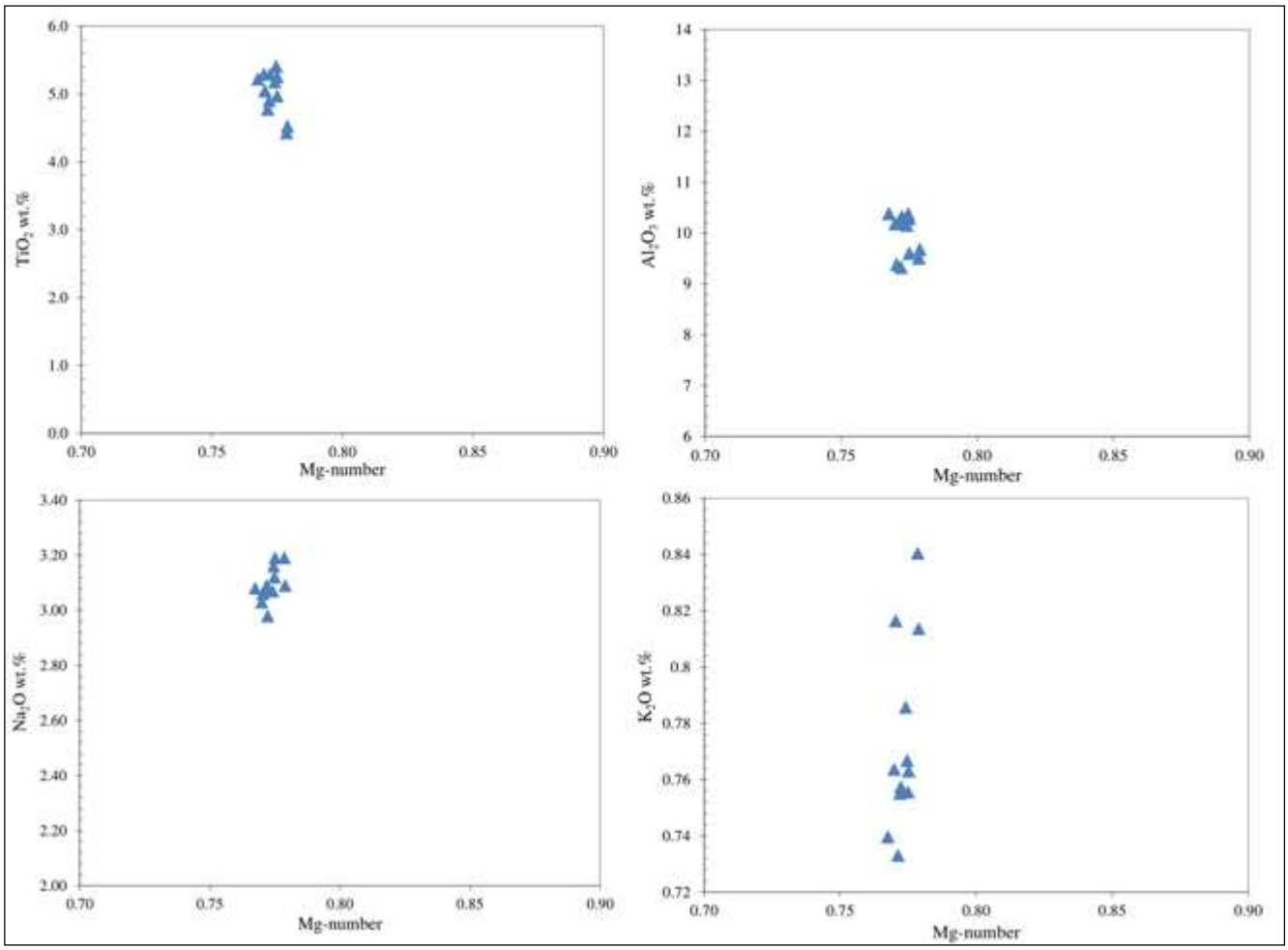

Figure 68 - Mg-number vs TiO_2, Al_2O_3, Na_2O and K_2O contents of amphibole from Pilgüjarvi sill, Pechenga Complex.

The chondrite-normalized REE patterns are hump-shaped with LREE (La_N/Sm_N = 0.86 ± 0.21; La_N/Yb_N = 4.62 ± 0.81) and HREE (Gd_N/Yb_N = 2.9-4.3) depletion relative to MREE (at about 230 times C1 chondrite) (Fig. 69; Tab. 14 Appendix B). The incompatible element pattern reveals a strong depletion in Li, Rb, B, and Pb relative to the neighbouring elements and slightly negative anomalies in Zr and Ti (Fig. 70). The Nb/Ta and Zr/Hf ratios are 22.03 and 27.12, respectively. As mentioned before, amphibole is enriched in Ba (Rb/Ba = 0.01; Ba = 408 ± 10 ppm), whereas Sr show mean value of 398 ± 62 ppm. Ni content is homogeneous with mean value of 384 ± 33 ppm. The amphibole is strongly enriched in Cr (2891 ppm), whereas Sc and V mean contents are 63 ppm and 517 ppm, respectively (Tab. 14 Appendix B).

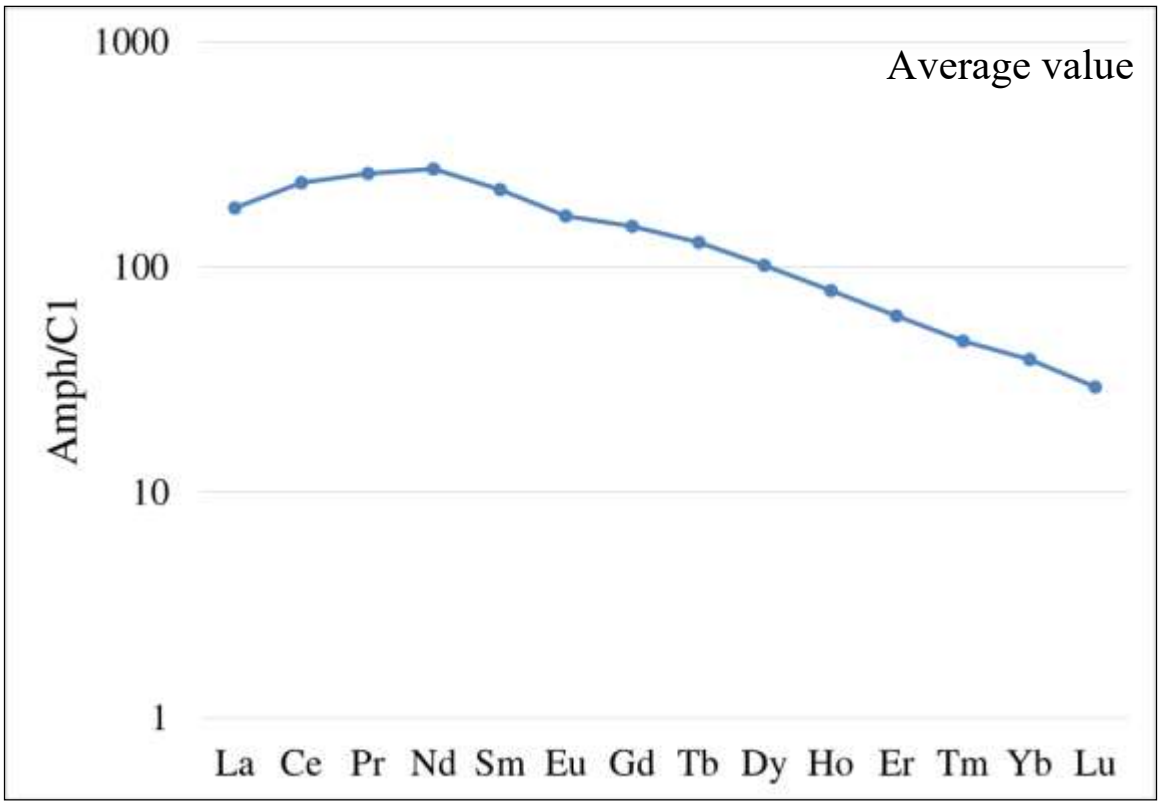

Figure 69 - Chondrite-normalized REE pattern of amphibole from Pilgüjarvi sill, Pechenga Complex (C1 chondrite from McDonough & Sun, 1995).

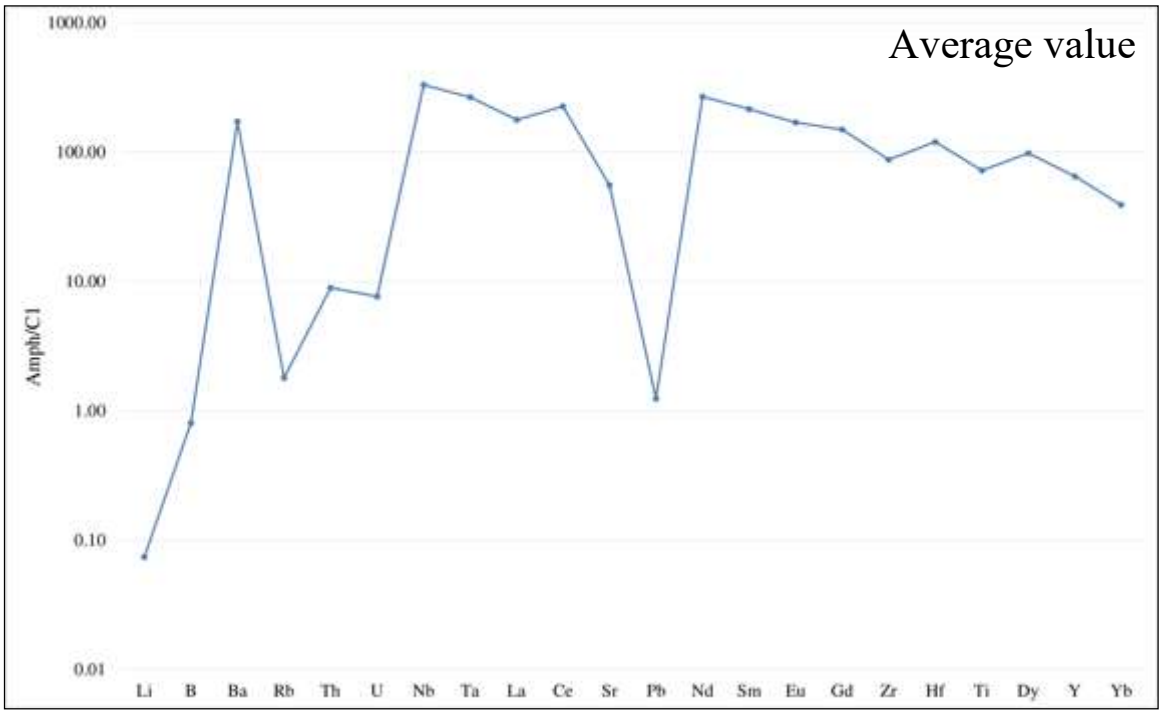

Figure 70 - Chondrite-normalized incompatible pattern of amphibole from Pilgüjarvi sill, Pechenga Complex (C1 chondrite from McDonough & Sun, 1995).

In-situ ion probe analyses (Tab. 45 Appendix B) reveal Li and B average contents of 0.11 ppm and 0.72 ppm, respectively. Brown amphibole has H_2O mean content of 0.98 ± 0.2 wt. % (Tab. 45

Appendix B). The average contents of fluorine and chlorine are 4461 ppm and 937 ppm, respectively (Tab. 45 Appendix B). The δD of amphibole shows an average value of -121.2 ± 5.2 ‰ (Tab. 49 Appendix B). The $\delta^{18}O$ mean value is 4.5 ± 1.5 ‰ (Tab. 49 Appendix B).

Spinel has a wide compositional variation. The chromium contents of spinel are variable (Cr_2O_3 = 16.2-27.3 wt.%), whereas alumina values are homogeneous (Al_2O_3 = 8-8.7 wt.%). Spinel shows strongly variable MgO contents (1.48-7.71 wt.%), and exhibits iron enrichment (FeO_T = 46.5-58.9 wt.%). Spinel is Ti-rich (TiO_2 = 8.2-12.3 wt.%) and MnO contents are in the range 0.26-1.35 wt.%.

Pilgüjarvi sill (sample 106-44)

Olivine has Fo contents slightly varying between 77 and 78 mol (Tab. 15 Appendix A). Olivine has variable contents of Cr between 66 and 186 ppm, and Ni values ranging between 1760 and 1973 ppm (Tab. 15 Appendix B).

Clinopyroxene is augitic in composition and has Mg-number value of 0.84 mol (Fig. 71; Tab. 16 Appendix A). Mg-number shows negatively correlation with alumina (1.9-5.3 wt.%) and TiO_2 contents (1.2-2.41 wt.%). Clinopyroxene exhibits a range of Cr_2O_3 (0.65-0.94 wt.%) without correlation with Mg-number. The Na_2O average content is 0.43 ± 0.06 wt.% (Fig. 71; Tab. 16 Appendix A).

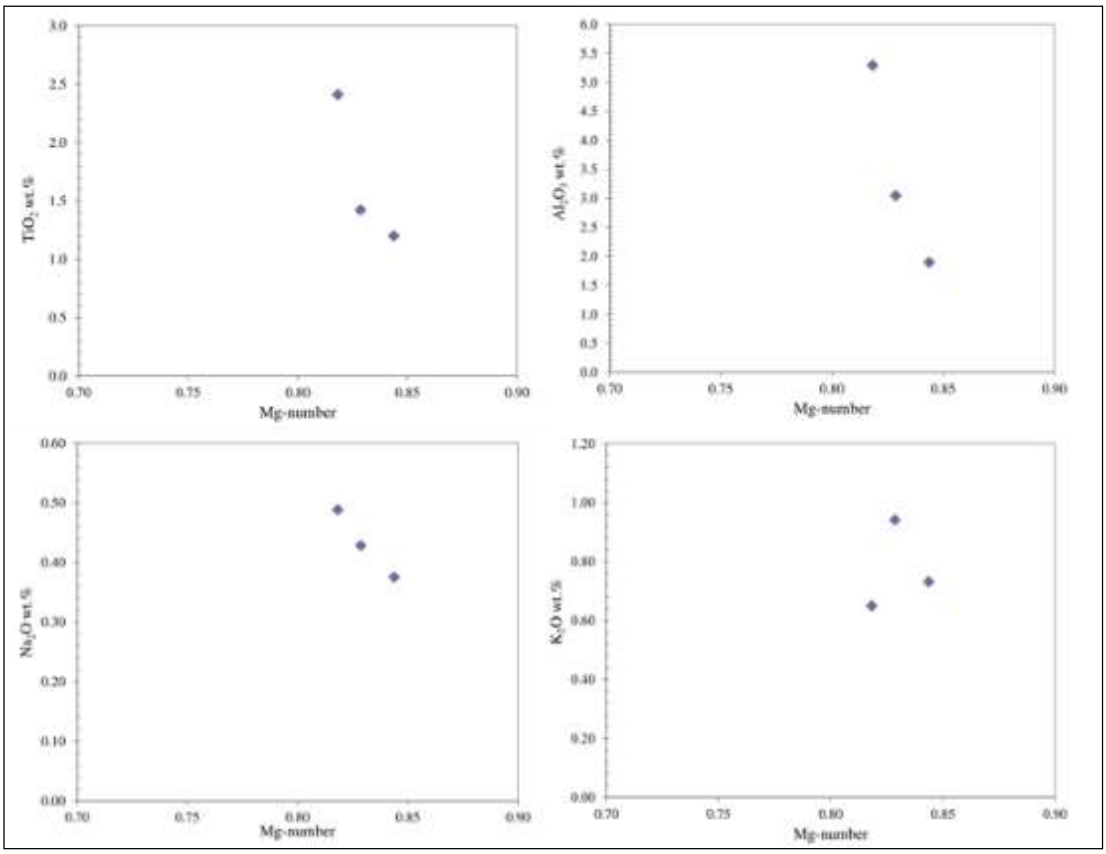

Figure 71 – Mg-number vs TiO_2, Al_2O_3, Na_2O and K_2O contents of clinopyroxene from Pilgüjarvi sill, Pechenga Complex.

The chondrite-normalized REE patterns of clinopyroxene are hump-shaped and characterized by LREE (La_N/Sm_N = 0.42) and to HREE (Gd_N/Yb_N = 4.01) depletion relative to MREE (La_N/Yb_N = 2.10) that are roughly 75 times the CI chondrite values (Fig. 72; Tab. 16 Appendix B). The chondrite-normalized patterns of the incompatible elements display negative anomalies in Th, U, Nb and Pb relative to the neighbouring elements (Fig. 73). A slightly depletion is observed for Zr and Ti. Europium does not show any significant anomaly, with an Eu/Eu* mean ratio of 0.94. The Ni and Cr contents are 250 ± 22 ppm and 4613 ± 396 ppm, respectively (Tab. 16 Appendix B).

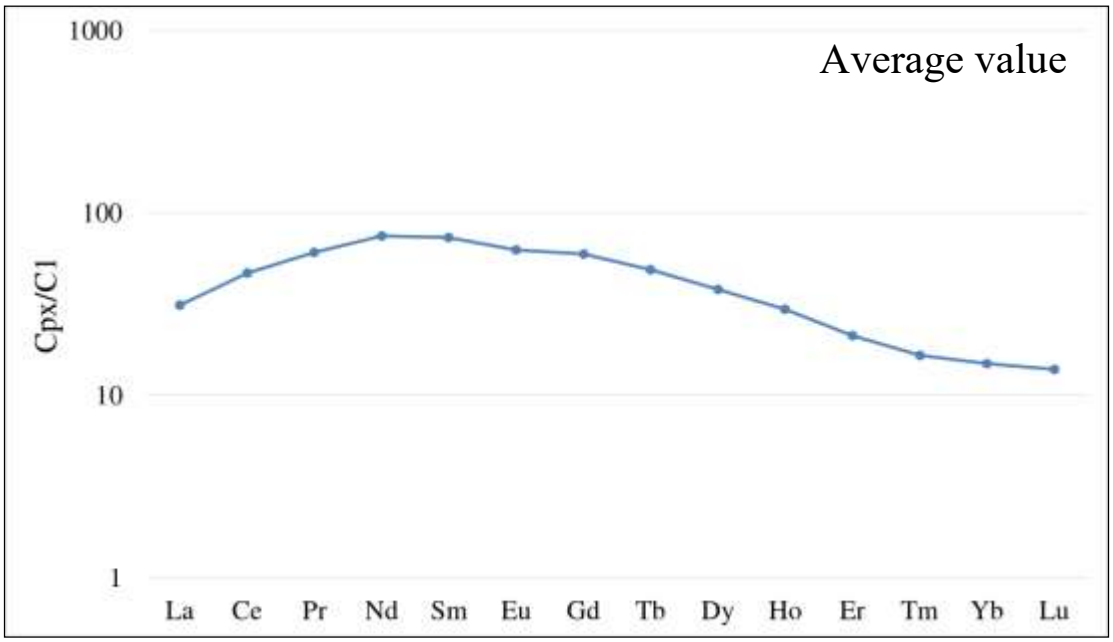

Figure 72 - Chondrite-normalized REE pattern of clinopyroxene from Pilgüjarvi sill, Pechenga Complex (C1 chondrite from McDonough & Sun, 1995).

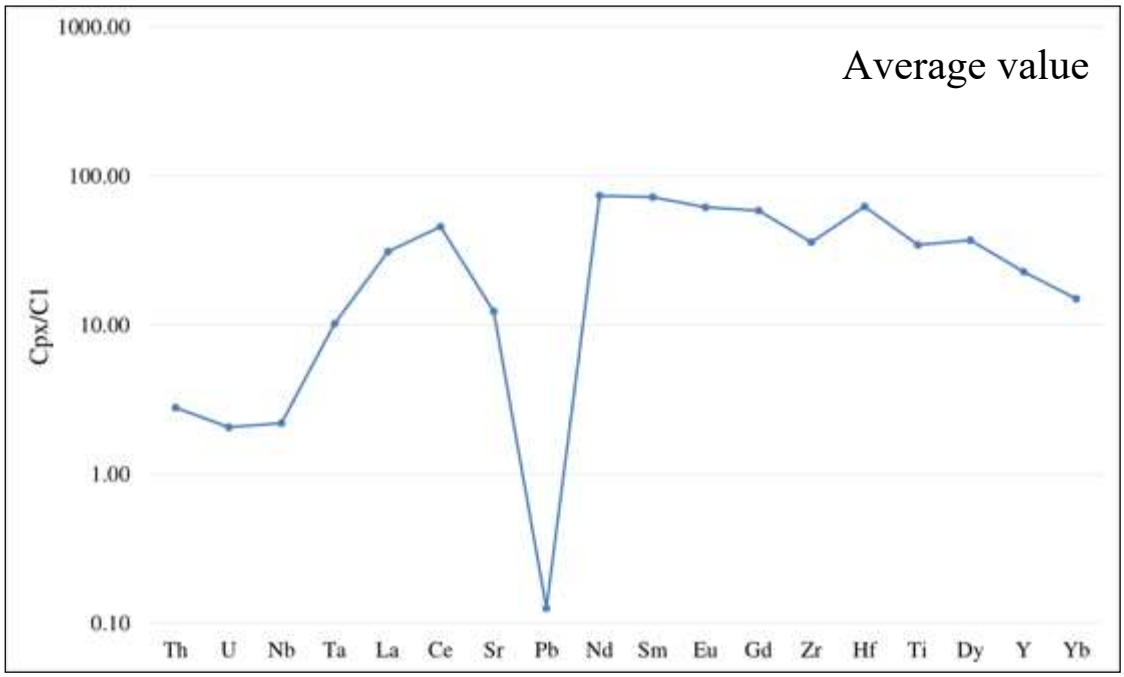

Figure 73 - Chondrite-normalized incompatible pattern of clinopyroxene from Pilgüjarvi sill, Pechenga Complex (C1 chondrite from McDonough & Sun, 1995).

Brown amphibole is pargasite with Mg-number of 0.76 mol (Fig. 74; Tab 17 Appendix A). No significant intra-grain zoning was observed. The titanium contents are homogeneous (5.02-5.92 wt.% TiO_2) as the Al_2O_3 contents (11.59-12.64 wt.%). Mg-number does not show correlation with titanium and alumina. The CaO has mean value of 11.71 ± 0.10 wt.% and is positive correlated with Mg-number. The Na_2O and K_2O mean contents are 2.92 ± 0.20 wt.% and 0.58 ± 0.03 wt.%, respectively, and are not observed correlation with Mg-number.

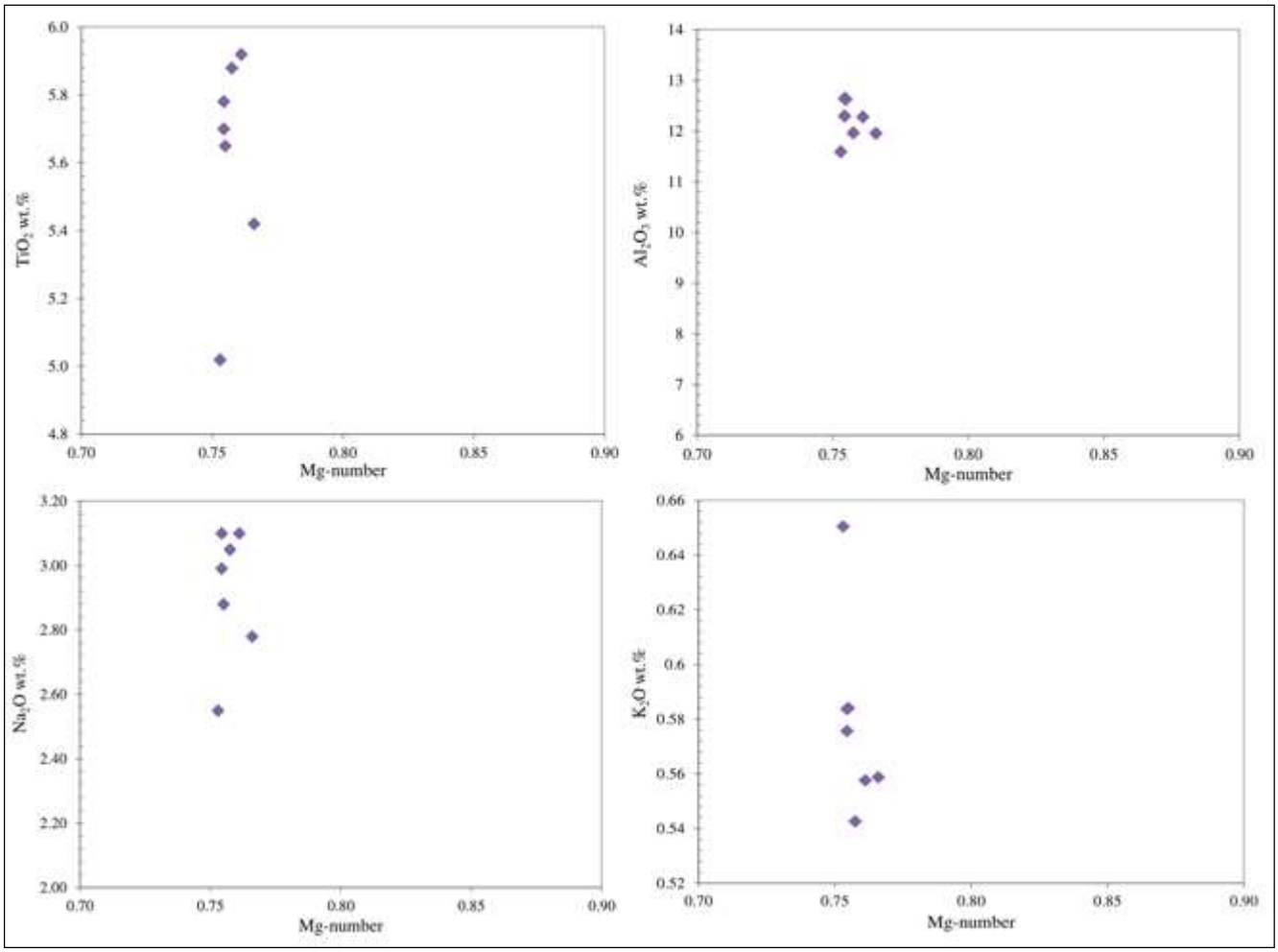

Figure 74 - Mg-number vs TiO_2, Al_2O_3, Na_2O and K_2O contents of amphibole from Pilgüjarvi sill, Pechenga Complex.

The chondrite-normalized REE patterns are characterized by a slightly depletion of LREE (La_N/Sm_N = 0.59 ± 0.21) and by a decrease from MREE to HREE (La_N/Yb_N = 3.29 ± 1.26; Gd_N/Yb_N = 3.93 ± 1.31), which are approximately 103 times the CI chondritic (Fig. 75; Tab. 17 Appendix B). The europium does not show negative anomaly (Eu/Eu* = 1.05). The incompatible element pattern reveals depletion in Rb, U and Pb relative to the neighbouring elements (Fig. 76). Furthermore, there are distinguished a slightly negative anomalies in La and Zr. The Nb/Ta and Zr/Hf average ratios are 19.46 and 26.48, respectively. About the LILE, the Rb/Ba ratio is 0.01 as highlighted by rubidium depletion (1.74-2.55 ppm) and barium enrichment (277-300 ppm). Sr shows homogeneous concentrations in the range 764-816 ppm. The Ni and Cr contents are variables in the ranges 472-660 ppm and 1061-4246 ppm, respectively. On the contrary, the Sc and V show homogeneous values, which are 43 ± 8 ppm and 467 ± 46 ppm, respectively (Tab. 17 Appendix B).

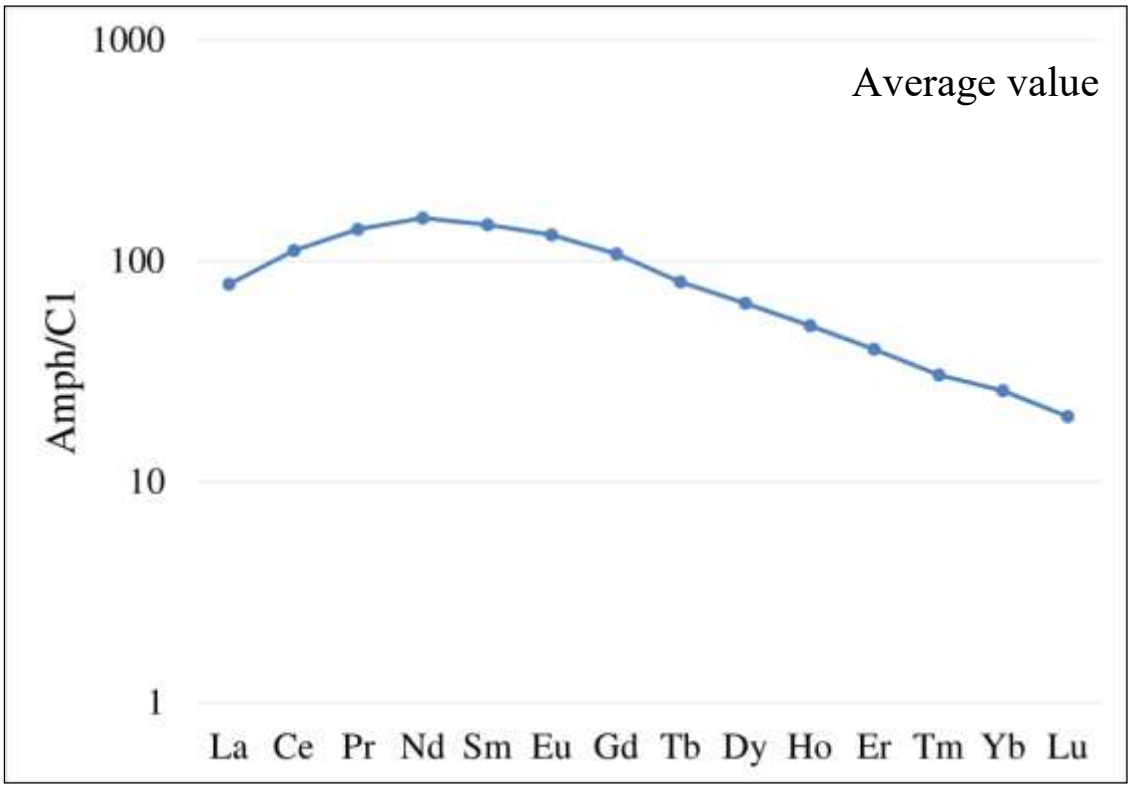

Figure 75 - Chondrite-normalized REE pattern of amphibole from Pilgüjarvi sill, Pechenga Complex (C1 chondrite from McDonough & Sun, 1995).

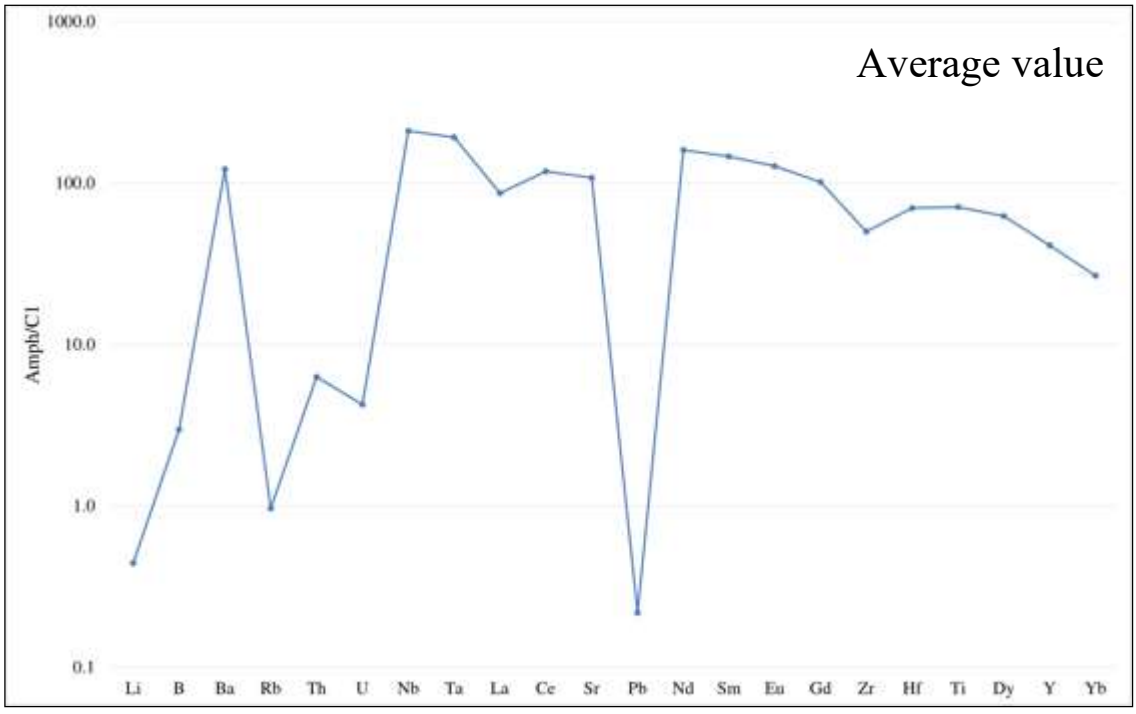

Figure 76 - Chondrite-normalized incompatible pattern of amphibole from Pilgüjarvi sill, Pechenga Complex (C1 chondrite from McDonough & Sun, 1995).

In-situ ion probe analyses (Tab. 45 Appendix B) of pargasite have remarked H_2O contents of 1.12 wt.% and fluorine and chlorine contents of 3156 ppm and 766 ppm, respectively. Amphiboles

display variable contents for Li (0.5-1.1 ppm) and B (2.68-7.16 ppm) (Tab. 45 Appendix B). The δD ratio of amphibole shows an average value of -129.8 ± 8.4 ‰ (Tab. 49 Appendix B). Oxygen isotope analysis were not performed due to the lack of good spots on amphibole grains (Tab. 49 Appendix B).

Spinel has chromite composition, with chromium value of 41.14 wt.%. The TiO_2 and Al_2O_3 contents of chromite are 3.16 wt.% and 9.96 wt.%, respectively. The contents of MgO and MnO are 5.57 wt.% and 0.24 wt.%, respectively.

Pilgüjarvi sill (sample 116-6)

Clinopyroxene is augite and its Mg-number values range between 0.75 ± 0.02 mol (Fig. 77; Tab. 18 Appendix A). Alumina (2.73-4.38 wt.%) and TiO_2 contents (1.23-2.07 wt.%) are homogeneous. The Cr_2O_3 (0.01-0.02 wt.%) does not show correlation with Mg-number. The Na_2O contents are homogeneous (0.36 ± 0.06 wt.%) and show negative correlation with Mg-number (Fig. 77).

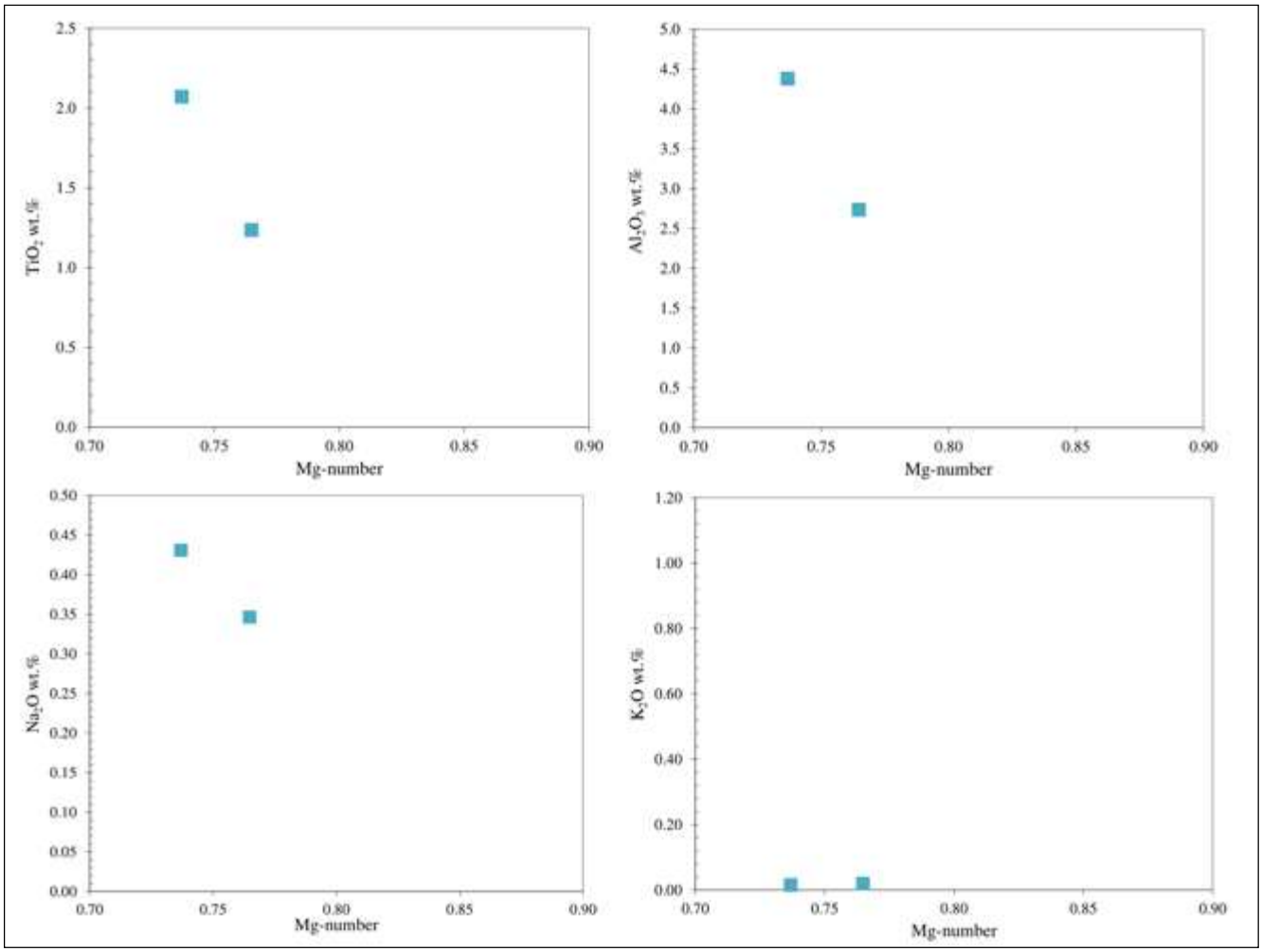

Figure 77 – Mg-number vs TiO_2, Al_2O_3, Na_2O and K_2O contents of clinopyroxene from Pilgüjarvi sill, Pechenga Complex.

The chondrite-normalized REE patterns of clinopyroxene are hump-shaped, with LREE (La_N/Sm_N = 0.42) and HREE (Gd_N/Yb_N = 2.8-3.3) depletion relative to the MREE (La_N/Yb_N = 1.64; at about 25 times C1 chondrite) (Fig. 78 and 79; Tab. 18 Appendix B). Negative anomaly in Eu are not observed (Eu/Eu* = 0.90). The clinopyroxene of the magnetite-olivine have the lowest Ni (114 ± 6 ppm) and Cr (13 ± 5 ppm) contents of the clinopyroxene analysed from the Pechenga Complex (Tab. 18 Appendix B).

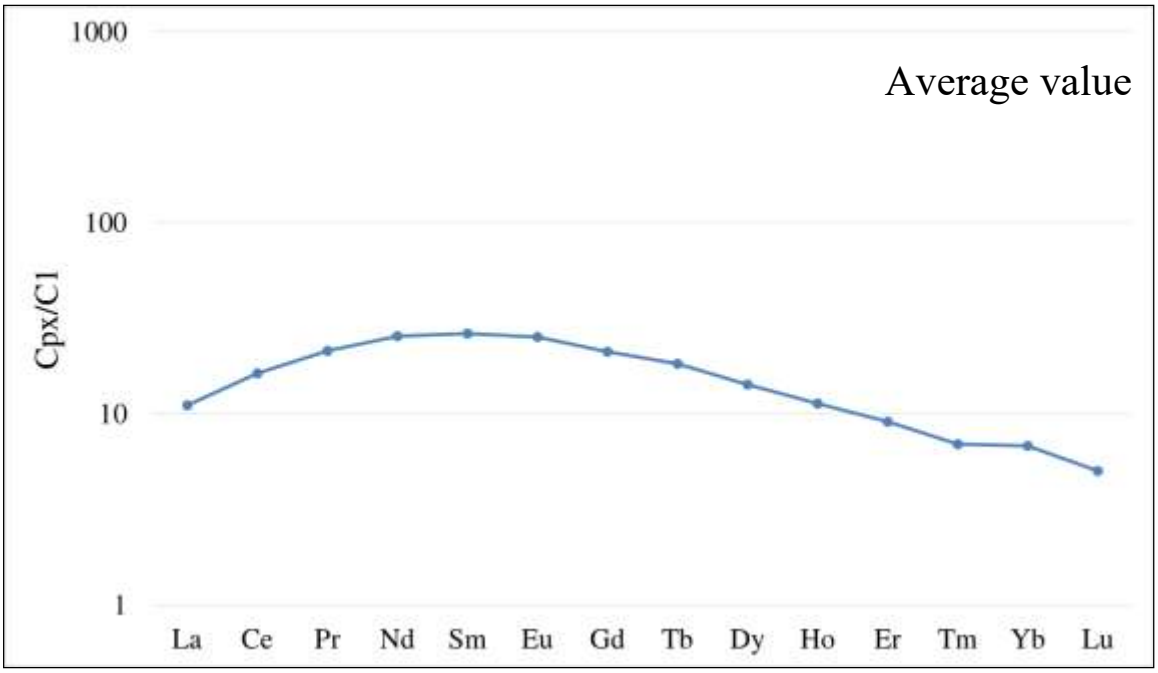

Figure 78 - Chondrite-normalized REE pattern of clinopyroxene from Pilgüjarvi sill, Pechenga Complex (C1 chondrite from McDonough & Sun, 1995).

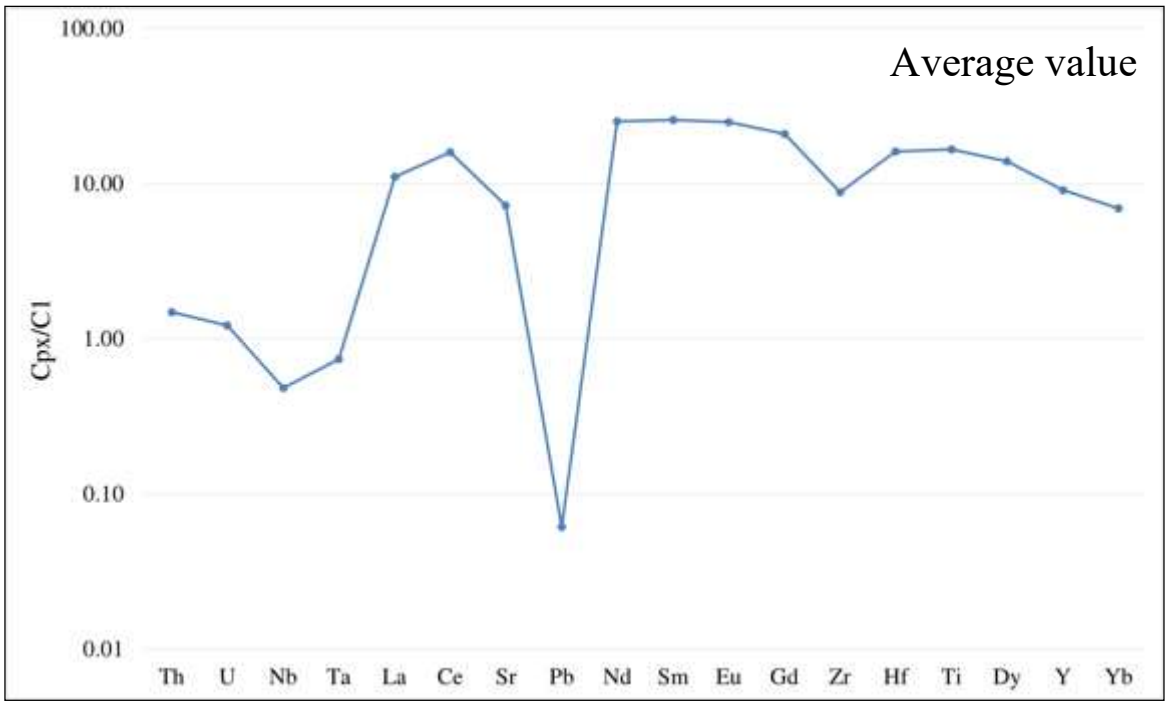

Figure 79 - Chondrite-normalized incompatible pattern of clinopyroxene from Pilgüjarvi sill, Pechenga Complex (C1 chondrite from McDonough & Sun, 1995).

Brown amphibole is pargasite with Mg-number of 0.69 mol. No significant intra-grain zoning was observed (Fig. 80; Tab. 19 Appendix A). Amphibole has TiO_2 average value of 5.25 ± 0.25 wt.% which show a negative correlation with Mg-number. The Al_2O_3 contents are homogeneous (11.35-12.13 wt.%) as the iron values (FeO_{tot}) which are in the range 10.70-11.22 wt.%. The Na_2O mean content is 3.09 ± 0.08 wt.%, whereas the K_2O mean value is 0.93 ± 0.07 wt.% (Fig. 80; Tab. 19 Appendix A).

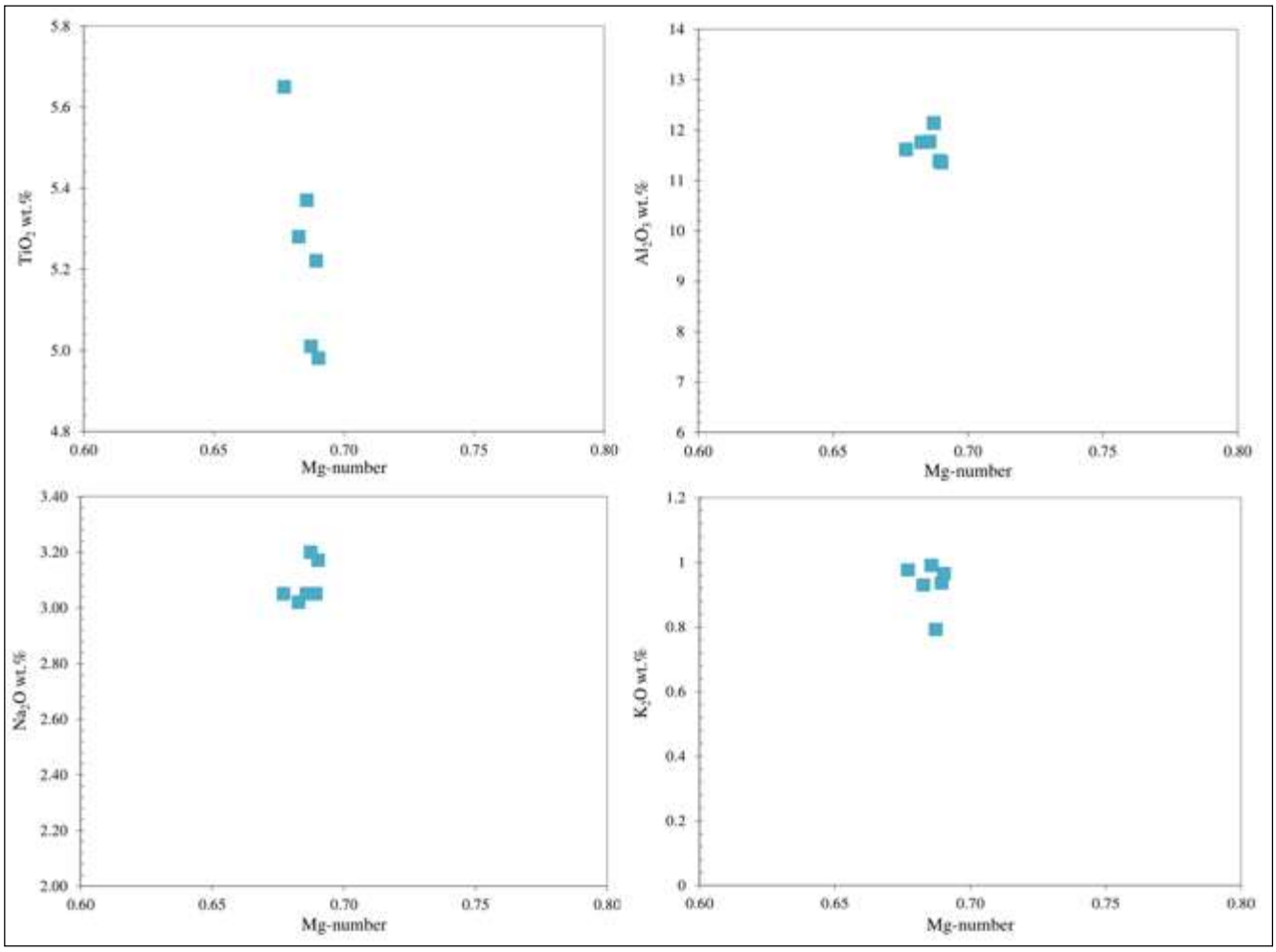

Figure 80 - Mg-number vs TiO_2, Al_2O_3, Na_2O and K_2O contents of amphibole from Pilgüjarvi sill, Pechenga Complex.

The chondrite-normalized REE patterns are characterized by a steady decrease from LREE to HREE (La_N/Yb_N = 1.73; Gd_N/Yb_N = 2.93), which are about 90-100 times the CI chondrite (Fig. 81; Tab. 19 Appendix B). Europium does not show anomalies (Eu/Eu* = 0.97). The incompatible element pattern reveals a depletion in Li, Rb, Sr, Pb and Zr relative to the neighbouring elements (Fig. 82; Tab. 19 Appendix B). The Nb/Ta and Zr/Hf ratios are 22.96 and 31.33, respectively. The Rb/Ba ratio (0.02) confirms the depletion in Rb (5.74 ± 056 ppm) and the enrichment in Ba (380 ± 36 ppm). The amphiboles exhibit homogeneous values for Sc (115 ± 10 ppm) and V (835 ± 97 ppm) which are about 15-20 times the CI chondrite, whereas amphiboles are depleted in Cr (19 ± 5.70 ppm) relative to other amphiboles of Pechenga Complex. Ni contents are variable between 188 and 260 ppm (Tab. 19 Appendix B).

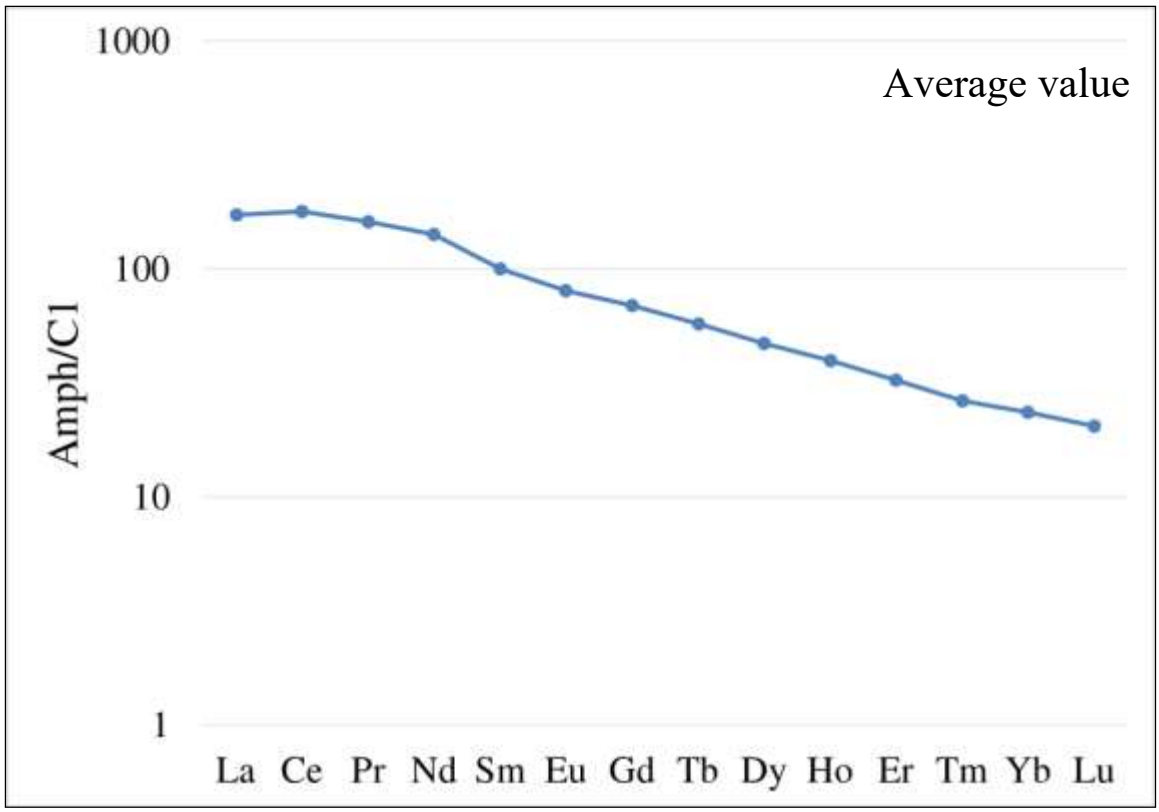

Figure 81 - Chondrite-normalized REE pattern of amphibole from Pilgüjarvi sill, Pechenga Complex (C1 chondrite from McDonough & Sun, 1995).

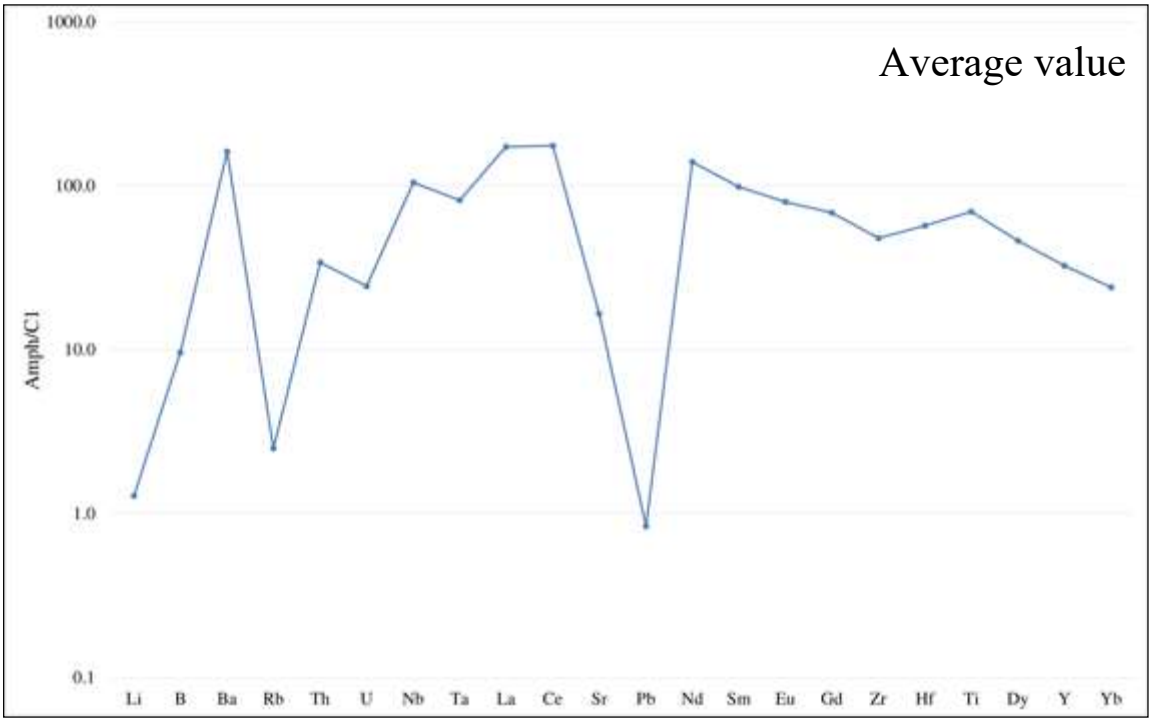

Figure 82 - Chondrite-normalized incompatible pattern of amphibole from Pilgüjarvi sill, Pechenga Complex (C1 chondrite from McDonough & Sun, 1995).

Brown amphibole has H_2O contents ranging between 0.73 and 0.93 wt.% (Tab. 45 Appendix B). Amphibole has high B contents (mean value of 59.08 ± 14.57 ppm) and shows Li mean content of 1.09

± 0.72 ppm. The average contents of fluorine and chlorine are 2316 ± 201 ppm and 1392 ± 117 ppm, respectively (Tab. 45 Appendix B). The δD ratio of amphibole shows an average value of -104.3 ± 4.5 ‰, whereas the $\delta^{18}O$ has high value of 6.4 ± 0.99 ‰ (Tab. 49 Appendix B).

Kammikivi sill (57a-HV-28)

Olivine has Fo values of 80 mol and has contents of Cr between 140 and 253 ppm (Tab. 20 Appendix A and Tab. 20 Appendix B). The Ni contents ranging between 2764 and 2892 ppm (Tab. 20 Appendix B).

Clinopyroxene is augite with Mg-number value of 0.82 mol (Fig. 83; Tab. 21 Appendix A). Mg-number shows negative correlation with alumina (0.91-1.75 wt.%) and TiO_2 contents (0.27-0.54 wt.%). Clinopyroxene exhibits a range of Cr_2O_3 (0.7-0.9 wt.%) without correlation with Mg-number. The CaO contents are homogeneous (21.97 ± 0.18 wt.%). The Na_2O (0.45 ± 0.05 wt.%) values display negative correlation with Mg-number.

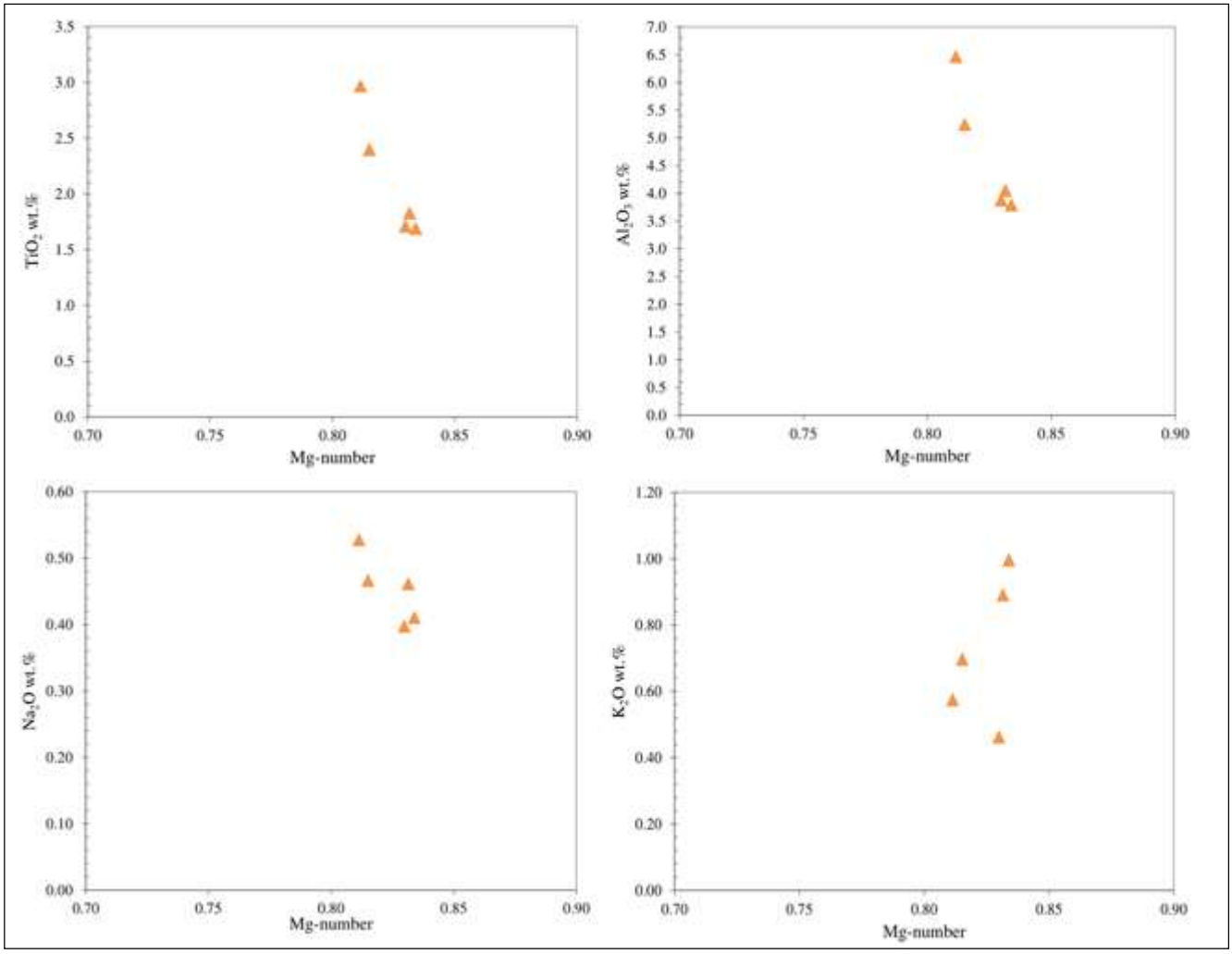

Figure 83 – Mg-number vs TiO_2, Al_2O_3, Na_2O and K_2O contents of clinopyroxene from Kammikivi sill, Pechenga Complex.

The chondrite-normalized REE patterns of clinopyroxene are hump-shaped and characterized by MREE enrichment (La_N/Sm_N = 0.39; La_N/Yb_N = 1.38) relative to LREE and HREE values (Gd_N/Yb_N = 2.72) that are 40 times the CI chondrite (Fig. 84; Tab. 21 Appendix B). The europium does not show negative, or positive, anomalies (Eu/Eu* = 1.11). The chondrite-normalized patterns of the incompatible elements show negative anomalies in Nb, Pb and Zr (Fig. 85; Tab. 21 Appendix B). The Nb/Ta and Zr/Hf ratios are 4.45 and 18.99. The Ni values are in the range 373-435 ppm, whereas the Cr contents are variable (2282-5253 ppm). Sc and V average values are 83 ± 11 and 326 ± 39 ppm, respectively (Tab. 21 Appendix B).

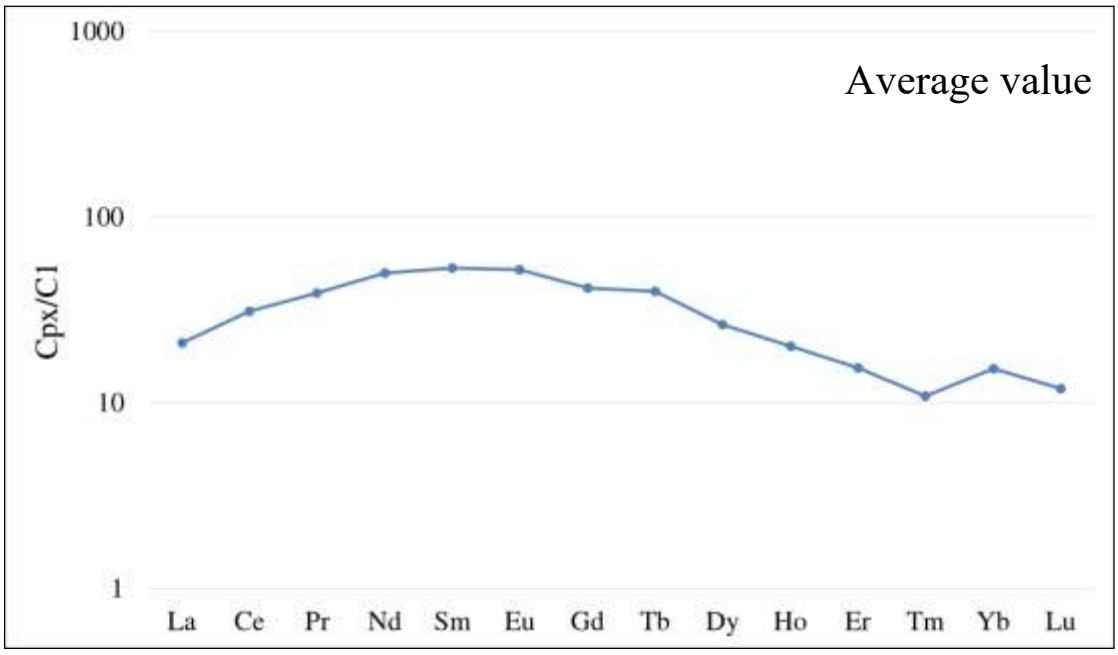

Figure 84 - Chondrite-normalized REE pattern of clinopyroxene from Kammikivi sill, Pechenga Complex (C1 chondrite from McDonough & Sun, 1995).

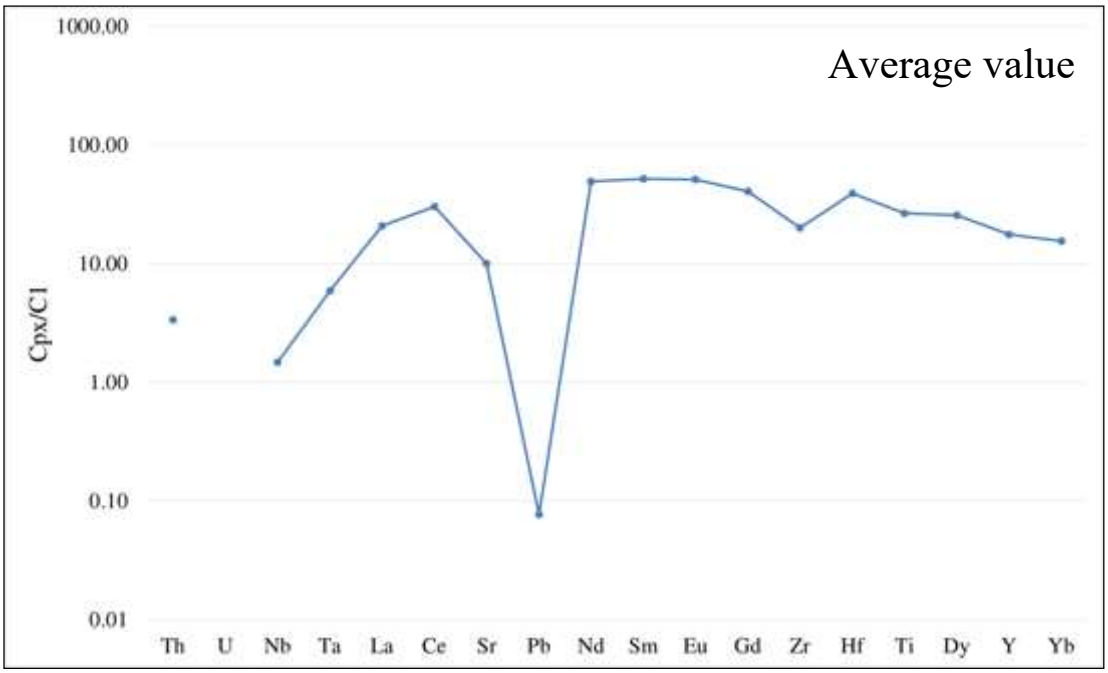

Figure 85 - Chondrite-normalized incompatible pattern of clinopyroxene from Kammikivi sill, Pechenga Complex (C1 chondrite from McDonough & Sun, 1995).

Brown amphibole is pargasite with Mg-number of 0.79 mol (Fig. 86; Tab. 22 Appendix A). Pargasite has TiO_2 contents in the range 4.43-6.48 wt.% and Al_2O_3 values between 9.02 and 12.34 wt.%. Titanium and alumina show slightly negative correlation with Mg-number. The Na_2O content is homogeneous with average value of 3.13 ± 0.12 wt.% as the K_2O value which is 0.78 ± 0.12 wt.%. Na_2O and K_2O display positive correlation with Mg-number (Fig. 86; Tab. 22 Appendix A).

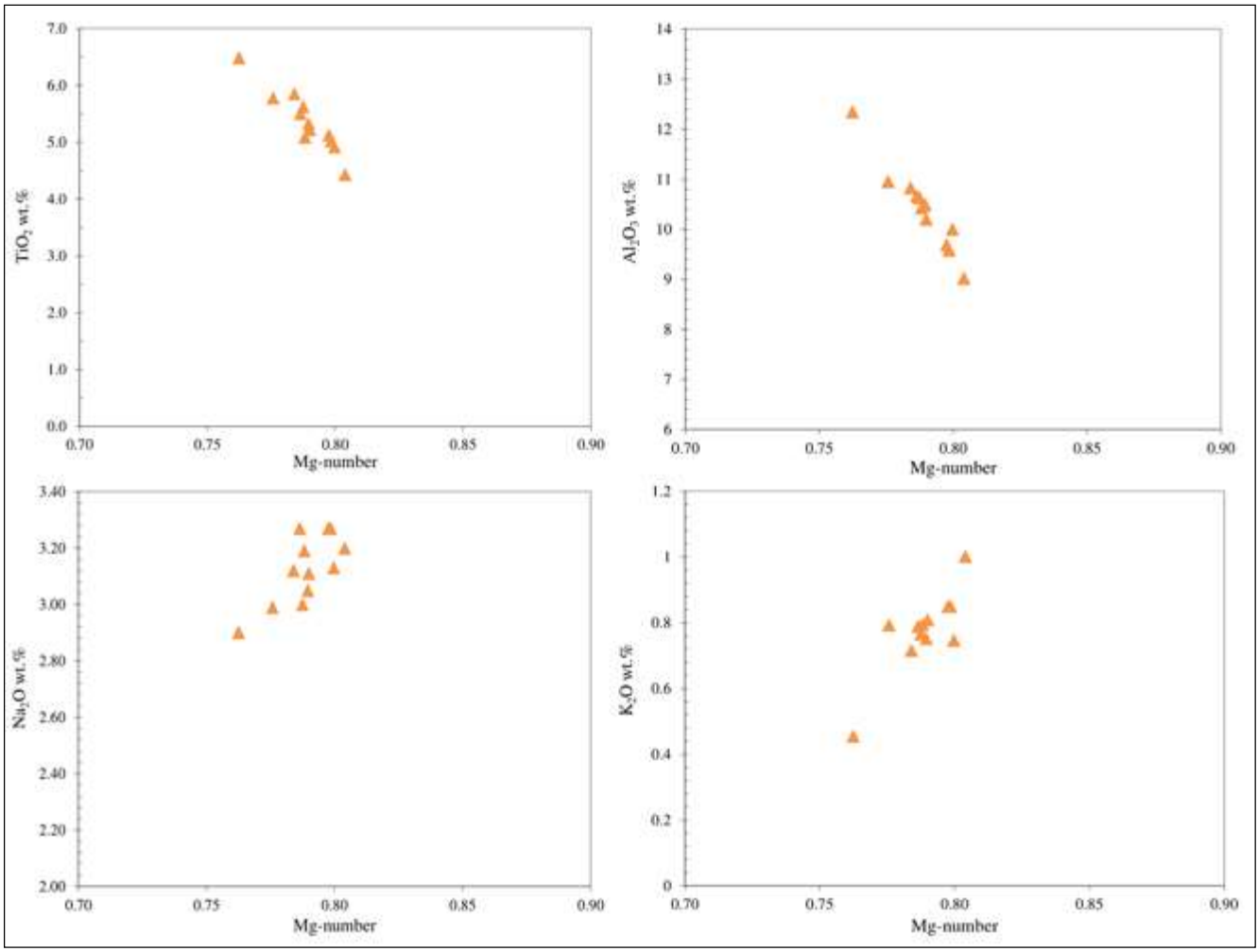

Figure 86 - Mg-number vs TiO_2, Al_2O_3, Na_2O and K_2O contents of amphibole from Kammikivi sill, Pechenga Complex.

The chondrite-normalized REE patterns are hump-shaped with LREE (La_N/Sm_N = 0.85 ± 0.21; La_N/Yb_N = 5.08 ± 0.81) and HREE (Gd_N/Yb_N = 3.05-4.78) depletion relative to MREE (at about 230 times C1 chondrite) (Fig. 87; Tab. 22 Appendix B). The incompatible element pattern reveals a strong depletion in Li, Rb, and Pb relative to the neighbouring elements and slightly negative anomalies in Zr and Ti (Fig. 88; Tab. 22 Appendix B). Positive anomalies are observed for Ba, Nb-Ta, Ce, Nd and Sm. The Nb/Ta and Zr/Hf ratios are 23.29 and 27.15, respectively. The europium does not show negative or positive anomalies (Eu/Eu* = 0.93). About LILE, Ba (421 ± 40 ppm) and Rb (3.43 ± 0.50 ppm) are 179 and 1.6 times the CI chondrite, respectively. Amphiboles display variable contents for the transition metals (Ni = 671-815 ppm; Cr = 1287-4033 ppm; V = 490-598 ppm; Sc = 23-86 ppm) (Tab. 22 Appendix B).

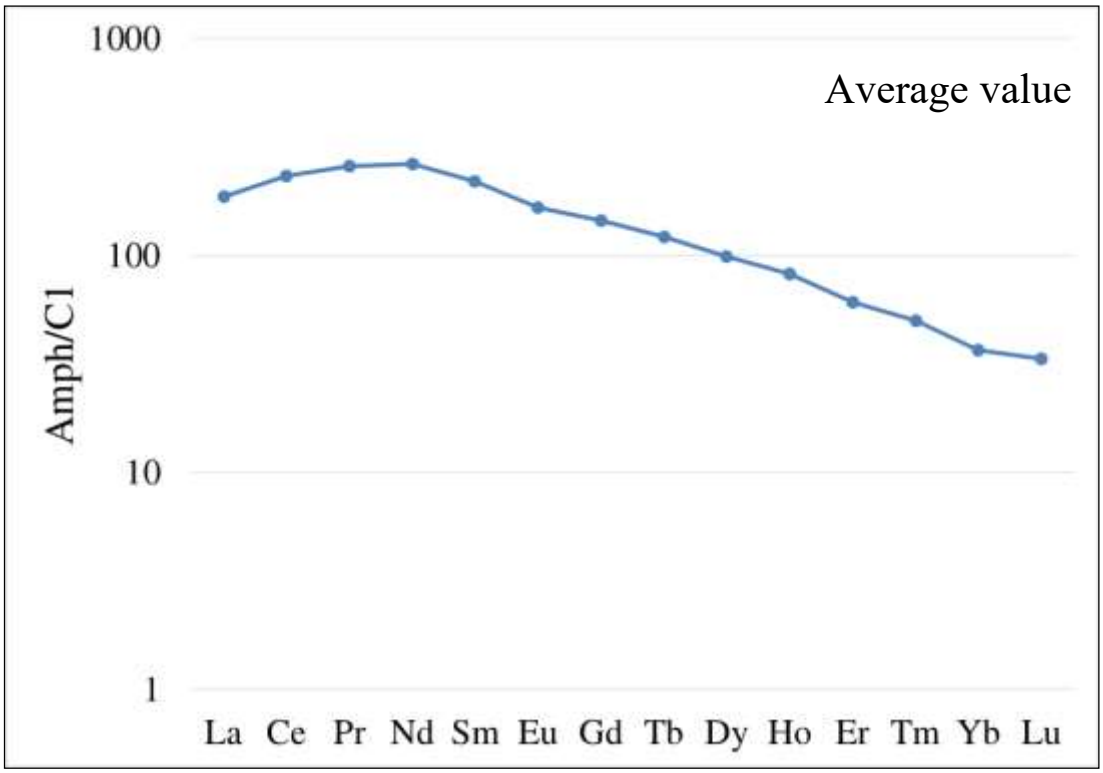

Figure 87 - Chondrite-normalized REE pattern of amphibole from Kammikivi sill, Pechenga Complex (C1 chondrite from McDonough & Sun, 1995).

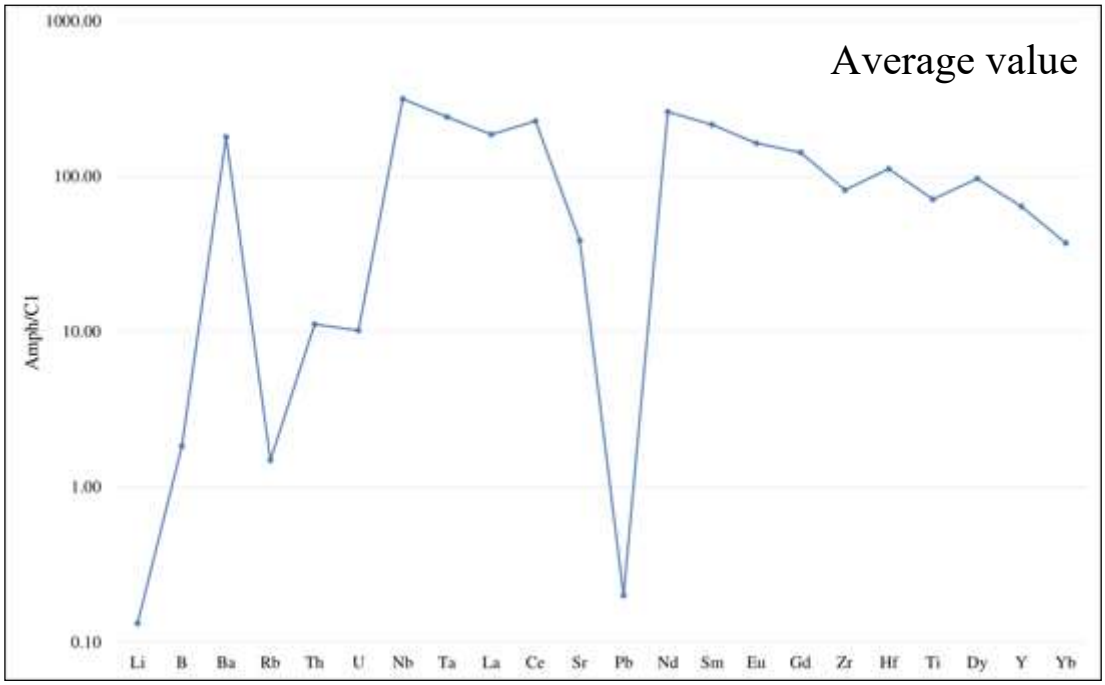

Figure 88 - Chondrite-normalized incompatible pattern of amphibole from Kammikivi sill, Pechenga Complex (C1 chondrite from McDonough & Sun, 1995).

Average H_2O content of amphibole is 1.72 ± 0.09 wt.% and a fluorine high contents are observed (5788 ± 1700 ppm) (Tab. 45 Appendix B). The average content of chlorine is 858 ± 328 ppm. Amphibole has high B contents (mean value of 51.39 ± 18.83 ppm) and shows Li mean content of 0.27 ± 0.09 ppm.

The δD and $\delta^{18}O$ ratios of amphibole show average values of -117.4 ± 46.3 ‰ and 4.3 ± 0.43 ‰ (Tab. 49 Appendix B).

Spinel has a slightly compositional variation, showing strongly variable alumina contents (Al_2O_3 = 3.96-12.52 wt.%). The others major elements contents are quite homogeneous: spinel is Ti- and Mn-rich (TiO_2 = 9.61-12 wt.%; MnO = 2.8-4.18 wt.%) and has chromium contents in the range 16.67-21.14 wt.%. MgO values of spinel differ from 1.42 to 2.44 and the iron mean value is 53.8 wt.%.

Nyasyukka dike complex (samples N-2 and N-3)

Trace trace element compositions of amphibole of sample N-3 are from Fiorentini et al. (2008).

Olivine has very low and variable Fo contents in the 2 samples between 61 and 72 mol (Tab. 23 and 24 Appendix A) and its contents of Cr ranging between 40 and 92 ppm in sample (Tab. 23 Appendix B). Ni values ranging between 1651 and 1824 ppm.

Clinopyroxene has Mg-number values ranging between 0.77 and 0.80 mol. Mg-number shows positive correlation with Cr_2O_3 (0.06-0.7 wt.%) (Tab. 25 Appendix A). Clinopyroxene exhibits alumina (1.83-3.27 wt.%) and TiO_2 contents (0.58-1.62 wt.%) without correlation with Mg-number (Tab 25 Appendix A). The clinopyroxene grains were not analysed for trace elements due to the small size of the relict grains almost substitute by secondary phases.

Brown amphibole is pargasite in composition with Mg-number of 0.70 mol (Fig. 89; Tab. 26 and 27 Appendix A). No significant intra-grain zoning was observed. The TiO_2 (4.78-4.91 wt.%) and Al_2O_3 (10.09-10.64 wt.%) contents are homogeneous and only alumina displays positive correlation with Mg-number (Fig. 89; Tab. 26 and 27 Appendix A). The Na_2O and K_2O mean contents are 2.94 ± 0.13 wt.% and 0.76 ± 0.03 wt.%, respectively, and the sodium shows a positive correlation with Mg-number (Fig. 89; Tab. 26 and 27 Appendix A).

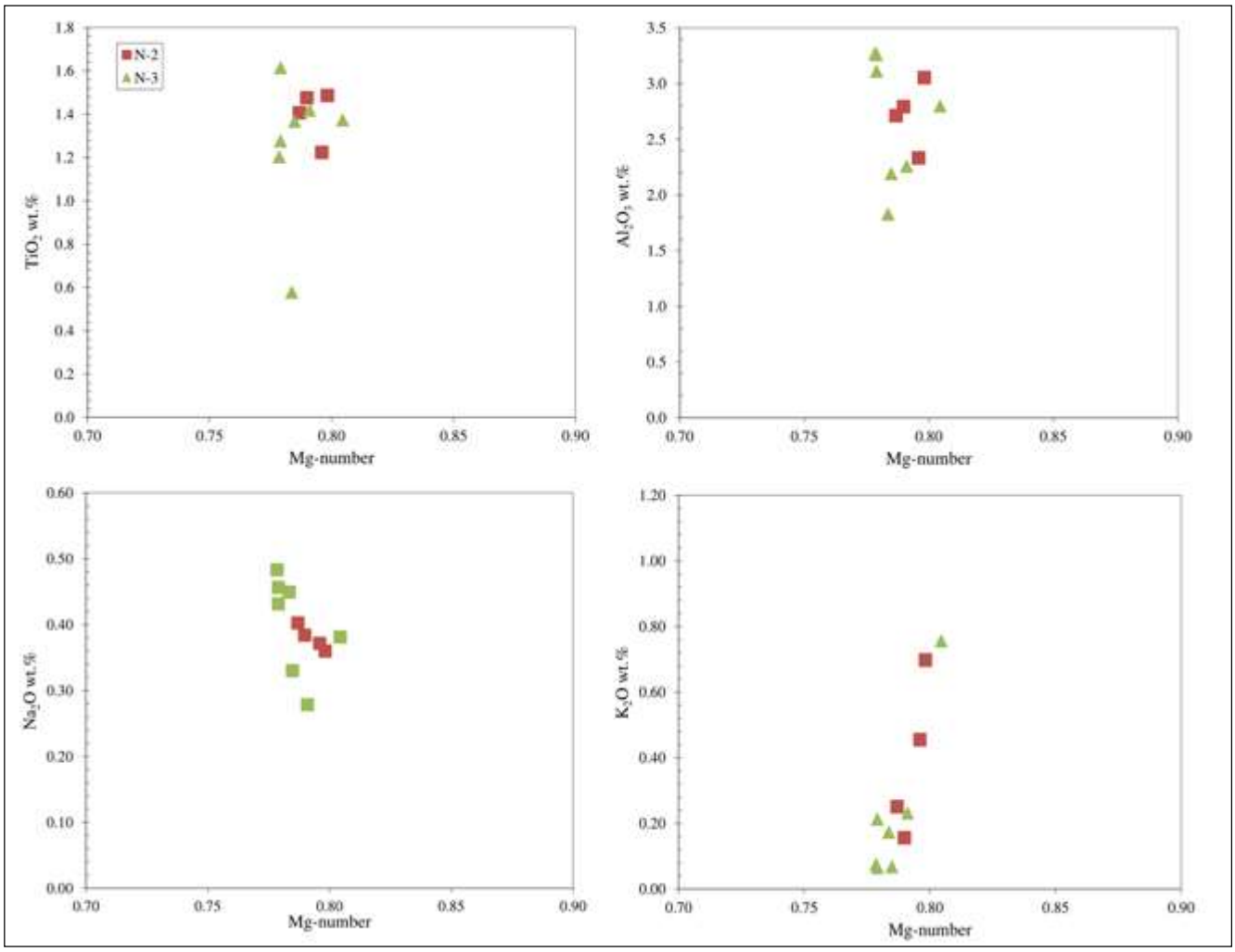

Figure 89 - Mg-number vs TiO_2, Al_2O_3, Na_2O and K_2O contents of amphibole from Nyasyukka dike complex, Pechenga Complex.

The trace elements data of amphibole of the sample N-3 are those from Fiorentini et al. (2008). The chondrite-normalized REE patterns are hump-shaped and show decrease from MREE to HREE (La_N/Yb_N = 0.64-1.78; Gd_N/Yb_N = 2.54-3.69), which are about 160 times the CI chondrite (Fig. 90; Tab. 24 and 25 Appendix B). The LREE are depleted (La_N/Sm_N = 0.88-1.22) with no europium anomaly (Eu/Eu* = 0.98). The chondrite-normalized incompatible element patterns reveal depletion in Li, Rb, B and Pb relative to the neighbouring elements (Fig. 91; Tab. 24 and 25 Appendix B). Nb/Ta and Zr/Hf ratios are 20.20 and 28.30, respectively. Rb and Ba have homogeneous values of 3.70 ± 26 ppm and 301-330 ppm, respectively. The Ni contents are variable between 412 and 507 ppm as the Cr that shows a wide range of 947-2130 ppm. On the contrary, the V and Sc contents are homogeneous in two restricted range of 535-562 ppm and 56-66 ppm, respectively (Tab. 24 and 25 Appendix B).

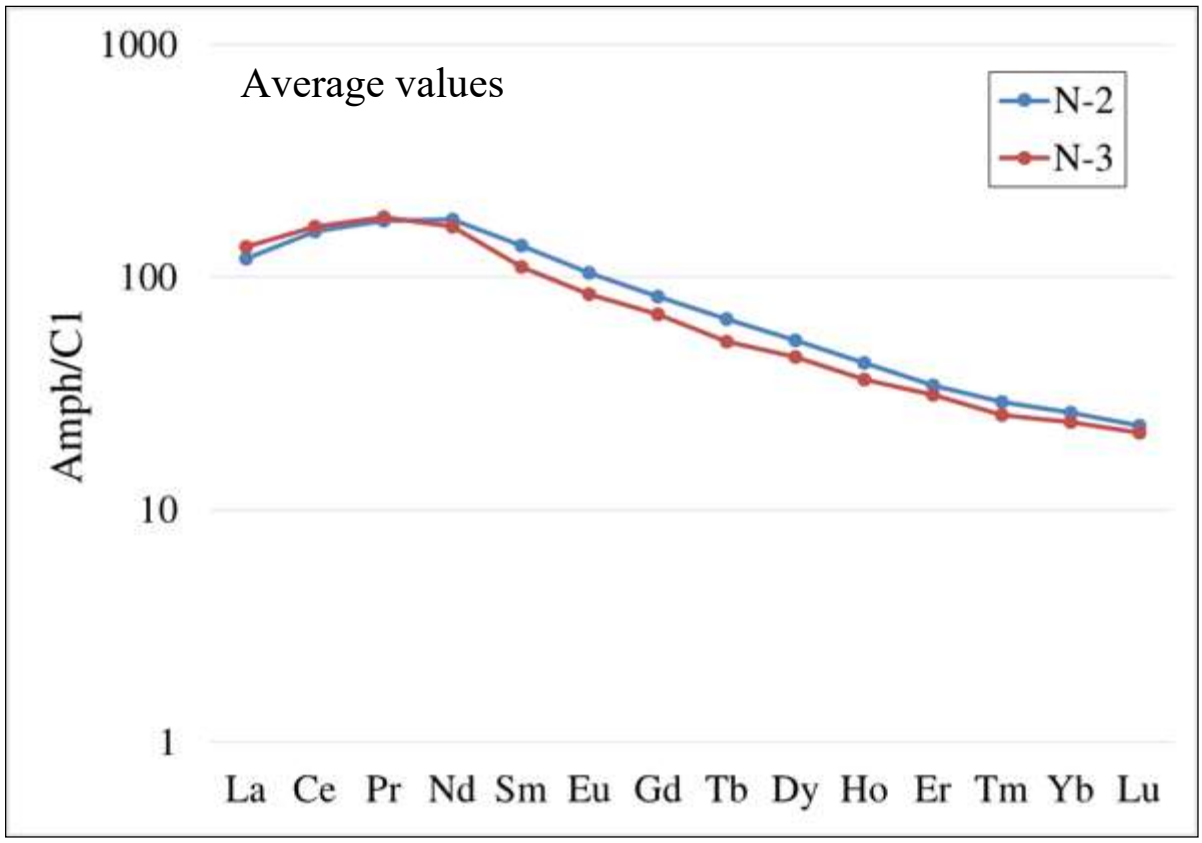

Figure 90 - Chondrite-normalized REE pattern of amphibole from Nyasyukka dike complex, Pechenga Complex (C1 chondrite from McDonough & Sun, 1995); data from Fiorentini et al. (2008).

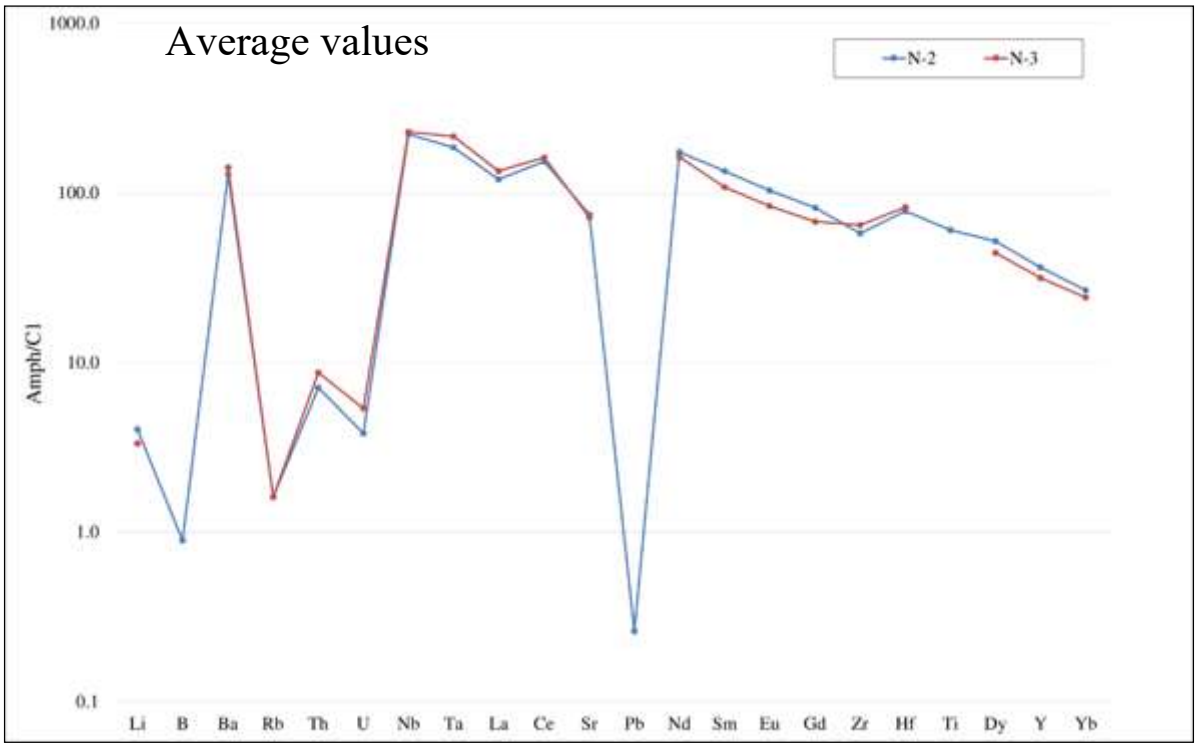

Figure 91 - Chondrite-normalized incompatible pattern of amphibole from Nyasyukka dike complex, Pechenga Complex (C1 chondrite from McDonough & Sun, 1995). Data from Fiorentini et al. (2008).

Analysed H_2O in brown amphiboles ranges between 1.02 and 1.35 wt. % (Tab. 45 Appendix B). The same analysis technique is used for Li and B which contents are 3.89-6.02 ppm and 0.35-0.80 ppm, respectively (Tab. 45 Appendix B). Furthermore, the chlorine and fluorine contents are variables in the ranges 1098-1566 ppm and 873-1646 ppm, respectively (Tab. 45 Appendix B). The amphiboles from Nyasyukka complex show values for δD ratio between -108.7 ‰ and -99.5 ‰, whereas the $\delta^{18}O$ ratio is in the range 3.0-5.0 ‰ (Tab. 49 Appendix B).

3.3 Major, trace elements and isotope compositions of Phanerozoic samples

In the following section are reported the compositions of olivine, clinopyroxene and amphibole of Phanerozoic samples that were selected for SIMS analysis on amphibole.

Antarctica (Ross Orogen): Husky Ridge (TT329)

Major and trace elements composition of sample TT329 are from Tiepolo and Tribuzio (2008).

Clinopyroxene associated to brown amphibole is augite with a Mg-number of 0.79 mol (Tab. 28 Appendix A). The Al_2O_3 contents are variable and range from 0.69 to 5.96 wt.%, the TiO_2 contents are nearly 0.30 wt.%. The Na_2O contents are variable (0.27-0.93) wt.% (Tab. 28 Appendix A). The chondrite-normalized REE patterns (not shown) are bell-shaped with the maximum at the MREE at about 4 times the C1 chondrite values (Tab. 26 Appendix B). The La_N/Sm_N ratio ranges between 0.4 and 0.5 and no Eu anomaly is observed. The incompatible element patterns reveal depletion in Ba, Nb, Pb and Ti relative to the nearby elements. Enrichments relative to the neighbouring elements in Th and U are observed. Cr contents are in the range 1130-2000 ppm (Tab. 26 Appendix B).

Brown amphibole is edenite and has Mg-number of 0.71 mol (Tab. 29 Appendix A). The amphibole has homogeneous TiO_2 (mean value 1.51 wt.%) and Al_2O_3 (about 10.77 wt.%) contents. The Na_2O and K_2O contents are homogeneous with mean values of 1.53 wt.% and 0.38 wt.%, respectively (Tab. 29 Appendix A). The chondrite-normalized REE patterns vary from flat to slightly convex downward (La_N/Sm_N = 0.577; La_N/Yb_N = 1.04) with MREE at 20 times CI chondrite values (Fig. 92; Tab. 26 Appendix B). No Eu anomalies are observed (Eu/Eu* = 0.88).

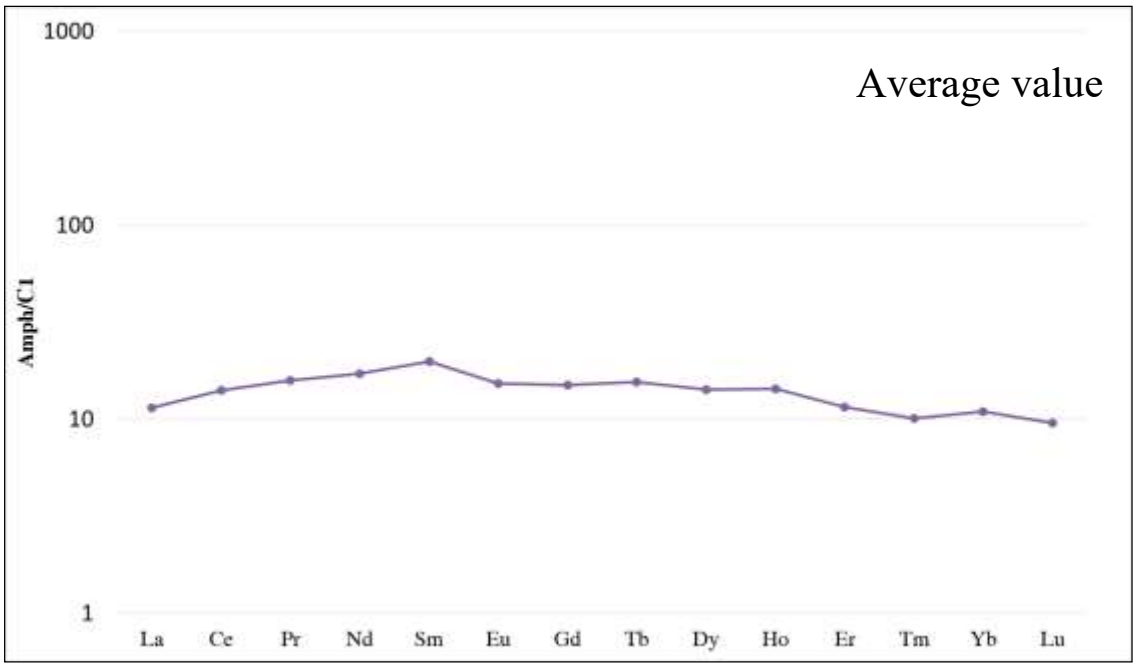

Figure 92- Chondrite-normalized REE pattern of amphibole from Husky Ridge, Ross Orogen (C1 chondrite from McDonough & Sun, 1995).

Chondrite-normalized pattern of trace elements display distinctive negative Th, Nb, Ta, Sr, Pb and Zr anomalies and positive U and La anomalies (Fig. 93; Tab. 26 Appendix B). About the LILE, Ba has homogeneous contents of 14.45 ± 1.25 ppm. The Cs mean value is 0.03 ppm. Brown amphibole shows high concentrations in Cr (mean value 582 ppm), Sc (63.05 ppm) and V (483 ppm). The Ni mean content is 412 ± 14.14 ppm (Tab. 26 Appendix B).

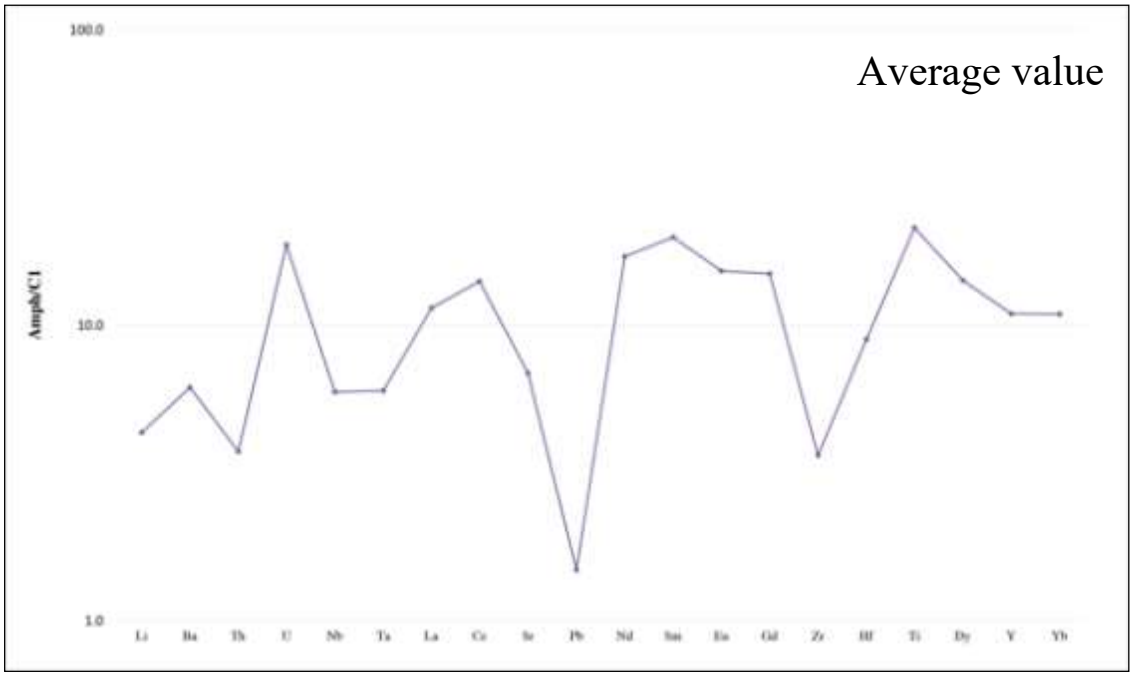

Figure 93 - Chondrite-normalized incompatible pattern of amphibole from Husky Ridge, Ross Orogen (C1 chondrite from McDonough & Sun, 1995).

The volatile contents of the amphibole (Tab. 46 Appendix B), as well as the hydrogen and oxygen isotopes analysis (Tab. 50 Appendix B) were carried out in this study. In-situ ion probe analyses reveal H_2O contents ranging between 0.95 and 1.06 wt.% whereas Li and B mean contents of 6.49 ± 0.42 ppm and 4.24 ± 0.74 ppm, respectively (Tab. 46 Appendix B). Amphibole from Husky Ridge Qtz-diorite shows fluorine mean content of 959 ± 36 ppm and chlorine values ranging between 929 and 1020 ppm (Tab. 46 Appendix B). The δD ratio of amphibole shows an average value of -61.5 ± 7.3 ‰ and $\delta^{18}O$ ratio is in the range 6.1-8.4 ‰ (Tab. 50 Appendix B).

Iran (Zagros orogen): Sanandaj Sirjan Zone (AL89)

Major and trace elements data are from Esna-Ashari et al. (2016).

Olivine has very low and variable Fo contents between 71 and 84 mol (Tab. 30 Appendix A) and its contents of Cr ranging between 84 and 262 ppm (Tab. 27 Appendix B). Ni values ranging between 1155 and 1457 ppm (Tab. 27 Appendix B).

Clinopyroxene has Mg-number mean value of 0.88 mol. Mg-number shows positive correlation with Cr_2O_3 (0.3-1.1 wt.%) (Tab. 31 Appendix A). Clinopyroxene exhibits alumina (0.5-2.6 wt.%) and TiO_2 contents (0.07-0.25 wt.%) without correlation with Mg-number. The CaO contents are homogeneous (21.68 ± 1.3 wt.%). The Na_2O (0.17 ± 0.05 wt.%) values display negative correlation with Mg-number (Tab. 31 Appendix A). The chondrite-normalized REE pattern of clinopyroxene vary from flat to slightly convex downward and depleted in LREE (La_N/Sm_N = 0.49; La_N/Yb_N = 0.45) and MREE that are 3 times the CI chondrite (Tab. 27 Appendix B). The HREE values (Gd_N/Yb_N = 1.22) are 4 times the CI values. The europium shows slightly negative anomaly (Eu/Eu* = 0.72). The chondrite-normalized pattern of the incompatible elements shows negative anomalies in Nb, Pb and Zr, whereas positive anomalies are observed for Th, La-Ce and Nd-Sm (Tab. 27 Appendix B). The Ni values are in the range 137-151 ppm, whereas the Cr contents are variable (4534-6712 ppm). Sc and V average values are 74 ± 10 and 733 ± 119 ppm, respectively (Tab. 27 Appendix B).

Brown amphibole is pargasite with Mg-number of 0.83 mol (Tab. 32 Appendix A). No significant intra-grain zoning was observed. The TiO_2 (2.75 ± 0.21 wt.%) and Al_2O_3 (11.1 ± 0.14 wt.%) contents are homogeneous. The Na_2O and K_2O mean contents are 2.17 ± 0.38 wt.% and 0.61 ± 0.02 wt.%, respectively (Tab. 32 Appendix A). The chondrite-normalized REE pattern are hump-shaped in the LREE region (La_N/Sm_N = 1.18) and the europium show slightly negative anomalies (Eu/Eu* = 0.72) (Fig. 94; Tab. 27 Appendix B). About MREE and HREE the pattern is almost flat (La_N/Yb_N = 2.69; Gd_N/Yb_N = 1.35), which are about 26 times the CI chondrite (Fig. 94; Tab. 27 Appendix B).

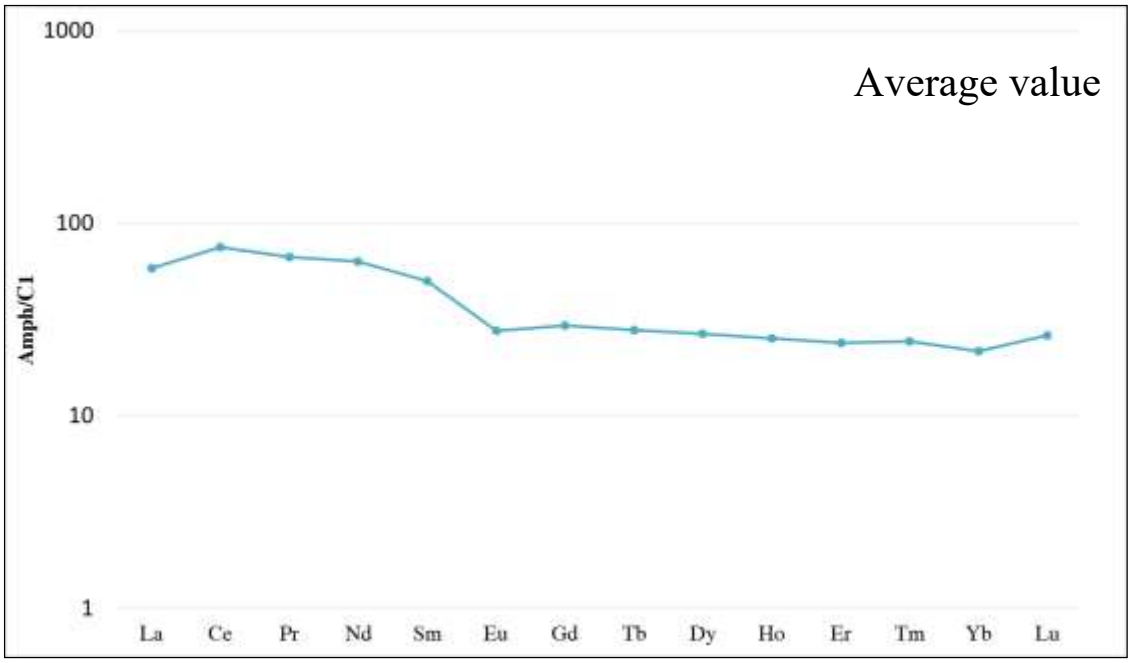

Figure 94 - Chondrite-normalized REE pattern of amphibole from Sanandaj Sirjan Zone, Zagros Orogen, Iran (C1 chondrite from McDonough & Sun, 1995).

The chondrite-normalized incompatible element pattern reveals negative anomalies in Rb, Pb and Zr (Fig. 95; Tab. 27 Appendix B). Nb/Ta and Zr/Hf ratios are 20 and 23.5, respectively. Rb has homogeneous mean values of 2.6 ± 0.6 ppm and whereas Ba is variable with mean value of 42 ± 22.6 ppm (Tab. 27 Appendix B). The Ni contents are homogeneous (365 ± 16 ppm) whereas the Cr has high content (2950 ± 363 ppm). On the contrary, the V and Sc contents are homogeneous in two restricted range of 362-469 ppm and 64.5-70 ppm, respectively (Tab. 27 Appendix B).

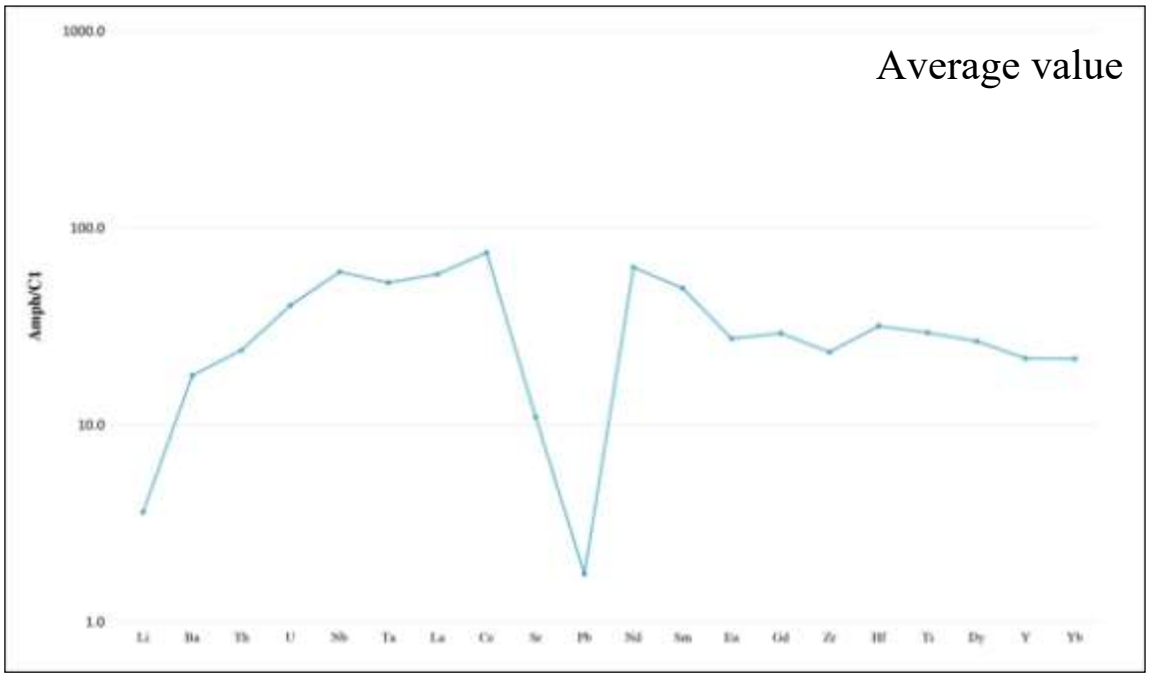

Figure 95 - Chondrite-normalized incompatible pattern of amphibole from Sanandaj Sirjan Zone, Zagros Orogen, Iran (C1 chondrite from McDonough & Sun, 1995).

Ion probe analyses of brown amphiboles give H_2O contents of 0.64-0.71 wt.% (Tab. 46 Appendix B). The same analysis technique is used for Li and B which contents are 4.82-5.80 ppm and 0.93-1.94 ppm, respectively (Tab. 46 Appendix B). Furthermore, the chlorine and fluorine contents are variables in the ranges 429-579 ppm and 645-742 ppm, respectively (Tab. 46 Appendix B). About isotopic in-situ analysis, amphibole shows values for δD ratio between -94 and -110 ‰, whereas the $\delta^{18}O$ ratio is in the range 5.7-6.9 ‰ (Tab. 50 Appendix B).

Japan Arc: Taku (TK1B)

Olivine has very low Fo contents of 0.70 mol (Tab. 33 Appendix A) and its contents of Cr ranges between 5.03 and 8.19 ppm (Tab. 28 Appendix B). Ni values are between 326 and 426 ppm (Tab. 28 Appendix B).

Clinopyroxene has augitic composition and Mg-number values ranging between 0.76 and 0.86 mol (Tab. 34 Appendix A). Mg-number does not show correlation with alumina (2.04 ± 0.73 wt.%), TiO_2 (0.27 ± 0.14 wt.%) and Cr_2O_3 (0.31 ± 0.19 wt.%) contents (Tab. 34 Appendix A). The Na_2O contents are homogeneous (0.23 ± 0.07 wt.%) and show negative correlation with Mg-number. Clinopyroxene has Ni values in the range 1737-1868 ppm, whereas the Cr contents are variable (2777-10909 ppm) (Tab. 28 Appendix B). Sc and V average values are 335-520 and 979-2313 ppm, respectively (Tab. 28 Appendix B).

Brown amphibole is pargasite with Mg-number of 0.74 mol (Tab. 35 Appendix A). No significant intra-grain zoning was observed. The TiO_2 (1.20-2.09 wt.%) and Al_2O_3 (11.24-12.66 wt.%) contents are homogeneous and only alumina displays positive correlation with Mg-number. The Na_2O and K_2O mean contents are 1.67 ± 0.15 wt.% and 0.69 ± 0.03 wt.%, respectively (Tab. 35 Appendix A). The chondrite-normalized REE pattern is hump-shaped and show decrease from MREE to HREE (La_N/Yb_N = 1.10; Gd_N/Yb_N = 1.76), which are about 20 times the CI chondrite (Fig. 96; Tab. 29 Appendix B). The LREE are depleted (La_N/Sm_N = 0.49) and the europium shows marginally negative anomaly (Eu/Eu* = 0.84). The chondrite-normalized incompatible element pattern reveals depletion in B, Rb, Pb and Zr relative to the neighbouring elements (Fig. 97; Tab. 29 Appendix B). Nb/Ta and Zr/Hf ratios are 19.13 and 24.66, respectively. Rb and Ba have homogeneous values of 3.51 ± 0.33 ppm and 65.10 ± 4.22 ppm, respectively. The Ni contents are high (136 ± 11.1 ppm) as the Cr that shows a mean concentrations of 1129 ± 167 ppm (Tab. 29 Appendix B). The V and Sc contents are homogeneous with mean values of 491 ± 54.8 ppm and 73.10 ± 3.41 ppm, respectively (Tab. 29 Appendix B).

Brown amphibole has H_2O contents between 1.04 and 1.22 wt.% (Tab. 46 Appendix B). The same analysis technique is used for Li and B which contents are 1.4-1.8 ppm and 1.21-1.54 ppm, respectively (Tab. 46 Appendix B). Furthermore, the chlorine and fluorine contents vary in the ranges 652-780 ppm and 501-542 ppm, respectively. The amphiboles were also analysed for hydrogen and oxygen isotopes and show values for δD ratio between -112 and -124 ‰, whereas the $\delta^{18}O$ ratio is in the range 5.4-6.4 ‰ (Tab. 50 Appendix B).

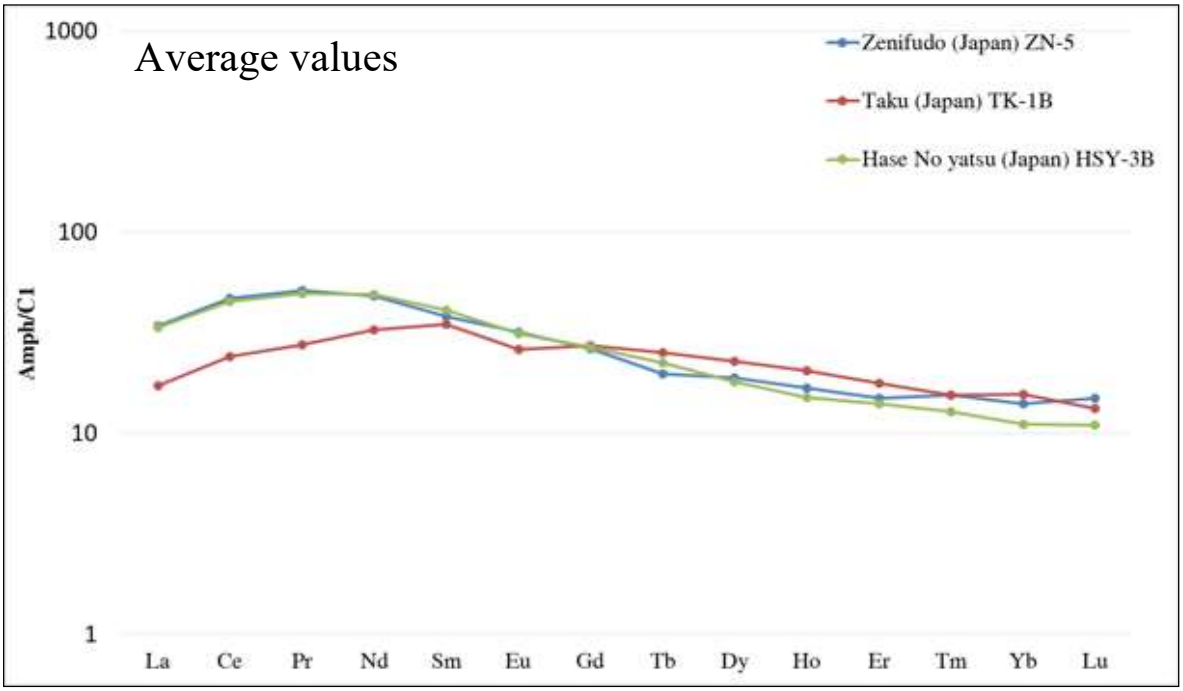

Figure 96 - Chondrite-normalized REE pattern of amphiboles from Taku, Zenifudo and Hase no Yatsu, Japan Arc (C1 chondrite from McDonough & Sun, 1995).

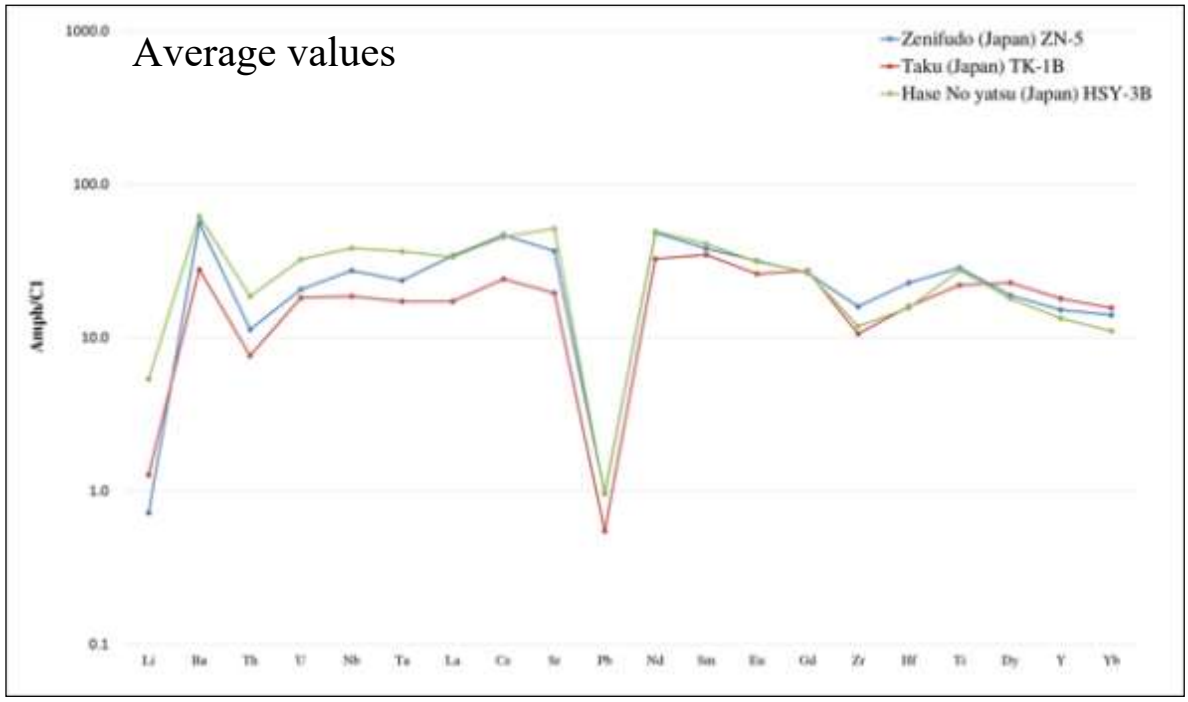

Figure 97 - Chondrite-normalized incompatible pattern of amphibole from Taku, Zenifudo and Hase no Yatsu, Japan Arc (C1 chondrite from McDonough & Sun, 1995).

Japan Arc: Zenifudo (ZN5)

Olivine has very low and variable Fo contents of 0.76 mol (Tab. 36 Appendix A) and its contents of Cr are extremely variable ranging between 5.83 and 138.23 ppm (Tab. 30 Appendix B). Ni values ranging between 174 and 236 ppm (Tab. 30 Appendix B).

Clinopyroxene is augite (Mg-number 0.82-0.85 mol) (Tab. 37 Appendix A). Mg-number does not show correlation with alumina (2.75-4.02 wt.%), TiO_2 (0.19 -0.67 wt.%) and Cr_2O_3 (0.27 ± 0.08 wt.%) contents (Tab. 37 Appendix A). The Na_2O contents are homogeneous with mean value of 0.23 ± 0.06 wt.% (Tab. 37 Appendix A). The chondrite-normalized REE pattern of clinopyroxene are hump-shaped, with LREE (La_N/Sm_N = 0.37-0.70) and HREE (Gd_N/Yb_N = 1.1-2.5) depletion relative to the MREE (La_N/Yb_N = 0.94-1.43; at about 8 times C1 chondrite) (Tab. 31 Appendix B). Negative anomaly in Eu are not observed (Eu/Eu* = 1.06). The chondrite-normalized pattern of the incompatible elements shows negative anomalies in Nb, Pb, Zr and Hf, whereas positive anomalies are observed for Th, U relative to the neighbouring elements (Tab 31 Appendix B). The Ni values are in the range 15.74-28.22 ppm, whereas the Cr contents are extremely variable (693-2204 ppm). Sc and V average values are 84.02 ± 9.8 and 230 ± 42.4 ppm, respectively (Tab. 31 Appendix B).

Brown amphibole is pargasite with Mg-number of 0.73 mol (Tab. 38 Appendix A). No significant intra-grain zoning was observed. The TiO_2 (2.18 ± 0.6 wt.%) and Al_2O_3 (12.33 ± 0.25 wt.%) contents are homogeneous and no correlation with Mg-number were observed. The Na_2O and K_2O mean

contents are 2.31 ± 0.09 wt.% and 0.66 ± 0.04 wt.%, respectively (Tab. 38 Appendix A). The chondrite-normalized REE patterns are hump-shaped and show decrease from MREE to HREE (La_N/Yb_N = 0.90; Gd_N/Yb_N = 1.88), which are about 16 times the CI chondrite (Fig. 96; Tab. 32 Appendix B). The LREE are slightly enriched (La_N/Sm_N = 0.90) and the europium does not show negative or positive anomalies (Eu/Eu* = 1). The chondrite-normalized incompatible element pattern reveals negative anomalies in Li, Rb, B and Pb relative to the neighbouring elements (Fig. 97; Tab. 32 Appendix B). Nb/Ta and Zr/Hf ratios are 21.21 and 26.27, respectively. Rb and Ba have homogeneous values of 2.34 ± 0.33 ppm and 130 ± 9.14 ppm, respectively (Tab. 32 Appendix B). The Ni contents are homogeneous with mean content of 59 ± 5.49 ppm whereas the Cr shows a range of 1279-1994 ppm. The contents of V and Sc are homogeneous in two restricted range of 379 ± 61.5 ppm and 64.1 ± 6 ppm, respectively (Tab. 32 Appendix B). Brown amphiboles are analysed with ion probe for H_2O contents that are almost homogeneous in the range 0.8 and 0.98 wt.% (Tab. 46 Appendix B). The same analysis technique is used for Li and B which contents are 0.8-1.6 ppm and 0.39-0.92 ppm, respectively (Tab. 46 Appendix B). Furthermore, the chlorine and fluorine contents are homogeneous in the ranges 531-672 ppm and 344-406 ppm, respectively (Tab. 46 Appendix B). The isotopic analysis for hydrogen and oxygen have revealed exceptionally variable values for δD ratio between -29 and -84 ‰, whereas the $\delta^{18}O$ ratio is in the range 5.5-6.7 ‰ (Tab. 50 Appendix B).

Japan Arc: Hase no Yatsu (HSY3B)

Data from Langone et al. (2009).

Olivine has very low and variable Fo contents between 0.60 and 0.71 mol (Tab. 39 Appendix A) and its contents of Cr ranging between 3.46 and 12.61 ppm (Tab. 33 Appendix B). Ni values ranging between 163 and 246 ppm (Tab. 33 Appendix B).

Clinopyroxene associated to brown amphibole is augitic in composition with a Mg-number of 0.83 mol (Tab. 40 Appendix A). The Al_2O_3 and Na_2O contents are variable (1.19-2.91 wt.% and 0.11-0.40, respectively), whereas the TiO_2 mean content is nearly 0.35 wt.% (Tab. 40 Appendix A). The chondrite-normalized REE pattern is characterized by a depletion in LREE and HREE (La_N/Sm_N = 0.43; Gd_N/Yb_N = 2.80) relative to MREE (La_N/Yb_N = 1.54), which is at about 11 times CI chondrite and no Eu anomalies were observed (Eu/Eu* = 0.96) (Tab. 34 Appendix B). The incompatible element pattern reveals enrichment in Th, U, Nd and Sm relative to the neighbouring elements and negative anomalies were observed for Nb, Pb and Zr (Tab. 34 Appendix B). Cr contents are in the range 599-2204 ppm whereas Ni values are almost homogeneous with average content of 21.13 ± 4.16 ppm (Tab. 34 Appendix B).

Brown amphibole is pargasite with Mg-number of 0.70 mol (Tab. 41 Appendix A). About major elements composition no significant intra-grain zoning was observed. The TiO_2 (1.24 ± 0.16 wt.%) and Al_2O_3 (13.42 ± 0.34 wt.%) contents are homogeneous and are not observed correlation with Mg-number (Tab. 41 Appendix A). The Na_2O and K_2O mean contents are 1.95 ± 0.10 wt.% and 1.29 ± 0.11 wt.%, respectively. The chondrite-normalized REE pattern is hump-shaped and show decrease from MREE to HREE (La_N/Yb_N = 3.02; Gd_N/Yb_N = 2.42), which are about 15 times the CI chondrite (Fig. 96; Tab. 35 Appendix B). The LREE are depleted (La_N/Sm_N = 0.82) and the Eu does not show negative or positive anomalies (Eu/Eu* = 0.94). The chondrite-normalized incompatible element pattern reveals depletion in Li, Rb, Pb and Zr relative to the neighbouring elements (Fig. 97; Tab. 35 Appendix B). Positive anomalies are observed for Ba, Nb-Ta, Nd and Ti. Nb/Ta and Zr/Hf ratios are 19.0 and 26.6, respectively. About LILE, Rb and Ba have homogeneous values of 6.90 ± 0.46 ppm and 145 ± 13 ppm, respectively. The Ni contents are homogeneous with average concentration of 60.58 ± 3.12 ppm whereas the Cr shows a wide range of 243-740 ppm (Tab. 35 Appendix B). Furthermore, the V and Sc contents are heterogeneous in two ranges of 265-627 ppm and 59-118 ppm, respectively (Tab. 35 Appendix B). Brown amphiboles are analysed with ion probe for H_2O contents that ranging between 0.8 and 0.86 wt. % (Tab. 46 Appendix B). The same analysis technique is used for Li and B which contents are 1.7-2.4 ppm and 3.81-4.13 ppm, respectively (Tab. 46 Appendix B). Furthermore, the fluorine and chlorine contents are quite variables in the ranges 749-867 ppm and 321-443 ppm, respectively (Tab. 46 Appendix B). The amphiboles of sample HSY3B show variable values for δD ratio between -51 and +31 ‰ and the highest $\delta^{18}O$ ratio of the studied samples with values in the range 8.5-10.9 ‰ (Tab. 50 Appendix B).

Tibet: Himalayan Orogen (14JT50)

Clinopyroxene associated to brown amphibole is augite with a Mg-number of 0.82 mol (Tab. 42 Appendix A). The Al_2O_3 contents are homogeneous in a range from 2.33 to 3.85 wt.% whereas the TiO_2 contents are quite variable (0.26-0.67 wt.%). The Na_2O contents are homogeneous with an average value of 0.41 ± 0.11 wt.% (Tab. 42 Appendix A). The chondrite-normalized REE patterns are bell-shaped with the maximum at the MREE at about 11 times the C1 chondrite values (Tab. 36 Appendix B). The LREE and HREE (La_N/Sm_N = 0.42; Gd_N/Yb_N = 1.48) are depleted relative to MREE (La_N/Yb_N = 0.73) and no Eu anomalies were observed (Eu/Eu* = 0.96). The incompatible element pattern reveals depletion in Ba, Nb, Pb, Zr and Ti relative to the neighbouring elements (Tab. 36 Appendix B). Positive anomalies are observed in Th, U and La. The Cr and Ni contents are heterogeneous with average values of 507 ± 95.26 ppm and 139 ± 20.45 ppm, respectively (Tab. 36 Appendix B).

Brown amphibole is hornblende and has Mg-numbers of 0.76 mol (Tab. 43 Appendix A). The amphibole has homogeneous TiO_2 (mean value 1.52 ± 0.20 wt.%) and Al_2O_3 (about 12.88 ± 0.66 wt.%) contents. The Na_2O and K_2O contents are homogeneous with mean values of 2.20 ± 0.14 wt.% and 0.31 ± 0.09 wt.%, respectively (Tab. 43 Appendix A). The chondrite-normalized REE pattern is hump-shaped with depleted LREE and HREE (La_N/Sm_N = 0.36; Gd_N/Yb_N = 1.73) relative to MREE (La_N/Yb_N = 0.78) at 20 times CI chondrite values (Fig. 98; Tab. 37 Appendix B). No Eu anomalies are observed (Eu/Eu* = 1.04).

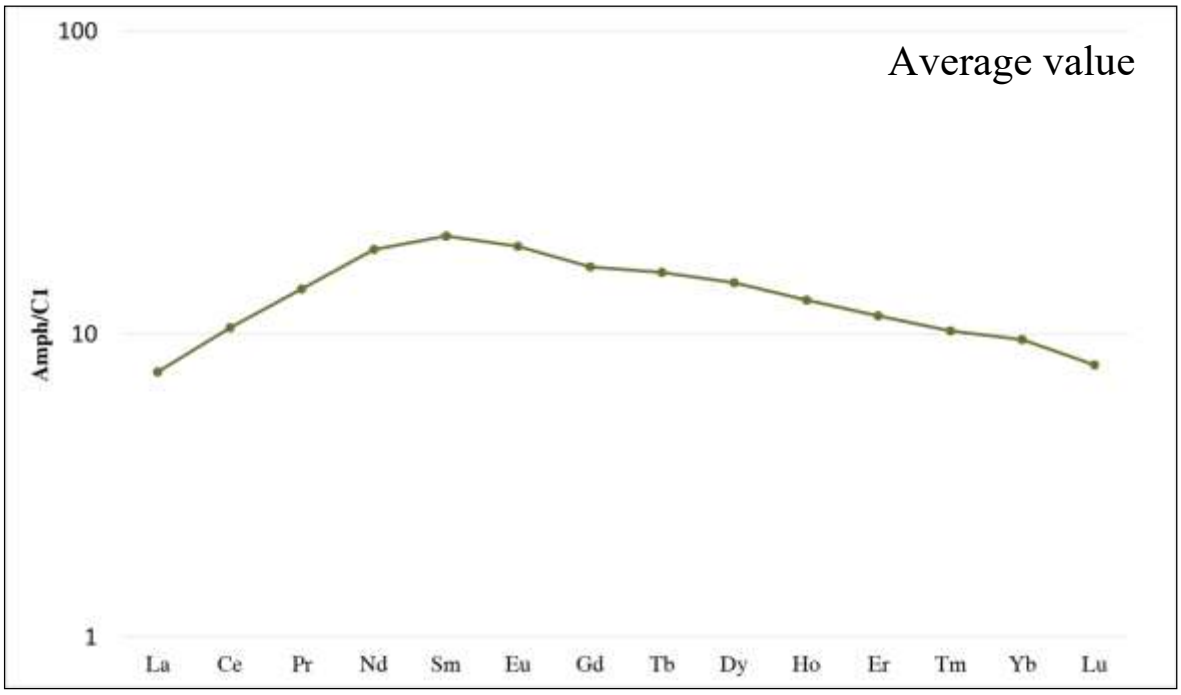

Figure 98 - Chondrite-normalized REE pattern of amphibole from Milin, Himalayan Orogen, China (C1 chondrite from McDonough & Sun, 1995).

Chondrite-normalized pattern of trace elements displays negative Rb, Th, Pb and Zr anomalies (Fig. 99; Tab. 37 Appendix B). About the LILE, Ba and Rb have homogeneous contents of 59.88 ± 3.49 ppm and 1.85 ± 0.28 ppm, respectively. Brown amphibole shows relatively high concentrations in Cr (mean value 507 ± 95.2 ppm), Sc (65.77 ± 4.15 ppm) and V (509 ± 45.28 ppm). The Ni mean content is 138 ± 20.44 ppm (Tab. 37 Appendix B).

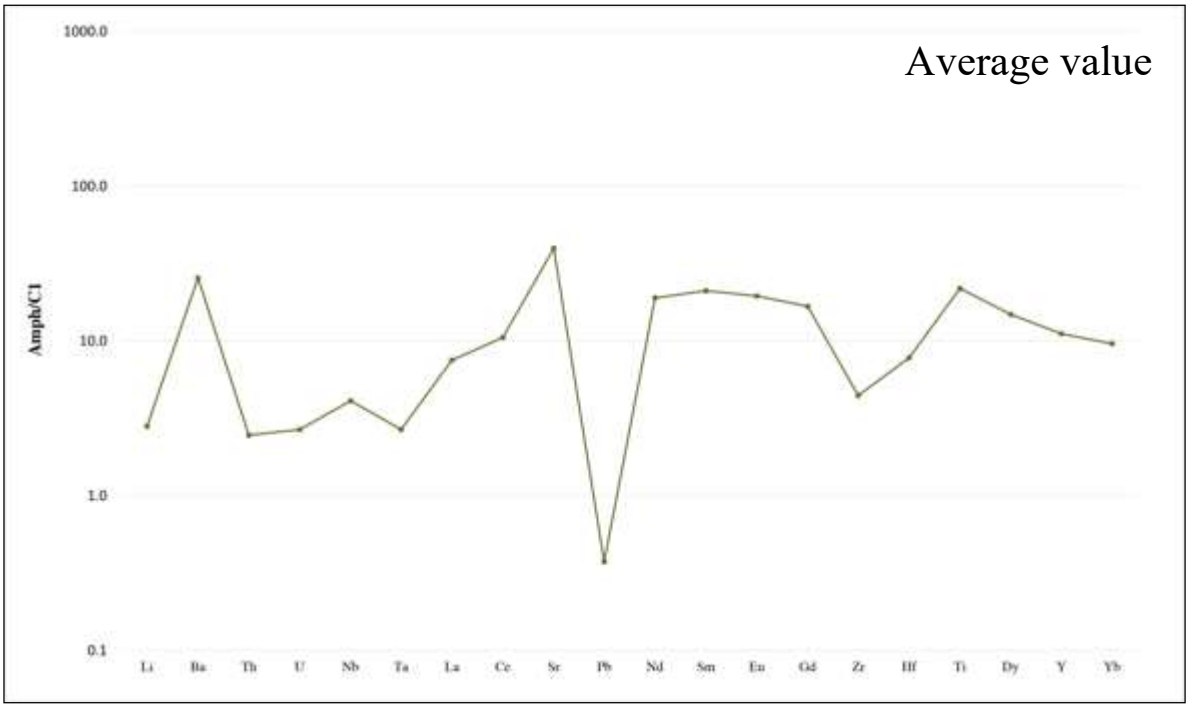

Figure 99 - Chondrite-normalized incompatible pattern of amphibole from Milin, Himalayan Orogen, China (C1 chondrite from McDonough & Sun, 1995).

In-situ ion probe analyses reveal homogeneous H_2O contents ranging between 0.94 and 0.99 wt.% (Tab. 46 Appendix B). Furthermore, in-situ analysis on amphibole have shown Li and B mean contents of 4.20 ± 1.43 ppm and 1.30 ± 0.60 ppm, respectively (Tab. 46 Appendix B). Amphibole also shows fluorine mean content of 1033 ± 47 ppm and chlorine values ranging between 460 and 610 ppm (Tab. 46 Appendix B). The δD ratio of amphibole shows an average value of -74.7 ± 8.5 ‰ and $\delta^{18}O$ ratio is variable in the range 4.2-7.9 ‰ (Tab. 50 Appendix B).

Italy: Alps Orogen (MAT15)

Data from Tiepolo et al. (2011).

Olivine has very low and variable Fo contents of 0.83 ± 0.09 mol (Tab. 44 Appendix A) and its contents of Cr ranging between 8.53 and 19.20 ppm (Tab. 38 Appendix B). Ni values ranging between 832 and 1581 ppm (Tab. 38 Appendix B).

Clinopyroxene shows homogeneous Mg-number value (0.86 mol) whereas the TiO_2 (0.28-0.58 wt.%) and Al_2O_3 (2.42-3.46 wt.%) are quite variables (Tab. 45 Appendix A). The Cr_2O_3 contents (0.28 wt.%) are positively correlated with Mg-number, whereas the Na_2O content (0.26 wt.%) does not show correlation with Mg-number (Tab. 45 Appendix A). The chondrite-normalized REE pattern of clinopyroxene is characterized by a depletion in LREE (La_N/Sm_N = 0.35; La_N/Yb_N = 0.57) relative to

HREE values (Gd_N/Yb_N = 1.71) at about 5 times C1 chondrite (Tab. 38 Appendix B). The Eu/Eu* ratio has value of 1.04. The chondrite-normalized pattern of incompatibles exhibit negative anomalies in Th, U, Pb and Hf relative to the neighbouring elements (Tab. 38 Appendix B). The Cr values are in the range 1670-2522 ppm. The Sc and V contents are 180 ppm and 231 ppm, respectively (Tab. 38 Appendix B).

Brown amphibole is pargasite with Mg-number of 0.77 mol (Tab. 46 Appendix A). No significant major elements intra-grain zoning was observed. The TiO_2 (1.57 ± 0.10 wt.%) and Al_2O_3 (12.75 ± 0.17 wt.%) contents are homogeneous and only alumina displays positive correlation with Mg-number. The Na_2O and K_2O mean contents are 2.15 ± 0.08 wt.% and 0.32 ± 0.01 wt.%, respectively (Tab. 46 Appendix A). The chondrite-normalized REE patterns are hump-shaped and show almost flat pattern from MREE to HREE (La_N/Yb_N = 0.84; Gd_N/Yb_N = 1.13), which are about 20 times the CI chondrite (Fig. 100; Tab. 38 Appendix B). The LREE are depleted compared to the MREE (La_N/Sm_N = 0.60) and the europium does not show negative or positive anomalies (Eu/Eu* = 1.14).

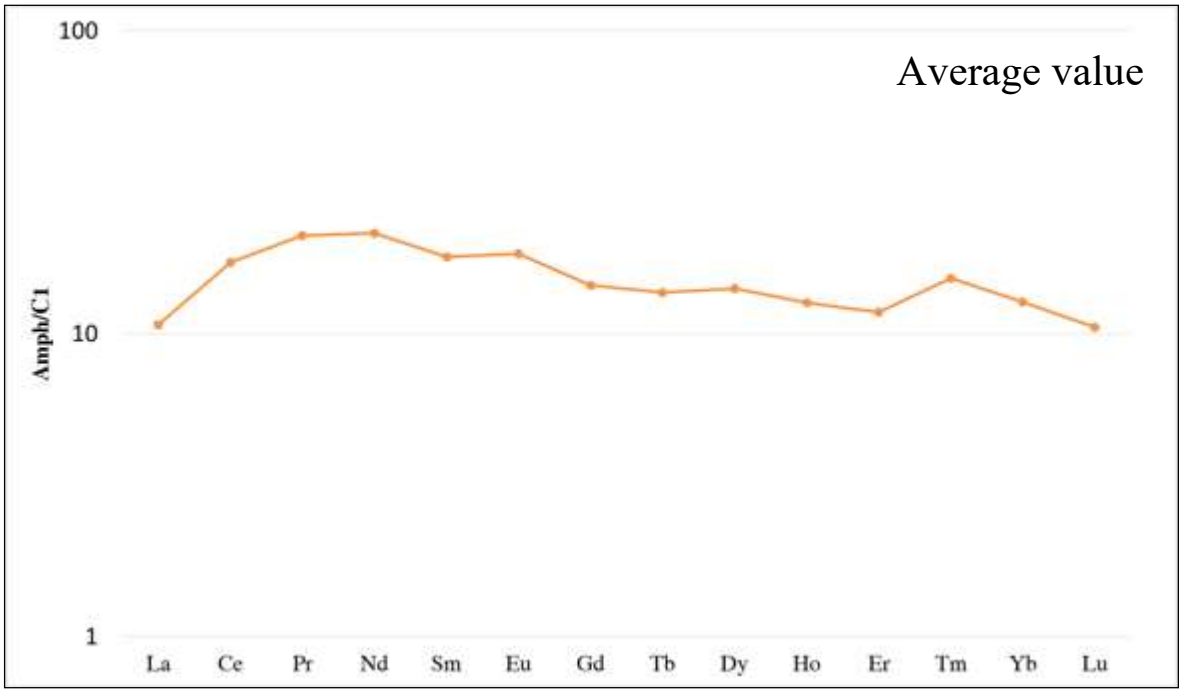

Figure 100 - Chondrite-normalized REE pattern of amphibole from Mt. Mattoni, Adamello batholith (C1 chondrite from McDonough & Sun, 1995).

The chondrite-normalized incompatible element patterns reveal depletion in Li, Rb, B, Pb and Zr relative to the neighbouring elements (Fig. 101; Tab. 38 Appendix B). Nb/Ta and Zr/Hf ratios are 14.29 and 20.15, respectively. Rb and Ba have homogeneous values of 1.10 ± 0.18 ppm and 49.90 ± 6.58 ppm, respectively (Tab. 38 Appendix B). The Ni contents are homogeneous 243 ± 26.77 ppm as the Cr that shows a wide range of 2067-2515 ppm. The V contents are homogeneous (484-498 ppm) whereas the Sc has variable values in the range 99-132 ppm (Tab. 38 Appendix B).

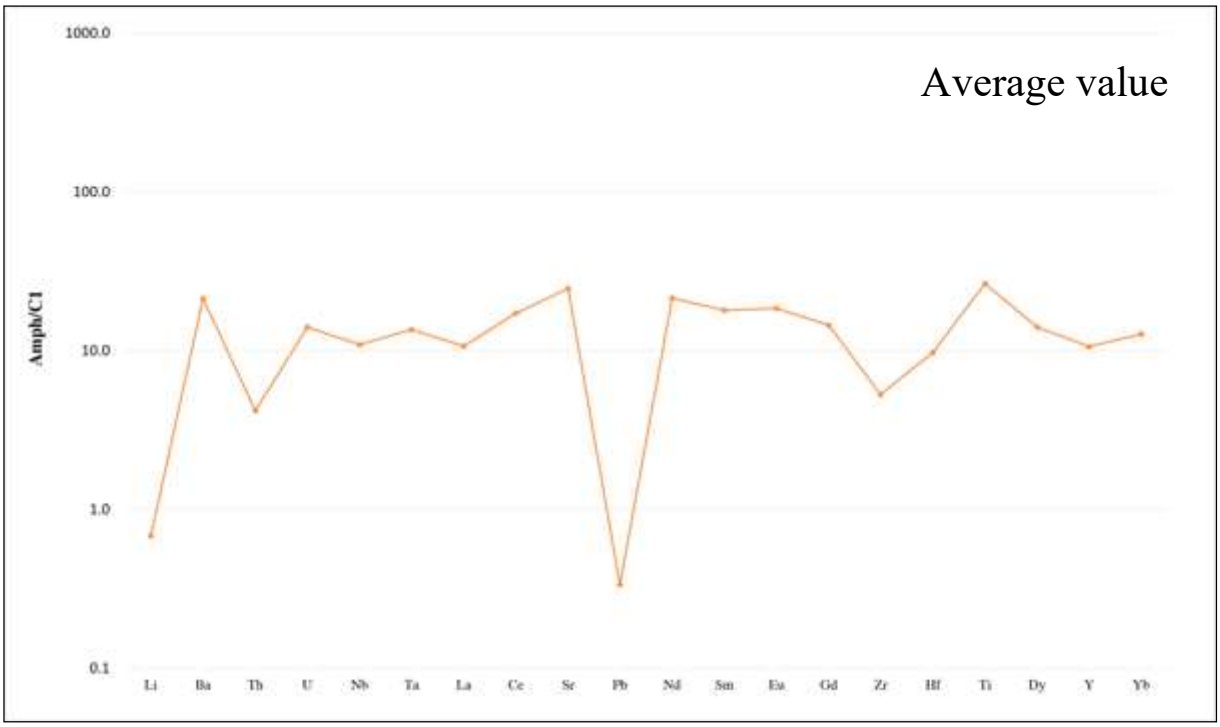

Figure 101 - Chondrite-normalized incompatible pattern of amphibole from Mt. Mattoni, Adamello batholith (C1 chondrite from McDonough & Sun, 1995).

The H_2O contents measured with ion probe technique reveals for brown amphiboles a range between 0.79 and 0.82 wt. % (Tab. 46 Appendix B). The Li and B contents measured with ion probe are 1.02 ± 0.10 ppm and 1.41 ± 0.99 ppm, respectively (Tab. 46 Appendix B). Furthermore, the chlorine and fluorine contents are variables in the ranges 397-499 ppm and 492-708 ppm, respectively (Tab. 46 Appendix B). The isotopic analysis for hydrogen and oxygen reveal values for δD ratio between -66 and -80 ‰, whereas the $\delta^{18}O$ ratio is in the range 4.2-6.4 ‰ (Tab. 50 Appendix B).

Italy: Alps Orogen (VS9)

Data from Tiepolo et al. (2002).

Olivine has very low and variable Fo contents of 0.82 mol (Tab. 47 Appendix A). The Cr and Ni values are homogeneous with average concentrations of 3.35 ± 0.30 ppm and 358.97 ± 0.95 ppm, respectively (Tab. 39 Appendix B).

Clinopyroxene associated to brown amphibole is augitic in composition with a Mg-number of 0.82 mol (Tab. 48 Appendix A). The Al_2O_3 contents are homogeneous in a range from 2.33 to 3.85 wt.% whereas the TiO_2 contents are quite variable (0.26-0.67 wt.%). The Na_2O contents are homogeneous with an average value of 0.41 ± 0.11 wt.% (Tab. 48 Appendix A). The chondrite-normalized REE patterns are well bell-shaped with the maximum at the MREE at about 11 times the C1 chondrite values (Tab.

39 Appendix B). The LREE and HREE (La_N/Sm_N = 0.42; Gd_N/Yb_N = 1.48) are depleted relative to MREE (La_N/Yb_N = 0.73) and no Eu anomalies were observed (Eu/Eu* = 0.96). The incompatible element pattern reveals depletion in Ba, Nb, Pb, Zr and Ti relative to the neighbouring elements (Tab. 39 Appendix B). The Cr and Ni contents are heterogeneous with average values of 507 ± 95.26 ppm and 139 ± 20.45 ppm, respectively (Tab. 39 Appendix B).

Brown amphibole is pargasite in composition with Mg-number ranging from 0.67 to 0.73 mol (Tab. 49 Appendix A). No significant intra-grain zoning was observed. The TiO_2 contents are homogeneous in the range 1.31-1.97 wt.% whereas Al_2O_3 values are variable (10.46-14.05 wt.%). The Na_2O and K_2O mean contents are 1.98 ± 0.33 wt.% and 0.48 ± 0.07 wt.%, respectively (Tab. 49 Appendix A). The chondrite-normalized REE pattern varies from flat to slightly convex downward from MREE to HREE (La_N/Yb_N = 0.37; Gd_N/Yb_N = 1.30), which are about 20 times the CI chondrite (Fig. 102; Tab. 39 Appendix B). The LREE are depleted (La_N/Sm_N = 0.27) and the europium shows marginally negative anomaly (Eu/Eu* = 0.86).

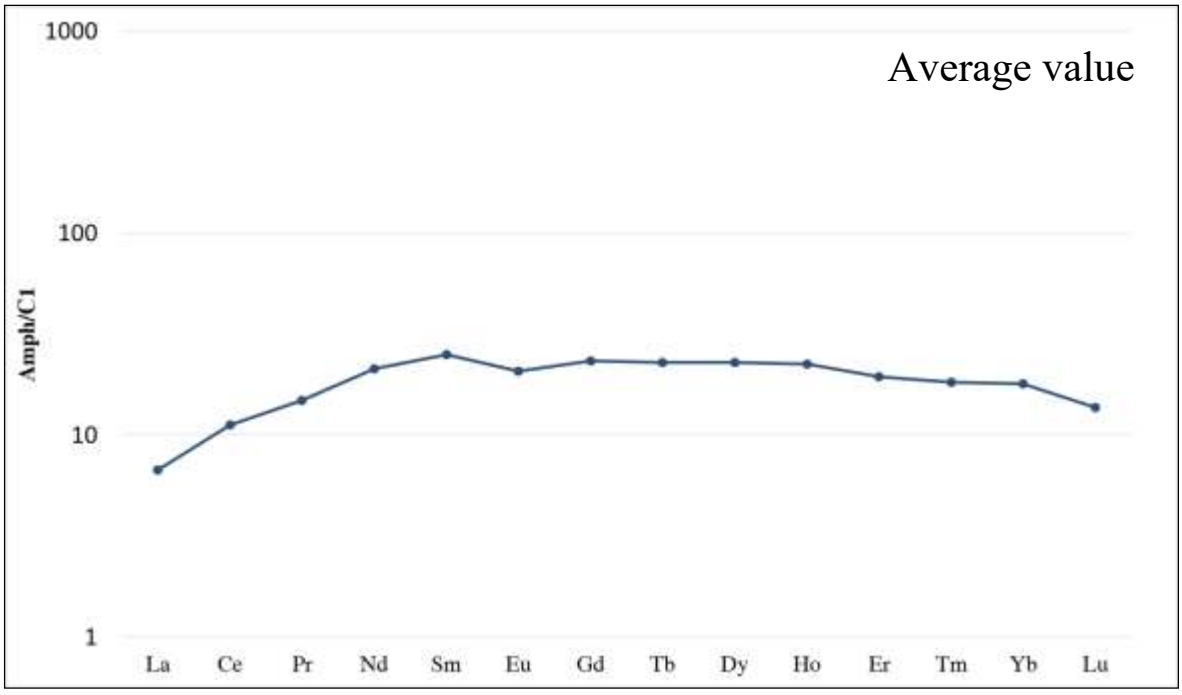

Figure 102 - Chondrite-normalized REE pattern of amphibole from Val Masino, Bregaglia pluton (C1 chondrite from McDonough & Sun, 1995).

The chondrite-normalized incompatible element pattern reveals depletion in Li, Rb, B, Pb and Zr relative to the neighbouring elements (Fig. 103; Tab. 39 Appendix B). Nb/Ta and Zr/Hf ratios are 17.90 and 21.30, respectively. Rb and Ba have homogeneous values of 2.58 ± 0.08 ppm and 41.09 ± 5.78 ppm, respectively (Tab. 39 Appendix B). The Ni contents are also consistent with mean value of 124 ± 4.44 ppm whereas the Cr have variable concentrations in a wide range of 258-526 ppm (Tab. 39

Appendix B). The same contents variability is observable for V (540-853 ppm) and Sc (74-145 ppm) (Tab. 39 Appendix B).

Figure 103 - Chondrite-normalized incompatible pattern of amphibole Val Masino, Bregaglia pluton (C1 chondrite from McDonough & Sun, 1995).

Brown amphiboles of Bregaglia were not analysed for H_2O, F and Cl contents. Nevertheless, amphiboles were analysed with ion probe for Li and B contents (Tab. 46 Appendix B). Li and B have variable concentrations (1.37-4.24 ppm and 0.33-3.51 ppm, respectively). Only oxygen isotopic analyses were carried out on amphibole from Bregaglia with the $\delta^{18}O$ ratio in the range 4.0-6.2 ‰ (Tab. 50 Appendix B).

Sunda Arc: Batu Hijau (SRD02305)

Brown amphibole is hornblende with Mg-number of 0.72 mol (Tab. 50 Appendix A). No significant intra-grain zoning was observed. The TiO_2 (1.28 ± 0.14 wt.%) and Al_2O_3 (6.75 ± 0.78 wt.%) contents are homogeneous (Tab. 50 Appendix A). The Na_2O and K_2O mean contents are1.38 ± 0.22 wt.% and 0.18 ± 0.05 wt.%, respectively (Tab. 50 Appendix A). The chondrite-normalized REE pattern is hump-shaped and show marginally decrease from MREE to HREE (La_N/Yb_N = 0.47; Gd_N/Yb_N = 1.53), which are about 53 times the CI chondrite (Fig. 104; Tab. 40 Appendix B). The LREE are strongly depleted (La_N/Sm_N = 0.26) and Eu shows markedly negative anomaly (Eu/Eu* = 0.64).

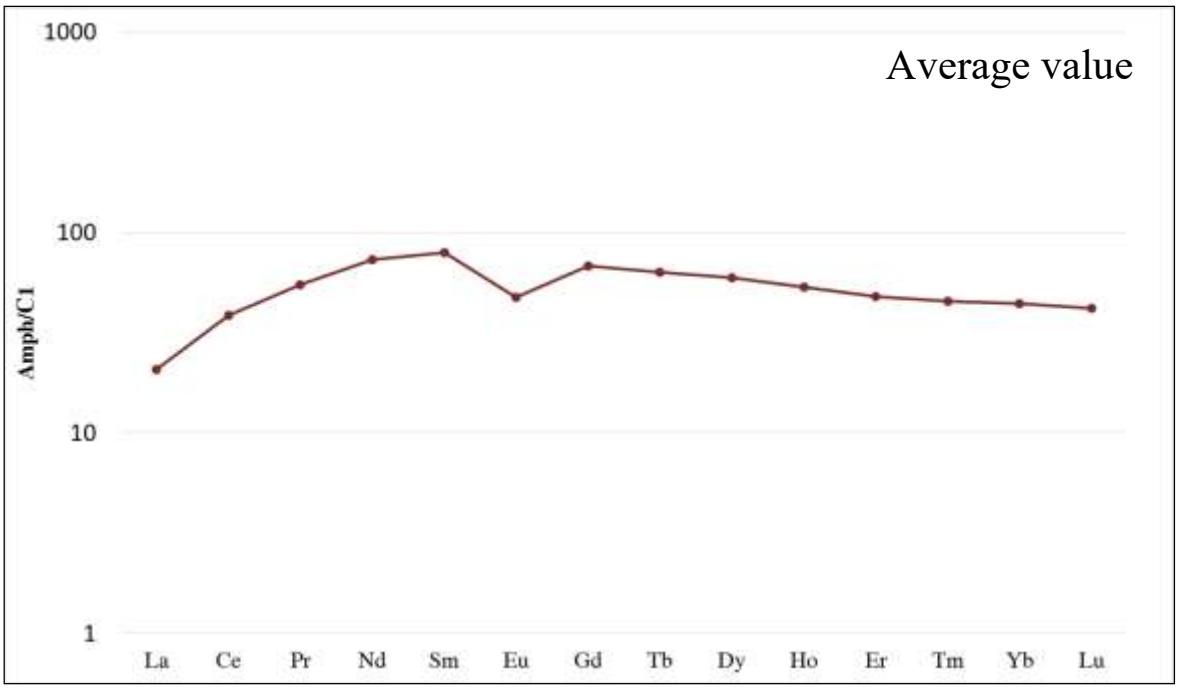

Figure 104 - Chondrite-normalized REE pattern of amphibole from Batu Hijau, Sunda Arc, Indonesia (C1 chondrite from McDonough & Sun, 1995).

The chondrite-normalized incompatible element patterns reveal depletion in Li, Rb, B, Ta, Pb, Zr and Ti relative to the neighbouring elements (Fig. 105; Tab. 40 Appendix B). Positive anomalies are observed for Ba, Nb, Nd, Sm and Gd. Nb/Ta and Zr/Hf ratios are 39.30 and 22.40, respectively. Rb and Ba have homogeneous values of 0.33 ± 0.05 ppm and 36.89 ± 4.01 ppm, respectively (Tab. 40 Appendix B). The Ni contents are consistent with an average value of 61.22 ± 9.55 ppm as the Cr concentrations (28.33 ± 5.80 ppm) (Tab. 40 Appendix B). On the contrary, the amphibole is enriched in V (305 ± 31.76 ppm) and Sc (114 ± 13.47 ppm) (Tab. 40 appendix B).

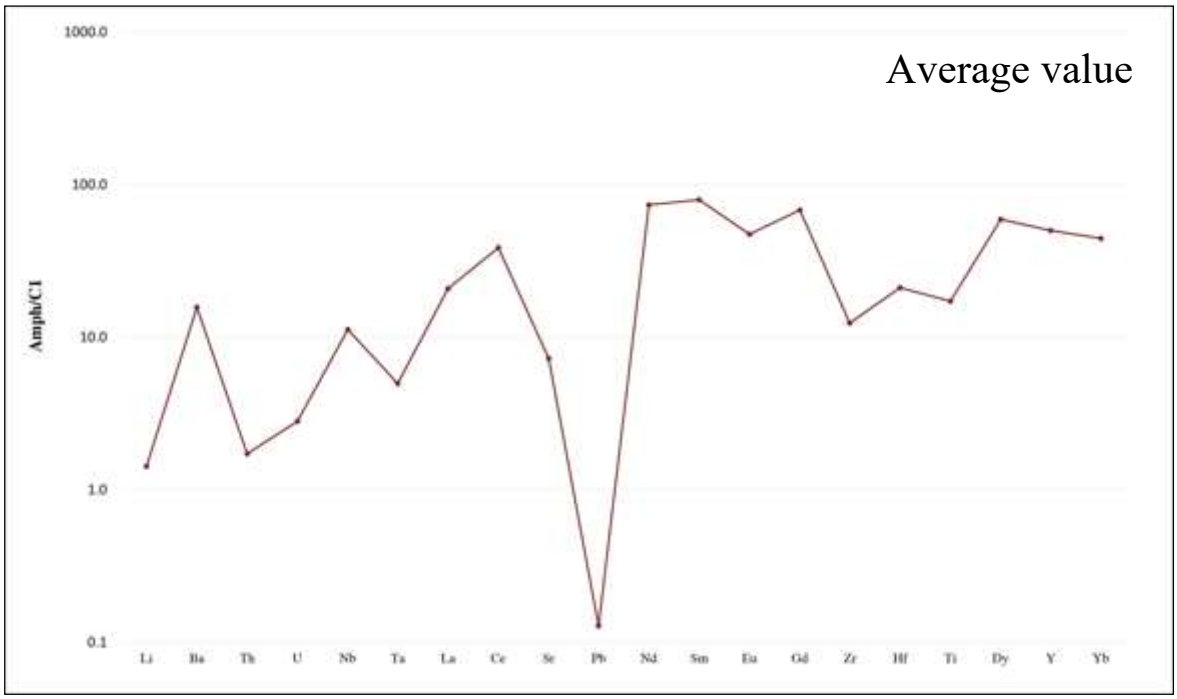

Figure 105 - Chondrite-normalized incompatible pattern of amphibole from Batu Hijau, Sunda Arc, Indonesia (C1 chondrite from McDonough & Sun, 1995).

H_2O contents in amphibole varies between 1.16 and 1.30 wt. % (Tab. 46 Appendix B). The same analysis technique is used for Li and B which contents are 0.90-1.60 ppm and 0.77-1.06 ppm, respectively (Tab. 46 Appendix B). Furthermore, the chlorine and fluorine contents are variables in the ranges 1301-1613 ppm and 1130-1509 ppm, respectively (Tab. 46 Appendix B). Amphiboles from Batu Hijau show δD ratio between -100 and -110 ‰, whereas the $\delta^{18}O$ ratio is in the range 3.1-4.0 ‰ (Tab. 50 Appendix B).

Alkaline lavas from South west USA: Hoover Dam (MGT)

Brown amphibole is kaersutite with Mg-number ranging between 0.71 and 0.75 mol (Tab. 51 Appendix A). No significant intra-grain zoning was observed. The TiO_2 (5.70 ± 0.13 wt.%) and Al_2O_3 (14.37 ± 0.15 wt.%) contents are homogeneous and only alumina displays positive correlation with Mg-number. The Na_2O and K_2O mean contents are 2.42 ± 0.10 wt.% and 1.93 ± 0.03 wt.%, respectively (Tab. 51 Appendix A). The chondrite-normalized REE patterns are hump-shaped and show decrease from MREE to HREE (La_N/Yb_N = 3.53; Gd_N/Yb_N = 3.26), which are about 25 times the CI chondrite (Fig. 106; Tab. 41 Appendix B). The LREE are depleted (La_N/Sm_N = 0.76) with no europium anomalies (Eu/Eu* = 1.06). The chondrite-normalized incompatible element patterns reveal depletion in Li, Rb, B, Th, U, La-Ce, Pb and Zr relative to the neighbouring elements (Fig. 107; Tab. 41 Appendix B). Nb/Ta and Zr/Hf ratios are 17.65 and 27.05, respectively (Tab. 41 Appendix B). Rb and Ba have homogeneous

values of 6.89 ± 0.64 ppm and 278.32 ± 8.13 ppm, respectively (Tab. 41 Appendix B). The Ni contents are variable between 108 and 366 ppm as the Cr that shows a wide range of 302-745 ppm. On the contrary, the V and Sc contents are homogeneous in two restricted range of 492 ± 36.21 ppm and 45.72 ± 2.34 ppm, respectively (Tab. 41 Appendix B).

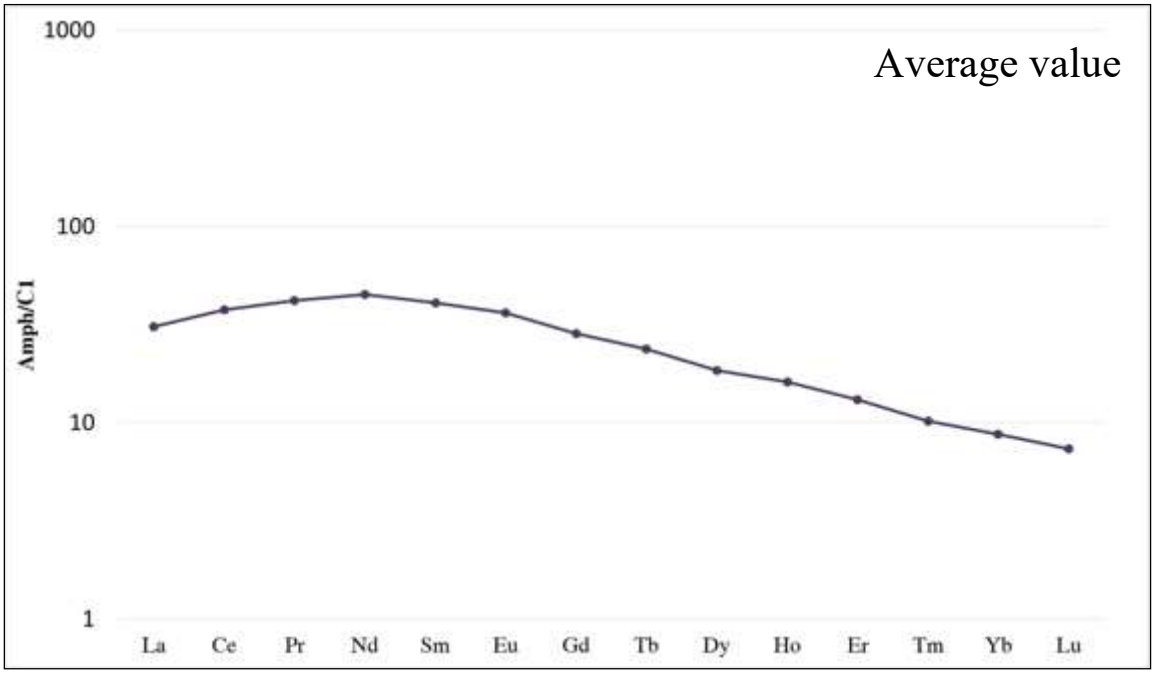

Figure 106 - Chondrite-normalized REE pattern of amphibole from Hoover Dam, Arizona (C1 chondrite from McDonough & Sun, 1995).

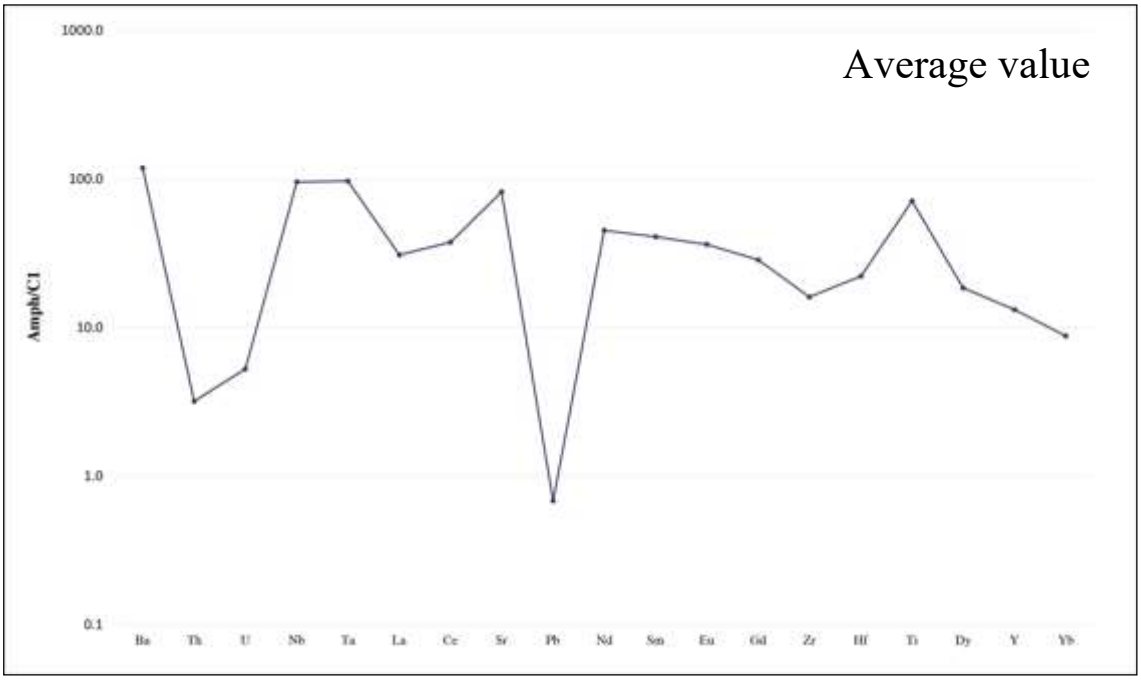

Figure 107 - Chondrite-normalized incompatible pattern of amphibole Hoover Dam, Arizona (C1 chondrite from McDonough & Sun, 1995).

The amphibole megacrysts from Hoover Dam were collected in a second time in respect the first sample selection and were not analysed by ion probe. The data of water, Cl and F contents as well as the hydrogen and oxygen isotopic values reported in the Discussion Chapter 4 are from literature (Boettcher and O'Neill, 1980).

Alkaline lavas from South west USA: Dish Hill (DH)

Brown amphibole is kaersutite in composition with Mg-number in the range 0.56-0.65 mol (Tab. 52 Appendix A). No significant intra-grain major elements compositional zoning was observed. The TiO_2 (4.65-5.24 wt.%) and Al_2O_3 (14.11-14.77 wt.%) contents are homogeneous and were not observed correlation with Mg-number. The Na_2O and K_2O mean contents are 2.66 ± 0.10 wt.% and 1.63 ± 0.06 wt.%, respectively (Tab. 52 Appendix A). The chondrite-normalized REE patterns are bell-shaped and show decrease from MREE to HREE (La_N/Yb_N = 3.51; Gd_N/Yb_N = 3.13), which are about 30 times the CI chondrite (Fig. 108; Tab. 42 Appendix B). The LREE are slightly depleted (La_N/Sm_N = 0.81) and the europium does not show negative or positive anomalies (Eu/Eu* = 1.09).

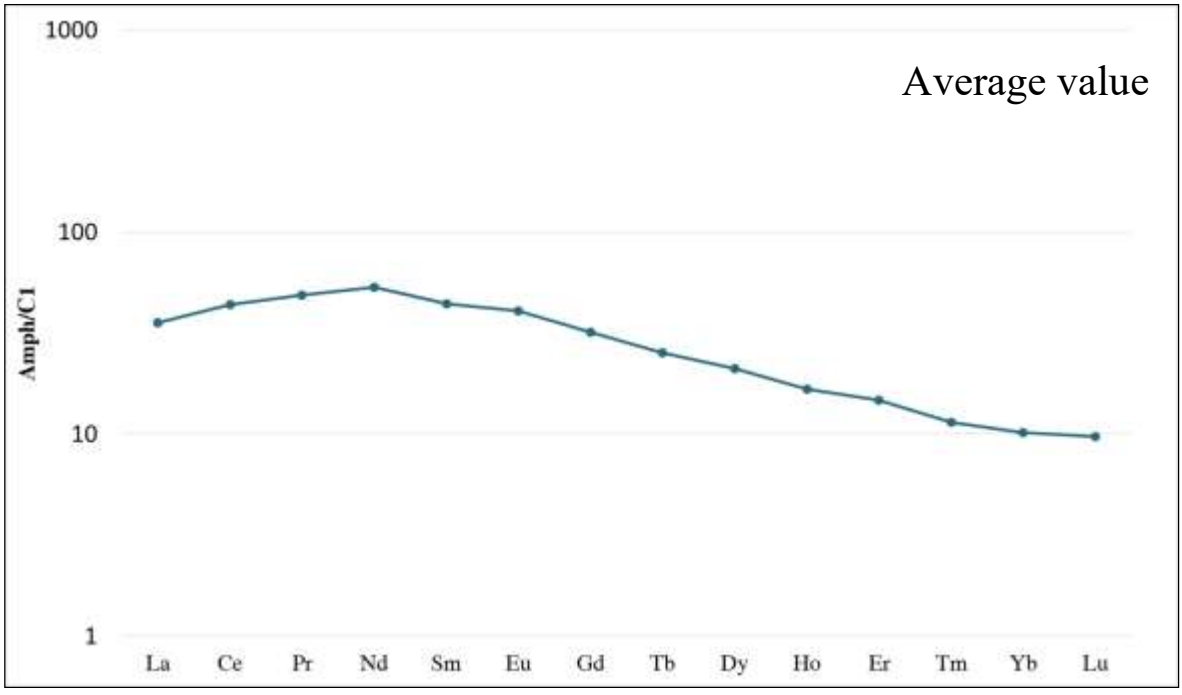

Figure 108 - Chondrite-normalized REE pattern of amphibole from Dish Hill, California (C1 chondrite from McDonough & Sun, 1995).

The chondrite-normalized incompatible element patterns reveals depletion in Li, Rb, B, Th, U, La-Ce and Pb relative to the neighbouring elements (Fig. 109; Tab. 42 Appendix B). Positive anomalies are

observed for Ba, Nb-Ta, Sr Nd and Ti. Nb/Ta and Zr/Hf ratios are 19.24 and 26.08, respectively. Rb and Ba have homogeneous values of 10.64 ± 0.49 ppm and 257 ± 21.37 ppm, respectively (Tab. 42 Appendix B). The Ni contents are variable between 5.65 and 11.77 ppm as the Cr that has a wide concentration between 3.41 ppm and 19.74 ppm (Tab. 42 Appendix B). Vanadium displays the same variability contents in the range 277-450 ppm whereas Sc contents are homogeneous (35.81 ± 4.18 ppm) (Tab. 42 Appendix B).

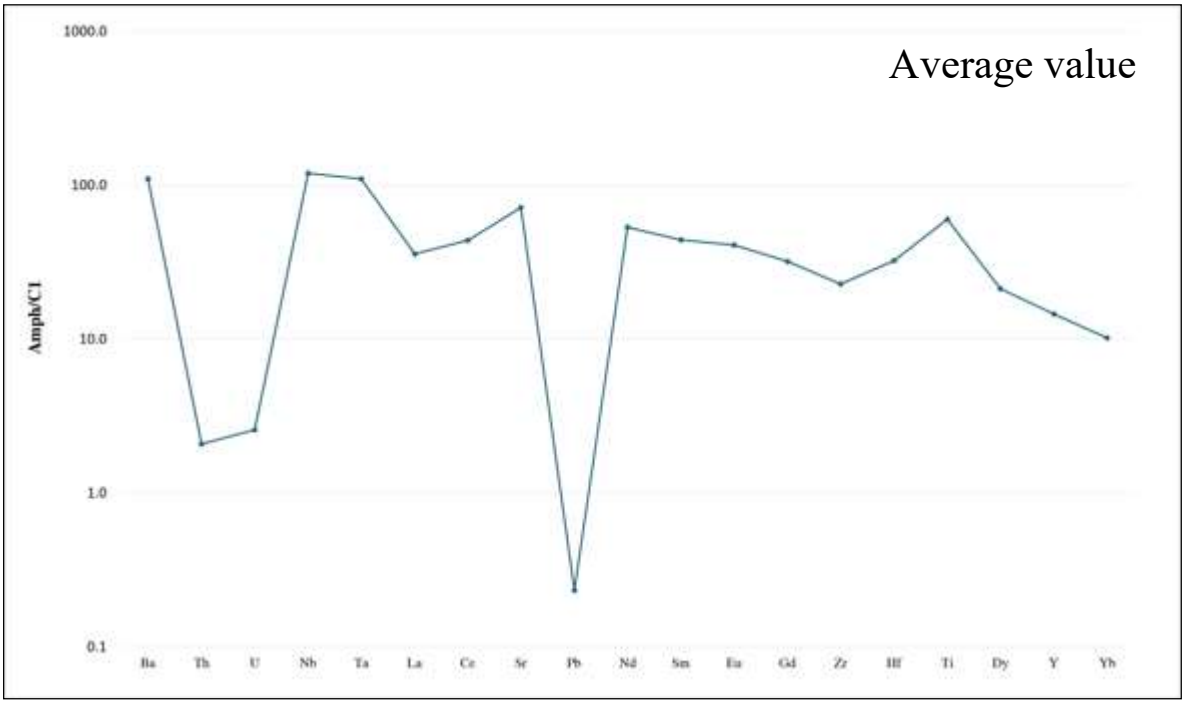

Figure 109 - Chondrite-normalized incompatible pattern of amphibole from Dish Hill, California (C1 chondrite from McDonough & Sun, 1995).

As described above for amphiboles from Hoover Dam, the samples from Dish Hill were not analysed for volatile contents as well as isotopic data. The values reported in the Chapter 4 are those from literature (Boettcher and O'Neill, 1980).

Chapter 4

Discussion

4.1 Amphibole stability in igneous environment

Amphibole crystallisation conditions are dependent mainly from water contents and chemical composition of the equilibrium melts. Experimental data on hydrous basaltic systems suggests that the maximum thermal stability of amphibole is about 1.100°C, thus supporting the formation of clinopyroxene before amphibole, which grows at the expense of the earlier-formed minerals (clinopyroxene and/or olivine; Foden and Green, 1992; Melekhova et al., 2013; Smith, 2014). Basalts, and in general subalkaline melts, typically have on the liquid line of descent spinel → olivine → clinopyroxene → plagioclase (Sisson and Grove 1993). Amphibole is stabilised only at high water contents (>3 wt%; Sisson and Grove 1993; Smith et al., 2009). The evidence in all the studied rocks is that amphibole follows clinopyroxene in the crystallisation order and precedes plagioclase in the few samples in which this mineral is present. High H_2O contents and rapid crystallisation in closed system conditions would improve amphibole, clinopyroxene and spinel crystallisation (Johnson et al., 1991; Stone et al., 2003; Müntener & Ulmer 2006). High water contents in basaltic melts have the effect of destabilising silicate minerals, and plagioclase in particular (Gaetani et al. 1993; Sisson and Grove 1993). Plagioclase is thus suppressed at high water contents (>3-4 wt.% H_2O; Zimmer et al., 2010) and high pressure as a fuction of bulk-rock composition (0.8-1.5 GPa; Borghini et al., 2009; Falloon et al., 2008). The stability curve for amphibole is however subparallel to decompression pathways (Fig. 110, from Davidson et al., 2007). Crossing this boundary down-pressure will result in resorption, rather than precipitation. For this reason, a H_2O-saturated magma from the mantle will precipitate amphibole as soon as it encounters the amphibole stability curve (1.5–2 GPa; Allen and Boettcher, 1983) but can also resorb amphibole at shallow depths.

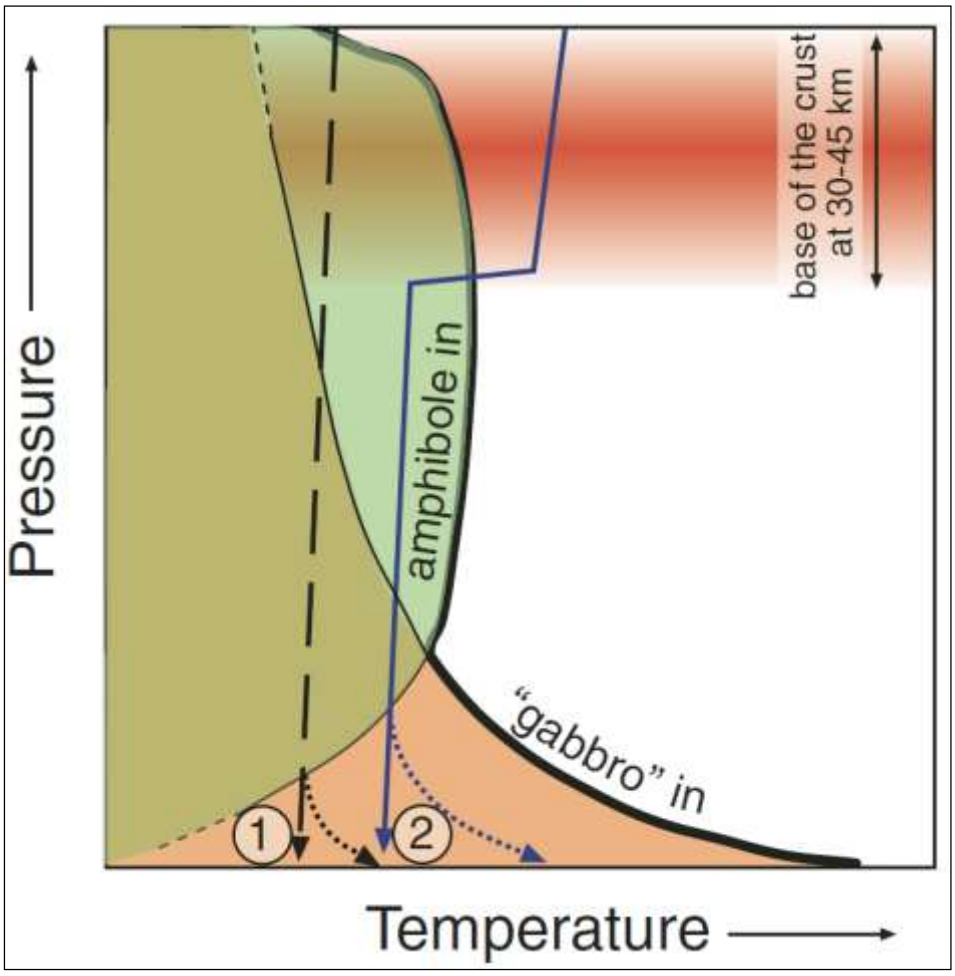

Figure 110 - Amphibole crystallisation field, showing topology of phase boundaries for amphibole and for gabbro (cpx + pl ± olivine) and Curves 1–2 represent P-T paths of magma ascent. Dashed extensions represent possible heating during decompression crystallization (from Davidson et al., 2007).

At depth, it is likely that differentiation of arc magmas is open-system and the geochemical signature of amphibole might reflect melting of basalts with residual amphibole, rather than simply amphibole crystallisation from an evolving melt (Davidson et al., 2007). Several studies on Phanerozoic amphiboles have demonstrated that amphibole fractionation is consistent with the high water contents that characterize primitive magmas at subduction zones (Fischer and Marty, 2005; Wallace, 2005). Thus, amphibole fractionation is cryptic, with the observed (typically gabbroic) silicate phase assemblage representing crystallisation in the shallow subvolcanic system, or remobilization of shallow cumulates (Dungan and Davidson, 2004), and having limited leverage on compositions. A significant role for amphibole is borne out by a survey of cumulate xenoliths found in arc lavas that are commonly amphibole bearing (Davidson et al., 2007). Arculus and Wills (1980) reported amphibole in cumulate nodules from along the arc in the Lesser Antilles, despite its rarity in erupted lavas. Amphibole-magnetite–bearing cumulates are also important components of Alaskan-type ultramafic complexes. If

the Phanerozoic arc magmas can easily reach the range of H_2O contents favorable for amphibole formation, this has not to be taken for granted for the Archean mantle-derived melts. Amphibole also occurs as megacrysts in alkali basalts. This phase, together with clinopyroxene, orthopyroxene, feldspars, garnet and other minerals, has been interpreted as high-pressure phenocrysts that was, at some stage, in equilibrium with basaltic melts (e.g., Irving 1974). However, many authors (e.g., Wilshire and Trask, 1971; Boettcher and O'Neil, 1980) proposed that the amphibole megacrysts at Dish Hill, California, resulted from fragmentation of peridotite that contains the amphibole-bearing veins. The amphibole megacrysts would not necessarily be in chemical equilibrium with the host basalt (Boettcher and O'Neil, 1980). Many studies about amphibole megacrysts from composite mantle xenoliths of alkaline basalts from the Carpathian-Pannonian region have proven that the megacrysts represent cumulate phases formed during an early upwelling of basaltic magma, and which were brought to the surface by subsequent magma pulse (e.g. Demeny et al., 2005).

The Precambrian rocks considered in this thesis share many petrographic and textural similarities with hornblendites and amphibole-bearing pyroxenites from Phanerozoic orogenic settings. However chemical compositions of Precambrian amphiboles are more comparable with those characterising amphibole megacrysts from alkaline lavas (Fig. 111). A detailed petrologic study on the origin of amphibole in both Proterozoic and Archean rocks is thus mandatory. These similarities open to several possibilities about amphibole origin in the Archean and Proterozoic rocks.

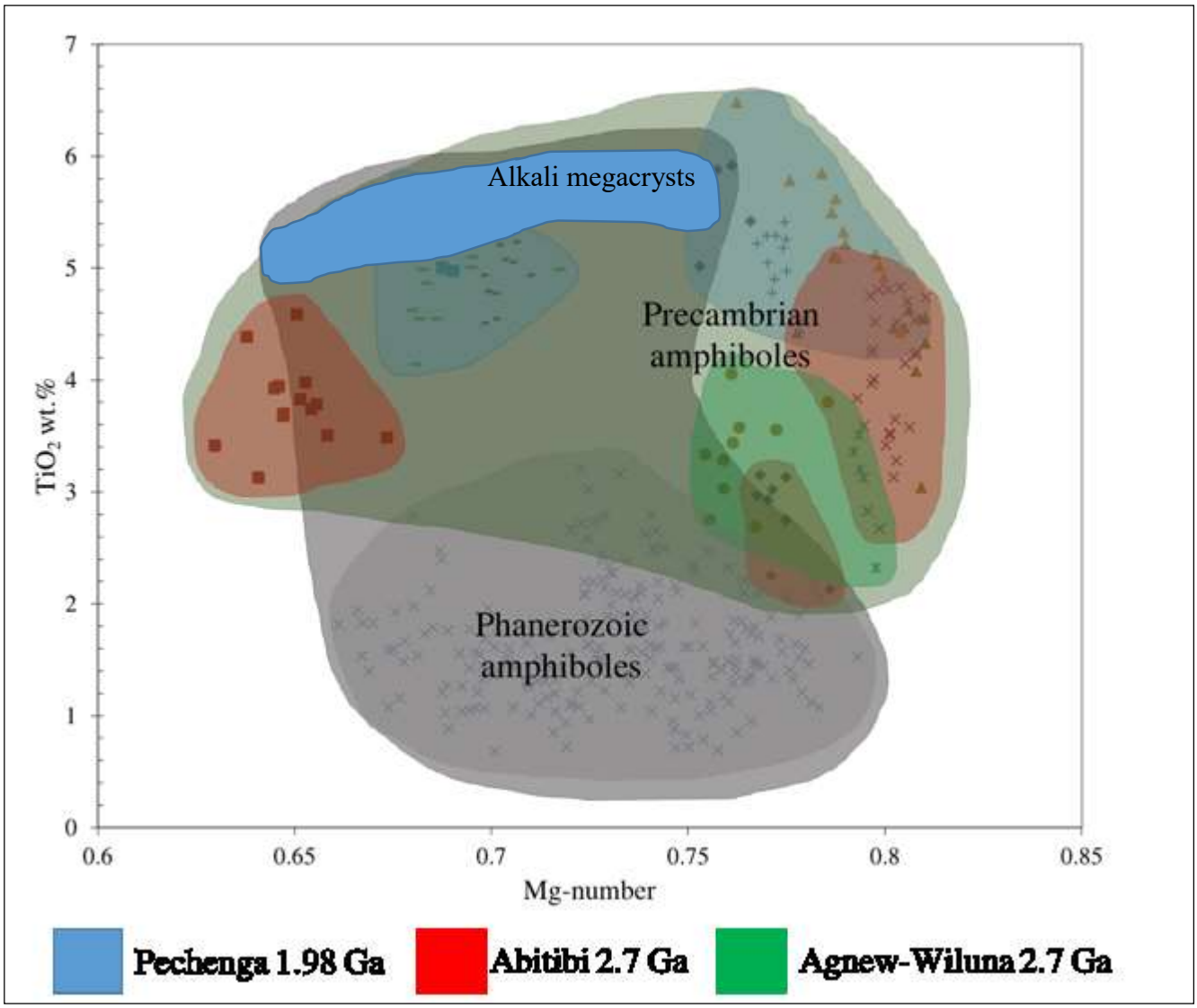

Figure 111 - Mg-number versus TiO_2 wt.% in the studied amphiboles.

4.2 Amphibole geothermobarometry

The Al-in-hornblende barometer of Hammerstrom and Zen (1986) is one of the most influential petrologic tools yet calibrated. Their barometer was immediately used to place granitic magmatism within a crustal framework (e.g., Ague and Brimhall 1988; Pickett and Saleeby 1993), and led to several new calibrations (e.g., Hollister et al. 1987; Johnson and Rutherford 1989a,b; Schmidt 1992; Anderson and Smith 1995). More recently Ridolfi and Renzulli (2011) have calibrated a hornblende-only barometer, and other models for volcanic systems, and Molina et al. (2015) have a new amphibole thermometer and saturation model. Ridolfi and Renzulli (2011) recognize that experimental error can limit model precision, and they show that amphibole compositions alone can be used to predict magmatic intensive variables. Because of the temperature (T°C)-sensitivity of Al-in-hornblende and the potential

for re-equilibration, Blundy and Holland (1990) warned that without reliable thermal information, "the Al geobarometer is unlikely to be of much practical value". Anderson and Smith (1995) responded with a T°C-sensitive barometer. But as they make clear, useful P estimates derive only from highly restricted circumstances, e.g., near-solidus, multiply saturated granitic systems (Hollister et al. 1987), where T < 800 °C, and amphibole Fe/(Fe+Mg) < 0.65 (Anderson and Smith 1995), and where multiple saturated phases and contact metamorphic rocks allow for independent estimates of P (e.g., Hollister et al. 1987; Anderson 1996; Anderson et al. 2008; Barnes et al. 2012). Amphibole-based barometry is in fact fraught with very real and under-appreciated challenges. Aluminum contents of amphiboles are clearly more sensitive to T°C and Al_2O_3 contents of coexisting liquids than to P. Notwithstanding, amphibole-based barometry is of common use. The T°C-sensitivity is especially evident when Al^T is compared to Si in amphibole, for which it mostly substitutes: except for a few high-Al^T outliers, amphiboles crystallized in the P range of 0–2 kbar encompass the entire span of Al^T-Si at 6–10 kbar. In contrast, when separated into T°C intervals, mean Si and Al^T contents systematically decrease and increase, respectively, from 650 to 1175°C. The challenges facing amphibole barometry can be further illustrated from a thermodynamic point of view. If a P-signal can be extracted, such should be driven by molar volume contrasts between competing amphibole components and coexisting liquids. For amphiboles, molar volume differences upon crystallisation are much smaller and less well differentiated. From such comparisons we might anticipate that pyroxene-based barometers should be nearly seven times more sensitive to P than their amphibole counterparts, although even the pyroxene-based barometers have standard errors of estimate (or SEE; or model root mean square errors) that are not small: ±0.7 kbar when multiple estimates are averaged, ±1.2–2.0 kbar for individual estimates (Putirka 2008). These results do not impugn careful barometric results on near-solidus granitic systems, where P estimates are tested against independent igneous and metamorphic equilibria (e.g., Hollister et al. 1987; Anderson and Smith 1995; Anderson 1996; Anderson et al. 2008). However, it remains quite unclear if P can be predicted from amphibole in systems exhibiting high thermodynamic variance – igneous systems saturated with just one or a few phases. Ridolfi and Renzulli (2011) argued that a stronger P signal could further be recovered by limiting calibrations to experiments that report small compositional errors and that yield amphibole compositions most similar to those found in nature. However, the Ridolfi and Renzulli (2011) data restrictions mean that <12% of current experimental data are used. This may reject possibly useful data, where compositional errors are not reported; there is value in performing calibrations on data that span a wider range of compositions compared to nature to minimize or eliminate model extrapolation. Recent studies have highlighted how calcic, igneous amphiboles are of special interest as their compositional diversity and common occurrence provide ample potential to investigate magmatic processes (Putirka 2016). But not all amphibole-based barometers lead to geologically useful

information: recent and new tests reaffirm prior studies (e.g., Erdman et al. 2014), indicating that amphibole barometers are generally unable to distinguish between experiments conducted at 1 atm and at higher pressures, except under highly restrictive conditions. The problem may relate to an intrinsic sensitivity of amphiboles to temperature and liquid composition, rather than pressure. The exceptional conditions are those identified by Anderson and Smith (1995): current amphibole barometers are more likely to be useful when T < 800 °C and $Fe\#^{Amp} = Fe^{Amp}/(Fe^{Amp}+Mg^{Amp}) < 0.65$. Such analysis reveals that amphiboles are vastly less complex than may be inferred from published catalogues of end-member components. And nearly all remaining compositional variation can be described with just four components: alumino-tschermakite, a Na-K-gedrite-like component, a ferri-ferrotschermakite-like component, and an as yet unrecognized component with 3 to 4 Al atoms per formula unit (apfu), 1 apfu each of Na and Ca, and <6 Si apfu, here termed aluminous kaersutite. None of these components, however, are significantly P-sensitive, leaving the Al-in-amphibole approach, with all its challenges, the best existing hope for an amphibole barometer. A new empirical barometer based on D_{Al} successfully differentiates experimental amphiboles crystallized at 1 to 8 kbar, at least when multiple P estimates, from multiple amphibole compositions, are averaged. Without such averaging however, amphibole barometry is a less certain proposition, providing ±2 kbar precision on individual estimates for calibration data, and ±4 kbar at best for test data; independent checks on P are thus needed. Amphibole compositions, however, provide for very effective thermometers, here based on D_{Ti}, D_{Na}, and amphibole compositions alone, with precisions of ±30 °C (Putirka 2016).

To compare the pressure of crystallisation of the Precambrian amphibole with the P-T crystallisation conditions of the early cumulus phases, clinopyroxene and clinopyroxene-orthopyroxene geothermobarometers were applied. Using chemistry-structure coefficients reported in Nimis (1995), the P conditions of clinopyroxene formation can be calculated as a function of atomic fractions (Nimis and Ulmer, 1998). The cpx-opx geothermobarometer is that expressed in the study of Putirka (2008). The two-pyroxenes thermometer provides somewhat greater precision, but precision is further improved if the calibration data base is restricted to include only Mg-rich systems, in this case defined as those cpx-opx pairs where $Mg\text{-number}^{cpx}>0.75$. The barometer is based on the Mercier et al. (1984) approach and is also calibrated using only high Mg-number compositions, with P precision to ± 2.8 kbar and R^2 = 0.82 (Putirka, 2008).

The Al-in-amphibole geobarometer was used to constrain the pressure crystallisation conditions of the Precambrian amphiboles target of this study. In literature, the Al-in-amphibole geobarometer was developed starting from plutonic quartz-diorites, gabbros and granites. These systems are different from

the ultramafic and mafic systems of the rocks studied in this thesis. However, the error related to the system composition was considered and the geobarometer was used to compare the P crystallisation conditions between amphibole and clinopyroxene. The methods used are those developed by Hammarstrom and Zen (1986), Johnson and Rutherford (1989) and Schmidt (1992). The calculated P conditions reveal mean value for the Australian amphiboles from Mt. Keith of 5 ± 1 kbar. About the other Australian locality, Mount Clifford, the calculated P crystallisation conditions of amphiboles have a mean value of 4.26 ± 0.67 kbar. The T°C conditions calculated using the method of Putirka (2016) are 903 ± 18.69 °C and 993 ± 6.56 °C for Mt. Keith and Mt. Clifford, respectively. The pressure conditions obtained are more controversial compared with those calculated with the Al-in-amphibole barometers (27.1 ± 0.11 kbar for Mt. Keith and 24.1 ± 0.36 kbar for Mt. Clifford). These high P values are unrealistic and could be the results of the alkali-poor compositions of the whole-rock used for the calculation. About the Canadian amphiboles, the calculated pressure conditions with Al-in-amph geobarometer for amphibole formation are 2.35 ± 0.56 kbar, 6.40 ± 0.83 kbar and 3.83 ± 0.43 for Theo's Flow, Boston Creek and Ghost Range, respectively. The P-T conditions for the amphiboles calculated with the geothermobarometer by Putirka (2016) reveal mean T°C of 937 ± 20.61°C and P of 5.7 ± 0.95 kbar for Theo's Flow, T°C of 961.4 ± 11.18 °C and P of 5.0 ± 1.27 kbar for Boston Creek, and T°C of 999.5 ± 11.60 °C and P of -1.0 ± 0.56 kbar for Ghost Range. Furthermore, P conditions have been calculated for the clinopyroxene of Theo's Flow (5.80 ± 0.58 kbar) and Boston Creek (-1.58 ± 0.62 kbar). The data of Boston Creek suggest contrasting P crystallisation conditions for amphibole and clinopyroxene whereas at Theo's Flow the two phases are crystallised relatively deep in the crust. However, this is in disagreement with the flow structure of the hosting volcanic suite. For the komatiite rocks of the Ghost Range, the geothermobarometers reveal calculated P formation conditions for pyroxenes of 2.35 ± 0.97 kbar (clinopyroxene barometer) and 2.4 ± 0.5 kbar for orthopyroxene-clinopyroxene geobarometer. As a matter of fact, the samples from Ghost Range are the only ones for which the two-pyroxenes geothermobarometer can be used. The differences between pressure conditions values determined for amphibole and pyroxenes are not so wide for the Ghost Range komatiite and, as in the other localities, indicate formation of the relevant minerals in a relatively deep level of the crust. About the Proterozoic Pechenga Complex, the calculated P conditions reveal mean values of 5.47 ± 0.76 kbar and 4.88 ± 0.72 kbar for amphibole from the Pilgüjarvi and Kammikivi sills, respectively. On the contrary, the P-T conditions obtained with the method of Putirka (2016) are more indicative of crystallisation of amphiboles at the surface (-1.7 ± 0.74 kbar and 1017 ± 11.42 °C for the Pilgüjarvi sill; -2.0 ± 0.66 kbar and 1023.1 ± 11.83 °C). However, the calculated P conditions of clinopyroxene formation in the Pilgüjarvi sill are different, with P values in the range 3.91-0.03 kbar. This variability can be ascribed to the different nature of the suites. On the contrary, the Kammikivi sill shows P crystallisation conditions

for clinopyroxene of 3.58 ± 0.56 kbar. These values suggest that crystallisation conditions occur not near the surface but deep in the crust.

In Table 4.2.1 the calculated pressures and temperatures are summarised.

Region	Localities Sample ID	Phase	P (kbar) Al-in-amph geobarometer; Ridolfi and Renzulli (2011)	P (kbar) Geobarometer (Putirka, 2016)	T (°C) Geothermometer (Putirka, 2016)
Australia – Agnew-Wiluna GB	Mt. Keith MKD1	Amph	5.07 ± 0.73		903 ± 18.69
	Mt. Clifford 85437	Amph	4.26 ± 0.67		993 ± 6.56
Canada – Abitibi GB	Theo's Flow T-2	Amph	2.35 ± 0.56	5.7 ± 0.95	937 ± 20.61
		Cpx		5.80 ± 0.58	
	Boston Creek B-5	Amph	6.40 ± 0.83	5.0 ± 1.27	961.4 ± 11.18
		Cpx		-1.58 ± 0.62	
	Ghost Range GR1; GR2	Amph	3.83 ± 0.43	-1.0 ± 0.56	999.5 ± 11.60
		Cpx		2.35 ± 0.97	
		Opx-Cpx		2.4 ± 0.5	
Russia – Pechenga Complex	Pilgüjarvi sill Pilg 8-38; 106-44; 116-6	Amph	5.47 ± 0.76	-1.7 ± 0.74	1017 ± 11.42
		Cpx		3.91-0.03	
	Kammikivi sill 57HV28	Amph	4.88 ± 0.72	-2.0 ± 0.66	1023.1 ± 11.83
		Cpx		3.58 ± 0.56	

GB: greenstone belt; Amph: amphibole; Cpx: clinopyroxene; Opx: orthopyroxene

In summary, the geobarometric calculation on Proterozoic rocks reveal large uncertainty on pressure estimates in agreement with the conclusion of Putirka (2016). However, all the Al-in amphibole geobarometric calculations reveal crystallisation pressures for amphibole >3 kbar, thus amphibole crystallisation might have occurred at depths >9.9 km (depth estimates using a geobarometric gradient of 3.3 km/1 kbar; Hagemann and Brown, 1996). The crystallisation of amphibole is unlikely to be related to the surficial emplacement of the host volcanic rocks. The calculated pressures obtained with the application of geobarometer by Putirka (2016) are in agreement with those calculated with Al-in amphibole for few localities. Thus, the estimate pressures are plausible. The samples with negative pressures suggest very low P crystallization conditions of amphibole.

4.3 Is amphibole a reaction product between melt and clinopyroxene precursor?

Several studies have revealed that amphibole in primitive arc magmas starts crystallising at the expense of clinopyroxene precursors (Davidson et al., 2007; Erdmann et al., 2014; Smith et al., 2014). It is well documented that intermediate and more evolved (and hydrous) arc magmas are generated in "hot zones" which are partially molten domains in the lower crust where melts of different type and origin can be distinguished: (1) mantle melts undergoing fractional crystallisation and evolving towards residual H_2O-rich compositions and (2) melts from the partial melting of pre-existing crustal rocks mixing with the mantle melts (Annen et al., 2006). All "hot zone" melts are H_2O-rich, therefore they have low density and viscosity and can readily separate from their source and ascend rapidly. In the case of adiabatic ascent, the magma attains a super-liquidus state, because of the relative slopes of the adiabat and the liquidus. This leads to resorption of any entrained crystals or country rock xenoliths, while crystallisation begins only when the ascending magma intersects its H_2O-saturated liquidus at shallow depths. This crystallisation mechanism takes place at shallow depths on timescales of decades or less and is run by decompression and degassing. Degassing and crystallisation at shallow depths lead to large increases in viscosity and stalling of the magma to form volcano-feeding magma chambers and shallow plutons (Annen et al., 2006).

In this frame, amphibole crystallisation can be theoretically achieved from residual H_2O-rich melts reacting with earlier-formed clinopyroxene mushes at different crustal levels. Melt segregation in hot zones affords mechanisms by which a largely crystal-free melt is separated from the early-formed clinopyroxene and reaction-replacement amphiboles. This does not exclude amphibole formation in low-pressure conditions. Sobolev et al. (2016) have calculated the primary melt liquidus temperature for

Abitibi komatiites that is close to 1,530 °C ± 20 °C, for a pressure of 250 bar. This temperature is about 60 °C lower than the temperature of anhydrous komatiite liquidus. The authors estimated the potential T of the mantle source considering an H_2O content of 0.6 ± 0.1 wt% and they obtained a T of 1,730 ± 50 °C. This value exceeds average estimates of the potential temperature for the Archaean non-arc basalts and the maximum estimates for Phanerozoic plumes for at least about 100 °C. This is consistent with a plume origin of Abitibi komatiites and a higher overall mantle temperature in the Archaean (Sobolev et al., 2016).

Phenocryst formation is decoupled from this process, and as a result, fractionation of amphibole in arc magmas may be cryptic (Smith, 2014). As described in the study by Smith (2014), clinopyroxene has reasonably limited influence on residual melt SiO_2, i.e., the melts participating in amphibole-forming melt–mush reactions are expected to be low SiO_2 (basalt or basaltic andesite), with relatively low abundances of incompatible trace elements, albeit higher than the melt before clinopyroxene crystallisation. Furthermore, melts reacting with clinopyroxene need not be co-genetic: clinopyroxene may be formed as a cumulate from earlier magmas and progressively replaced with amphibole by later melts ascending through the cumulate pile. The lower thermal stability of amphibole means that these cumulates may be periodically re-melted by the addition of high-temperature (>1110 °C) primitive melts.

Two scenarios may be thus proposed for the crystallisation of Precambrian amphiboles in the studied rocks and will be investigated in the forthcoming sections:

i) close-system - the parental liquid evolved in closed system becoming rich in water by fractional crystallisation of anhydrous phases until the stability of amphibole is reached. In this case amphibole and clinopyroxene lie on the same liquid line of descent and equilibrium between the two phases is expected;
ii) open-system – H_2O-rich residual melts percolated the cumulate pile reacting with clinopyroxene and inducing amphibole crystallisation.

4.4 Amphibole-Clinopyroxene equilibrium

In order to assess if amphibole and clinopyroxene are on the same liquid line of descent, the amphibole-clinopyroxene equilibrium is the first constrain that has to be verified. There are several ways to check equilibrium between amphibole and clinopyroxene. Textural relationships between the two minerals (see sections 2.1 and 2.1) and distribution of major and trace elements are the most robust

proxies to evaluate equilibrium conditions. Among major elements, information on the equilibrium conditions can be gathered from the exchange coefficient $^{amph/cpx}Kd_{Fe/Mg}$ and thus in turn from the ratio between the Mg-number [$Mg/(Mg+Fe_{tot})$] of the two phases (Fig. 112). Data in the literature are scarce and limited to the experimental work of Müntener et al. (2001). The authors crystallised amphibole and clinopyroxene from a natural arc-magma composition at 1.2 GPa and found that at equilibrium the ratio of $Mg\text{-number}_{AMPH}/Mg\text{-number}_{CPX}$ is 0.97.

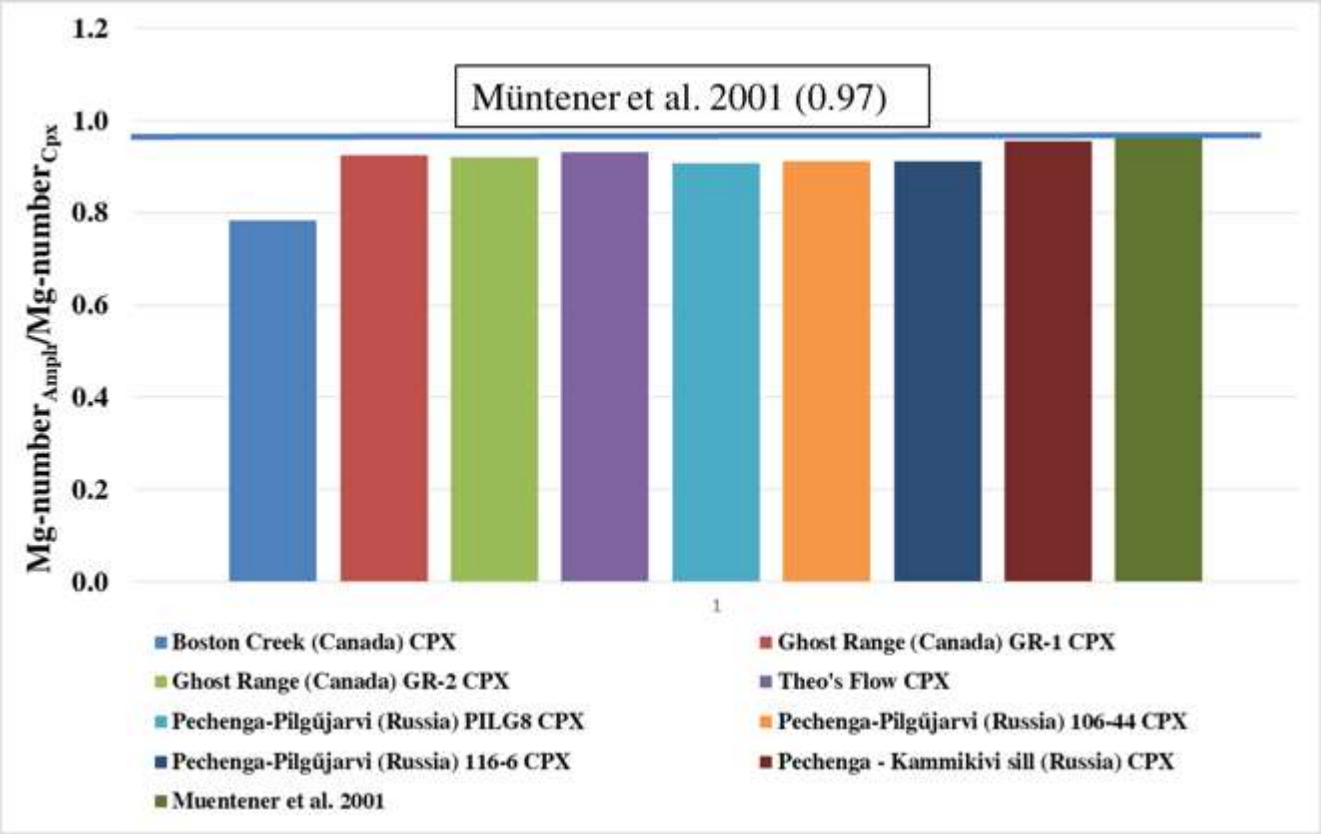

Figure 112 - Comparison of Mg-number of amphibole and clinopyroxene. The blue line is the equilibrium $Mg\text{-number}_{AMPH}/Mg\text{-number}_{CPX}$ after Müntener et al. (2001)

REE are also informative on equilibrium between amphibole and clinopyroxene. Because REE are incorporated in amphibole and clinopyroxene in equivalent sites with the same crystal chemical mechanism, $^{Amph/Cpx}D$ for the REE at equilibrium should be close to unity and never exceeding 3-4 (Zanetti et al., 1996). These two equilibrium constraints were tested on all the amphibole-clinopyroxene couples of the dataset. Note that the equilibrium conditions could not be evaluated for Australians samples because of absence of preserved clinopyroxene.

Abitibi Greenstone Belt

Amphiboles in the iron-picrite from Boston Creek are interstitial to olivine grains and occupys the same intercumulus domains of clinopyroxene with no apparent replacement textures, thus with no evidence for textural disequilibrium. However, the Mg-number$_{AMPH}$/Mg-number$_{CPX}$ ratio is 0.78 and is much lower than the value of 0.97 reported by Müntener et al. (2001) for equilibrium conditions. The REE pattern of the $^{Amph/Cpx}D$ (Fig. 113) reveals that at Boston Creek amphibole and clinopyroxene are not in equilibrium and a marked fractionation of the $^{Amph/Cpx}D_{REE}$ pattern with $^{Amph/Cpx}D_{LREE}$ at about 50 and $^{Amph/Cpx}D_{HREE}$ at about 20 is observed. This suggests that the equilibrium melt of amphibole was significantly enriched in REE (and LREE in particular) relative to that in equilibrium with clinopyroxene.

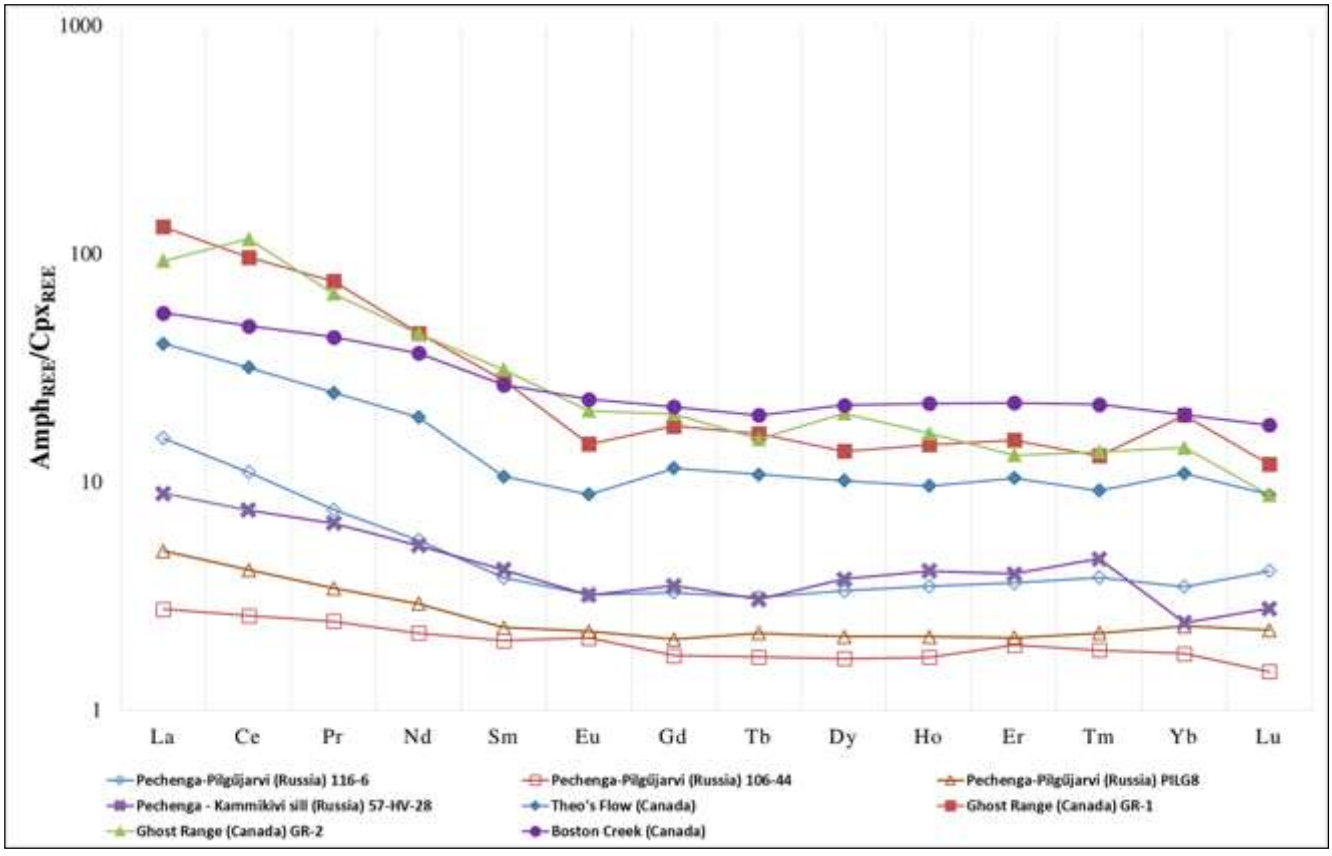

Figure 113 - $^{Amph/Cpx}D_{REE}$ pattern for the Precambrian samples.

In the Theo's Flow rocks, the textural relationships between amphibole and clinopyroxene are not preserved and the ratio of Mg-number$_{AMPH}$/Mg-number$_{CPX}$ is 0.93 that is very close to the equilibrium literature value of 0.97. The solid/solid partitioning of REE between amphibole and clinopyroxene however reveals values for LREE and HREE of 25 and 10, respectively, that are much higher than the equilibrium range. This trend is almost the same $^{amph/cpx}D$ pattern of Boston Creek except for a lesser

fractionation for MREE. According to mechanisms of solid/solid partitioning of REE, amphibole and clinopyroxene may have been originated by different melts.

At Ghost Range amphibole has poikilitic texture and shows sharp contact with pyroxenes. Only in few cases amphibole overgrows clinopyroxene. Amphiboles and clinopyroxenes show a Mg-number$_{AMPH}$/Mg-number$_{CPX}$ ratio of 0.92, not far from the equilibrium value from literature. The amphibole/clinopyroxene partitioning of REE displays overall values higher than the equilibrium range and enrichment in LREE (up to enrichment factor of 67) relative to HREE (up to an enrichment factor of 15). The melt in equilibrium with amphibole was more enriched in LREE and, to a lesser extent, in HREE compared to melt in equilibrium with clinopyroxene.

Pechenga complex

In the Paleoproterozoic Pechenga Complex, amphibole of the Pilgüjarvi sill shows poikilitic to intercumulus textures with sharp contacts with clinopyroxene. However, in the magnetite-olivine peridotite amphibole overgrows clinopyroxene grains suggesting disequilibrium conditions (Fig. 20, section 2.1). Amphibole of the Kammikivi sill has poikilitic texture that in some spots shows replacement of the intercumulus clinopyroxene. The Mg-number$_{AMPH}$/Mg-number$_{CPX}$ ratio in the Pilgüjarvi sill shows a mean value of 0.91 that is not far from the literature value of 0.97 at equilibrium conditions. The Mg-number$_{AMPH}$/Mg-number$_{CPX}$ ratio in the Kammikivi sill is 0.96, thus very close to the 0.97 equilibrium value from the literature. Results from major elements are however not supported by trace elements. The solid/solid $^{Amph/Cpx}D$ show patterns with a slightly decrease from LREE (3.2) to HREE at 2.2 close to the equilibrium range, whereas amphibole and pyroxene of the magnetite-olivine peridotites have HREE partition coefficients at 4 with a significant enrichment in LREE (at about 15). For the amphibole and clinopyroxene of the Kammikivi sill, the $^{Amph/Cpx}D$ REE values show a pattern decreasing from LREE (at about 7) to MREE and HREE (at about 4). This pattern is comparable with that of magnetite-olivine peridotite of Pilgüjarvi sill and suggests that amphibole and clinopyroxene crystallisation conditions are slightly shifted from those predicted at equilibrium.

Summary

According to the above textural and chemical evidences, amphibole and clinopyroxene in most of the Precambrian samples considered, and especially the Archean ones, do not fulfil the conditions required for equilibrium. To summarize, the Canadian samples are those apparently most far from equilibrium whereas those from the Proterozoic Pechenga Complex (Pilgüjarvi and Kammikivi sills) are closer to equilibrium conditions. Amphibole crystallisation in most of the studied rocks seems to occur from a more differentiated melt, i.e. with lower Mg-number and enriched in REE (and in LREE over

HREE in particular). These evidences suggest that amphibole and clinopyroxene did not crystallise "on site" from the same melt. Two different scenarios can be envisaged: i) amphibole originated from the same parental melt of clinopyroxene (in this case the two minerals would be on the same liquid line of descent) but amphibole crystallised from a liquid much more differentiated that back migrated the cumulate pile and crystallised interstitial between early cumulus minerals; ii) amphibole crystallised from an exotic melt with no relations with the parental liquid of the early crystallised cumulus minerals. In the latter case, a new magmatic pulse from the mantle is required.

4.5 Modelling of melt evolution

In order to assess if amphibole and clinopyroxene were derived from melts evolved from the same parent liquid the equilibrium melts were calculated and the possibility was evaluated for deriving one melt (amph) or the other (cpx) by fractional crystallisation of the cumulus minerals. The incompatible trace element composition of the melts in equilibrium with clinopyroxenes and amphiboles were calculated by applying $^{Sol/Liq}D$ for P-T-X conditions suitable for the studied rocks. The $^{Cpx/Liq}D$ used are those from Adam and Green (2006) for similar clinopyroxene composition whereas for amphibole the $^{Amph/Liq}D$ are from Tiepolo et al. (2007).

Melt calculation

The N-MORB-normalized incompatible trace element patterns for the melt in equilibrium with clinopyroxene is reported in Fig. 114. The patterns of the tholeiites of Theo's Flow and Ghost Range are characterized by a slight LREE/HREE fractionation (La_N/Yb_N = 3.79), nearly flat HREE (Gd_N/Yb_N = 1.59) and negative anomalies in Zr and Hf (0.22 and 0.16 times the N-MORB values). Th and U concentrations are very high (40 times the N-MORB values). The N-MORB-normalized incompatible trace element patterns for the melts in equilibrium with amphibole are shown in Fig. 115 A and B. The patterns of the Canadians tholeiites of Theo's Flow and Ghost Range are characterized by fractionation of LREE/HREE (La_N/Yb_N = 12.02 for Theo's Flow; La_N/Yb_N = 14.46-16.64 for Ghost Range), slightly hump-shaped HREE (Gd_N/Yb_N = 1.48 for Theo's Flow; Gd_N/Yb_N = 1.35-1.85 for Ghost Range). Negative anomalies are observed in Ba, Sr and, to a lesser extent, in Ti (0.47 and 0.96 times the N-MORB value) for calculated amphibole-equilibrium melts from the two localities. Positive anomalies in 115 B (173 and 1400 times the N-MORB value for Theo's Flow and Ghost Range, respectively), Th and a slightly enrichment in Zr-Hf is observed for Ghost Range amphibole-equilibrium melt. The calculated melts for amphibole and clinopyroxene from Theo's Flow (Fig. 116 A) do not show similarities in their respective positive or negative anomalies as well as in the level of incompatible trace element concentrations. In particular, the Sr and Ti negative anomalies characterising amphibole-equilibrium

melt are not observed in the melt in equilibrium with clinopyroxene. Furthermore, the negative Zr-Hf negative anomaly of clinopyroxene-equilibrium melt is not reflected by the pattern of melt in equilibrium with amphibole. The comparison of the N-MORB-normalized incompatible trace element patterns for the melts in equilibrium with clinopyroxene and amphibole from Ghost Range reveals significant differences. In particular the negative anomalies in Sr and Ti that characterise the amphibole-melt are not present in the melt in equilibrium with clinopyroxene. In addition, the pattern of clinopyroxene-equilibrium melt shows a slightly Zr-Hf negative anomaly that is positive in the amphibole-equilibrium melt.

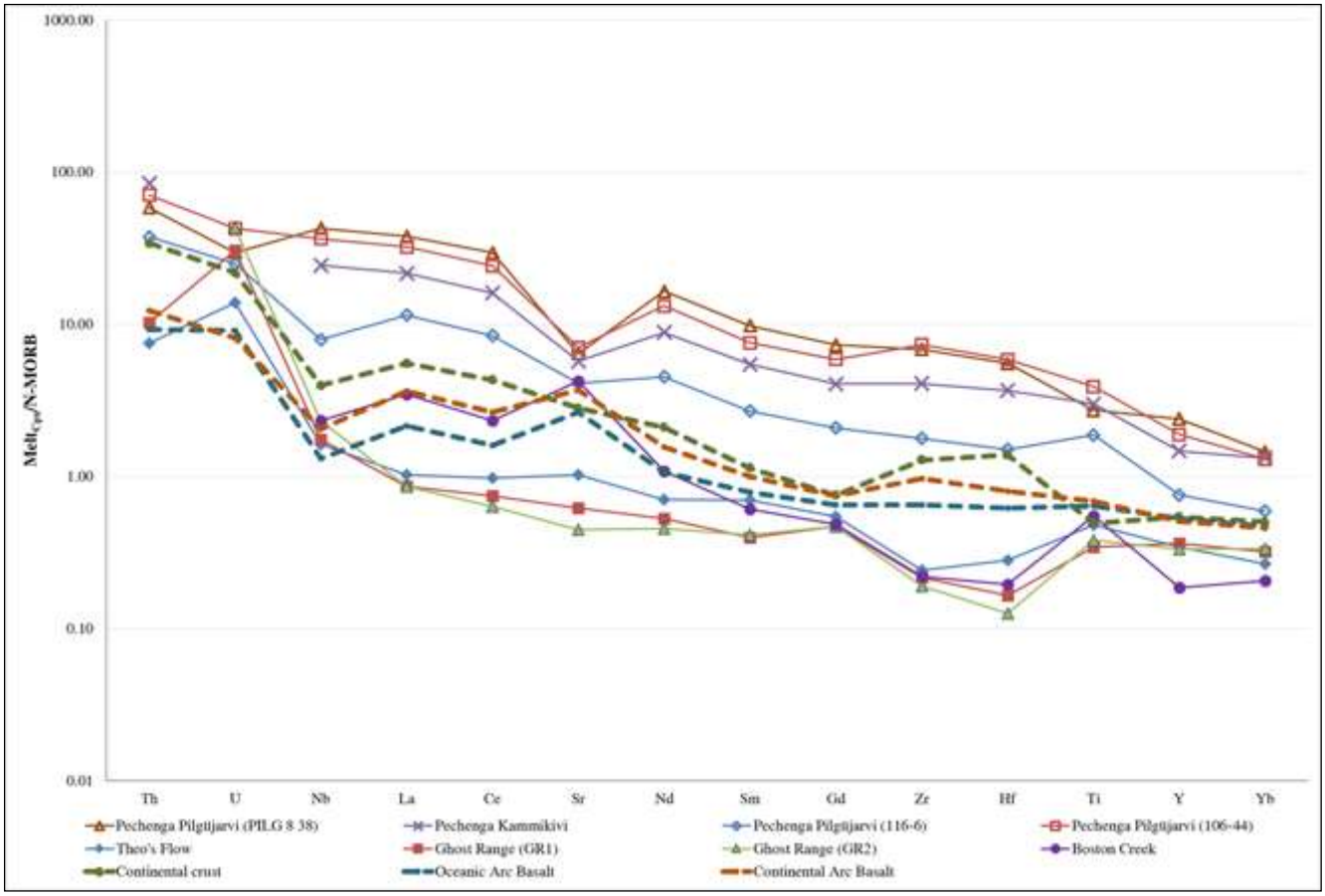

Figure 114 - The N-MORB-normalized incompatible trace element patterns for the melt in equilibrium with clinopyroxene, from the Precambrian localities. N-MORB and Continental Crust values are from McDonough and Sun, 1995. Continental and Oceanic Arc Basalt values are from Kelemen et al., 2003.

The N-MORB-normalized pattern of the melt in equilibrium with clinopyroxene from Boston Creek is characterized by enrichments in LREE over HREE (La_N/Yb_N = 16.74), which are almost flat (Gd_N/Yb_N = 2.34). The incompatible element patterns reveal positive anomaly in Sr and high Th and U contents as well as negative anomalies in Zr-Hf (0.22 and 0.19 times the N-MORB concentrations). The N-MORB normalized trace elements patterns of the melt in equilibrium with amphibole from Boston Creek display enrichment in LREE over HREE (La_N/Yb_N = 45.01), which are almost flat (Gd_N/Yb_N =

1.99). The incompatible element pattern reveals slightly negative anomalies in Sr, Pb, Zr, Hf and Ti compared to the neighbour elements. Positive anomalies are observed for B and Th. The patterns of the melts in equilibrium with clinopyroxene and amphibole from Boston Creek are characterized by similarities in Zr-Hf negative anomalies as well as enrichment in B. However, the clinopyroxene-equilibrium melt has REE at 0.5 times the N-MORB values whereas the melt in equilibrium with amphibole is at 3 times the N-MORB. The difference is highlighted by the incompatible element patterns that are 3-4 (clinopyroxene) and 70 (amphibole) times the N-MORB values.

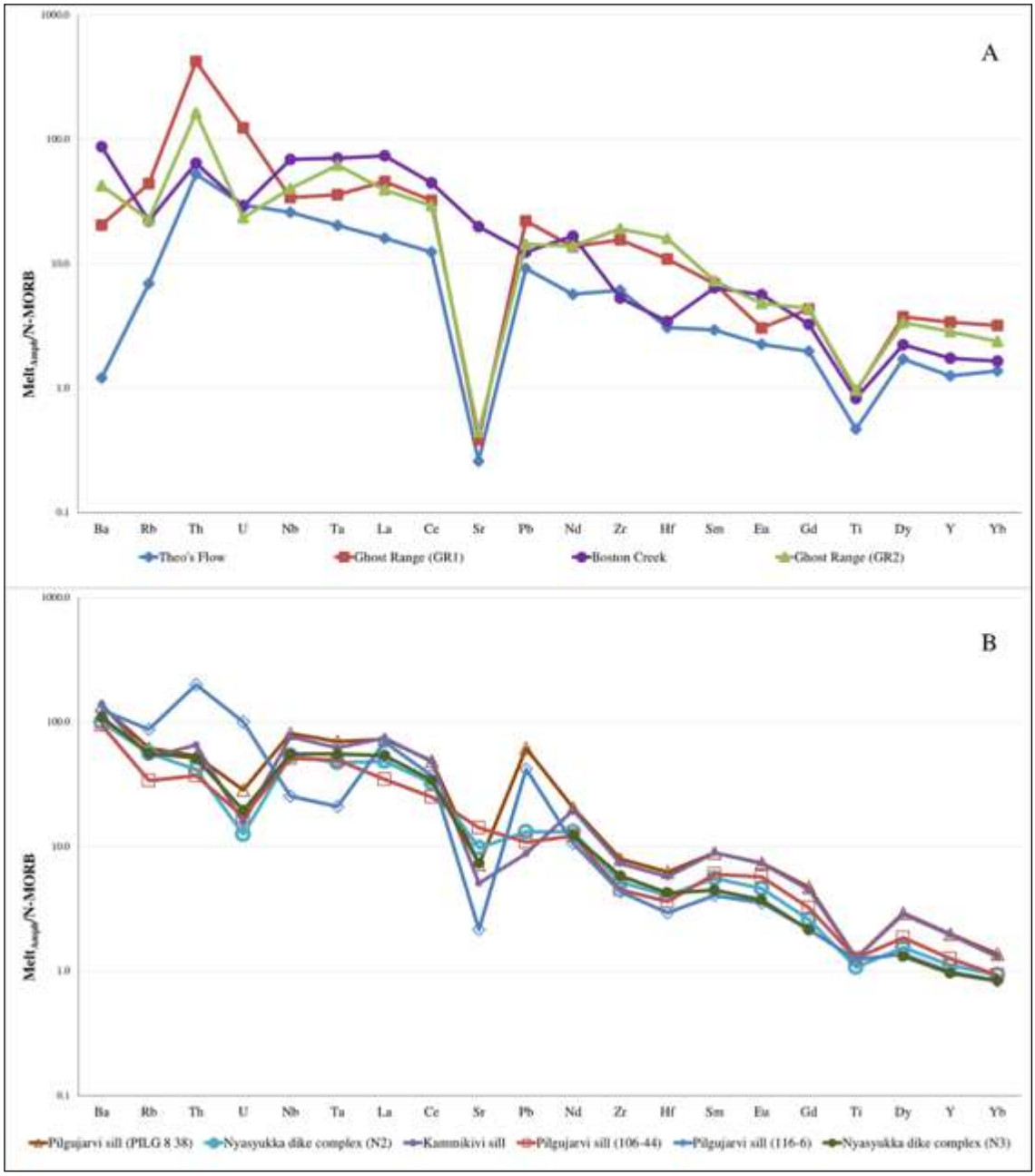

Figure 115 A, B - The N-MORB-normalized incompatible trace element patterns for the melts in equilibrium with (A) Canadian and (B) Russian amphiboles.

The patterns of the melts in equilibrium with clinopyroxene from the Pilgüjarvi and Kammikivi sills are characterized by low HREE (0.20 times the N-MORB value; $Gd_N/Yb_N = 4.05$) marked LREE enrichment over HREE ($La_N/Yb_N = 21.64$), negative anomaly in Sr, slightly positive anomalies in Zr-Hf, and high Th and U concentrations (up to 84 N-MORB concentration; Fig. 114). The N-MORB normalized trace elements patterns of the melts in equilibrium with amphibole from Pechenga Complex are characterized by enrichment in LREE ($La_N/Yb_N = 37.40$-83.07 for the Pilgüjarvi sill; $La_N/Yb_N = 57.75$ for Kammikivi sill) that decrease to HREE ($Gd_N/Yb_N = 2.59$-3.47 for the Pilgüjarvi sill; $Gd_N/Yb_N = 3.49$ for Kammikivi sill) (Fig. 115 B). Despite the different locations of samples, the incompatible element patterns of the equilibrium melts with amphibole are characterized by comparable concentrations and have negative anomalies in U, Sr, Zr, Hf and Ti. Positive anomalies are observed for B (except one melt of Pilgüjarvi sill), Nb and Ta. Two patterns of the Pilgüjarvi sill reveal positive anomaly in Pb. Only one amphibole-equilibrium melt (calculated starting from the amphibole of olivine-magnetite) has positive Th and U and negative Nb-Ta anomalies compared to the other melts. The normalized N-MORB patterns of melts in equilibrium with clinopyroxene and amphibole reveal comparable concentrations for all the considered incompatible trace elements (Fig. 116 B)

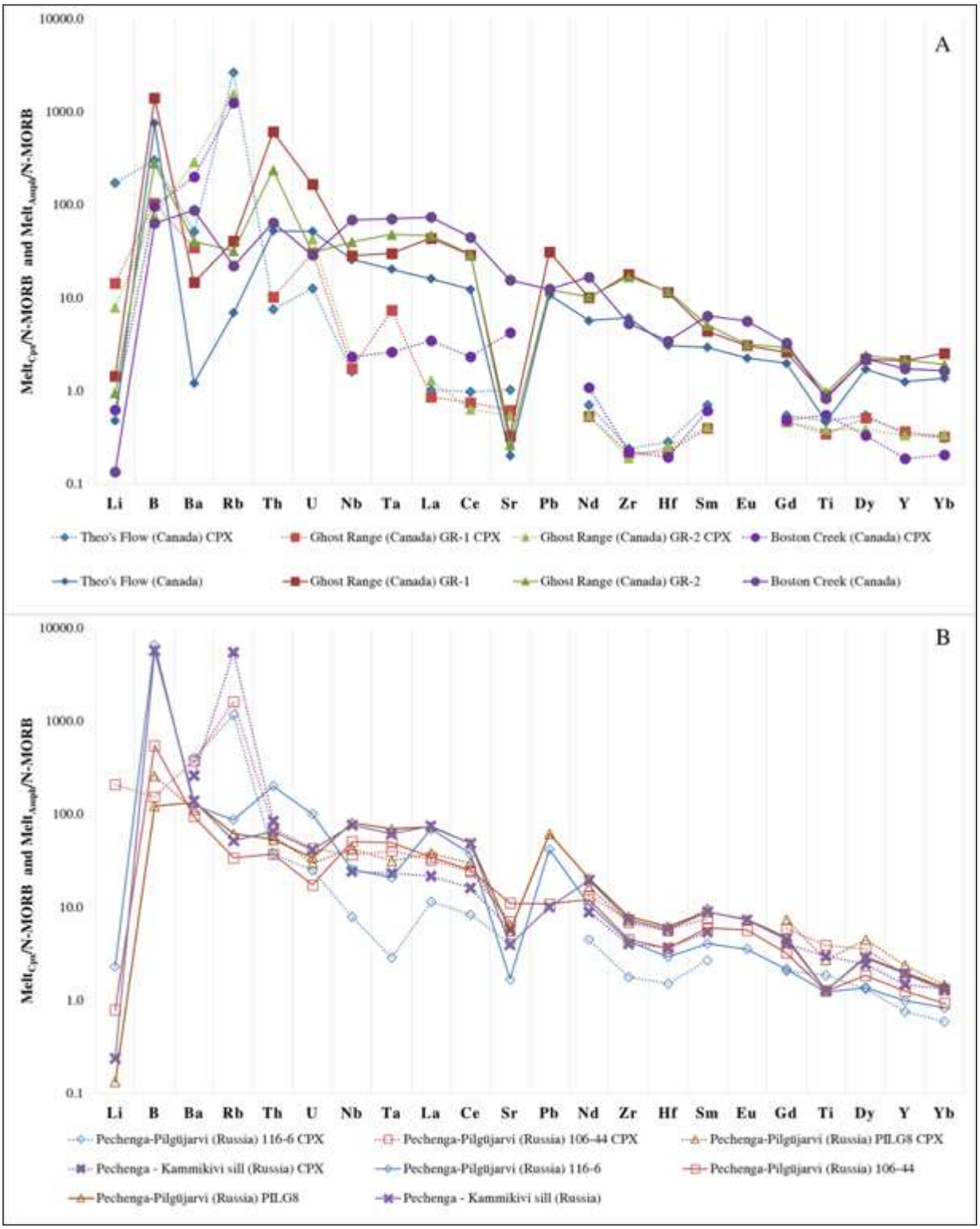

Figure 116 A, B - The N-MORB-normalized incompatible trace element patterns for the melts in equilibrium with (A) Canadian clinopyroxene-amphibole and (B) Russian clinopyroxene-amphibole.

Modelling

The first approach was to test if the melt in equilibrium with amphibole can be a melt circulating into the cumulate pile after the crystallisation of clinopyroxene and with only amphibole in equilibrium. A process of fractional crystallisation driven exclusively by amphibole was simulated by considering different residual melt fractions (F = 0.9 – 0.1) and starting from the composition of the melt in equilibrium with clinopyroxene (Fig. 117). The fractional crystallisation model is obtained by applying the formula:

$$C_L = C_0 \times F \wedge (^{Amph/L}D-1)$$

where C_L is the composition of the liquid in equilibrium with amphibole at different residual melt fraction, C_0 is the starting melt composition (namely the melt in equilibrium with clinopyroxene) and $^{Amph/L}D$ is the partition coefficient of amphibole (amph vol% x $^{Amph/L}D_{REE}$). In Figure 117 the REE chondritic-normalized patterns of calculated and amphibole-equilibrium melt compositions are reported.

For the Canadian Theo's Flow, the model reveals similarities between analysed concentrations of REE in amphibole and calculated compositions for low fractions of residual melts (F = 0.2). However, the LREE in amphibole-equilibrium melt have lower concentrations (40 vs 70 times Cl chondritic value) compared to those in calculated melt. The modelled REE chondritic-normalized pattern of Boston Creek displays concentrations of MREE and HREE comparable with analysed amphibole for high crystallisation degree (F = 0.1). However, the LREE values of natural amphibole are, also in this case, lower (140 vs 400 times Cl) compared to the low fractions of residual melts of the model. For the Ghost Range, the calculated amphibole compositions at F = 0.1 have comparable concentrations with those of analysed amphiboles. In general, the concentrations of HREE observed in the crystallisation models show an enrichment in these elements for high fractionation degrees, whereas natural amphibole shows slight depletion in HREE for corresponding fractionation grade. However, these results are in agreement with textural observation of no evidences of clinopyroxene substitution by amphibole. At Pechenga Complex, the model yields comparable compositions for REE between calculated and analysed amphiboles. In two samples from Pilgüjarvi and Kammikivi sills, the modelled amphibole composition is in agreement with crystallisation at differentiation degrees F = 0.7 - 0.8 . For the other two samples from Pilgüjarvi sill, the amphiboles have compositions comparable with those of calculated amphiboles in early stages after clinopyroxene formation at F = 0.9 - 1. However, in the latter samples, LREE concentrations in natural amphiboles are depleted if compared to those predicted in the models.

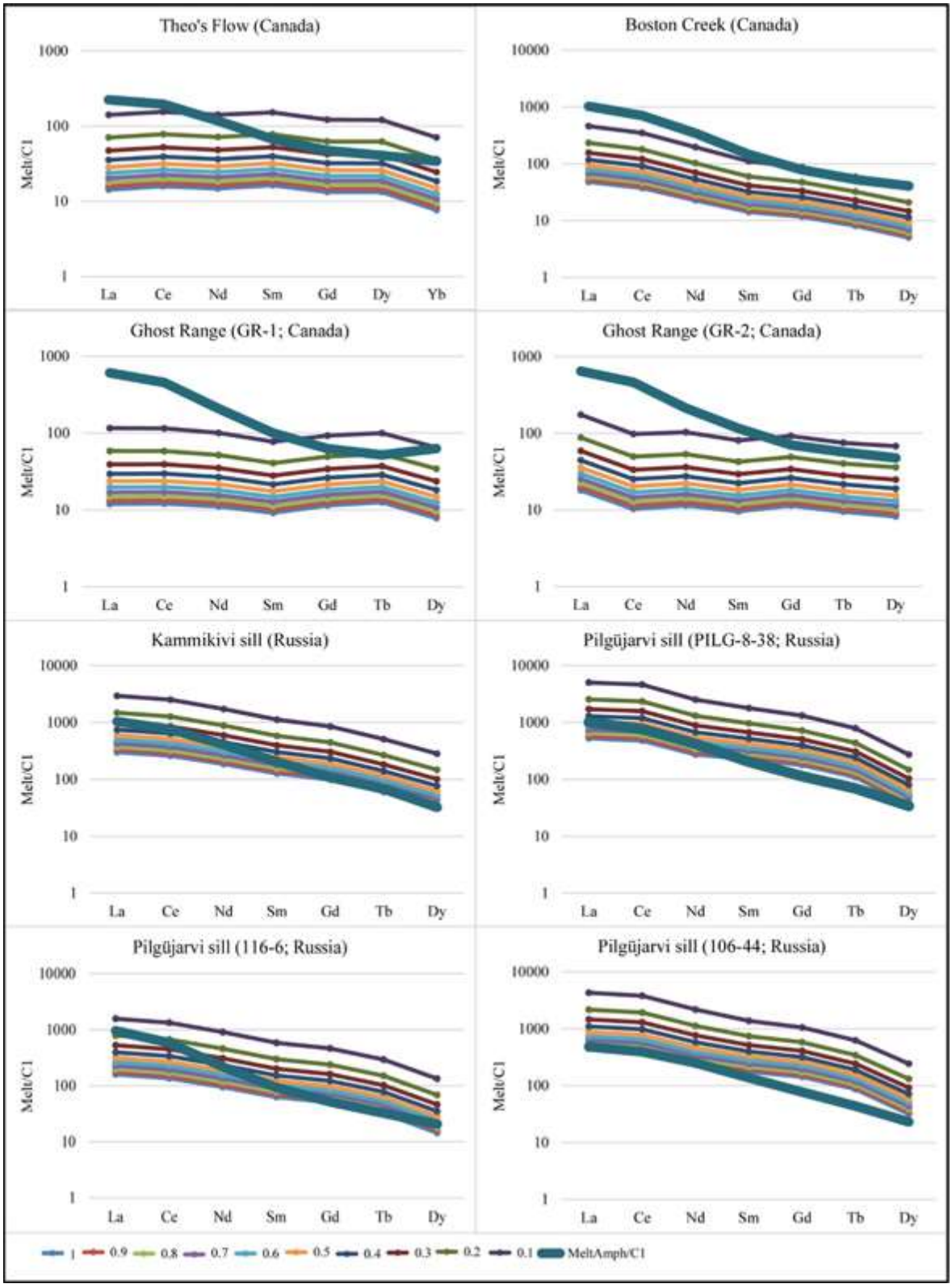

Figure 117 – Model of fractional crystallisation driven by amphibole considering different residual melt fraction (F = 0.9 – 0.1) and starting from the composition of the melt in equilibrium with clinopyroxene.

In summary the model shows that the melt in equilibrium with amphibole cannot be considered derived from that in equilibrium with clinopyroxene by the sole crystallisation of amphibole. The

mismatch in LREE between the analysed and the calculated compositions suggests a further component that amplifies the LREE enrichment in the melt in equilibrium with amphibole. Two possibilities can account for this LREE enrichment: i) the fractional crystallisation of mineral phases much more LREE-depleted than amphibole (such as olivine and orthopyroxene) or ii) a contribution of an exotic component rich in LREE. In order to address this point, a second model of fractional crystallisation was carried out by considering primitive bulk compositions from the same suites of the studied rocks and evolving the melt by crystallisation of all the early cumulus minerals (olivine, orthopyroxene and clinopyroxene). As starting melt composition, for each locality the bulk-rock trace element composition of the least differentiated rock (representative of a melt composition) found in the literature was considered.

The composition of the liquids in equilibrium with amphibole and clinopyroxene were then compared with the compositions calculated from the fractional crystallisation curves. The bulk-rock composition considered in the calculation for the different suites of studied samples are the following: the bulk-rock composition of Theo's Flow is from Lentz et al. (2011) and Stone et al. (1995 and 1996); for the Boston Creek the whole-rock data are from Stone et al. (1995). Regarding Ghost Range, literature for whole-rock trace elements composition data are not available. Data used in the model are from Fan and Kerrich (1997) and Xie Qianli and Kerrich (1994) and derived from a tholeiitic sequence geologically coeval and coherent with that of the Ghost Range. Data of the bulk-rock composition for the Pechenga Complex suites used for the model are from Fiorentini et al. (2008 and 2011). The used $^{Sol/Liq}D$ for olivine are from Adam and Green (2006) and Lee et al. (2007), for clinopyroxene ad orthopyroxene from Adam and Green (2006) and for amphibole from Tiepolo et al. (2007).

Results reveal that amphibole-equilibrium melt compositions in the Precambrian samples are different from the modelled melt compositions (Fig. 118). The matching between computed and observed compositions for Theo's Flow and Ghost Range suggests that amphibole crystallised during the late stages of melt differentiation (around 10-15 % of residual melt). This is in agreement with the textural evidences and is not far from the observed volume percentages of amphiboles in the rocks. However, at Ghost Range the amphibole-equilibrium melts still possess LREE concentrations considerably higher (460 times the Cl value) compared to those of the modelled melt fractionations (230 times the Cl concentrations). The model for the iron-picrite of Boston Creek suggests that amphibole crystallisation occurred between 10 % and 20 % of residual melt, which is not in agreement with the modal percentages of amphibole in the rock. Also, in this case, LREE are more enriched in the amphibole-equilibrium melt than in the calculated one, thus suggesting an exotic input for LREE in the system. The mismatch between the model and the volume % of amphibole observed in the sample implies a fraction of melt that escaped the system. About the Pechenga Complex, the differentiation

model for REE shows that amphibole crystallisation should have occurred between 20 and 50 % of residual melt, based on the different suites. In particular, the crystallisation model shows that in the Kammikivi sill and in one sample from the Pilgüjarvi sill amphibole starts to crystallise at 20 - 30 % of residual melt. In the others two samples from Pilgüjarvi sill the model suggests that amphibole crystallisation starts at F = 0.5-0.6 of residual fraction of melt.

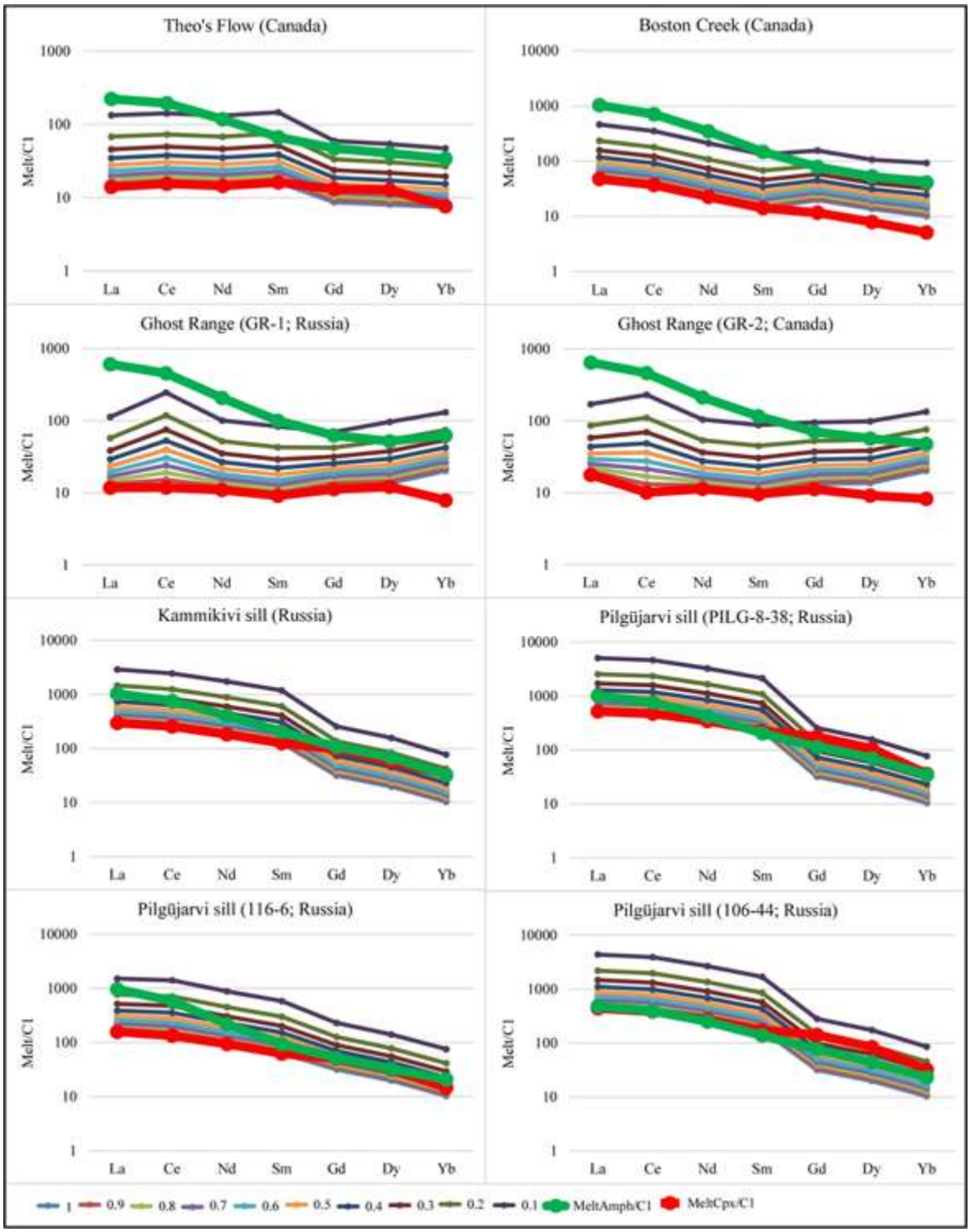

Figure 118 – Model of fractional crystallisation considering the bulk compositions of the studied rocks and evolving the melt by crystallisation of all the early cumulus minerals (ol + opx + cpx). The numbers from 0.1 to 1 are the fraction of residual melt (F)

The crystallisation model shows that measured amphibole REE composition can be obtained in all localities, with the exception of Canada, by differentiation of the primary melt by fractional crystallisation of the early cumulus minerals (Ol + Opx + Cpx), thus implying that a completely external

melt is not required. For the Canadian localities, the model fails to reproduce the strong LREE enrichment, hence an exotic LREE component has to be supposed after the crystallisation of clinopyroxene, thus during the late stages of crystallisation. The models of fractional crystallisation for the samples from Pechenga Complex support the crystallisation of amphibole in closed-system conditions although the melt is slightly more evolved than that in equilibrium with clinopyroxene. In conclusion, amphibole crystallized from a melt likely evolved by fractional crystallisation from the primary melt but the disequilibrium between amphibole and clinopyroxene suggests that this melt was highly mobile in the cumulate pile, and likely amphibole crystallisation occurred during melt migration within the cumulate pile.

4.6 The role of external components

As outlined in the previous section, several evidences suggest that parental melts of the studied samples underwent chemical differentiation before amphibole crystallisation. According to the fractional crystallisation model based on REE, amphibole has the same geochemical affinity of the bulk rock and likely crystallized for high degrees of melt differentiations.

Several examples suggesting the middle and lower crust as the dominant source of evolved magmas are described in the literature; e.g. the Deep Crustal Hot Zones (DCHZ; Annen et al., 2006) or Melting-Assimilation-Storage-Hybridization (MASH) zones (Hildreth and Moorbath, 1988). Various thermodynamic models have also demonstrated that the intrusion of mantle-derived primary magmas into the lower crust can produce large volumes of partial melt by heating and melting of the crust (e.g. Annen et al., 2006). Furthermore, H_2O-rich intermediate to silicic residual melts are also generated by incomplete crystallization of newly arrived basalt in the hot zone, with some contribution from remelting of earlier intrusions (i.e., Petford and Gallagher, 2001; Annen et al., 2006; Solano et al., 2014). Jackson et al. (2003) and Solano et al. (2012, 2014) argued that the DCHZ is in a mush state for most of its lifetime, except when a new inflow of basaltic magma generates a transient magma chamber. Partial melt in the mush migrates upwards along grain boundaries, and accumulates near the top of the DCHZ, forming one or more high porosity layers. The melt fraction accumulates until it reaches the “solid-to-liquid” transition, at which step the mush disaggregates yielding a mobile magma comprising melt and suspended crystals. Such melt-rich layer is unlikely to be stable, and the magma will ascend to higher crustal levels via dikes, faults or fractures to erupt directly, or form upper crustal magma chambers and plutons (i.e., Grosfils, 2007; Karlstrom et al., 2010). Jackson et al. (2003, 2005) also argued that the melt in the high porosity layer is chemically evolved, because it has equilibrated with solid at low

temperatures near the top of the DCHZ. Thus, the coupled processes of melt migration and chemical reaction through a temperature gradient give rise to evolved magma in DCHZ (Solano et al., 2012).

4.6.1 Constrains from transition metals

The differentiation processes are also highlighted by the distribution of the transition metals. In the Theo's Flow, Cr and Sc contents in clinopyroxene are 2.09 and 10.94 ppm, respectively, while in amphibole are 0.45 ppm for Cr and 6.78 ppm for Sc (Fig. 119 A). On the contrary, Ni, Co and Zn display higher contents for amphibole compared to those of clinopyroxene. These elements have a high compatibility for the high temperature mafic phases of subalkaline melts, e.g., olivine and clinopyroxene. Being amphibole a lower-temperature phase it is expected to be depleted in Ni, Zn and Co relative to clinopyroxene. Thus, amphibole and clinopyroxene do not follow the same liquid line of descendent. Clinopyroxene in the Boston Creek sample shows higher Cr and Sc contents compared to those of the associated amphibole and this is consistent with the late fractional crystallisation of amphibole relative to clinopyroxene, as expected. In the Ghost Range peridotites the Cr content of amphibole (3.34-3.61 ppm) is slightly higher that of clinopyroxene (2.09-3.12 ppm). A similar incongruity is also observed for other highly compatible elements such as Ni, V and Co, thus suggesting that the two minerals do not lie on the same liquid line of descent. Transition metals in particular suggest that the melt at the origin of amphibole assimilated mafic phases rich in transition metals such as olivine (rich in Ni and Co) and pyroxene (rich in Cr and V). For this reason, amphibole in the Ghost Range peridotites may be interpreted as a reaction product between olivine and clinopyroxene with an amphibole-forming liquid of exotic origin.

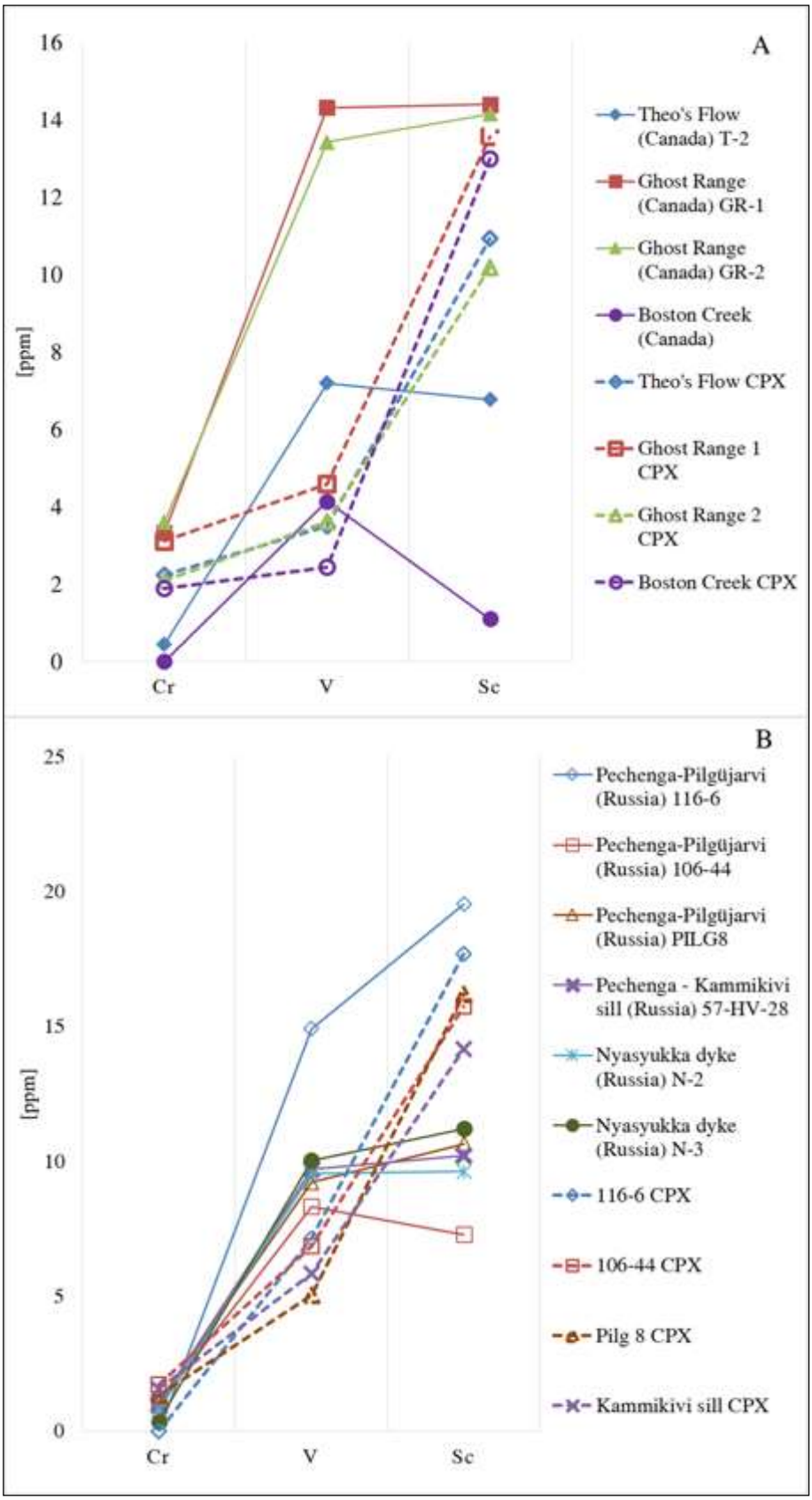

Figure 119 A, B – Transition metals contents are compared for clinopyroxene and amphibole in (A) Canadian and (B) Russian samples.

In the Pilgüjarvi and Kammikivi sill, the transition metal distribution shows slightly higher Cr contents in clinopyroxene compared to amphibole (Fig. 119 B). The latter, however, has higher contents in V, Co, Ni and Zn. This supports the hypothesis that amphibole crystallisation is related to a melt/rock reaction process between a primary assemblage (likely olivine + magnetite/ilmenite + clinopyroxene) and a more evolved melt in equilibrium with amphibole that promoted the partial resorption of the primocrystic phases and thus the mobilisation of Ni (from olivine) and Cr (from pyroxene).

4.6.2 Constrains from fluid-mobile elements

The origin of amphibole from the hydration of the cumulate pile (in particular of clinopyroxene) in response to the circulation of seawater-derived fluids cannot be also *a priori* excluded. Proxies for the magmatic vs. metamorphic origin of amphibole are fluid-mobile elements such as Cl, F, Ba, B and Sr but also some fluid-immobile elements such as Nb. Chlorine is expected to be high in seawater-derived fluids (about 20,000 ppm in seawater; e.g., Von Damm, 1990) and low in silicate melts (20 to 50 ppm in primitive magmas; Michael and Schilling, 1989). In contrast, F is relatively high in evolved silicate melts (commonly ~300 ppm; Michael and Schilling, 1989) and low in seawater-derived fluids (2 ppm in seawater; Faure, 1991). Chlorine incorporation into amphibole is dependent on its K, Fe^{2+}, $^{(IV)}Al$, and Mg contents (Oberti et al., 1993; Aranovich and Safonov 2018). However, when all amphibole compositions are considered there is no correlation between the abundances of these elements and that of Cl, suggesting that Cl in the fluid phases (silicate or aqueous based) was the dominant control on amphibole Cl contents. Nb is considered an immobile element, even under amphibolite facies metamorphic conditions (e.g., Weaver and Tarney, 1981) and for which amphibole may have a compatible behaviour (Tiepolo et al., 2000). The circulation of seawater-derived fluids in the cumulate pile is expected to give low Nb amphiboles. On the contrary, evolved hydrous silicate melts crystallise amphiboles that are enriched in Nb primarily for the highly incompatible behaviour of Nb in most of the high T°C phases. The Nb/La ratio in magmatic amphibole is expected to greatly exceed Nb/La in hydrothermal amphibole. Hence, both Nb abundances and Nb/La should be able to distinguish between magmatic and hydrothermal amphiboles (Coogan et al., 2001).

Primary arc melts (picrite and boninite) in sub-arc mantle xenoliths, and arc-related melt inclusions in general, are strongly enriched in Cl in comparison with MORB and possess high Cl/F ratio (Benard et al., 2017). Fluxed melting involving fluids with high Cl/F and derived from subducted serpentinite or altered crust can account for this sub-arc signature. Amphibole (and/or mica) in the deep mantle wedge near the slab is suggested to control the Cl/F signatures of metasomatic agents ascending to the sources of arc and back-arc magmas (Benard et al., 2017). The positive correlations between slab depth and F abundances in primitive arc melt inclusions possibly result from amphibole (and/or mica)

breakdown in the deep metasomatised mantle near the slab (Benard et al., 2017). During exsolution of a volatile phase from a magma, Cl preferentially partitions into the fluid over F leading to an increase of Cl/F. High Cl contents in melt inclusions from Gorgona komatiites were also attributed to assimilation of altered oceanic crustal rocks (Kamenetsky et al., 2003). In modern magmatic settings, chlorine assimilation occurs up to depths of 800 m below seafloor (Gillis et al., 2003). Gillis et al. (2003) observed that N-MORB glasses from the East Pacific Ridge (EPR) are enriched in Cl relative to expected values for the fractionation products of mantle-derived melts; feature that has been interpreted to be related to interaction with seawater-derived components. For the authors, assimilation was proposed to be the most likely explanation, at least for Cl, due to the large difference between enrichment seen at the fast-spreading EPR and slow-spreading Mid Atlantic Ridge. Magmatic amphiboles from the upper gabbros at Hess Deep display similar chlorine enrichments as EPR glasses, thereby confirming that assimilation must be prevalent along the roof and margins of axial magma chambers.

The F and Cl contents of the Precambrian and Phanerozoic amphiboles were compared (Fig. 120) to concentrations in amphiboles from gabbroic and ultra-mafic rocks of MORB and arc setting (Coogan et al., 2001; Gillis and Meyer, 2001; Benard et al., 2017). The Canadians tholeiites of Ghost Range are enriched in both F and Cl whereas the tholeiite at Theo's Flow display amphiboles that are strongly F-enriched (up to 10321 ppm) and relatively depleted in Cl (2435 ppm). These high concentrations in halogens may reflect the strongly evolved nature (90-95 %) of the melt crystallizing amphibole which concentrates Cl and F due to their strongly incompatible behaviour with regard to the high-temperature mineral phases (Gillis and Mayer, 2001; Benard et al., 2017). Amphiboles in the Fe-picrite of Boston Creek have Cl and F contents comparable with those of replacive amphiboles described by Coogan et al. (2001) for gabbroic rocks in MORB. However, the halogen concentrations are also comparable with those of Phanerozoic amphiboles of arc settings with a clear input of subducted material. The Australian Archean amphiboles, both from Mt. Clifford and Mt. Keith, have high Cl concentrations (up to 4421 ppm) and relatively low F contents (about 340 ppm). Data of Russian Proterozoic ferropicrites of Pilgüjarvi and Kammikivi sills confirm their F-enriched nature and the relatively low Cl values, whereas the amphiboles from Nyasyukka dike complex show relatively high concentrations in Cl (up to 1566 ppm) and F (1646 ppm). The generally higher concentrations in Cl and F relative to amphiboles from MORB and arc settings can be related to melt differentiation that has been shown to be consistent in the previous section.

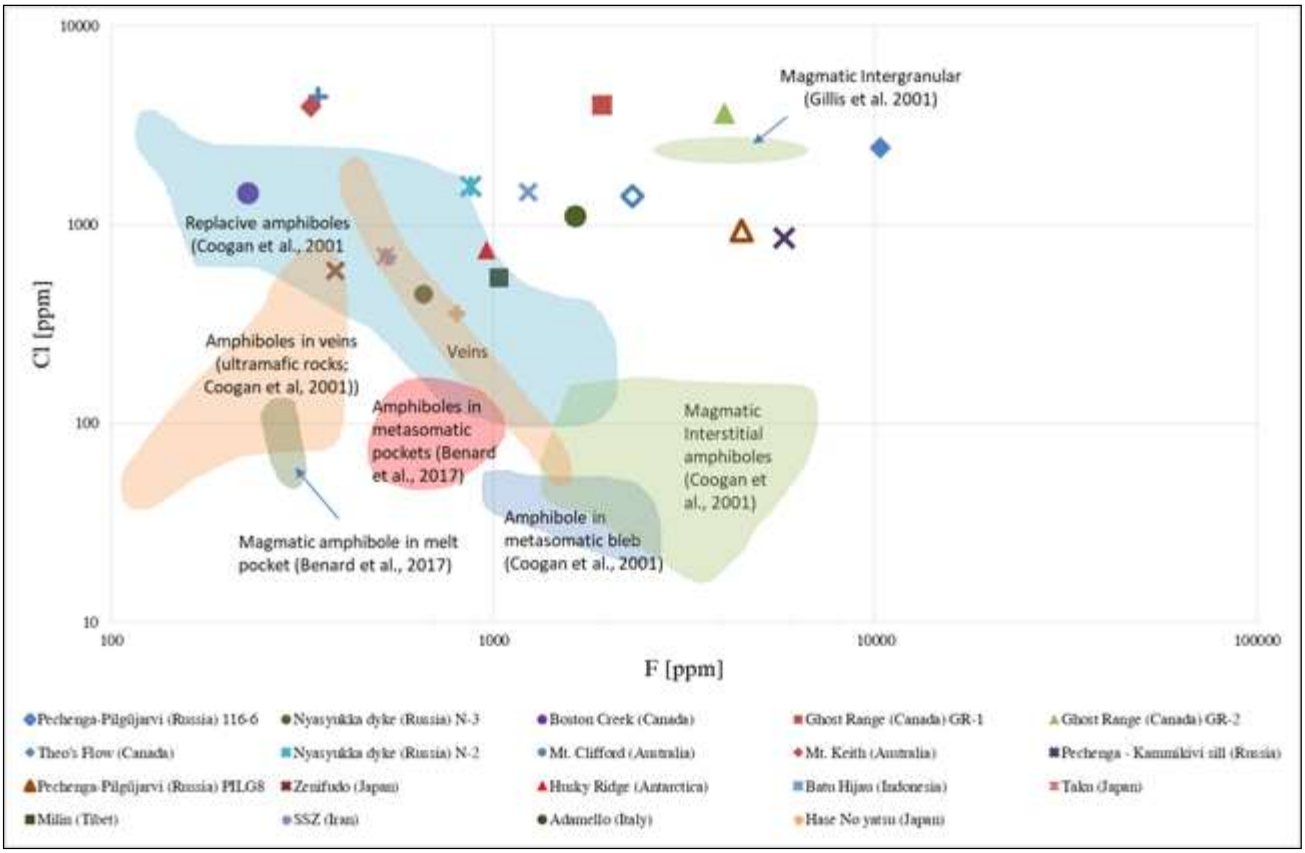

Figure 120 - Fluorine and chlorine contents of the Precambrian and Phanerozoic amphiboles were compared to concentrations in amphiboles from gabbroic and ultra-mafic rocks of MORB and arc setting from literature.

More accurate information can be obtained from ratios of elements with similar compatibility. Nb-La and Cl-F couples have almost the same incompatibility during the crystallisation of ol-opx-cpx-spl. Ratios between these elements are thus not expected to be significantly fractionated. In Fig. 121 the ratio Cl/F versus Nb/La of Precambrian and, for comparison, Phanerozoic amphiboles is reported. The field labelled “amphiboles with complex origin”, that fall between the end-members, may form either from the interaction of exsolved magmatic fluids with igneous plagioclase and clinopyroxene or from seawater-derived fluids interacting with magmatic amphibole (Coogan et al., 2001).

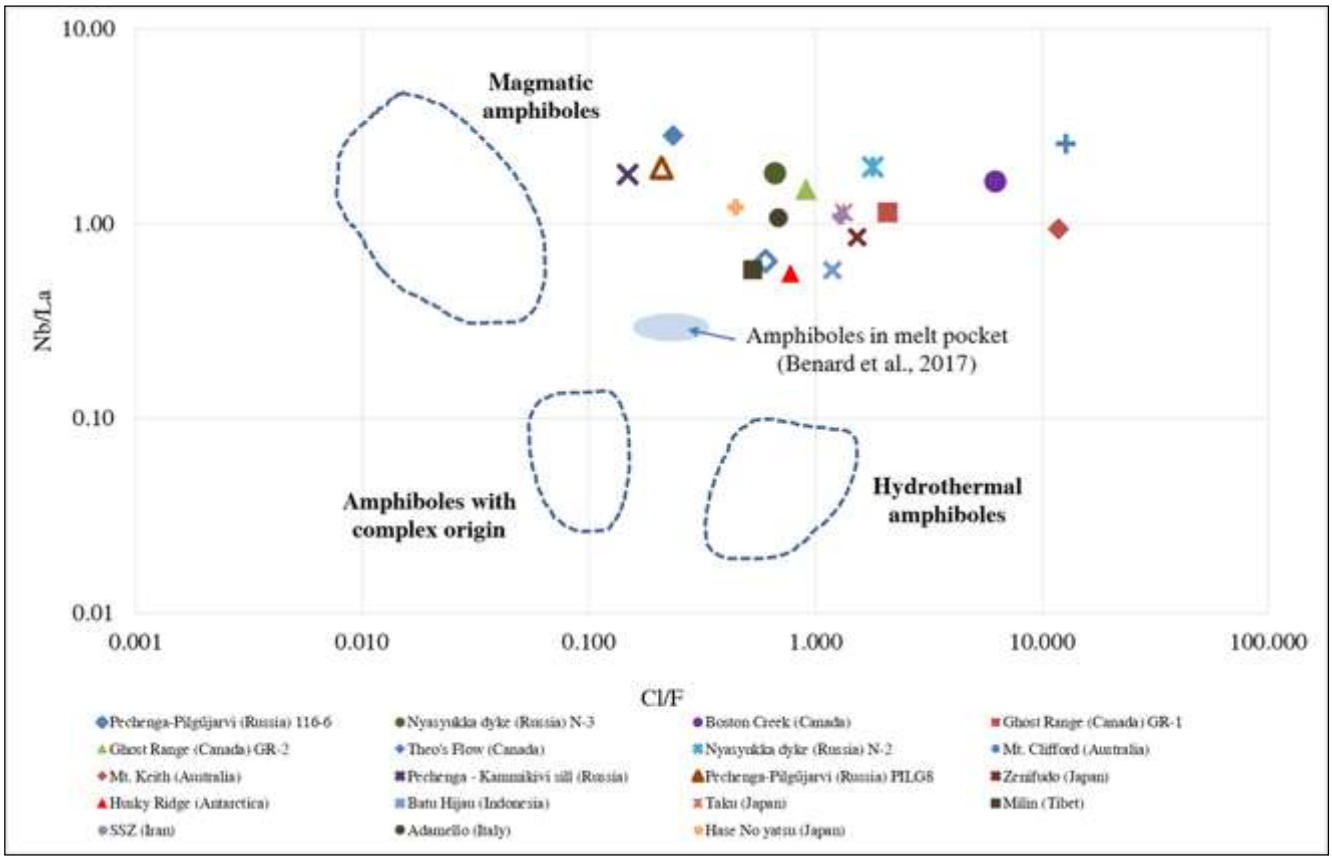

Figure 121 - The ratio Cl/F versus Nb/La of Precambrian and Phanerozoic amphiboles is reported. The amphibole compositional fields are those from Coogan et al. (2001) for magmatic and hydrothermal amphiboles in a suite of gabbros from the Mid-Atlantic Ridge.

The Precambrian and Phanerozoic amphiboles do not fall in any of the reported fields. They have Nb/La ratios similar to the field of magmatic amphiboles whereas the Cl/F ratios are higher and comparable with those of hydrothermal amphiboles. Benard and co-authors (2017) suggest that F is compatible in amphibole at temperatures typical of the shallow mantle lithosphere and the slab-mantle interface. This result is in good agreement with the experimentally determined $0.7 < {}^{amph/melt}D_F < 1.85$ (Edgar and Pizzolato, 1995; Hauri et al., 2006; Van den Bleeken and Koga, 2015). These experiments cover a broad range of P–T conditions (0.5–2.5 GPa and 750–1200 °C) and mineral compositions, suggesting that the compatible behaviour of F is preserved over a wide range of conditions (Edgar and Pizzolato, 1995; Hauri et al., 2006; Van den Bleeken and Koga, 2015). Amphibole crystallisation is expected to deplete the residual melt in F respect to Cl. Benard et al. (2017) reported that amphibole crystallisation may deplete residual melt in F by a factor of about 100 relative to Cl. The shift toward high F/Cl ratio, at constant Nb/La ratios, can be likely related to the F depletion induced in the melt by fractional crystallisation of amphibole. However, we cannot exclude that the high Cl/F ratios is a primary feature of the mantle sources. The boron contents in amphibole are another useful tracer for mineral-

seawater interaction. Boron is a quintessentially crustal element with high concentrations in rocks of continental affinity and in rocks that interacted with the hydrosphere. Oceanic sediments and altered oceanic basalts and peridotites show very high B abundances (10–200 ppm), whereas the depleted mantle is characterised by very low B contents (<0.1 ppm; Leeman and Sisson, 1996; Marshall et al., 2017). Enrichment of B may be attributed to interaction with hydrothermally altered material (Perfit et al., 1999). Where this contamination occurs is uncertain: it could result from fluid–melt interaction as magma is transported to the seafloor, interaction at seafloor during emplacement (Bourdon et al., 2000), or assimilation of hydrothermally altered roof rock and/or seawater-derived fluid into a magma chamber (Gillis et al., 2003; Fiorentini et al., 2008). In Fig. 122 Sr versus B concentrations are reported for Precambrian and Phanerozoic amphiboles. Compositions of amphiboles from oceanic gabbros are also reported as well as the data of seawater and vent fluids (Coogan et al., 2001). The Precambrian amphiboles are Sr-enriched and, generally, B-depleted. The data from literature for amphibole from gabbroic oceanic crust does not show any correlation in composition with Precambrian amphiboles, except for amphiboles from Canadian tholeiite of Ghost Range and Australian komatiites. At Ghost Range, the amphiboles have B contents comparable with those of replacive- and veins-amphiboles in gabbros altered by seawater interaction. Furthermore, the Australian amphiboles have B and Sr contents comparable with amphiboles in reaction blebs with vent fluids of modern gabbroic rocks. In summary, although amphiboles crystallised from differentiated melt, the B contents are generally low, thus suggesting that a contribution from seawater-derived fluid is unlikely.

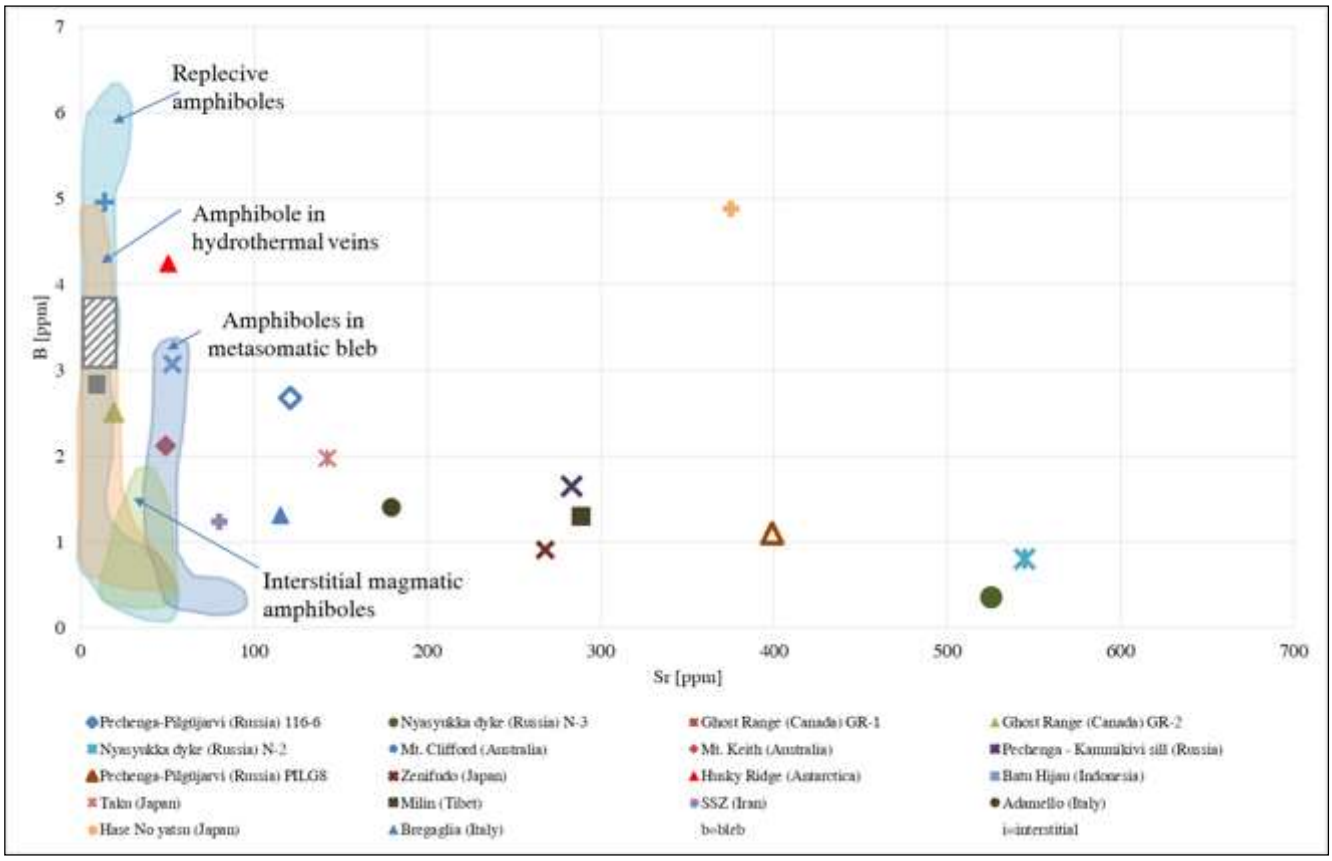

Figure 122 – Sr versus B contents in amphiboles. The fields are those from Coogan et al. (2001). The stripped grey field and the grey square are the reported composition for vent fluids and seawater, respectively (Coogan et al., 2001).

4.6.3 Constraints from $\delta^{18}O$ and δD

In order to better evaluate the origin of amphibole and the role of hydrothermal fluids, additional information can be gathered from the hydrogen isotopic data and water contents (Fig. 123). H_2O concentrations are comparable between the Precambrian and Phanerozoic amphiboles, with evidences of the incomplete occupancy of the $^{O3}O^{2-}$ structural crystalline site of the amphibole. This is another evidence against a metamorphic origin. Furthermore, the range of δD values observed in Archean and Paleoproterozoic amphiboles is consistent with a magmatic origin for water. In particular, the δD vs. H_2O diagram highlights the low hydrogen isotope values for both the Archean and Paleoproterozoic amphiboles (blue field) that are mostly close to the mantle δD range. This δD signature is thus in contrast with an origin of amphibole by hydration of the cumulate minerals by seawater or crustal derived fluids. Hydrogen isotopes, which are diagnostic and reliable indicators of external water source inputs, are generally pushed towards lighter values upon alteration processes (Kyser et al. 1986; Fiorentini et al., 2012). Only the amphiboles from the Canadian tholeiite of Ghost Range show anomalous and extremely low hydrogen isotope values (-197.6 ± 16 ‰ and -236.3 ± 23.6 ‰). Exceptionally low δD values were previously reported for mantle xenoliths (Deloule et al.,1991) and melt inclusions from Koolau volcano

in the Hawaiian Islands (Hauri, 2002) and from Mariana arc system (Shaw et al., 2008). In all these cases the source of low δD values was ascribed to a significant recycled slab component (Eiler et al., 1996; Hauri, 1996; Lassiter and Hauri, 1998). Based on studies of submarine glasses (Kyser and O'Neil, 1984), melt inclusions from Hawaii (Hauri, 2002), as well as experimental hydrogen isotope fractionation studies (Pineau et al., 1998), degassing of H_2O from silicate melts leads to low δD values and to a positive correlation with H_2O contents when magma H_2O contents are <2 wt.% (Shaw et al., 2008). In particular, subduction-related dehydration results in a slab with low δD values and a mantle wedge with high δD values. The consequence is that a slab with low δD values can be subducted into the deeper mantle. If slab dehydration is particularly efficient, as inferred for example from low H_2O/Ce ratios of plumes containing recycled lithosphere (Dixon et al., 2002), the residual water in the subducting slab would become extremely D-depleted (up to δD = -243 ‰ for 92 % water loss from a slab at δD = -50 ‰). The model proposed by Shaw et al. (2008) predicts that modern OIBs with recycled slab components should have low δD values, while OIBs containing recycled mantle wedge material should exhibit high δD values.

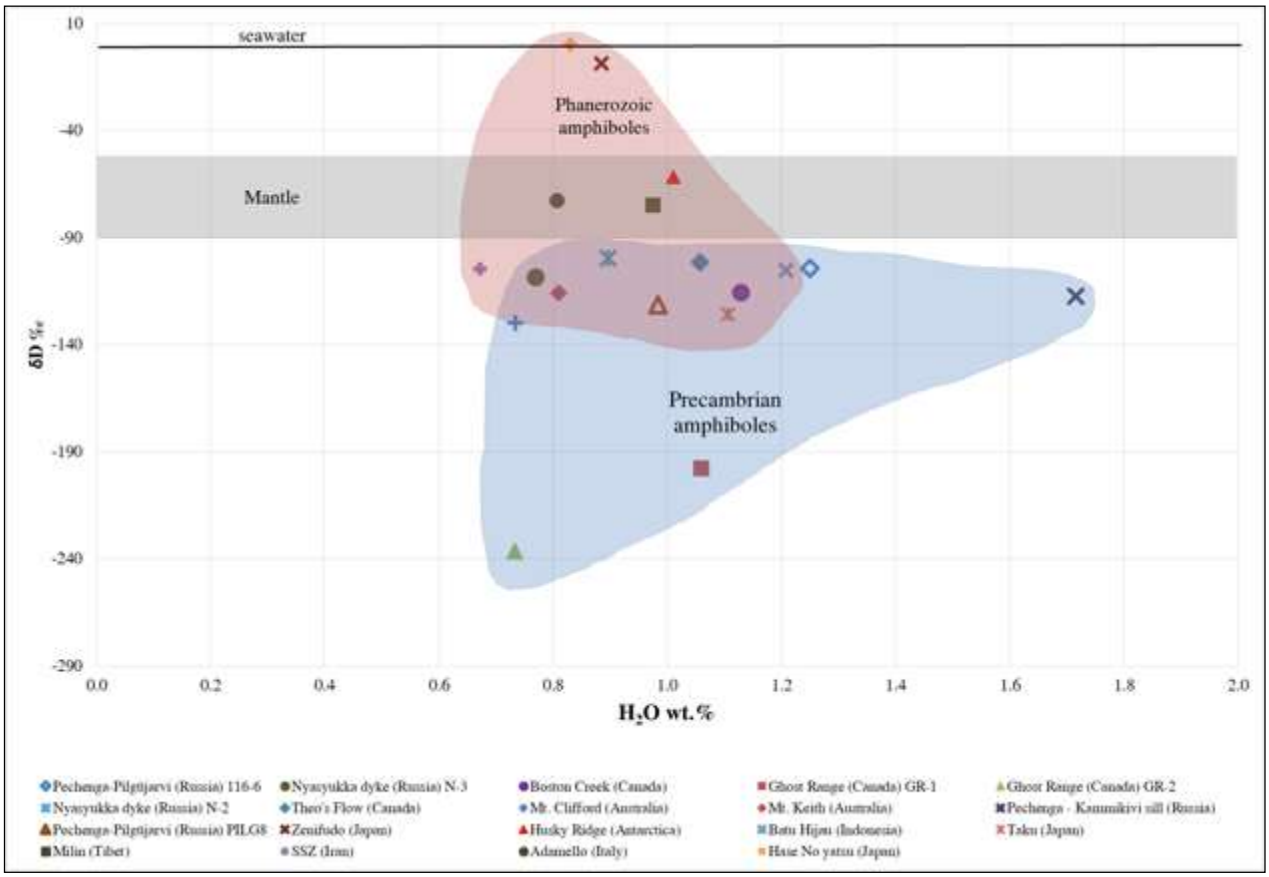

Figure 123 – The hydrogen isotopic data and water contents of Precambrian and Phanerozoic amphiboles. The mantle field and seawater δD values are from Deloule et al. (1991) and Shaw et al. (2008), respectively.

The range of δD values of the Precambrian amphiboles is between -99.5 ‰ and -129.8 ‰, that is slightly low compared to the mantle range. Fiorentini et al. (2008, 2012) proposed that the relatively heavy isotopic composition of hydromagmatic amphiboles from the cumulate portions of the komatiitic dunites of the Agnew-Wiluna greenstone belt is comparable to that of magmatic amphiboles from ferropicritic intrusions in the Pechenga Complex (Hanski and Smolkin, 1989) and komatiitic sills from the Munro Lake Sill in the Abitibi greenstone belt (MacRae 1969; Stone et al. 2003). The authors argued that the amphiboles formed upon crystallization of a hydrous ultramafic magma under sufficient confining pressures, so that volatiles were not completely exsolved. However, the minor dispersion of δD values (within the heavy isotopic magmatic range; Kyser and O'Neil 1984) in the amphiboles from the Mt. Keith suggests that these phases formed during incipient degassing of the melt, which crystallized in a subvolcanic environment (Rosengren et al. 2005; Fiorentini et al. 2007a, 2012). On the basis of experimental work by Deloule et al. (1991), it is possible to ascribe the minor δD dispersion to either H_2O loss, which decreases D/H ratios and water contents, or H_2 loss, which increases D/H ratios while slightly decreasing the water content. Both H_2O loss and/or H_2 loss occur during degassing. For Fiorentini et al. (2012), the nature of isotopic variation that is documented in the primary hydromagmatic amphibole grains from the Agnew-Wiluna greenstone belt intrusions is not associated with alteration, which would push δD toward much lighter values (Kyser et al. 1986).

For H_2O, the H isotope fractionation between water and magma is positive (δD gas/melt > 0), such that the escaping gas would be enriched in D and the residual magma progressively depleted in D during degassing (Stone et al., 2005; Fiorentini et al., 2008). In the dehydration process, the δD values of the residual melt shift from an initial mantle value to more negative values. However, for reduced species (e.g. H_2, H_2S, HCl, etc.), the H isotope fractionation between gas and magma is negative (δD gas/melt < 0), such that escaped H gas would be isotopically lighter (i.e. with a lower δD value) and residual H_2O isotopically heavier (i.e. with a higher δD).

The hypothesis of a crustal contribution in the origin of the amphiboles and its parental liquid was addressed also by means of the analysis of oxygen isotopes in amphiboles. The variability in oxygen isotope compositions observed in unaltered mantle-derived rocks (OIB, MORB and peridotite xenoliths) is fairly low and suggests that modern upper mantle has an average oxygen isotope composition $\delta^{18}O$ of 5.5 ± 0.5‰ (Byerly et al., 2017). The oxygen isotope composition of igneous amphiboles from primitive island arc lavas and from mantle peridotites is in the range $\delta^{18}O$ = +4.9 ‰ to +5.8 ‰ (Demeny et al, 2004, 2010; Vroon et al., 2001; Chazot et al., 1997) suggesting minor fractionation during crystallisation from mantle derived melts. Large-scale fractionation of oxygen isotopes is confined to processes that

occur at or near the Earth's surface; thus, changes from the average $\delta^{18}O$ of mantle-derived rocks, either positively or negatively, are typically ascribed to the presence of recycled crustal material in the mantle source or interaction of mantle-derived melts with crustal material upon ascent (Byerly et al., 2017). In Fig. 124 the oxygen isotopic range for crustal material ($\delta^{18}O$ = from 6 to 42 ‰) and seawater ($\delta^{18}O$ = 0) are reported. It is also worth noting that pore-waters in the oceanic crust are initially low in $\delta^{18}O$ (close to 0 ‰ near the sediment-water interface to -3 ‰ at depths of several hundred meters; Eiler, 2001, and references therein). Oxygen isotopic compositions of nominally anhydrous minerals (olivine and pyroxene) do not show systematic difference in hydrous and anhydrous lherzolites (Chazot et al., 1997). The same study showed that the oxygen isotopic composition of amphibole ($\delta^{18}O$ = 5.3-5.6 ‰) is in equilibrium with the peridotitic minerals, thus suggesting that in the fluid and the mantle had the same oxygen isotopic composition.

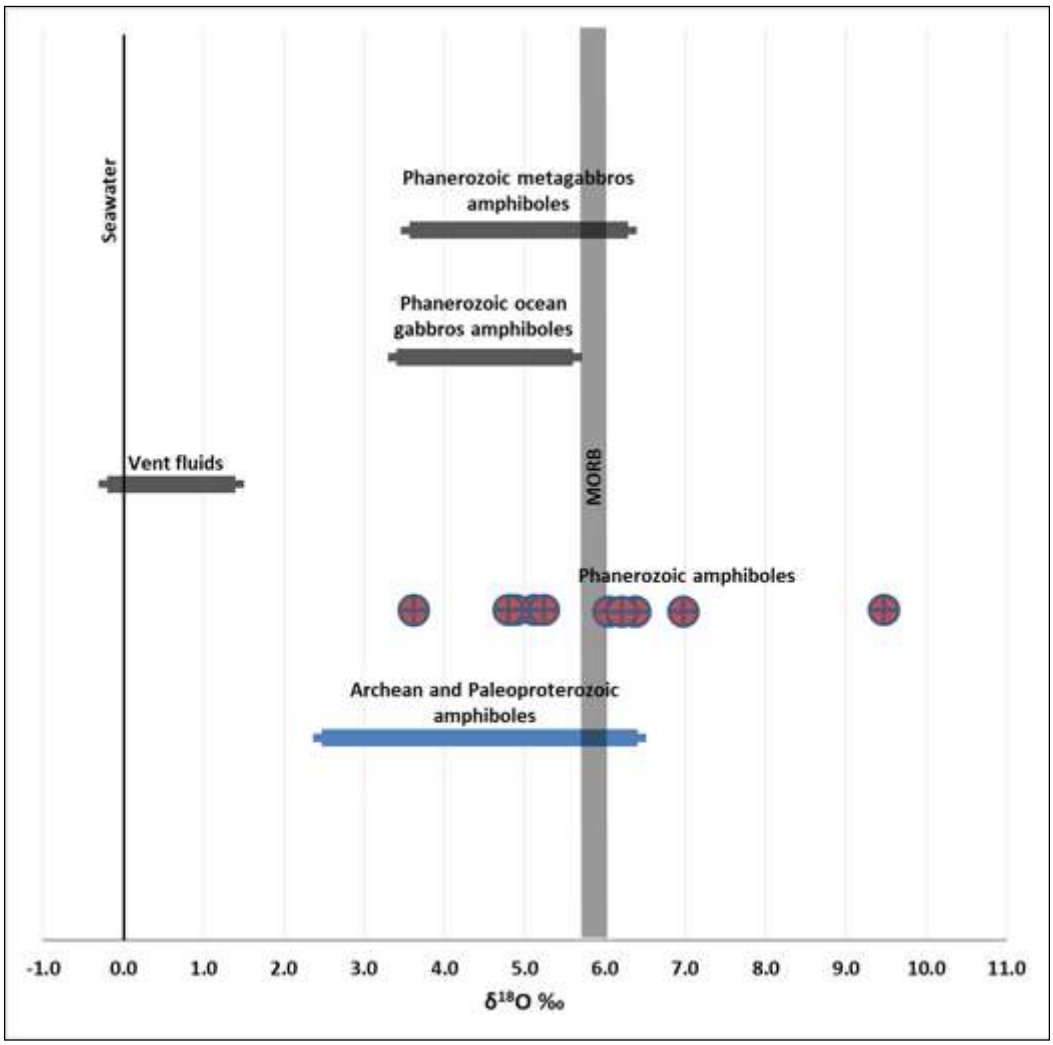

Figure 124 - Oxygen isotopes values for the Precambrian and Phanerozoic amphiboles. The data of Phanerozoic gabbros and metagabbros are from Gillis et al. (2001) and references therein. Seawater and MORB $\delta^{18}O$ range are from Eiler (2001) and references therein.

The $\delta^{18}O$ values of the studied Precambrian amphiboles (see Chapter 3 for details) cover a wide range from 2.5 to 6.4 ‰. The higher value (6.4 ± 0.99 ‰) pertain to the olivine-magnetite peridotite from the Pilgüjarvi sill of the Pechenga Complex whereas the Canadian and Russian amphiboles have mean values of 3.9 ± 0.3 ‰ and 4.2 ± 0.9 ‰, respectively. The oxygen isotopic compositions of Australian amphiboles are 2.5 ± 0.42 ‰ and 5.0 ± 0.30‰ for Mt. Keith and Mt. Clifford, respectively. With the exception of the olivine-magnetite peridotite from the Pechenga Complex, the light oxygen isotopic signatures for Precambrian amphiboles exclude a crustal input which would shift the $\delta^{18}O$ towards higher values. A small crustal contribution could be supposed for the amphibole of the olivine-magnetite peridotite in the Pechenga Complex. Low $\delta^{18}O$ values might be ascribed to the interaction of the amphiboles parental melts with seawater ($\delta^{18}O = 0$). Many studies have shown that submarine weathering and low temperature ($T < 225$ °C) hydrothermal alteration of the upper oceanic crust lead to an enrichment in $\delta^{18}O$ in the bulk rock. On the contrary, higher temperature ($T > 300$ °C) seawater-rock interactions produce depletions in ^{18}O in the lower crust and upper mantle sequences (e.g. Gregory and Taylor, 1981; Alt et al., 1986; Früh-Green et al., 2001). Fluid-mobile elements and hydrogen isotopes have already suggested that seawater apparently was not involved in the petrogenesis of the studied amphiboles. Notwithstanding, oxygen isotopes were correlated with the Cl and B seawater proxies as well as the Cl/F ratio. As show in the Fig. 125 A and B, the $\delta^{18}O$ isotopic signatures of amphiboles do not show any correlation with the seawater-enriched elements mentioned above. These evidences have two implications: i) they further confirm that seawater was not involved in petrogenesis of the studied amphiboles; ii) the low $\delta^{18}O$ signature of most of the Archean and Paleoproterozoic amphiboles is likely a primary feature of the mantle source.

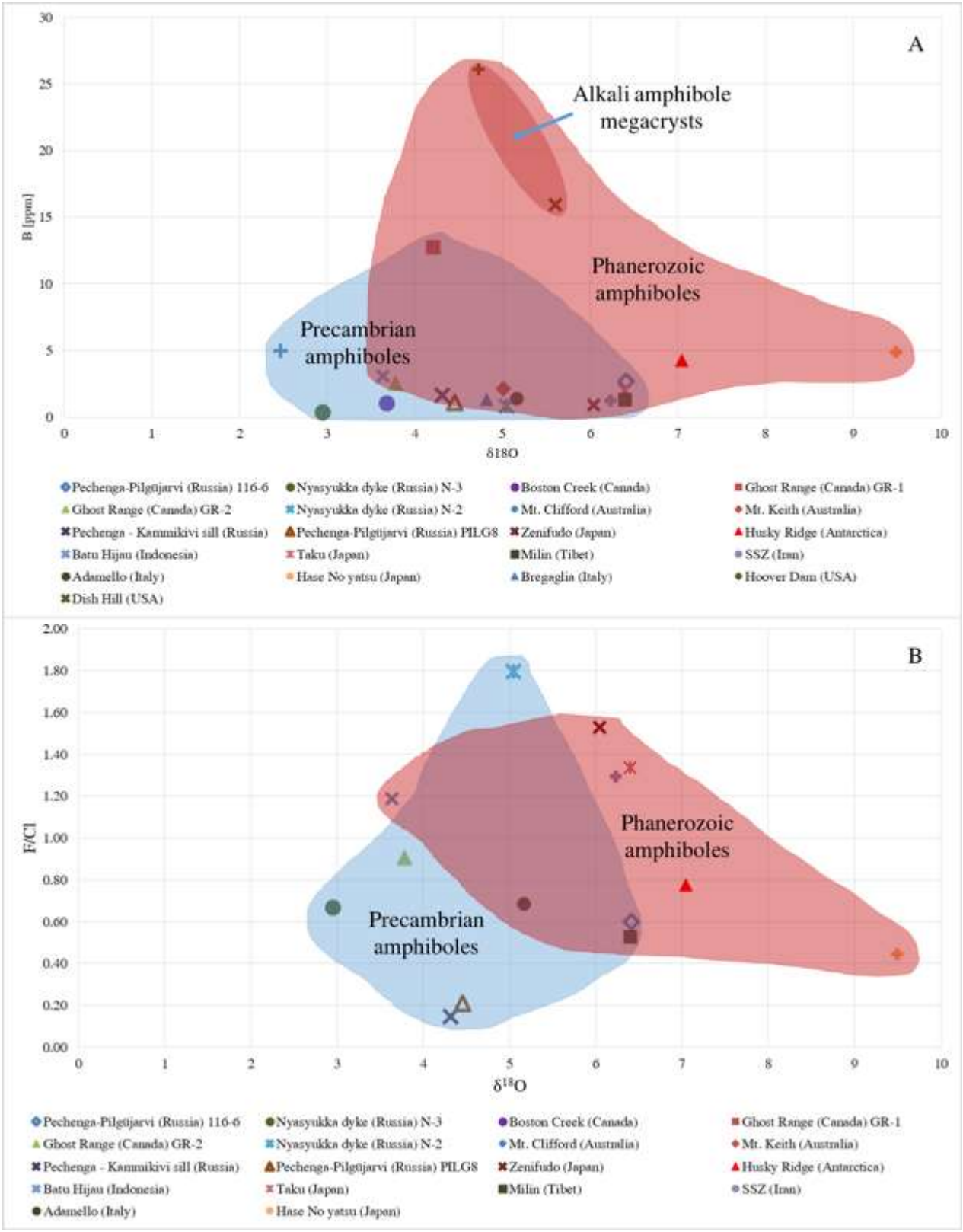

Figure 125 A, B - Oxygen isotopic ratios are compared to (A) B contents and (B) F/Cl ratios for Archean, Early Proterozoic (Precambrian) and Phanerozoic amphiboles.

4.7 Water contents of primary melts

The water contents in primary melts of the Archean and Paleoproterozoic samples can be estimated by applying amphibole/melt exchange coefficient for water. A mean value of $^{amph/L}X_{H2O} = 0.3$ has been assumed according to the experimental work of Tiepolo et al. (1999) and considering that this value is in agreement with the few data reported in the literature (e.g. Hauri et al., 2006). As previously mentioned, amphiboles are residual after a significant crystallisation of clinopyroxene and olivine. Thus, the primary melt had likely a different composition than the melt in equilibrium with amphibole. In order to estimate the composition in H_2O of the parental liquid, the contribution of olivine and clinopyroxene has to be subtracted because their crystallisation leads to a concentration of the volatiles into the residual liquids. Olivine and clinopyroxene contribution have been subtracted according to their modal proportions in the rock (see Tab. 2.2 of Chapter 2).

In Fig. 126 the water contents calculated for the melts in equilibrium with amphiboles are reported. In Precambrian amphibole-forming melts the water contents are almost comparable to those of Phanerozoic age. The Precambrian melts have H_2O contents in the range 2.44 - 4.17 wt. % that is consistent with the geobarometric results regarding conditions for amphibole crystallisation.

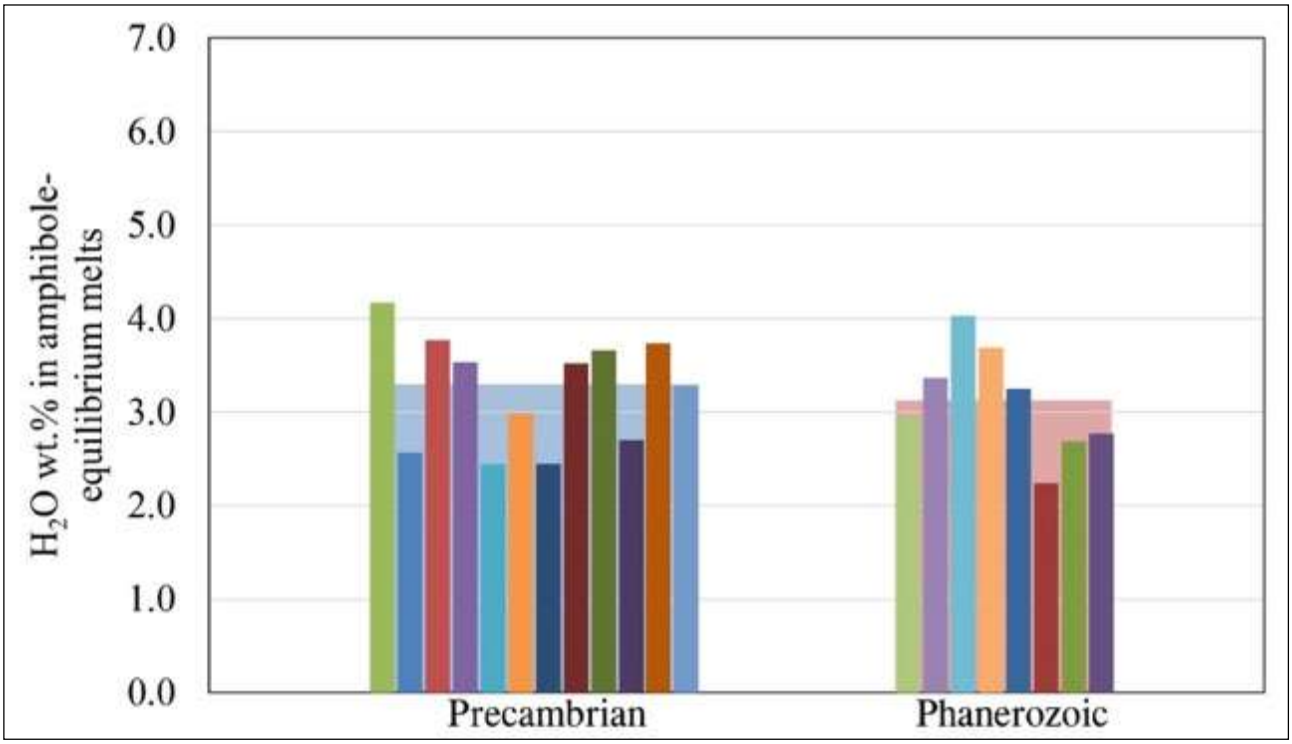

Figure 126 – Calculated water contents in amphibole-equilibrium melts. The blue and the pink fields enveloping the histogram bars are the average water contents for the Precambrian and Phanerozoic amphibole-equilibrium melts, respectively.

In Fig. 127 the calculated water contents in primary melts of Precambrian and Phanerozoic samples are reported together with the experimental data of water contents determined in melt inclusions hosted in olivines in the komatiites of the Belingwe Greenstone Belt (Zimbabwe; Asafov et al., 2018) and of the Abitibi Greenstone Belt (Sobolev et al., 2016). The water contents of primary melts in Canadian samples considered in this study are in the range between 0.11 and 0.38 wt.%. The Australian primary melts have water contents of 0.37 wt.% and 0.41 wt.% at Mt. Clifford and Mt. Keith, respectively. In the Pechenga Complex, the water contents calculated for primary melts are in the range 0.13-0.37 wt.% for the Pilgüjarvi sill and 0.29 wt.% for the Kammikivi sill. The variability of the Pilgüjarvi sill primary melts is related to the low H_2O concentration (0.13 wt.%) obtained for the magnetite-olivine peridotite while the other two samples have water contents in primary melts of 0.33 wt.% and 0.37 wt.%. The calculated parental melts of the Nyasyukka dike complex have H_2O values between 0.90 wt.% and 1.03 wt.%. If calculated values are compared with data from literature, the tholeiites of Abitibi Greenstone Belt, Theo's Flow and Ghost Range, have H_2O concentrations comparable to those in komatiites of Belingwe Greenstone Belt (0.2 wt.%) but lower than those proposed by Sobolev et al. (2016) for the komatiites of the Abitibi Greenstone Belt (0.6 wt.% estimated from of melt inclusion in olivine). Australian komatiites of Mt. Keith and Mt. Clifford as well as the Fe-picrites of Boston Creek (Abitibi Greenstone Belt) and in those of the Pilgüjarvi and Kammikivi sill have H_2O contents in the range reported by the literature (0.2-0.6 wt.%; Asafov et al., 2018; Sobolev et al., 2016).

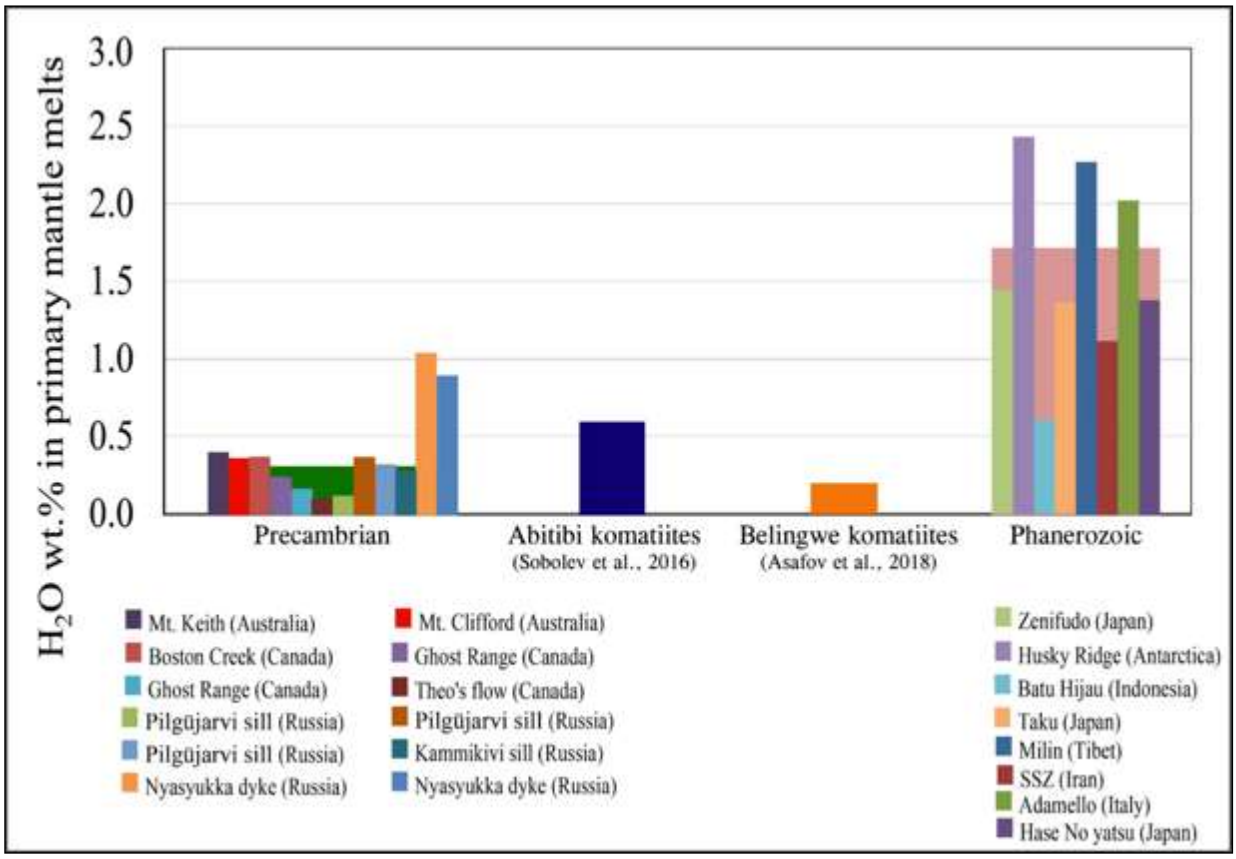

Figure 127 – Comparison between the calculated water contents for primary melts of Precambrian and Phanerozoic age. The water values for the Abitibi and Belingwe komatiites are from Sobolev et al. (2016) and Asafov et al. (2018), respectively.

4.8 Chlorine and Fluorine contents of primary melts

The F and Cl contents in primary melts of the Archean and Paleoproterozoic samples were estimated by applying amphibole/melt exchange coefficients for F and Cl. A mean value of $^{amph/L}D_F$ = 1.84 and $^{amph/L}D_{Cl}$ = 0.21 have been assumed according to the experimental work by Tiepolo and coworkers (unpublished) and considering that this value is in agreement with the few data reported in the literature (Dalou et al., 2014; Hauri et al., 2006; Van den Bleeken and Koga, 2015). As previously mentioned for the water content calculation, amphibole is residual after crystallization of clinopyroxene and olivine. In order to have the F and Cl parental liquid composition the contribution of olivine and clinopyroxene was subtracted according to their modal proportions in the rock.

In Fig. 128 A, B the calculated F (A) and Cl (B) contents in primary melts of Precambrian and Phanerozoic samples are reported. The F and Cl contents of primary melts in Canadian samples are extremely heterogeneous in the range 12.4-168.3 ppm and 347.9-1340.4, respectively. The lower end in the range of F contents was obtained for the Boston Creek Fe-picrite parental melt. The primary melts

of the Australian komatiites have Cl and F contents of 3858 and 28.32 ppm, respectively, at Mt. Clifford and, 2804 ppm and 27.15, respectively, at Mt. Keith. In the Pechenga Complex, the calculated primary liquids of Pilgüjarvi and Kammikivi sill show a twofold variation of F (157.3-242.5 ppm) and Cl contents (204.3-446.3 ppm). The parental liquid of the magnetite-olivine peridotite of the Pilgüjarvi sill has low F (37.7 ppm) and Cl contents (198.8 ppm). The calculated parental melts of the Nyasyukka dike complex show Cl enrichment (1829-2610 ppm) whereas fluorine values are in the range (165.9-313.1 ppm), thus in the range of the other rocks of the Pechenga Complex.

The Australian komatiites show similar fluorine contents but extremely different Cl values if compared to those of parental melts of the Belingwe komatiites (Asafov et al., 2018). The Canadian tholeiites are generally F- and Cl-enriched compared to the Belingwe komatiites. Exception is made for the Cl contents of the Theo's Flow tholeiite that are almost similar to those of African komatiites. The Fe-picrites of Boston Creek (Abitibi Greenstone Belt) and those of the Pechenga Complex display higher F concentrations and relatively high Cl contents compared to those of the Belingwe komatiites but almost comparable concentrations with those of Phanerozoic arc-related amphiboles. Nevertheless, the primary melts of the Pilgüjarvi and Kammikivi sills have Cl values similar to those of the Belingwe komatiites. The parental liquid of the Nyasyukka dike complex is also comparable for Cl and F concentrations with that of Phanerozoic arc-related amphiboles.

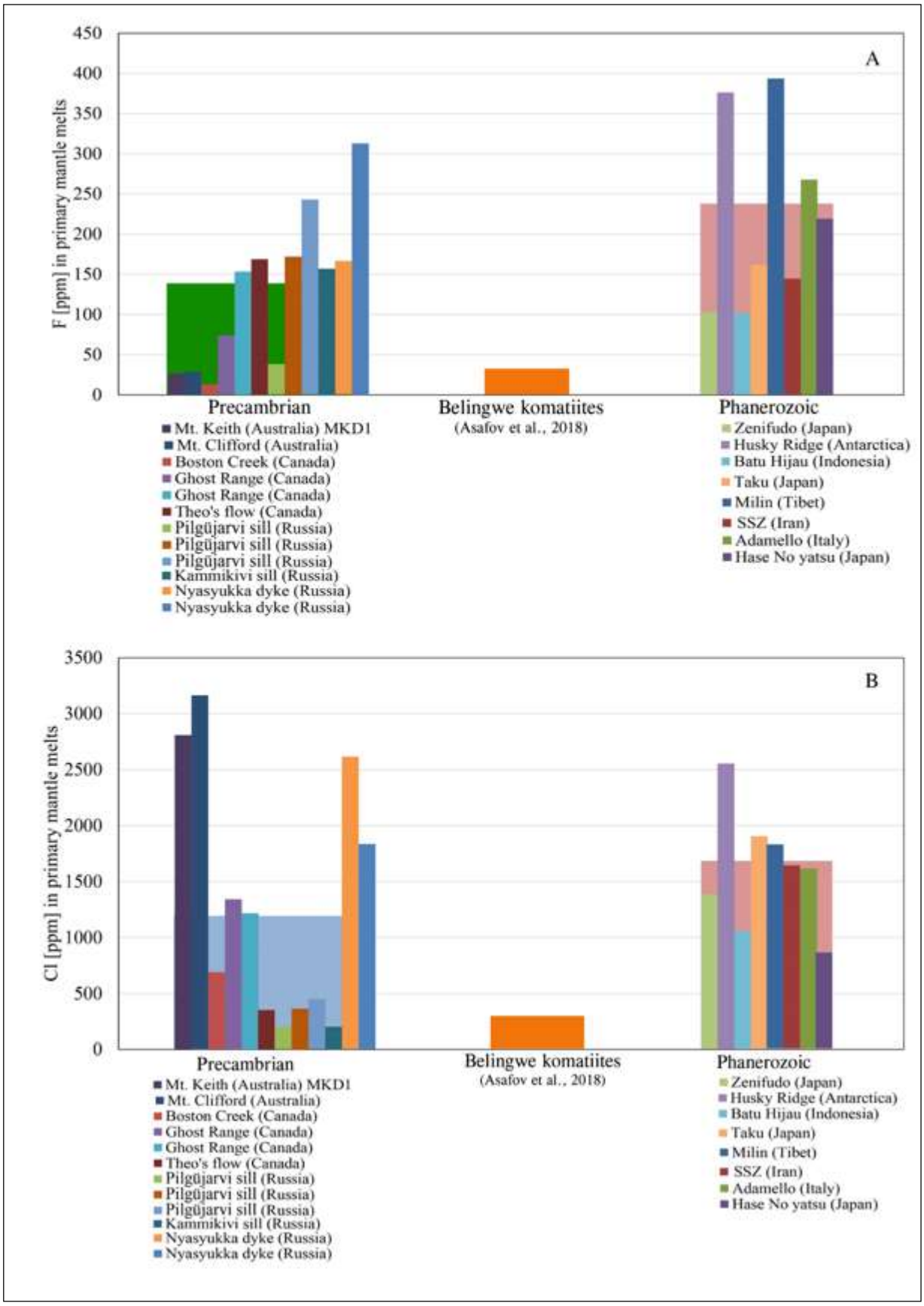

Figure 128 A, B – (A) F and (B) Cl contents calculated for primary melts. The data for F and Cl compositions of parental melt of Belingwe komatiites are those from literature (Asafov et al., 2018).

4.9 Implications on the secular evolution of the Earth's mantle

The calculated compositions of melts generated by mantle melting during Archean and Proterozoic times represent a unique chance to investigate differences with Phanerozoic mantle-derived melts and thus to identify possible secular variations in the mantle composition and melting processes. A direct comparison of absolute values between calculated melts and modern analogues can give only limited information because biased by the evolved and not primary nature of the melts in equilibrium with Precambrian amphiboles. More robust information from absolute values can be gathered only from the components or elements behaving as highly incompatible towards the early crystallising minerals, such as water or the other volatiles (F-Cl) and for which a back calculation of the primary melt composition is possible by subtracting the contribution of olivine and clinopyroxene. In all the other cases the most robust information on possible secular variations may be achieved from ratios between elements with a similar compatibility that are, consequently, not fractionated during the differentiation process.

4.9.1 Inferences from incompatible trace element composition

Although the melt in equilibrium with amphibole is not a primary melt, its incompatible trace element composition can give some information on the geochemical affinity of the parental liquid and, in turn, on the geodynamic setting and on the mantle sectors activated during Archean and Proterozoic. Olivine and clinopyroxene, which are early crystallising minerals relative to amphibole, are not expected to impart to the residual melts significant changes in the geochemical signature for the petrologically relevant elements.

The reader would consider that there is no general consensus that komatiites were exclusively produced at plumes (e.g. Arndt et al., 1998, 2008; Sobolev et al., 2016). A subduction origin for komatiites has been also proposed based on the high-SiO_2 komatiites (such as the 3.5-3.2 Ga-old South African komatiites in the Commondale, Nondweni and Barberton greenstone belts; Parman et al., 1997; Wilson and Versfeld, 1994; Wilson et al., 2003). These basaltic komatiites strongly resemble the composition of modern boninites (Cameron et al., 1979; Parman et al., 2001, 2003). Neither theory seems to satisfactorily explain all the observed compositions, suggesting perhaps that komatiites were produced in more than one tectonic setting, as basalts are today (Parman and Grove, 2005). Worth of mention are also studies (e.g., Asahara and Ohtani, 2001; Sobolev et al., 2016) proposing komatiites as the products of melting in hydrous plumes, which is a sort of hybrid hypothesis of the plume and subduction ideas. Such models try to reconcile the two sides of the debate by incorporating the evidence for relatively high magmatic H_2O contents into the plume-melting process. Moreover, large interest of the scientific community, and also not a general consensus, is on the significance of the ferropicrites of

Archean age (e.g. Milidragovic et al., 2016). The widespread emplacement of ca. 2.7 Ga ferropicrites occurred synchronously with the emplacement of ubiquitous komatiites and Mg-tholeiites during the global Neoarchean mantle melting event (Condie, 1998, 2000; Rino et al., 2004; Stein and Hofmann, 1994) that contributed significant volumes of juvenile material to continental crust (Condie et al., 2009; Hawkesworth et al., 2009; Milidragovic and Francis, 2014). The ubiquity of Archean ferropicrites is compatible with a model in which domains of Fe-rich peridotite and pyroxenite existed as ‘‘plums” (Sun, 1985) in a predominantly pyrolitic peridotite mantle (Milidragovic et al., 2016). The compositions of the Fe-rich domains appear to have been as diverse as the present-day upper mantle, yielding magmas that ranged in affinity from modern OIB to MORB. Milidragovic et al. (2016) argued that the Archean alkaline ferropicrites have fractionated trace element profiles, including the absence of HFSE anomalies relative to REE of similar compatibility, which broadly resemble the modern ‘‘alkaline” OIB, and in contrast with archetypal Archean komatiitic, tholeiitic, and calcalkaline magmas. Furthermore, they have relatively high Ni concentrations, which exceed the Ni contents of primary melts equilibrated with normal mantle peridotite (Herzberg, 2011), but are similar to those of the olivine tholeiites from Hawaii (Sobolev et al., 2005). The relative paucity of ferropicrites younger than ca. 2.7 Ga (Lightfoot et al., 1993; Wooden et al., 1993; Hanski and Smolkin, 1995; Gibson et al., 2000; Ichiyama et al., 2006; Heinonen and Luttinen, 2008) may reflect a lower abundance of Fe-rich domains in the post-Archean terrestrial mantle. This observation suggests that most Fe-rich plumes were melted out during the Neoarchean melting event, which accompanied the peak in mantle potential temperatures (Korenaga, 2008; Herzberg et al., 2010; Milidragovic et al., 2016).

The melts in equilibrium with amphiboles were calculated as previously described in the section 4.4. The N-MORB normalized patterns of the incompatible element composition of the melt in equilibrium with amphibole were compared with the present-day composition of primary mantle-derived melts from different geodynamic settings: mid-ocean ridge basalt, MORB; ocean island basalt, OIB; island arc basalt, IAB. For the Abitibi Greenstone Belt, the N-MORB normalized incompatible trace element pattern (Figure 129) of the Theo’s Flow tholeiite and Ghost Range are completely different in terms of both overall values and element fractionation from both N-MORB and IAB. Calculated melts parallel the trace element pattern of modern OIB at generally higher values (approximately 5 times). Significant differences with OIB are the negative anomalies in Ti, Ba and Sr and the positive anomalies in Th. The melt in equilibrium with the Boston Creek amphibole with Fe-picrite affinity does not show anomalies in Ba and Sr and has a N-MORB normalized incompatible element pattern almost paralleling that of modern OIB.

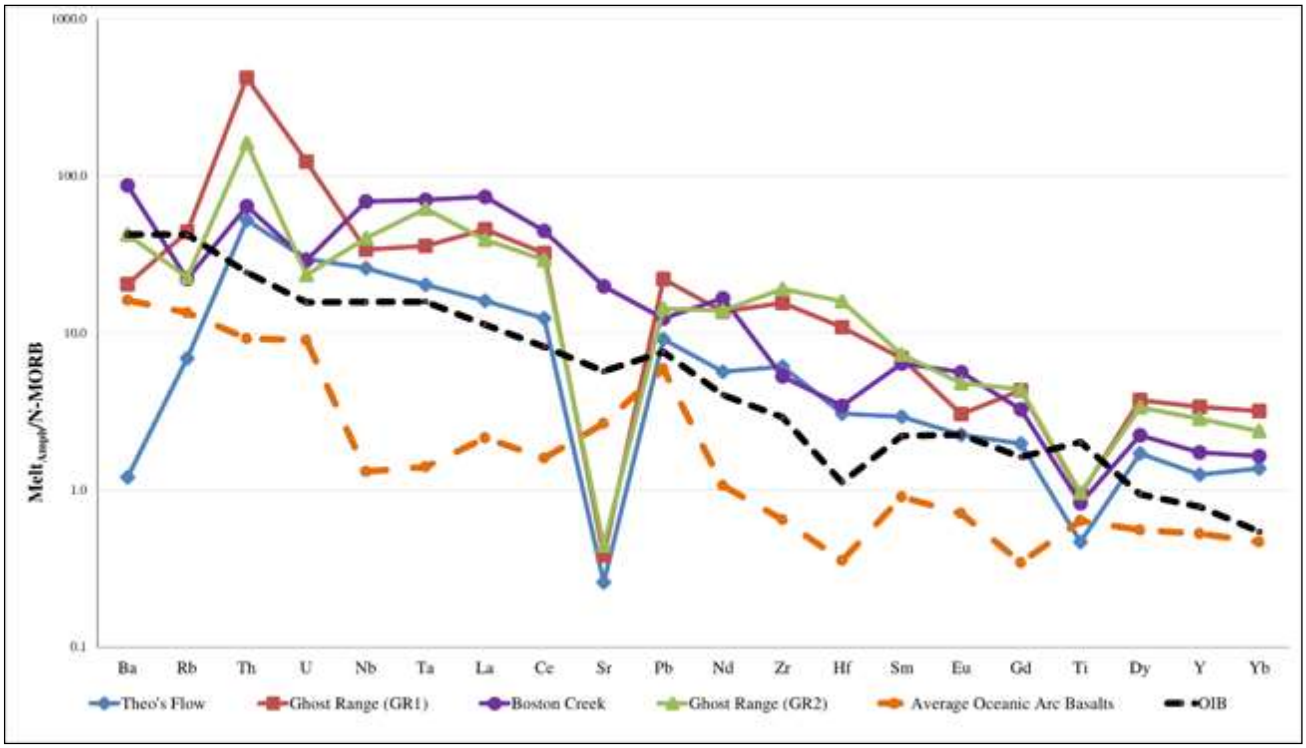

Figure 129 - The N-MORB normalized incompatible trace element patterns for the calculated melts in equilibrium with amphibole, in the samples from Abitibi greenstone belt (Canada). The data of OIB and IAB compositions are from McDonough and Sun (1995) and Kelemen (2003), respectively.

The N-MORB normalized incompatible trace element pattern of the melt in equilibrium with the Australian amphiboles of Mt. Keith and Mt. Clifford (Fig. 130) is different in terms of both overall values and element fractionation from both N-MORB and IAB. It parallels at slightly higher values the pattern of modern OIB and similarly to the melts from the Abitibi greenstone belt it shows positive Th-U and negative Sr and Ti anomalies that are not observed in modern OIBs. A weak Nb-Ta negative anomaly is also observed: this is in agreement with the derivation of this melts from komatiites. As shown in Figure 130, Archean komatiites are characterised by negative Nb-Ta anomalies; thus, this feature appears to be preserved in spite of the residual character of the liquid.

Figure 130 - The N-MORB normalized incompatible trace element patterns for the calculated melts in equilibrium with amphibole, in the samples from Agnew-Wiluna greenstone belt (Australia). The data of OIB and IAB compositions are from McDonough and Sun (1995) and Kelemen (2003), respectively.

In the Pechenga Complex, the N-MORB normalized incompatible trace elements patterns of the melts in equilibrium with amphibole have strong affinity with modern OIB and show significant differences with both N-MORB and IAB (Fig. 131). Overall values of incompatible trace elements are higher than modern OIB but parallel the general trend. Exceptions are for Sr, Ti and, to a lesser extent, U, which show negative anomalies. A completely different behaviour is observed for the melt in equilibrium with amphibole in the olivine-magnetite peridotite of the Pilgüjarvi sill. Here the N-MORB normalized incompatible trace element patterns reveal a marked negative Nb and Ta anomaly similar to that observed in IAB but at significantly higher values for Nb and Ta. This signature is not representative of the primary melt; instead, it is likely related to the abundant crystallisation of Ti-bearing oxides for which Nb and Ta have a high compatibility (e.g. Xiong et al., 2011).

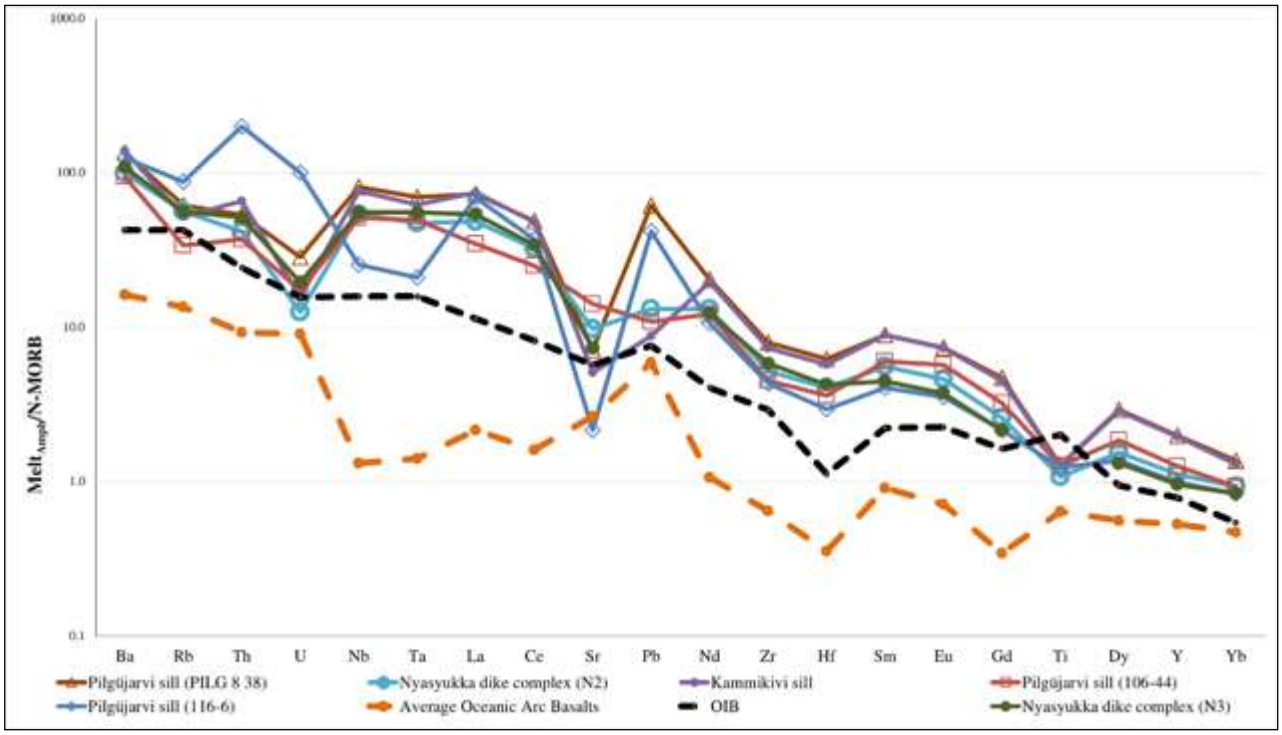

Figure 131 - The N-MORB normalized incompatible trace element patterns for the calculated melts in equilibrium with amphibole, in the samples from Pechenga Complex (Russia). The data of OIB and IAB compositions are from McDonough and Sun (1995) and Kelemen (2003), respectively.

In general, all the melts in equilibrium with amphibole from Archean and Proterozoic rocks do not resemble present-day MORB or IAB. In particular, none of the calculated melts possesses the typical pronounced Nb-Ta negative anomaly of IAB. A weak Nb-Ta negative anomaly is shown only by the melts from the Agnew Wiluna greenstone belt (Australia) in agreement with their komatiitic affinity. Data seem to exclude a subduction contribution in the genesis of the parental liquids of the studied amphiboles. In order to evaluate the alkaline affinity of the calculated melt, the Nb/Y ratio (normalized to the primordial mantle; McDonough and Sun, 1995) has been used (Milidragovic et al., 2015; Saccani, 2015). In the Figure 132 the Nb/Y ratios of the Precambrian amphibole-equilibrium melts are shown and, for comparison, those of Phanerozoic age (subduction-related zones and alkaline megacrysts). Nb is strongly enriched in alkaline basalts relative to tholeiitic basalts and Y is used as an element that does not participate in processes (therefore causing mantle heterogeneity) and that behaves as incompatible during partial melting and fractional crystallisation processes (Pearce, 1982). The relatively high Nb/Y ratios (Nb/Y_{PM}=5.24-6.36) confirm the alkaline affinity of the Fe-picrites from Abitibi Greenstone Belt and Pechenga Complex, except for the amphiboles of olivine-magnetite cumulate from the Pilgujarvi intrusion that have ratios suggesting a sub-alkaline signature. Furthermore, amphiboles from Archean tholeiites (from Abitibi Greenstone Belt) and komatiites (Agnew-Wiluna Greenstone Belt) have low Nb/Y_{PM} ratios suggesting a sub-alkaline affinity.

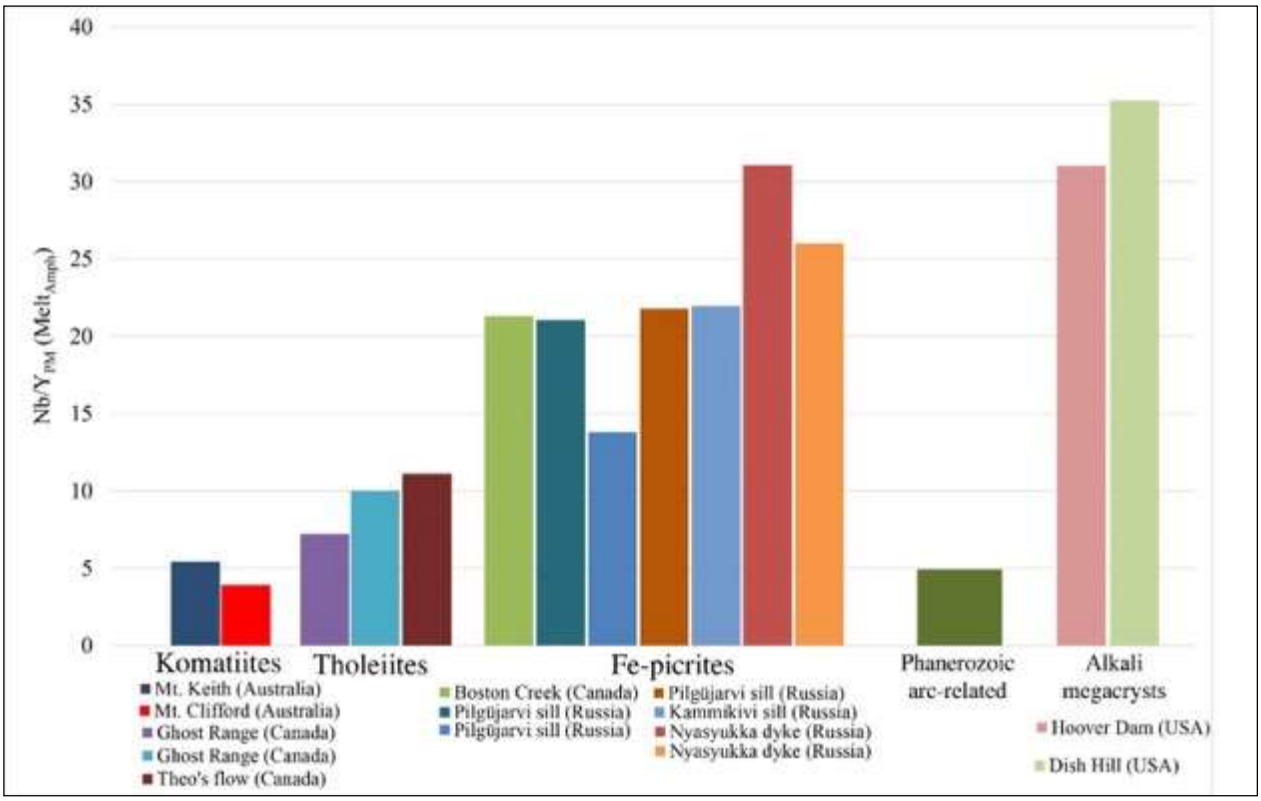

Figure 132 – Nb/Y ratio, normalised to the primordial mantle (McDonough and Sun, 1995), of the calculated amphibole-equilibrium melts.

In the Figure 133, the Archean and Paleoproterozoic amphiboles follow a different trend compared to the Phanerozoic amphiboles from subduction-related zones and megacrysts. The latter show higher Nb/Y_{PM} ratios (Nb/Y_{PM}=7.59-12.21), thereby confirming the efficiency of the Nb/Y_{PM} ratio as a proxy for the alkalinity signature of the magma source. The amphiboles from subduction-related settings display a sub-alkaline ratio (Nb/Y_{PM}<3.01) that is comparable with those of Theo's Flow tholeiite, Australian komatiites and the olivine-magnetite from Pechenga.

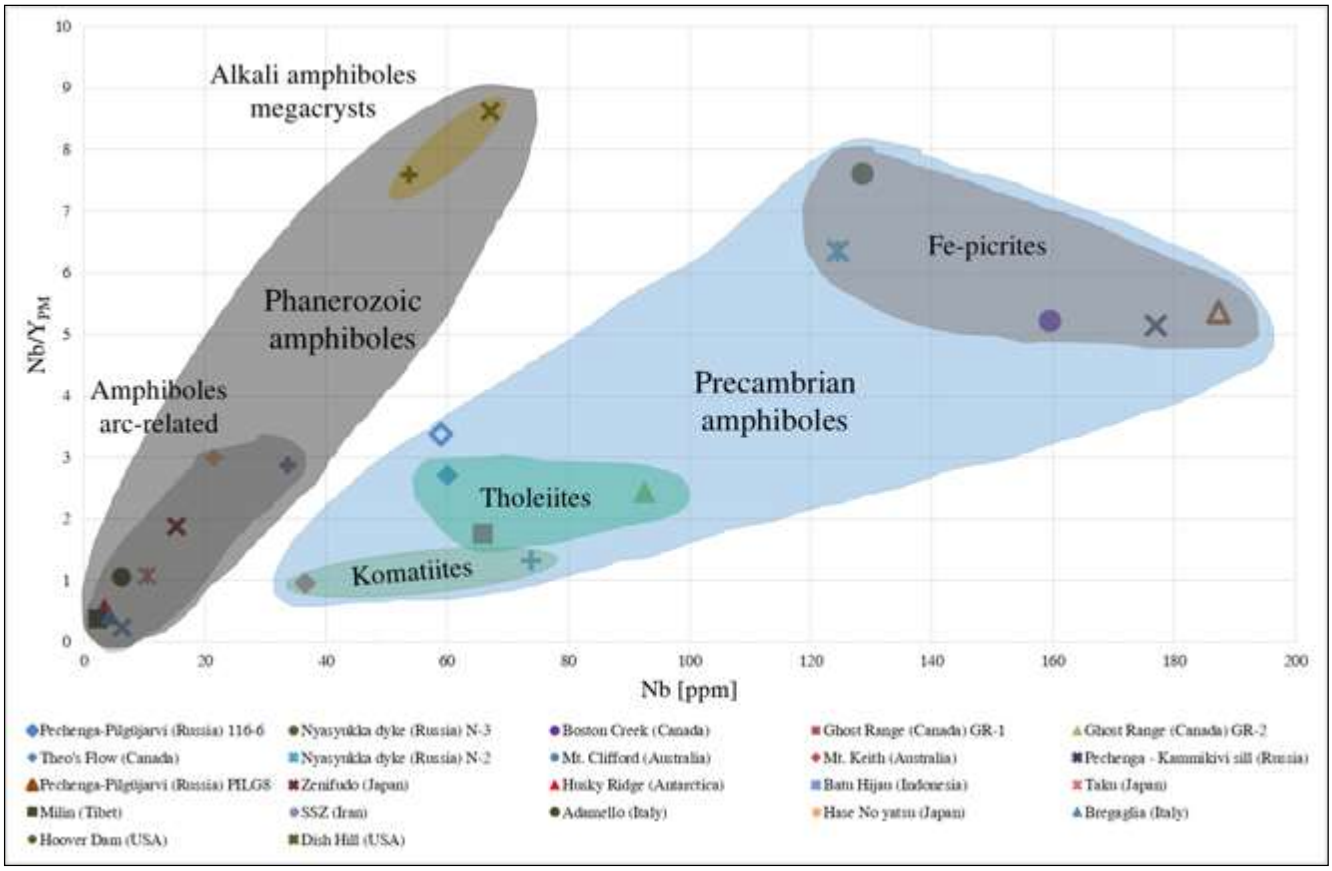

Figure 133 – Nb versus Nb/Y ratios normalized to primordial mantle (McDonough and Sun, 1995) of the Precambrian and Phanerozoic amphiboles.

In summary all the studied amphiboles from Precambrian complexes are in equilibrium with melts that reflect the alkaline affinity of the primary melt, suggested for the origin of the different igneous complexes, and that possess incompatible trace element patterns that parallel the modern OIB signature at higher values. These overall higher incompatible trace element values with respect to present-day OIB can be easily interpreted as the result of melt differentiation prior the crystallisation of amphibole, as described in the section 4.4. Of not easy interpretation are the negative anomalies in Sr and Ti characterising almost all the computed melts. Such features are likely not related to an original signature of the mantle source but likely related to differentiation and possibly to the crystallisation of mineral phases with a high compatibility for Sr and Ti. Stone et al. (2003) argued that clinopyroxene concentrate Sr relative to LREE (Sobolev et al., 1996; Ivanov et al., 1997). A fractionation of Sr from LREE can also be operated by amphibole (Tiepolo et al., 2007). Hence, the depletion of Sr in the Precambrian amphiboles can be related to the relative incompatibility and compatibility, respectively, of these elements in clinopyroxene and possibly amphibole. Alternatively, given the presence of minor phlogopite in some of the studied samples and the high compatibility of both Ti and Sr in this mineral

(e.g., Smith et al., 2014), the crystallisation of small amount of phlogopite (also in association with clinopyroxene and amphibole) could be responsible of the observed depletion.

4.9.2 Inferences from the Nb/Ta ratio and its bearing with the Nb-paradox

The geochemical elements niobium (Nb), tantalum (Ta), zirconium (Zr) and hafnium (Hf) display broadly similar ionic radius and charge. As a result, these elements tend to behave alike during a wide range of geological processes. However, during partial melting of the mantle and fractional crystallization of any derived magmas, the smaller dimensions of Ta and Hf relative to Nb and Zr lead to relative partition coefficient ratios between refractory sources (S) and liquids (L) - $^{S/L}D_{Nb}/^{S/L}D_{Ta}$ and $^{S/L}D_{Zr}/^{S/L}D_{Hf}$ - to be generally lower than unity (Tiepolo & Vannucci, 2014). Consequently, it has been postulated that during planet differentiation over time all silicate reservoirs would have been dispersed on a unique positive Nb/Ta and Zr/Hf array, which aligns along chondritic Nb/Ta and Zr/Hf values. However, this array is commonly displaced to significantly lower Nb/Ta values at chondritic Zr/Hf ratios (Münker et al., 2003). In other words, the Nb/Ta ratio is lower than predicted under the assumption that Earth originally accreted from asteroidal material 'chondritic' in composition. This geochemical anomaly is known as the "terrestrial Nb-Ta paradox". A better understanding of its debated origin would underpin new knowledge on the differentiation of our planet and the evolution of its geochemical reservoirs.

In order to account for the Nb-Ta paradox two opposite scenarios were proposed. The first is based on experimental evidence showing that at high pressure Nb displays a more siderophile behavior with respect to Ta, and especially to Zr and Hf (Wade & Wood, 2001). The inference is that Nb was partitioned from the primordial magma ocean into the core. Accordingly, the observed depleted Nb/Ta signature of the silicate Earth would have been imparted with core-mantle equilibration at 4.533 Ga (Kleine et al., 2002; Yin et al., 2002; Schoenberg et al., 2002). This hypothesis has been recently refined with the finding that Nb is also more chalcophile than Ta under moderately reducing conditions at low pressures (sub-GPa), compatible with conditions typical for small asteroidal bodies at the boundary between silicate mantle and metal- and sulfur-rich core domains (Münker et al., 2017). Accordingly, it is conceivable that the subchondritic Nb/Ta ratio of the Earth's silicate mantle would have also been inherited during the main stages of planet accretion from the silicate portions of reduced asteroidal building blocks, which have relatively low Nb/Ta ratios in contrast to their cores. An alternative hypothesis is the presence of a hidden superchondritic Nb/Ta reservoir/s in the silicate Earth, which would counterbalance the commonly observed subchondritic Nb/Ta signature. Potential candidates were

identified in lower crustal granulites (Stepanov & Hermann, 2013), in the amphibole-rich lower crust (Tiepolo & Vannucci, 2014) and in the subcontinental lithospheric mantle (Pfänder et al., 2012).

In order to address the Nb-Ta paradox, and in particular to verify a time-dependence the Nb/Ta depletion, the secular variation in Nb-Ta in the melt in equilibrium with selected amphiboles has been monitored. The calculation of the Nb/Ta ratio of the silicate melt in equilibrium with amphibole is biased by the selective incorporation of Nb and Ta as a function of its crystal chemistry. Variations in the partitioning of Nb relative to Ta between amphibole and melt can be described in terms of Mg# and Ti contents of amphibole (Tiepolo et al., 2000). According to each mean amphibole composition, we calculated the $^{Amph/L}D_{Nb}/^{Amph/L}D_{Ta}$ ratio and we computed that of the equilibrium melt starting from the amphibole Nb/Ta ratio. Variations in amphibole composition and in turn of the amphibole structure do not significantly influence the $^{Amph/L}D_{Zr}/^{Amph/L}D_{Hf}$ ratio (e.g. Tiepolo et al., 2001). We thus calculated the Zr/Hf ratios of the melt in equilibrium with amphibole by considering a constant mean $^{Amph/L}D_{Zr}/^{Amph/L}D_{Hf}$ ratio of 0.6 (Tiepolo et al., 2007).

Most of the calculated Nb/Ta and Zr/Hf values lies along an array with slightly lower slope (but within error) in relation to the known terrestrial one (Münker et al., 2003), intersecting the Zr/Hf chondritic value at the significantly subchondritic Nb/Ta value of 13 ± 1.6 (Fig. 134). The reason behind the slightly lower slope could reflect a shift in the Zr/Hf ratios related to the occurrence of pyroxene fractionation prior to amphibole, which is significant especially in Archean magmas. However, the striking aspect of our dataset is the fact that a significant number of calculated melts deviates from the main array, showing anomalously high Nb/Ta ratios even at chondritic Zr/Hf values.

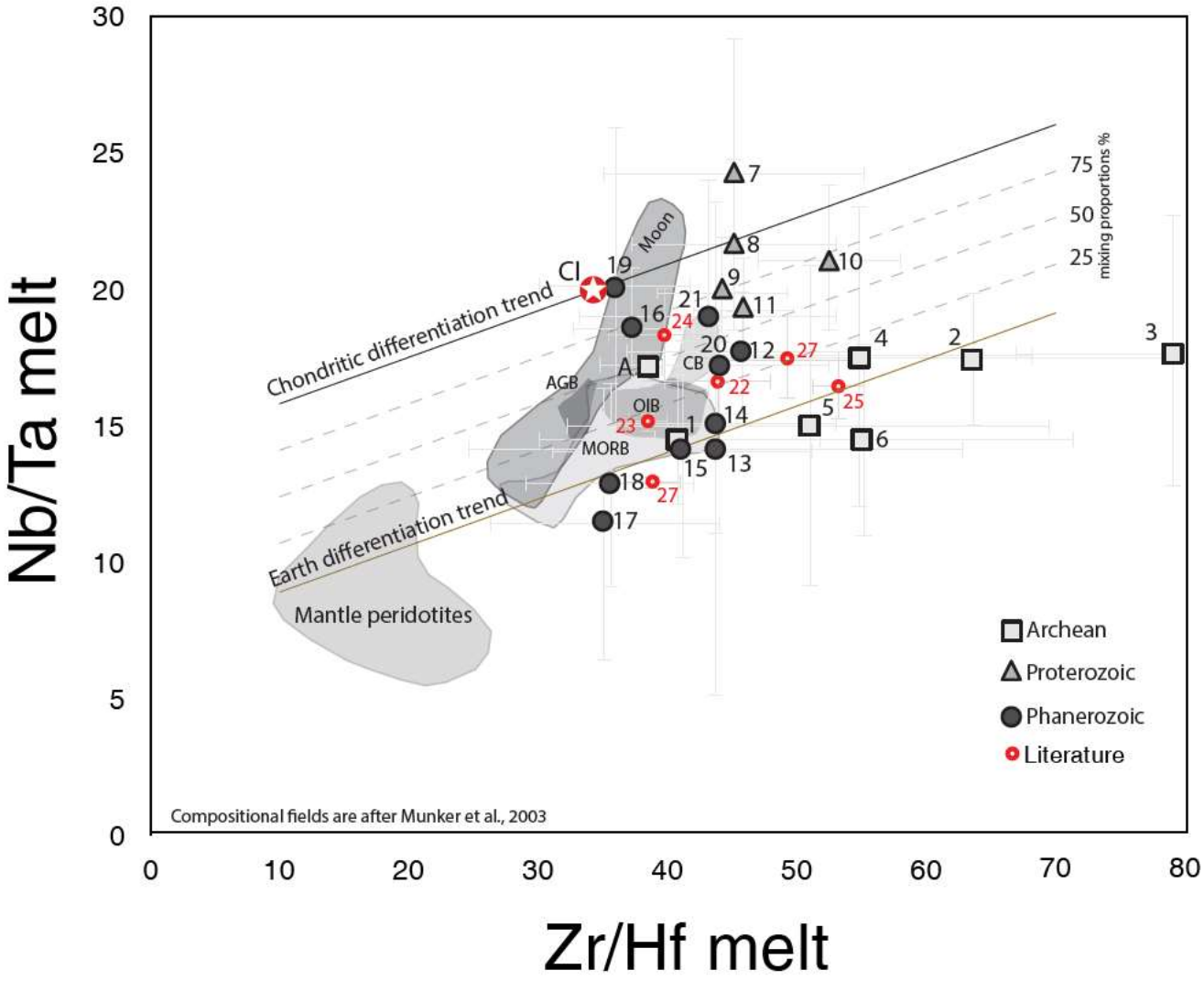

Figure 134 - Variations of the Nb/Ta vs. Zr/Hf ratios in melts in equilibrium with amphibole. Compositional fields are from (Münker et al., 2003). The chondritic differentiation trend has been obtained translating the Earth differentiation trend to the chondritic Nb/Ta and Zr/Hf values of 19 and 34.3, respectively (Münker et al., 2003). Dashed lines represent different mixing proportions of the two differentiation trends. Numerical codes refer to: the 2.7 Ga komatiites of Mt. Keith (1) and Mt. Clifford (2) in the Agnew-Wiluna greenstone belt (Australia); the 2.7 Ga tholeiites of the Theo's Flow (3) and Ghost Range (4-5) and the 2.7 Ga Fe-picrite of Boston Creek (6) in the Abitibi greenstone belt (Canada); the 1.98 Ga Fe-picrites of the Kammikivi (7) sill, Pilgujarvi sill (8-9-10) and the 1.95 Ga Fe-picrite of Nyasyukka Dike Complex (11) in the Pechenga Complex (Russia). Phanerozoic amphiboles are from: the 165 Ma Aligoodarz igneous complex in the Sanandaj–Sirjan Zone (12) (Zagros Orogen); the 117 Ma Hase no Yatsu (13) and the 70 Ma Zenifudo intrusion (14) in Central Japan and the 116 Ma Kita-Taku pluton in SW Japan (15); the 82 Ma hornblendite from Milin area in the Gangdese Batolith (16) (Himalayan orogen); the 30-42 Ma hornblendites from Mt. Mattoni (17) in the Adamello batholith and from the Bregaglia pluton (18) in the Alpine Orogen; the 5 Ma porphyritic tonalites from the Batu Hijau (19); the amphibole megacrysts from Hoover Dam (20) and Dish Hill (21) in the quaternary alkaline lavas in southwest USA; (22) Jeju Island, South Korea (Yang et al., 2012); (23) Rhön area, Germany (Mayer et al., 2014); (24) Charpatio-pannonian basin, Austria, Hungary, Slovakia and Romania (Demeny et al., 2005); (25) Massif central (Woodland et al., 2007); (26) Carpatho pannonian basin, Hungary (Dobosi et al., 2003); (27) Canary Islands (Demeny et al., 2008); 3.2 Ga komatiite (A) from the Weltevreden greenstone belt (South Africa; Putchel et al., 2014).

These melts lie on trends parallel to the differentiation trend of the silicate Earth, but variably shifted towards higher Nb/Ta values, in between the trend defined by a hypothetical chondritic reservoir ("Chondritic differentiation trend" in Fig. 134) and the array defined by the Nb/Ta subchondritic silicate Earth ("Earth differentiation trend" in Fig. 134). We argue that these samples are genuinely anomalous and do not simply divert vertically (i.e., along the y axis) from the silicate Earth differentiation trend, as is the case for some of the magmas emplaced in present-day arcs in which rutile is retained to play a petrogenetic role in the mantle source (Beier et al., 2017). In fact, a role of Ti-rich minerals during crystallization is negligible in the investigated samples, because all rocks are rutile-free and display petrographic evidence of accessory ilmenite postdating amphibole in the crystallization sequence. Furthermore, fractional crystallization cannot account for the observed Nb/Ta anomaly because neither olivine nor clinopyroxene incorporate significant amount of Nb and Ta. More importantly, it appears that anomalously Nb/Ta enriched melts are not restricted to any specific setting or geological time, but rather occur throughout the evolution of the planet in different environments.

The heterogeneity of the >2.7 Ga Earth's mantle is well documented in the variable platinum group element (PGE) concentrations as well as in terms of hafnium, neodymium (Putchel et al., 2013; 2014) and oxygen (Byerly et al., 2017) isotope systematics. The earliest documented evidence of an enriched Nb/Ta mantle source (with values up to 18.2; Putchel et al., 2013) occurs in the 3.27 Ga Weltevreden komatiite lavas (South Africa; Connolly et al., 2011), which also display anomalous oxygen isotope composition (Byerly et al., 2017). The source of the Weltevreden komatiites was likely a deep mantle domain, which crystallized from the primordial magma ocean at about 4.4 Ga (Putchel et al., 2013). This piece of evidence argues against the hypothesis that Nb was homogenously partitioned and sequestered from the primordial magma ocean into the core at 4.533 Ga (Kleine et al., 2002; Yin et al., 2002; Schoenberg et al., 2002). Alternatively, on the basis of recent experimental work it could be argued that the anomalously Nb/Ta enriched portions of the lower mantle – effectively the source regions of Archean komatiites (Campbell et al., 1992) - may reflect domains that survived equilibration with the core. Reactions involving garnet and perovskite would dissolve ferric iron and produce iron metal droplets (Okuchi, 1997; Frost et al., 2004), which would adhere to the deep mantle solid silicate assemblage and escape sequestration into the core, effectively concentrating siderophile and chalcophile elements, including niobium.

However, this hypothesis contradicts evidence from the secular evolution of the PGE concentration in komatiites, which indicates that in the early Archean these lavas were sourced from a highly PGE-depleted lower mantle reservoir that recorded equilibration with the core (Maier et al., 2009). In fact, if the observed anomalous Nb/Ta signature reflected a perovskite-mediated preferential enrichment of the siderophile element Nb in lower mantle domains, an even more pronounced enriched

signature would be observed for the highly siderophile platinum group elements, which is not the case (Maier et al., 2009). An alternative hypothesis to explain the origin of the Nb/Ta enriched lower mantle domains that sourced the early Archean Weltevreden komatiites involves the presence of a non-terrestrial component derived from the proto-solar nebula (Hashizume & Chaussidon, 2005). Timing of the inferred extra-terrestrial input could be bracketed between the time of core-mantle equilibration (~4.5 Ga) and the time of isolation of the oldest recorded Nb/Ta enriched mantle domains (i.e., the source of the Weltevreden komatiites at ~4.4 Ga; Putchel et al., 2013).

The question arises as to what sort of process(-es) may have produced an anomalously enriched Nb/Ta signature in the lower mantle. A hint may lie in the fact that the anomalously enriched terrestrial samples appear to align along Nb/Ta-Zr/Hf trends that are consistent with a Moon affinity (Fig. 134; Münker et al., 2003). The Moon formed when Earth collided with a large extra-terrestrial body with chondritic Nb/Ta composition; the estimated timing of this giant impact is thought to have occurred ~95 Ma after core-mantle equilibration (Jacobson et al., 2014). If the variably subchondritic to chondritic Nb/Ta signature of the Moon samples resulted from mixing between the impactor and the already Nb/Ta depleted silicate Earth upon collision (Münker et al., 2003), the newly discovered nearly chondritic signature of some terrestrial mantle domains may well reflect the scattered presence of non-homogenized fragments of the giant impactor, which partially mixed with proto-Earth mantle and did not escape the Earth system to form the Moon.

In summary, the observed anomalously enriched Nb/Ta signature that occurs in some of the investigated magmas spanning in space and time throughout the complex evolution of the planet has to be a primary feature of their mantle sources. These new data are inconsistent with the interpretation of a secular homogeneity of the subchondritic Nb/Ta signature of the silicate Earth. Conversely, the observed heterogeneous Nb/Ta signature of the Earth's silicate mantle resulted from the complex assembly of non-homogeneous geochemical reservoirs over a protracted geological time. The tapping of anomalously enriched mantle domains throughout the entire evolution of the planet, since the early Archean through to the Phanerozoic, implies that some "early" moon-like deep mantle domains (the source of the early Archean komatiites) escaped complete equilibration with the subchondritic Earth's mantle and reached the shallower source of the Phanerozoic melts. However, any inference on the abundance of these enriched domains in the Earth's mantle is speculative due to the paucity of samples so far considered.

4.9.3 Inferences from variations in water, fluorine and chlorine

Inferences on the secular variations in the volatile element composition of the mantle has been evaluated by comparing the calculated F, Cl and water concentrations in primary melts of Archean and

early Proterozoic amphiboles with those of modern primary MORB, IAB (Sobolev and Chaussidon, 1996) and OIB magmas (Hauri, 2002). In the comparison the melts in equilibrium with amphibole megacrysts from alkaline lavas were also considered (Boettcher and O'Neill, 1980; Figure 135).

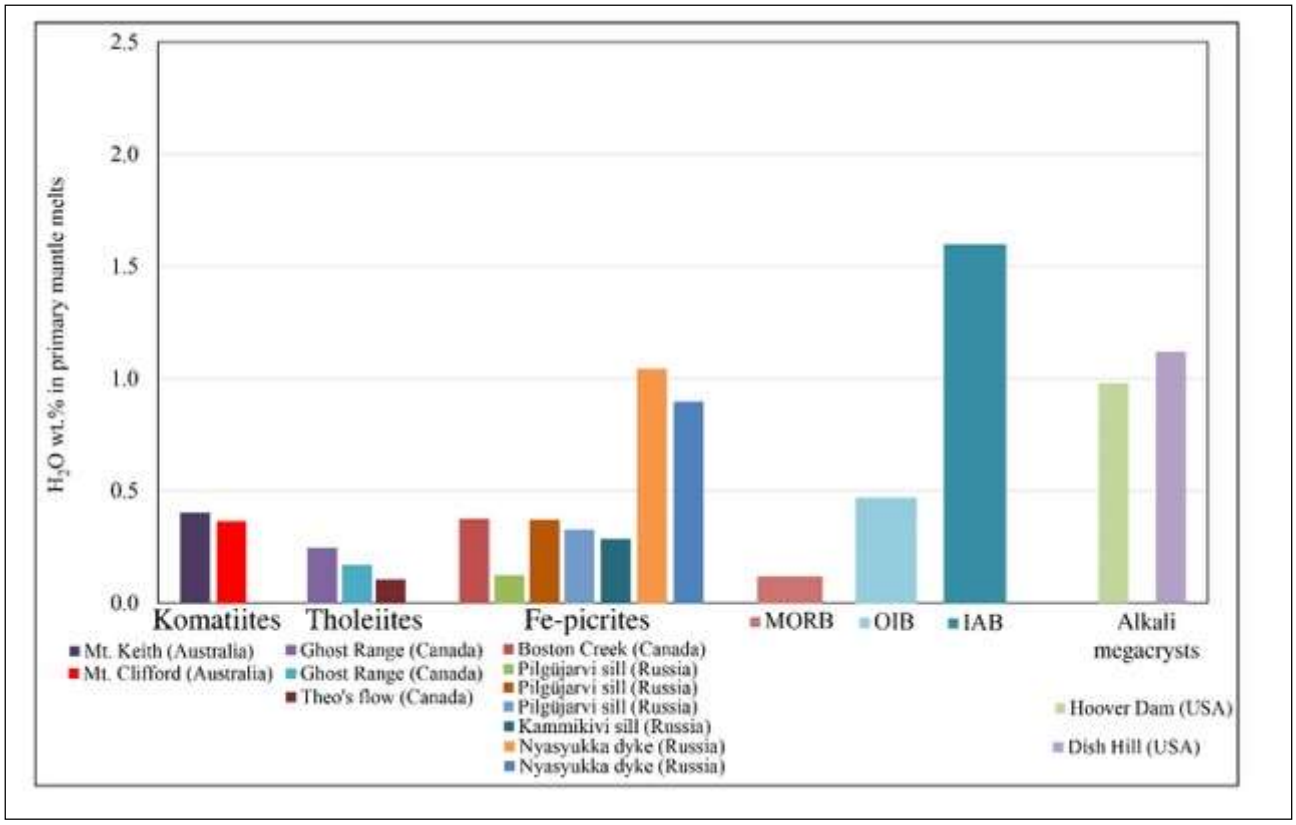

Figure 135 - Comparison between the water contents of Precambrian primary melts and modern MORB, OIB, IAB (Sobolev and Chaussidon, 1996; Hauri, 2002) and alkali megacrysts (Boettcher and O'Neill, 1980).

The H_2O content of the Australian komatiites of the Agnew Wiluna Greenstone Belt is much higher than present-day MORB, much lower than IAB and closely resembles that of modern OIB. Tholeiites from the Abitibi Greenstone Belt show lower water contents than komatiites even approaching the values of modern N-MORB. H_2O contents of Fe-picrites are highly variable and generally inbetween values of modern MORB and OIB. Only in the case of the Nyasyukka dike the H_2O contents are more similar to those of melt in equilibrium with amphibole megacrysts of alkaline lavas and only slightly lower than the water contents of modern IAB. The calculated primary melts have an extreme heterogeneity in the F/Cl ratios (Fig. 136). Fe-picrites of the Pilgüjarvi and Kammikivi sill show F/Cl ratios comparable with those of modern IAB (Churikova et al., 2007) and also with those of alkali megacrysts from Hoover Dam (USA). Remarkably, the Fe-picrite of the Kammikivi sill has the highest F/Cl ratios. The Canadian Fe-picrite of Boston Creek shows, instead, very low F/Cl ratios which are comparable with those of the Australian komatiites. The Canadian tholeiites have F/Cl ratios similar to

those of magnetite-olivine peridotite from Pilgüjarvi sill and the ferropicrites of Nyasyukka dike complex. In summary, the Cl-enrichment of Archean komatiite primary melts is in agreement with the findings of Asafov et al. (2018) that estimated 290 ppm of Cl (and 32 ppm of F; F/Cl = 0.11) in the melt in equilibrium with Fo = 93.5 for the Belingwe komatiites.

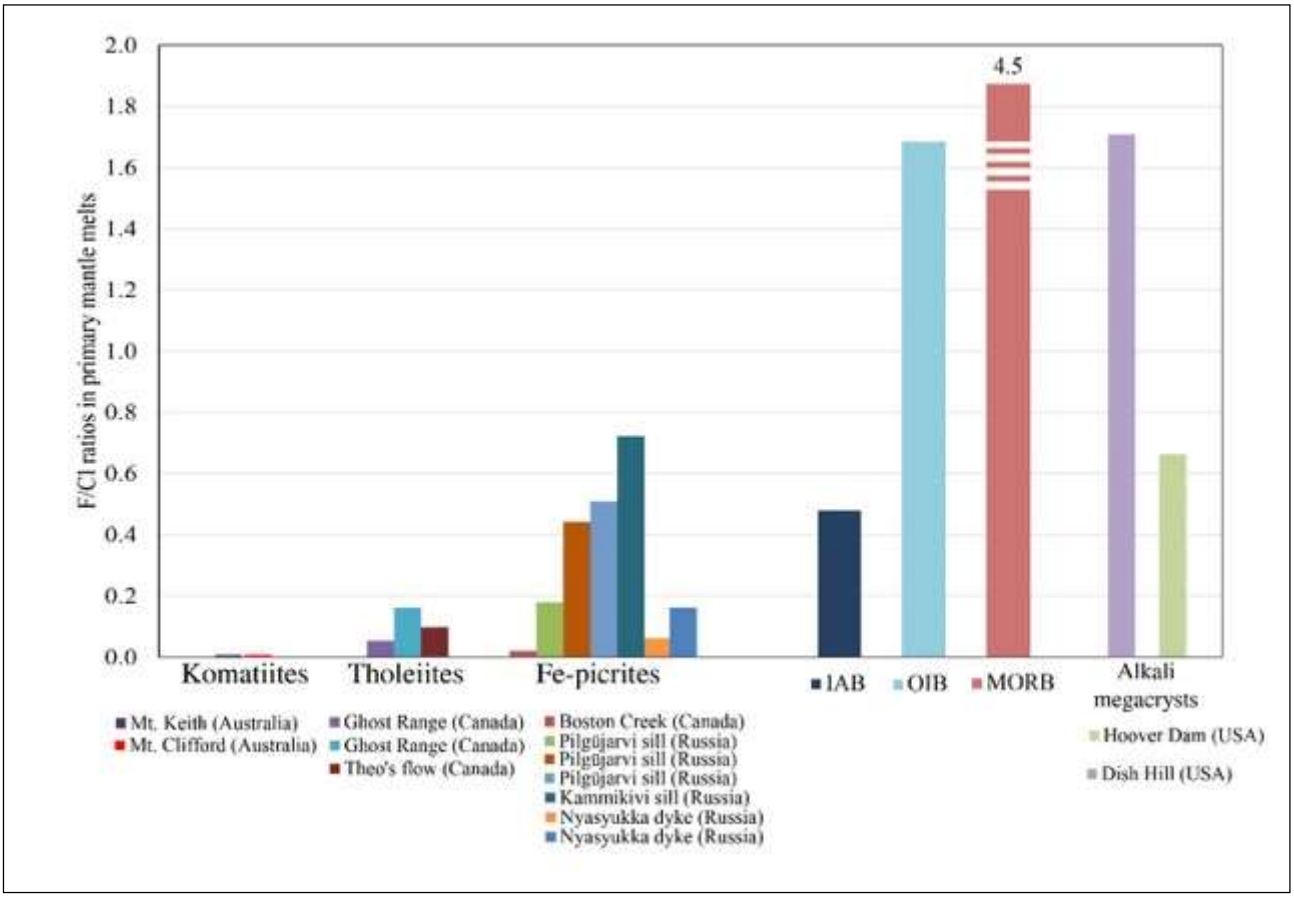

Figure 136 - Comparison between the F/Cl ratios of Precambrian primary melts and modern MORB, OIB, IAB (Sobolev and Chaussidon, 1996; Hauri, 2002) and alkali megacrysts (Boettcher and O'Neill, 1980).

In the interpretation of the above data and in particular those relative to the H_2O contents, the reader has to consider that similar volatile contents in primary melts can be obtained from different mantle sources by varying the degree of partial melting. For example, for low degree of partial melting a H_2O depleted mantle source can give the same water content in the melt as a more enriched mantle source undergoing higher degree of melting. In this frame the similar water contents of komatiites and modern OIB do not imply the same H_2O content in the mantle sources. There is large consensus that komatiites were produced by relatively high degrees of melting given the higher thermal regime of the Earth during Archean times (e.g. Arndt et al., 1998; 2008). It follows that according to the data of this thesis the Archean mantle source of the komatiites had a much higher water content than that characterizing present day OIB. Sobolev et al. (2016) argued that the mantle transition zone at 410–660

km depth is a possible water source for primary melts of the Abitibi komatiites. Experimental studies have shown that the high-pressure polymorphs of olivine—wadsleyite and ringwoodite— can accommodate significant amounts of Cl, F and H_2O (Roberge et al., 2015; Roberge et al., 2017; Asafov et al., 2018). Accordingly, the transitional zone peridotite could have exceptionally high ratios of H_2O, F, (and possibly Cl) to LREE, Nb, K, Rb, B and Ba. The recent finding of H_2O-rich ringwoodite in diamond provides evidence that transition-zone peridotite indeed contains at least 1 wt. % of H_2O (Pearson et al., 2014). More difficult is to give conclusions about tholeiites. Their fractionated trace element pattern paralleling that of OIB suggests that the mantle source was relatively enriched, as that of present-day OIB. However, the low water content is much similar to that of melts produced by a depleted mantle (N-MORB). Different combinations of source mantle composition and degree of partial melting can account for these contrasting features. Because these tholeiites are associated with komatiites (e.g., Ghost Range; Jensen and Langfron, 1985) completely different mantle sources or melting processes are unlikely. The low water contents may thus reflect local heterogeneities of the mantle or different depths at which partial melting occurred. The water-depleted tholeiites could be accordingly originated from shallower, much water-depleted levels of the Archean mantle. In the case of Fe-picrites, given the similar incompatible trace element patterns (resembling that of modern OIB) but the different water contents, the observed variation can be reconciled only by supposing a large heterogeneity in the water composition of the mantle source. This is in agreement with the hypothesis of Milidragovic et al. (2016) that Archean ferropicrites were derived from domains of Fe-rich peridotite and pyroxenite in a predominantly pyrolitic peridotite mantle. Remarkably, water contents in alkaline melts similar to those of modern IAB suggest, in agreement with results on komatiites, that during Archean partial melting took place in a mantle much more water-rich than that feeding present-day OIB.

More in general, results of this work support the previous work of Sobolev et al. (2016) and Herzberg (2016) arguing that mantle ingassing during a ‘cool’ Hadean could describe the elevated volatile contents that have been modelled for and observed in some late-Archean komatiites. This ingassing might have introduced large-scale oxygen isotope heterogeneities in the Archean mantle that were homogenized or are no longer sampled by modern processes (Byerly et al., 2017). Puchtel et al. (2014) suggest that the source of the Weltevreden komatiites is the product of crystallization of a magma ocean at about 4.4 Ga followed by long term isolation from the convecting mantle prior to eruption. Byerly et al. (2018) argued that the low $\delta^{18}O$ of the Weltevreden source could be the result of the same early Earth processes that created these mantle heterogeneities some with low $\delta^{18}O$. Impressive is the similar light oxygen isotope composition of the source of the Archean and early Proterozoic amph-bearing rocks of this thesis and the Weltevreden komatiites. Nevertheless, Maier et al. (2009) and Fiorentini et al. (2011) suggest that the concentration of PGE in the deep mantle progressively increased

throughout the Archean and that this was the consequence of slow descendent mixing of meteoritic Late Veneer during the period between the Late Heavy Bombardment (4.3-3.9 Ga) and 2.7 Ga. Moreover, Milidragovic and co-authors (2016) observed geochemical similarity between the late Archean subalkaline ferropicrites and differentiated basaltic (SNC and HED) meteorites. For the authors the source of Fe-rich enrichment in the Archean mantle may be the late meteoritic infall that followed the formation of the Earth's core.

4.9.4 Inferences from Sc/V and its bearing on mantle oxygen fugacity

Vanadium exists in four potential valence states in magmas, V^{2+}, V^{3+}, V^{4+} and V^{5+}. In melts at terrestrial fO_2s only V^{3+}, V^{4+} and V^{5+} are likely to be present, the abundance of V^{4+} and V^{5+} is small, and the proportion of V^{3+} decreases substantially with increasing fO_2 (Canil, 2002). The crystal structures of most liquidus phases in mafic and ultramafic magmas prefer to incorporate V^{3+}, and for this reason experimentally measured $^{crystal/liquid}D_V$ decreases with increasing fO_2 (Canil, 2002). In this way, increased fO_2 during melting or crystallization will decrease the overall compatibility of V. The low mobility of V during alteration and metamorphism favours the preservation of this redox memory even in rocks more than 3 Ga old (Canil, 2002). The behaviour of V and Sc during mantle melting is such that these elements are more similar to each other than to any other elements, as evidenced by their similar enrichments in continental crust, arc magmas and MORB relative to primitive mantle (Sun & McDonough, 1989; McDonough & Sun, 1995; Rudnick & Fountain, 1995). V and Sc are both mildly incompatible during the formation of MORB and arc lavas, and they are not mobile in fluids (Lee et al., 2005). However, the speciation and, thus, the partitioning of V are redox-sensitive, whereas those of Sc are not (Lee et al., 2005). The use of Sc/V ratios rather than V alone helps to reduce the effects of magmatic differentiation processes that may dilute V and Sc concentrations, but not significantly modify their relative proportions (Lee et al., 2005).

The Sc and V concentrations in primary melts were calculated for Precambrian and Phanerozoic samples by applying amphibole/melt partition coefficient for Sc and V. Mean values of $^{amph/L}D_{Sc} = 3.47$ and $^{amph/L}D_V = 5.24$ have been assumed according to the experimental work of Tiepolo (1999) and considering that these values are in agreement with the few data reported in the literature (Sisson, 1994). As previously described for H_2O, F and Cl contents calculation, amphiboles are residual after crystallization of clinopyroxene and olivine. In order to have the Sc and V parental liquid composition, the contribution of olivine and clinopyroxene was subtracted according to their modal proportions in the rock. Fig. 137 reports the Sc/V ratios of calculated primary melts for Precambrian, Phanerozoic arc-related and amphibole megacrysts from alkali lavas.

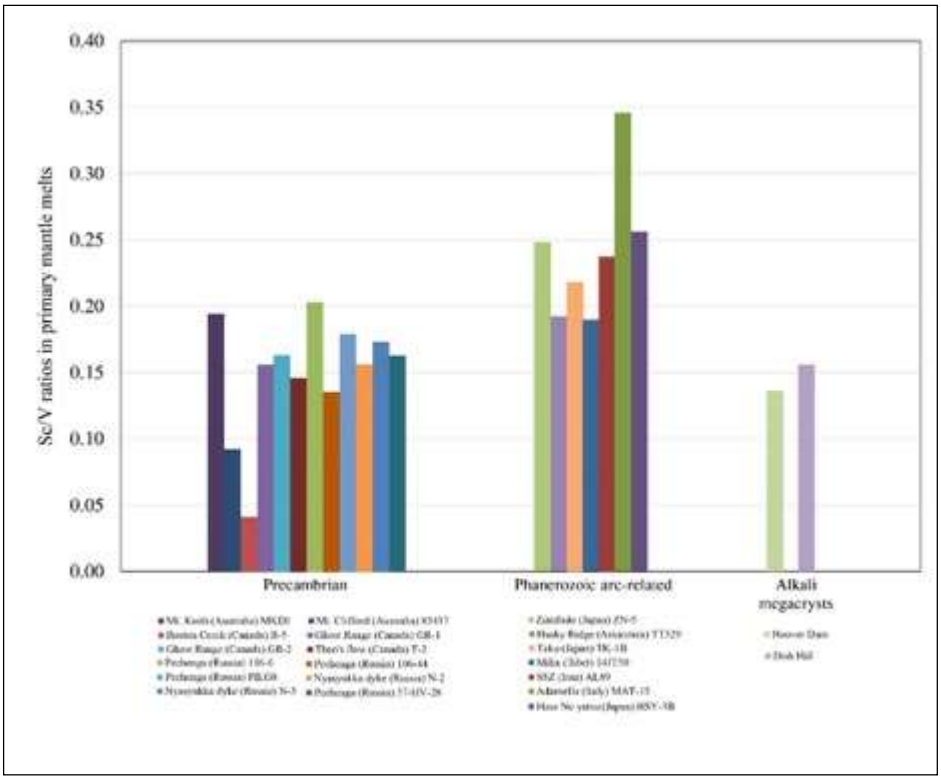

Figure 137 - the Sc/V ratios of calculated primary melts of Precambrian, Phanerozoic arc-related and amphibole megacrysts from alkali lavas.

The Archean and early Proterozoic calculated melts are characterized by relatively homogeneous Sc/V ratios, except for the Australian komatiite of Mt. Clifford and the Canadian Fe-picrite of Boston Creek that have exceptionally low Sc/V ratios (0.04-0.10 Sc/V). Sc/V ratios of Archean and early Proterozoic melts are almost comparable with those of amphibole megacrysts from alkali lavas (Sc/V = 0.15), thus suggesting that the oxygen fugacity conditions of the mantle source in the Archean and early Proterozoic were similar to those of alkaline lavas during Phanerozoic. Noteworthy is that for similar geodynamic settings amphiboles of the present study do not show any significant variation in the oxygen fugacity conditions from Archean to Phanerozoic. The lower Sc/V ratios characterising Archean and early Proterozoic amphiboles with respect to Phanerozoic arc-related melts is a further evidence that in the Archean and early Proterozoic there is no evidence of a subduction-related component in the source of mafic melts (at least those having amphibole as a late crystallising mineral).

5. SUMMARY AND CONCLUSIONS

Planet Earth since its formation underwent a complex evolution that progressively changed its original composition. All the early differentiation events left an indelible mark on the Archean Earth's mantle. However, our knowledge on the Archean mantle composition is still fragmentary arising a series of problems spanning from the effective chondritic composition of the Earth to how volatile elements were added to the Earth and how their deep cycle evolved through time giving origin to life. This thesis has explored the potential of a novel approach in deciphering the Archean mantle geochemical signature that consists in deriving the geochemical fingerprint of the Archean mantle from amphibole of Archean igneous ultramafic rocks. The project aimed to explore the suitability of amphibole to track secular changes in composition and oxidation state of the Archean mantle and in particular in the volatile content.

The oldest samples found with igneous amphibole are Late Archean komatiites (c.a. 2.7 Ga) from the Agnew-Wiluna belt in Western Australia and from the Abitibi greenstone belt in Canada. Other Proterozoic amphibole-bearing ultramafic samples considered in the thesis derive from different units of the 1.9 Ga Pechenga Complex in Russia. The Archean and Early Proterozoic amphiboles have petrographic and textural features that closely resemble those of igneous cumulates (hornblendites) from Phanerozoic arc settings that were thus considered for comparison. Major and trace element composition of Archean and Early Proterozoic amphibole, especially from the Fe-picrites, is close to that of Phanerozoic amphibole megacrysts of alkaline lavas. For this reason, a series of amphibole megacrysts from southwest USA (Hoover Dam and Dish Hill) were also considered for comparison.

In the Archean and Early Proterozoic samples at first the origin of amphibole was constrained. The geobarometric calculations reveal large uncertainty on crystallisation pressures. The Al-in amphibole geobarometric calculations reveal a crystallisation P for amphibole > 3 kbar (at depth > 9.9 km, estimates using a geobarometric gradient of 3.3 km/1 kbar; Hagemann and Brown, 1996). For few localities, these P estimates are confirmed also by the application of the geobarometer of Putirka (2016), thus suggesting their reliability. Others localities yield negative pressure estimates pointing to very low P crystallization conditions of amphibole.

In order to understand the significance of amphibole in rocks that should be virtually anhydrous, the equilibrium between amphibole and primary clinopyroxene was tested using a textural and geochemical approach based on the Fe-Mg and REE partitioning. The amph-bearing rock from the Abitibi Greenstone Belt are those in which amphibole is apparently most far from equilibrium with the associated clinopyroxene. In the amph-bearing rock from the Pechenga Complex (Pilgüjarvi and

Kammikivi sills) amphibole and clinopyroxene are instead very close to equilibrium conditions. Amphibole crystallisation in most of the studied rocks seems to occur from a more differentiated melt, i.e. with low Mg-number and enriched in REE (LREE over HREE in particular). These evidences of disequilibrium between amphibole and clinopyroxene suggests that amphibole did not crystallised "on site" from the same melt of the clinopyroxene. Two different scenarios were proposed to explain this disequilibrium: i) amphibole and clinopyroxene have the same parental liquid that evolved in closed system becoming rich in water by fractional crystallisation of anhydrous phases until the stability of amphibole is reached. ii) H_2O-rich melts have percolated the cumulate pile reacting with clinopyroxene and inducing amphibole crystallisation.

In order to constrain which of these hypotheses are the most reliable, a model of fractional crystallisation was carried out considering the bulk compositions of the studied rocks and evolving the melt by crystallisation of the early cumulus minerals (olivine, orthopyroxene and clinopyroxene). The crystallisation model shows that the measured amphibole REE composition can be obtained in all localities (with the exception for Canada samples) by differentiation of the primary melt by fractional crystallisation of the early cumulus minerals, thus implying that a completely external melt is not required. For the Canadian localities, the model fails to reproduce the strong LREE enrichment and a LREE exotic component may be taken into account. My conclusion is that amphibole in the Archean and Early Proterozoic rocks crystallized from a melt likely evolved by fractional crystallisation from the primary melt. The disequilibrium between amphibole and clinopyroxene highlights that amphibole crystallisation likely occurred during melt migration within the cumulate pile. Other evidences denote that fractional crystallisation is however not the only differentiation process recorded by amphibole. The distribution of the transition metals in amphibole and clinopyroxene supports the hypothesis that amphibole crystallisation follows a melt/rock reaction process between a primary assemblage (likely olivine + magnetite/ilmenite + clinopyroxene) and a melt (likely more evolved) that promoted the partial reabsorption of the primocrystic phases and induced the mobilisation of Ni (from olivine) and Cr (from pyroxene).

Another step towards the understanding of the significance of amphibole in rocks that should be virtually anhydrous is to constrain the origin of water. In particular, the origin of amphibole from the hydration of the cumulate pile (in particular of clinopyroxene) in response to the circulation of seawater-derived fluids cannot be also a priori excluded. Proxies for this process are fluid-mobile elements such as Cl, F, Ba, B and Sr. The Archean and early Proterozoic amphiboles do not fall in any of the known magmatic and hydrothermal fields: they have Nb/La ratios falling in the magmatic amphiboles field whereas the Cl/F ratios are higher and comparable with those of hydrothermal amphiboles. The shift

toward high Cl/F ratio, at constant Nb/La ratios, can be however likely related to the F depletion induced in the melt by fractional crystallisation of amphibole itself. However, we cannot exclude that the high Cl/F ratios is a primary feature of the mantle sources. The Archean and early Proterozoic amphiboles are also Sr-enriched and, generally, B-depleted. All these features thus suggest that a contribution of seawater-derived fluid is unlikely.

The H_2O concentrations in the Archean and early Proterozoic amphiboles are comparable to those of either subduction related or amphibole megacrysts of alkaline lavas. A common feature is also a not full occupancy of the $^{O3}O^{2-}$ structural crystalline site of the amphibole, typical of all high temperature igneous amphiboles. To constrain the origin of water in amphibole the δD and $\delta^{18}O$ were determined in situ by ion microprobe (e.g., SIMS technique). The range of δD values of the Archean and Paleoproterozoic amphiboles is between -99.5 ‰ and -129.8 ‰, that is slightly lower if compared to the mantle range but still consistent with a magmatic origin for water. This δD signature is thus also in contrast with an origin of amphibole by hydration of the cumulate minerals by seawater fluids, as proposed by their Cl/F ratios and Sr-B budgets. However, the hypothesis of a crustal contribution in the origin of the amphiboles, and in turn a non-mantellic origin of water, seems supported by the oxygen isotope signature of amphibole. All amphiboles show $\delta^{18}O$ values lighter than those of the mantle with the sole exception of the olivine-magnetite peridotite from the Pechenga Complex (for which a small crustal input is thus not excluded). The light $\delta^{18}O$ values of amphiboles in Archean and early Proterozoic rocks could be ascribed to the interaction of the amphibole parental melts with recycled altered oceanic materials, which are the most suitable input of seawater-like geochemical anomalies into the mantle during time. Nevertheless, this is unlikely because fluid-mobile elements and hydrogen isotopes have already suggested that seawater apparently was not involved in the petrogenesis of the studied amphiboles. Furthermore, oxygen isotope do not show any correlation with the seawater proxies (e.g., B, Cl). All these geochemical evidences pointed out that the light $\delta^{18}O$ signature of most of the Archean and Paleoproterozoic amphiboles is likely a primary feature of the mantle source.

All studied amphiboles are in equilibrium with melts resembling the alkaline affinity of the primary melt that has been suggested in the literature for the different igneous complexes. The incompatible trace element pattern parallels at higher values that of modern OIB (with respect to MORB and IAB) even if display negative Sr and Ti anomalies. This higher overall incompatible trace element values with respect present day OIB can be easily interpreted as the result of melt differentiation prior the crystallisation of amphibole. Sr and Ti anomalies are likely related to the crystallisation of mineral phases with a high compatibility for Sr and Ti such as amphibole itself or phlogopite.

A main conclusion of this thesis based on the comparison of the water content in primary melts from Archean-early Proterozoic amphiboles and present-day OIB, MORB and IAB is that the Archean mantle source of the komatiites had a much higher water content than that characterizing present day OIB. This is in agreement with the finding that the high-pressure polymorphs of olivine could have exceptionally high concentrations of H_2O and F, (and possibly Cl) thus representing a good volatile-reservoir in the deep mantle. Conclusions about tholeiites are more problematic. The fractionated trace element pattern of these melts, paralleling that of OIB, suggests that the mantle source was relatively enriched in incompatible elements even if the water content is low and similar to that of present-day N-MORB. These contrasting features may reflect local heterogeneities of the mantle or different depths (shallower) at which partial melting has occurred. The early Proterozoic Fe-picrites yield an incompatible trace element patterns resembling that of modern OIB but with highly variable water contents suggesting a large heterogeneity in the water composition of the mantle source. Heterogeneity of the mantle through the Earth's history was also observed for the Nb/Ta signature. Some of the calculated melts (since early Proterozoic) show an enriched Nb/Ta signature that is independent from space (geological setting) and time and that was interpreted as a primary feature of the different mantle sources. The observed heterogeneous Nb/Ta signature of the Earth's mantle was interpreted as related to the addition of extra-terrestrial material after the mantle-core equilibration and prior 4.4 Ga and to a not complete equilibration of these domains during the Earth's evolution.

I documented the occurrence in the Archean and Early Proterozoic of mantle domains producing melts with the trace element signature close to modern OIB but enriched in volatile components, especially in H_2O. This volatile element enrichment of the mantle was likely a deep signature and unrelated to subduction processes as known today. I also documented a Nb/Ta extra-terrestrial signature for some mantle domains and I do not exclude that these features are mutually related. Results of this thesis are fragmentary and still incomplete but suggests that the Earth's mantle still possess domains that escaped a complete equilibration or with the core or with the rest of the mantlein case of an extra-terrestrial origin and are thus records of the Early Earth history.

Amphibole, given its highly versatile structure, has been demonstrated to be a very important source of information about the equilibrium melts and in turn on mantle source.

References

Adam, J., and Green, T. Trace element partitioning between mica- and amphibole-bearing garnet lherzolite and hydrous basanitic melt: 1. Experimental results and the investigation of controls on partitioning behaviour. Contrib Mineral Petrol 152, 1–17 (2006).

Agard, A., Omrani, J., Jolivet, L., Whitechurch, H., Vrielynck, B., Spakman, W., Monte, P., Meyer, B., Wortel, R. Zagros orogeny: a subduction-dominated process. Geological Magazine 148, 692- 725 (2011).

Ague, J.J., and Brimhall, G.H. Regional variations in bulk chemistry, mineralogy, and the compositions of mafic and accessory minerals in the batholiths of California. Geological Society of America Bulletin, 100, 891–911 (1988).

Alavi, M. Regional stratigraphy of the Zagros fold–thrust belt of Iran and its proforeland evolution. American Journal of Science 304, 1–20 (2004).

Allen, J.C., and Boettcher, A.L. The stability of amphibole in andesite and basalt at high pressures: American Mineralogist, v. 68, 307–314 (1983).

Allibone, A., & Wysoczanski, R. Initiation of magmatism during the Cambrian-Ordovician Ross orogeny in southern Victoria Land, Antarctica. Geological Society of America Bulletin 114, 1007-1018 (2002).

Alt, J.C., Muehlenbachs, K., Honnerez, J. An oxygen isotopic profile through the upper kilometre of the oceanic crust, DSDP Hole 504B. Eart Planet Sci Lett 80, 217-229 (1986).

Anderson, J.L. Status of thermobarometry in granitic batholiths. Transactions of the Royal Society of Edinburgh: Earth Sciences, 87, 125–138 (1996).

Anderson, J.L., and Smith, D.R. The effects of temperature and fO_2 on the Al-in-hornblende barometer. American Mineralogist, 80, 549–599 (1995).

Anderson, J.L., Barth, A.P., Wooden, J.L., and Mazdab, F. Thermometers and thermobarometers in granitic systems. Reviews in Mineralogy and Geochemistry, 69, 121–142 (2008).

Annen, C., Blundy, J.D., and Sparks, R.S.J. The genesis of intermediate and silicic magmas in deep crustal hot zones: Journal of Petrology, v. 47, p. 505–539 (2006).

Aranovich, L, Safonov, O. Halogens in high-grade metamorphism. In: Harlov DE, Aranovich L (eds) The role of halogens in terrestrial and extraterrestrial geochemical processes: surface, crust, and mantle. Springer, Berlin, 713–757 (2018).

Arculus, R.J., and Wills, K.J.A. The petrology of plutonic blocks and inclusions from the Lesser Antilles Island arc: Journal of Petrology, v. 21, 743–799 (1980).

Armstrong, R.A., Compston, W., Retief, E.A., Williams, I.S., and Welke, H.J. Zircon ion microprobe studies bearing on the age and evolution of the Witwatersrand triad. Precambrian Res. 53, 243–266 (1991).

Arndt N. T. & Jenner G. A. Crustally contaminated komatiites and basalts from Kambalda, Western Australia. Chemical Geology 56, 229–255 (1986).

Arndt, N. High Ni in Archean tholeiites. Tectonophysics, 187, 411–420 (1991).

Arndt, N. Komatiites, kimberlites, and boninites. J. Geophys. Res., 108 (B6), 2293 (2003).

Arndt, N. Spinifex and swirling olivines in a komatiite lava lake, Munro Township, Canada. Precambrian Research, 34, 139-155 (1986).

Arndt, N.T. Thick, layered peridotite-gabbro lava flows in Munro Township, Ontario: Canadian Journal of Earth Sciences, v. 14, p. 2620–2637 (1977).

Arndt, N.T. Ultramafic Rocks of Munro Township and their Volcanic Setting [Ph.D. dissertation]: Toronto, University of Toronto, 295 p. (1975).

Arndt, N.T., 2008, Komatiite: New York, Cambridge University Press, 467 p. (2008).

Arndt, N.T., Albarede, F., Nisbet, E.G. Mafic and ultramafic magmatism. In: M. J. de Wit and L.D. Ashwal (eds.) Greenstone Belts, New York: Oxford University Press., 233–254 (1997).

Arndt, N.T., Barnes, S.J., Lesher, C.M. Komatiite. Cambridge University Press, Cambridge (2008).

Arndt, N.T., Naldrett, A.J., and Pyke, D.R., 1977, Komatiitic and iron-rich tholeiitic lavas of Munro Township, northeast Ontario: Journal of Petrology, v. 18, p. 319–369 (1977).

Asafov, E.V., Sobolev, A.V., Gurenko, A.A., Arndt, N.T., Batanova, V.G., Portnyagina, M.V., Garbe-Schönberge, D., Krasheninnikova, S.P. Belingwe komatiites (2.7 Ga) originate from a plume with moderate water content, as inferred from inclusions in olivine. Chemical Geology 478, 39–59 (2017).

Asahara, Y., and Ohtani, E. Melting relations of the hydrous primitive mantle in the CMAS- H2O system at high pressures and temperatures, and implications for generation of komatiites: Physics of the Earth and Planetary Interiors, v. 125, 31–44 (2001).

Aulbach, S., & Stagno, V. Evidence for a reducing Archean ambient mantle and its effects on the carbon cycle. Geology, v. 44, 751–754 (2016).

Barley, M.E., Brown, S.J., Krapež, R.B., and Cas, R.A.F. Tectonostratigraphic analysis of the eastern Yilgarn craton: An improved geological framework for exploration in Archaean terranes. Australian Minerals Industry Association Report 437A (2002).

Barley, M.E., Eisenlohr, B.N., Groves, D.I., Perring, C.S., and Vearncombe, J.R. Late Archean convergent margin tectonics and gold mineralization: A new look at the Norseman-Wiluna belt, Western Australia. Geology, v. 17, 826–829 (1989).

Barley, M.E., Stuart, J.A., Krapež, B., and Kositcin, N., 2008, Physical volcanology and geochemistry of a Late Archean volcanic arc: Kurnalpi and Gindalbie terranes, Eastern Goldfields superterrane, Western Australia. Precambrian Research, v. 161, 53–76 (2008).

Barnes, S. J. Komatiites: petrology, volcanology, metamorphism and geochemistry. Society of Economic Geologists Special Publication 13, 13–49 (2006).

Barnes S. J., Lesher C. M. & Sproule R. A. Geochemistry of komatiites in the Eastern Goldfields Superterrane, Western Australia and the Abitibi Greenstone Belt, Canada, and implications for the distribution of associated Ni–Cu–PGE deposits. Applied Earth Science Transactions IMM B 116, 167–187 (2007).

Barnes, S.J., and Fiorentini, M.L., 2012, Komatiite magmas and sulfide nickel deposits: A comparison of variably endowed terranes. Economic Geology, v. 107, 755–780 (2012).

Barnes, S.J., and Van Kranendonk, M.F. Archaean andesites in the east Yilgarn craton, Australia: Products of plume-crust interaction? Lithosphere, v. 6, 80–92 (2014).

Barnes, S.J., Fiorentini, M.J.L., Duuring, P, Grguric, B.A., and Perring, C.S. The Perseverance and Mount Keith nickel deposits of the Agnew-Wiluna belt, Yilgarn craton, Western Australia. Reviews in Economic Geology, v. 17, 51–88 (2011).

Barnes, S.J., Fiorentini, M.L. and Fardon, C.M. Platinum group element and nickel sulphide ore tenors of the Mount Keith nickel deposit, Yilgarn craton, Australia. Mineralium Deposita, v. 47, 129–150 (2012).

Bateman, R., Costa, S., Swe, T., and Lambert, D. Archaean mafic magmatism in the Kalgoorlie area of the Yilgarn craton, Western Australia: A geochemical and Nd isotopic study of the petrogenetic and tectonic evolution of a greenstone belts: Precambrian Research, v. 108, 27–112 (2001).

Begg, G.C., Hronsky, J.A.M., Arndt, N.T., Griffin, W.L., O'Reilly, S.Y., Hayward, N. Lithospheric, cratonic, and geodynamic setting of Ni-Cu-PGE sulfide deposits. Econ Geol 105, 1057–1070 (2010).

Beier, C., Haase, K. M., Brandl, P. A., Krumm, S. H. Primitive andesites from the Taupo Volcanic Zone formed by magma mixing. Contrib. Mineral. Petrol. 172, 33 (2017).

Bell, D.R., & Hoering, T.C. D/H ratios and H_2O contents of mantle-derived amphibole megacrysts from Dish Hill, California. Deep Earth and planetary volatiles, (1994).

Benard, A. Koga, K.T., Shimizu, Kendrick, N.M.A., Ionov, D.A., Nebel, O., Arculus, R.J. Chlorine and fluorine partition coefficients and abundances in sub-arc mantle xenoliths (Kamchatka, Russia): Implications for melt generation and volatile recycling processes in subduction zones. Geochimica et Cosmochimica Acta 199, 324–350 (2017).

Beresford, S., Fiorentini, M., Barley, M., Hronsky, J., Grguric, B., Duuring, P., Rosengren, N., Saleem, A., Cass, R., Tait, M., Bleeker, W., Barnes, S., Cassidy, K., and Champion, D. Cratonic to camp scale footprint of the world's largest komatiite-hosted Ni-Cu belt, Agnew-Wiluna belt, W.A. Biennial SGA Meeting, 10th, Townsville, 2009, Proceedings, 149–151 (2009).

Berry, A.J., Danyushevsky, L.V., O'Neill, H.S.C., Newville, M., Sutton, S.R. Oxidation state of iron in komatiitic melt inclusions indicates hot Archean mantle. Nature 455, 960–964 (2008).

Black, L.P., & Sheraton, J.W. The influence of Precambrian source components on the U-Pb zircon age of a Palaeozoic granite from Northern Victoria Land, Antarctica. Precambrian Research 46, 275-293 (1990).

Blewett, R.S. and Czarnota, K. A new integrated tectonic framework of the Eastern Goldfields superterrane. Geoscience Australia Record 2007/14, 27–32 (2007a).

Blewett, R.S. and Czarnota, K. The Y1-P763 project final report November 2005, Module 3— terrane structure: Tectonostratigraphic architecture and uplift history of the Eastern Yilgarn craton. Geoscience Australia Record 2007/15, 114 (2007b).

Blewett, R.S., Czarnota, K., and Henson, P.A. Structural-event framework for the eastern Yilgarn craton, Western Australia, and its implications for orogenic gold. Precambrian Research, v. 183, 203–229 (2010a).

Blewett, R.S., Henson, P.A., Roy, I.G., Champion, D.C., and Cassidy K.F. Scale integrated architecture of a world-class gold mineral system: the Archaean eastern Yilgarn craton, Western Australia. Precambrian Research, v. 183, 230–250 (2010b).

Blundy, J. D. & Sparks, R. S. J. Petrogenesis of mafic inclusions in granitoids of the Adamello Massif, Italy. Journal of Petrology 33, 1039–1104 (1992).

Blundy, J.D., and Holland, T.J.B. Calcic amphibole equilibria and a new amphibole-plagioclase geothermometer. Contributions to Mineralogy and Petrology, 104, 208–224 (1990).

Boettcher, A.L., and O'Neil, J. R. Stable isotope, chemical, and petrographic studies of high-pressure amphiboles and micas: evidence for metasomatism in the mantle source regions of alkali basalts and kimberlites. American Journal of Science, 280-A, 594–621 (1980).

Boger, S. D. & Miller, J. McL. Terminal suturing of Gondwana and the onset of the Ross-Delamerian orogeny: the cause and effect of an Early Cambrian reconfiguration of plate motions. Earth and Planetary Science Letters 219, 35-48 (2004).

Borg, S.C., & De Paolo, D.J. A tectonic model of the Antarctic Gondwana margin with implication for southeastern Australia: isotopic and geochemical evidence. Tectonophysics 196, 339-358 (1991).

Borghini, G., Fumagalli, P., and Rampone, E. The Stability of Plagioclase in the Upper Mantle: Subsolidus Experiments on Fertile and Depleted Lherzolite. Journal of Petrology, v. 51, 229-254 (2009).

Bottke, W.F., Vokrouhlický, D., Minton, D., Nesvorný, D., Morbidelli, A., Brasser, R., Simonson, B., Levison, H.F. An Archaean heavy bombardment from a destabilized extension of the asteroid beltNature, 485 (2012), pp. 78-81

Brueckner, H.K., Carswell, D.A., & Griffin, W.L. Paleozoicdiamonds within a Precambrian peridotite lens in UHP gneissesof the Norwegian Caledonides. Earth and Planetary Science Letters 203, 805-816 (2002).

Buick, R., Dunlop, J.S.R., and Groves, D.I. Stromatolite recognition in ancient rocks: an appraisal of irregularly laminated structures in an Early Archaean chert-barite unit from North Pole, Western Australia. Alcheringa, 5, 161-181 (1981).

Burt, D.R.L., Sheppy, N.R. Mount Keith nickel sulfide deposit. In: Knight CL (ed) Economic geology of Australia and Papua New Guinea, vol. 1. Metals Australasian Institute of Mining and Metallurgy, Carlton South, 159–168 (1975).

Byerly, B. L., Kareem, K., Bao, H. & Byerly, G. R. Early Earth mantle heterogeneity revealed by light oxygen isotopes of Archean komatiites. Nature Geosciences 10, 871-875 (2017).

Callegari, E. & Brack, P. Geological map of the Tertiary Adamello batholith (Northern Italy). Explanatory notes and legend. Memorie di Scienze Geologiche 54, 19-49 (2002).

Callegari, E. & Dal Piaz, G.B. Field relationships between the main igneous masses of the Adamello Intrusive Massif (N. Italy). Memorie degli Istituti Geologia e Mineralogia dell'Universita' di Padova 24, 1-38 (1973).

Cameron, W.E., Nisbet, E.G., and Dietrich, V.J. Boninites, komatiites and ophiolitic basalts: Nature, v. 280, 550–553 (1979).

Campbell, I. & Schenk, E. T. Camptonite dikes near Boulder Dam, Arizona. Contrib. of the Division of the Geological Sciences 539, 671-692 (1950).

Campbell, I. H., & Griffiths, R. W. The Changing Nature of mantle Hotspots through Time: Implications for the Chemical Evolution of the Mantle. The Journal of Geology 100, 497-523 (1992).

Campbell, I.H. and Hill, R.I. A two-stage model for the formation of granite-greenstone terrains of the Kalgoorlie-Norseman area, Western Australia: Earth and Planetary Sciences Letters, v. 90, 11–25 (1988).

Campbell, I.H., & O'Neill, H. St C. Evidence against a chondritic Earth. Nature 483, 553-558 (2012).

Campbell, I.H., Griffiths, R.W., and Hill, R.I. Melting in an Archaean mantle plume: Heads it's basalts, tails it's komatiites. Nature, v. 339, 697–699 (1989).

Canil, D. Vanadium in peridotites, mantle redox and tectonic environments: Archean to present. Earth Planet. Sci. Lett., 195, 75-90 (2002).

Canil, D. Vanadium partitioning and the oxidation state of Archean komatiite magmas. Nature 389, 842-845 (1997).

Canil, D., & Fedortchouk, Y. Olivine-liquid partitioning for vanadium and other trace elements with applications to modern and ancient picrites. Can. Mineral. 39, 319-330 (2001).

Cassidy, K.F., Champion, D.C., Krapež, B., Barley, M.E., Brown, S.J.A., Blewett, R.S., Groenewald, P.B., and Tyler, I.M. A revised geological framework for the Yilgarn craton, Western Australia. Geological Survey of Western Australia Record 2006/8, 8 (2006).

Champion, D.C., and Cassidy, K.F. An overview of the Yilgarn craton and its crustal evolution: Geoscience Australia Record 2007/14, 8–13 (2007).

Champion, D.C., and Sheraton, J.W. Geochemistry and Nd systematics of Archaean granites of the Eastern Goldfields, Yilgarn craton, Australia: Implications for crustal growth processes: Precambrian Research, v. 109, 109–132 (1997).

Chazot, G., Lowry, D., Menzies, M., and Mattey, D. Oxygen isotopic composition of hydrous and anhydrous mantle peridotites. V. 61, 161-169 (1997).

Chu, M.F., Chung, S.L., Song, B., Liu, D., O'Reilly, S.Y., Pearson, N.J., Ji, J., Wen, D.J. Zircon U–Pb and Hf isotope constraints on the Mesozoic tectonics and crustal evolution of southern Tibet. Geology 34, 745–748 (2006).

Chung, S.L., Liu, D., Ji, J., Chu, M.F., Lee, H.Y., Wen, D.J., Lo, C.H., Lee, T.Y., Qian, Q., Zhang, Q. Adakites from continental collision zones: melting of thickened lower crust beneath southern Tibet. Geology 31, 1021–1024 (2003).

Churikova, T., Worner, G., Mironov, N., and Kronz, A. Volatile (S, Cl and F) and fluid mobile trace element compositions in melt inclusions: implications for variable fluidsources across the Kamchatka arc. Contrib. Mineral. Petrol. 154, 217–239 (2007).

Compston, W, Williams, I.S., Campbell, I.H., and Gresham, J.J. Zircon xenocrysts from the Kambalda volcanics: Age constraints and direct evidence for older continental crust below the Kambalda-Norseman greenstones. Earth and Planetary Science Letters, v. 76, 299–311 (1986).

Condie, C.K., & Kröner, A. When did plate tectonics begin? Evidence from the geologic record. The Geological Society of America Special Paper 440, 281-294 (2008).

Condie, K. C. Incompatible element ratios in oceanic basalts and komatiites: Tracking deep mantle sources and continental growth rates with time. Geochem. Geophys. Geosyst. 4(1), 1005 (2003).

Condie, K. C. Secular variation in the composition of basalts: an index to mantle evolution. Journal of Petrology, 26, 545–563 (1984).

Condie, K. C., Greenstones through time, in Archean Crustal Evolution, edited by K. C. Condie, Elsevier Sci., New York, chap. 3, 85–120 (1994).

Condie, K.C. Archaean Greenstone Belts. Elsevier, Amsterdam, 434 p (1981).

Condie, K.C. Episodic continental growth and supercontinents: a mantle avalanche connection? Earth Planet. Sci. Lett. 163, 97–108 (1998).

Condie, K.C. Episodic continental growth models: afterthoughtsand extensions. Tectonophysics 322, 153–162 (2000).

Condie, K.C. Geochemical characteristics of Precambrian basaltic greenstones, in Early Precambrian Basic Magmatism, edited by R. P. Hall and D. J. Hughes, , Blackie Acad. & Prof., New York, 40–55 (1990).

Condie, K.C., Belousova, E., Griffin, W.L., and Sircombe, K.N. Granitoid events in space and time: constraints from igneous and detrital zircon age spectra. Gondwana Res. 15, 228– 242 (2009).

Connolly, B. D., Puchtel, I. S., Walker, R. J., Arevalo, R. J., Piccoli, P. M., Byerly, G., Robin-Popieul, C., Arndt, N. Highly siderophile element systematics of the 3.3 Ga Weltevreden komatiites, South Africa: implications for early Earth history. Earth Planet. Sci. Lett. 311, 253-263 (2011).

Coogan, L.A., Wilson, R.N., Gillis, K.M., and Macleod, C.J. Near-solidus evolution of oceanic gabbros: Insights from amphibole geochemistry. Geochimica et Cosmochimica Acta, v. 65, 4339–4357 (2001).

Cooper, R.A., & Tulloch, A.J. Early Palaeozoic terranes in New Zeland and their relationships to the Lachlan Fold Belt. Tectonophysics 214, 129-144 (1992).

Corfu, F., Noble, S.R. Genesis of the southern Abitibi greenstone belt: evidence from zircon Hf-isotope analysis using a single filament technique. Geochim Cosmochim 56, 2527-2531 (1992).

Czarnota, K., Champion, D.C., Goscombe, B., Blewett, R.S., Cassidy, K.F., Henson, P.A., and Groenewald, P.B. Geodynamics of the eastern Yilgarn craton. Precambrian Research, v. 183, 175–202 (2010).

Dallai, L., Ghezzo, C., & Sharp, Z.D. Oxygen isotope evidence for crustal assimilation and magma mixing in the Granite Harbour Intrusives, Northern Victoria Land, Antarctica. Lithos 67, 135-151 (2003).

Dalou C., Koga, K.T., Le Voyer, M., and Shimizu, N. Contrasting partition behavior of F and Cl during hydrous mantle melting: implications for Cl/F signature in arc magmas. Prog. Earth Planet. Sci. 1, 26–42 (2014).

Dann, J.C. Vesicular komatiites, 3.5-Ga Komati Formation, Barberton Greenstone Belt, South Africa: inflation of submarine lavas and origin of spinifex zones. Bull Volcanol 63, 462–481 (2001)

Davidson, J., Turner, S., Handley, H., Macpherson, C. & Dosseto, A. Amphibole sponge in arc crust? Geology 35, 787–790 (2007).

Davies, J.H., von Blanckenburg, F. Slab breakoff: A model of lithosphere detachment and its test in the magmatism and deformation of collisional orogens. Earth and Planetary Science Letters, 129, 85-102 (1995).

De Joux, A., Thordarson, T., Denny, M., Hinton, R.W., and de Joux, A.J. U-Pb dating constraints on the felsic and intermediate volcanic sequence of the nickel-sulphide bearing Cosmos succession, Agnew-Wiluna greenstone belt, Yilgarn craton, Western Australia: Precambrian Research, v. 236, 85–105 (2013).

Del Moro, A., Ferrara, G., Tonarini, S., & Callegari, E. Rb-Sr systematics on the rocks from the Adamello batholith (Southern Alps). Memorie della Societa' Geologica Italiana 26, 261-284 (1983).

Delano, J.W. Redox history of the Earth's interior since ~3900 Ma: implications for prebiotic molecules, Orig. Life Evol. Biosph. 31, 311– 341 (2001).

Deloule, E., Albarede, F., & Sheppard, S.M.F. Hydrogen isotope heterogeneities in the mantle from ion probe analysis of amphiboles from ultramafic rocks. Earth and Planetary Science Letters, 105, 543–553 (1991a).

Deloule, E., France-Lanord, C., and Albarede, F. D/H analysis of minerals by ion probe, in ''Stable Isotope Geochemistry: A Tribute to Samuel Epstein''. Geochem. Soc. Spec. Publ., 3, 53 – 62 (1991b).

Demény, A., Casillas, R., Hegner, E., Vennemann, T.W., Nagy, G., Sipos, P. Geochemical and H-O-Sr-Nd isotope evidence for magmatic processes and meteoric-water interactions in the basal complex of La Gomera, Canary Islands. Miner Petrol 98, 181–195 (2010).

Demény, A., Casillas, R., Vennemann, T.W., Hegner, E., Nagy, G., Ahijado, A., De La Nuez, J., Sipos, P., Pilet, S. & Milton, J. Plume-related stable isotope compositions and fluid-rock interaction processes in the Basal complex of La Palma, Canary Islands Spain. In Metasomatism in oceanic and continental lithospheric mantle. Eds. Coltorti and Gregoire. Geological Society, London, Special Publication, 293, 155-175 (2008).

Demény, A., Vennemann, T.W., Hegner, E., Ahijado, A., Casillas, R., Nagy, G., Homonnay, Z., Gutierrez, M. s S H, O, Sr, Nd and Pb isotopic evidence for recycled oceanic crust in the Transitional Volcanic Group of Fuerteventura, Canary Islands, Spain. Chem Geol 205, 37–54 (2004).

Demény, A., Vennemann, T.W., Homonnay, Z., Milton, A., Embey-Isztin A. & Nagy, G. Origin of amphibole megacrysts in the Pliocene-Pleistocene basalts of the Carpathian-Pannonian region. Geolog. Carpathica, 56, 179-189 (2005).

DePaolo, D.J. Trace element and isotopic effects of combined wall-rock assimilation and fractional crystallization. Earth and Planetary Science Letters 53, 189-202 (1981).

Dewey, J.F., Pitman, W.C., Ryan, W.B.F., Bonnin, J. Plate tectonics and the evolution of the Alpine System. Geological Society of America Bulletin 84, 3137–3180 (1973).

Di Vincenzo, G., & Rocchi, S. Origin and interaction of mafic and felsic magmas in an evolving late orogenic setting: the Early Paleozoic Terra Nova Intrusive Complex, Antarctica. Contributions to Mineralogy and Petrology 137, 15-35 (1999).

Di Vincenzo, G., Palmeri, R., Talarico, F., Andriessen, P.A.M., & Ricci, C.A. Petrology and geochronology of eclogites from the Lanterman Range, Antarctica. Journal of Petrology 38, 1391-1417 (1997).

Dixon, J.E., Leist, L., Langmuir, C., & Schilling, J.G. Recycled dehydrated lithosphere observed in plume-influenced mid-ocean-ridge basalt. Nature 420, 385-389 (2002).

Dobosi, G., Downes, H., Embey-Isztin A. & Jenner G.A. Origin of megacrysts and pyroxenite xenoliths from the Pliocene alkali basalts of the Pannonian Basin (Hungary). N. Jb. Miner. Abh. 178, 3, 217-237 (2003).

Donaldson, M.J. Mount Clifford-Marshall pool area. In: Groves DI, Lesher CM (eds) Regional geology and nickel deposits of the Norseman-Wiluna belt, Western Australia: Nedlands. University of Western Australia Extension Service, Western Australia, C53–C67 (1982).

Donaldson, M.J., Lesher, C.M., Groves, D.I., Gresham, J.J. Comparison of Archaean dunites and komatiites associated with nickel mineralization in Western Australia: implications for dunite genesis. Mineralium Deposita 21, 296–305 (1986).

Dowling, S.E., and Hill, R.E.T. Rivers of fire: the physical volcanology of komatiites of the Mount Keith region, Norseman-Wiluna belt, Western Australia. Commonwealth Scientific and Industrial Research Organisation, Exploration Geoscience Restricted Report, v. 103R, 170 p. (1990).

Dowling, S.E., and Hill, R.E.T. The Mount Keith ultramafic complex and the Mount Keith nickel deposit. Australian Geological Survey Organization Record 1993/54, 165–170 (1993).

Drummond, B.J., Goleby, B.R., and Swager, C.P. Crustal signature of Late Archean tectonic episodes in the Yilgarn craton, Western Australia: Evidence from deep seismic sounding. Tectonophysics, v. 329, 193–221 (2000).

Duggan, B., Perring, C., Seat, Z., and Smith, P., 2008, Spinifex Park: Final exploration summary: BHP Billiton unpub. memorandum, 37 p. (2008).

Dungan, M.A., and Davidson, J.P. Partial assimilative recycling of the mafic plutonic roots of arc volcanoes: An example from the Chilean Andes: Geology, v. 32, p. 773–776 (2004).

Eiler, J.M. Oxygen isotope variations of basaltic lavas and upper mantle rocks. In: VALLEY, J. W. & COLE, D. R. (eds) Stable Isotope Geochemistry. Mineralogical Society of America, Reviews in Mineralogy and Geochemistry, 43, 319–364 (2001).

Eiler, J.M., Farley, K.A, Valley, J.W., Hauri, E., Craig, H., Hart, S., and Stolper, E.M. Oxygen isotope variations in ocean island basalt phenocrysts, Geochim. Cosmochim. Acta, 61, 2281–2293 (1996).

Elkins-Tanton, L. T. Linked magma ocean solidification and atmospheric growth for Earth and Mars. EPSL 271, 181-191 (2008).

Erdman, S., Martel, C., Pichavant, M., and Kushnir, A. Amphibole as an archivist of magmatic crystallization conditions: problems, potential, and implications for inferring magma storage prior to the paroxysmal 2010 eruption of Mount Merapi, Indonesia. Contributions to Mineralogy and Petrology, (2014).

Esna-Ashari, A., Tiepolo, M. & Hassanzadeh, J. On the occurrence and implications of Jurassic primary continental boninite-like melts in the Zagros orogen. Lithos 258-259, 37-57 (2016)

Falloon, T.J., Green, D.H., Danyushevsky, L.V., and Mcneill, A.W. The Composition of Near-solidus Partial Melts of Fertile Peridotite at 1 and 1.5 GPa: Implications for the Petrogenesis of MORB. Journal of Petrology, v. 591-613

Fan, J., and Kerrich, R. Geochemical characteristics of aluminum depleted and undepleted komatiites and HREE-enriched Iow-Ti tholeiites, western Abitibi greenstone belt: A heterogeneous mantle plume-convergent margin environment. Geochimica et Cosmochimica Acta, v. 61, 4723-4744 (1997).

Farquhar, J., Zerkle, A.L., Bekker, A. Geological constraints on the origin of oxygenic photosynthesis. Photosynth Res. 107, 11-36 (2011).

Faure, G. Principles and Applications of Geochemistry. Prentice Hall, Englewood Cliffs, NJ. (1991)

Fiorentini, M. L. & Garwin, S. L. Evidence of a mantle contribution in the genesis of magmatic rocks from the Neogene Batu Hijau district in the Sunda Arc, South Western Sumbawa, Indonesia. Contrib. Mineral. Petrol. 159, 819-837 (2010).

Fiorentini, M. L., Beresford, S. W., Deloule, E., Hanski, E., Stone, W. E., Pearson, N. J. The role of mantle-derived volatiles in the petrogenesis of Palaeoproterozoic ferropicrites in the Pechenga Greenstone Belt, northwestern Russia: Insights from in-situ microbeam and nanobeam analysis of hydromagmatic amphibole. Earth Planet. Sci. Lett. 268, 2-14 (2008).

Fiorentini, M.L., Beresford, S.W., Rosengren, N., Barley, M.E., and McCuaig, T.C. Contrasting komatiite belts, associated Ni–Cu–(PGE) deposit styles and assimilation histories, Australian Journal of Earth Sciences, 57, 543-566 (2010).

Fiorentini, M. L., Beresford, S. W., Stone, W. E., Deloule, E. Evidence of water degassing during emplacement and crystallization of 2.7 Ga komatiites from the Agnew-Wiluna greenstone belt, Western Australia. Contrib. Mineral. Petrol. 164, 143-155 (2012).

Fiorentini, M.L., Barnes, S.J., Maier, W.D., Burnham, O.M., and Heggie, G. Global Variability in the Platinum-group Element Contents of Komatiites. Journal of Petrology, v. 52, 83-112 (2011).

Fiorentini, M.L., Rosengren, N., Beresford, S.W., Grguric, B., Barley, M.E. Controls on the emplacement and genesis of the MKD5 and Sarah's Find Ni-Cu-PGE deposits, Mount Keith, Agnew-Wiluna Greenstone Belt, Western Australia. Mineralium Deposita 126, 847–877 (2007).

Fiorentini, M.L., Stone, W.E., Beresford3, S.W., and Barley, M.E. Platinum-group element alloy inclusions in chromites from Archaean mafic-ultramafic units: evidence from the Abitibi and the Agnew-Wiluna Greenstone Belts. Mineralogy and Petrology 82, 341–355 (2004).

Fischer, T.P., and Marty, B. Volatile abundances in the sub-arc mantle: Insights from volcanic and hydrothermal gas discharges: Journal of Volcanology and Geothermal Research, v. 140, 205–216 (2005).

Foden, J.D., & Green, D.H. Possible role of amphibole in the origin of andesite: some experimental and natural evidence. Contrib. Mineral. Petrol. 109, 479–493 (1992).

Foster, D.A., Gray, D.R., & Spaggiari, C. Timing of subduction and exhumation along the Cambrian East Gondwana margin, and the formation of the Palaeozoic backarc basins. Geological Society of America Bulletin, 117, 105-116 (2005).

Francis, D. The implications of picritic lavas for the mantle sources of terrestrial magmatism. Lithos, 34, 89–106 (1995).

Francis, D., Ludden, J., Johnstone, R., Davis, W. Picrite evidence for more Fe in Archean mantle reservoirs. Earth and Planetary Science Letters, 167, 197–213 (1999).

Frost, D.J., Liebske, C., Lagenhorst, F., McCammon, C.A., Tronnes, R.G. & Rubie, D.C. Experimental evidence for the existence of iron-rich metal in the Earth's lower mantle. Nature 428, 409-412 (2004).

Früh-Green, G.L., Scambelluri, M., Vallis, F. O-H isotope ratios of high pressure ultramafic rocks: implications for fluid sources and mobility in the subducted hydrous mantle Contrib Mineral Petrol 141, 145-159 (2001).

Gaetani, G.A., Grove, T.L., & Bryan, W.B. The influence of water on the petrogenesis of subduction-related igneous rocks. Nature, 365, 332-334 (1993).

Gao, S., Liu, X., Yuan, H., Hattendorf, B., Gunther, D., Chen, L., Hu, S. Determination of Forty Two Major and Trace Elements in USGS and NIST SRM Glasses by laser ablation-inductively Coupled plasma mass spectrometry. Geostand. Newsl. 26, 181-196 (2002).

Garcia, O.M., Musnow, D.W., and Liu, N.W.K. Volatiles in Ti-rich amphibole megacrysts, southwest USA. American Mineralogist, v. 65, 306-312 (1980).

Garwin, S. The geologic setting of intrusion-related hydrothermal systems near the Batu Hijau porphyry copper-gold deposit Sumbawa, Indonesia. In: Goldfarb RJ, Nielsen R (eds) Integrated methods for discovery, Soc Econ Geol Special Publ 9, 333–366 (2002).

Gentili, S., Bonadiman, C., Comodi, P., Coltorti, M., Zucchini, A., Ottolini, L. Oxo-amphiboles in mantle xenoliths: evidence for H_2O-rich melt interacting with the lithospheric mantle of Harrow Peaks (Northern Victoria Land, Antarctica). Mineral. Petrol., 109, 741-759 (2015)

Giacomini, F., Tiepolo, M., Dallai, L., & Ghezzo, C. On the onset and evolution of the Ross orogeny magmatism in North Victoria Land, Antarctica. Chemical Geology 240, 103-128 (2007).

Gibson, S.A., Thompson, R.N., and Dickin, A.P. Ferropicrites: geochemical evidence for Fe-rich streaks in upwelling mantle plumes. Earth Planet. Sci. Lett. 174, 355–374 (2000).

Gillis, K.M., Coogan, L.A., Chaussidon, M. Volatile element (B, Cl, F) behaviour in the roof of an axial magma chamber from the East Pacific Rise. Earth Planet Sci Lett 213, 447–462 (2003)

Gillis, K.M., Meyer, P.S. Metasomatism of oceanic gabbros by late-stage melts and hydrothermal fluids: evidence from the rare earth element composition of amphiboles. Geochem. Geophys. Geosyst. 2 2000GC000087 (2001).

Goldstein, S. B., and Francis, D. The petrogenesis and mantle source of Archaean ferropicrites from the western Superior Province, Ontario, Canada. J. Petrol., 49, 1729–1753 (2008).

Gole, M.J., Barnes, S.J., and Hill, R.E.T. The geology of the Agnew nickel deposit, Western Australia: Canadian Institute of Mining and Metallurgy Bulletin, v. 82, 46–56 (1989).

Gole, M.J., Robertson, J., and Barnes, S.J. Extrusive origin and structural modification of the komatiitic Mount Keith ultramafic unit. Economic Geology, v. 108, p. 1731–1752 (2013).

Goscombe, B., Blewett, R.S, Czarnota, K., Maas, R., Groenewald, B.A. Broad thermo-barometric evolution of the Eastern Goldfields Superterrane, in: Bierlein, F.P., Knox-Robinson, C.M., (Eds.) (2007). Proceedings of Geoconferences (WA) Inc. Kalgoorlie 07' Conference. Geoscience Australia Record 2007/14, 33–38 (2007).

Greber, N.D., Dauphas, N., Bekker, A., Ptáček1, M.P., Bindeman, I.N., Hofmann, A. Titanium isotopic evidence for felsic crust and plate tectonics 3.5 billion years ago. Science, v. 357, 1271-1274 (2017).

Green, D.H. Petrogenesis of Archean ultramafic magmas and implications for Archaean tectonics. In: A. Kroner (ed.) Precambrian Plate Tectonics, pp. 469–490 (1981).

Green, J.C., and Schulz, K.J. Iron-rich basaltic komatiites in the early Precambrian Vermillion District, Minnesota. Can. J. Earth Sci. 14, 2181–2192 (1997).

Grosfils, E.B. Magma reservoir failure on the terrestrial planets: Assessing the importance of gravitational loading in simple elastic models: Journal of Volcanology and Geothermal Research, v. 166, 47–75 (2007).

Gunn, G.M., & Warren, G. Geology of Victoria Land between Mawson and Mullock Glaciers, Antarctica. New Zealand Geological Survey Bulletin 71, 85-100 (1962).

Hagemann, S.G., and Brown, P.E. Geobarometry in Archean lode-gold deposits Eur. J. Mineral., 8, 937-960 (1996).

Hammerstrom, J.M., and Zen, E. Aluminum in hornblende: an empiricaligneous geobarometer. American Mineralogist, 71, 1297–1313 (1986)

Hansen, V.L. Venus: A thin-lithosphere analog for early Earth? In Van Kranendonk, M.J., Smithies, R.H., and Bennett, V.C., eds., Earth's Oldest Rocks (>3.2 Ga): Amsterdam, Netherlands, Elsevier, 971–983 (2007).

Hanski, E. Petrology of the Pechenga ferropicrites and cogenetic, Nibearing gabbro–wehrlite intrusions, Kola Peninsula, Russia. Geol. Soc. Finland, Bull. 367, 192 (1992).

Hanski, E., Huhma, H., Smolkin, V.F., Vaasjoki, M. The age of the ferropicritic volcanics and comagmatic Ni-bearing intrusions at Pechenga, Kola Peninsula. Geol. Soc. Finland, Bull. 62, 123–133 (1990).

Hanski, E., Smolkin, V.F. Pechenga ferropicrites and other early Proterozoic picrites in the eastern part of the Baltic Shield. Precamb. Res. 45, 63–82 (1989).

Hanski, E., Smolkin, V.F., 1995. Iron and LREE-enriched mantle source for Early Proterozoic intraplate magmatism as exemplified by the Pechenga ferropicrites, Kola Peninsula, Russia. Lithos 34, 107–125 (1995).

Hanski, E.J., Hannu H., Melezhiket V.A. New isotopic and geochemical data from the Palaeoproterozoic Pechenga Greenstone Belt, NW Russia: Implication for basin development and duration of the volcanism. Precambrian Research. 245, 51–65 (2014).

Hansmann, W. Age determination on the Tertiary Masino- Bregaglia (Bergell) intrusives (Italy, Switzerland): a review. Schweiz Mineral Petrogr Mitt 76, 421–451 (1996).

Hanson, G.N., Langmuir, C.H. Modelling of major elements in mantle-melt systems using a trace element approach. Geochimica et Cosmochimica Acta, 42, 725–741 (1978).

Hashizume, K. & Chaussidon, M. A non-terrestrial ^{16}O-rich isotopic composition for the protosolar nebula. Nature 434, 619-622 (2005).

Hauri, E.H. SIMS analysis of volatiles in silicate glasses, 2: isotopes and abundances in Hawaiian melt inclusions. Chemical Geology 183, 115–141 (2002).

Hauri, E.H. Volatiles in melt inclusions from Hawaiian volcanoes: an ion microprobe study. EOS Trans. Am. Geophys U. 77, 811 (1996).

Hauri, E.H., Gaetani, G.A., Green, T.H. Partitioning of water during melting of the Earth's upper mantle at H_2O-undersaturated conditions. Earth and Planetary Science Letters 248, 715–734 (2006).

Hawkesworth, C., Cawood, P., Kemp, T., Storey, C., and Dhuime, B. A matter of preservation. Science 323, 49–50 (2009).

Heinonen, J.S., and Luttinen, A.V. Jurassic dikes of Vestfjella, western Dronning Maud Land, Antarctica: geochemical tracing of ferropicrite sources. Lithos 105, 347–364 (2008).

Herzberg C. Petrological Evidence from Komatiites for an Early Earth Carbon and Water Cycle. Journal of Petrology 57, 2271–2288 (2016).

Herzberg, C. Generation of plume magmas through time: An experimental perspective. Chemical Geology 126, 1–16 (1995).

Herzberg, C. Identification of source lithology in the Hawaiian and Canary Islands: implications for origins. J. Petrol. 52, 113–146 (2011).

Herzberg, C., Condie, K., and Korenaga, J. Thermal history of the Earth and its petrological expression. Earth Planet. Sci. Lett. 292, 79–88 (2010).

Hildreth, W., & Moorbath, S. Crustal contribution to arc magmatism in the Andes of Central Chile. Contributions to Mineralogy and Petrology 98, 455–489 (1988).

Hill, R.E.T., Barnes, S.J., Gole, M.J., and Dowling, S.E. Physical volcanology of komatiites: A field guide to the komatiites of the Norseman-Wiluna greenstone belt, Eastern Goldfields province, Yilgarn block, Western Australia: Geological Survey of Western Australia Excursion Guide Book 1, 100 p. (1990).

Hill, R.E.T., Barnes, S.J., Gole, M.J., and Dowling, S.E. The volcanology of komatiites as deduced from field relationships in the Norseman-Wiluna greenstone belt, Western Australia. Lithos, v. 34, 159–188 (1995).

Hollister, L.S., Grissom, G.C., Peters, E.K., Stowell, H.H., and Sisson, V.B. Confirmation of the empirical correlation of Al in hornblende with pressure of solidification of calc-alkaline plutons. American Mineralogist, 72, 231–239 (1987).

Houlé, M.G., Préfontaine, S., Fowler, A.D., Gibson, H.L. Endogenous growth in channelized komatiite lava flows: evidence from spinifex-textured sills at Pyke Hill and Serpentine Mountain, Western Abitibi Greenstone Belt, Northeastern Ontario, Canada. Bull Volcanol 71, 881–901 (2009).

Hudson, D.R., and Travis, G.A. A native nickel-heazlewoodite-ferroan trevorite assemblage from Mount Clifford, Western Australia: Economic Geology, v. 76, 1686–1697 (1981).

Ichiyama, Y., Ishiwatari, A., Hirahara, Y., and Shuto, K. Geochemical and isotopic constraints on the genesis of the Permian ferropicritic rocks from the Mino-Tamba belt, SW Japan. Lithos 89, 47–65 (2006).

Irving, A.J. Pyroxene-rich ultramafic xenoliths in the Newer Basalts of Victoria, Australia. Neues Jahrb. Mineralogie Abh., v. 120, 147-167 (1974).

Ivanov, D.A., Griffin, W.L., O'Reilly, S.Y. Volatile-bearing minerals and lithophile trace elements in the upper mantle. Chem Geol 141, 153-184 (1997).

Jackson, M.D., Cheadle, M.J., and Atherton, M.P. Quantitative modeling of granitic melt generation and segregation in the continental crust: Journal of Geophysical Research-Solid Earth, v. 108, p. 2332 (2003).

Jackson, M.D., Gallagher, K., Petford, N., and Cheadle, M.J. Towards a coupled physical and chemical model for tonalite–trondhjemite– granodiorite magma formation. Lithos, v. 79, 43–60 (2005)

Jackson, S.L. and Harrap, R.M., 1989. Geology of parts of Pacand, In: Summary of Field Work and Other Activities 1989. Ont. Geol. Surv., Misc. Pap. 146, 125-131 (1989).

Jacobson, S.A., Morbidelli, A., Raymond, S.N., O'Brien, D.P., Walsh, K.J. & Rubie, D. C. Highly siderophile elements in Earth's mantle as a clock for the Moon-forming impact. Nature 508, 84-87 (2014).

Jahn, B.M., Gruau, G., Glickson, A.Y. Komatiites of the Onverwacht Group, South Africa: REE chemistry, Sm–Nd age and mantle evolution. Contributions to Mineralogy and Petrology, 80, 25–40 (1982).

Jensen L.S., milne, V.G., White, O.L., Barlow, R.B., and Kustra, C.R. Larder Lake Synoptic Mapping Project. District of Cochrane and Timiskaming. Summary of Field Work, Ontario Geological Survey, Miscellaneous paper, 64-69 (1979).

Jensen, L.S. and Langford, F. F. Geology and Petrogenesis of the Archean Abitibi Belt in the Kirkland Lake Area, Ontario. Ontario Geological Survey, Miscellaneous Paper 123, 130 p. (1985)

Jensen, L.S. Stratigraphy and petrogenesis of Archean metavolcanic sequences, southwestern Abitibi Subprovince, Ontario. In: L.D. Ayres, P.C. Thurston, K.D. Card and W. Weber (Editors), Evolution of Archean Supracrustal Sequences. Geol. Assoc. Can., Spec. Pap. 28, 65-87 (1985).

Ji, W.Q., Wu, F.Y., Chung, S.L., Li, J.X., Liu, C.Z. Zircon U–Pb geochronology and Hf isotopic constraints on petrogenesis of the Gangdese batholith, southern Tibet. Chemical Geology 262, 229–245 (2009).

Johnson, M.C., and Rutherford, M.J. Experimental calibration of an aluminum-in-hornblende geobarometer applicable to calc-alkaline rocks. EOS, 69, 1511 (1989).

Johnson, M.C., and Rutherford, M.J. Experimental calibration of an aluminum-in-hornblende geobarometer applicable to Long Valley caldera (California) volcanic rocks. Geology, 17, 837–841 (1989).

Johnson, M.C., Rutherford, M.J., and Hess., P.C. Chassigny petrogenesis: Melt compositions, intensive parameters, and water contents of Martian (?) magmas. Geochimica et Cosmochimica Acta, 55 349-366 (1991).

Johnstone, R.M. Geology of the Stoughton-Roquemaure Group, Beatty and Munro Townships, Northwestern Ontario [M.S. thesis]: Ottawa, Carleton University, p. 325 (1987).

Jolly, W. T. Development and degradation of Archean lavas Abitibi area, Canada in light of major element geochemistry. Jour. Petrology, v. 21, p. 323-363 (1980).

Jones, A.P., Mutanen, T., Tuisku, P., Hanski, E., Price, G.D. The Pechenga structure, Russia: giant Ni-Cu mineralisation related to large meteorite impact? Fermor Flagship meeting. World class mineral deposits and Earth evolution, 19–21 Aug 2003, Cardiff University and The National Museum of Wales, Abstracts, Trans Inst Min Metal: Sect B: Appl Earth Sci 112, B149–B150 (2003).

Kagami, H., Ulmer, P., Hansmann, W., Dietrich, V., Steiger, R. Nd-Sr isotopic and geochemical characteristics of the southern Adamello (northern Italy) intrusives: implications for crustal versus mantle origin. J Geophys Res 96B9, 331–346 (1991).

Kamei, A., Owada, M., Nagao, T., Shiraki, K. High-Mg diorites derived from sanukitic HMA magmas, Kyushu Island, southwest Japan arc: evidence from clinopyroxene and whole rock compositions. Lithos 75, 359-371 (2004).

Kamenetsky, V.S., Sobolev, A.V., McDonough, W.F. Melt inclusion evidence for a volatile-enriched (H2O, Cl, B) component in parental magmas of Gorgona Island komatiites. Geophys Res Abst 5, 14774 (2003).

Karlstrom, L., Dufek, J., Manga, M. Magma chamber stability in arc and continental crust. Journal of Volcanology and Geothermal Research, 190, 249–270 (2010).

Kelemen, P.B., Hanghøj, K., and Greene, A.R. One view of the geochemistry of subduction-related magmatic arcs, with an emphasis on primitive andesite and lower crust. The Crust, Treatise on Geochemistry, ed. Rudnick RL (Elsevier-Pergamon, Oxford), v. 3, 593–659 (2003).

Kent, A.J.R., and Hagemann, S. Constraints on the timing of lode-gold mineralisation in the Wiluna greenstone belt, Yilgarn Craton, Western Australia. Australian Journal of Earth Sciences, 43, 573-588 (1996).

Kerr, A., Marriner, G., Arndt, N.T. The petrogenesis of Gorgona komatiites, picrites and basalts: new field, petrographic and geochemical constraints. Lithos, 37, 245–260 (1995).

Kitayama, Y.C., and Francis, D. Iron-rich alkaline magmatism in the Archean Wawa greenstone belts (Ontario, Canada). Precambrian Res. 252, 53–70 (2014).

Kleine, T., Münker, C., Mezger, K. & Palme, H. Rapid accretion and early core formation on asteroids and the terrestrial planets from Hf-W chronometry. Nature 418, 952-955 (2002).

Korenaga, J. Urey ratio and the structure and evolution of Earth's mantle. Rev. Geophys. 46, 1–32 (2008).

Kositcin, N., Brown, S.J.A., Barley, M.E., Krapež, B., Cassidy, K.F, and Champion, D.C. SHRIMP U-Pb age constraints on the Later Archaean tectonostratigraphic architecture of the Eastern Goldfields superterrane, Yilgarn craton, Western Australia: Precambrian Research, v. 161, 5–33 (2008).

Krapež, B. and Hand, J.L. Late Archaean deep-marine volcaniclastic sedimentation in an arc-related basin: the Kalgoorlie sequence of the Eastern Goldfields superterrane, Yilgarn craton, Western Australia. Precambrian Research, v. 161, 89–113 (2008).

Krapež, B. Brown, S.J.A., Hand, J, Barley, M.E., and Cas, R.A.F. Age constraints on recycled crust and supracrustal sources of Archean metasedimentary sequences, Eastern Goldfields province, Western Australia. Evidence from SHRIMP zircon dating: Tectonophysics, v. 322, p. 89–133 (2000).

Krapež, B. Sequence-stratigraphic concepts applied to the identification of depositional basins and global tectonic cycles. Australian Journal of Earth Science, v. 44, 1–36 (1997).

Krapež, B., Barley, M.E., and Brown, S.J.A. Late Archaean synorogenic basins of the Eastern Goldfields superterrane, Yilgarn craton, Western Australia. Part 1. Kalgoorlie and Gindalbie terranes. Precambrian Research, v. 161, 135–153 (2008).

Kyser, T.K., Cameron, W.E., Nisbet, E.G. Boninite petrogenesis and alteration history: constraints from stable isotope compositions of boninites from Cape Vogel, New Caledonia and Cyprus. Contrib Miner Petrol 93, 222–226 (1986).

Kyser, T.K., O'Neil, J.R. Hydrogen isotope systematics of submarine basalts. Geochim Cosmochim Acta 48, 2123–2133 (1984).

Laflèche, M.R., Dupuy, C., Bougault, H. Geochemistry and petrogenesis of Archean mafic volcanic rocks of the southern Abitibi belt, Quebec. Precambrian Research, 57, 207–241 (1992).

Langone, A., Tiepolo, M., Morishita, T., Tribuzio, R. Cretaceous amphibole-rich intrusives with high-Mg andesite affinity from Japan: a petrological and geochronological study. (AGU 2009)

Larson, M.S., Stone, W.E., Morris, W.A. & C rocket, J.H. Magnetic signature of magnetite-enriched rocks hosting platinum-group element mineralization within the Archean Boston Creek Flow. Geophysics 63, 40-445 (1998).

Lassiter, J.C., and Hauri, E.H. Osmium-isotope variations in Hawaiian lavas: evidence for recycled oceanic lithosphere in the Hawaiian plume. Earth and Planetary Science Letters 164, 483–496 (1998).

Laubscher, H.P. Jura, Alps and the boundary of the Adria subplate. Tectonophysics, 483, 223–239 (2010).

Laubscher, H.P. The late Alpine (Periadriatic) intrusions and the Insubric Line. Memorie della Società Geologica Italiana, 26, 21–20 (1983).

Leake, B.E., Woolley, A.R., Arps, C.E.S., Birch, W.D., Gilbert, M.C., Grice, J.D., Hawthorne, F.C., Kato, A., Kisch, H.J., Krivovichev, V.G., Linthout, K., Laird, J., Mandarino, J.A., Maresch, W.V., Nickel, E.H., Rock, N.M.S., Schumacher, J.C., Smith, D.C., Stephenson, N.C.N., Ungaretti, L., Whittaker, E.J.W., Guo, Y.Z. Nomenclature of amphiboles: report of the subcommittee on amphiboles of the International Mineralogical Association, commission on new minerals and mineral names. Am Miner 82, 1019–1037 (1997).

Lee, C.T.A., Harbert, A., Leeman, W.P. Extension of lattice strain theory to mineral/mineral rare-earth element partitioning: An approach for assessing disequilibrium and developing internally consistent partition coefficients between olivine, orthopyroxene, clinopyroxene and basaltic melt. Geochimica et Cosmochimica Acta 71, 481–496 (2007).

Lee, C.T.A., Leeman, W.P, Dante Canil, D., and A Li, Z.X. Similar V/Sc Systematics in MORB and Arc Basalts: Implications for the Oxygen Fugacities of their Mantle Source Regions. Journal of Petrology 46, 2313–2336 (2005).

Leeman, W.P., and Sisson, V.B. Geochemistry of boron and its implications for crustal and mantle processes. In Boron: Mineralogy, Petrology and Geochemistry, vol. 33, 645–695 (1996).

Lentz, R.C.F., McCoy, T.J., Collins, L.E., Corrigan, C.M., Benedix, G.K., Taylor, G.J., and Harvey, R.P. Theo's Flow, Ontario, Canada: A terrestrial analog for the Martian nakhlite meteorites. The Geological Society of America, Special Paper 483 (2011).

Lesher, C.M., and Arndt, N.T. REE and Nd isotope geochemistry, petrogenesis and volcanic evolution of contaminated komatiites at Kambalda, Western Australia. Lithos, 34, 127–158 (1995).

Li, Z.-X. A., Lee, C.-T. A. The constancy of upper mantle fO_2 through time inferred from V/Sc ratios in basalts. Earth and Planetary Science Letters, 228, 483–493 (2004).

Lightfoot, P.C., Hawkesworth, C.J., Hergt, J., Naldrett, A.J., Gorbachev, N.S., Fedorenko, V.A., Doherty, W. Remobilisation of the continental lithosphere by a mantle plume; major-, traceelement, and Sr-, Nd-, and Pb-isotope evidence from picritic and tholeiitic lavas of the Noril'sk District, Siberian Trap, Russia. Contributions to Mineralogy and Petrology, 114, 171-188 (1993).

Liu, S.F., Champion, D.C., and Cassidy, K.F. Geology of the Sir Samuel 1:250000 sheet area, Western Australia. Geoscience Australia Record 2002/14, 57 p. (2002).

Locmelis, M., Barnes, S. J., Pearson, N. J. & Fiorentini, M. L. Anomalous Sulfur-Poor Platinum Group Element Mineralization in Komatiitic Cumulates, Mount Clifford, Western Australia. Economic Geology 104, 841-855 (2009).

Luffi, P., Saleeby, J.B, Lee, C.T.A., and Ducea, M.N. Lithospheric mantle duplex beneath the central Mojave Desert revealed by xenoliths from Dish Hill, California. Journal of Geophysical Research, v. 114, B03202 (2009).

Ma, L., Wang, Q., Li, Z.X., Wyman, D.A., Jiang, Z.Q., Yang, J.H., Gou, G.N., Guo, H.F. Late Cretaceous (ca. 93 Ma) norites and hornblendites in the Milin area, eastern Gangdese: Lithosphere–asthenosphere interaction during slab roll-back and an insight into early Late Cretaceous (ca. 100–80 Ma) magmatic "flare-up" in southern Lhasa (Tibet). Lithos 172-173, 17-30 (2013).

Ma, L., Wang, Q., Wyman, D. A., Jiang, Z. Q., Yang, J. H., Li, Q.L., Gou, G.N., Guo, H.F. Late Cretaceous crustal growth in the Gangdese area, southern Tibet: Petrological and Sr–Nd–Hf–O isotopic evidence from Zhengga diorite–gabbro. Chemical Geology, 349–350, 54–70 (2013).

MacRae, N.D. Ultramafic intrusion of the Abitibi Area, Ontario; Can. Journ. Earth Sciences, Vol 6, 281-303 (1969).

Maier, W. D., Barnes, S. J., Campbell, I. H., Fiorentini, M. L., Poltonen, P., Barnes S. J. & Smithies, R. H. Progressive mixing of meteoritic veneer into the early Earth's deep mantle. Nature 460, 620-623 (2009)

Mangan, M.T., and Marsh, B.D. Solidification front fractionation in phenocryst-free sheet-like magma bodies: The Journal of Geology, v. 100, 605–620, (1992).

Marshall, H.R., Wanless, V.D., Shimizu, N., Philip, von Strandmann, P.A.E., Elliott, T., Monteleone, B.D. The boron and lithium isotopic composition of mid-ocean ridge basalts and the mantle. Geochimica et Cosmochimica Acta 207, 102–138 (2017).

Martin, R. F. Amphiboles in the Igneous Environment. Rev. Mineralogy & Geochemistry 67, 323-358 (2007).

Mayer, B., Jung, S., Romer, R.L., Pfänder, J.A., Klugel, A., Pack, A. & Groner, E. Amphibole in alkaline basalts from intraplate settings: implications for the petrogenesis of alkaline lavas from the metasomatised lithospheric mantle. Contrib. Mineral. Petrol. 167:989 (2014).

McDonough, W.F., Sun, S.S., The chemical composition of the Earth. Chem. Geol. 120, 223–253 (1995).

McIver, J.R., Cawthorn, R.G., and Wyatt, B.A. The Ventersdorp Supergroup – the youngest komatiitic sequence in southern Africa. In Komatiites (eds. N. T. Arndt and E. G. Nisbet). Allen and Unwin, Boston, pp. 81–90 (1982).

Melekhova, E., Annen, C. & Blundy, J. Compositional gaps in igneous rock suites controlled by magma system heat and water content. Nat. Geosci. 6, 385–390 (2013).

Melezhik, V.A., Hanski, E.J., 2012. The Pechenga Greenstone Belt. In: Melezhik, V.A., Prave, A.R., Hanski, E.J., Fallick, A.E., Lepland, A., Kump, L.R., Strauss, H. (Eds.), Reading the Archive of Earth's Oxygenation. Volume 1: The Palaeoproterozoicof Fennoscandia as Context for the Fennoscandian Arctic Russia – Drilling EarlyEarth Project. Springer-Verlag, Berlin, Heidelberg, 289–385 (2012).

Melezhik, V.A., Hudson-Edwards, K.A., Skuf'in, P.K., Nilson, L.P. Pechenga area, Russia: Part 1. Geological setting and comparison with Pasvik, Norway. Trans. Inst. Mime. Metall., Sect. B, Appl. Earth Sci., 103, B129–B145 (1994).

Melezhik, V.A., Sturt, B.A. General geology and evolutionary history ofthe early Proterozoic Polmak–Pasvik–Pechenga–Imandra/Varzuga–Ust'Ponoy Greenstone Belt in the northeastern Baltic Shield. Earth-Sci. Rev., 36, 205–241 (1994).

Melezhik, V.A., Fallick, A.E. A widespread positive $\delta^{13}C_{carb}$ anomaly at around 2.33–2.06 Ga on the Fennoscandian Shield: a paradox? Terra Nova 8, 141–157 (1996).

Michael, P.J., and Schilling, J. Chlorine in mid-ocean ridge magmas: evidence for assimilation of seawater-influenced components. Geochim. Cosmochim. Acta 53, 3131–3143 (1989).

Milidragovic, D., and Francis, D., Ferropicrite-driven reworking of the Ungava craton and the genesis of Neoarchean pyroxene-granitoids. Earth Planet. Sci. Lett. 386, 138–148 (2014).

Milidragovic, D., Francis, D. Ca. 2.7 Ga ferropicritic magmatism: A record of Fe-rich heterogeneities during Neoarchean global mantle melting. Geochim. Cosmochim. Acta 185, 44–63 (2016).

Milidragovic, D., Francis, D., Weis, D. and Constantin, M. Neoarchean (c. 2.7 Ga) plutons of the Ungava Craton, Que´bec, Canada: parental magma compositions and implications for Fe-rich mantle source regions. Journal of Petrology 55, 2481–2511 (2014).

Miller, G.H., Stolper, E.M., & Ahrens, T.J. The equation of state of a molten komatiite 1. Shock wave compression to 36 GPa. Journal of Geophysical Research 96, 831–848 (1991).

Mole, D.R. Evaluating the lithospheric architecture of the Archaean Yilgarn craton in space and time: Implications for komatiite volcanism and earth evolution. PhD thesis, University of Western Australia, 746 p (2012).

Mole, D.R., Fiorentini, M.L., Cassidy, K.F., Kirkland, C.L., Thebaud, N., McCuaig, T.C., Doublier, M.P., Duuring, M.L., Romano, S.S., Maas, E.A., Belousova, E.A., Barnes, S.J., and Miller, J. Crustal evolution, intracratonic architecture and the metallogeny of an Archaean craton. Geological Society London, Special Publication 393, 23–80 (2013).

Mole, D.R., Fiorentini, M.L., Thebaud, N., Cassidy, K.F., McCuaig, T.C., Kirkland, C.L, Romano, S.S., Doublier, M.P., Belousova, E.A., Barnes, S.J., and Miller, J. Archean komatiite volcanism controlled by the evolution of early continents: Proceedings of National Academy of Sciences, v. 111, 10,083–10,088 (2014).

Molina, J.F., Moreno, J.A., Castro, A., Rodruiguez, C., and Fershtater, G.B. Calcic amphibole thermobarometry in metamorphic and igneous rocks: new calibrations based on plagioclase/amphibole Al-Si partitioning and amphiboleliquid Mg partitioning. Lithos, 232, 286–305 (2015).

Montrasio, A., Tromsdorff, V. Guida all'escursione del massiccio di Val Masino-Bregaglia Val Malenco occidentale, Sondrio. Mem Soc Geol It 26, 421–434 (1983).

Morris, P.A. and Witt, W.K. Geochemistry and tectonic setting of two contrasting felsic volcanic associations in the Eastern Goldfields, Western Australia: Precambrian Research, v. 83, p. 83–107 (1997).

Morris, P.A. Archaean mafic and ultramafic rocks, Menzies to Norseman, Western Australia. Geological Survey of Western Australia Report 55, 80 p (1993).

Münker, C. and Crawford, A. Cambrian arc along the SE Gondwana active margin: a synthesis from Tasmania-New Zealand-Australia-Antarctica correlations. Tectonics 19, 415-432 (2000).

Münker, C., Fonseca, R. O. C. & Schulz, T. Silicate Earth's missing niobium may have been sequestered into asteroidal cores. Nature Geosciences 10, 822-826 (2017).

Münker, C., Pfänder, J. A., Weyer, S., Büchl, A., Kleine, T., Mezger, K. Evolution of Planetary Cores and the Earth-Moon System from Nb/Ta Systematics. Science 301, 84-87 (2003).

Müntener, O., & Ulmer, P. Experimentally derived high-pressure cumulates from hydrous arc magmas and consequences for the seismic velocity structure of lower arc crust. Geophysical Research Letters, v. 33, L21308 (2006).

Müntener, O., Kelemen, P.B., and T. L. Grove. The role of H_2O during crystallization of primitive arc magmas under uppermost mantle conditions and genesis of igneous pyroxenites: An experimental study, Contrib. Mineral. Petrol., 141, 643– 658 (2001).

Myers, J.S. The generation and assembly of an Archaean supercontinent: Evidence from the Yilgarn craton, Western Australia. Geological Society of London Special Publication 95, p. 1–10 (1997).

Negrutsa, V.Z. Evolution of exogenic prosesses in the Pechenga paleobasin. F.P. Mitrofanov, V.F. Smolkin (Eds.), Magmatism, Sedimentogenesis and Geodynamics of the Pechenga Paleorift. Geological Institute, Kola Science Centre, Russian Academy of Sciences, 101-123 (1995). (in Russian)

Nelson, D.R. Evolution of the Archaean granite-greenstone terranes of the Eastern Goldfields, Western Australia: SHRIMP U-Pb zircon constraints. Precambrian Research, v. 83, p. 57–81 (1997).

Nesbitt, R.W., Sun, S.S., Purvis, A.C. Komatiites: geochemistry and genesis. Canadian Mineralogist, 17, 165–186 (1979).

Nimis, P. A clinopyroxene geobarometer for basaltic systems based on crystal-structure modeling. Contrib Mineral Petrol 121, 115-125 (1995).

Nimis, P., and Ulmer, P. Clinopyroxene geobarometry of magmatic rocks Part 1: An expanded structural geobarometer for anhydrous and hydrous, basic and ultrabasic systems. Contrib Mineral Petrol (1998) 133, 122-135 (1998).

Nisbet, E.G. The tectonic setting and petrogenesis of komatiites. In: N.T. Arndt and E.G. Nisbet (eds.) Komatiites. 501–520. London: George Allen and Unwin. (1982)

Oberti, R., Ungaretti, L., Cannillo, E., and Hawthorne, F.C. The mechanism of Cl incorporation into amphibole. Am. Mineral. 78, 746–752 (1993)

Ohtani, E. Generation of komatiite magma and gravitational differentiation in the deep upper mantle. Earth and Planetary Science Letters, 67, 261–272 (1984).

Ohtani, E., Suzuki, A., Kato, T. Flotation of olivine and diamond in mantle melt at high pressure: implications for fractionation in the deep mantle and ultra-deep origin of diamond. In: M. H. Manghnani and T. Yagi (eds) Properties of Earth and Planetary Materials, 227–239 (1998).

Okuchi, T. Hydrogen Partitioning into Molten Iron at High Pressure: Implications for Earth's Core. Science 278, 1781-1784 (1997).

Ottolini, L., Bottazzi, P., Zanetti, A. Quantitative analysis of hydrogen, fluorine and chlorine in silicates using energy filtering. Proceedings of the Ninth International Conference on Secondary Ion Mass Spectrometry (SIMS IX), Yokohama, Japan, 7-11 November 1993. Eds. Benninghoven, A., Nihei, Y., Shimizu, R., Werner, H.W., Jhon Wiley & Son, 191-194 (1994).

Ottolini, L., Bottazzi, P., Zanetti, A., Vannucci, R. Determination of hydrogen in silicates by secondary ion mass spectrometry. Analyst (London), 120, 1309-1313 (1995).

Ottolini, L.P., and Le Févre, B. SIMS analysis of chlorine in metasomatised upper-mantle rocks. Microchim. Acta, 161, 329-336 (2008).

Parman, S.W., and Grove, T.L. Komatiites in the plume debate. Geological Society of America Special Paper 388, 249-256 (2005).

Parman, S.W., Dann, J.C., Grove, T.L., and de Wit, M.J. Emplacement conditions of komatiite magmas from the 3.49 Ga Komati Formation, Barberton Greenstone Belt, South Africa: Earth and Planetary Science Letters, v. 150, 303–323 (1997).

Parman, S.W., Grove, T.L., and Dann, J.C. The production of Barberton komatiites in an Archean subduction zone: Geophysical Research Letters, v. 28, 2513–2516 (2001).

Parman, S.W., Shimizu, N., Grove, T.L., and Dann, J.C. Constraints on the pre-metamorphic trace element composition of Barberton komatiites from ion probe analyses of preserved clinopyroxenes: Contributions to Mineralogy and Petrology, v. 144, 383–396 (2003).

Pearce, J.A. Trace element characteristics of lavas from destructive plate boundaries. In: R.S. Thorp (Ed.) - Andesites: Orogenic Andesites and Related Rocks, John Wiley and Sons, New York, 525–548 (1982).

Pearson, D.G., Brenker, F.E., Nestola, F., McNeill, J., Nasdala, L., Hutchison, M.T., Matveev, S., Mather, K., Silversmit, G., Schmitz, S., Vekemans, B., and Vincze, L. Hydrous mantle transition zone indicated by ringwoodite included within diamond. Nature, v. 507, 221-224 (2014).

Pepin, R.O., Porcelli, D. Xenon isotope systematics, giant impacts, and mantle degassing of the early Earth. Earth and Planetary Science Letters, 250, 470-485 (2006).

Perring, C. Volcanological and Structural Controls on Mineralization at the Mount Keith and Cliffs Komatiite-Associated Nickel Sulfide Deposits, Agnew-Wiluna Belt, Western Australia—Implications for Ore Genesis and Targeting. Economic Geology, v. 110, 1669–1695 (2015).

Perring, C.S. A 3-D geological and structural synthesis of the Leinster area of the Agnew-Wiluna belt, Yilgarn craton, Western Australia, with special reference to the volcanological setting of komatiite-associated nickel sulfide deposits. Economic Geology, v. 110, 469–503 (2015).

Petford, N., and Gallagher, K. Partial melting of mafic (amphibolitic) lower crust by periodic influx of basaltic magma: Earth and Planetary Science Letters, v. 193, p. 483 (2001).

Pfänder, J. A., Münker, C., Stracke, A., Mezger, K. Nb/Ta and Zr/Hf in ocean island basalts — Implications for crust–mantle differentiation and the fate of Niobium. Earth Planet. Sci. Lett. 254, 158-172 (2007).

Pfänder, J., Jung, S., Münker, C., Strake, A., Mezger, K. A possible high Nb/Ta reservoir in the continental lithospheric mantle and consequences on the global Nb budget — evidence from continental basalts from Central Germany. Geochim. Cosmochim. Acta 77, 232–251 (2012).

Pickett, D.A., and Saleeby, J.B. Thermobarometric constraints on the depth of exposure and conditions of plutonism and metamorphism at deep levels of the Sierra Nevada Batholith, Tehachipi Mountains, California. Journal of Geophysical Research, 98, 609–629 (1993).

Pineau, F., Shilobreeva, S., Kadik, A., Javoy, M. Water solubility and D/H fractionation in the system basaltic andesite–H_2O at 1250 °C and between 0.5 and 3 kbars. Chemical Geology, 147, 173-184 (1998).

Predovsky, A.A., Fedotov, Zh.A., Zhangurov, A.M. Geochemistry of the Pechenga Complex. Nauka, Leningrad (1974) (in Russian).

Puchtel, I. S., Walker, R. J., Touboul, M., Nisbet, E. G. & Byerly, G. R. Insights into early Earth from the Pt-Re-Os isotope and highly siderophile element abundance systematics of Barberton komatiites. Geochim. Cosmochim. Acta 125, 394-413 (2014).

Putchel, I. S., Blichert-Toft, J., Touboul, M., Walker, R. J., Byerly, G. R., Nisbet, E. G., Anhaeusser, C. R. Insights into early Earth from Barberton komatiites: Evidence from lithophile isotope and trace element systematics. Geochim. Cosmochim. Acta 108, 63-90 (2013).

Putirka, K.D. Amphibole thermometers and barometers for igneous systems and some implications for eruption mechanisms of felsic magmas at arc volcanoes. Amer Mineral, v. 101, 841–858 (2016).

Putirka, K.D. Thermometers and barometers for volcanic systems. Reviews in Mineralogy and Geochemistry, 69, 61–120 (2008).

Rajamani, V., Shivkumar, K., Hanson, G.N., and Shirey, S.B. Geochemistry and petrogenesis of amphibolites, Kolar Schist Belt, South India: evidence for komatiitic magma derived by low percentages of melting of the mantle. Journal of Petrology, 26, 92–123 (1985).

Ridolfi, F., and Renzulli, A. Calcic amphiboles in calc-alkaline and alkaline magmas: thermobarometric and chemometric empirical equations valid up to 1,130 °C and 2.2 GPa. Contrib Mineral Petrol 163, 877–895 (2012).

Rigden, S.B., Ahrens, T.J., Stolper, E.M. Densities of liquid silicates at high pressure. Science, 226, 1071–1074 (1984).

Righter, K., and Carmichael, I.S.E. Mega-xenocrystsi n alkali olivine basalts: Fragments of disrupted mantle assemblages. American Mineralogist, 78, 1230-1245 (1993).

Ringwood, A.E., and Major, A. Synthesis of majorite and other high-pressure garnets and perovskites. Earth and Planetary Science Letters 12, 411–418 (1971).

Rino, S., Komiya, T., Windley, B.F., Katayama, I., Motoki, A., and Hirata, T. Major episodic increases of continental crustal growth determined from zircon ages of river sands; implications for mantle overturns in the Early Precambrian. Phys. Earth Planet. Inter. 146, 369–394 (2004).

Roberge, M., Bureau, H., Bolfan-Casanova, N., Frost, D.J., Raepsaet, C., Surble, S., Khodja, H., Auzende, A.-L., Fiquet, G. Is the transition zone a deep reservoir for fluorine? Earth Planet. Sci. Lett. 429, 25–32 (2015).

Roberge, M., Bureau, H., Bolfan-Casanova, N., Raepsaet, C., Surble, S., Khodja, H., Auzende, A.-L., Cordier, P., Fiquet, G. Chlorine in wadsleyite and ringwoodite: an experimental study. Earth Planet. Sci. Lett. 467, 99–107 (2017).

Robin-Popieul, C.C.M., Arndt, N.T., Chauvel, C., Byerly, G.R., Sobolev, A.V., and Wilson, A. A new model for Barberton komatiites: deep critical melting with high melt retention. Journal of Petrology 53, 2191–2229 (2012).

Rocchi, S., Di Vincenzo, G. & Ghezzo, C. The Terra Nova Intrusive Complex (Victoria Land, Antarctica). Terra Antarctica Reports 10, 49 pp (2004).

Rocchi, S., Tonarini, S., Armienti, P., Innocenti, F. & Manetti, P. Geochemical and isotopic structure of the early Paleozoic active margin of Gondwana in northern Victoria Land, Antarctica.Tectonophysics 284, 261-281 (1998).

Rose-Koga, E.F., Koga, K.T., Hamada, M., Hélouis, T., Whitehouse, M.J., Shimizu, N. Volatile (F and Cl) concentrations in Iwate olivine-hosted melt inclusions indicating low-temperature subduction. Earth Planets Space 66, 81 (2014).

Rosengren, N. M., Cas, R. A. F., Beresford, S. W., Palich, B. M. Reconstruction of an extensive Archaean dacitic submarine volcanic complex associated with the komatiite-hosted Mt Keith nickel deposit, Agnew-Wiluna Greenstone Belt, Yilgarn Craton, Western Australia. Precambrian Research 161, 34-52 (2008).

Rosengren, N.M. Architecture and emplacement origin of an archaean komatiitic dunite and associated NiS mineralisation: Mt Keith, Agnew-Wiluna Greenstone Belt, Yilgarn Craton, Western Australia, Unpublished PhD Thesis, Monash University, Australia (2004).

Rosengren, N.M., Beresford, S.W., Grguric, B.A., Cas, R.A.F. An intrusive origin for the komatiitic-dunite hosted Mount Keith disseminated nickel sulphide deposit, Western Australia. Econ Geol 100, 149–156 (2005).

Rudnick, R.L., and Fountain, D.M. Nature and composition of the continental crust: a lower crustal perspective. Reviews of Geophysics, 33, 267-309 (1995).

Saccani, S. A new method of discriminating different types of post-Archean ophiolitic basalts and their tectonic significance using Th-Nb and Ce-Dy-Yb systematics Geoscience Frontiers, v. 6, 481-501 (2015).

Sandeman, H., Hanmer, S., Davis, W., Ryan, J., and Peterson, T. Neoarchaean volcanic rocks, Central Hearne supracrustal belt, Western Churchill Province, Canada: geochemical and isotopic evidence supporting intra-oceanic, supra-subduction zone extension. Precambrian Res. 134, 113–141 (2004).

Sato, D., Matsuura, H., Yamamoto, T. Timing of the Late Cretaceous ignimbrite flare-up at the eastern margin of the Eurasian Plate: New zircon U–Pb ages from the Aioi–Arima–Koto region of SW Japan. J. of Volcanology and Geothermal Research 310, 89-97 (2016).

Satterly, J. Geology of Munro Township: Ontario Department of Mines Annual Report 60 (8), 1–60 (1951).

Satterly, J. Geology of Harker Township. Ontario Department of Mines, Annual Report for 1951, Vol 60, part 7, 47 p. (1952).

Satterly, J. Geology of the North Half of Holloway Township. Ontario Department of Mines, Annual Report for 1952, Vol 61, part 7, 38 p. (1954).

Schmidt, M.W. Amphibole composition in tonalite as a function of pressure: an experimental calibration of the Al-in-hornblende barometer. Contributions to Mineralogy and Petrology, 110, 304–310 (1992).

Schoenberg, R., Kamber, B. S., Collerson, K. D. & Moorbarth, S. Tungsten isotope evidence from ~3.8-Gyr metamorphosed sediments for early meteorite bombardment of the Earth. Nature 418, 403-405 (2002).

Schulz, K.J. Magnesian basalts from the Archean terrains of Minnesota. In Komatiites (eds. N. T. Arndt and E. G. Nisbet). George Allen & Unwin, London, 171–186 (1982).

Schweitzer, J., and Kröner, A. Geochemistry and petrogenesis of Early Proterozoic intracratonic volcanic rocks of the Ventersdorp Supergroup, South Africa. Chem. Geol. 51, 265–288 (1985).

Sengör, A.M.C. The Cimmeride Orogenic System and the Tectonics of Eurasia. Geological Society of America Special Paper, p. 195 (1984).

Shaw, A.M., Hauri, E.H., Fischer, T.P., Hilton, D.R., Kelley K.A. Hydrogen isotopes in Mariana arc melt inclusions: Implications for subduction dehydration and the deep-Earth water cycle. Earth and Planetary Science Letters, 275, 138–145 (2008).

Shirey, S.B. Initial Os isotopic compositions of Munro Township, Ontario, komatiites revisited: Additional evidence for near-chondritic, late-Archean convecting mantle beneath the Superior Province. Abstracts of the 7th Goldschmidt Conference: LPI Contribution 921, Abstract 2375.

Sisson, T.W. Hornblende-Melt Trace-Element Partitioning Measured by Ion Microprobe. Chemical Geology, 117, 331-344 (1994).

Sisson, T.W., and Grove, T.L. Experimental investigations of the role of H2O in calc-alkaline differentiation and subduction zone magmatism: Contributions to Mineralogy and Petrology, v. 113, 143–166 (1993).

Skuf'in, P.K. Evolution of the volcanism of the ore-bearing Pechenga structure (Kola Peninsula). Geology of Ore Deposits 35, 271–283 (1993) (in Russian).

Skuf'in, P.K., Bayanova, T.B. Early Proterozoic central-type volcano in thePechenga Structure and its relation to the ore-bearing gabbro-wehrlite complexof the Kola Peninsula. Petrology 14, 609–627 (2006).

Skuf'in, P.K., Theart, H.F.J. Geochemical and tectono-magmatic evolution ofthe volcano-sedimentary rocks of Pechenga and other greenstone fragments ofthe Kola Greenstone Belt. Precambrian Research 141, 1–48 (2005).

Smith, D.J. Clinopyroxene precursors to amphibole sponge in arc crust. Nature Communications, 5, 4329 (2014).

Smith, D.J., Petterson, M.G., Saunders, A.D., Millar, I.L., Jenkin, G.R.T., Toba, T., Naden, J., Cook, J.M. The petrogenesis of sodic island arc magmas at Savo volcano, Solomon Islands. Contrib Mineral Petrol 158, 785–801 (2009).

Smithies, R.H., and Champion, D.C. Geochemistry of felsic igneous alkaline rocks in the Eastern Goldfields, Yilgarn craton, Western Australia: A result of lower crustal delamination—implications for late Archaean tectonic evolution. Journal of the Geological Society of London, v. 156, 561–576 (1999).

Smolkin V. F., Borisova V. V. Nickel-bearingintrusive magmatism (gabbro-wehrlite formation). In: F. P. Mitrofanov and V. F. Smolkin (Eds.). Magmatism, Sedimentogenesis, and Geodynamics of the Pechenga Paleorift, Russian Academy of Sciences, Kola Science Centre, Apatity, 183–219 (1995) (in Russian).

Smolkin, V.F. Petrology of the Pilgüjarvi ore-bearing intrusion. VINITI, No. 2114-77. Geological Institute of the Academy of Science of the USSR, Apatity, p. 216 (1977) (in Russian).

Smolkin, V.F., Balashov, Yu.A., Hanski, E., Huhma, H., Vaasjoki, M., Walker, R. The isotopic age of the ferropicritic volcano-plutonic association of the Pechengazone. In: Bibikova, E.V. (Ed.), Isotopic Dating of Endogenic Ore Formations.Nauka, Moscow, pp. 56–73 (1993) (in Russian).

Smolkin, V.F., Bayanova, T.B., Fedotov, Zh.A. Ore-bearing maficultramafic rocks of the Pechenga–Allarechka area, Kola region: isotopic dating. Proceedings of the II Russian Conference on Isotope Geochemistry. St. Petersburg, pp. 467–470 (2003) (in Russian).

Smolkin, V.F., Hanski, E., Huhma, H., Fedotov, H.Zh. Sm-Nd and U-Pb Isotopic Study of The Nyasyukka Dike Complex, Kola Peninsula, Russia. (2015)

Smolkin, V.F., Kozhevnikov, V.N., Kapitonov, I.N. First results of in situ U-Pbdating of zircon from the Pechenga metasediments and turbidites and geo-dynamic reconstructions. In: Voytekhovsky, Yu.L. (Ed.), Mineralogy, Petrologyand Ores of the Kola Region. Proceedings of VIII All-Russian Fersman Scientific Session Dedicated to the 135th Anniversary of Birth of Acad. D.S. Belyankin, April18–19, 2011. Publishing House K & M, Apatity, pp. 208–213 (2011) (in Russian).

Sobolev, A.V, Hofmann, A.W., Sobolev, S.V., and Nikogosian, I.K. An olivine-free mantle source of Hawaiian shield basalts. Nature, 434, 590-597 (2005).

Sobolev, A.V., Chaussidon, M. H_2O concentrations in primary melts from suprasubduction zones and mid-ocean ridges: implications for H_2O storage and recycling in the mantle. Earth Planet. Sci. Lett. 137, 45–55 (1996).

Sobolev, A.V., Hofmann, A.W., Kuzmin, D.V., Yaxley, G.M., Nicholas T. Arndt, N.T., Chung, S.L., Danyushevsky, L.V., Elliott, T., Frey, F.A., Garcia, M.O., Andrey A. Gurenko, A.A., Kamenetsky, V.S., Kerr, A.C., Krivolutskaya, N.A., Matvienkov, V.V., Nikogosian, I.K., Rocholl, A., Sigurdsson, I.A., Sushchevskaya, N.M., Tekla, M. The Amount of Recycled Crust in Sources of Mantle-Derived Melts. Science, 316, 412-417 (2007).

Sobolev, A.V., Migdisov, A.A., Portnyagin, M.V. Incompatible element partitioning between clinopyroxene and basalt revealed by the study of melt inclusions inminerals from Troodos lavas, Cyprus. Petrol 4, 307-317 (1996)

Solano, J.M.S., Jackson, M.D., Sparks, R.S.J., Blundy, J.D. Evolution of major and trace element composition during melt migration through crystalline mush: implications for chemical differentiation in the crust. American Journal of Science, v. 314, 895–939 (2014).

Solano, J.M.S., Jackson, M.D., Sparks, R.S.J., Blundy, J.D., and Annen, C. Melt Segregation in Deep Crustal Hot Zones: a Mechanism for Chemical Differentiation, Crustal Assimilation and the Formation of Evolved Magmas: Journal of Petrology, v. 53, 1999–2026 (2012).

Sossi, S.A., Eggins, S.M., Nesbitt, R.W., Nebel1, O., Hergt, J.M., Campbell, I.H., O'Neill1, H.St.C., Van Kranendonk, M., and Davies, D.R. Petrogenesis and Geochemistry of Archean Komatiites. Journal of Petrology, v. 0, 1–38 (2016).

Squire, R.J., Cas, R.A.F., and Champion, D.C. The Black Flag Group: A vector to ore at St Ives. Geoscience Australia Record 2007/14, 13–35 (2007).

Stein, M., and Hofmann, A.W. Mantle plumes and episodic crustal growth. Nature 372, 63–68 (1994).

Stepanov, A. S. and Hermann, J. Fractionation of Nb and Ta by biotite and phengite: Implications for the "missing Nb paradox". Geology 41, 303-306 (2013).

Stone W.E., Crocket, J.H., and Fleet, M.E. Sulfide-poor platinum-group mineralization in komatiitic systems: Boston Creek flow, layered basaltic komatiite, Abitibi belt, Ontario. Econ. Geol. 88, 817-836 (1993).

Stone, W. E., Crocket, J. H., Dickin, A. P. & Fleet, M. E. Origin of Archean ferropicrites: geochemical constraints from the Boston creek Flow, Abitibi greenstone belt, Ontario, Canada. Chemical Geology 121, 51-71 (1995).

Stone, W. E., Crocket, J. H., Fleet, M. E. Differentation processes in an unusual iron-rich alumina-poor Archean ultramafic/mafic igneous body, Ontario. Contrib. Mineral. Petrol. 119, 287-300 (1995)

Stone, W. E., Jensen, L. S. & Church, W. R. Petrography and geochemistry of an unusual Fe-rich basaltic komatiite from Boston Township, northeastern Ontario. Can. J. Earth Sci. 24, 2537-2550 (1987).

Stone, W.E., Crocket, J.H., and Fleet, M.E. Platinum-group mineral occurrence associated with flow-top amygdule sulfides in komatiitic basalt, Abitibi greenstone belt, Ontario. Mineralogy and Petrology, v. 56, 1–24 (1996).

Stone, W.E., Deloule, E., Larson, M.S., and Lesher, C.M. Evidence for hydrous high-MgO melts in the Precambrian. Geology 25, 143-146 (1997).

Stone, W.E., Deloule, E., Stone, M.S., 2003. Hydromagmatic amphibole in komatiitic, tholeiitic and ferropicritic units, Abitibi Greenstone Belt, Ontario and Québec: evidence for Archaean wet basic and ultrabasic melts. Mineral. Petrol. 77, 39–65 (2003).

Stone, W.E., Fleet, M.E., Crocket, J.H., and Kingston, D.M. Platinum-group minerals in pyroxenite from the Boston Creek Flow basaltic komatiite, Abitibi greenstone belt, Ontario. Can. Mineral. 30, 109-119 (1992).

Stone, W.E. Deloule, E., Beresford, S.W., Fiorentini, M.L. Anomalously high δD values for Archean ferropicrite melt: implications for magmatic degassing. Can. Mineral. 43, 1735–1744 (2005).

Stump, E. The Ross Orogen of the Transantarctic Mountains. Cambridge: Cambridge University Press, p. 284 (1995).

Sun, S.-S. Geochemical characteristics of Archean ultramafic and mafic volcanic rocks: implications for mantle composition and evolution. In: A. Kröner, G.N. Hanson and A.M. Goodwin (eds.) Archaean Geochemistry, 25–47 (1984).

Sun, S.-S. Ocean islands – plums or plumes? Nature 316, 103–104 (1985).

Sun, S.-S., and McDonough, W.F. Chemical and isotopic systematics of oceanic basalts: implications for mantle compositions and processes. Spec. Publ. Vol. Geol. Soc. London 42, 313–345 (1989).

Swager, C.P. Tectono-stratigraphy of late Archaean greenstone terranes in the southeastern Eastern Goldfields, Western Australia. Precambrian Research, v. 83, 11–42 (1997).

Takahashi, E. Space–time distribution of Late Mesozoic to Early Cenozoic magmatism in East Asia and its tectonic implication. In Hashimoto M. & Uyeda S. (eds). Accretion Tectonics in the Circum-Pacific Regions, 69–88 (1983).

Thurston, P.C., Ayer, J.A., Goutier, J., Hamilton, M.A. Depositional gaps in Abitibi greenstone belt stratigraphy: a key to exploration for syngenetic mineralization. Econ Geol 103, 1097–1134 (2008).

Tiepolo, M., Langone, A., Morishita, T., and Yuhara, M. On the Recycling of Amphibole-rich Ultramafic Intrusive Rocks in the Arc Crust: Evidence from Shikanoshima Island (Kyushu, Japan). Journal of Petrology, 53, 1255-1285 (2012).

Tiepolo, M. & Vannucci, R. The contribution of amphibole from deep arc crust to the silicate Earth's Nb budget. Lithos 208-209, 16-20 (2014).

Tiepolo, M., and Tribuzio, R. Petrology and U-Pb Zircon Geochronology of Amphibole-rich Cumulates with Sanukitic Affinity from Husky Ridge (NorthernVictoria Land, Antarctica): Insights into the Role of Amphibole in the Petrogenesis of Subduction-related Magmas. Journal of Petrology v. 49, 937-970 (2008).

Tiepolo, M., Bottazzi, P., Foley, S. F., Oberti, R., Vannucci, R. & Zanetti, A. Fractionation of Nb and Ta from Zr and Hf at Mantle Depths: the Role of titanian Pargasite and Kaersutite. Journal of Petrology 42, 221-232 (2001).

Tiepolo, M., Langone, A., Morishita, T., and Yuhara, M. On the Recycling of Amphibole-rich Ultramafic Intrusive Rocks in the Arc Crust: Evidence from Shikanoshima Island (Kyushu, Japan). Journal of Petrology, v. 53, 1255-1285 (2009).

Tiepolo, M., Oberti, R., Zanetti, A., Vannucci, R. and Foley S. Trace-Element Partitioning Between Amphibole and Silicate Melt: Mineralogical Society of America, Reviews in Mineralogy and Petrology v. 67, p. 417-452 (2007).

Tiepolo, M., Tribuzio, R. & Langone, A. High-Mg Andesite Petrogenesis by Amphibole Crystallization and Ultramafic Crust Assimilation: Evidence from Adamello Hornblendites (Central Alps, Italy). Journal of Petrology 52, 1011-1045 (2011).

Tiepolo, M., Tribuzio, R., Ji, Wu, F.Y., and Lustrino, M., Alpine Tethys closure as revealed by amphibole-rich mafic and ultramafic rocks from the Adamello and the Bergell intrusions (Central Alps). Journal of the Geological Society, 171, 793–799 (2014).

Tiepolo, M., Tribuzio, R., Vannucci, R. The compositions of mantle-derived melts developed. Contrib. Mineral. Petrol. 144, 1-15 (2002).

Tiepolo, M., Vannucci, R., Oberti, R., Foley, S., Bottazzi, P., Zanetti, A. Nb and Ta incorporation and fractionation in titanian pargasite and kaersutite: crystal-chemical constraints and implications for natural systems. Earth Planet. Sci. Lett. 176, 185-201 (2000).

Tiepolo, M., Zanetti, A., and Oberti, R. Detection, crystal-chemical mechanisms and petrological implications of $^{[6]}Ti^{4+}$ partitioning in pargasite and kaersutite. Eur. J. Mineral., 11, 345-354 (1999).

Tiepolo, M., Zanetti, A., Oberti, R., Brumm, R., Foley, S. & Vannucci, R. Trace-element partitioning between synthetic potassic-richterites and silicate melts, and contrasts with the partitioning behavior of pargasites and kearsutites. Eur. J. Mineral. **15**, 329-340 (2003).

Treiman, A.H. The nakhlite meteorites: Augite-rich igneous rocks from Mars: Chemie der Erde, v. 65, p. 203–270 (2005),

Tribuzio, R., Tiepolo, M. and Fiameni, S. A mafic-ultramafic cumulate sequence derived from boninite-type melts (Niagara Icefall, northern Victoria Land, Antarctica). Contributions to Mineralogy and Petrology, 155, 619–633 (2007).

Trofimovs, J., Tait, M.A., Cas, R.A.F., McArthur, A., Beresford, S.W. Can the role of thermal erosion in strongly deformed komatiite–Ni–Cu–(PGE) deposits be determined? Perseverance, Agnew-Wiluna Belt, Western Australia. Austr. J. Earth Sci. 50, 199–214 (2003).

Ulmer, P., Callegari, E., Sonderegger, U.C. Genesis of the mafic and ultramafic rocks and their genetical relations to the tonalitic-trondhjemitic granitoids of the southern part of the Adamello batholith (Northern Italy). Mem Soc Geol It 26, 171–222 (1983).

Van den Bleeken, G., and Koga, K.T. Experimentally determined distribution of fluorine and chlorine upon hydrous slab melting, and implications for F-Cl cycling through subduction zones. Geochim. Cosmochim. Acta 171, 353–373 (2015).

Van der Westhuizen, W.A., de Brutyn, H., and Meintjes, P.G. The Ventersdorp Supergroup: an overview. J. Afr. Earth Sci. 13, 83–105 (1991).

Van Kranendonk, M.J., Altermann, W., Beard, B.L., Hoffman, P.F., Johnson, C.M., Kasting, J.F., Melezhik, V.A., Nutman, A.P., Papineau, D., and Pirajno, F. A chronostratigraphic division of the Precambrian. In The Geologic Time Scale 2012 (eds. F. M. Gradstein, J. G. Ogg, M. Schmitz and G. Ogg). Elsevier B.V., 299–392 (2012).

Von Damm, K.L. Seafloor hydrothermal activity: Black smoker chemistry and chimneys. Ann. Rev. Earth Planet. Sci. 18, 173–204 (1990).

Vroon, P.Z., Lowry, D., van Bergen, M.J., Boyce, A.J., Mattey, D.P. Oxygen isotopic systematics of the Banda Arc: low δ18O despite involvement of subducted continental materials in magma genesis. Geochim. Cosmochim. Acta, 65, 589-609 (2001).

Wade, J. & Wood, B. J. The Earth's 'missing' niobium may be in the core. Nature 409, 75-78 (2001).

Wakita, K. Geology and tectonics of Japanese islands: A review – The key to understanding the geology of Asia. Journal of Asian Earth Sciences, 72, 75–87 (2013).

Wallace, P.J. Volatiles in subduction zone magmas: Concentrations and fl uxes based on melt inclusion and volatile gas data: Journal of Vol canology and Geothermal Research, v. 140, p. 217–240 (2005)

Walter, M.J. Melting of garnet peridotite and the origin of komatiite and depleted lithosphere. Journal of Petrology 39, 29–60 (1998).

Wen, D.R., Chung, S.L., Song, B., Iizuka, Y., Yang, H.J., Ji, J.Q., Liu, D.Y., Gallet, S.. Late Cretaceous Gangdese intrusions of adakitic geochemical characteristics, SE Tibet: petrogenesis and tectonic implications. Lithos 105, 1–11 (2008b).

Wen, D.R., Liu, D.Y., Chung, S.L., Chu, M.F., Ji, J.Q., Zhang, Q., Song, B., Lee, T.Y., Yeh, M.W., Lo, C.H.,. Zircon SHRIMP U–Pb ages of the Gangdese batholith and implications for Neotethyan subduction in southern Tibet. Chemical Geology, 252, 191–201 (2008a).

Wilshire, H. G., and Trask, N. J. Structural and textural relationships of amphibole and phlogopite in peridotite inclusions, Dish Hill, California: Amer. Mineral. 56, 240-255 (1971).

Wilshire, H. G., Schwarzman, E. C., and Trask, N. J. Distribution of ultramafic xenoliths at 12 North American Sites. U.S. Geological Survey Interagency Report: Astrogeology 42, 87 p. (1972).

Wilshire, H.G., Nielson Pike, J.E., Meyer, C.E., and Schwarzman, E.C. Amphibole-rich neins in lherzolite xenoliths, Dish Hill and Deadman Lake, California. American Journal of Science, 280-A, 576-593 (1980).

Wilson, A.H., and Versfeld, J.A. The early Archaean Nondweni greenstone belt, southern Kaapvaal Craton, South Africa, part II: Characteristics of the volcanic rocks and constraints on magma genesis: Precambrian Research, v. 67, 277–320 (1994).

Wilson, A.H., Shirey, S.B., and Carlson, R.W. Archaean ultra-depleted komatiites formed by hydrous melting of cratonic mantle. Nature, v. 423, 858-861 (2003).

Wooden, J.L., Czamanske, G.K., Fedorenko, V.A., et al. Isotopic and traceelement constraints on mantle and crustal contributions to Siberian continental flood basalts, Noril'sk area, Siberia. Geochimica et Cosmochimica Acta, 57, 3677–3704 (1993).

Woodland, A.B. & Jugo, P.J. A complex magmatic system beneath the Devès volcanic field, Massif Central, France: evidence from clinopyroxene megacrysts. Contrib. Mineral. Petrol. 153, 719-731 (2007).

Xie, Q., and Kerrich, R. Silicate-perovskite and majorite signaturekomatiites from the Archean Abitibi greenstone belt: Implications for early mantle differentiation and stratification, J. Geophys. Res., 99, 15799–15812, (1994).

Xiong, X., Keppler, H., Audetat, A., Ni, H., Sun, W., Li, Y. Partitioning of Nb and Ta between rutile and felsic melt and the fractionation of Nb/Ta during partial melting of hydrous metabasalt. Geochimica et Cosmochimica Acta 75, 1673–1692 (2011).

Yang, K., Arai, S., Yu, J., Yun, S.H., Kim, J.S. & Hwang, J.Y. Gabbroic xenoliths and megacrysts in the Pleisto-Holocene alkali basalts Jeju island, south Corea: the implications for the metasomatism of the lower continental crust. Lithos, 142-143, 201-215 (2012).

Yin, Q., Jacobsen, S. B., Yamashita, K., Blichert-Toft, J., Telouk, P. & Albarede, F. A short timescale for terrestrial planet formation from Hf–W chronometry of meteorites. Nature 418, 949-952 (2002).

Zagorodny, V.G., Mirskaya, D.D., Suslova, S.N. Geology of the PechengaSedimentary-Volcanogenic Series. Nauka, Leningrad (1964) (in Russian).

Zak, S., Makarov, V.N., Proskuryakov, V.V., Kochnev-Pervukhov, V.I., Zaskind, E.S., Batashev, E.V. Geology, magmatism and mineralization of the Pechenga ore field. Nedra, Leningrad, 112 p. (1982)

Zhang, J. & Herzberg, C. Melting experiments on anhydrous peridotite KLB-1 from 5.0 to 22.5 GPa. Journal of Geophysical Research 99, 17729 (1994).

Zhang, Z.M., Zhao, G.C., Santosh, M., Wang, J.L., Dong, X., Shen, K. Late Cretaceous charnockite with adakitic affinities from the Gangdese batholith, southeastern Tibet: evidence for Neo-Tethyan mid-ocean ridge subduction? Gondwana Research 17, 615–631 (2010).

Zibra, I., Gessner, K., Pawley, M.J., Wyche, S., .Chen, S.F., Korsch, R.J., Blewett, R.S.,Jones, T., Milligan, P., Jones, L.E.A., Doublier, M.P., Hall, C.E., Romano, S.S., Ivanic, T.J., Patison, N., Kennett, B.L.N., and Van Kranendonk, M.J., 2013, Preliminary interpretation of deep seismic line 10GA-YU2: Youanmi terrane and western Kalgoorlie terrane. Geological Survey of Western Australia Record 2013/6, 83–90 (2013).

Acknowledgments

I would like to thank my PhD supervisor Massimo Tiepolo for the continuous support of my PhD study and related research, for his patience, motivation, and immense knowledge. His supervision helped me in all the time of research and writing of this thesis. I could not have imagined having a better advisor and mentor for my PhD study.

A big thank also goes to Dr. Marilena Moroni. She has always helped me in my research and gave me precious life coaching, in addition to preparing fantastic jams, during sadness times.

A special thanks goes to Prof. Marco Fiorentini for the precious scientific support to my PhD and for providing the extraordinary sample collection that allowed this work.

I would to thank Dr. Elena Ferrari for helping me in the laboratory experiences and, especially, for the precious friendship gained during this years.

I am also grateful to Dr. Enrico Cannaò for his steadfast support and sincerely interest in my research.

I would like to thank Dr Simone Tumiati, Prof. Diego Gatta and Prof. Marco Merlini for their support in sci, but also for the hard question, which incented me to widen my research from various perspectives.

My sincere thanks also goes to Mr. Andrea Risplendente (University of Milan), Dr. Antonio Langone (IGG-CNR of Pavia) and Dr. Etienne Deloule (CRPG-CNRS of Nancy), who gave access to the laboratory and who helped me during the analytical sessions. Without they precious support it would not be possible to conduct this research. I am also grateful to Mr. Fabio Marchesini for help me in sample preparation.

A very special gratitude goes out to all down at Research Fund and also Rich Foundation for helping and providing the funding for the work. This work was carried out as part of foundation research project ‘‘Metal Sources and Transport Mechanisms in the Deep Lithosphere” in the Australian Research Council (ARC) – Australia – Centre of Excellence for Core to Crust Fluid Systems (CCFS, CE11E0070) and with the support of MURST grants (from the Italian Ministry of Research and University – Italy).

I am also grateful to my PhD fellows and colleagues Luca Samuele Capizzi, Alessandro Da Mommio, Davide Comboni, Marilena Moroni, Elena Ferrari, Micol Bussolesi, Sula Milani, Chiara Zuffetti, Mattia Bonazzi, Simone Tumiati, Giovanni Grieco, and Enrico Cannaò for the many beautiful moments spent together.

I want to thank all my friends, especially Federico, Simone, Laura, Davide, Cristina, Alessandro, Andrea, Jacopo for the memorable evenings and barbecues.

Last but not the least, I would like to thank my family: my mother and my brother for supporting me spiritually throughout my PhD experence and my life in general. I never could have done this without their help.

Table 1 - Electron microprobe analyses of brown amphibole of the sample MKD1 (Mt. Keith – Agnew-Wiluna greenstone belt, Western Australia).

	Amphibole								
SiO_2	45.50	43.14	43.03	43.42	43.20	44.32	44.84	45.85	45.26
TiO_2	0.39	3.20	3.13	3.36	3.51	2.32	1.51	0.83	1.16
Al_2O_3	10.69	10.60	10.53	10.66	10.74	10.60	11.10	10.87	10.73
Cr_2O_3	0.34	0.90	1.03	1.24	0.95	0.79	1.41	1.05	1.11
FeOtot	7.60	7.46	7.44	7.51	7.47	7.58	7.28	7.27	7.12
MnO	0.05	0.07	0.04	0.08	0.05	0.06	0.14	0.14	0.08
NiO	0.28	0.44	0.34	0.34	0.28	0.31	0.10	0.09	0.12
MgO	17.66	16.12	16.17	16.06	16.11	16.79	16.98	17.36	17.41
CaO	12.43	12.13	12.15	12.13	11.96	12.19	11.42	11.79	11.87
Na_2O	2.41	2.47	2.49	2.58	2.45	2.44	2.54	2.52	2.62
K_2O	0.49	0.88	0.92	0.92	0.91	0.82	0.81	0.67	0.71
Cl	0.39	0.39	0.39	0.39	0.39	0.39	0.39	0.39	0.39
O=Cl									
Total	97.84	97.41	97.27	98.29	97.65	98.22	98.13	98.44	98.18
Si	6.550	6.299	6.295	6.287	6.285	6.395	6.444	6.549	6.494
Ti	0.043	0.352	0.344	0.366	0.384	0.252	0.163	0.089	0.125
Al	1.814	1.824	1.815	1.819	1.842	1.802	1.880	1.830	1.814
Cr	0.038	0.103	0.119	0.142	0.109	0.090	0.161	0.118	0.126
Fe^{2+}	0.915	0.911	0.911	0.910	0.909	0.914	0.875	0.868	0.854
Fe^{3+}	0.000	0.000	0.000	0.000	0.000	0.000	0.000	0.000	0.000
Mn	0.007	0.009	0.005	0.010	0.006	0.008	0.016	0.016	0.009
Ni	0.032	0.052	0.040	0.039	0.033	0.036	0.012	0.011	0.014
Mg	3.786	3.505	3.524	3.464	3.491	3.608	3.634	3.693	3.720
Ca	1.916	1.898	1.905	1.882	1.865	1.885	1.759	1.804	1.825
Na	0.671	0.700	0.705	0.724	0.692	0.684	0.708	0.698	0.729
K	0.090	0.165	0.171	0.169	0.168	0.150	0.149	0.123	0.130
cations	15.862	15.818	15.833	15.813	15.786	15.824	15.801	15.799	15.840
$Mg/(Mg+Fe_{TOT})$	0.81	0.79	0.79	0.79	0.79	0.80	0.81	0.81	0.81
(Na+K)A	0.76	0.82	0.83	0.81	0.79	0.82	0.80	0.80	0.84

Note: Oxide values are in wt.%. All other values are calculated with normalization program Norm.

Table 2 - Electron microprobe analyses of brown amphibole of the sample 85437 (Mt. Clifford – Agnew-Wiluna greenstone belt, Western Australia).

	Amphibole									
SiO_2	43.42	43.98	44.84	43.22	43.38	43.58	44.16	43.31	42.96	43.11
TiO_2	3.58	3.56	3.81	4.06	3.45	2.75	3.29	3.04	3.34	2.69
Al_2O_3	10.04	9.74	8.45	9.19	9.28	9.95	9.33	9.84	9.87	9.86
Cr_2O_3	0.64	0.82	0.68	0.67	0.80	0.62	0.60	0.63	0.42	0.64
FeOtot	8.78	8.38	8.09	8.81	8.81	9.24	8.98	8.97	9.15	8.70
MnO	0.08	0.06	0.09	0.09	0.10	0.08	0.11	0.11	0.11	0.08
NiO	0.19	0.18	0.24	0.19	0.12	0.19	0.13	0.17	0.23	0.14
MgO	15.87	15.96	16.62	15.74	15.78	16.02	15.87	15.85	15.78	16.09
CaO	11.47	11.68	11.00	11.62	11.56	11.91	11.89	11.93	11.74	11.80
Na_2O	2.86	2.91	3.00	2.88	2.84	2.80	2.67	2.80	2.92	2.73
K_2O	0.51	0.52	0.57	0.52	0.46	0.40	0.41	0.37	0.43	0.35
Cl	0.44	0.44	0.44	0.44	0.44	0.44	0.44	0.44	0.44	0.44
O=Cl										
Total	97.43	97.78	97.39	96.98	96.57	97.55	97.44	97.01	96.94	96.20
Si	6.348	6.397	6.527	6.365	6.405	6.377	6.453	6.369	6.334	6.381
Ti	0.393	0.389	0.417	0.449	0.383	0.303	0.362	0.336	0.371	0.299
Al	1.730	1.669	1.449	1.595	1.614	1.717	1.607	1.705	1.714	1.719
Cr	0.074	0.095	0.078	0.078	0.093	0.072	0.070	0.073	0.049	0.074
Fe2+	1.073	1.019	0.985	1.085	1.088	1.131	1.097	1.103	1.129	1.077
Fe3+	0.000	0.000	0.000	0.000	0.000	0.000	0.000	0.000	0.000	0.000
Mn	0.009	0.007	0.011	0.011	0.013	0.010	0.013	0.014	0.013	0.010
Ni	0.023	0.020	0.028	0.023	0.014	0.023	0.015	0.020	0.027	0.017
Mg	3.455	3.457	3.604	3.451	3.470	3.492	3.454	3.471	3.464	3.547
Ca	1.796	1.820	1.717	1.833	1.829	1.868	1.862	1.880	1.854	1.872
Na	0.810	0.821	0.846	0.821	0.813	0.795	0.756	0.800	0.834	0.784
K	0.095	0.096	0.106	0.098	0.087	0.075	0.077	0.069	0.081	0.066
cations	15.808	15.790	15.768	15.809	15.808	15.860	15.764	15.840	15.871	15.848
$Mg/(Mg+Fe_{TOT})$	0.76	0.77	0.79	0.76	0.76	0.76	0.76	0.76	0.75	0.77
(Na+K)A	0.81	0.79	0.79	0.85	0.81	0.86	0.76	0.84	0.87	0.85

Note: Oxide values are in wt.%. All other values are calculated with normalization program Norm.

Table 3 - Electron microprobe analyses of clinopyroxene of the sample T-2 (Theo's Flow – Abitibi greenstone belt, Canada).

	Clinopyroxene		
SiO_2	53.40	53.35	54.02
TiO_2	0.46	0.35	0.27
Al_2O_3	2.23	1.65	1.56
Cr_2O_3	0.47	0.96	1.12
Fe_2O_3	0.00	0.00	0.00
FeO	6.82	6.01	5.34
MnO	0.17	0.22	0.14
NiO	0.05	0.09	0.13
MgO	16.09	16.95	17.15
CaO	20.87	20.44	21.16
Na_2O	0.30	0.27	0.29
K_2O	0.00	0.00	0.00
Total	100.87	100.29	101.19
Si	1.950	1.953	1.956
Ti	0.013	0.010	0.007
Al	0.096	0.071	0.067
Cr	0.014	0.028	0.032
Fe^{3+}	0.000	0.000	0.000
Fe^{2+}	0.208	0.184	0.162
Mn	0.005	0.007	0.004
Ni	0.001	0.003	0.004
Mg	0.876	0.925	0.926
Ca	0.816	0.802	0.821
Na	0.021	0.019	0.021
K	0.000	0.000	0.000
Wollastonite	0.39	0.38	0.39
Enstatite	0.44	0.46	0.47
Ferrosilite	0.10	0.09	0.08
Pyroxmangite	0.00	0.00	0.00
Acmite	0.00	0.00	0.00
Jadeite	0.02	0.02	0.02
xMgonM1	0.75	0.78	0.80
xMgonM2	0.13	0.14	0.13
xMgFe(II+)	0.81	0.83	0.85
xMgFe(tot)	0.81	0.83	0.85

Note: Oxide values are in wt.%.
All other values are calculated with normalization program Norm.

Table 4 - Electron microprobe analyses of brown amphibole of the sample T-2 (Theo's Flow – Abitibi greenstone belt, Canada).

	Amphibole						
SiO_2	46.46	46.62	45.15	46.03	46.73	47.89	49.61
TiO_2	2.97	3.02	2.25	3.15	3.13	2.75	2.13
Al_2O_3	7.61	7.34	11.38	7.37	7.44	7.29	7.22
Cr_2O_3	0.38	0.20	0.41	0.04	0.15	0.06	0.31
FeOtot	9.17	9.07	8.54	9.03	8.93	8.92	8.56
MnO	0.14	0.15	0.04	0.13	0.13	0.18	0.13
NiO	0.02	0.10	0.09	0.08	0.11	0.03	0.14
MgO	17.00	17.19	16.15	16.81	17.26	17.25	17.64
CaO	10.94	10.48	12.35	10.65	10.61	10.42	11.02
Na_2O	2.61	2.95	1.41	2.58	2.54	3.05	1.32
K_2O	0.52	0.44	0.45	0.57	0.46	0.41	0.17
Cl	0.24	0.24	0.24	0.24	0.24	0.24	0.24
O=Cl							
Total	97.82	97.57	98.21	96.45	97.49	98.25	98.26
Si	6.721	6.754	6.471	6.747	6.760	6.859	7.025
Ti	0.323	0.329	0.243	0.347	0.341	0.296	0.227
Al	1.297	1.253	1.922	1.273	1.268	1.231	1.205
Cr	0.043	0.023	0.046	0.005	0.017	0.007	0.035
Fe^{2+}	1.109	1.099	1.024	1.107	1.080	1.068	1.014
Fe^{3+}	0.000	0.000	0.000	0.000	0.000	0.000	0.000
Mn	0.017	0.018	0.005	0.016	0.016	0.022	0.016
Ni	0.003	0.012	0.010	0.009	0.012	0.003	0.016
Mg	3.662	3.709	3.447	3.669	3.719	3.679	3.720
Ca	1.696	1.627	1.897	1.673	1.645	1.599	1.672
Na	0.732	0.829	0.392	0.733	0.712	0.847	0.363
K	0.096	0.082	0.082	0.107	0.085	0.076	0.031
cations	15.700	15.734	15.539	15.687	15.655	15.687	15.324
$Mg/(Mg+Fe_{TOT})$	0.77	0.77	0.77	0.77	0.77	0.77	0.79
(Na+K)A	0.70	0.73	0.47	0.69	0.66	0.69	0.32

Note: Oxide values are in wt.%. All other values are calculated with normalization program Norm.

Table 5 - Electron microprobe analyses of clinopyroxene of the sample B-5 (Boston Creek – Abitibi greenstone belt, Canada).

	Clinopyroxene							
SiO_2	52.60	52.73	53.54	53.65	53.82	54.06	53.91	53.64
TiO_2	0.54	0.50	0.34	0.35	0.27	0.27	0.36	0.30
Al_2O_3	1.75	1.51	1.13	1.19	1.14	0.91	1.19	0.94
Cr_2O_3	0.76	0.75	0.71	0.90	0.81	0.74	0.87	0.72
Fe_2O_3	2.17	1.73	0.79	0.35	0.54	0.30	0.00	1.47
FeO	4.27	4.29	5.15	5.34	5.18	5.25	5.66	4.35
MnO	0.12	0.11	0.07	0.12	0.17	0.13	0.09	0.07
NiO	0.02	0.00	0.05	0.01	0.00	0.00	0.00	0.08
MgO	15.19	15.13	15.56	15.77	15.86	15.89	15.70	15.98
CaO	23.22	23.22	23.11	22.91	23.02	23.19	23.06	23.15
Na_2O	0.46	0.51	0.37	0.33	0.32	0.32	0.31	0.38
K_2O	0.01	0.01	0.00	0.00	0.00	0.00	0.00	0.00
Total	101.10	100.49	100.82	100.93	101.14	101.06	101.15	101.08
Si	1.923	1.937	1.958	1.959	1.960	1.970	1.964	1.955
Ti	0.015	0.014	0.009	0.010	0.007	0.008	0.010	0.008
Al	0.075	0.065	0.049	0.051	0.049	0.039	0.051	0.040
Cr	0.022	0.022	0.020	0.026	0.024	0.021	0.025	0.021
Fe3+	0.060	0.048	0.022	0.010	0.015	0.008	0.000	0.040
Fe2+	0.131	0.132	0.157	0.163	0.158	0.160	0.172	0.133
Mn	0.004	0.003	0.002	0.004	0.005	0.004	0.003	0.002
Ni	0.001	0.000	0.002	0.000	0.000	0.000	0.000	0.002
Mg	0.828	0.828	0.848	0.858	0.861	0.863	0.853	0.868
Ca	0.910	0.914	0.906	0.896	0.898	0.905	0.900	0.904
Na	0.032	0.036	0.026	0.024	0.023	0.023	0.022	0.027
K	0.001	0.000	0.000	0.000	0.000	0.000	0.000	0.000
Wollastonite	0.43	0.43	0.44	0.43	0.43	0.44	0.44	0.44
Enstatite	0.41	0.41	0.43	0.43	0.43	0.43	0.43	0.44
Ferrosilite	0.07	0.07	0.08	0.08	0.08	0.08	0.09	0.07
Pyroxmangite	0.00	0.00	0.00	0.00	0.00	0.00	0.00	0.00
Acmite	0.03	0.04	0.02	0.01	0.02	0.01	0.00	0.03
Jadeite	0.00	0.00	0.00	0.01	0.01	0.01	0.02	0.00
xMgonM1	0.78	0.79	0.79	0.79	0.80	0.81	0.79	0.81
xMgonM2	0.05	0.04	0.06	0.06	0.06	0.06	0.06	0.06
xMgFe(II+)	0.86	0.86	0.84	0.84	0.85	0.84	0.83	0.87
xMgFe(tot)	0.81	0.82	0.83	0.83	0.83	0.84	0.83	0.83

Note: Oxide values are in wt.%. All other values are calculated with normalization program Norm.

Table 6 - Electron microprobe analyses of brown amphibole of the sample B-5 (Boston Creek – Abitibi greenstone belt, Canada).

	Amphibole						
SiO_2	41.75	41.65	41.78	41.45	40.85	41.18	41.62
TiO_2	3.83	3.51	3.13	3.74	3.68	3.98	3.49
Al_2O_3	11.47	11.64	11.56	11.97	12.26	12.26	11.58
Cr_2O_3	0.00	0.06	0.02	0.03	0.00	0.02	0.00
FeOtot	12.06	12.12	12.67	12.16	12.39	12.06	11.56
MnO	0.12	0.19	0.16	0.12	0.13	0.08	0.05
NiO	0.08	0.13	0.07	0.04	0.00	0.09	0.05
MgO	12.66	13.11	12.69	12.92	12.75	12.73	13.38
CaO	11.59	11.49	11.24	11.71	11.77	11.81	11.68
Na_2O	3.27	3.26	3.41	3.47	3.10	3.29	3.33
K_2O	0.38	0.36	0.42	0.43	0.38	0.42	0.43
Cl	0.14	0.14	0.14	0.14	0.14	0.14	0.14
O=Cl							
Total	97.21	97.52	97.15	98.04	97.32	97.92	97.17
Si	6.216	6.186	6.238	6.133	6.091	6.097	6.190
Ti	0.429	0.392	0.352	0.416	0.413	0.443	0.390
Al	2.013	2.038	2.034	2.087	2.155	2.139	2.030
Cr	0.000	0.007	0.003	0.003	0.001	0.003	0.000
Fe^{2+}	1.502	1.505	1.582	1.505	1.545	1.493	1.438
Fe^{3+}	0.000	0.000	0.000	0.000	0.000	0.000	0.000
Mn	0.015	0.024	0.021	0.015	0.017	0.010	0.007
Ni	0.010	0.015	0.008	0.005	0.000	0.011	0.006
Mg	2.807	2.900	2.822	2.847	2.832	2.807	2.963
Ca	1.849	1.829	1.798	1.856	1.881	1.874	1.861
Na	0.944	0.939	0.987	0.995	0.896	0.944	0.960
K	0.072	0.069	0.080	0.082	0.072	0.079	0.082
cations	15.857	15.903	15.925	15.944	15.902	15.900	15.926
$Mg/(Mg+Fe_{TOT})$	0.65	0.66	0.64	0.65	0.65	0.65	0.67
(Na+K)A	0.87	0.90	0.93	0.94	0.90	0.90	0.93

Continued Table 6

	Amphibole						
SiO_2	41.02	40.21	40.70	40.98	41.09	39.77	40.85
TiO_2	3.79	4.59	4.39	3.93	3.70	3.42	3.95
Al_2O_3	12.49	12.32	12.52	12.14	12.32	17.32	12.86
Cr_2O_3	0.00	0.00	0.01	0.00	0.02	0.00	0.04
FeOtot	12.00	11.99	12.52	12.21	12.24	12.23	12.10
MnO	0.14	0.09	0.08	0.12	0.13	0.13	0.15
NiO	0.07	0.09	0.10	0.00	0.03	0.03	0.11
MgO	12.82	12.53	12.38	12.45	12.61	11.68	12.39
CaO	11.79	11.78	11.43	11.65	11.80	11.05	11.49
Na_2O	3.23	3.22	3.41	3.52	3.10	3.38	3.41
K_2O	0.42	0.44	0.41	0.39	0.43	0.41	0.40
Cl	0.14	0.14	0.14	0.14	0.14	0.14	0.14
O=Cl							
Total	97.76	97.27	97.95	97.39	97.46	99.42	97.75
Si	6.081	6.006	6.039	6.107	6.112	5.773	6.058
Ti	0.423	0.516	0.490	0.441	0.414	0.373	0.441
Al	2.182	2.169	2.189	2.132	2.160	2.963	2.248
Cr	0.000	0.000	0.001	0.000	0.002	0.000	0.004
Fe^{2+}	1.488	1.498	1.553	1.522	1.523	1.485	1.501
Fe^{3+}	0.000	0.000	0.000	0.000	0.000	0.000	0.000
Mn	0.017	0.012	0.011	0.015	0.017	0.016	0.019
Ni	0.008	0.011	0.012	0.000	0.003	0.003	0.013
Mg	2.830	2.787	2.736	2.763	2.794	2.525	2.737
Ca	1.873	1.885	1.817	1.860	1.881	1.719	1.826
Na	0.928	0.933	0.981	1.017	0.894	0.951	0.981
K	0.079	0.085	0.077	0.074	0.081	0.077	0.077
cations	15.909	15.902	15.906	15.932	15.880	15.886	15.903
$Mg/(Mg+Fe_{TOT})$	0.66	0.65	0.64	0.64	0.65	0.63	0.65
(Na+K)A	0.91	0.90	0.91	0.95	0.88	0.89	0.90

Note: Oxide values are in wt.%. All other values are calculated with normalization program Norm.

Table 7 - Electron microprobe analyses of olivine of the sample GR-1 (Ghost Range – Abitibi greenstone belt, Canada).

	Olivine								
SiO_2	40.11	40.04	40.08	40.28	40.41	40.33	39.76	40.09	40.32
TiO_2	0.02	0.05	0.01	0.02	0.01	0.02	0.09	0.00	0.00
Al_2O_3	0.01	0.04	0.00	0.02	0.00	0.05	0.05	0.00	0.01
Cr_2O_3	0.00	0.05	0.04	0.01	0.03	0.00	0.00	0.00	0.00
FeO	16.53	16.43	16.72	16.42	16.18	16.61	16.77	17.03	17.01
MnO	0.24	0.28	0.25	0.30	0.30	0.28	0.31	0.25	0.23
NiO	0.29	0.24	0.29	0.26	0.27	0.36	0.35	0.35	0.30
MgO	43.83	43.72	43.97	44.76	43.96	43.99	44.17	43.99	43.70
CaO	0.05	0.06	0.06	0.07	0.04	0.07	0.07	0.05	0.08
Na_2O	0.00	0.00	0.01	0.01	0.00	0.01	0.00	0.00	0.00
K_2O	0.01	0.00	0.00	0.00	0.00	0.02	0.02	0.01	0.00
Total	101.10	100.92	101.43	102.15	101.19	101.75	101.58	101.78	101.66
Si	1.004	1.005	1.001	0.996	1.010	1.004	0.991	0.998	1.006
Ti	0.000	0.001	0.000	0.000	0.000	0.000	0.002	0.000	0.000
Al	0.000	0.001	0.000	0.001	0.000	0.002	0.001	0.000	0.000
Cr	0.000	0.001	0.001	0.000	0.001	0.000	0.000	0.000	0.000
Fe^{2+}	0.346	0.345	0.349	0.340	0.338	0.346	0.350	0.355	0.355
Mn	0.005	0.006	0.005	0.006	0.006	0.006	0.007	0.005	0.005
Ni	0.006	0.005	0.006	0.005	0.006	0.007	0.007	0.007	0.006
Mg	1.636	1.635	1.636	1.650	1.638	1.632	1.641	1.633	1.625
Ca	0.002	0.002	0.002	0.002	0.001	0.002	0.002	0.001	0.002
Na	0.000	0.000	0.000	0.001	0.000	0.001	0.000	0.000	0.000
K	0.000	0.000	0.000	0.000	0.000	0.001	0.001	0.000	0.000
Forsterite	0.82	0.82	0.82	0.82	0.82	0.82	0.82	0.82	0.82
Fayalite	0.17	0.17	0.18	0.17	0.17	0.17	0.17	0.18	0.18
Tephroite	0.00	0.00	0.00	0.00	0.00	0.00	0.00	0.00	0.00
Monticellit	0.00	0.00	0.00	0.00	0.00	0.00	0.00	0.00	0.00
Kirschstein	0.00	0.00	0.00	0.00	0.00	0.00	0.00	0.00	0.00
Glaukocroit	0.00	0.00	0.00	0.00	0.00	0.00	0.00	0.00	0.00
Ni-Olivine	0.00	0.00	0.00	0.00	0.00	0.00	0.00	0.00	0.00
xMg	0.82	0.82	0.82	0.82	0.82	0.82	0.82	0.82	0.82
xFe	0.17	0.17	0.18	0.17	0.17	0.17	0.17	0.18	0.18

Note: Oxide values are in wt.%. All other values are calculated with normalization program Norm.

Table 8 - Electron microprobe analyses of olivine of the sample GR-2 (Ghost Range – Abitibi greenstone belt, Canada).

	Olivine										
SiO_2	39.89	39.93	39.90	40.06	40.18	40.34	39.98	40.18	40.42	40.14	40.06
TiO_2	0.02	0.00	0.01	0.00	0.01	0.04	0.02	0.04	0.05	0.05	0.03
Al_2O_3	0.01	0.01	0.02	0.02	0.03	0.02	0.01	0.00	0.01	0.02	0.00
Cr_2O_3	0.00	0.00	0.00	0.01	0.03	0.01	0.00	0.03	0.00	0.04	0.06
FeO	17.05	16.93	16.01	15.85	16.16	16.20	15.82	15.93	16.20	16.44	16.60
MnO	0.29	0.31	0.23	0.21	0.27	0.25	0.21	0.26	0.24	0.18	0.25
NiO	0.37	0.23	0.36	0.23	0.30	0.24	0.16	0.30	0.22	0.29	0.22
MgO	44.25	43.92	44.81	44.52	44.58	44.55	44.45	44.38	44.04	44.28	44.37
CaO	0.09	0.08	0.12	0.17	0.09	0.14	0.09	0.10	0.06	0.12	0.11
Na_2O	0.00	0.00	0.00	0.00	0.00	0.00	0.01	0.00	0.00	0.02	0.00
K_2O	0.01	0.00	0.00	0.01	0.01	0.00	0.00	0.00	0.00	0.00	0.01
Total	101.97	101.41	101.45	101.07	101.65	101.79	100.74	101.23	101.25	101.58	101.70
Si	0.991	0.998	0.992	0.999	0.998	1.001	1.000	1.002	1.010	0.999	0.996
Ti	0.000	0.000	0.000	0.000	0.000	0.001	0.000	0.001	0.001	0.001	0.001
Al	0.000	0.000	0.001	0.001	0.001	0.001	0.000	0.000	0.000	0.001	0.000
Cr	0.000	0.000	0.000	0.000	0.001	0.000	0.000	0.001	0.000	0.001	0.001
Fe^{2+}	0.354	0.354	0.333	0.331	0.336	0.336	0.331	0.332	0.338	0.342	0.345
Mn	0.006	0.007	0.005	0.004	0.006	0.005	0.004	0.006	0.005	0.004	0.005
Ni	0.007	0.005	0.007	0.005	0.006	0.005	0.003	0.006	0.005	0.006	0.004
Mg	1.638	1.635	1.660	1.656	1.651	1.648	1.658	1.650	1.640	1.643	1.644
Ca	0.002	0.002	0.003	0.004	0.003	0.004	0.003	0.003	0.002	0.003	0.003
Na	0.000	0.000	0.000	0.000	0.000	0.000	0.000	0.000	0.000	0.001	0.000
K	0.000	0.000	0.000	0.000	0.000	0.000	0.000	0.000	0.000	0.000	0.000
Forsterite	0.82	0.82	0.83	0.83	0.83	0.83	0.83	0.83	0.82	0.82	0.82
Fayalite	0.18	0.18	0.17	0.17	0.17	0.17	0.17	0.17	0.17	0.17	0.17
Tephroite	0.00	0.00	0.00	0.00	0.00	0.00	0.00	0.00	0.00	0.00	0.00
Monticellit	0.00	0.00	0.00	0.00	0.00	0.00	0.00	0.00	0.00	0.00	0.00
Kirschstein	0.00	0.00	0.00	0.00	0.00	0.00	0.00	0.00	0.00	0.00	0.00
Glaukocroit	0.00	0.00	0.00	0.00	0.00	0.00	0.00	0.00	0.00	0.00	0.00
Ni-Olivine	0.00	0.00	0.00	0.00	0.00	0.00	0.00	0.00	0.00	0.00	0.00
xMg	0.82	0.82	0.83	0.83	0.82	0.82	0.83	0.83	0.82	0.82	0.82
xFe	0.18	0.18	0.17	0.17	0.17	0.17	0.17	0.17	0.17	0.17	0.17

Note: Oxide values are in wt.%. All other values are calculated with normalization program Norm.

Table 9 - Electron microprobe analyses of clinopyroxene of the samples GR-1 and GR-2 (Ghost Range – Abitibi greenstone belt, Canada).

	Clinopyroxene (GR-1)								*Clinopyroxene (GR-2)*	
SiO_2	55.73	56.23	56.63	56.57	56.57	56.51	56.42	56.13	52.90	54.48
TiO_2	0.23	0.28	0.51	0.48	0.19	0.31	0.49	0.19	0.25	0.27
Al_2O_3	1.36	1.37	0.73	0.81	1.03	1.04	0.75	1.27	2.52	1.01
Cr_2O_3	0.46	0.45	0.23	0.29	0.4	0.37	0.23	0.47	0.98	0.66
Fe_2O_3	0	0	0	0	0	0	0	0.4	0.17	0.50
FeO	9.95	10.04	10.81	10.8	10.1	10.09	10.64	9.91	4.67	3.39
MnO	0.26	0.22	0.25	0.28	0.3	0.21	0.26	0.3	0.16	0.12
NiO	0.13	0.06	0.05	0.02	0.11	0.09	0.11	0.03	0.11	0.07
MgO	30.09	30.28	30.96	30.53	30.31	30.19	31.06	30.57	16.66	16.33
CaO	1.91	1.96	1.02	1.11	1.94	1.79	1.13	1.94	21.57	23.81
Na_2O	0.03	0.01	0.03	0.04	0	0.04	0	0.01	0.25	0.47
K_2O	0	0.01	0	0	0.01	0	0	0	0.01	0.01
Total	100.15	100.91	101.22	100.94	100.97	100.63	101.08	101.22	100.27	101.12
Si	1.965	1.968	1.976	1.982	1.980	1.984	1.970	1.958	1.932	1.971
Ti	0.006	0.007	0.013	0.013	0.005	0.008	0.013	0.005	0.007	0.007
Al	0.057	0.057	0.030	0.034	0.042	0.043	0.031	0.052	0.108	0.043
Cr	0.013	0.012	0.006	0.008	0.011	0.010	0.007	0.013	0.028	0.019
Fe^{3+}	0.000	0.000	0.000	0.000	0.000	0.000	0.000	0.010	0.005	0.014
Fe^{2+}	0.293	0.294	0.315	0.316	0.296	0.296	0.311	0.289	0.143	0.103
Mn	0.008	0.007	0.008	0.008	0.009	0.006	0.008	0.009	0.005	0.004
Ni	0.004	0.002	0.001	0.001	0.003	0.002	0.003	0.001	0.003	0.002
Mg	1.581	1.579	1.610	1.594	1.581	1.580	1.616	1.589	0.907	0.881
Ca	0.072	0.074	0.038	0.042	0.073	0.067	0.042	0.073	0.844	0.923
Na	0.002	0.001	0.002	0.003	0.000	0.003	0.000	0.001	0.018	0.033
K	0.000	0.000	0.000	0.000	0.001	0.000	0.000	0.000	0.001	0.000
Wollastonite	0.02	0.02	0.01	0.02	0.03	0.03	0.01	0.02	0.39	0.45
Enstatite	0.79	0.79	0.81	0.80	0.79	0.79	0.81	0.80	0.46	0.44
Ferrosilite	0.15	0.15	0.16	0.16	0.15	0.15	0.16	0.15	0.07	0.05
Pyroxmangite	0.00	0.00	0.00	0.00	0.01	0.00	0.00	0.00	0.00	0.00
Acmite	0.00	0.00	0.00	0.00	0.00	0.00	0.00	0.00	0.01	0.01
Jadeite	0.00	0.00	0.00	0.00	0.00	0.00	0.00	0.00	0.01	0.01
xMgonM1	0.81	0.81	0.81	0.80	0.81	0.80	0.82	0.81	0.79	0.85
xMgonM2	0.78	0.77	0.80	0.79	0.77	0.78	0.80	0.78	0.12	0.04
xMgFe(II+)	0.84	0.84	0.84	0.83	0.84	0.84	0.84	0.85	0.86	0.90
xMgFe(tot)	0.84	0.84	0.84	0.83	0.84	0.84	0.84	0.84	0.86	0.88

Note: Oxide values are in wt.%. All other values are calculated with normalization program Norm.

Table 10 - Electron microprobe analyses of brown amphibole of the sample GR-1 (Ghost Range – Abitibi greenstone belt, Canada).

	Amphibole									
SiO_2	44.78	44.28	44.54	44.55	44.66	44.77	44.87	44.51	44.67	45.09
TiO_2	3.65	3.84	3.97	3.58	4.55	4.81	4.01	4.25	3.28	3.13
Al_2O_3	8.82	8.89	9.11	8.92	8.40	8.27	8.66	8.43	9.02	9.50
Cr_2O_3	1.55	1.60	1.44	1.41	1.17	0.92	1.49	1.59	1.48	1.55
FeOtot	7.06	7.47	7.22	7.12	6.95	7.11	7.37	7.25	7.06	7.28
MnO	0.11	0.09	0.11	0.08	0.13	0.13	0.04	0.03	0.11	0.07
NiO	0.11	0.08	0.06	0.12	0.04	0.09	0.02	0.08	0.11	0.09
MgO	16.12	16.06	15.89	16.63	16.55	16.05	16.27	15.93	16.14	16.57
CaO	11.75	11.64	11.81	11.70	11.29	11.24	11.46	11.59	11.66	11.64
Na_2O	2.76	2.77	2.81	2.93	2.91	2.89	2.89	2.78	2.76	2.67
K_2O	0.76	0.75	0.77	0.71	0.51	0.60	0.78	0.78	0.76	0.77
Cl	0.40	0.40	0.40	0.40	0.40	0.40	0.40	0.40	0.40	0.40
O=Cl										
Total	97.47	97.46	97.73	97.75	97.16	96.88	97.86	97.22	97.05	98.37
Si	6.505	6.450	6.460	6.459	6.491	6.528	6.496	6.492	6.513	6.483
Ti	0.399	0.421	0.433	0.390	0.497	0.528	0.437	0.466	0.360	0.338
Al	1.510	1.526	1.557	1.524	1.439	1.421	1.478	1.449	1.550	1.610
Cr	0.178	0.184	0.165	0.162	0.135	0.106	0.171	0.183	0.171	0.176
Fe^{2+}	0.858	0.910	0.876	0.863	0.845	0.867	0.892	0.884	0.861	0.875
Fe^{3+}	0.000	0.000	0.000	0.000	0.000	0.000	0.000	0.000	0.000	0.000
Mn	0.013	0.011	0.013	0.010	0.016	0.016	0.005	0.004	0.014	0.009
Ni	0.013	0.009	0.007	0.014	0.005	0.011	0.003	0.009	0.013	0.011
Mg	3.488	3.484	3.432	3.591	3.582	3.485	3.508	3.460	3.505	3.548
Ca	1.829	1.817	1.835	1.817	1.758	1.756	1.778	1.811	1.822	1.793
Na	0.777	0.782	0.790	0.824	0.820	0.817	0.811	0.786	0.780	0.744
K	0.140	0.139	0.143	0.131	0.095	0.112	0.144	0.146	0.141	0.141
cations	15.710	15.734	15.712	15.785	15.682	15.646	15.721	15.691	15.728	15.729
$Mg/(Mg+Fe_{TOT})$	0.80	0.79	0.80	0.81	0.81	0.80	0.80	0.80	0.80	0.80
(Na+K)A	0.75	0.76	0.77	0.80	0.75	0.70	0.75	0.75	0.74	0.73

Continued Table 10

	Amphibole									
SiO_2	44.34	44.96	44.35	44.34	44.92	44.32	44.62	44.30	44.10	43.90
TiO_2	4.81	4.52	4.52	4.27	4.74	4.83	4.71	3.51	3.53	3.42
Al_2O_3	8.36	8.32	8.86	8.63	8.14	8.09	8.00	8.88	8.97	8.99
Cr_2O_3	1.23	1.30	1.12	1.22	1.16	1.18	1.10	1.34	1.40	1.53
FeOtot	7.21	7.05	7.25	7.17	6.83	7.06	7.00	6.94	7.11	7.09
MnO	0.05	0.07	0.12	0.10	0.06	0.07	0.09	0.10	0.03	0.09
NiO	0.06	0.15	0.12	0.15	0.04	0.06	0.08	0.15	0.06	0.06
MgO	16.03	16.14	16.04	15.80	16.40	16.24	16.30	15.71	16.09	15.96
CaO	11.23	11.33	11.49	11.29	11.34	11.19	11.28	11.49	11.65	11.73
Na_2O	2.90	2.80	2.91	3.06	2.73	2.94	2.79	2.81	2.76	2.79
K_2O	0.77	0.78	0.72	0.70	0.80	0.61	0.67	0.79	0.73	0.78
Cl	0.40	0.40	0.40	0.40	0.40	0.40	0.40	0.40	0.40	0.40
O=Cl										
Total	96.99	97.43	97.50	96.73	97.16	96.59	96.65	96.02	96.43	96.33
Si	6.476	6.527	6.446	6.494	6.528	6.491	6.526	6.527	6.476	6.463
Ti	0.528	0.494	0.494	0.470	0.518	0.532	0.518	0.389	0.390	0.379
Al	1.439	1.423	1.518	1.490	1.394	1.396	1.379	1.542	1.552	1.560
Cr	0.142	0.149	0.129	0.141	0.133	0.137	0.128	0.156	0.163	0.178
Fe^{2+}	0.881	0.856	0.881	0.878	0.830	0.865	0.856	0.855	0.873	0.873
Fe^{3+}	0.000	0.000	0.000	0.000	0.000	0.000	0.000	0.000	0.000	0.000
Mn	0.006	0.009	0.015	0.012	0.008	0.009	0.012	0.012	0.003	0.011
Ni	0.007	0.018	0.014	0.018	0.005	0.007	0.009	0.018	0.007	0.007
Mg	3.487	3.489	3.472	3.446	3.550	3.542	3.550	3.447	3.519	3.499
Ca	1.757	1.762	1.789	1.772	1.766	1.756	1.768	1.814	1.833	1.850
Na	0.821	0.788	0.820	0.869	0.769	0.835	0.791	0.803	0.786	0.796
K	0.143	0.145	0.133	0.131	0.149	0.113	0.126	0.149	0.137	0.146
cations	15.687	15.660	15.712	15.720	15.649	15.684	15.661	15.711	15.738	15.761
$Mg/(Mg+Fe_{TOT})$	0.80	0.80	0.80	0.80	0.81	0.80	0.81	0.80	0.80	0.80
(Na+K)A	0.77	0.71	0.75	0.77	0.73	0.80	0.76	0.77	0.76	0.79

Continued Table 10

	Amphibole							
SiO_2	44.38	45.07	44.69	45.07	45.03	45.03	43.83	44.83
TiO_2	4.53	4.22	2.67	4.25	2.83	4.15	3.59	4.75
Al_2O_3	9.03	8.64	9.24	8.17	8.82	8.12	8.53	8.17
Cr_2O_3	1.42	1.52	1.43	1.49	1.50	1.45	1.53	0.90
FeOtot	6.79	6.98	7.39	6.93	7.39	7.00	7.28	7.38
MnO	0.07	0.06	0.10	0.09	0.11	0.07	0.08	0.10
NiO	0.04	0.08	0.08	0.06	0.06	0.12	0.06	0.14
MgO	16.02	16.47	16.47	16.38	16.15	16.23	15.82	16.19
CaO	11.38	11.45	11.89	11.34	11.65	11.40	11.60	11.56
Na_2O	2.94	2.87	2.75	2.74	2.68	2.76	2.81	2.81
K_2O	0.50	0.54	0.79	0.78	0.73	0.79	0.77	0.75
Cl	0.40	0.40	0.40	0.40	0.40	0.40	0.40	0.40
O=Cl								
Total	97.09	97.91	97.50	97.29	96.95	97.12	95.91	97.58
Si	6.452	6.501	6.498	6.546	6.571	6.557	6.488	6.510
Ti	0.495	0.458	0.292	0.464	0.311	0.455	0.400	0.519
Al	1.547	1.469	1.583	1.399	1.517	1.393	1.488	1.398
Cr	0.163	0.173	0.164	0.171	0.173	0.167	0.179	0.104
Fe^{2+}	0.826	0.842	0.899	0.842	0.902	0.852	0.901	0.896
Fe^{3+}	0.000	0.000	0.000	0.000	0.000	0.000	0.000	0.000
Mn	0.009	0.008	0.013	0.010	0.013	0.008	0.010	0.012
Ni	0.004	0.010	0.010	0.006	0.007	0.014	0.008	0.017
Mg	3.469	3.538	3.566	3.543	3.510	3.520	3.488	3.501
Ca	1.773	1.770	1.852	1.765	1.822	1.779	1.840	1.799
Na	0.829	0.803	0.775	0.772	0.758	0.779	0.807	0.791
K	0.092	0.099	0.146	0.145	0.135	0.147	0.146	0.138
cations	15.658	15.671	15.797	15.663	15.720	15.671	15.754	15.685
$Mg/(Mg+Fe_{TOT})$	0.81	0.81	0.80	0.81	0.80	0.81	0.79	0.80
(Na+K)A	0.69	0.70	0.80	0.72	0.72	0.72	0.79	0.78

Note: Oxide values are in wt.%. All other values are calculated with normalization program Norm.

Table 11 - Electron microprobe analyses of amphibole of the sample GR-2 (Ghost Range – Abitibi greenstone belt, Canada).

	Amphibole								
SiO_2	44.35	44.02	43.46	43.86	43.31	42.31	45.06	44.69	45.11
TiO_2	4.33	4.08	4.63	4.55	5.10	4.42	4.47	4.47	3.04
Al_2O_3	9.12	8.78	9.55	9.71	10.52	12.33	8.70	8.72	8.65
Cr_2O_3	1.46	1.51	1.02	1.04	0.16	0.37	1.53	1.47	1.27
FeOtot	6.73	6.78	6.81	6.74	7.53	7.84	7.02	7.08	6.95
MnO	0.07	0.05	0.13	0.04	0.11	0.10	0.11	0.05	0.04
NiO	0.02	0.04	0.03	0.05	0.04	0.09	0.08	0.07	0.13
MgO	16.13	16.01	15.89	16.15	15.63	15.39	15.99	16.40	16.54
CaO	11.18	11.26	11.72	11.59	11.57	11.29	11.39	11.27	11.41
Na_2O	3.09	3.10	3.10	3.20	3.07	3.29	3.23	3.14	2.96
K_2O	0.55	0.62	0.55	0.55	0.22	0.29	0.61	0.65	0.63
Cl	0.37	0.37	0.37	0.37	0.37	0.37	0.37	0.37	0.37
O=Cl									
Total	97.03	96.26	96.89	97.48	97.26	97.71	98.20	98.00	96.74
Si	6.451	6.467	6.351	6.361	6.293	6.136	6.493	6.455	6.580
Ti	0.474	0.451	0.509	0.496	0.557	0.482	0.485	0.486	0.334
Al	1.564	1.520	1.645	1.660	1.802	2.107	1.478	1.484	1.487
Cr	0.168	0.175	0.118	0.119	0.018	0.042	0.174	0.168	0.147
Fe^{2+}	0.819	0.833	0.832	0.817	0.915	0.951	0.846	0.855	0.848
Fe^{3+}	0.000	0.000	0.000	0.000	0.000	0.000	0.000	0.000	0.000
Mn	0.009	0.006	0.016	0.005	0.014	0.012	0.014	0.006	0.005
Ni	0.002	0.005	0.003	0.006	0.004	0.010	0.009	0.008	0.016
Mg	3.494	3.503	3.458	3.488	3.382	3.324	3.432	3.528	3.593
Ca	1.742	1.773	1.835	1.801	1.801	1.754	1.759	1.744	1.783
Na	0.871	0.883	0.878	0.900	0.865	0.925	0.902	0.879	0.837
K	0.101	0.116	0.103	0.101	0.040	0.053	0.113	0.120	0.118
cations	15.696	15.734	15.750	15.754	15.692	15.796	15.704	15.733	15.747
$Mg/(Mg+Fe_{TOT})$	0.81	0.81	0.81	0.81	0.79	0.78	0.80	0.80	0.81
(Na+K)A	0.72	0.77	0.82	0.80	0.71	0.80	0.77	0.79	0.75

Note: Oxide values are in wt.%. All other values are calculated with normalization program Norm.

Table 11 - Electron microprobe analyses of amphibole of the sample GR-2 (Ghost Range – Abitibi greenstone belt, Canada).

	Amphibole								
SiO_2	44.35	44.02	43.46	43.86	43.31	42.31	45.06	44.69	45.11
TiO_2	4.33	4.08	4.63	4.55	5.10	4.42	4.47	4.47	3.04
Al_2O_3	9.12	8.78	9.55	9.71	10.52	12.33	8.70	8.72	8.65
Cr_2O_3	1.46	1.51	1.02	1.04	0.16	0.37	1.53	1.47	1.27
FeOtot	6.73	6.78	6.81	6.74	7.53	7.84	7.02	7.08	6.95
MnO	0.07	0.05	0.13	0.04	0.11	0.10	0.11	0.05	0.04
NiO	0.02	0.04	0.03	0.05	0.04	0.09	0.08	0.07	0.13
MgO	16.13	16.01	15.89	16.15	15.63	15.39	15.99	16.40	16.54
CaO	11.18	11.26	11.72	11.59	11.57	11.29	11.39	11.27	11.41
Na_2O	3.09	3.10	3.10	3.20	3.07	3.29	3.23	3.14	2.96
K_2O	0.55	0.62	0.55	0.55	0.22	0.29	0.61	0.65	0.63
Cl	0.37	0.37	0.37	0.37	0.37	0.37	0.37	0.37	0.37
O=Cl									
Total	97.03	96.26	96.89	97.48	97.26	97.71	98.20	98.00	96.74
Si	6.451	6.467	6.351	6.361	6.293	6.136	6.493	6.455	6.580
Ti	0.474	0.451	0.509	0.496	0.557	0.482	0.485	0.486	0.334
Al	1.564	1.520	1.645	1.660	1.802	2.107	1.478	1.484	1.487
Cr	0.168	0.175	0.118	0.119	0.018	0.042	0.174	0.168	0.147
Fe^{2+}	0.819	0.833	0.832	0.817	0.915	0.951	0.846	0.855	0.848
Fe^{3+}	0.000	0.000	0.000	0.000	0.000	0.000	0.000	0.000	0.000
Mn	0.009	0.006	0.016	0.005	0.014	0.012	0.014	0.006	0.005
Ni	0.002	0.005	0.003	0.006	0.004	0.010	0.009	0.008	0.016
Mg	3.494	3.503	3.458	3.488	3.382	3.324	3.432	3.528	3.593
Ca	1.742	1.773	1.835	1.801	1.801	1.754	1.759	1.744	1.783
Na	0.871	0.883	0.878	0.900	0.865	0.925	0.902	0.879	0.837
K	0.101	0.116	0.103	0.101	0.040	0.053	0.113	0.120	0.118
cations	15.696	15.734	15.750	15.754	15.692	15.796	15.704	15.733	15.747
$Mg/(Mg+Fe_{TOT})$	0.81	0.81	0.81	0.81	0.79	0.78	0.80	0.80	0.81
(Na+K)A	0.72	0.77	0.82	0.80	0.71	0.80	0.77	0.79	0.75

Note: Oxide values are in wt.%. All other values are calculated with normalization program Norm.

Table 12 - Electron microprobe analyses of olivine of the sample Pilg 8 38
(Pilgüjarvi sill – Pechenga Complex, Russia).

	Olivine					
SiO_2	38.79	39.11	38.91	38.99	39.74	39.28
TiO_2	0.06	0.06	0.00	0.08	0.00	0.00
Al_2O_3	0.03	0.01	0.00	0.01	0.02	0.05
Cr_2O_3	0.00	0.00	0.04	0.03	0.01	0.03
FeO	20.12	20.16	20.99	20.79	20.46	21.26
MnO	0.37	0.20	0.32	0.26	0.21	0.21
NiO	0.10	0.19	0.09	0.04	0.11	0.15
MgO	41.78	41.97	40.53	41.51	40.81	41.18
CaO	0.20	0.16	0.18	0.12	0.16	0.17
Na_2O	0.06	0.00	0.00	0.00	0.09	0.05
K_2O	0.01	0.00	0.00	0.00	0.00	0.00
Total	101.52	101.86	101.07	101.83	101.61	102.38
Si	0.980	0.985	0.994	0.985	1.008	0.990
Ti	0.001	0.001	0.000	0.002	0.000	0.000
Al	0.001	0.000	0.000	0.000	0.001	0.002
Cr	0.000	0.000	0.001	0.001	0.000	0.001
Fe^{2+}	0.425	0.425	0.448	0.439	0.434	0.448
Mn	0.008	0.004	0.007	0.006	0.004	0.004
Ni	0.002	0.004	0.002	0.001	0.002	0.003
Mg	1.574	1.576	1.543	1.563	1.542	1.546
Ca	0.005	0.004	0.005	0.003	0.004	0.005
Na	0.003	0.000	0.000	0.000	0.004	0.002
K	0.000	0.000	0.000	0.000	0.000	0.000
Forsterite	0.78	0.78	0.77	0.78	0.78	0.77
Fayalite	0.21	0.21	0.22	0.22	0.22	0.22
Tephroite	0.00	0.00	0.00	0.00	0.00	0.00
Monticellit	0.00	0.00	0.00	0.00	0.00	0.00
Kirschstein	0.00	0.00	0.00	0.00	0.00	0.00
Glaukocroit	0.00	0.00	0.00	0.00	0.00	0.00
Ni-Olivine	0.00	0.00	0.00	0.00	0.00	0.00
xMg	0.78	0.78	0.77	0.78	0.77	0.77
xFe	0.21	0.21	0.22	0.22	0.22	0.22

Note: Oxide values are in wt.%.
All other values are calculated with normalization program Norm.

Table 13 - Electron microprobe analyses of clinopyroxene of the sample Pilg 8 38 (Pilgüjarvi sill – Pechenga Complex, Russia).

	Clinopyroxene				
SiO_2	53.05	51.88	51.17	52.54	51.05
TiO_2	1.06	0.93	1.34	1.24	1.57
Al_2O_3	2.24	2.31	3.54	2.39	3.49
Cr_2O_3	0.73	0.86	0.52	0.65	0.59
Fe_2O_3	0.00	1.16	0.69	0.21	0.00
FeO	5.68	4.63	5.29	5.49	5.68
MnO	0.08	0.12	0.15	0.17	0.06
NiO	0.01	0.00	0.00	0.01	0.00
MgO	15.98	16.00	14.96	15.73	14.75
CaO	22.01	21.99	22.17	22.16	22.00
Na_2O	0.30	0.31	0.41	0.40	0.42
K_2O	0.00	0.00	0.00	0.00	0.00
Total	101.14	100.18	100.24	100.98	99.62
Si	1.931	1.907	1.883	1.917	1.891
Ti	0.029	0.026	0.037	0.034	0.044
Al	0.096	0.100	0.154	0.103	0.152
Cr	0.021	0.025	0.015	0.019	0.017
Fe^{3+}	0.000	0.032	0.019	0.006	0.000
Fe^{2+}	0.173	0.142	0.163	0.168	0.176
Mn	0.003	0.004	0.005	0.005	0.002
Ni	0.000	0.000	0.000	0.000	0.000
Mg	0.867	0.877	0.821	0.855	0.814
Ca	0.859	0.866	0.874	0.866	0.873
Na	0.021	0.022	0.029	0.028	0.030
K	0.000	0.000	0.000	0.000	0.000
Wollastonite	0.41	0.40	0.40	0.41	0.40
Enstatite	0.43	0.44	0.41	0.43	0.41
Ferrosilite	0.09	0.07	0.08	0.08	0.09
Pyroxmangite	0.00	0.00	0.00	0.00	0.00
Acmite	0.00	0.02	0.02	0.01	0.00
Jadeite	0.02	0.00	0.01	0.02	0.03
xMgonM1	0.77	0.78	0.74	0.77	0.74
xMgonM2	0.10	0.09	0.08	0.08	0.08
xMgFe(II+)	0.83	0.86	0.83	0.84	0.82
xMgFe(tot)	0.83	0.83	0.82	0.83	0.82

Note: Oxide values are in wt.%.
All other values are calculated with normalization program Norm.

Table 14 - Electron microprobe analyses of brown amphibole of the sample Pilg 8 38 (Pilgüjarvi sill – Pechenga Complex, Russia).

	Amphibole				
SiO_2	45.00	42.05	39.38	39.23	38.24
TiO_2	3.32	4.99	5.25	5.57	5.40
Al_2O_3	8.31	10.64	12.25	12.57	12.57
Cr_2O_3	0.55	0.49	0.09	0.06	0.04
FeOtot	9.56	8.14	10.16	9.86	10.54
MnO	0.09	0.08	0.14	0.09	0.13
NiO	0.24	0.17	0.16	0.15	0.18
MgO	15.35	14.89	13.72	13.81	13.38
CaO	11.65	12.38	12.40	12.56	12.50
Na_2O	3.14	3.01	2.84	2.76	2.78
K_2O	0.38	0.70	0.73	0.73	0.74
Cl	0.00	0.00	0.00	0.00	0.00
O=Cl					
Total	97.58	97.53	97.11	97.39	96.51
Si	6.583	6.169	5.878	5.831	5.769
Ti	0.366	0.550	0.589	0.623	0.613
Al	1.432	1.839	2.154	2.201	2.235
Cr	0.063	0.057	0.010	0.007	0.005
Fe^{2+}	1.169	0.998	1.268	1.226	1.330
Fe^{3+}	0.000	0.000	0.000	0.000	0.000
Mn	0.012	0.010	0.017	0.012	0.017
Ni	0.028	0.021	0.019	0.018	0.022
Mg	3.344	3.253	3.050	3.057	3.007
Ca	1.826	1.946	1.984	2.000	2.021
Na	0.891	0.855	0.823	0.797	0.813
K	0.070	0.131	0.138	0.138	0.143
cations	15.784	15.826	15.931	15.910	15.975
$Mg/(Mg+Fe_{TOT})$	0.74	0.77	0.71	0.71	0.69
(Na+K)A	0.79	0.93	0.94	0.94	0.96

Note: Oxide values are in wt.%.
All other values are calculated with normalization program Norm.

Table 15 - Electron microprobe analyses of olivine of the sample 106-44 (Pilgüjarvi sill – Pechenga Complex, Russia).

	Olivine		
SiO_2	39.14	38.91	38.75
TiO_2	0.03	0.07	0.06
Al_2O_3	0.00	0.01	0.04
Cr_2O_3	0.05	0.06	0.05
FeO	19.26	19.71	18.88
MnO	0.27	0.31	0.23
NiO	0.24	0.36	0.20
MgO	40.90	41.11	41.33
CaO	0.25	0.22	0.27
Na_2O	0.05	0.06	0.06
K_2O	0.00	0.00	0.00
Total	100.20	100.82	99.88
Si	1.003	0.992	0.993
Ti	0.001	0.001	0.001
Al	0.000	0.000	0.001
Cr	0.001	0.001	0.001
Fe^{2+}	0.413	0.420	0.405
Mn	0.006	0.007	0.005
Ni	0.005	0.007	0.004
Mg	1.562	1.562	1.579
Ca	0.007	0.006	0.008
Na	0.003	0.003	0.003
K	0.000	0.000	0.000
Forsterite	0.78	0.78	0.79
Fayalite	0.21	0.21	0.20
Tephroite	0.00	0.00	0.00
Monticellit	0.01	0.01	0.01
Kirschstein	0.00	0.00	0.00
Glaukocroit	0.00	0.00	0.00
Ni-Olivine	0.00	0.00	0.00
xMg	0.78	0.78	0.79
xFe	0.21	0.21	0.20

Note: Oxide values are in wt.%.
All other values are calculated with normalization program Norm.

Table 16 - Electron microprobe analyses of clinopyroxene of the sample 106-44 (Pilgüjarvi sill – Pechenga Complex, Russia).

	Clinopyroxene		
SiO_2	48.34	51.62	50.29
TiO_2	2.41	1.20	1.43
Al_2O_3	5.30	1.90	3.05
Cr_2O_3	0.65	0.73	0.94
Fe_2O_3	1.43	0.60	1.71
FeO	4.22	4.66	4.03
MnO	0.11	0.13	0.02
NiO	0.08	0.06	0.08
MgO	13.92	15.75	15.11
CaO	22.22	21.93	22.14
Na_2O	0.49	0.38	0.43
K_2O	0.01	0.01	0.00
Total	99.17	98.97	99.23
Si	1.804	1.920	1.871
Ti	0.068	0.034	0.040
Al	0.233	0.083	0.134
Cr	0.019	0.022	0.028
Fe^{3+}	0.040	0.017	0.048
Fe^{2+}	0.132	0.145	0.125
Mn	0.003	0.004	0.001
Ni	0.002	0.002	0.002
Mg	0.774	0.873	0.838
Ca	0.888	0.874	0.883
Na	0.035	0.027	0.031
K	0.000	0.001	0.000
Wollastonite	0.38	0.41	0.40
Enstatite	0.39	0.44	0.42
Ferrosilite	0.07	0.07	0.06
Pyroxmangite	0.00	0.00	0.00
Acmite	0.04	0.02	0.03
Jadeite	0.00	0.00	0.00
xMgonM1	0.71	0.79	0.76
xMgonM2	0.06	0.08	0.08
xMgFe(II+)	0.86	0.86	0.87
xMgFe(tot)	0.82	0.84	0.83

Note: Oxide values are in wt.%. All other values are calculated with normalization program Norm.

Table 17 - Electron microprobe analyses of brown amphibole of the sample 106-44 (Pilgüjarvi sill – Pechenga Complex, Russia).

	Amphibole						
SiO_2	41.08	41.85	41.26	41.23	42.04	40.66	41.52
TiO_2	5.78	5.42	5.92	5.88	5.02	5.65	5.70
Al_2O_3	12.30	11.95	12.28	11.96	11.59	12.63	12.64
Cr_2O_3	0.57	0.46	0.40	0.54	0.31	0.64	0.42
FeOtot	8.17	7.87	7.92	8.04	8.42	8.18	8.13
MnO	0.07	0.09	0.07	0.09	0.07	0.11	0.06
NiO	0.11	0.09	0.05	0.00	0.00	0.02	0.18
MgO	14.09	14.46	14.17	14.10	14.41	14.15	14.02
CaO	11.80	11.78	11.76	11.71	11.51	11.75	11.68
Na_2O	3.10	2.78	3.10	3.05	2.55	2.88	2.99
K_2O	0.58	0.56	0.56	0.54	0.65	0.58	0.58
Cl	0.08	0.08	0.08	0.08	0.08	0.08	0.08
O=Cl							
Total	97.66	97.31	97.49	97.14	96.57	97.25	97.91
Si	6.008	6.113	6.029	6.050	6.188	5.969	6.040
Ti	0.636	0.595	0.651	0.649	0.556	0.624	0.624
Al	2.120	2.057	2.115	2.069	2.010	2.185	2.167
Cr	0.066	0.053	0.047	0.062	0.036	0.074	0.049
Fe^{2+}	0.999	0.961	0.968	0.987	1.036	1.004	0.989
Fe^{3+}	0.000	0.000	0.000	0.000	0.000	0.000	0.000
Mn	0.009	0.011	0.009	0.011	0.009	0.014	0.007
Ni	0.013	0.011	0.006	0.000	0.000	0.002	0.021
Mg	3.069	3.146	3.084	3.082	3.159	3.093	3.037
Ca	1.849	1.844	1.841	1.841	1.815	1.848	1.820
Na	0.879	0.787	0.878	0.868	0.728	0.820	0.843
K	0.109	0.104	0.104	0.102	0.122	0.109	0.107
cations	15.757	15.682	15.731	15.720	15.658	15.742	15.704
$Mg/(Mg+Fe_{TOT})$	0.75	0.77	0.76	0.76	0.75	0.75	0.75
(Na+K)A	0.84	0.73	0.82	0.81	0.66	0.78	0.77

Note: Oxide values are in wt.%.
All other values are calculated with normalization program Norm.

Table 18 - Electron microprobe analyses of clinopyroxene of the sample 116-6 (Pilgüjarvi sill – Pechenga Complex, Russia).

	Clinopyroxene	
SiO_2	51.42	49.23
TiO_2	1.23	2.07
Al_2O_3	2.73	4.38
Cr_2O_3	0.02	0.01
Fe_2O_3	1.30	2.28
FeO	6.88	6.53
MnO	0.13	0.16
NiO	0.00	0.04
MgO	14.69	13.49
CaO	21.69	21.80
Na_2O	0.35	0.43
K_2O	0.00	0.01
Total	100.44	100.43
Si	1.900	1.830
Ti	0.034	0.058
Al	0.119	0.192
Cr	0.001	0.000
Fe^{3+}	0.036	0.064
Fe^{2+}	0.213	0.203
Mn	0.004	0.005
Ni	0.000	0.001
Mg	0.809	0.747
Ca	0.859	0.868
Na	0.025	0.031
K	0.000	0.001
Wollastonite	0.40	0.38
Enstatite	0.41	0.37
Ferrosilite	0.11	0.10
Pyroxmangite	0.00	0.00
Acmite	0.03	0.03
Jadeite	0.00	0.00
xMgonM1	0.72	0.67
xMgonM2	0.09	0.08
xMgFe(II+)	0.79	0.79
xMgFe(tot)	0.77	0.74

Note: Oxide values are in wt.%.
All other values are calculated with normalization program Norm.

Table 19 - Electron microprobe analyses of brown amphibole of the sample 116-6 (Pilgüjarvi sill - Pechenga Complex, Russia).

	Amphibole					
SiO_2	41.35	42.28	40.69	41.71	42.40	41.74
TiO_2	5.65	5.22	5.28	5.37	4.98	5.01
Al_2O_3	11.61	11.38	11.75	11.76	11.35	12.13
Cr_2O_3	0.04	0.05	0.09	0.01	0.03	0.00
FeOtot	11.22	10.70	10.93	10.95	10.80	10.77
MnO	0.01	0.07	0.02	0.10	0.07	0.09
NiO	0.02	0.00	0.00	0.11	0.00	0.00
MgO	13.21	13.34	13.21	13.42	13.52	13.30
CaO	11.67	11.65	11.59	11.56	11.46	11.24
Na_2O	3.05	3.05	3.02	3.05	3.17	3.20
K_2O	0.98	0.93	0.93	0.99	0.96	0.79
Cl	0.00	0.00	0.00	0.00	0.00	0.00
O=Cl						
Total	98.80	98.68	97.51	99.03	98.75	98.27
Si	6.060	6.174	6.039	6.087	6.188	6.115
Ti	0.623	0.573	0.589	0.590	0.547	0.552
Al	2.005	1.959	2.055	2.023	1.952	2.094
Cr	0.004	0.006	0.011	0.001	0.004	0.000
Fe^{2+}	1.375	1.307	1.357	1.336	1.318	1.319
Fe^{3+}	0.000	0.000	0.000	0.000	0.000	0.000
Mn	0.002	0.009	0.003	0.012	0.009	0.011
Ni	0.002	0.000	0.000	0.013	0.000	0.000
Mg	2.883	2.901	2.920	2.917	2.939	2.902
Ca	1.833	1.823	1.843	1.808	1.792	1.764
Na	0.867	0.864	0.869	0.863	0.897	0.909
K	0.182	0.174	0.176	0.184	0.180	0.148
cations	15.837	15.789	15.861	15.835	15.825	15.814
$Mg/(Mg+Fe_{TOT})$	0.68	0.69	0.68	0.69	0.69	0.69
(Na+K)A	0.88	0.86	0.89	0.86	0.87	0.82

Note: Oxide values are in wt.%.
All other values are calculated with normalization program Norm.

Table 20 - Electron microprobe analyses of olivine of the sample 57-HV-28 (Kammikivi sill – Pechenga Complex, Russia).

	Olivine				
SiO_2	39.68	39.45	39.65	39.61	39.64
TiO_2	0.00	0.08	0.11	0.01	0.06
Al_2O_3	0.03	0.03	0.04	0.04	0.04
Cr_2O_3	0.04	0.02	0.01	0.01	0.06
FeO	17.37	18.17	17.68	17.09	17.63
MnO	0.29	0.25	0.25	0.29	0.28
NiO	0.38	0.31	0.35	0.42	0.45
MgO	43.13	42.16	42.34	42.92	42.85
CaO	0.25	0.17	0.25	0.31	0.22
Na_2O	0.02	0.02	0.03	0.01	0.05
K_2O	0.00	0.01	0.00	0.00	0.02
Total	101.2	100.67	100.71	100.71	101.3
Si	0.9968	1.0005	1.0038	0.9996	0.9964
Ti	0.0001	0.0016	0.0020	0.0002	0.0011
Al	0.0008	0.0009	0.0013	0.0012	0.0010
Cr	0.0008	0.0003	0.0001	0.0002	0.0011
Fe^{2+}	0.3649	0.3854	0.3743	0.3607	0.3706
Mn	0.0062	0.0053	0.0054	0.0062	0.0060
Ni	0.0077	0.0063	0.0071	0.0085	0.0091
Mg	1.6150	1.5937	1.5976	1.6144	1.6054
Ca	0.0068	0.0047	0.0068	0.0083	0.0061
Na	0.0008	0.0011	0.0014	0.0006	0.0025
K	0.0000	0.0002	0.0001	0.0000	0.0006
Forsterite	0.807	0.799	0.802	0.808	0.804
Fayalite	0.182	0.193	0.188	0.181	0.186
Tephroite	0.003	0.003	0.003	0.003	0.003
Monticellit	0.006	0.004	0.006	0.007	0.005
Kirschstein	0.001	0.001	0.001	0.002	0.001
Glaukocroit	0.000	0.000	0.000	0.000	0.000
Ni-Olivine	0.004	0.003	0.004	0.004	0.005
xMg	0.806	0.797	0.800	0.807	0.801
xFe	0.182	0.193	0.188	0.180	0.185

Note: Oxide values are in wt.%.
All other values are calculated with normalization program Norm.

Table 21 - Electron microprobe analyses of clinopyroxene of the sample 57-HV-28 (Kammikivi sill – Pechenga Complex, Russia).

	Clinopyroxene				
SiO_2	47.64	50.96	50.82	49.07	49.95
TiO_2	2.97	1.71	1.69	2.40	1.83
Al_2O_3	6.47	3.88	3.79	5.24	4.05
Cr_2O_3	0.57	0.46	1.00	0.70	0.89
Fe_2O_3	1.10	0.10	0.22	0.74	1.23
FeO	4.64	5.48	5.13	5.06	4.26
MnO	0.12	0.15	0.12	0.09	0.07
NiO	0.03	0.07	0.08	0.05	0.08
MgO	13.59	15.24	15.01	14.17	14.83
CaO	21.94	21.67	22.06	22.02	22.14
Na_2O	0.53	0.40	0.41	0.47	0.46
K_2O	0.02	0.00	0.01	0.00	0.01
Total	99.62	100.12	100.34	100.01	99.80
Si	1.771	1.875	1.869	1.815	1.848
Ti	0.083	0.047	0.047	0.067	0.051
Al	0.284	0.168	0.164	0.229	0.177
Cr	0.017	0.014	0.029	0.020	0.026
Fe^{3+}	0.031	0.003	0.006	0.021	0.034
Fe^{2+}	0.144	0.169	0.158	0.157	0.132
Mn	0.004	0.005	0.004	0.003	0.002
Ni	0.001	0.002	0.002	0.001	0.002
Mg	0.753	0.836	0.823	0.781	0.818
Ca	0.874	0.854	0.869	0.873	0.877
Na	0.038	0.028	0.029	0.034	0.033
K	0.001	0.000	0.001	0.000	0.000
Wollastonite	0.36	0.39	0.39	0.38	0.39
Enstatite	0.38	0.42	0.41	0.39	0.41
Ferrosilite	0.07	0.08	0.08	0.08	0.07
Pyroxmangite	0.00	0.00	0.00	0.00	0.00
Acmite	0.03	0.00	0.01	0.02	0.03
Jadeite	0.01	0.03	0.02	0.01	0.00
xMgonM1	0.68	0.74	0.74	0.71	0.74
xMgonM2	0.07	0.09	0.08	0.08	0.08
xMgFe(II+)	0.84	0.83	0.84	0.83	0.86
xMgFe(tot)	0.81	0.83	0.83	0.82	0.83

Note: Oxide values are in wt.%.
All other values are calculated with normalization program Norm.

Table 22 - Electron microprobe analyses of brown amphibole of the sample 57-HV-28 (Kammikivi sill – Pechenga Complex, Russia).

	Amphibole					
SiO_2	42.18	42.70	43.79	43.57	42.90	44.56
TiO_2	5.50	5.78	4.92	5.09	5.62	4.43
Al_2O_3	10.66	10.95	10.00	10.43	10.63	9.02
Cr_2O_3	0.47	0.32	0.21	0.22	0.10	0.41
FeOtot	7.40	7.83	7.02	7.39	7.43	7.02
MnO	0.06	0.10	0.10	0.11	0.09	0.11
NiO	0.05	0.16	0.06	0.12	0.14	0.11
MgO	15.30	15.21	15.74	15.43	15.46	16.16
CaO	11.63	11.53	11.54	11.42	11.52	11.20
Na_2O	3.27	2.99	3.13	3.19	3.00	3.20
K_2O	0.79	0.79	0.75	0.79	0.77	1.00
Cl	0.09	0.09	0.09	0.09	0.09	0.09
O=Cl						
Total	97.31	98.36	97.25	97.76	97.65	97.22
Si	6.170	6.177	6.366	6.315	6.232	6.483
Ti	0.605	0.629	0.538	0.555	0.614	0.485
Al	1.838	1.867	1.713	1.782	1.820	1.547
Cr	0.054	0.037	0.024	0.025	0.011	0.047
Fe^{2+}	0.905	0.947	0.853	0.896	0.903	0.854
Fe^{3+}	0.000	0.000	0.000	0.000	0.000	0.000
Mn	0.007	0.012	0.012	0.013	0.011	0.014
Ni	0.006	0.019	0.007	0.013	0.016	0.013
Mg	3.333	3.277	3.408	3.331	3.345	3.502
Ca	1.823	1.787	1.797	1.774	1.793	1.746
Na	0.927	0.839	0.882	0.897	0.845	0.903
K	0.147	0.146	0.139	0.147	0.142	0.186
cations	15.816	15.735	15.738	15.748	15.732	15.779
$Mg/(Mg+Fe_{TOT})$	0.79	0.78	0.80	0.79	0.79	0.80
(Na+K)A	0.90	0.77	0.82	0.82	0.78	0.83

Continued Table 22

	Amphibole					
SiO_2	43.58	43.81	41.01	43.16	42.45	42.06
TiO_2	5.02	5.13	6.48	5.22	5.32	5.85
Al_2O_3	9.58	9.69	12.34	10.20	10.49	10.83
Cr_2O_3	0.14	0.06	0.41	0.41	0.23	0.27
FeOtot	7.12	7.24	7.82	7.32	7.42	7.40
MnO	0.06	0.13	0.09	0.08	0.08	0.06
NiO	0.22	0.12	0.11	0.09	0.10	0.07
MgO	15.84	16.02	14.09	15.46	15.63	15.08
CaO	11.31	11.29	11.78	11.33	11.60	11.55
Na_2O	3.27	3.27	2.90	3.11	3.05	3.12
K_2O	0.85	0.85	0.45	0.81	0.75	0.72
Cl	0.09	0.09	0.09	0.09	0.09	0.09
O=Cl						
Total	96.98	97.61	97.48	97.19	97.13	97.02
Si	6.368	6.359	5.989	6.297	6.210	6.161
Ti	0.552	0.560	0.712	0.573	0.585	0.645
Al	1.650	1.658	2.124	1.754	1.809	1.870
Cr	0.016	0.007	0.048	0.047	0.027	0.032
Fe^{2+}	0.870	0.879	0.955	0.893	0.908	0.907
Fe^{3+}	0.000	0.000	0.000	0.000	0.000	0.000
Mn	0.007	0.016	0.011	0.010	0.010	0.008
Ni	0.026	0.014	0.013	0.011	0.012	0.008
Mg	3.447	3.463	3.065	3.359	3.405	3.290
Ca	1.771	1.756	1.843	1.771	1.818	1.813
Na	0.926	0.920	0.821	0.880	0.865	0.886
K	0.158	0.157	0.085	0.151	0.140	0.134
cations	15.790	15.788	15.666	15.745	15.790	15.753
$Mg/(Mg+Fe_{TOT})$	0.80	0.80	0.76	0.79	0.79	0.78
(Na+K)A	0.86	0.83	0.75	0.80	0.82	0.83

Note: Oxide values are in wt.%. All other values are calculated with normalization program Norm.

Table 23 - Electron microprobe analyses of olivine of the sample N-2 (Nyasyukka dike complex – Pechenga Complex, Russia).

	Olivine							
SiO_2	37.92	37.89	37.48	37.85	39.25	38.13	38.25	38.29
TiO_2	0.07	0	0.07	0.03	0.03	0.02	0.03	0.04
Al_2O_3	0.02	0	0	0.01	0.02	0	0	0
Cr_2O_3	0	0	0	0	0	0	0.02	0
FeO	30.53	29.08	34.11	29.24	24.95	30.35	28.95	27.08
MnO	0.51	0.49	0.6	0.43	0.31	0.43	0.47	0.35
NiO	0.27	0.18	0.29	0.26	0.23	0.17	0.07	0.2
MgO	33.89	34.6	31.34	34.66	38.08	34.09	34.87	36.74
CaO	0.02	0.06	0.04	0.02	0.06	0.03	0.03	0.04
Na_2O	0	0	0	0	0	0.03	0	0
K_2O	0	0	0	0	0	0	0	0
Total	103.23	102.3	103.93	102.51	102.93	103.25	102.68	102.74
Si	0.992	0.994	0.990	0.991	1.003	0.995	0.998	0.988
Ti	0.001	0.000	0.001	0.001	0.001	0.001	0.001	0.001
Al	0.001	0.000	0.000	0.000	0.001	0.000	0.000	0.000
Cr	0.000	0.000	0.000	0.000	0.000	0.000	0.000	0.000
Fe^{2+}	0.668	0.638	0.754	0.640	0.533	0.663	0.632	0.585
Mn	0.011	0.011	0.013	0.010	0.007	0.010	0.010	0.008
Ni	0.006	0.004	0.006	0.006	0.005	0.004	0.001	0.004
Mg	1.321	1.352	1.234	1.352	1.450	1.326	1.356	1.413
Ca	0.001	0.002	0.001	0.001	0.002	0.001	0.001	0.001
Na	0.000	0.000	0.000	0.000	0.000	0.002	0.000	0.000
K	0.000	0.000	0.000	0.000	0.000	0.000	0.000	0.000
Forsterite	0.658	0.674	0.614	0.673	0.726	0.662	0.678	0.703
Fayalite	0.333	0.318	0.375	0.319	0.267	0.331	0.316	0.291
Tephroite	0.006	0.005	0.007	0.005	0.003	0.005	0.005	0.004
Monticellit	0	0.001	0.001	0	0.001	0.001	0.001	0.001
Kirschstein	0	0.001	0	0	0	0	0	0
Glaukocroit	0	0	0	0	0	0	0	0
Ni-Olivine	0.003	0.002	0.003	0.003	0.002	0.002	0.001	0.002
xMg	0.658	0.674	0.614	0.673	0.726	0.662	0.678	0.703
xFe	0.332	0.318	0.375	0.319	0.267	0.33	0.316	0.291

Note: Oxide values are in wt.%. All other values are calculated with normalization program Norm.

Table 24 - Electron microprobe analyses of olivine of the sample N-3 (Nyasyukka dike complex – Pechenga Complex, Russia).

	Olivine											
SiO_2	38.25	37.42	38.00	38.35	37.68	37.26	38.23	38.56	38.38	38.79	38.62	38.04
TiO_2	0.00	0.00	0.03	0.05	0.02	0.04	0.00	0.02	0.04	0.07	0.01	0.02
Al_2O_3	0.03	0.03	0.00	0.02	0.00	0.02	0.00	0.03	0.00	0.04	0.00	0.02
Cr_2O_3	0.00	0.01	0.01	0.00	0.00	0.00	0.00	0.00	0.00	0.00	0.00	0.00
FeO	25.85	33.08	27.75	27.37	30.42	32.52	28.77	25.95	26.56	25.50	25.49	30.41
MnO	0.42	0.45	0.37	0.40	0.41	0.35	0.46	0.40	0.33	0.43	0.39	0.52
NiO	0.15	0.10	0.20	0.13	0.18	0.20	0.22	0.24	0.34	0.24	0.18	0.21
MgO	37.03	31.81	35.82	35.80	33.67	31.70	34.98	36.84	37.08	37.44	37.66	33.54
CaO	0.01	0.00	0.11	0.10	0.03	0.04	0.00	0.04	0.02	0.04	0.04	0.01
Na_2O	0.01	0.04	0.00	0.00	0.01	0.00	0.00	0.03	0.03	0.00	0.02	0.00
K_2O	0.00	0.00	0.00	0.00	0.00	0.00	0.00	0.00	0.01	0.02	0.00	0.00
Total	101.74	102.96	102.30	102.22	102.44	102.14	102.66	102.11	102.79	102.55	102.42	102.76
Si	0.993	0.993	0.989	0.999	0.993	0.996	0.997	0.999	0.988	0.998	0.993	1.000
Ti	0.000	0.000	0.001	0.001	0.001	0.001	0.000	0.000	0.001	0.001	0.000	0.000
Al	0.001	0.001	0.000	0.001	0.000	0.001	0.000	0.001	0.000	0.001	0.000	0.001
Cr	0.000	0.000	0.000	0.000	0.000	0.000	0.000	0.000	0.000	0.000	0.000	0.000
Fe^{2+}	0.561	0.734	0.604	0.596	0.670	0.727	0.628	0.562	0.572	0.549	0.548	0.669
Mn	0.009	0.010	0.008	0.009	0.009	0.008	0.010	0.009	0.007	0.009	0.009	0.012
Ni	0.003	0.002	0.004	0.003	0.004	0.004	0.005	0.005	0.007	0.005	0.004	0.004
Mg	1.432	1.258	1.390	1.389	1.322	1.263	1.360	1.422	1.423	1.435	1.444	1.314
Ca	0.000	0.000	0.003	0.003	0.001	0.001	0.000	0.001	0.001	0.001	0.001	0.000
Na	0.000	0.002	0.000	0.000	0.001	0.000	0.000	0.001	0.001	0.000	0.001	0.000
K	0.000	0.000	0.000	0.000	0.000	0.000	0.000	0.000	0.000	0.001	0.000	0.000
Forsterite	0.71	0.63	0.69	0.70	0.66	0.63	0.68	0.71	0.71	0.72	0.72	0.66
Fayalite	0.28	0.37	0.30	0.30	0.33	0.36	0.31	0.28	0.29	0.27	0.27	0.33
Tephroite	0.01	0.01	0.00	0.00	0.01	0.00	0.01	0.00	0.00	0.01	0.00	0.01
Monticellit	0.00	0.00	0.00	0.00	0.00	0.00	0.00	0.00	0.00	0.00	0.00	0.00
Kirschstein	0.00	0.00	0.00	0.00	0.00	0.00	0.00	0.00	0.00	0.00	0.00	0.00
Glaukocroit	0.00	0.00	0.00	0.00	0.00	0.00	0.00	0.00	0.00	0.00	0.00	0.00
Ni-Olivine	0.00	0.00	0.00	0.00	0.00	0.00	0.00	0.00	0.00	0.00	0.00	0.00
xMg	0.71	0.63	0.69	0.69	0.66	0.63	0.68	0.71	0.71	0.72	0.72	0.66
xFe	0.28	0.37	0.30	0.30	0.33	0.36	0.31	0.28	0.28	0.27	0.27	0.33

Note: Oxide values are in wt.%. All other values are calculated with normalization program Norm.

Table 25 - Electron microprobe analyses of clinopyroxene of the samples N-2 and N-3 (Nyasyukka dike complex - Pechenga Complex, Russia)

	Clinopyroxene (N-2)				*Clinopyroxene (N-3)*						
SiO_2	52.44	51.30	51.44	51.48	51.63	50.32	52.85	51.03	51.74	50.69	51.55
TiO_2	1.22	1.49	1.47	1.41	1.42	1.20	0.58	1.62	1.37	1.28	1.37
Al_2O_3	2.33	3.05	2.79	2.71	2.26	3.27	1.83	3.26	2.19	3.11	2.80
Cr_2O_3	0.45	0.70	0.16	0.25	0.23	0.08	0.17	0.21	0.07	0.06	0.76
Fe_2O_3	1.27	1.42	1.85	2.05	0.82	3.14	1.70	1.46	1.47	2.75	1.22
FeO	6.02	5.51	5.58	5.42	6.40	4.55	6.09	6.09	6.00	4.97	5.48
MnO	0.14	0.06	0.21	0.15	0.14	0.17	0.27	0.10	0.10	0.19	0.13
NiO	0.01	0.10	0.00	0.09	0.00	0.04	0.05	0.08	0.00	0.05	0.01
MgO	15.68	15.08	15.27	15.07	15.16	14.53	15.48	14.64	15.00	14.74	15.19
CaO	21.83	22.22	21.89	22.20	21.98	22.13	21.57	21.94	22.41	21.98	22.15
Na_2O	0.37	0.36	0.38	0.40	0.28	0.48	0.45	0.43	0.33	0.46	0.38
K_2O	0.00	0.00	0.00	0.00	0.00	0.00	0.00	0.00	0.01	0.00	0.01
Total	101.77	101.29	101.04	101.23	100.32	99.91	101.03	100.86	100.69	100.28	101.05
Si	1.906	1.877	1.885	1.885	1.907	1.867	1.935	1.877	1.905	1.874	1.888
Ti	0.033	0.041	0.041	0.039	0.039	0.034	0.016	0.045	0.038	0.036	0.038
Al	0.100	0.132	0.121	0.117	0.098	0.143	0.079	0.141	0.095	0.136	0.121
Cr	0.013	0.020	0.005	0.007	0.007	0.002	0.005	0.006	0.002	0.002	0.022
Fe^{3+}	0.035	0.039	0.051	0.057	0.023	0.088	0.047	0.040	0.041	0.077	0.034
Fe^{2+}	0.183	0.169	0.171	0.166	0.198	0.141	0.187	0.187	0.185	0.154	0.168
Mn	0.004	0.002	0.006	0.005	0.004	0.005	0.008	0.003	0.003	0.006	0.004
Ni	0.000	0.003	0.000	0.003	0.000	0.001	0.001	0.002	0.000	0.002	0.000
Mg	0.849	0.822	0.834	0.823	0.834	0.804	0.845	0.803	0.823	0.812	0.829
Ca	0.850	0.871	0.860	0.871	0.870	0.880	0.846	0.865	0.884	0.871	0.869
Na	0.026	0.026	0.027	0.029	0.020	0.035	0.032	0.031	0.024	0.033	0.027
K	0.000	0.000	0.000	0.000	0.000	0.000	0.000	0.000	0.000	0.000	0.001
Wollastonite	0.40	0.39	0.39	0.40	0.41	0.39	0.40	0.39	0.41	0.39	0.40
Enstatite	0.43	0.41	0.42	0.41	0.42	0.40	0.42	0.40	0.41	0.41	0.42
Ferrosilite	0.09	0.08	0.09	0.08	0.10	0.07	0.09	0.09	0.09	0.08	0.08
Pyroxmangite	0.00	0.00	0.00	0.00	0.00	0.00	0.00	0.00	0.00	0.00	0.00
Acmite	0.03	0.03	0.03	0.03	0.02	0.04	0.03	0.03	0.02	0.03	0.03
Jadeite	0.00	0.00	0.00	0.00	0.00	0.00	0.00	0.00	0.00	0.00	0.00
xMgonM1	0.75	0.74	0.75	0.74	0.75	0.74	0.75	0.72	0.75	0.74	0.75
xMgonM2	0.10	0.08	0.09	0.08	0.09	0.07	0.09	0.08	0.07	0.08	0.08
xMgFe(II+)	0.82	0.83	0.83	0.83	0.81	0.85	0.82	0.81	0.82	0.84	0.83
xMgFe(tot)	0.80	0.80	0.79	0.79	0.79	0.78	0.78	0.78	0.79	0.78	0.80

Note: Oxide values are in wt.%. All other values are calculated with normalization program Norm.

Table 26 - Electron microprobe analyses of brown amphibole of the sample N-2 (Nyasyukka dike complex - Pechenga Complex, Russia)

	Amphibole									
SiO_2	42.73	42.76	42.76	42.28	42.43	42.41	42.11	42.84	41.81	42.48
TiO_2	4.94	4.55	4.78	5.08	4.80	5.24	5.21	4.51	5.06	4.94
Al_2O_3	10.35	10.17	10.42	10.68	10.52	11.01	11.15	10.40	10.90	10.81
Cr_2O_3	0.40	0.36	0.40	0.36	0.34	0.14	0.23	0.30	0.19	0.17
FeOtot	10.70	10.61	10.59	10.53	10.74	10.31	10.53	10.77	10.26	10.11
MnO	0.12	0.10	0.15	0.17	0.11	0.15	0.15	0.10	0.11	0.07
NiO	0.05	0.08	0.13	0.06	0.03	0.13	0.10	0.06	0.01	0.01
MgO	13.85	13.94	13.90	13.98	13.98	13.89	13.90	13.96	13.76	13.85
CaO	11.41	11.42	11.42	11.59	11.57	11.75	11.59	11.40	11.70	11.53
Na_2O	2.83	3.05	3.31	3.01	2.89	3.01	2.93	3.05	2.96	2.91
K_2O	0.75	0.73	0.76	0.73	0.73	0.77	0.75	0.72	0.77	0.77
Cl										
O=Cl										
Total	98.12	97.76	98.62	98.46	98.14	98.81	98.65	98.11	97.53	97.65
Si	6.267	6.296	6.251	6.189	6.229	6.179	6.149	6.285	6.172	6.242
Ti	0.545	0.504	0.526	0.559	0.530	0.574	0.572	0.498	0.562	0.546
Al	1.789	1.765	1.795	1.843	1.820	1.890	1.919	1.798	1.896	1.872
Cr	0.047	0.042	0.046	0.041	0.039	0.016	0.027	0.034	0.022	0.019
Fe^{2+}	1.312	1.306	1.295	1.289	1.319	1.256	1.286	1.321	1.267	1.242
Fe^{3+}	0.000	0.000	0.000	0.000	0.000	0.000	0.000	0.000	0.000	0.000
Mn	0.014	0.012	0.019	0.021	0.014	0.019	0.019	0.013	0.014	0.009
Ni	0.006	0.009	0.015	0.007	0.004	0.015	0.011	0.007	0.001	0.002
Mg	3.025	3.057	3.026	3.048	3.057	3.014	3.023	3.050	3.025	3.031
Ca	1.793	1.802	1.789	1.818	1.820	1.834	1.813	1.792	1.851	1.815
Na	0.805	0.871	0.938	0.854	0.823	0.850	0.830	0.868	0.847	0.829
K	0.139	0.138	0.141	0.137	0.137	0.144	0.140	0.136	0.146	0.144
cations	15.742	15.801	15.842	15.805	15.791	15.791	15.790	15.802	15.803	15.752
$Mg/(Mg+Fe_{TOT})$	0.70	0.70	0.70	0.70	0.70	0.71	0.70	0.70	0.70	0.71
(Na+K)A	0.74	0.81	0.87	0.81	0.79	0.83	0.79	0.80	0.84	0.79

Note: Oxide values are in wt.%. All other values are calculated with normalization program Norm.

Table 27 - Electron microprobe analyses of brown amphibole of the sample N-3 (Nyasyukka dike complex - Pechenga Complex, Russia)

	Amphibole									
SiO_2	42.33	42.12	42.28	42.69	42.05	42.03	43.61	42.96	43.25	42.94
TiO_2	4.99	4.87	4.96	4.99	5.10	5.01	4.14	4.55	4.63	4.55
Al_2O_3	10.51	10.05	10.21	10.14	10.60	10.75	9.47	9.58	9.93	9.63
Cr_2O_3	0.13	0.15	0.21	0.20	0.11	0.16	0.23	0.21	0.22	0.34
FeOtot	11.04	11.26	10.86	9.98	10.70	10.65	11.65	11.58	11.39	11.30
MnO	0.14	0.15	0.11	0.16	0.11	0.05	0.10	0.12	0.16	0.12
NiO	0.08	0.13	0.02	0.01	0.12	0.06	0.07	0.10	0.04	0.09
MgO	13.32	13.67	13.45	14.23	13.70	13.62	13.95	13.92	13.58	13.86
CaO	11.40	11.48	11.45	11.47	11.64	11.60	11.21	11.19	11.30	11.22
Na_2O	2.73	2.81	2.82	2.97	2.90	2.91	2.96	2.75	3.06	2.99
K_2O	0.77	0.75	0.76	0.78	0.80	0.80	0.85	0.77	0.78	0.80
Cl										
O=Cl										
Total	97.43	97.44	97.13	97.62	97.83	97.64	98.24	97.73	98.34	97.84
Si	6.261	6.249	6.272	6.278	6.201	6.203	6.407	6.346	6.345	6.337
Ti	0.555	0.543	0.553	0.552	0.566	0.556	0.458	0.506	0.511	0.505
Al	1.832	1.757	1.785	1.758	1.842	1.870	1.640	1.668	1.717	1.675
Cr	0.015	0.018	0.025	0.023	0.013	0.019	0.027	0.024	0.026	0.039
Fe^{2+}	1.366	1.397	1.347	1.227	1.319	1.315	1.431	1.431	1.398	1.395
Fe^{3+}	0.000	0.000	0.000	0.000	0.000	0.000	0.000	0.000	0.000	0.000
Mn	0.017	0.018	0.014	0.020	0.014	0.006	0.013	0.015	0.020	0.015
Ni	0.009	0.015	0.002	0.001	0.014	0.007	0.008	0.012	0.004	0.010
Mg	2.934	3.021	2.972	3.117	3.009	2.994	3.052	3.063	2.967	3.046
Ca	1.807	1.825	1.820	1.807	1.839	1.834	1.765	1.771	1.776	1.774
Na	0.783	0.808	0.811	0.847	0.829	0.833	0.843	0.788	0.870	0.856
K	0.145	0.142	0.145	0.147	0.150	0.151	0.159	0.146	0.146	0.151
cations	15.724	15.795	15.747	15.776	15.796	15.788	15.803	15.769	15.781	15.804
$Mg/(Mg+Fe_{TOT})$	0.68	0.68	0.69	0.72	0.70	0.69	0.68	0.68	0.68	0.69
(Na+K)A	0.73	0.79	0.78	0.80	0.82	0.82	0.80	0.77	0.79	0.80

Note: Oxide values are in wt.%. All other values are calculated with normalization program Norm.

Table 28 - Electron microprobe analyses of clinopyroxene of the sample TT329 (Husky Ridge – Antarctica). Data from Tiepolo and Tribuzio(2008).

	Clinopyroxene							
SiO_2	52.13	51.38	53.74	53.71	53.85	53.99	55.03	54.37
TiO_2	0.69	0.78	0.23	0.10	0.11	0.13	0.16	0.27
Al_2O_3	4.73	5.96	1.58	1.19	1.19	0.88	2.58	2.97
Cr_2O_3	0.04	0.09	0.11	0.17	0.04	0.10	0.10	0.24
Fe_2O_3	0.00	0.00	0.48	0.61	1.27	0.57	0.00	0.00
FeO	9.01	9.54	6.14	5.90	5.49	5.72	8.63	9.65
MnO	0.21	0.17	0.20	0.27	0.27	0.22	0.24	0.27
MgO	15.58	16.56	14.94	14.49	14.47	14.64	18.26	17.96
CaO	16.83	12.71	23.10	24.22	24.26	24.43	12.67	12.81
Na_2O	0.70	0.93	0.39	0.27	0.40	0.29	0.31	0.43
K_2O	0.21	0.20	0.03	0.01	0.00	0.00	0.12	0.24
Total	100.13	98.32	100.94	100.94	101.35	100.97	98.10	99.21
Si	1.916	1.911	1.966	1.971	1.968	1.978	2.053	2.010
Ti	0.019	0.022	0.006	0.003	0.003	0.004	0.005	0.008
Al	0.205	0.261	0.068	0.052	0.051	0.038	0.113	0.129
Cr	0.001	0.003	0.003	0.005	0.001	0.003	0.003	0.007
Fe^{3+}	0.000	0.000	0.013	0.017	0.035	0.016	0.000	0.000
Fe^{2+}	0.277	0.297	0.188	0.181	0.168	0.175	0.269	0.298
Mn	0.007	0.005	0.006	0.008	0.008	0.007	0.008	0.009
Mg	0.853	0.918	0.815	0.792	0.788	0.800	1.015	0.990
Ca	0.663	0.507	0.905	0.952	0.950	0.959	0.506	0.507
Na	0.050	0.067	0.028	0.019	0.028	0.021	0.022	0.031
K	0.010	0.010	0.001	0.001	0.000	0.000	0.006	0.011
Wollastonite	0.30	0.22	0.44	0.46	0.46	0.47	0.25	0.25
Enstatite	0.43	0.46	0.41	0.40	0.39	0.40	0.51	0.50
Ferrosilite	0.14	0.15	0.09	0.09	0.08	0.09	0.14	0.15
Pyroxmangite	0.00	0.00	0.00	0.00	0.00	0.00	0.00	0.00
Acmite	0.00	0.00	0.01	0.02	0.03	0.02	0.00	0.00
Jadeite	0.06	0.08	0.02	0.00	0.00	0.01	0.03	0.04
xMgonM1	0.65	0.61	0.77	0.78	0.78	0.79	0.70	0.66
xMgonM2	0.21	0.31	0.05	0.02	0.01	0.01	0.36	0.34
xMgFe(II+)	0.76	0.76	0.81	0.81	0.82	0.82	0.79	0.77
xMgFe(tot)	0.76	0.76	0.80	0.80	0.80	0.81	0.79	0.77

Note: Oxide values are in wt.%. All other values are calculated with normalization program Norm.

Table 29 - Electron microprobe analyses of brown amphibole of the sample TT329 (Husky Ridge – Antarctica) Data from Tiepolo and Tribuzio (2008).

	Amphibole						
SiO_2	45.90	45.94	46.18	46.06	46.02	46.16	46.13
TiO_2	1.54	1.55	1.57	1.42	1.52	1.57	1.43
Al_2O_3	10.42	10.81	10.90	10.94	10.72	10.73	10.88
Cr_2O_3	0.06	0.07	0.09	0.08	0.16	0.10	0.08
FeOtot	11.33	10.92	10.93	10.68	10.27	10.14	10.23
MnO	0.08	0.19	0.26	0.23	0.19	0.18	0.19
NiO							
MgO	13.60	14.10	14.04	14.11	14.26	14.66	14.30
CaO	12.40	12.20	12.35	12.21	12.27	12.42	12.18
Na_2O	1.46	1.63	1.41	1.68	1.54	1.45	1.59
K_2O	0.46	0.32	0.32	0.25	0.43	0.45	0.47
Cl	0.07	0.07	0.07	0.07	0.07	0.07	0.07
O=Cl							
Total	97.26	97.72	98.06	97.66	97.38	97.86	97.49
Si	6.706	6.664	6.672	6.675	6.683	6.667	6.688
Ti	0.169	0.169	0.171	0.155	0.167	0.170	0.156
Al	1.794	1.849	1.857	1.868	1.835	1.827	1.859
Cr	0.007	0.008	0.010	0.009	0.018	0.011	0.009
Fe^{2+}	1.385	1.324	1.321	1.294	1.247	1.225	1.240
Fe^{3+}	0.000	0.000	0.000	0.000	0.000	0.000	0.000
Mn	0.009	0.023	0.032	0.029	0.023	0.022	0.023
Ni	0.000	0.000	0.000	0.000	0.000	0.000	0.000
Mg	2.960	3.047	3.021	3.047	3.083	3.154	3.088
Ca	1.942	1.895	1.913	1.896	1.910	1.923	1.892
Na	0.414	0.459	0.396	0.472	0.434	0.405	0.447
K	0.086	0.059	0.059	0.046	0.080	0.083	0.088
cations	15.473	15.497	15.451	15.490	15.481	15.487	15.489
$Mg/(Mg+Fe_{TOT})$	0.68	0.70	0.70	0.70	0.71	0.72	0.71
(Na+K)A	0.47	0.50	0.45	0.49	0.48	0.49	0.49

Note: Oxide values are in wt.%. All other values are calculated with normalization program Norm.

Table 30 - Electron microprobe analyses of olivine of the sample AL89 (Sanandaj Sirjan Zone - Iran). Data from Esna-Ashari et al. (2016).

	Olivine												
SiO_2	39.40	40.20	38.90	40.20	39.40	39.00	39.30	39.40	39.60	38.50	39.30	39.30	37.40
TiO_2	0.00	0.02	0.06	0.00	0.00	0.06	0.03	0.00	0.03	0.01	0.00	0.00	0.00
Al_2O_3	0.01	0.01	0.00	0.00	0.00	0.05	0.00	0.03	0.00	0.01	0.00	0.02	0.00
Cr_2O_3	0.01	0.04	0.02	0.00	0.02	0.00	0.02	0.06	0.00	0.02	0.04	0.00	0.07
FeO	20.60	17.20	23.30	14.90	20.20	20.60	16.50	16.80	17.20	21.80	20.60	16.20	25.10
MnO	0.34	0.25	0.28	0.21	0.25	0.28	0.21	0.27	0.33	0.26	0.30	0.21	0.28
NiO	0.17	0.09	0.11	0.15	0.22	0.17	0.17	0.15	0.18	0.13	0.18	0.27	0.08
MgO	41.30	43.80	39.70	45.30	40.90	40.40	43.10	43.40	42.90	39.30	40.30	44.00	36.50
CaO	0.01	0.00	0.03	0.03	0.00	0.00	0.01	0.02	0.00	0.07	0.01	0.01	0.03
Na_2O	0.01	0.00	0.00	0.00	0.02	0.03	0.00	0.00	0.00	0.00	0.00	0.00	0.00
K_2O	0.00	0.02	0.00	0.00	0.00	0.00	0.00	0.00	0.01	0.00	0.00	0.00	0.02
Total	101.85	101.63	102.40	100.78	101.02	100.59	99.34	100.14	100.26	100.10	100.73	100.01	99.48
Si	0.996	1.003	0.989	1.001	1.004	1.000	1.002	0.997	1.003	0.998	1.007	0.992	0.991
Ti	0.000	0.000	0.001	0.000	0.000	0.001	0.001	0.000	0.001	0.000	0.000	0.000	0.000
Al	0.000	0.000	0.000	0.000	0.000	0.002	0.000	0.001	0.000	0.000	0.000	0.001	0.000
Cr	0.000	0.001	0.000	0.000	0.001	0.000	0.000	0.001	0.000	0.000	0.001	0.000	0.002
Fe^{2+}	0.436	0.359	0.496	0.310	0.431	0.442	0.352	0.355	0.365	0.473	0.442	0.342	0.556
Mn	0.007	0.005	0.006	0.004	0.005	0.006	0.005	0.006	0.007	0.006	0.007	0.005	0.006
Ni	0.004	0.002	0.002	0.003	0.005	0.004	0.004	0.003	0.004	0.003	0.004	0.006	0.002
Mg	1.556	1.629	1.505	1.681	1.554	1.544	1.637	1.636	1.620	1.518	1.540	1.655	1.442
Ca	0.000	0.000	0.001	0.001	0.000	0.000	0.000	0.001	0.000	0.002	0.000	0.000	0.001
Na	0.000	0.000	0.000	0.000	0.001	0.002	0.000	0.000	0.000	0.000	0.000	0.000	0.000
K	0.000	0.001	0.000	0.000	0.000	0.000	0.000	0.000	0.000	0.000	0.000	0.000	0.001
Forsterite	0.78	0.82	0.75	0.84	0.78	0.77	0.82	0.82	0.81	0.76	0.77	0.83	0.72
Fayalite	0.22	0.18	0.25	0.16	0.22	0.22	0.18	0.18	0.18	0.24	0.22	0.17	0.28
Tephroite	0.00	0.00	0.00	0.00	0.00	0.00	0.00	0.00	0.00	0.00	0.00	0.00	0.00
Monticellit	0.00	0.00	0.00	0.00	0.00	0.00	0.00	0.00	0.00	0.00	0.00	0.00	0.00
Kirschstein	0.00	0.00	0.00	0.00	0.00	0.00	0.00	0.00	0.00	0.00	0.00	0.00	0.00
Glaukocroit	0.00	0.00	0.00	0.00	0.00	0.00	0.00	0.00	0.00	0.00	0.00	0.00	0.00
Ni-Olivine	0.00	0.00	0.00	0.00	0.00	0.00	0.00	0.00	0.00	0.00	0.00	0.00	0.00
xMg	0.78	0.82	0.75	0.84	0.78	0.77	0.82	0.82	0.81	0.76	0.77	0.82	0.72
xFe	0.22	0.18	0.25	0.16	0.22	0.22	0.18	0.18	0.18	0.24	0.22	0.17	0.28

Note: Oxide values are in wt.%. All other values are calculated with normalization program Norm.

Table 31 - Electron microprobe analyses of clinopyroxene of the sample AL89 (Sanandaj Sirjan Zone - Iran).
Data from Esna-Ashari et al. (2016).

	Clinopyroxene								
SiO_2	53.80	53.50	54.10	53.40	53.70	54.70	54.80	52.80	52.90
TiO_2	0.17	0.20	0.17	0.20	0.25	0.09	0.07	0.21	0.18
Al_2O_3	2.50	2.10	2.10	2.60	2.40	1.10	0.50	2.60	2.30
Cr_2O_3	1.08	0.82	0.73	0.98	1.10	0.36	0.30	0.78	0.79
Fe_2O_3	0.00	0.00	0.00	0.00	0.00	0.00	0.00	0.00	0.00
FeO	4.10	4.20	4.60	4.60	3.70	3.60	3.30	4.00	3.90
MnO	0.13	0.10	0.17	0.16	0.12	0.13	0.12	0.09	0.11
NiO	0.05	0.00	0.00	0.02	0.08	0.00	0.00	0.03	0.06
MgO	17.60	17.80	18.40	18.10	16.30	16.80	17.10	16.30	16.00
CaO	20.80	20.90	20.00	20.10	22.40	22.90	23.80	22.10	22.20
Na_2O	0.17	0.11	0.14	0.17	0.20	0.23	0.12	0.15	0.24
K_2O	-	-	-	-	-	-	-	-	-
Total	100.40	99.73	100.41	100.33	100.25	99.91	100.11	99.06	98.68
Si	1.954	1.954	1.960	1.938	1.961	1.998	1.997	1.949	1.962
Ti	0.005	0.006	0.005	0.006	0.007	0.003	0.002	0.006	0.005
Al	0.107	0.090	0.090	0.111	0.103	0.047	0.022	0.113	0.101
Cr	0.031	0.024	0.021	0.028	0.032	0.010	0.009	0.023	0.023
Fe^{3+}	0.000	0.000	0.000	0.000	0.000	0.000	0.000	0.000	0.000
Fe^{2+}	0.125	0.128	0.139	0.140	0.113	0.110	0.101	0.124	0.121
Mn	0.004	0.003	0.005	0.005	0.004	0.004	0.004	0.003	0.004
Ni	0.002	0.000	0.000	0.001	0.002	0.000	0.000	0.001	0.002
Mg	0.953	0.969	0.994	0.979	0.887	0.915	0.929	0.897	0.884
Ca	0.809	0.818	0.776	0.782	0.877	0.896	0.929	0.874	0.882
Na	0.012	0.008	0.010	0.012	0.014	0.016	0.009	0.011	0.017
K	-	-	-	-	-	-	-	-	-
Wollastonite	0.38	0.39	0.37	0.36	0.42	0.45	0.46	0.42	0.42
Enstatite	0.48	0.49	0.50	0.49	0.45	0.46	0.46	0.45	0.44
Ferrosilite	0.06	0.06	0.07	0.07	0.06	0.06	0.05	0.06	0.06
Pyroxmangite	0.00	0.00	0.00	0.00	0.00	0.00	0.00	0.00	0.00
Acmite	0.00	0.00	0.00	0.00	0.00	0.00	0.00	0.00	0.00
Jadeite	0.01	0.01	0.01	0.01	0.01	0.02	0.01	0.01	0.02
xMgonM1	0.80	0.82	0.81	0.80	0.79	0.84	0.88	0.80	0.80
xMgonM2	0.16	0.15	0.18	0.18	0.09	0.07	0.05	0.10	0.09
xMgFe(II+)	0.88	0.88	0.88	0.88	0.89	0.89	0.90	0.88	0.88
xMgFe(tot)	0.88	0.88	0.88	0.88	0.89	0.89	0.90	0.88	0.88

Note: Oxide values are in wt.%. All other values are calculated with normalization program Norm.

Table 32 - Electron microprobe analyses of brown amphibole of the sample AL89 (Sanandaj Sirjan Zone - Iran). Data from Esna-Ashari et al. (2016).

	Amphibole	
SiO_2	44.90	44.30
TiO_2	2.60	2.90
Al_2O_3	11.00	11.20
Cr_2O_3	0.58	0.63
FeOtot	5.96	6.08
MnO	0.05	0.10
NiO	0.07	0.09
MgO	17.10	16.50
CaO	11.30	11.40
Na_2O	1.90	2.44
K_2O	0.63	0.60
Cl	0.07	0.07
O=Cl		
Total	96.09	96.24
Si	6.505	6.437
Ti	0.283	0.317
Al	1.878	1.918
Cr	0.066	0.072
Fe^{2+}	0.722	0.739
Fe^{3+}	0.000	0.000
Mn	0.006	0.012
Ni	0.008	0.011
Mg	3.690	3.571
Ca	1.754	1.775
Na	0.534	0.687
K	0.116	0.111
cations	15.564	15.650
$Mg/(Mg+Fe_{TOT})$	0.84	0.83
(Na+K)A	0.56	0.65

Note: Oxide values are in wt.%.
All other values are calculated with normalization program Norm.

Table 33 - Electron microprobe analyses of olivine of the sample TK1B (Taku - Japan).

	Olivine						
SiO_2	38.09	37.15	37.03	37.54	37.32	37.14	37.26
TiO_2	0.00	0.00	0.00	0.00	0.00	0.03	0.00
Al_2O_3	0.00	0.00	0.01	0.04	0.02	0.01	0.00
Cr_2O_3	0.06	0.04	0.00	0.00	0.01	0.19	0.00
FeO	26.32	30.68	31.19	27.82	27.68	29.32	28.51
MnO	0.33	0.55	0.46	0.39	0.38	0.43	0.45
NiO	0.05	0.08	0.06	0.09	0.03	0.03	0.12
MgO	37.02	33.22	32.49	34.98	35.76	34.19	34.70
CaO	0.03	0.02	0.02	0.02	0.02	0.02	0.01
Na_2O	0.01	0.00	0.00	0.04	0.00	0.03	0.02
K_2O	0.00	0.00	0.00	0.01	0.01	0.01	0.00
Total	101.91	101.74	101.26	100.93	101.23	101.40	101.07
Si	0.988	0.987	0.992	0.992	0.981	0.984	0.986
Ti	0.000	0.000	0.000	0.000	0.000	0.001	0.000
Al	0.000	0.000	0.000	0.001	0.001	0.000	0.000
Cr	0.001	0.001	0.000	0.000	0.000	0.004	0.000
Fe^{2+}	0.571	0.682	0.699	0.615	0.608	0.649	0.631
Mn	0.007	0.012	0.010	0.009	0.009	0.010	0.010
Ni	0.001	0.002	0.001	0.002	0.001	0.001	0.003
Mg	1.431	1.316	1.297	1.378	1.400	1.350	1.369
Ca	0.001	0.001	0.001	0.001	0.001	0.001	0.000
Na	0.001	0.000	0.000	0.002	0.000	0.002	0.001
K	0.000	0.000	0.000	0.000	0.000	0.000	0.000
Forsterite	0.71	0.65	0.65	0.69	0.69	0.67	0.68
Fayalite	0.28	0.34	0.35	0.31	0.30	0.32	0.31
Tephroite	0.00	0.01	0.01	0.00	0.00	0.01	0.01
Monticellit	0.00	0.00	0.00	0.00	0.00	0.00	0.00
Kirschstein	0.00	0.00	0.00	0.00	0.00	0.00	0.00
Glaukocroit	0.00	0.00	0.00	0.00	0.00	0.00	0.00
Ni-Olivine	0.00	0.00	0.00	0.00	0.00	0.00	0.00
xMg	0.71	0.65	0.65	0.69	0.69	0.67	0.68
xFe	0.28	0.34	0.35	0.31	0.30	0.32	0.31

Note: Oxide values are in wt.%. All other values are calculated with normalization program Norm.

Table 34 - Electron microprobe analyses of clinopyroxene of the sample TK1B (Taku - Japan).

	Clinopyroxene					
SiO_2	52.14	51.81	52.10	52.01	52.40	53.61
TiO_2	0.34	0.45	0.29	0.39	0.52	0.10
Al_2O_3	3.10	3.09	2.38	2.59	2.65	1.02
Cr_2O_3	0.75	0.32	0.15	0.33	0.27	0.18
Fe_2O_3	0.00	0.32	0.19	0.17	0.00	0.00
FeO	6.35	5.48	7.09	6.39	5.19	6.85
MnO	0.20	0.13	0.15	0.22	0.14	0.23
NiO	0.02	0.00	0.00	0.03	0.08	0.04
MgO	15.40	15.22	15.35	15.43	15.33	15.26
CaO	21.46	22.01	21.10	21.70	22.75	22.13
Na_2O	0.24	0.30	0.20	0.13	0.14	0.22
K_2O	0.01	0.01	0.00	0.00	0.00	0.00
Total	100.01	99.14	99.00	99.39	99.47	99.64
Si	1.921	1.922	1.942	1.930	1.938	1.988
Ti	0.009	0.013	0.008	0.011	0.015	0.003
Al	0.135	0.135	0.105	0.113	0.116	0.045
Cr	0.022	0.009	0.004	0.010	0.008	0.005
Fe^{3+}	0.000	0.009	0.005	0.005	0.000	0.000
Fe^{2+}	0.196	0.170	0.221	0.198	0.161	0.212
Mn	0.006	0.004	0.005	0.007	0.004	0.007
Ni	0.001	0.000	0.000	0.001	0.002	0.001
Mg	0.846	0.841	0.853	0.853	0.845	0.844
Ca	0.847	0.875	0.843	0.863	0.902	0.879
Na	0.017	0.022	0.015	0.009	0.010	0.016
K	0.001	0.001	0.000	0.000	0.000	0.000
Wollastonite	0.39	0.40	0.40	0.40	0.43	0.44
Enstatite	0.42	0.42	0.43	0.43	0.42	0.42
Ferrosilite	0.10	0.09	0.11	0.10	0.08	0.11
Pyroxmangite	0.00	0.00	0.00	0.00	0.00	0.00
Acmite	0.00	0.01	0.01	0.01	0.00	0.00
Jadeite	0.02	0.01	0.01	0.01	0.01	0.02
xMgonM1	0.74	0.76	0.74	0.76	0.78	0.77
xMgonM2	0.11	0.08	0.11	0.10	0.07	0.08
xMgFe(II+)	0.81	0.83	0.79	0.81	0.84	0.80
xMgFe(tot)	0.81	0.83	0.79	0.81	0.84	0.80

Note: Oxide values are in wt.%. All other values are calculated with normalization program Norm.

Table 35 - Electron microprobe analyses of brown amphibole of the sample TK1B (Taku - Japan).

	Amphibole								
SiO_2	42.96	44.01	43.67	43.87	44.08	45.08	43.35	44.93	43.76
TiO_2	1.48	1.79	1.77	1.52	1.56	1.21	1.26	1.31	2.09
Al_2O_3	12.54	12.13	12.37	12.66	11.89	12.34	12.41	11.24	12.60
Cr_2O_3	0.18	0.18	0.16	0.14	0.20	0.15	0.20	0.25	0.23
FeOtot	10.72	11.42	11.00	10.94	11.21	11.16	11.29	10.54	9.99
MnO	0.10	0.11	0.08	0.15	0.15	0.12	0.13	0.09	0.09
NiO	0.01	0.05	0.09	0.07	0.02	0.00	0.08	0.00	0.00
MgO	14.34	13.95	14.05	14.61	14.14	13.79	14.28	14.43	14.68
CaO	11.45	11.34	11.48	11.73	11.56	11.40	11.29	11.99	11.64
Na_2O	1.79	1.71	1.73	1.84	1.62	1.52	1.66	1.35	1.79
K_2O	0.67	0.70	0.69	0.69	0.66	0.69	0.76	0.70	0.66
Cl	0.07	0.07	0.07	0.07	0.07	0.07	0.07	0.07	0.07
O=Cl									
Total	96.22	97.39	97.08	98.23	97.10	97.46	96.72	96.83	97.53
Si	6.360	6.444	6.408	6.367	6.469	6.559	6.397	6.583	6.365
Ti	0.164	0.197	0.195	0.166	0.172	0.132	0.140	0.145	0.229
Al	2.188	2.093	2.139	2.166	2.057	2.116	2.158	1.941	2.160
Cr	0.021	0.021	0.018	0.016	0.023	0.018	0.023	0.029	0.027
Fe^{2+}	1.327	1.398	1.350	1.328	1.376	1.358	1.393	1.291	1.215
Fe^{3+}	0.000	0.000	0.000	0.000	0.000	0.000	0.000	0.000	0.000
Mn	0.012	0.014	0.010	0.019	0.019	0.015	0.017	0.012	0.011
Ni	0.001	0.006	0.010	0.008	0.003	0.000	0.010	0.000	0.000
Mg	3.162	3.042	3.071	3.158	3.091	2.988	3.139	3.149	3.180
Ca	1.816	1.779	1.805	1.824	1.818	1.777	1.785	1.882	1.814
Na	0.514	0.485	0.492	0.518	0.461	0.429	0.475	0.383	0.505
K	0.126	0.130	0.129	0.129	0.124	0.127	0.143	0.130	0.122
cations	15.691	15.610	15.628	15.699	15.612	15.520	15.681	15.545	15.627
$Mg/(Mg+Fe_{TOT})$	0.70	0.69	0.69	0.70	0.69	0.69	0.69	0.71	0.72
(Na+K)A	0.64	0.61	0.62	0.65	0.59	0.52	0.62	0.51	0.63

Note: Oxide values are in wt.%. All other values are calculated with normalization program Norm.

Table 36 - Electron microprobe analyses of olivine of the sample ZN5 (Zenifudo - Japan). Data from Langone et al. (2009)

	Olivine										
SiO_2	38.53	37.84	38.08	37.83	38.00	38.62	38.59	38.84	38.62	38.69	38.82
TiO_2	0.00	0.00	0.01	0.01	0.03	0.04	0.03	0.00	0.07	0.00	0.00
Al_2O_3	0.01	0.00	0.00	0.02	0.00	0.01	0.00	0.03	0.02	0.02	0.01
Cr_2O_3	0.04	0.00	0.00	0.00	0.01	0.02	0.00	0.02	0.00	0.00	0.00
FeO	22.43	22.11	24.16	21.73	21.19	21.50	22.02	22.61	22.65	22.57	21.92
MnO	0.32	0.37	0.40	0.40	0.35	0.36	0.33	0.31	0.36	0.35	0.37
NiO	0.09	0.03	0.06	0.06	0.08	0.06	0.00	0.05	0.01	0.00	0.00
MgO	40.31	39.86	38.52	40.22	40.85	40.73	40.05	40.12	39.15	39.90	40.41
CaO	0.01	0.03	0.00	0.02	0.02	0.04	0.04	0.03	0.02	0.00	0.03
Na_2O	0.02	0.00	0.00	0.02	0.02	0.01	0.00	0.01	0.02	0.02	0.03
K_2O	0.00	0.02	0.01	0.00	0.00	0.01	0.01	0.01	0.01	0.01	0.00
Total	101.76	100.26	101.24	100.31	100.55	101.40	101.07	102.03	100.93	101.56	101.59
Si	0.981	0.978	0.984	0.975	0.974	0.984	0.989	0.988	0.996	0.989	0.989
Ti	0.000	0.000	0.000	0.000	0.001	0.001	0.001	0.000	0.001	0.000	0.000
Al	0.000	0.000	0.000	0.001	0.000	0.000	0.000	0.001	0.001	0.001	0.000
Cr	0.001	0.000	0.000	0.000	0.000	0.000	0.000	0.000	0.000	0.000	0.000
Fe^{2+}	0.478	0.478	0.522	0.468	0.454	0.458	0.472	0.481	0.488	0.482	0.467
Mn	0.007	0.008	0.009	0.009	0.008	0.008	0.007	0.007	0.008	0.008	0.008
Ni	0.002	0.001	0.001	0.001	0.002	0.001	0.000	0.001	0.000	0.000	0.000
Mg	1.530	1.535	1.484	1.545	1.560	1.546	1.530	1.521	1.504	1.520	1.534
Ca	0.000	0.001	0.000	0.001	0.001	0.001	0.001	0.001	0.001	0.000	0.001
Na	0.001	0.000	0.000	0.001	0.001	0.001	0.000	0.001	0.001	0.001	0.002
K	0.000	0.001	0.000	0.000	0.000	0.000	0.000	0.000	0.000	0.000	0.000
Forsterite	0.76	0.76	0.74	0.76	0.77	0.77	0.76	0.76	0.75	0.76	0.76
Fayalite	0.24	0.24	0.26	0.23	0.22	0.23	0.24	0.24	0.24	0.24	0.23
Tephroite	0.00	0.00	0.00	0.00	0.00	0.00	0.00	0.00	0.00	0.00	0.00
Monticellit	0.00	0.00	0.00	0.00	0.00	0.00	0.00	0.00	0.00	0.00	0.00
Kirschstein	0.00	0.00	0.00	0.00	0.00	0.00	0.00	0.00	0.00	0.00	0.00
Glaukocroit	0.00	0.00	0.00	0.00	0.00	0.00	0.00	0.00	0.00	0.00	0.00
Ni-Olivine	0.00	0.00	0.00	0.00	0.00	0.00	0.00	0.00	0.00	0.00	0.00
xMg	0.76	0.76	0.74	0.76	0.77	0.77	0.76	0.76	0.75	0.76	0.76
xFe	0.24	0.24	0.26	0.23	0.22	0.23	0.24	0.24	0.24	0.24	0.23

Note: Oxide values are in wt.%. All other values are calculated with normalization program Norm.

Table 37 - Electron microprobe analyses of clinopyroxene of the sample ZN5 (Zenifudo - Japan).

	Clinopyroxene									
SiO_2	50.72	50.23	49.85	49.68	51.61	50.47	51.59	52.51	51.54	52.64
TiO_2	0.49	0.48	0.35	0.42	0.35	0.67	0.31	0.25	0.39	0.19
Al_2O_3	4.02	3.89	3.39	3.79	3.40	3.79	2.94	2.75	3.83	2.84
Cr_2O_3	0.27	0.48	0.24	0.80	0.27	0.19	0.29	0.33	0.27	0.19
Fe_2O_3	1.18	1.76	2.67	2.97	0.69	0.65	0.56	0.85	0.15	0.42
FeO	4.99	4.32	4.13	3.73	5.66	5.51	4.57	5.62	5.92	5.07
MnO	0.18	0.14	0.12	0.17	0.18	0.19	0.20	0.17	0.17	0.19
NiO	0.00	0.03	0.08	0.03	0.00	0.02	0.02	0.04	0.04	0.00
MgO	16.08	15.61	16.01	16.51	16.55	15.09	16.34	17.66	15.82	16.21
CaO	20.55	21.09	20.43	19.61	19.95	21.39	21.17	19.38	20.79	21.52
Na_2O	0.20	0.25	0.19	0.28	0.23	0.20	0.20	0.19	0.22	0.30
K_2O	0.00	0.00	0.00	0.00	0.02	0.00	0.00	0.00	0.00	0.00
Total										
Si	1.89	1.88	1.88	1.86	1.91	1.89	1.92	1.92	1.91	1.94
Ti	0.01	0.01	0.01	0.01	0.01	0.02	0.01	0.01	0.01	0.01
Al	0.18	0.17	0.15	0.17	0.15	0.17	0.13	0.12	0.17	0.12
Cr	0.01	0.01	0.01	0.02	0.01	0.01	0.01	0.01	0.01	0.01
Fe^{3+}	0.03	0.05	0.08	0.08	0.02	0.02	0.02	0.02	0.00	0.01
Fe^{2+}	0.16	0.14	0.13	0.12	0.18	0.17	0.14	0.17	0.18	0.16
Mn	0.01	0.00	0.00	0.01	0.01	0.01	0.01	0.01	0.01	0.01
Ni	0.00	0.00	0.00	0.00	0.00	0.00	0.00	0.00	0.00	0.00
Mg	0.89	0.87	0.90	0.92	0.91	0.84	0.91	0.96	0.87	0.89
Ca	0.82	0.84	0.83	0.79	0.79	0.86	0.85	0.76	0.82	0.85
Na	0.01	0.02	0.01	0.02	0.02	0.01	0.01	0.01	0.02	0.02
K	0.00	0.00	0.00	0.00	0.00	0.00	0.00	0.00	0.00	0.00
Wollastonite	0.359	0.368	0.358	0.330	0.356	0.385	0.388	0.346	0.371	0.394
Enstatite	0.445	0.435	0.451	0.461	0.457	0.422	0.454	0.483	0.437	0.444
Ferrosilite	0.078	0.068	0.065	0.058	0.088	0.086	0.071	0.086	0.092	0.078
Pyroxmangite	0.003	0.002	0.002	0.003	0.003	0.003	0.003	0.003	0.003	0.003
Acmite	0.014	0.018	0.014	0.020	0.017	0.015	0.014	0.013	0.004	0.012
Jadeite	0.000	0.000	0.000	0.000	0.000	0.000	0.000	0.000	0.012	0.010
xMgonM1	0.753	0.755	0.763	0.756	0.758	0.744	0.791	0.777	0.745	0.782
xMgonM2	0.138	0.115	0.137	0.166	0.155	0.1	0.116	0.187	0.128	0.106
xMgFe(II+)	0.852	0.866	0.873	0.887	0.839	0.83	0.864	0.849	0.827	0.851
xMgFe(tot)	0.826	0.825	0.814	0.821	0.824	0.815	0.851	0.831	0.823	0.841

Note: Oxide values are in wt.%. All other values are calculated with normalization program Norm.

Table 38 - Electron microprobe analyses of brown amphibole of the sample ZN5 (Zenifudo - Japan).

	Amphibole																
SiO_2	41.87	41.66	50.47	54.45	42.28	42.34	42.53	43.06	42.18	41.80	42.09	43.11	43.57	41.69	41.99	42.01	46.82
TiO_2	2.86	2.64	0.71	0.26	2.09	2.29	1.83	2.48	3.04	2.87	2.89	1.22	0.54	2.46	2.24	2.40	0.77
Al_2O_3	12.03	11.68	4.73	0.90	12.36	12.40	13.29	10.29	11.62	12.33	12.39	12.43	12.94	12.21	12.22	12.38	9.22
Cr_2O_3	0.06	0.10	0.16	0.07	0.23	0.14	0.15	0.10	0.21	0.01	0.04	0.16	0.12	0.17	0.13	0.08	0.01
FeOtot	8.42	8.43	6.04	7.19	8.71	8.30	8.19	8.70	8.50	8.66	8.97	8.88	8.28	8.67	8.46	8.80	8.02
MnO	0.07	0.10	0.13	0.15	0.13	0.17	0.07	0.11	0.07	0.14	0.11	0.14	0.16	0.04	0.12	0.12	0.13
NiO	0.02	0.04	0.00	0.04	0.00	0.00	0.00	0.04	0.04	0.00	0.00	0.00	0.00	0.07	0.00	0.00	0.00
MgO	14.84	14.55	18.74	18.49	14.93	14.94	14.70	14.64	14.77	14.48	15.09	15.52	15.03	15.31	14.87	14.72	16.74
CaO	11.48	12.10	12.23	12.79	11.79	11.65	11.72	11.83	11.78	11.80	11.41	11.40	11.76	11.37	12.04	11.51	11.70
Na_2O	2.50	2.31	0.85	0.14	2.27	2.25	2.14	2.15	2.59	2.58	2.46	2.49	2.16	2.56	2.44	2.38	1.81
K_2O	0.47	0.44	0.11	0.02	0.57	0.51	0.59	0.53	0.48	0.50	0.45	0.55	0.73	0.51	0.59	0.62	0.38
Cl	0.06	0.06	0.06	0.06	0.06	0.06	0.06	0.06	0.06	0.06	0.06	0.06	0.06	0.06	0.06	0.06	0.06
O=Cl																	
Total	94.61	94.06	94.17	94.51	95.37	94.99	95.21	93.94	95.27	95.17	95.90	95.90	95.29	95.06	95.10	95.02	95.61
Si	6.269	6.288	7.364	7.900	6.288	6.302	6.299	6.496	6.285	6.238	6.228	6.362	6.441	6.226	6.268	6.273	6.842
Ti	0.322	0.300	0.078	0.029	0.234	0.256	0.204	0.281	0.341	0.322	0.322	0.135	0.060	0.276	0.252	0.270	0.084
Al	2.123	2.078	0.813	0.154	2.166	2.175	2.320	1.829	2.041	2.169	2.161	2.162	2.255	2.149	2.150	2.179	1.588
Cr	0.007	0.012	0.018	0.008	0.027	0.017	0.017	0.012	0.024	0.001	0.004	0.018	0.015	0.020	0.015	0.010	0.001
Fe^{2+}	1.054	1.064	0.737	0.872	1.083	1.033	1.014	1.098	1.059	1.081	1.110	1.096	1.024	1.083	1.056	1.099	0.980
Fe^{3+}	0.000	0.000	0.000	0.000	0.000	0.000	0.000	0.000	0.000	0.000	0.000	0.000	0.000	0.000	0.000	0.000	0.000
Mn	0.009	0.013	0.016	0.018	0.017	0.021	0.008	0.013	0.008	0.017	0.014	0.017	0.020	0.005	0.016	0.015	0.017
Ni	0.002	0.005	0.000	0.005	0.000	0.000	0.000	0.005	0.004	0.000	0.000	0.000	0.000	0.008	0.000	0.000	0.000
Mg	3.309	3.271	4.072	3.995	3.307	3.312	3.243	3.289	3.278	3.218	3.325	3.411	3.309	3.405	3.306	3.273	3.643
Ca	1.842	1.957	1.912	1.988	1.879	1.858	1.860	1.912	1.881	1.887	1.809	1.803	1.863	1.819	1.926	1.841	1.832
Na	0.726	0.676	0.240	0.038	0.655	0.649	0.615	0.629	0.748	0.747	0.706	0.712	0.619	0.741	0.706	0.689	0.513
K	0.090	0.085	0.021	0.004	0.108	0.097	0.112	0.103	0.091	0.096	0.085	0.104	0.138	0.097	0.112	0.118	0.072
cations	15.752	15.748	15.272	15.012	15.763	15.719	15.692	15.668	15.761	15.776	15.764	15.821	15.743	15.832	15.807	15.767	15.571
$Mg/(Mg+Fe_{TOT})$	0.76	0.75	0.85	0.82	0.75	0.76	0.76	0.75	0.76	0.75	0.75	0.76	0.76	0.76	0.76	0.75	0.79
(Na+K)A	0.75	0.75	0.26	0.03	0.76	0.72	0.69	0.67	0.76	0.78	0.76	0.82	0.74	0.83	0.81	0.77	0.57

Note: Oxide values are in wt.%. All other values are calculated with normalization program Norm.

Table 39 - Electron microprobe analyses of clinopyroxene of the sample HSY3b (Hase no Yatsu - Japan). Data from Langone et al. (2009).

	Olivine													
SiO_2	36.92	37.20	37.05	36.92	37.41	37.33	37.57	37.03	37.67	37.43	37.35	37.06	37.20	36.94
TiO_2	0.00	0.03	0.00	0.02	0.00	0.02	0.01	0.02	0.02	0.01	0.00	0.00	0.03	0.00
Al_2O_3	0.00	0.01	0.00	0.00	0.00	0.00	0.01	0.00	0.00	0.00	0.00	0.00	0.00	0.00
Cr_2O_3	0.00	0.00	0.00	0.00	0.05	0.01	0.03	0.00	0.03	0.00	0.00	0.00	0.00	0.00
FeO	31.77	31.62	32.06	31.92	29.79	29.37	27.15	27.75	27.57	28.63	30.67	32.81	30.71	32.58
MnO	0.57	0.57	0.56	0.55	0.59	0.55	0.44	0.50	0.44	0.51	0.50	0.64	0.56	0.58
NiO	0.01	0.06	0.05	0.04	0.03	0.03	0.02	0.00	0.01	0.01	0.00	0.01	0.00	0.03
MgO	33.64	33.51	33.39	33.34	34.68	34.88	36.77	36.42	36.60	35.44	34.27	32.79	34.14	32.61
CaO	0.01	0.05	0.01	0.02	0.01	0.05	0.02	0.02	0.01	0.03	0.02	0.02	0.04	0.04
Na_2O	0.01	0.00	0.00	0.00	0.02	0.02	0.00	0.01	0.01	0.00	0.01	0.01	0.00	0.00
K_2O	0.00	0.00	0.00	0.00	0.00	0.00	0.00	0.00	0.00	0.00	0.00	0.00	0.01	0.00
Total	102.94	103.05	103.12	102.81	102.59	102.25	102.03	101.75	102.36	102.06	102.82	103.35	102.69	102.77
Si	0.970	0.977	0.974	0.973	0.979	0.978	0.975	0.966	0.977	0.979	0.978	0.976	0.976	0.978
Ti	0.000	0.001	0.000	0.000	0.000	0.000	0.000	0.000	0.000	0.000	0.000	0.000	0.001	0.000
Al	0.000	0.000	0.000	0.000	0.000	0.000	0.000	0.000	0.000	0.000	0.000	0.000	0.000	0.000
Cr	0.000	0.000	0.000	0.000	0.001	0.000	0.001	0.000	0.001	0.000	0.000	0.000	0.000	0.000
Fe^{2+}	0.698	0.695	0.705	0.704	0.652	0.644	0.590	0.605	0.598	0.626	0.672	0.722	0.674	0.721
Mn	0.013	0.013	0.013	0.012	0.013	0.012	0.010	0.011	0.010	0.011	0.011	0.014	0.012	0.013
Ni	0.000	0.001	0.001	0.001	0.001	0.001	0.001	0.000	0.000	0.000	0.000	0.000	0.000	0.001
Mg	1.318	1.312	1.308	1.310	1.353	1.362	1.423	1.416	1.414	1.382	1.338	1.287	1.335	1.287
Ca	0.000	0.001	0.000	0.001	0.000	0.001	0.001	0.001	0.000	0.001	0.001	0.001	0.001	0.001
Na	0.000	0.000	0.000	0.000	0.001	0.001	0.000	0.001	0.000	0.000	0.000	0.000	0.000	0.000
K	0.000	0.000	0.000	0.000	0.000	0.000	0.000	0.000	0.000	0.000	0.000	0.000	0.000	0.000
Forsterite	0.65	0.65	0.65	0.65	0.67	0.67	0.70	0.70	0.70	0.68	0.66	0.64	0.66	0.64
Fayalite	0.34	0.34	0.35	0.35	0.32	0.32	0.29	0.30	0.30	0.31	0.33	0.36	0.33	0.36
Tephroite	0.01	0.01	0.01	0.01	0.01	0.01	0.01	0.01	0.01	0.01	0.01	0.01	0.01	0.01
Monticellite	0.00	0.00	0.00	0.00	0.00	0.00	0.00	0.00	0.00	0.00	0.00	0.00	e 0.001	0.00
Kirschstein	0.00	0.00	0.00	0.00	0.00	0.00	0.00	0.00	0.00	0.00	0.00	0.00	. 0.000	0.00
Glaukocroit	0.00	0.00	0.00	0.00	0.00	0.00	0.00	0.00	0.00	0.00	0.00	0.00	0.00	0.00
Ni-Olivine	0.00	0.00	0.00	0.00	0.00	0.00	0.00	0.00	0.00	0.00	0.00	0.00	0.00	0.00
xMg	0.65	0.65	0.65	0.65	0.67	0.67	0.70	0.70	0.70	0.68	0.66	0.64	0.66	0.64
xFe	0.34	0.34	0.35	0.35	0.32	0.32	0.29	0.30	0.30	0.31	0.33	0.36	0.33	0.36

Note: Oxide values are in wt.%. All other values are calculated with normalization program Norm.

Table 40 - Electron microprobe analyses of clinopyroxene of the sample HSY3b (Hase no Yatsu - Japan). Data from Langone et al. (2009).

	Clinopyroxene													
SiO_2	53.36	51.84	51.96	52.04	53.61	52.37	52.88	53.14	52.25	52.96	52.21	53.10	52.74	52.26
TiO_2	0.22	0.47	0.48	0.48	0.23	0.40	0.53	0.30	0.37	0.31	0.31	0.23	0.33	0.19
Al_2O_3	1.60	2.91	1.92	2.19	1.19	2.25	2.25	1.42	2.75	1.44	2.29	1.40	1.52	1.33
Cr_2O_3	0.05	0.12	0.05	0.05	0.09	0.12	0.22	0.05	0.26	0.19	0.07	0.00	0.17	0.07
Fe_2O_3	0.80	2.26	1.67	1.49	0.60	1.52	0.40	0.71	1.87	1.16	2.26	0.89	0.95	1.15
FeO	5.16	3.73	3.87	4.07	4.35	4.18	4.85	5.81	3.40	3.88	3.04	4.43	4.32	4.70
MnO	0.17	0.15	0.13	0.15	0.12	0.15	0.14	0.21	0.13	0.17	0.14	0.18	0.15	0.16
NiO	0.03	0.04	0.01	0.00	0.00	0.00	0.00	0.04	0.01	0.00	0.00	0.00	0.00	0.00
MgO	14.63	14.94	14.84	14.83	15.58	14.97	15.16	14.55	15.62	15.26	15.59	15.32	15.16	14.58
CaO	24.59	23.47	24.53	24.44	24.57	24.05	24.17	24.46	23.06	24.63	23.68	24.28	24.31	24.14
Na_2O	0.23	0.38	0.14	0.15	0.12	0.24	0.15	0.11	0.40	0.17	0.28	0.15	0.14	0.19
K_2O	0.00	0.01	0.01	0.00	0.01	0.02	0.01	0.00	0.01	0.01	0.03	0.00	0.02	0.00
Total	100.84	100.31	99.60	99.89	100.47	100.26	100.77	100.79	100.13	100.17	99.92	99.98	99.80	98.78
Si	1.956	1.905	1.926	1.923	1.963	1.926	1.934	1.954	1.915	1.948	1.920	1.956	1.948	1.955
Ti	0.006	0.013	0.013	0.013	0.006	0.011	0.015	0.008	0.010	0.009	0.009	0.007	0.009	0.005
Al	0.069	0.126	0.084	0.095	0.051	0.098	0.097	0.062	0.119	0.062	0.099	0.061	0.066	0.059
Cr	0.001	0.004	0.002	0.002	0.003	0.003	0.006	0.002	0.008	0.006	0.002	0.000	0.005	0.002
Fe^{3+}	0.022	0.062	0.047	0.041	0.016	0.042	0.011	0.020	0.052	0.032	0.063	0.025	0.026	0.033
Fe^{2+}	0.158	0.115	0.120	0.126	0.133	0.129	0.148	0.179	0.104	0.119	0.094	0.137	0.133	0.147
Mn	0.005	0.005	0.004	0.005	0.004	0.005	0.005	0.006	0.004	0.005	0.005	0.006	0.005	0.005
Ni	0.001	0.001	0.000	0.000	0.000	0.000	0.000	0.001	0.000	0.000	0.000	0.000	0.000	0.000
Mg	0.799	0.818	0.820	0.817	0.850	0.821	0.826	0.798	0.853	0.837	0.855	0.841	0.835	0.813
Ca	0.966	0.924	0.974	0.968	0.964	0.948	0.947	0.964	0.906	0.971	0.933	0.958	0.962	0.968
Na	0.016	0.027	0.010	0.010	0.009	0.017	0.011	0.008	0.029	0.012	0.020	0.010	0.010	0.014
K	0.000	0.000	0.000	0.000	0.000	0.001	0.001	0.000	0.000	0.000	0.001	0.000	0.001	0.000
Wollastonite	0.464	0.421	0.457	0.452	0.467	0.443	0.448	0.463	0.416	0.463	0.431	0.460	0.459	0.464
Enstatite	0.400	0.410	0.410	0.408	0.425	0.410	0.413	0.399	0.427	0.418	0.427	0.421	0.417	0.406
Ferrosilite	0.079	0.057	0.060	0.063	0.067	0.064	0.074	0.089	0.052	0.060	0.047	0.068	0.067	0.074
Pyroxmangite	0.003	0.002	0.002	0.002	0.002	0.002	0.002	0.003	0.002	0.003	0.002	0.003	0.002	0.003
Acmite	0.016	0.028	0.011	0.011	0.009	0.018	0.011	0.008	0.029	0.012	0.021	0.011	0.011	0.014
Jadeite	0.000	0.000	0.000	0.000	0.000	0.000	0.000	0.000	0.000	0.000	0.000	0.000	0.000	0.000
xMgonM1	0.789	0.78	0.81	0.802	0.83	0.795	0.795	0.779	0.799	0.826	0.818	0.819	0.815	0.801
xMgonM2	0.011	0.038	0.01	0.015	0.02	0.026	0.032	0.018	0.055	0.01	0.037	0.022	0.019	0.011
xMgFe(II+)	0.835	0.877	0.872	0.867	0.864	0.864	0.848	0.817	0.891	0.875	0.901	0.86	0.862	0.847
xMgFe(tot)	0.816	0.822	0.831	0.83	0.85	0.828	0.838	0.801	0.846	0.847	0.845	0.839	0.839	0.819

Note: Oxide values are in wt.%. All other values are calculated with normalization program Norm.

Table 41 - Electron microprobe analyses of brown amphibole of the sample HSY3b (Hase no Yatsu - Japan). Data from Langone et al. (2009).

	Amphibole							
SiO_2	43.82	43.53	42.43	42.90	42.76	41.58	42.94	43.62
TiO_2	1.28	1.08	1.56	1.22	1.07	1.31	1.26	1.16
Al_2O_3	13.26	12.73	13.66	13.55	13.70	13.63	13.62	13.18
Cr_2O_3	0.14	0.10	0.11	0.07	0.11	0.03	0.06	0.02
FeOtot	10.88	11.54	9.45	10.63	10.51	9.81	10.29	11.25
MnO	0.15	0.16	0.08	0.12	0.09	0.10	0.07	0.14
NiO	0.00	0.00	0.00	0.01	0.01	0.00	0.00	0.00
MgO	13.51	13.39	14.96	13.70	14.15	14.54	14.12	13.22
CaO	12.54	12.31	12.32	12.50	12.47	12.29	12.27	12.17
Na_2O	1.80	1.88	2.08	1.90	2.03	2.03	2.04	1.86
K_2O	1.11	1.14	1.41	1.36	1.31	1.30	1.37	1.29
Cl	0.04	0.04	0.04	0.04	0.04	0.04	0.04	0.04
O=Cl								
Total	98.48	97.86	98.06	97.96	98.21	96.62	98.06	97.90
Si	6.363	6.386	6.182	6.278	6.241	6.163	6.265	6.383
Ti	0.139	0.119	0.171	0.134	0.117	0.146	0.139	0.128
Al	2.269	2.201	2.346	2.337	2.357	2.381	2.342	2.273
Cr	0.016	0.011	0.012	0.008	0.013	0.004	0.007	0.002
Fe^{2+}	1.321	1.416	1.151	1.301	1.283	1.216	1.256	1.377
Fe^{3+}	0.000	0.000	0.000	0.000	0.000	0.000	0.000	0.000
Mn	0.018	0.020	0.010	0.015	0.011	0.012	0.009	0.017
Ni	0.000	0.000	0.000	0.001	0.001	0.000	0.000	0.000
Mg	2.922	2.926	3.246	2.986	3.076	3.210	3.068	2.881
Ca	1.951	1.935	1.923	1.960	1.950	1.952	1.918	1.908
Na	0.507	0.535	0.588	0.539	0.574	0.583	0.577	0.528
K	0.205	0.213	0.262	0.254	0.244	0.246	0.255	0.241
cations	15.711	15.762	15.892	15.812	15.866	15.913	15.837	15.736
$Mg/(Mg+Fe_{TOT})$	0.69	0.67	0.74	0.70	0.71	0.73	0.71	0.68
(Na+K)A	0.71	0.75	0.85	0.79	0.82	0.83	0.83	0.74

Note: Oxide values are in wt.%. All other values are calculated with normalization program Norm.

Table 42 - Electron microprobe analyses of clinopyroxene of the sample 14JT50 (Milin - Tibet).

	Clinopyroxene								
SiO_2	51.34	51.14	51.30	52.37	51.90	52.49	52.87	53.36	54.04
TiO_2	0.67	0.50	0.39	0.27	0.40	0.45	0.45	0.32	0.14
Al_2O_3	3.85	3.09	3.79	3.78	3.65	3.72	3.21	2.33	1.50
Cr_2O_3	0.00	0.05	0.00	0.32	0.36	0.37	0.37	0.18	0.22
Fe_2O_3	2.78	2.36	2.93	2.04	1.04	0.93	0.00	0.00	0.00
FeO	3.55	3.71	3.51	4.25	4.79	4.92	5.67	4.95	5.69
MnO	0.21	0.20	0.09	0.23	0.18	0.19	0.17	0.06	0.21
NiO	0.00	0.07	0.00	0.08	0.01	0.00	0.05	0.02	0.09
MgO	14.78	14.73	14.84	14.85	14.51	14.66	14.88	15.38	14.17
CaO	22.79	23.19	22.50	23.12	23.61	22.81	23.35	23.67	24.18
Na_2O	0.58	0.36	0.61	0.46	0.29	0.58	0.23	0.27	0.51
K_2O	0.01	0.00	0.00	0.02	0.00	0.00	0.00	0.00	0.02
Total	100.55	99.40	99.96	101.80	100.74	101.11	101.26	100.54	100.76
Si	1.881	1.898	1.888	1.896	1.901	1.911	1.925	1.949	1.981
Ti	0.019	0.014	0.011	0.007	0.011	0.012	0.012	0.009	0.004
Al	0.166	0.135	0.164	0.161	0.158	0.160	0.138	0.100	0.065
Cr	0.000	0.002	0.000	0.009	0.011	0.011	0.011	0.005	0.006
Fe^{3+}	0.077	0.066	0.081	0.056	0.029	0.025	0.000	0.000	0.000
Fe^{2+}	0.109	0.115	0.108	0.129	0.147	0.150	0.173	0.151	0.174
Mn	0.006	0.006	0.003	0.007	0.006	0.006	0.005	0.002	0.007
Ni	0.000	0.002	0.000	0.002	0.000	0.000	0.002	0.001	0.003
Mg	0.807	0.815	0.814	0.802	0.792	0.795	0.808	0.837	0.774
Ca	0.895	0.922	0.887	0.897	0.926	0.890	0.911	0.926	0.950
Na	0.041	0.026	0.043	0.033	0.021	0.041	0.017	0.019	0.036
K	0.000	0.000	0.000	0.001	0.000	0.000	0.000	0.000	0.001
Wollastonite	0.40	0.42	0.39	0.40	0.42	0.41	0.42	0.44	0.47
Enstatite	0.40	0.41	0.41	0.40	0.40	0.40	0.41	0.42	0.39
Ferrosilite	0.05	0.06	0.05	0.06	0.07	0.08	0.09	0.08	0.09
Pyroxmangite	0.00	0.00	0.00	0.00	0.00	0.00	0.00	0.00	0.00
Acmite	0.04	0.03	0.04	0.03	0.02	0.03	0.00	0.00	0.00
Jadeite	0.00	0.00	0.00	0.00	0.00	0.02	0.02	0.02	0.04
xMgonM1	0.76	0.77	0.76	0.75	0.75	0.74	0.75	0.79	0.77
xMgonM2	0.05	0.04	0.06	0.05	0.04	0.05	0.06	0.05	0.01
xMgFe(II+)	0.88	0.88	0.88	0.86	0.84	0.84	0.82	0.85	0.82
xMgFe(tot)	0.81	0.82	0.81	0.81	0.82	0.82	0.82	0.85	0.82

Note: Oxide values are in wt.%. All other values are calculated with normalization program Norm.

Table 43 - Electron microprobe analyses of brown amphibole of the sample 14JT50 (Milin - Tibet).

	Amphibole								
SiO_2	43.89	44.77	42.82	44.09	42.57	43.55	44.08	43.87	44.13
TiO_2	1.49	1.50	1.85	1.44	1.49	1.31	1.29	1.65	1.52
Al_2O_3	12.56	13.27	13.10	12.46	13.44	12.67	11.66	13.85	12.99
Cr_2O_3	0.12	0.13	0.27	0.28	0.08	0.08	0.11	0.05	0.07
FeOtot	10.63	10.11	10.09	9.78	10.45	10.20	10.40	10.12	9.40
MnO	0.07	0.18	0.20	0.03	0.18	0.10	0.09	0.18	0.16
NiO	0.06	0.00	0.00	0.06	0.05	0.01	0.02	0.00	0.02
MgO	18.53	18.68	18.31	18.29	18.59	18.60	18.64	18.20	18.53
CaO	12.52	12.36	12.45	12.55	12.42	12.41	12.44	12.56	12.58
Na_2O	2.09	2.14	1.98	2.13	2.10	2.16	2.12	2.14	2.07
K_2O	0.20	0.21	0.24	0.22	0.23	0.21	0.22	0.33	0.23
Cl	0.05	0.05	0.05	0.05	0.05	0.05	0.05	0.05	0.05
O=Cl									
Total	102.15	103.35	101.32	101.33	101.60	101.29	101.07	102.95	101.70
Si	6.136	6.155	6.035	6.189	5.994	6.130	6.223	6.070	6.158
Ti	0.157	0.155	0.196	0.152	0.158	0.138	0.137	0.171	0.160
Al	2.069	2.150	2.176	2.061	2.230	2.102	1.940	2.259	2.136
Cr	0.013	0.015	0.031	0.031	0.009	0.009	0.012	0.005	0.007
Fe^{2+}	1.243	1.162	1.189	1.148	1.231	1.201	1.228	1.171	1.097
Fe^{3+}	0.000	0.000	0.000	0.000	0.000	0.000	0.000	0.000	0.000
Mn	0.008	0.021	0.024	0.003	0.022	0.011	0.011	0.022	0.019
Ni	0.007	0.000	0.000	0.007	0.006	0.001	0.003	0.000	0.002
Mg	3.858	3.825	3.843	3.824	3.898	3.899	3.919	3.750	3.851
Ca	1.875	1.821	1.880	1.888	1.874	1.872	1.882	1.862	1.881
Na	0.566	0.570	0.541	0.580	0.573	0.589	0.580	0.574	0.560
K	0.035	0.036	0.043	0.039	0.040	0.038	0.040	0.058	0.040
cations	15.967	15.911	15.958	15.922	16.035	15.990	15.974	15.943	15.911
$Mg/(Mg+Fe_{TOT})$	0.76	0.77	0.76	0.77	0.76	0.76	0.76	0.76	0.78
(Na+K)A	0.60	0.61	0.58	0.62	0.61	0.63	0.62	0.63	0.60

Note: Oxide values are in wt.%. All other values are calculated with normalization program Norm.

Table 44 - Electron microprobe analyses of olivine of the sample MAT15 (Adamello - Italy). Data from Tiepolo et al. (2011)

	Olivine				
SiO_2	39.58	39.07	39.83	38.78	39.73
TiO_2	0.00	0.01	0.00	0.01	0.00
Al_2O_3	0.00	0.00	0.02	0.02	0.00
Cr_2O_3	0.01	0.00	0.03	0.00	0.00
FeO	16.54	16.59	16.63	16.55	16.74
MnO	0.29	0.34	0.29	0.30	0.31
NiO	0.12	0.11	0.16	0.15	0.12
MgO	43.64	44.06	44.33	44.06	44.29
CaO	0.02	0.02	0.04	0.02	0.01
Na_2O	0.00	0.00	0.01	0.00	0.00
K_2O	0.00	0.01	0.00	0.01	0.01
Total	100.21	100.21	101.35	99.91	101.22
Si	0.993	0.980	0.992	0.991	0.991
Ti	0.000	0.000	0.000	0.000	0.000
Al	0.001	0.001	0.000	0.001	0.001
Cr	0.001	0.000	0.000	0.000	0.000
Fe^{2+}	0.347	0.350	0.350	0.303	0.334
Mn	0.006	0.006	0.007	0.005	0.006
Ni	0.003	0.003	0.002	0.004	0.002
Mg	1.648	1.659	1.649	1.696	1.664
Ca	0.001	0.001	0.000	0.001	0.001
Na	0.001	0.000	0.000	0.000	0.001
K	0.000	0.000	0.000	0.000	0.000
Forsterite	0.82	0.82	0.82	0.84	0.83
Fayalite	0.17	0.17	0.17	0.15	0.17
Tephroite	0.00	0.00	0.00	0.00	0.00
Monticellit	0.00	0.00	0.00	0.00	0.00
Kirschstein	0.00	0.00	0.00	0.00	0.00
Glaukocroit	0.00	0.00	0.00	0.00	0.00
Ni-Olivine	0.00	0.00	0.00	0.00	0.00
xMg	0.82	0.82	0.82	0.84	0.83
xFe	0.17	0.17	0.17	0.15	0.17

Note: Oxide values are in wt.%. All other values are calculated with normalization program Norm.

Table 45 - Electron microprobe analyses of clinopyroxene of the sample MAT15 (Adamello - Italy). Data from Tiepolo et al. (2011)

	Clinopyroxene				
SiO_2	53.21	52.11	52.56	53.46	50.84
TiO_2	0.28	0.58	0.80	0.32	0.40
Al_2O_3	2.42	3.46	2.47	2.09	4.12
Cr_2O_3	0.23	0.34	0.27	0.19	0.92
Fe_2O_3	0.48	0.91	0.03	0.38	1.18
FeO	3.74	3.48	4.01	3.95	4.01
MnO	0.13	0.12	0.14	0.13	0.15
NiO	0.01	0.00	0.01	0.02	0.01
MgO	15.14	15.04	14.97	15.25	14.68
CaO	24.83	25.07	25.34	24.67	22.69
Na_2O	0.26	0.06	0.05	0.28	0.37
K_2O	0.00	0.01	0.01	0.01	0.01
Total	100.73	101.18	100.66	100.75	99.38
Si	1.940	1.895	1.922	1.949	1.883
Ti	0.008	0.016	0.022	0.009	0.011
Al	0.104	0.148	0.107	0.090	0.180
Cr	0.007	0.010	0.008	0.006	0.027
Fe^{3+}	0.013	0.025	0.001	0.011	0.033
Fe^{2+}	0.114	0.106	0.123	0.120	0.124
Mn	0.004	0.004	0.004	0.004	0.005
Ni	0.000	0.000	0.000	0.001	0.000
Mg	0.823	0.815	0.816	0.829	0.810
Ca	0.970	0.977	0.993	0.963	0.900
Na	0.018	0.004	0.004	0.020	0.027
K	0.000	0.001	0.001	0.001	0.001
Wollastonite	0.46	0.44	0.47	0.46	0.40
Enstatite	0.41	0.41	0.41	0.42	0.41
Ferrosilite	0.06	0.05	0.06	0.06	0.06
Pyroxmangite	0.00	0.00	0.00	0.00	0.00
Acmite	0.01	0.01	0.00	0.01	0.03
Jadeite	0.01	0.00	0.00	0.01	0.00
xMgonM1	0.82	0.80	0.82	0.82	0.75
xMgonM2	0.01	0.01	0.00	0.01	0.06
xMgFe(II+)	0.88	0.89	0.87	0.87	0.87
xMgFe(tot)	0.87	0.86	0.87	0.86	0.84

Note: Oxide values are in wt.%. All other values are calculated with normalization program Norm.

Table 46 - Electron microprobe analyses of brown amphibole of the sample MAT15 (Adamello - Italy).

	Amphibole							
SiO_2	43.84	44.00	44.21	44.62	45.42	41.83	43.18	43.94
TiO_2	1.46	1.60	1.64	1.21	1.12	2.04	1.69	1.32
Al_2O_3	12.61	12.69	12.94	11.94	11.72	14.35	13.33	12.35
Cr_2O_3	0.25	0.30	0.32	0.34	0.30	0.44	0.37	0.31
FeOtot	8.44	8.27	8.19	8.31	8.34	7.96	8.22	8.37
MnO	0.15	0.10	0.09	0.13	0.11	0.09	0.14	0.12
NiO	0.02	0.03	0.02	0.08	0.06	0.09	0.08	0.03
MgO	15.64	16.43	16.05	16.44	16.71	15.42	15.75	16.35
CaO	12.15	11.96	12.15	11.78	11.67	12.40	12.28	11.94
Na_2O	2.11	2.25	2.10	2.14	1.94	2.40	2.40	2.21
K_2O	0.31	0.32	0.33	0.30	0.28	0.36	0.35	0.30
Cl	0.00	0.00	0.00	0.00	0.00	0.00	0.00	0.00
O=Cl								
Total	96.98	97.95	98.05	97.28	97.67	97.37	97.79	97.25
Si	6.373	6.329	6.345	6.452	6.522	6.080	6.241	6.369
Ti	0.160	0.173	0.177	0.132	0.121	0.223	0.184	0.144
Al	2.160	2.151	2.189	2.035	1.984	2.458	2.271	2.110
Cr	0.029	0.034	0.037	0.038	0.034	0.051	0.042	0.036
Fe^{2+}	1.026	0.995	0.983	1.005	1.002	0.968	0.994	1.015
Fe^{3+}	0.000	0.000	0.000	0.000	0.000	0.000	0.000	0.000
Mn	0.019	0.012	0.011	0.016	0.013	0.011	0.018	0.015
Ni	0.002	0.004	0.003	0.010	0.007	0.010	0.009	0.004
Mg	3.386	3.520	3.431	3.540	3.574	3.338	3.390	3.529
Ca	1.892	1.843	1.868	1.825	1.796	1.931	1.902	1.854
Na	0.595	0.628	0.584	0.600	0.540	0.676	0.673	0.621
K	0.057	0.058	0.061	0.055	0.052	0.066	0.065	0.055
cations	15.699	15.747	15.688	15.707	15.644	15.813	15.788	15.752
$Mg/(Mg+Fe_{TOT})$	0.77	0.78	0.78	0.78	0.78	0.78	0.77	0.78
(Na+K)A	0.65	0.69	0.65	0.65	0.59	0.74	0.74	0.68

Note: Oxide values are in wt.%. All other values are calculated with normalization program Norm.

Table 47 - Electron microprobe analyses of olivine of the sample VS 9 (Adamello - Italy). Data from Tiepolo et al. (2002).

	Olivine	
SiO_2	40.05	40.11
TiO_2	0.08	0.02
Al_2O_3	0.07	0.06
Cr_2O_3	0.00	0.00
FeO	16.31	15.64
MnO	0.53	0.56
MgO	44.30	44.95
CaO	0.05	0.02
Na_2O	0.00	0.11
K_2O	0.03	0.02
Total	101.42	101.49
Si	0.998	0.994
Ti	0.002	0.000
Al	0.002	0.002
Cr	0.000	0.000
Fe^{2+}	0.340	0.324
Mn	0.011	0.012
Mg	1.645	1.661
Ca	0.001	0.001
Na	0.000	0.005
K	0.001	0.001
Forsterite	0.82	0.83
Fayalite	0.17	0.16
Tephroite	0.01	0.01
Monticellit	0.00	0.00
Kirschstein	0.00	0.00
Glaukocroit	0.00	0.00
Ni-Olivine	0.00	0.00
xMg	0.82	0.83
xFe	0.17	0.16

Note: Oxide values are in wt.%.
All other values are calculated with normalization program Norm.

Table 48 - Electron microprobe analyses of clinopyroxene of the sample VS 9 (Adamello - Italy). Data from Tiepolo et al. (2002).

	Clinopyroxene			
SiO_2	51.38	52.21	51.15	52.35
TiO_2	0.64	0.55	0.56	0.37
Al_2O_3	4.39	3.55	2.51	2.84
Cr_2O_3	0.00	0.00	0.00	0.00
Fe_2O_3	2.56	0.54	1.33	1.48
FeO	3.46	4.69	3.49	3.82
MnO	0.26	0.14	0.25	0.26
MgO	14.62	14.94	14.59	15.48
CaO	23.46	23.44	24.12	22.88
Na_2O	0.45	0.31	0.20	0.38
K_2O	0.03	0.00	0.03	0.06
Total	101.25	100.36	98.23	99.92
Si	1.870	1.912	1.918	1.923
Ti	0.018	0.015	0.016	0.010
Al	0.188	0.153	0.111	0.123
Cr	0.000	0.000	0.000	0.000
Fe^{3+}	0.070	0.015	0.038	0.041
Fe^{2+}	0.105	0.144	0.109	0.117
Mn	0.008	0.004	0.008	0.008
Mg	0.793	0.815	0.815	0.848
Ca	0.915	0.920	0.969	0.900
Na	0.032	0.022	0.015	0.027
K	0.001	0.000	0.001	0.003
Wollastonite	0.40	0.42	0.45	0.42
Enstatite	0.40	0.41	0.41	0.42
Ferrosilite	0.05	0.07	0.06	0.06
Pyroxmangite	0.00	0.00	0.00	0.00
Acmite	0.03	0.02	0.02	0.03
Jadeite	0.00	0.01	0.00	0.00
xMgonM1	0.75	0.77	0.81	0.79
xMgonM2	0.04	0.05	0.01	0.05
xMgFe(II+)	0.88	0.85	0.88	0.88
xMgFe(tot)	0.82	0.84	0.85	0.84

Note: Oxide values are in wt.%. All other values are calculated with normalization program Norm.

Table 49 - Electron microprobe analyses of clinopyroxene of the sample VS 9 (Adamello - Italy). Data from Tiepolo et al. (2002).

	Amphibole							
SiO_2	47.31	45.99	42.35	42.68	43.62	43.32	42.88	42.27
TiO_2	0.97	1.31	1.93	1.97	1.78	1.89	1.75	1.58
Al_2O_3	9.67	10.46	14.05	13.92	13.43	13.33	13.19	12.67
Cr_2O_3	0.00	0.00	0.00	0.00	0.00	0.00	0.00	0.00
FeOtot	10.53	10.80	11.38	11.21	10.05	9.98	10.08	9.59
MnO	0.15	0.17	0.16	0.14	0.12	0.16	0.19	0.16
NiO	0.00	0.00	0.00	0.00	0.00	0.00	0.00	0.00
MgO	15.58	14.97	13.30	13.39	14.70	15.12	14.60	14.97
CaO	12.81	12.74	12.39	12.37	12.01	11.76	12.28	12.33
Na_2O	1.43	1.50	2.13	2.08	2.24	2.27	2.10	2.09
K_2O	0.43	0.45	0.47	0.49	0.42	0.48	0.65	0.44
Cl	0.00	0.00	0.00	0.00	0.00	0.00	0.00	0.00
O=Cl								
Total	98.88	98.39	98.16	98.25	98.37	98.31	97.72	96.10
Si	6.771	6.640	6.183	6.215	6.295	6.260	6.256	6.261
Ti	0.104	0.142	0.212	0.216	0.193	0.205	0.192	0.176
Al	1.631	1.780	2.417	2.389	2.284	2.270	2.268	2.212
Cr	0.000	0.000	0.000	0.000	0.000	0.000	0.000	0.000
Fe^{2+}	1.260	1.304	1.389	1.365	1.213	1.206	1.230	1.188
Fe^{3+}	0.000	0.000	0.000	0.000	0.000	0.000	0.000	0.000
Mn	0.018	0.021	0.020	0.017	0.015	0.020	0.023	0.020
Ni	0.000	0.000	0.000	0.000	0.000	0.000	0.000	0.000
Mg	3.321	3.219	2.892	2.904	3.160	3.254	3.172	3.302
Ca	1.964	1.971	1.938	1.930	1.857	1.821	1.920	1.957
Na	0.397	0.420	0.603	0.587	0.627	0.636	0.594	0.600
K	0.079	0.083	0.088	0.091	0.077	0.088	0.121	0.083
cations	15.546	15.579	15.742	15.714	15.721	15.761	15.776	15.799
$Mg/(Mg+Fe_{TOT})$	0.72	0.71	0.68	0.68	0.72	0.73	0.72	0.74
(Na+K)A	0.48	0.50	0.69	0.68	0.70	0.72	0.71	0.68

Note: Oxide values are in wt.%. All other values are calculated with normalization program Norm.

Table 50 - Electron microprobe analyses of brown amphibole of the sample SRD02305 (Batu Hijau - Indonesia).

	Amphibole												
SiO_2	47.55	49.14	47.82	47.91	47.63	47.80	50.14	47.76	48.21	49.21	46.80	47.80	46.41
TiO_2	1.40	1.03	1.45	1.11	1.33	1.36	1.12	1.28	1.32	1.09	1.43	1.31	1.44
Al_2O_3	7.24	5.84	6.41	6.66	6.89	7.32	4.78	7.38	7.27	6.30	7.61	6.87	7.20
Cr_2O_3	0.00	0.04	0.01	0.05	0.00	0.04	0.00	0.00	0.00	0.04	0.02	0.01	0.03
FeOtot	13.30	11.05	10.78	10.84	10.84	11.20	9.60	11.32	11.44	10.68	11.66	10.96	11.35
MnO	0.40	0.32	0.36	0.38	0.36	0.39	0.45	0.34	0.31	0.35	0.29	0.33	0.21
NiO	0.08	0.00	0.10	0.07	0.00	0.07	0.01	0.01	0.00	0.04	0.00	0.06	0.00
MgO	15.09	15.67	15.15	15.69	15.37	14.73	17.10	15.49	14.84	15.59	14.89	15.33	14.72
CaO	11.25	10.74	11.21	10.78	10.90	10.98	10.86	10.93	10.92	10.84	10.96	10.97	11.04
Na_2O	1.24	1.03	1.16	1.20	1.21	1.34	1.35	1.28	1.73	1.58	1.69	1.56	1.60
K_2O	0.18	0.13	0.14	0.16	0.19	0.18	0.32	0.18	0.16	0.17	0.21	0.19	0.15
Cl	0.01	0.15	0.15	0.15	0.15	0.15	0.15	0.15	0.15	0.15	0.15	0.15	0.15
O=Cl													
Total	97.73	95.00	94.58	94.86	94.71	95.40	95.73	95.97	96.20	95.89	95.56	95.39	94.14
Si	6.950	7.261	7.126	7.111	7.083	7.070	7.324	7.024	7.077	7.210	6.948	7.073	6.985
Ti	0.153	0.115	0.162	0.124	0.148	0.151	0.124	0.142	0.146	0.120	0.160	0.146	0.163
Al	1.247	1.017	1.126	1.165	1.208	1.276	0.823	1.279	1.258	1.088	1.332	1.198	1.277
Cr	0.000	0.005	0.001	0.006	0.000	0.005	0.000	0.000	0.000	0.005	0.002	0.001	0.003
Fe^{2+}	1.626	1.366	1.343	1.346	1.348	1.385	1.173	1.392	1.404	1.309	1.448	1.356	1.429
Fe^{3+}	0.000	0.000	0.000	0.000	0.000	0.000	0.000	0.000	0.000	0.000	0.000	0.000	0.000
Mn	0.049	0.040	0.046	0.048	0.045	0.049	0.055	0.042	0.039	0.044	0.036	0.042	0.027
Ni	0.009	0.000	0.012	0.009	0.000	0.008	0.002	0.001	0.000	0.005	0.000	0.007	0.000
Mg	3.285	3.449	3.362	3.468	3.404	3.245	3.720	3.393	3.245	3.402	3.292	3.378	3.300
Ca	1.762	1.700	1.790	1.714	1.737	1.740	1.700	1.722	1.718	1.702	1.743	1.739	1.780
Na	0.351	0.295	0.335	0.346	0.348	0.383	0.382	0.364	0.492	0.449	0.486	0.448	0.467
K	0.033	0.025	0.026	0.031	0.036	0.034	0.059	0.034	0.029	0.031	0.040	0.035	0.028
cations	15.466	15.273	15.329	15.368	15.357	15.347	15.361	15.393	15.408	15.364	15.489	15.423	15.459
$Mg/(Mg+Fe_{TOT})$	0.67	0.72	0.71	0.72	0.72	0.70	0.76	0.71	0.70	0.72	0.69	0.71	0.70
(Na+K)A	0.38	0.27	0.33	0.37	0.36	0.35	0.36	0.39	0.41	0.36	0.49	0.42	0.46

Note: Oxide values are in wt.%. All other values are calculated with normalization program Norm.

Table 51 - Electron microprobe analyses of brown amphibole of the sample MGT (Hoover Dam - United States of America).

	Amphibole															
SiO_2	39.64	39.70	39.82	39.60	40.40	40.16	39.96	40.09	39.66	39.84	39.94	40.10	40.35	40.19	40.29	39.97
TiO_2	5.64	5.58	5.73	5.80	5.92	5.62	5.82	5.48	5.84	5.56	5.61	5.56	5.78	5.68	5.65	5.92
Al_2O_3	14.32	14.35	14.33	14.60	14.39	14.46	14.24	14.39	14.50	14.40	14.66	14.34	14.28	14.19	14.08	14.45
Cr_2O_3	0.00	0.00	0.01	0.06	0.10	0.08	0.15	0.08	0.05	0.05	0.10	0.12	0.04	0.00	0.08	0.01
FeOtot	9.68	9.59	9.53	9.61	8.25	8.36	8.56	8.25	8.14	8.36	8.47	8.52	8.53	8.52	8.32	8.44
MnO	0.10	0.12	0.10	0.11	0.10	0.07	0.12	0.06	0.05	0.11	0.07	0.04	0.03	0.12	0.07	0.08
NiO	0.02	0.00	0.00	0.02	0.09	0.00	0.00	0.04	0.00	0.04	0.07	0.05	0.04	0.06	0.10	0.00
MgO	13.06	13.20	13.23	13.07	13.61	13.67	13.96	13.91	14.00	14.07	13.95	14.23	14.05	13.94	14.06	14.16
CaO	11.10	11.01	10.96	10.94	10.81	10.81	11.00	10.83	10.98	10.94	10.97	10.99	10.95	10.96	10.80	10.88
Na_2O	2.61	2.54	2.54	2.39	2.33	2.24	2.40	2.30	2.44	2.37	2.46	2.32	2.43	2.42	2.50	2.42
K_2O	1.88	1.93	1.89	1.93	1.94	1.96	1.93	1.94	2.00	1.95	1.96	1.93	1.89	1.90	1.92	1.92
Cl																
O=Cl																
Total	98.05	98.02	98.14	98.13	97.94	97.42	98.14	97.37	97.66	97.68	98.25	98.19	98.38	97.98	97.87	98.24
Si	5.831	5.837	5.842	5.813	5.893	5.889	5.838	5.883	5.814	5.841	5.825	5.849	5.870	5.875	5.890	5.824
Ti	0.624	0.617	0.632	0.640	0.650	0.620	0.640	0.605	0.644	0.613	0.615	0.610	0.632	0.625	0.621	0.649
Al	2.483	2.487	2.478	2.526	2.474	2.499	2.452	2.489	2.505	2.488	2.520	2.465	2.448	2.445	2.426	2.482
Cr	0.000	0.000	0.001	0.007	0.011	0.009	0.017	0.009	0.006	0.006	0.011	0.014	0.005	0.000	0.009	0.001
Fe^{2+}	1.191	1.179	1.169	1.180	1.006	1.025	1.046	1.013	0.998	1.025	1.033	1.039	1.038	1.042	1.017	1.029
Fe^{3+}	0.000	0.000	0.000	0.000	0.000	0.000	0.000	0.000	0.000	0.000	0.000	0.000	0.000	0.000	0.000	0.000
Mn	0.012	0.015	0.012	0.014	0.013	0.008	0.015	0.007	0.006	0.013	0.009	0.005	0.004	0.015	0.009	0.009
Ni	0.003	0.000	0.000	0.003	0.011	0.000	0.000	0.005	0.000	0.004	0.008	0.005	0.005	0.007	0.011	0.000
Mg	2.861	2.890	2.891	2.857	2.957	2.986	3.038	3.040	3.056	3.072	3.030	3.091	3.044	3.035	3.061	3.073
Ca	1.750	1.734	1.723	1.721	1.690	1.699	1.722	1.703	1.724	1.718	1.714	1.717	1.707	1.717	1.692	1.699
Na	0.744	0.724	0.722	0.680	0.659	0.637	0.680	0.654	0.693	0.674	0.696	0.656	0.685	0.686	0.709	0.684
K	0.353	0.362	0.354	0.361	0.361	0.367	0.360	0.363	0.374	0.365	0.365	0.359	0.351	0.354	0.358	0.357
cations	15.852	15.846	15.824	15.801	15.725	15.738	15.807	15.772	15.821	15.819	15.825	15.810	15.789	15.798	15.804	15.806
$Mg/(Mg+Fe_{TOT})$	0.71	0.71	0.71	0.71	0.75	0.74	0.74	0.75	0.75	0.75	0.75	0.75	0.75	0.74	0.75	0.75
(Na+K)A	0.85	0.85	0.82	0.80	0.72	0.74	0.81	0.77	0.82	0.82	0.82	0.81	0.79	0.80	0.80	0.81

Note: Oxide values are in wt.%. All other values are calculated with normalization program Norm.

Table 52 - Electron microprobe analyses of brown amphibole of the sample DH (Dish Hill - United States of America).

	Amphibole											
SiO_2	39.35	39.22	39.54	39.20	39.26	38.66	39.33	39.23	38.99	38.86	39.20	39.29
TiO_2	5.24	4.98	5.15	4.98	4.71	4.65	4.82	4.72	4.82	4.66	4.85	4.89
Al_2O_3	14.77	14.53	14.45	14.70	14.11	14.35	14.16	14.39	14.24	14.22	14.25	14.17
Cr_2O_3	0.04	0.00	0.03	0.00	0.00	0.03	0.02	0.08	0.00	0.01	0.03	0.00
FeOtot	11.94	11.90	12.27	11.77	14.51	14.59	14.41	14.33	14.32	14.46	14.38	14.56
MnO	0.17	0.11	0.14	0.13	0.24	0.21	0.22	0.22	0.23	0.21	0.21	0.17
NiO	0.01	0.00	0.03	0.00	0.07	0.00	0.00	0.00	0.03	0.07	0.00	0.00
MgO	12.20	12.16	12.52	12.34	10.92	10.81	10.72	10.78	10.76	10.66	10.64	10.48
CaO	10.74	10.81	10.88	10.70	11.00	10.99	10.98	10.96	10.90	11.04	10.92	10.99
Na_2O	2.49	2.59	2.60	2.60	2.74	2.60	2.69	2.83	2.63	2.78	2.62	2.79
K_2O	1.72	1.66	1.69	1.74	1.58	1.59	1.62	1.57	1.61	1.56	1.61	1.61
Cl												
O=Cl												
Total	98.67	97.96	99.30	98.17	99.14	98.48	98.97	99.11	98.53	98.52	98.71	98.96
Si	5.799	5.823	5.803	5.805	5.838	5.792	5.852	5.829	5.828	5.819	5.845	5.852
Ti	0.581	0.556	0.569	0.555	0.527	0.524	0.539	0.527	0.542	0.525	0.544	0.548
Al	2.565	2.542	2.499	2.566	2.473	2.534	2.483	2.520	2.508	2.510	2.504	2.487
Cr	0.005	0.000	0.004	0.000	0.000	0.004	0.003	0.009	0.000	0.001	0.004	0.001
Fe^{2+}	1.472	1.477	1.506	1.458	1.805	1.828	1.793	1.781	1.790	1.811	1.793	1.813
Fe^{3+}	0.000	0.000	0.000	0.000	0.000	0.000	0.000	0.000	0.000	0.000	0.000	0.000
Mn	0.022	0.014	0.017	0.017	0.030	0.027	0.028	0.028	0.029	0.026	0.027	0.022
Ni	0.001	0.000	0.003	0.000	0.009	0.000	0.000	0.000	0.004	0.008	0.000	0.000
Mg	2.678	2.689	2.737	2.722	2.419	2.412	2.375	2.385	2.395	2.377	2.363	2.325
Ca	1.696	1.719	1.711	1.698	1.753	1.764	1.750	1.745	1.746	1.771	1.745	1.754
Na	0.711	0.746	0.740	0.747	0.790	0.755	0.776	0.815	0.762	0.807	0.757	0.806
K	0.323	0.314	0.316	0.329	0.300	0.304	0.308	0.298	0.307	0.298	0.306	0.306
cations	15.852	15.880	15.905	15.895	15.943	15.945	15.908	15.936	15.911	15.953	15.889	15.912
$Mg/(Mg+Fe_{TOT})$	0.65	0.65	0.65	0.65	0.57	0.57	0.57	0.57	0.57	0.57	0.57	0.56
(Na+K)A	0.85	0.88	0.90	0.89	0.94	0.94	0.91	0.94	0.91	0.95	0.89	0.91

Note: Oxide values are in wt.%. All other values are calculated with normalization program Norm.

Appendix B - Tables of trace element compositions and isotopic ratios of the samples.

Table 1 - LA-ICP-MS analyses of brown amphibole of the sample MKD1 (Mt. Keith – Agnew-Wiluna greenstone belt, Western Australia).

	Amphibole						
Sc	72.82	91.90	86.78	107.25	82.21	88.67	101.55
Ti	18932.81	22625.98	27446.77	26776.62	21158.29	28954.99	24721.46
V	651.43	664.29	667.70	774.52	633.99	685.75	686.56
Cr	8703.27	7224.60	6308.69	8305.01	7501.56	4566.98	6876.28
Co	51.56	49.68	52.41	54.97	50.77	54.86	53.71
Ni	880.73	835.50	846.28	887.38	826.09	930.44	905.99
Zn	45.44	44.22	46.33	45.45	44.54	44.88	38.68
Rb	4.44	3.15	2.53	3.27	3.15	2.90	3.13
Sr	35.43	47.64	54.09	54.29	43.57	53.57	55.17
Y	78.63	105.06	123.55	113.09	88.08	152.30	118.63
Zr	237.19	155.68	129.88	133.97	136.90	161.93	189.12
Nb	21.65	16.21	14.21	15.82	15.10	14.58	16.13
Cs	<0,0069	0.01	<0,0073	0.01	0.03	0.02	0.02
Ba	158.03	155.67	155.54	163.86	138.69	153.10	159.94
La	22.79	16.33	14.85	15.13	15.74	17.18	18.49
Ce	72.16	56.11	52.91	53.08	53.14	61.08	62.21
Pr	10.64	9.18	9.35	9.17	8.63	10.93	10.21
Nd	50.61	50.90	54.99	52.58	46.71	65.38	56.98
Sm	12.99	15.45	18.04	16.76	13.98	22.59	18.74
Eu	2.84	3.08	3.63	3.42	2.77	4.13	3.62
Gd	13.07	18.50	22.42	20.89	15.72	27.73	22.05
Tb	2.11	3.12	4.03	3.46	2.58	4.83	3.82
Dy	13.59	19.88	24.11	21.19	15.91	29.60	22.56
Ho	2.89	4.04	5.10	4.27	3.47	5.99	4.47
Er	8.08	10.54	12.44	10.88	8.91	14.40	11.60
Tm	1.11	1.38	1.57	1.38	1.12	1.79	1.56
Yb	7.07	8.09	8.95	8.86	7.62	11.49	8.80
Lu	0.88	1.09	1.09	1.15	0.93	1.37	1.19
Hf	9.04	6.68	5.62	5.67	5.44	7.11	6.69
Ta	1.30	0.93	0.88	0.87	0.84	0.80	0.92
Pb	1.08	0.74	0.64	1.03	1.06	1.11	1.15
Th	0.50	0.23	0.31	0.29	0.60	0.33	0.69
U	0.10	0.05	0.06	0.05	0.24	0.06	0.21
Nb/Y	0.28	0.15	0.12	0.14	0.17	0.10	0.14
Nb/Ta	16.71	17.39	16.24	18.23	18.08	18.27	17.53
Zr/Hf	26.24	23.31	23.11	23.63	25.17	22.77	28.27

Note: values are in ppm.

Table 2 - LA-ICP-MS analyses of brown amphibole of the sample 85437 (Mt. Clifford – Agnew-Wiluna greenstone belt, Western Australia).

	Amphibole			
Sc	81.79	31.38	56.20	34.85
Ti	19224.58	21974.87	22922.83	23928.63
V	753.54	808.34	837.83	838.32
Cr	5097.17	5947.71	3709.53	3686.48
Co	53.49	56.01	57.31	57.78
Ni	533.47	562.56	604.86	576.42
Zn	97.29	93.77	96.61	92.09
Rb	2.24	2.14	2.03	2.17
Sr	14.64	12.40	12.47	15.01
Y	116.22	141.20	294.62	94.79
Zr	471.89	626.16	587.56	822.52
Nb	21.74	31.19	61.18	17.30
Cs	0.36	0.06	0.10	0.07
Ba	66.40	70.74	87.21	76.64
La	19.65	29.56	37.34	18.93
Ce	58.43	89.73	154.96	54.10
Pr	8.71	12.47	29.12	8.27
Nd	44.32	60.21	165.92	42.75
Sm	15.14	18.43	54.70	13.72
Eu	2.81	3.35	5.22	3.24
Gd	17.98	21.05	57.02	15.95
Tb	3.39	4.09	10.42	2.87
Dy	20.94	25.65	61.20	17.72
Ho	4.53	5.52	11.80	3.76
Er	12.11	15.49	29.10	9.73
Tm	1.69	2.17	3.46	1.39
Yb	11.68	13.99	19.13	9.72
Lu	1.42	1.83	2.37	1.19
Hf	11.12	16.18	16.06	21.71
Ta	1.09	1.33	2.73	0.91
Pb	1.26	1.33	0.87	1.44
Th	2.62	2.59	0.39	2.74
U	0.15	0.15	0.09	0.21
Nb/Y	0.19	0.22	0.21	0.18
Nb/Ta	19.89	23.54	22.41	19.05
Zr/Hf	42.44	38.70	36.59	37.89

Note: values are in ppm.

Table 3 - LA-ICP-MS analyses of clinopyroxene of the sample T-2 (Theo's Flow – Abitibi greenstone belt, Canada).

	Clinopyroxene						
Sc	55.28	81.70	59.64	56.49	56.31	88.42	55.69
Ti	1580.89	2887.93	1663.42	1496.28	1446.36	2652.65	1444.70
V	160.78	282.32	183.39	159.91	155.01	282.40	153.21
Cr	4658.53	6104.45	6326.99	5548.76	6525.08	6672.63	5972.12
Co	45.40	46.11	46.02	43.52	47.86	45.61	45.03
Ni	343.13	325.20	371.19	350.72	381.30	342.59	360.60
Zn	39.55	46.36	27.54	34.72	40.35	58.02	31.46
Rb	0.03	0.02	0.10	0.03	0.03	0.16	0.02
Sr	12.53	14.86	12.47	12.41	11.28	16.49	12.21
Y	4.94	9.85	6.44	4.42	4.93	10.16	4.34
Zr	3.10	9.40	2.99	2.67	2.67	8.74	2.84
Nb	0.01	0.03	0.05	0.01	--	0.04	--
Cs	0.01	0.01	0.08	0.01	0.01	0.01	0.01
Ba	0.09	0.02	0.08	0.04	0.05	0.13	0.03
La	0.23	0.33	0.10	0.23	0.16	0.39	0.20
Ce	1.03	1.59	0.86	1.00	0.92	1.79	0.82
Pr	0.24	0.29	0.28	0.18	0.19	0.45	0.21
Nd	1.17	3.34	1.32	1.45	1.15	2.65	1.52
Sm	0.51	1.45	1.42	0.54	1.06	1.35	0.73
Eu	0.29	0.41	0.38	0.23	0.24	0.55	0.20
Gd	0.80	2.10	1.52	0.51	0.41	1.55	0.77
Tb	0.16	0.37	0.22	0.16	0.14	0.29	0.15
Dy	0.94	2.22	2.04	1.01	0.96	2.09	0.71
Ho	0.18	0.44	0.16	0.22	0.16	0.45	0.26
Er	0.42	1.03	0.24	0.58	0.46	1.04	0.52
Tm	0.10	0.15	0.14	0.05	0.09	0.12	0.07
Yb	0.56	0.80	0.18	0.29	0.33	0.98	0.54
Lu	0.05	0.12	0.06	0.09	0.06	0.19	0.06
Hf	0.16	0.80	0.30	0.08	0.05	0.60	0.22
Ta	0.01	0.01	0.03	0.01	--	0.01	0.01
Pb	0.11	0.04	0.21	0.15	0.03	0.25	0.38
Th	0.01	0.01	--	0.01	0.01	0.01	--
U	--	0.01	--	--	0.01	0.01	--

Note: values are in ppm.

Table 4 - LA-ICP-MS analyses of amphibole of the sample T-2 (Theo's Flow – Abitibi greenstone belt, Canada).

	Amphibole						
Sc	52.66	57.75	31.45	50.57	18.97	29.04	40.51
Ti	11943.37	11784.43	11474.67	13005.37	11122.84	12151.11	9541.00
V	409.39	423.65	390.17	438.78	367.58	414.69	378.74
Cr	670.85	1270.68	400.30	580.11	1644.91	3310.13	534.94
Co	65.09	78.41	71.47	76.27	63.21	70.02	57.90
Ni	792.35	775.06	734.53	929.76	609.99	626.01	520.69
Zn	56.01	68.24	74.74	68.30	37.62	48.69	65.30
Rb	0.31	0.73	0.35	0.41	0.45	0.55	0.38
Sr	10.29	10.76	12.80	11.99	11.26	13.45	30.75
Y	69.66	63.31	77.43	77.42	59.14	72.50	30.69
Zr	171.83	283.87	450.97	438.82	204.90	162.98	140.74
Nb	27.84	31.72	29.78	34.84	21.70	29.79	11.42
Cs	0.05	0.04	0.04	0.10	0,044	0,038	0.13
Ba	3.83	3.11	3.62	4.24	3.22	4.52	3.22
La	11.71	6.59	9.39	8.68	9.90	14.88	4.88
Ce	42.09	26.00	36.70	33.85	36.30	60.49	18.39
Pr	6.98	4.97	7.24	5.67	6.92	10.17	3.23
Nd	40.06	27.66	32.63	33.28	36.06	56.08	16.23
Sm	11.59	10.11	13.71	9.01	8.70	17.08	4.42
Eu	3.43	2.81	2.70	3.19	2.23	3.36	2.48
Gd	13.33	10.95	12.08	11.62	12.79	20.06	6.86
Tb	2.51	1.60	2.72	2.86	2.54	2.75	1.10
Dy	15.37	13.56	17.02	15.55	15.96	16.87	6.45
Ho	2.23	2.76	3.51	2.90	2.31	2.86	1.29
Er	6.66	4.99	7.88	7.25	5.69	8.57	3.47
Tm	0.89	0.68	1.02	1.21	1.02	1.15	0.50
Yb	6.90	7.26	7.28	7.92	5.34	5.97	3.62
Lu	0.56	1.06	0.68	1.11	0.62	0.77	0.59
Hf	3.21	5.56	9.47	13.99	3.87	3.90	3.76
Ta	0.88	1.12	1.37	1.43	1.09	1.35	0.51
Pb	0.23	0,172	0.26	0.19	0.31	1.75	0.51
Th	0.18	0.20	0.36	0.15	0.14	0.51	0.27
U	0.03	0.06	0.13	0.09	0.03	0.17	0.01
Nb/Y	0.40	0.50	0.38	0.45	0.37	0.41	0.37
Nb/Ta	31.64	28.32	21.74	24.36	19.91	22.07	22.48
Zr/Hf	53.53	51.06	47.62	31.37	52.95	41.79	37.43

Note: values are in ppm.

Table 5 - LA-ICP-MS analyses of clinopyroxene of the sample B-5 (Boston Creek – Abitibi greenstone belt, Canada).

	Clinopyroxene						
Sc	85.83	72.81	72.96	72.92	71.91	80.84	81.41
Ti	3352.41	1817.09	1915.42	1865.50	1776.55	2272.76	2115.69
V	190.11	121.22	130.84	119.79	121.44	140.25	136.03
Cr	4820.50	4372.89	5468.48	5070.29	4794.27	4991.39	5775.25
Co	51.05	53.02	49.93	49.03	48.72	47.68	51.04
Ni	461.72	490.29	481.98	473.97	489.78	470.87	490.77
Zn	34.79	30.81	29.16	31.20	26.14	35.96	29.59
Rb	0.09	0.06	0.05	<0.046	<0.027	0.08	0.07
Sr	67.24	49.69	51.06	49.61	50.02	59.18	51.93
Y	5.87	2.92	2.97	2.90	2.82	3.54	3.51
Zr	9.11	2.77	3.12	2.92	2.75	5.05	3.88
Nb	0.02	0.02	0.08	0.02	0.03	0.03	0.03
Cs	0.01	0.02	0.01	0.04	0.02	0.01	0.02
Ba	0.03	0.40	0.43	0.50	0.09	0.04	0.03
La	1.35	0.66	0.79	0.66	0.48	0.83	0.75
Ce	5.04	2.09	2.10	2.17	1.99	3.14	2.53
Pr	0.79	0.33	0.45	0.40	0.39	0.58	0.40
Nd	4.88	2.33	2.29	2.14	2.30	3.27	2.23
Sm	1.60	0.54	0.75	0.97	0.60	1.25	0.42
Eu	0.49	0.25	0.29	0.27	0.19	0.41	0.29
Gd	2.02	0.85	0.75	0.60	0.79	1.17	0.58
Tb	0.21	0.15	0.17	0.16	0.12	0.18	0.16
Dy	1.64	0.64	0.96	0.62	0.89	0.95	0.38
Ho	0.22	0.15	0.14	0.15	0.13	0.19	0.14
Er	0.79	0.36	0.39	0.35	0.17	0.50	0.26
Tm	0.08	0.04	0.05	0.08	0.03	0.06	0.07
Yb	0.55	0.34	0.34	0.33	0.23	0.44	0.46
Lu	0.10	0.04	0.06	0.04	0.06	0.07	0.04
Hf	0.37	0.22	0.17	0.14	0.20	0.11	0.10
Ta	0.01	0.02	0.02	0.01	0.01	--	0.03
Pb	0.08	0.07	0.14	0.26	0.34	0.61	0.09
Th	0.03	0.04	0.02	0.02	0.02	0.03	0.02
U	0.03	0.02	--	0.02	0.02	0.02	0.03

Note: values are in ppm.

Table 6 - LA-ICP-MS analyses of amphibole of the sample B-5 (Boston Creek – Abitibi greenstone belt, Canada).

	Amphibole												
Sc	7.05	9.54	4.83	6.58	7.97	5.40	6.89	4.26	7.99	6.59	4.34	7.77	6.60
Ti	20015.86	23468.88	17976.27	19618.13	19566.96	19337.34	23025.78	16348.45	25299.42	22264.31	18173.96	21501.93	20172.46
V	212.94	283.40	194.35	228.98	264.39	210.44	267.10	147.16	305.68	264.71	179.35	257.87	204.44
Cr	21.37	35.38	14.95	18.70	59.87	27.55	11.67	11.37	24.18	23.71	23.80	32.10	21.14
Co	73.65	86.28	74.74	76.84	85.26	81.41	83.81	77.48	81.70	78.95	79.66	82.15	77.69
Ni	536.88	616.19	481.46	566.29	617.61	568.85	517.56	588.19	520.32	526.70	568.66	524.39	623.94
Zn	76.00	99.05	85.90	83.22	96.64	97.11	79.33	81.10	87.27	84.95	80.55	79.59	76.49
Rb	1.54	2.38	1.21	1.34	1.20	1.15	1.41	1.41	1.55	1.52	1.26	1.43	1.54
Sr	1031.47	1107.04	1019.26	979.25	1145.92	1268.98	1176.63	1026.94	1233.76	1180.85	1113.89	1098.69	1093.54
Y	77.96	90.41	91.30	76.27	97.92	96.53	87.22	75.98	102.24	102.36	82.57	86.53	89.52
Zr	181.87	229.87	176.55	191.98	343.98	290.76	206.06	214.19	250.52	226.35	258.23	190.86	225.09
Nb	57.78	70.30	60.61	67.88	93.98	82.16	63.11	74.38	70.84	66.05	76.69	64.06	74.87
Cs	0.08	0.09	0.02	0.06	0.04	<0.023	<0.0126	0.07	0.13	0.06	0.03	0.04	0.03
Ba	250.32	261.20	224.29	225.26	256.98	297.91	300.13	237.16	317.44	308.59	262.24	256.73	254.34
La	31.61	44.32	33.99	32.75	59.33	62.58	37.16	39.30	46.21	44.02	51.00	35.60	46.18
Ce	96.34	130.72	113.23	100.87	167.75	175.01	117.47	122.48	141.92	140.56	151.58	112.15	138.86
Pr	15.87	20.51	18.18	16.54	24.15	25.39	18.94	19.19	23.05	22.31	21.94	18.57	22.74
Nd	85.46	105.35	94.62	87.76	105.39	118.60	100.03	93.70	117.18	111.36	100.24	95.20	109.40
Sm	19.88	26.17	20.76	20.06	23.38	22.93	23.97	21.79	24.84	30.24	20.30	23.89	24.76
Eu	7.01	7.00	7.21	5.82	6.81	7.20	7.00	6.85	8.15	8.28	6.80	7.50	7.82
Gd	17.24	21.27	20.92	18.29	19.05	21.49	22.97	18.09	25.43	23.41	18.82	21.92	19.46
Tb	2.87	3.44	3.20	2.72	3.05	3.14	3.50	2.58	4.01	3.35	2.81	3.37	3.21
Dy	16.88	20.12	19.75	16.48	19.31	18.78	18.80	16.97	22.69	21.34	15.69	19.53	18.51
Ho	3.25	3.41	3.70	3.00	4.03	3.89	3.29	2.94	4.23	3.89	3.01	3.69	3.86
Er	7.96	8.97	9.93	7.26	10.50	9.72	8.03	8.01	9.96	9.60	8.21	8.97	9.19
Tm	1.09	1.18	1.30	0.98	1.46	1.12	1.15	0.96	1.37	1.42	1.18	1.33	1.38
Yb	6.72	7.22	7.39	6.12	9.88	8.24	6.89	6.68	8.03	8.32	7.80	7.44	7.92
Lu	0.89	1.04	1.02	0.83	1.25	1.25	0.95	0.88	1.02	1.04	1.05	0.89	1.18
Hf	5.04	7.30	5.90	6.75	9.92	9.58	6.59	6.27	8.71	5.83	7.61	5.47	6.06
Ta	3.27	4.07	2.98	3.53	4.56	5.06	3.69	3.97	4.13	3.43	3.93	3.71	3.80
Pb	0.70	0.64	0.12	0.24	0.62	3.36	0.16	0.31	0.45	0.41	0.26	0.29	0.58
Th	0.19	0.31	0.18	0.29	0.33	0.47	0.28	0.22	0.33	0.48	0.31	0.22	0.53
U	0.06	0.08	0.03	--	0.08	0.07	0.03	0.04	0.04	0.05	0.07	0.06	0.05
Nb/Y	0.74	0.78	0.66	0.89	0.96	0.85	0.72	0.98	0.69	0.65	0.93	0.74	0.84
Nb/Ta	17.67	17.27	20.34	19.23	20.61	16.24	17.10	18.74	17.15	19.26	19.51	17.27	19.70
Zr/Hf	36.09	31.49	29.92	28.44	34.68	30.35	31.27	34.16	28.76	38.83	33.93	34.89	37.14

Note: values are in ppm.

Table 7 - LA-ICP-MS analyses of olivine of the sample GR-1 (Ghost Range – Abitibi greenstone belt, Canada).

	Olivine		
Sc	8.76	8.20	6.38
Ti	99.43	146.86	73.35
V	7.29	6.96	4.41
Cr	90.84	100.84	121.20
Co	197.93	191.99	198.19
Ni	2050.84	1966.04	2060.95
Zn	139.94	120.45	105.92
Sr	0.03	0.06	--
Y	0.34	0.38	0.10
Zr	0.18	0.42	0.09

Note: values are in ppm.

Table 8 - LA-ICP-MS analyses of olivine of the sample GR-2 (Ghost Range – Abitibi greenstone belt, Canada).

	Olivine						
Sc	5.45	6.78	6.44	6.55	7.23	7.20	6.39
Ti	138.43	126.99	93.75	63.06	79.17	54.12	76.67
V	5.12	5.52	4.78	5.10	6.40	6.10	4.99
Cr	71.88	99.44	93.26	120.79	83.75	126.13	89.85
Co	199.10	193.06	193.63	196.95	199.75	195.53	191.33
Ni	1969.01	1845.24	1894.93	1883.78	1934.37	1859.51	1872.29
Zn	119.91	120.99	117.00	124.82	123.30	125.59	111.47
Sr	--	0.06	0.06	--	--	--	--
Y	0.45	0.35	0.09	0.14	0.15	0.39	0.38
Zr	0.36	0.07	--	0.04	--	0.09	0.09

Note: values are in ppm.

Table 9 - LA-ICP-MS analyses of clinopyroxene of the samples GR-1 and GR-2 (Ghost Range – Abitibi greenstone belt, Canada).

	Clinopyroxene (GR-1)				*Clinopyroxene (GR-2)*					
Sc	79.16	82.90	81.02	77.91	71.67	70.29	77.61	31.83	31.38	79.32
Ti	1300.54	1505.24	1297.06	1273.92	1457	1418	1505	1659	1437	1508
V	250.56	274.17	244.80	260.27	241.46	237.50	252.95	109.86	112.06	262.57
Cr	7916.69	8005.68	8605.17	8533.74	7171.48	6655.76	7316.40	2097.21	2043.62	7949.35
Co	43.99	42.67	43.41	43.48	47.55	44.71	49.26	74.36	71.25	46.43
Ni	380.72	361.80	365.77	366.84	334.89	328.64	364.34	436.30	424.39	489.76
Zn	30.15	30.06	30.33	23.69	26.96	27.15	31.53	74.72	75.10	32.82
Rb	0.05	0.03	0.07	0.07	0.08	0.08	0.17	0.06	0.03	0.05
Sr		8.34	8.15	7.39	9.03	8.15	8.39	0.06	0.05	8.85
Y	6.79	7.63	6.42	6.52	8.36	7.02	8.07	3.12	3.27	7.71
Zr	3.92	5.43	3.84	3.46	4.92	4.21	4.25	1.44	2.14	4.99
Nb	--	0.03	0.01	0.04	0.04	0.03	0.02	0.02	--	--
Cs	--	0.02	0.02	--	0.03	0.03	0.09	0.02	--	--
Ba	0.04	0.03	0.02	0.05	0.69	0.03	0.24	--	0.03	0.14
La	0.13	0.29	0.12	0.25	0.33	0.31	0.22	0.04	--	0.32
Ce	0.61	0.98	0.86	1.04	1.32	0.86	1.13	0.04	0.03	1.07
Pr	0.10	0.18	0.19	0.18	0.33	0.14	0.21	--	0.05	0.24
Nd	1.14	1.46	1.31	1.53	1.40	2.21	1.73	0.22	--	1.44
Sm	0.52	0.38	0.54	0.83	0.96	0.66	0.75	0.27	0.19	0.73
Eu	0.23	0.28	0.31	0.25	0.29	0.19	0.26	0.04	0.03	0.23
Gd	1.27	0.91	0.87	0.71	1.41	0.68	1.60	0.21	0.26	1.47
Tb	0.14	0.24	0.11	0.20	0.37	0.24	0.21	0.03	0.03	0.21
Dy	1.30	1.35	1.50	1.24	1.03	1.38	0.93	0.41	0.66	1.67
Ho	0.28	0.30	0.28	0.23	0.36	0.23	0.36	0.15	0.05	0.36
Er	0.67	0.78	0.78	0.93	0.96	1.01	1.16	0.62	0.40	0.71
Tm	0.12	0.14	0.12	0.12	0.14	0.09	0.14	0.11	0.08	0.08
Yb	0.92	0.22	0.49	0.76	0.67	0.80	0.83	0.37	0.41	0.67
Lu	0.10	0.12	0.11	0.10	0.14	0.09	0.17	0.14	0.09	0.09
Hf	0.27	0.36	0.11	0.17	0.26	0.10	0.23	--	0.11	0.36
Ta	--	0.01	0.04	0.03	0.02	0.02	--	--	--	0.01
Pb	0.08	0.19	0.21	0.14	0.09	0.11	0.16	0.06	0.14	0.09
Th	--	0.02	--	0.01	0.03	0.02	0.02	0.02	--	0.03
U	--	0.01	--	0.04	0.03	0.01	0.02	--	0.02	0.03

Note: values are in ppm.

Table 10 - LA-ICP-MS analyses of brown amphibole of the sample GR-1 (Ghost Range – Abitibi greenstone belt, Canada).

	Amphibole					
Sc	100.80	106.81	101.60	103.73	54.28	44.52
Ti	19739.33	21423.86	20072.66	19431.14	24643.30	24661.30
V	845.94	822.73	817.01	843.52	750.17	733.22
Cr	9331.74	9273.94	9337.76	9376.76	7148.29	8677.55
Co	57.04	54.27	51.66	55.28	55.21	58.48
Ni	614.47	572.62	589.32	569.48	563.60	590.29
Zn	47.04	60.54	61.85	54.77	36.89	36.82
Rb	2.35	2.68	2.84	2.98	2.61	2.60
Sr	22.53	21.22	23.62	23.94	23.87	26.17
Y	133.05	146.65	140.84	124.23	60.28	46.06
Zr	704.83	628.96	697.79	732.47	1011.30	890.15
Nb	21.05	28.87	29.88	19.35	35.06	41.60
Cs	0.02	--	0.09	0.09	--	0.04
Ba	47.88	52.09	50.28	61.15	26.33	29.33
La	22.74	28.46	26.87	25.07	27.00	23.84
Ce	83.45	97.10	92.25	84.28	79.12	70.71
Pr	12.75	14.22	14.32	13.35	10.26	9.15
Nd	69.04	75.80	74.33	63.57	44.52	39.28
Sm	17.55	22.75	21.31	16.47	9.18	8.26
Eu	3.91	4.86	4.06	4.07	3.80	2.91
Gd	21.14	24.13	21.93	17.91	7.80	6.30
Tb	3.15	4.22	3.71	3.22	1.42	1.11
Dy	22.47	28.18	22.70	20.05	9.83	7.10
Ho	4.54	5.54	5.21	4.29	2.39	1.86
Er	14.27	17.24	13.97	14.46	6.97	5.25
Tm	1.91	2.03	1.91	1.92	1.18	0.94
Yb	14.03	16.59	12.27	13.06	7.97	6.24
Lu	1.62	1.52	1.33	1.39	1.16	0.76
Hf	23.44	19.21	19.63	22.57	30.06	25.63
Ta	1.27	1.54	2.07	1.30	1.59	2.08
Pb	1.70	2.22	1.71	1.74	1.08	1.01
Th	2.82	3.79	3.24	2.48	3.16	2.57
U	0.29	0.51	0.27	0.29	0.28	0.31
Nb/Y	0.16	0.20	0.21	0.16	0.58	0.90
Nb/Ta	16.54	18.75	14.43	14.94	22.09	20.03
Zr/Hf	30.07	32.74	35.55	32.45	33.64	34.73

Note: values are in ppm.

Table 11 - LA-ICP-MS analyses of amphibole of the sample GR-2 (Ghost Range – Abitibi greenstone belt, Canada).

	Amphibole					
Sc	88.58	89.12	76.42	85.44	84.71	78.55
Ti	24034.34	24361.19	23147.20	23479.76	24206.82	23683.64
V	773.35	763.98	734.56	720.61	751.55	769.21
Cr	9589.77	9429.52	8812.74	9703.70	9644.15	10225.96
Co	58.38	56.61	55.06	57.22	58.53	58.15
Ni	617.24	615.25	619.36	614.28	614.08	586.80
Zn	36.77	33.75	39.08	41.15	40.02	37.04
Rb	2.00	1.68	1.31	2.44	2.09	3.06
Sr	19.42	22.53	27.24	14.50	14.71	15.02
Y	110.49	142.87	149.34	92.81	95.25	69.60
Zr	708.77	745.49	904.45	611.99	811.92	567.39
Nb	47.38	44.85	38.01	39.94	36.95	39.90
Cs	0.04	0.03	--	0.01	--	--
Ba	131.41	134.59	123.98	136.24	124.52	84.58
La	26.58	25.13	20.90	31.17	31.08	29.25
Ce	90.92	93.48	78.68	84.80	87.17	81.66
Pr	14.29	16.35	14.11	11.07	11.45	10.92
Nd	66.91	89.90	79.68	45.51	48.89	44.77
Sm	18.19	26.21	26.80	11.89	15.11	12.46
Eu	4.21	6.21	6.12	2.46	2.52	2.75
Gd	17.36	27.17	28.12	13.21	13.97	11.73
Tb	3.41	4.36	4.69	2.49	2.54	2.13
Dy	19.71	28.40	28.44	15.50	17.40	11.81
Ho	4.01	5.58	5.40	3.26	3.63	2.68
Er	11.21	13.26	14.89	8.54	9.06	6.74
Tm	1.52	1.79	1.98	1.10	1.25	1.06
Yb	9.95	10.63	11.22	7.36	7.55	6.20
Lu	1.09	1.28	1.37	0.78	0.99	0.80
Hf	27.35	32.77	32.15	16.28	21.87	13.49
Ta	3.67	3.77	2.97	2.16	1.76	1.40
Pb	0.56	0.73	0.72	0.34	0.65	0.74
Th	1.64	1.04	0.56	0.61	1.02	2.16
U	0.02	0.06	0.03	0.10	0.03	0.12
Nb/Y	0.43	0.31	0.25	0.43	0.39	0.57
Nb/Ta	12.91	11.90	12.80	18.49	21.01	28.48
Zr/Hf	25.91	22.75	28.13	37.59	37.12	42.06

Note: values are in ppm.

Table 12 - LA-ICP-MS analyses of olivine of the sample Pilg 8 38 (Pilgüjarvi sill – Pechenga Complex. Russia).

	Olivine			
Sc	3.62	3.93	3.02	5.19
Ti	203.96	184.96	236.40	173.53
V	4.73	4.65	5.88	5.47
Cr	65.74	66.67	88.12	79.05
Co	194.67	191.70	195.93	193.95
Ni	1264.80	1238.97	1264.71	1260.41
Zn	220.00	205.97	186.86	186.58
Sr	0.01	0.05	0.04	0.04
Y	0.39	0.51	0.35	0.46
Zr	0.24	0.16	0.36	0.11

Table 13 - LA-ICP-MS analyses of clinopyroxene of the sample Pilg 8 38 (Pilgüjarvi sill – Pechenga Complex. Russia).

	Clinopyroxene
Sc	95.82
Ti	10662.84
V	282.99
Cr	3506.47
Co	33.59
Ni	176.79
Zn	32.28
Rb	0.02
Sr	82.43
Y	44.94
Zr	131.56
Nb	0.65
Cs	--
Ba	0.14
La	8.61
Ce	34.64
Pr	6.78
Nd	42.39
Sm	14.07
Eu	4.26
Gd	14.63
Tb	2.15
Dy	11.75
Ho	2.09
Er	4.63
Tm	0.53
Yb	2.71
Lu	0.32
Hf	6.23
Ta	0.11
Pb	0.21
Th	0.07
U	0.01

Note: values are in ppm.

Table 14 - LA-ICP-MS analyses of amphibole of the sample Pilg 8 38 (Pilgüjarvi sill – Pechenga Complex, Russia).

	Amphibole					
Sc	58.86	69.65	63.18	56.68	52.92	77.11
Ti	29933.59	31558.12	35519.10	31219.04	29323.97	31399.33
V	505.29	520.83	624.18	515.70	463.48	470.30
Cr	3629.75	3204.75	3486.14	2840.61	2125.38	2059.88
Co	54.38	61.60	63.75	54.35	53.66	56.25
Ni	357.19	405.33	436.87	389.27	353.86	359.96
Zn	66.99	63.53	88.13	87.66	71.75	72.02
Rb	3.52	4.28	5.06	3.86	3.84	3.72
Sr	353.10	397.60	339.20	352.10	474.36	476.06
Y	103.58	123.42	90.01	93.04	93.23	105.85
Zr	358.29	351.39	394.43	369.61	272.88	311.92
Nb	86.09	86.43	93.23	90.66	73.05	70.64
Cs	--	0.07	0.07	0.02	--	0.01
Ba	420.20	413.57	410.79	388.55	406.07	409.95
La	48.32	45.23	51.29	45.58	32.36	34.34
Ce	156.56	155.44	165.58	143.05	112.79	122.54
Pr	25.14	26.20	24.09	22.76	19.20	21.92
Nd	127.11	147.33	121.98	115.95	110.28	120.89
Sm	32.37	36.54	28.02	30.69	31.44	35.09
Eu	8.44	11.12	8.29	8.47	9.64	10.48
Gd	29.65	37.38	23.09	27.52	28.57	32.96
Tb	4.51	6.41	3.47	4.04	4.30	5.28
Dy	25.29	31.36	18.57	22.75	23.05	26.91
Ho	4.38	5.24	3.82	4.15	3.98	4.70
Er	10.10	11.54	7.91	8.76	8.98	10.41
Tm	1.10	1.33	1.29	1.00	1.06	1.07
Yb	6.59	7.11	6.38	5.68	5.92	6.29
Lu	0.74	0.81	0.84	0.63	0.61	0.67
Hf	12.79	13.72	13.39	12.85	10.85	12.30
Ta	4.08	3.73	4.18	4.13	3.38	3.20
Pb	2.95	2.76	3.36	4.80	2.43	2.37
Th	0.29	0.27	0.30	0.31	0.20	0.22
U	0.09	0.09	--	0.06	0.04	0.05
Nb/Y	0.83	0.70	1.04	0.97	0.78	0.67
Nb/Ta	21.10	23.17	22.30	21.95	21.61	22.08
Zr/Hf	28.01	25.61	29.46	28.76	25.15	25.36

Note: values are in ppm.

Table 15 - LA-ICP-MS analyses of olivine of the sample 106-44 (Pilgüjarvi sill – Pechenga Complex. Russia).

	Olivine		
Sc	4.36	4.42	6.00
Ti	163.51	168.26	149.51
V	7.05	7.16	9.06
Cr	66.72	100.81	186.64
Co	198.12	192.81	195.27
Ni	1818.18	1760.46	1973.24
Zn	161.70	160.35	142.24
Sr	0.04	0.02	0.02
Y	0.24	0.36	0.24
Zr	0.10	0.06	0.05

Note: values are in ppm.

Table 16 - LA-ICP-MS analyses of clinopyroxene of the sample 106-44 (Pilgüjarvi sill – Pechenga Complex. Russia).

	Clinopyroxene				
Sc	94.17	100.13	85.20	93.12	93.75
Ti	18786.55	17524.74	12490.49	13223.77	14387.98
V	408.32	416.56	355.49	373.32	366.06
Cr	4546.04	5236.40	4414.61	4687.98	4178.20
Co	31.69	32.34	33.54	33.10	32.71
Ni	224.59	246.83	249.08	246.62	286.01
Zn	30.91	38.62	27.73	29.93	29.24
Rb	--	0.14	--	0.11	0.04
Sr	93.34	89.84	83.99	84.99	99.75
Y	41.26	35.18	30.04	29.61	41.39
Zr	183.70	159.23	94.19	109.97	158.27
Nb	0.75	0.58	0.26	0.52	0.65
Cs	0.02	--	--	0.03	--
Ba	0.41	0.71	0.16	0.59	0.43
La	7.99	7.68	6.01	6.21	8.82
Ce	32.27	28.61	23.20	24.08	33.39
Pr	6.12	5.72	4.45	4.30	6.49
Nd	39.29	33.32	27.28	28.96	40.71
Sm	12.06	11.38	9.95	7.51	13.38
Eu	4.14	3.61	2.83	3.03	3.95
Gd	14.48	12.01	10.42	9.30	12.56
Tb	2.09	1.56	1.56	1.54	2.11
Dy	10.47	9.79	7.93	7.23	10.91
Ho	2.09	1.66	1.34	1.27	1.92
Er	3.52	3.30	2.95	3.15	3.98
Tm	0.46	0.38	0.38	0.30	0.50
Yb	2.91	2.10	2.36	2.00	2.74
Lu	0.45	0.33	0.27	0.30	0.35
Hf	9.28	6.37	4.04	5.47	7.66
Ta	0.27	0.15	0.06	0.08	0.16
Pb	0.18	0.57	--	0.34	0.18
Th	0.05	0.07	0.06	0.14	0.10
U	0.02	0.01	0.02	0.02	0.01

Table 17 - LA-ICP-MS analyses of amphibole of the sample 106-44 (Pilgüjarvi sill – Pechenga Complex. Russia).

	Amphibole				
Sc	46.72	41.54	43.50	30.51	53.44
Ti	30477.51	30370.63	31499.53	30980.21	32813.41
V	422.82	453.90	437.46	478.33	540.52
Cr	1061.42	1851.94	2702.99	3061.43	4246.57
Co	51.61	52.56	52.61	54.19	53.70
Ni	472.26	496.27	483.42	504.63	660.75
Zn	45.51	42.37	43.92	73.13	41.31
Rb	1.74	2.39	2.55	2.25	2.18
Sr	816.11	790.86	808.40	764.33	771.63
Y	65.53	66.98	68.97	55.26	64.93
Zr	171.44	189.47	204.01	181.96	227.50
Nb	51.79	54.60	48.30	52.07	55.57
Cs	--	0.01	--	--	--
Ba	277.85	294.79	300.50	278.56	282.06
La	17.47	19.97	19.40	18.43	26.44
Ce	62.98	74.26	70.49	67.68	91.25
Pr	12.38	13.22	12.98	11.86	15.90
Nd	69.88	75.34	75.74	67.26	80.71
Sm	21.48	23.30	23.32	19.34	21.88
Eu	7.14	6.96	7.50	7.39	7.38
Gd	22.77	20.36	20.33	19.88	18.38
Tb	2.97	3.38	3.15	2.59	3.02
Dy	15.92	15.76	17.19	13.61	15.38
Ho	3.14	2.99	3.09	2.25	2.66
Er	6.90	6.67	6.39	5.64	6.96
Tm	0.76	0.82	0.81	0.63	0.69
Yb	4.26	4.91	4.75	3.51	3.98
Lu	0.43	0.57	0.59	0.42	0.49
Hf	7.12	7.32	7.51	6.55	8.29
Ta	2.53	2.91	2.71	2.61	2.72
Pb	0.47	0.39	0.40	0.79	0.70
Th	0.13	0.18	0.30	0.11	0.20
U	0.02	0.05	0.06	0.01	0.03
Nb/Y	0.79	0.82	0.70	0.94	0.86
Nb/Ta	20.47	18.76	17.82	19.95	20.43
Zr/Hf	24.08	25.88	27.17	27.78	27.44

Note: values are in ppm.

Table 18 - LA-ICP-MS analyses of clinopyroxene of the sample 116-6 (Pilgüjarvi sill – Pechenga Complex, Russia).

	Clinopyroxene		
Sc	100.93	105.85	107.38
Ti	7468.09	6963.48	7550.43
V	396.72	395.15	408.42
Cr	8.11	16.07	16.18
Co	54.20	53.84	53.58
Ni	113.99	122.23	108.45
Zn	34.83	37.87	36.48
Rb	0.06	0.07	0.02
Sr	50.54	53.44	54.17
Y	13.37	14.67	14.52
Zr	31.80	35.71	35.15
Nb	0.09	0.20	0.07
Cs	--	0.04	0.01
Ba	0.43	0.90	0.16
La	2.22	3.01	2.61
Ce	9.06	11.30	9.17
Pr	1.79	2.21	1.73
Nd	10.71	12.28	11.73
Sm	3.54	4.37	3.72
Eu	1.34	1.47	1.43
Gd	4.08	4.19	4.23
Tb	0.64	0.76	0.60
Dy	3.09	3.53	3.78
Ho	0.62	0.65	0.63
Er	1.45	1.61	1.27
Tm	0.16	0.17	0.18
Yb	1.03	1.23	1.06
Lu	0.11	0.13	0.13
Hf	1.45	1.54	2.08
Ta	0.01	0.01	0.01
Pb	0.20	0.20	0.07
Th	0.02	0.08	0.03
U	0.01	0.01	--

Table 19 - LA-ICP-MS analyses of brown amphibole of the sample 116-6 (Pilgüjarvi sill - Pechenga Complex, Russia).

	Amphibole				
Sc	106.92	115.73	104.33	128.44	122.83
Ti	26686.27	31702.12	34051.51	29429.79	30930.11
V	702.49	855.96	975.93	814.78	828.31
Cr	12.13	24.52	22.36	22.35	13.55
Co	167.11	73.27	75.99	69.21	70.64
Ni	204.51	227.57	260.40	188.11	201.86
Zn	46.81	48.93	47.91	46.25	46.61
Rb	5.33	5.74	6.70	5.61	5.33
Sr	109.38	119.15	129.96	116.17	129.81
Y	49.98	26.50	50.06	67.67	59.40
Zr	166.22	191.58	204.36	191.33	183.09
Nb	25.67	24.70	31.21	24.77	24.63
Cs	<0,0076	0.07	0.37	0.04	0.07
Ba	334.24	427.86	384.81	355.66	401.03
La	35.95	36.16	42.66	45.77	42.50
Ce	99.57	73.95	111.16	134.47	124.27
Pr	12.90	7.69	14.28	19.59	17.60
Nd	60.72	29.36	62.02	88.18	81.42
Sm	13.44	5.98	14.24	21.47	18.59
Eu	4.66	2.94	4.37	5.60	5.07
Gd	14.41	6.05	12.92	18.44	16.49
Tb	2.22	1.04	1.96	2.67	2.53
Dy	11.87	5.95	11.03	15.68	13.10
Ho	2.14	1.17	2.15	2.94	2.60
Er	4.72	3.44	5.41	6.55	5.92
Tm	0.62	0.46	0.65	0.79	0.69
Yb	3.74	2.98	3.80	4.29	4.43
Lu	0.49	0.40	0.50	0.58	0.53
Hf	5.03	5.86	6.38	6.28	6.34
Ta	1.05	1.04	1.34	1.03	1.25
Pb	1.78	2.70	2.27	1.99	1.82
Th	0.48	1.09	2.22	0.72	0.43
U	0.11	0.26	0.44	0.10	0.07
Nb/Y	0.51	0.93	0.62	0.37	0.41
Nb/Ta	24.56	23.73	23.22	24.10	19.77
Zr/Hf	33.05	32.69	32.03	30.47	28.88

Note: values are in ppm.

Table 20 - LA-ICP-MS analyses of olivine of the sample 57-HV-28 (Kammikivi sill – Pechenga Complex, Russia).

	Olivine					
Sc	5.28	6.31	4.96	6.31	5.54	5.88
Ti	177.07	163.14	153.44	201.32	176.50	182.92
V	8.71	10.53	6.57	8.40	8.45	7.85
Cr	183.49	253.63	140.81	172.23	175.71	166.71
Co	196.22	196.85	200.44	197.80	200.02	196.89
Ni	2825.50	2892.00	2764.47	2829.88	2856.80	2834.49
Zn	200.95	181.61	175.20	176.41	172.88	171.52
Sr	0.07	0.04	0.02	0.02	--	0.01
Y	0.22	0.29	0.31	0.20	0.26	0.13
Zr	0.09	0.04	0.08	0.08	0.04	0.03

Note: values are in ppm.

Table 21 - LA-ICP-MS analyses of clinopyroxene of the sample 57-HV-28 (Kammikivi sill – Pechenga Complex, Russia).

	Clinopyroxene		
Sc	87.83	92.23	71.38
Ti	8763.76	13954.24	12523.81
V	308.36	372.25	299.46
Cr	5253.37	5048.49	2282.69
Co	36.52	35.51	33.13
Ni	435.35	402.02	373.87
Zn	36.45	31.43	30.47
Rb	0.35	0.29	<0.111
Sr	63.11	76.45	80.90
Y	15.76	32.10	34.85
Zr	37.57	94.82	102.10
Nb	0.14	0.60	0.37
Cs	--	0.11	--
Ba	--	0.49	0.15
La	2.91	6.14	5.73
Ce	10.07	21.73	24.66
Pr	1.80	3.78	4.90
Nd	9.84	25.74	32.34
Sm	4.34	10.18	8.97
Eu	1.26	3.81	3.70
Gd	5.34	9.30	9.74
Tb	0.67	1.89	1.79
Dy	1.88	9.05	8.30
Ho	0.47	1.37	1.53
Er	1.28	2.56	3.49
Tm	0.20	0.28	0.31
Yb	1.62	2.94	2.85
Lu	0.29	0.30	0.28
Hf	2.55	4.89	4.91
Ta	0.03	0.05	0.08
Pb	0.20	0.19	0.14
Th	0.03	0.03	0.10
U	--	0.03	0.05

Table 22 - LA-ICP-MS analyses of brown amphibole of the sample 57-HV-28 (Kammikivi sill – Pechenga Complex, Russia).

	Amphibole							
Sc	58.50	48.04	53.26	62.43	86.20	75.50	77.16	23.13
Ti	30524.73	31299.99	29610.83	29826.76	35685.33	30915.02	32049.27	31437.35
V	535.16	558.02	499.83	598.66	578.91	490.14	551.96	542.25
Cr	3656.04	1819.84	1988.25	3474.21	4033.79	2758.32	1287.82	1648.34
Co	48.12	52.58	50.30	59.27	54.33	53.94	47.76	52.08
Ni	671.92	715.57	694.75	815.50	804.07	680.37	742.65	705.25
Zn	39.22	42.82	63.34	47.02	38.42	48.45	38.34	48.27
Rb	2.81	3.58	3.16	3.81	3.99	2.66	3.52	3.88
Sr	297.47	278.72	274.64	292.23	336.08	320.10	270.04	196.22
Y	114.69	106.96	97.84	70.57	107.37	85.05	159.23	58.06
Zr	302.20	360.64	270.04	266.83	302.91	222.20	387.04	426.75
Nb	73.13	83.13	87.73	75.24	63.96	61.15	88.06	97.46
Cs	0.08	--	0.13	0.18	0.10	0.19	--	--
Ba	421.66	454.90	391.98	392.09	429.50	356.99	486.41	437.74
La	45.40	54.71	36.35	30.13	45.24	26.93	64.33	47.50
Ce	153.94	173.76	120.27	100.75	138.67	94.55	205.45	139.97
Pr	25.53	25.86	20.32	16.84	24.53	16.32	35.42	19.25
Nd	131.61	142.90	112.76	73.46	137.68	90.55	178.75	87.16
Sm	36.88	33.23	34.18	18.92	33.48	24.77	54.11	22.90
Eu	9.99	10.07	8.47	8.00	8.75	7.25	13.89	8.26
Gd	26.99	35.40	30.32	19.48	33.22	20.78	46.96	15.16
Tb	5.56	4.37	4.17	2.53	3.99	3.93	7.56	3.35
Dy	25.08	29.22	21.43	17.40	23.42	21.23	39.88	14.81
Ho	4.78	4.81	4.01	3.51	4.70	3.27	8.30	3.18
Er	10.36	9.80	7.80	6.89	9.51	8.77	17.91	6.22
Tm	1.64	1.37	0.83	0.84	0.78	1.03	2.29	0.95
Yb	5.93	6.11	5.98	4.11	6.12	5.25	10.19	4.10
Lu	0.92	0.82	0.61	0.68	0.83	0.69	1.32	0.63
Hf	11.48	12.00	10.91	10.22	11.50	8.09	14.19	15.13
Ta	2.97	3.57	3.94	3.47	3.04	2.75	3.52	3.79
Pb	0.34	--	0.26	0.39	0.71	1.02	0.47	0.36
Th	0.20	0.39	0.25	0.33	0.46	0.20	0.30	0.48
U	0.09	--	--	--	--	0.08	--	0.08
Nb/Y	0.64	0.78	0.90	1.07	0.60	0.72	0.55	1.68
Nb/Ta	24.62	23.29	22.27	21.68	21.04	22.24	25.02	25.72
Zr/Hf	26.32	30.05	24.75	26.11	26.34	27.47	27.28	28.21

Note: values are in ppm.

Table 23 - LA-ICP-MS analyses of olivine of the sample N-2 (Nyasyukka dike complex – Pechenga Complex, Russia)

	Olivine		
Sc	5.03	5.02	5.59
Ti	170.04	161.68	134.85
V	5.07	4.66	7.03
Cr	45.35	40.34	92.90
Co	224.86	226.66	223.61
Ni	1651.82	1698.55	1824.88
Zn	330.88	320.67	277.39
Sr	--	--	0.09
Y	0.26	0.31	0.43
Zr	0.14	0.25	0.27

Note: values are in ppm.

Table 24 - LA-ICP-MS analyses of brown amphibole of the sample N-2 (Nyasyukka dike complex - Pechenga Complex, Russia)

	Amphibole				
Sc	56.21	57.54	53.92	55.52	61.60
Ti	26940.75	26552.16	26055.81	26084.04	26927.17
V	539.76	531.57	521.69	541.70	538.20
Cr	1776.37	2385.39	2305.93	2742.86	1441.65
Co	97.15	57.67	60.55	60.86	55.93
Ni	498.47	515.43	510.70	522.95	488.76
Zn	63.85	74.40	66.96	70.94	64.76
Rb	3.97	3.32	3.64	3.63	3.92
Sr	560.20	525.04	515.31	540.81	582.61
Y	56.33	54.13	54.07	55.93	63.93
Zr	222.74	236.10	221.73	244.62	202.96
Nb	53.54	60.26	56.27	58.91	47.75
Cs	0.03	0.02	--	--	--
Ba	317.56	287.64	279.35	311.78	312.35
La	27.85	30.42	26.74	31.43	24.88
Ce	94.22	99.11	91.96	102.10	88.08
Pr	15.29	15.94	14.43	16.57	15.29
Nd	78.37	80.42	72.70	81.51	86.18
Sm	20.90	18.42	18.93	18.70	24.06
Eu	5.72	5.69	5.32	6.09	6.60
Gd	17.05	14.26	14.97	15.07	20.27
Tb	2.50	2.17	2.05	2.15	3.07
Dy	12.52	11.42	11.58	13.23	16.06
Ho	2.58	2.18	2.02	2.38	2.81
Er	5.25	5.38	5.12	5.57	5.81
Tm	0.76	0.71	0.68	0.66	0.70
Yb	4.70	4.63	3.65	3.82	4.54
Lu	0.57	0.61	0.40	0.58	0.62
Hf	8.77	8.62	8.07	8.25	7.43
Ta	2.74	2.84	2.53	2.59	2.23
Pb	0.65	0.86	0.63	0.54	0.63
Th	0.26	0.23	0.15	0.21	0.18
U	0.03	0.02	0.02	0.06	--
Nb/Y	0.95	1.11	1.04	1.05	0.75
Nb/Ta	19.54	21.22	22.24	22.75	21.41
Zr/Hf	25.40	27.39	27.48	29.65	27.32

Table 25 - LA-ICP-MS analyses of amphibole of the sample N-3 (Nyasyukka dike complex – Pechenga Complex, Russia). From Fiorentini et al. (2008)

	Amphibole								
Sc	69.11	70.62	66.07	65.40	62.52	64.44	68.37	65.80	64.90
Ti	--	--	--	--	--	--	--	--	--
V	571.10	578.93	562.43	551.03	558.73	550.40	571.27	557.75	558.14
Cr	1049.37	1003.00	804.67	1094.27	907.83	985.10	1107.45	877.06	697.45
Co	59.52	58.74	56.52	58.06	57.68	56.34	58.60	58.22	55.93
Ni	421.10	418.34	403.28	422.10	413.71	403.60	419.92	409.35	403.00
Zn	--	--	--	--	--	--	--	--	--
Rb	3.68	3.67	3.73	3.75	3.59	3.65	3.96	3.61	3.67
Sr	457.10	479.19	468.08	518.47	586.14	517.13	553.72	585.18	564.68
Y	37.90	43.12	41.65	46.68	56.87	51.13	49.53	57.09	58.79
Zr	276.46	280.42	271.03	245.32	223.78	238.44	251.26	245.95	235.47
Nb	57.68	58.98	57.37	58.51	56.79	57.48	56.58	57.05	54.35
Cs	--	--	--	--	--	--	--	--	--
Ba	317.00	325.53	326.63	329.84	318.68	304.86	353.92	363.75	337.59
La	36.41	35.47	35.35	31.97	25.72	29.70	32.20	30.18	27.64
Ce	104.75	105.49	104.87	101.39	88.82	97.12	101.61	100.08	93.92
Pr	15.03	16.25	16.11	15.96	14.93	16.22	17.02	17.61	16.49
Nd	62.46	67.45	68.62	74.79	73.55	78.32	78.41	86.78	82.12
Sm	12.77	13.53	13.41	15.15	18.59	17.74	16.86	18.99	19.13
Eu	3.59	4.03	4.06	4.43	5.24	5.20	4.83	5.81	5.67
Gd	10.15	11.25	11.17	12.55	14.89	14.31	14.18	16.99	16.66
Tb	1.40	1.66	1.68	1.82	2.17	2.07	1.89	2.28	2.34
Dy	8.17	9.52	8.80	10.31	12.05	11.68	11.90	13.13	14.00
Ho	1.51	1.75	1.63	1.90	2.38	2.10	2.01	2.45	2.50
Er	3.90	4.50	4.21	4.76	4.98	4.82	4.90	6.42	5.94
Tm	0.50	0.57	0.56	0.68	0.71	0.55	0.61	0.69	0.74
Yb	3.19	3.65	3.47	3.71	4.16	4.10	4.41	4.05	4.03
Lu	0.50	0.49	0.47	0.50	0.58	0.48	0.49	0.57	0.60
Hf	8.96	9.70	8.96	8.45	7.23	8.34	8.46	8.85	8.79
Ta	3.26	3.31	3.10	2.92	2.70	2.90	2.96	2.83	3.13
Pb	--	--	--	--	--	--	--	--	--
Th	0.30	0.27	0.28	0.26	0.19	0.22	0.24	0.25	0.27
U	0.05	0.05	0.04	0.04	0.04	0.04	--	0.04	0.04
Nb/Y	1.52	1.37	1.38	1.25	1.00	1.12	1.14	1.00	0.92
Nb/Ta	17.69	17.82	18.51	20.04	21.03	19.82	19.11	20.16	17.36
Zr/Hf	30.85	28.91	30.25	29.03	30.95	28.59	29.70	27.79	26.79

Note: values are in ppm.

Table 26 - LA-ICP-MS analyses of clinopyroxene and amphibole of the sample TT329 (Husky Ridge – Antarctica). Data from Tiepolo and Tribuzio(2008).

	Clinopyroxene			*Amphibole*	
Sc	91.30	81.30	**Sc**	65.00	61.10
Ti	1038.00	999.00	**Ti**	9479.00	9339.00
V	214.40	217.20	**V**	505.00	460.00
Cr	1992.00	1128.00	**Cr**	573.00	591.00
Co	48.10	48.30	**Co**	61.30	58.80
Ni	--	--	**Ni**	422.00	402.00
Zn	--	--	**Zn**	70.50	77.50
Rb	0.06	0.13	**Rb**	1.37	1.41
Sr	24.90	25.50	**Sr**	57.30	43.30
Y	3.46	4.34	**Y**	16.70	17.40
Zr	6.15	8.76	**Zr**	14.80	13.60
Nb	0.04	0.06	**Nb**	1.28	1.69
Cs	--	--	**Cs**	0.02	0.04
Ba	0.68	0.74	**Ba**	15.33	13.56
La	0.50	0.44	**La**	2.20	3.17
Ce	1.69	1.41	**Ce**	7.98	9.02
Pr	0.30	0.32	**Pr**	1.26	1.56
Nd	2.05	2.02	**Nd**	8.05	7.40
Sm	0.59	0.59	**Sm**	2.88	2.96
Eu	0.20	0.20	**Eu**	0.84	0.87
Gd	0.81	0.91	**Gd**	2.82	3.07
Tb	0.12	0.18	**Tb**	0.50	0.62
Dy	0.89	0.95	**Dy**	3.16	3.74
Ho	0.17	0.23	**Ho**	0.79	0.81
Er	0.41	0.61	**Er**	1.73	1.95
Tm	0.07	0.07	**Tm**	0.27	0.22
Yb	0.38	0.53	**Yb**	1.69	1.86
Lu	0.06	0.07	**Lu**	0.23	0.23
Hf	0.41	0.46	**Hf**	0.93	0.95
Ta	0.00	0.00	**Ta**	0.08	0.09
Pb	0.78	0.74	**Pb**	3.70	3.82
Th	0.14	0.15	**Th**	0.11	0.11
U	0.05	0.08	**U**	0.18	0.12
			Nb/Y	0.08	0.10
			Nb/Ta	15.80	19.44
			Zr/Hf	15.90	14.32

Note: values are in ppm.

Table 27 - LA-ICP-MS analyses of olivine, clinopyroxene and amphibole of the sample AL89 (Sanandaj Sirjan Zone - Iran). Data from Esna-Ashari et al. (2016).

	Olivine			
Sc	7.20	6.40	8.00	8.00
Ti	51.00	39.00	71.00	119.00
V	8.10	6.70	13.50	1.20
Cr	84.00	76.00	262.00	--
Co	170.00	167.00	180.00	192.00
Ni	1457.00	1316.00	1155.00	1424.00
Zn	95.00	84.00	107.00	88.00
Sr	0.01	0.02	0.71	1.93
Y	--	--	--	--
Zr	--	--	--	--

	Clinopyroxene			
Sc	76.00	71.00	63.00	87.00
Ti	1297.00	1138.00	998.00	1357.00
V	798.00	617.00	651.00	869.00
Cr	5935.00	4534.00	4779.00	6712.00
Co	30.46	29.56	32.27	32.39
Ni	144.00	137.00	151.00	149.00
Zn	22.99	19.74	26.84	22.95
Rb	0.25	--	0.45	0.09
Sr	10.57	7.38	7.02	10.29
Y	5.07	4.85	4.13	5.54
Zr	2.95	2.38	1.63	3.21
Nb	0.03	--	--	--
Cs	--	--	--	--
Ba	1.59	0.04	2.26	0.05
La	0.53	0.30	0.19	0.43
Ce	1.80	1.23	0.91	1.48
Pr	0.32	0.21	0.22	0.27
Nd	1.80	1.43	0.89	1.66
Sm	0.67	0.36	0.30	0.54
Eu	0.19	0.13	0.08	0.18
Gd	1.02	0.72	0.61	0.74
Tb	0.12	0.12	0.06	0.12
Dy	1.20	1.02	0.57	1.15
Ho	0.25	0.21	0.17	0.29
Er	0.72	0.61	0.41	0.69
Tm	0.10	0.09	0.06	0.06
Yb	0.47	0.50	0.46	0.76
Lu	0.07	0.07	0.04	0.06
Hf	0.17	0.06	0.10	0.26
Ta	0.01	--	0.01	--
Pb	0.29	--	0.14	0.07
Th	0.14	0.00	--	--
U	0.03	0.01	0.00	0.01

	Amphibole	
Sc	64.50	70.00
Ti	10083.00	15757.00
V	362.00	469.00
Cr	2693.00	3207.00
Co	44.00	41.00
Ni	368.00	345.00
Zn	44.00	49.00
Rb	2.18	3.05
Sr	80.00	80.00
Y	30.00	38.00
Zr	103.00	80.00
Nb	14.49	15.47
Cs	0.03	0.01
Ba	26.00	58.00
La	17.15	10.24
Ce	48.07	42.52
Pr	6.35	5.51
Nd	26.86	30.20
Sm	6.94	7.66
Eu	1.62	1.45
Gd	4.88	6.63
Tb	0.81	1.20
Dy	4.85	8.06
Ho	1.11	1.69
Er	2.97	4.61
Tm	0.38	0.79
Yb	3.06	3.98
Lu	0.73	0.54
Hf	3.57	3.10
Ta	0.70	0.78
Pb	4.21	4.64
Th	0.79	0.60
U	0.36	0.29
Nb/Y	0.48	0.41
Nb/Ta	20.70	19.83
Zr/Hf	28.85	25.81

Note: values are in ppm.

Table 28 - LA-ICP-MS analyses of olivine and clinopyroxene of the sample TK1B (Taku - Japan).

	Olivine				
Sc	2.60	2.11	2.27	2.24	1.99
Ti	60.23	36.18	39.48	59.39	47.70
V	1.56	0.71	0.86	0.97	1.02
Cr	6.09	5.03	8.19	--	5.31
Co	202.62	219.40	210.30	240.24	200.89
Ni	368.41	368.62	363.34	426.61	326.11
Zn	256.89	315.22	313.53	257.08	231.17
Sr	0.11	--	--	0.01	0.02
Y	0.03	--	0.02	--	--
Zr	0.07	--	0.05	0.04	0.05

	Clinopyroxene			
Sc	520.31	335.26	360.84	479.05
Ti	19412.45	7330.25	9272.03	20822.30
V	1929.22	976.52	1036.38	2313.10
Cr	10909.39	5102.12	2777.73	6126.52
Co	1532.57	1658.99	1579.48	1508.33
Ni	1737.36	1868.13	1847.37	1741.85
Zn	3665.56	4247.24	3616.47	3302.20
Rb	1.39	--	--	--
Sr	4.90	1.03	2.06	1.09
Y	40.95	25.02	26.05	40.02
Zr	35.49	37.97	39.40	31.96
Nb	--	--	--	0.58
Cs	1.27	--	0.13	--
Ba	0.27	--	--	--
La	0.58	--	0.15	0.27
Ce	1.32	0.91	0.72	0.98
Pr	0.13	--	--	0.19
Nd	--	0.49	2.33	--
Sm	1.53	1.06	--	2.38
Eu	0.49	0.50	--	0.61
Gd	2.74	0.94	1.04	3.25
Tb	0.88	0.38	0.49	0.71
Dy	4.01	4.35	4.41	6.24
Ho	1.21	1.02	1.33	1.26
Er	5.67	4.47	3.78	5.65
Tm	1.09	0.58	0.68	0.74
Yb	8.35	4.96	7.10	10.74
Lu	1.83	1.10	1.11	1.77
Hf	2.45	1.15	0.80	2.65
Ta	--	0.08	--	--
Pb	--	0.29	--	0.50
Th	--	0.08	0.10	0.07
U	--	0.08	--	0.10

Note: values are in ppm.

Table 29 - LA-ICP-MS analyses of amphibole of the sample TK1B (Taku - Japan).

	Amphibole				
Sc	74.50	76.84	71.82	74.46	67.88
Ti	10874.56	10175.96	8326.33	9962.82	9176.39
V	549.35	542.15	423.68	490.07	452.33
Cr	1360.77	907.78	1097.11	1078.20	1202.41
Co	62.43	70.91	63.34	56.49	64.15
Ni	133.02	150.82	131.30	122.79	144.51
Zn	100.29	108.87	99.86	89.34	85.94
Rb	3.50	3.56	3.89	2.97	3.65
Sr	153.00	142.09	129.44	140.67	146.44
Y	27.21	29.24	28.38	29.88	25.58
Zr	35.16	42.81	53.27	39.49	35.62
Nb	3.80	4.28	6.60	4.66	3.80
Cs	0.01	--	--	0.01	0.01
Ba	63.29	68.10	70.97	61.53	61.65
La	3.22	4.38	5.27	3.73	3.52
Ce	12.38	14.99	19.19	13.63	12.51
Pr	2.15	2.51	3.07	2.38	2.20
Nd	13.33	15.61	17.26	14.17	13.29
Sm	4.93	5.52	5.54	4.93	4.59
Eu	1.45	1.50	1.48	1.45	1.41
Gd	5.49	5.74	5.31	5.73	4.62
Tb	0.97	0.85	0.93	0.95	0.88
Dy	5.63	5.70	5.50	5.80	5.07
Ho	1.13	1.32	1.08	1.23	0.94
Er	2.71	2.86	2.88	3.09	2.47
Tm	0.36	0.36	0.40	0.40	0.35
Yb	2.21	2.71	2.71	2.78	2.25
Lu	0.34	0.34	0.29	0.31	0.32
Hf	1.59	1.55	2.20	1.52	1.53
Ta	0.21	0.22	0.33	0.22	0.23
Pb	1.30	2.08	0.75	1.07	1.76
Th	0.09	0.43	0.15	0.19	0.26
U	0.08	0.27	0.03	0.11	0.23
Nb/Y	0.14	0.15	0.23	0.16	0.15
Nb/Ta	18.18	19.72	19.82	21.09	16.81
Zr/Hf	22.16	27.71	24.21	25.95	23.30

Note: values are in ppm.

Table 30 - LA-ICP-MS analyses of olivine of the sample ZN5 (Zenifudo - Japan). Data from Langone et al. (2009)

	Olivine												
Sc	2.31	0.84	5.30	2.49	3.06	1.67	1.82	1.57	1.90	1.99	1.39	2.13	2.51
Ti	39.78	14.23	30.86	31.22	45.77	45.25	76.76	45.44	27.31	61.29	56.95	28.40	34.87
V	0.35	<0.32	2.63	1.59	1.82	2.04	1.71	<0.30	0.67	1.47	1.01	0.72	--
Cr	7.26	5.83	61.53	16.57	17.00	19.96	9.06	26.11	14.33	13.97	9.05	9.26	5.91
Co	187.04	198.79	183.07	205.58	179.80	201.61	193.86	213.47	194.04	207.78	193.58	197.74	199.60
Ni	219.66	223.93	236.90	198.13	207.03	175.56	195.52	183.13	212.41	196.29	197.01	197.42	199.12
Zn	188.24	155.29	188.75	187.88	153.51	183.82	174.44	177.78	194.90	179.53	188.60	184.24	172.86
Sr	0.03	--	--	--	--	0.29	--	0.12	--	--	--	0.04	--
Y	--	0.02	0.09	--	0.02	--	0.08	--	--	0.05	--	--	--
Zr	0.18	--	0.12	0.11	--	0.10	0.09	0.04	0.05	--	0.08	0.10	0.12

Note: values are in ppm.

Table 31 - LA-ICP-MS analyses of clinopyroxene of the sample ZN5 (Zenifudo - Japan). Data from Langone et al. (2009)

	Clinopyroxene								
Sc	76.11	90.14	94.22	89.31	90.11	71.08	77.35	71.64	96.21
Ti	1547.36	2723.75	3084.98	2505.04	1776.14	1381.32	1774.56	1543.38	2866.69
V	191.08	265.51	286.73	246.21	215.56	183.05	204.56	189.52	288.73
Cr	3389.60	3709.27	3657.93	3858.32	4034.54	5186.20	4484.88	4480.56	3657.67
Co	25.91	24.99	28.22	26.96	30.20	30.77	26.64	30.28	27.99
Ni	28.92	25.49	27.98	26.67	32.49	34.87	26.44	32.22	25.29
Zn	23.29	27.13	30.19	26.34	28.86	20.94	29.46	23.89	30.23
Rb	--	0.16	0.35	--	--	0.09	0.11	--	0.06
Sr	38.55	45.08	45.49	43.65	39.46	44.78	46.34	45.17	46.67
Y	4.76	6.38	6.88	6.34	6.85	3.99	4.24	4.55	8.37
Zr	4.70	9.07	10.44	8.74	7.32	4.58	5.32	3.86	9.94
Nb	--	0.09	0.04	0.02	--	--	--	0.02	0.02
Cs	0.01	0.01	0.01	--	0.02	--	0.03	--	0.02
Ba	--	0.99	--	0.37	--	--	0.32	0.28	0.58
La	0.72	1.42	1.09	0.98	0.81	0.75	0.74	0.59	1.18
Ce	2.79	4.76	3.93	3.63	3.87	3.05	3.12	2.57	4.75
Pr	0.55	0.69	0.58	0.66	0.77	0.42	0.57	0.49	0.83
Nd	3.07	3.89	4.13	3.55	3.71	2.90	3.17	2.89	4.77
Sm	1.20	1.26	1.56	1.25	1.29	1.17	0.91	0.80	1.83
Eu	0.31	0.54	0.47	0.44	0.56	0.35	0.27	0.34	0.69
Gd	1.12	1.09	1.11	1.40	1.51	1.28	1.20	0.93	1.49
Tb	0.10	0.16	0.19	0.22	0.22	0.16	0.12	0.13	0.20
Dy	1.01	1.32	1.72	1.21	1.52	0.86	0.73	0.78	1.17
Ho	0.19	0.24	0.38	0.28	0.22	0.13	0.24	0.20	0.25
Er	0.45	0.60	0.77	1.06	0.69	0.53	0.44	0.53	0.77
Tm	0.10	0.11	0.11	0.15	0.11	0.04	0.07	0.07	0.11
Yb	0.46	0.89	0.80	0.56	0.51	0.41	0.50	0.43	0.57
Lu	0.12	0.10	0.13	0.12	0.14	0.10	0.09	0.09	0.13
Hf	0.10	0.16	0.29	0.19	0.44	0.25	0.14	0.15	0.23
Ta	--	0.01	--	0.01	0.01	--	--	--	--
Pb	0.04	0.24	0.68	0.26	0.16	0.14	0.08	0.06	0.09
Th	--	0.16	0.29	0.11	0.02	0.01	0.05	0.03	0.23
U	0.01	0.06	0.10	0.06	--	0.01	0.03	0.01	0.04

Note: values are in ppm.

Table 32 - LA-ICP-MS analyses of amphibole of the sample ZN5 (Zenifudo - Japan). Data from Langone et al. (2009)

	Amphibole										
Sc	70.45	61.15	65.4	60.75	69.32	67.32	49.34	70.39	61.81	63.4	66.41
Ti	15069.38	9504.59	7444.98	10489.72	15092.77	15886.67	10345.18	16245.19	11832.64	13111.55	13039.91
V	426.81	323.28	296.21	327.27	431.7	455.67	305.28	471.16	370.01	396.77	373.56
Cr	1994.84	1914.72	1438.07	1386.29	1692.01	1822.83	1279.41	1724.87	1556.42	1440.01	1414.53
Co	49.21	49.11	45.83	49.87	49.04	46.17	46.96	56.56	49.03	53.51	52.36
Ni	55.66	60.1	62.37	55.42	54.4	50.01	55.27	58.2	64.83	69.71	59.86
Zn	53.04	54.47	47.04	53.27	41.6	46.31	50.46	60.8	39.76	58.25	49.05
Rb	1.91	2.34	2.59	2.26	2.33	1.67	2.88	2.68	2.41	2.32	2.3
Sr	264.91	238.81	240.82	245.31	270.55	276.71	344.71	303.8	252.41	258.97	250.03
Y	25.41	19.56	19.82	22.5	26.38	26.66	19.46	27.76	24.13	24.05	24.62
Zr	52.71	64.82	72.56	69.05	53.66	51.37	56.24	65.63	69.54	66.21	62.59
Nb	6.17	8.02	8.58	6.96	5.15	5.31	5.94	7.19	7.39	7.59	6.62
Cs	--	--	--	0.0238	--	--	0.0126	--	--	--	--
Ba	129.91	120.99	127.74	127.24	129.48	123.74	142.45	151.05	124.36	131.53	121.6
La	6.31	8.36	9.8	8.98	6.56	6.42	9.06	7.74	8.88	8.24	7.68
Ce	23.82	29.58	32.69	30.78	23.45	22.48	27.09	29.77	30.7	31.12	28.39
Pr	4.11	4.64	5.17	4.98	4.26	4.03	4.08	4.65	4.77	4.77	4.52
Nd	20.53	20.55	21.66	22.38	19.34	20.65	18.67	24.35	23.89	22.8	24.55
Sm	6.07	5.58	4.57	5.28	5.64	5.19	4.9	6.95	5.92	5.69	5.65
Eu	1.83	1.446	1.486	1.61	1.68	1.71	1.67	2.69	1.64	1.86	1.92
Gd	5.28	6.04	3.76	5.1	6.05	4.82	3.7	6.64	5.14	5.92	4.59
Tb	0.732	0.688	0.495	0.693	0.948	0.662	0.547	0.825	0.751	0.788	0.718
Dy	4.45	4.12	3.76	4.47	5.49	4.94	3.16	4.96	5.16	5.04	4.72
Ho	1.138	0.796	0.629	0.884	0.94	0.977	0.826	1.134	1.049	0.997	0.913
Er	2.36	1.68	2.34	2.25	2.48	2.41	2.11	3.25	2.6	2.32	2.27
Tm	0.391	0.275	0.332	0.465	0.537	0.363	0.266	0.311	0.448	0.341	0.394
Yb	2.55	1.9	1.57	2.14	2.81	2.36	1.85	2.77	2.31	2.68	2.17
Lu	0.374	0.356	0.19	0.349	0.431	0.357	0.284	0.462	0.41	0.413	0.353
Hf	2.11	2.51	2.48	2.32	2.39	1.91	1.92	3.25	2.73	2.19	2.54
Ta	0.268	0.427	0.406	0.285	0.235	0.389	0.318	0.36	0.397	0.291	0.245
Pb	1.75	0.959	3.25	4	3.25	2.42	4.39	1.85	1.61	1.74	1.64
Th	0.094	0.107	0.442	0.365	0.242	0.197	1.58	0.125	0.236	0.097	0.108
U	0.059	0.0312	0.366	0.347	0.223	0.124	0.366	0.051	0.12	0.096	0.031
Nb/Y	0.24	0.41	0.43	0.31	0.20	0.20	0.31	0.26	0.31	0.32	0.27
Nb/Ta	23.02	18.78	21.13	24.42	21.91	13.65	18.68	19.97	18.61	26.08	27.02
Zr/Hf	24.98	25.82	29.26	29.76	22.45	26.90	29.29	20.19	25.47	30.23	24.64

Note: values are in ppm.

Table 33 - LA-ICP-MS analyses of olivine of the sample HSY3b (Hase no Yatsu - Japan). Data from Langone et al. (2009).

	Olivine										
Sc	3.11	2.61	3.16	2.05	1.68	2.73	3.51	4.36	3.41	2.03	3.07
Ti	104.23	50.91	25.07	81.27	59.98	50.95	29.46	25.69	41.86	9.38	11.23
V	3.93	--	0.64	--	1.22	0.49	1.00	1.98	1.06	--	0.66
Cr	--	11.88	6.82	--	--	5.11	--	12.61	3.46	--	4.23
Co	189.97	203.26	201.76	178.94	171.10	174.87	173.37	162.76	167.99	173.84	179.82
Ni	183.96	192.50	171.09	188.41	163.96	177.66	190.81	186.11	246.46	186.33	168.84
Zn	252.59	270.49	265.68	264.86	247.17	243.28	222.68	211.76	197.17	212.01	223.66
Sr	0.22	--	0.07	0.19	0.24	--	--	0.10	--	--	0.13
Y	0.03	0.04	--	0.03	--	--	--	0.05	--	--	--
Zr	0.16	0.20	--	0.14	--	0.11	0.09	--	--	0.04	--

Note: values are in ppm.

Table 34 - LA-ICP-MS analyses of clinopyroxene of the sample HSY3b (Hase no Yatsu - Japan). Data from Langone et al. (2009).

	Clinopyroxene										
Sc	81.58	83.28	104.19	115.55	98.62	105.06	78.49	87.74	57.27	128.41	79.60
Ti	1979.57	2248.32	3086.37	4029.97	3018.97	3423.88	2009.39	3208.99	1508.64	4142.99	2317.79
V	141.90	195.60	254.50	301.67	218.61	250.04	204.96	213.68	107.75	274.01	166.32
Cr	599.47	1967.58	933.03	789.48	1663.44	1220.06	693.58	1539.61	211.66	1031.63	2204.93
Co	24.58	23.18	27.97	27.41	23.50	25.35	22.85	24.38	22.92	26.57	26.24
Ni	17.53	21.27	24.08	24.34	15.74	21.59	26.24	28.22	16.44	18.65	18.34
Zn	32.69	37.60	37.42	38.94	38.43	29.17	35.15	23.52	26.15	28.67	33.68
Rb	--	--	0.06	--	0.13	0.14	0.12	0.12	0.06	0.12	0.09
Sr	45.83	59.09	53.34	60.18	57.75	59.44	80.11	73.89	31.78	71.67	69.38
Y	4.64	5.91	9.09	9.48	7.11	8.18	6.01	6.69	3.85	9.63	5.93
Zr	11.57	5.90	9.19	11.81	8.70	10.21	11.84	8.89	10.38	12.89	9.47
Nb	0.12	--	0.07	0.05	0.02	0.04	0.09	0.04	--	0.12	0.21
Cs	--	--	0.04	0.02	--	--	--	--	--	--	0.04
Ba	0.16	0.18	0.49	0.50	0.49	0.55	0.90	0.43	0.07	0.74	0.51
La	1.30	0.69	1.01	0.98	0.88	1.23	1.27	0.94	0.96	1.16	1.20
Ce	3.87	3.44	4.36	5.01	3.79	4.52	4.81	3.74	3.14	4.45	3.73
Pr	0.68	0.69	0.94	1.16	0.85	0.92	0.95	0.93	0.70	0.95	0.79
Nd	4.35	4.04	6.16	6.57	5.22	5.26	4.97	4.39	3.48	6.65	4.52
Sm	1.75	1.38	2.19	2.37	1.83	2.15	1.84	1.22	0.93	1.66	0.93
Eu	0.29	0.58	0.64	0.65	0.52	0.52	0.31	0.55	0.23	0.62	0.39
Gd	1.34	1.51	1.78	2.64	1.66	2.09	1.28	1.45	1.03	2.68	1.83
Tb	0.19	0.13	0.23	0.36	0.25	0.31	0.16	0.22	0.16	0.39	0.18
Dy	1.18	1.52	1.90	1.96	1.19	1.52	1.06	1.39	0.94	2.52	1.54
Ho	0.38	0.31	0.33	0.45	0.25	0.34	0.18	0.31	0.20	0.34	0.22
Er	0.30	0.52	1.09	1.36	0.69	1.10	0.65	0.73	0.36	1.15	0.59
Tm	0.07	0.08	0.10	0.18	0.08	0.10	0.08	0.09	0.06	0.11	0.11
Yb	0.35	0.58	0.49	1.04	0.50	0.39	0.60	0.35	0.25	0.94	0.67
Lu	0.04	0.09	0.10	0.11	0.08	0.06	0.05	0.10	0.04	0.12	0.11
Hf	0.65	0.60	0.34	0.97	0.39	0.45	0.81	0.10	0.31	0.71	0.33
Ta	--	--	--	--	0.01	--	--	--	0.02	0.02	0.02
Pb	1.06	0.17	0.17	0.32	0.31	0.15	0.31	0.19	0.16	0.29	0.20
Th	0.07	0.04	0.04	0.07	0.05	0.06	0.09	0.04	0.07	0.19	0.03
U	0.06	0.01	0.02	0.05	0.04	0.02	0.03	0.02	0.02	0.04	0.04

Note: values are in ppm.

Table 35 - LA-ICP-MS analyses of amphibole of the sample HSY3b (Hase no Yatsu - Japan). Data from Langone et al. (2009).

	Amphibole						
Sc	82.99	72.81	59.19	63.50	65.71	81.73	118.31
Ti	17916.79	13484.63	6890.15	7358.66	6215.23	14416.87	18518.98
V	606.27	511.80	265.36	270.79	273.05	566.64	627.70
Cr	380.86	490.79	454.30	538.28	652.29	253.85	593.08
Co	51.54	49.42	44.92	42.80	51.45	44.72	50.89
Ni	58.56	66.25	60.21	60.50	56.71	62.80	59.07
Zn	74.86	76.57	48.74	60.18	72.58	64.09	88.94
Rb	7.18	7.23	7.12	7.37	6.47	6.11	6.85
Sr	364.11	425.07	354.66	350.84	307.06	406.53	417.52
Y	21.95	21.49	20.48	21.10	19.88	20.49	20.12
Zr	36.30	41.51	60.50	54.86	71.14	31.20	28.29
Nb	7.76	7.71	14.18	12.51	14.14	6.08	4.36
Cs	0.50	0.06	0.11	0.12	0.04	0.28	0.12
Ba	140.83	160.21	122.38	143.40	138.79	155.20	155.52
La	7.21	6.80	9.85	9.57	10.94	6.14	4.36
Ce	21.80	24.66	34.44	32.95	39.16	22.28	15.63
Pr	3.84	4.21	5.48	5.36	5.48	3.50	2.93
Nd	20.00	22.19	26.32	25.37	26.24	19.20	16.30
Sm	6.64	6.14	5.63	6.86	6.51	5.51	4.78
Eu	1.86	1.78	1.65	1.73	1.56	1.93	1.74
Gd	4.70	5.73	4.79	5.48	4.80	5.37	6.07
Tb	0.92	0.75	0.73	0.77	0.72	0.89	0.88
Dy	3.95	4.87	3.87	4.34	4.60	3.90	5.00
Ho	0.83	0.83	0.96	0.88	0.89	0.67	0.79
Er	2.02	3.12	2.00	1.78	1.65	2.37	2.63
Tm	0.43	0.26	0.39	0.30	0.33	0.24	0.22
Yb	1.68	1.34	2.02	1.93	2.14	1.78	1.71
Lu	0.30	0.27	0.34	0.23	0.29	0.21	0.22
Hf	1.61	1.80	2.41	1.49	2.08	1.18	0.89
Ta	0.31	0.46	0.73	0.68	0.83	0.25	0.32
Pb	2.32	2.31	2.58	2.34	2.31	3.46	1.59
Th	1.09	0.68	0.50	0.50	0.42	0.36	0.23
U	0.52	0.25	0.28	0.24	0.17	0.22	0.14
Nb/Y	0.35	0.36	0.69	0.59	0.71	0.30	0.22
Nb/Ta	25.11	16.65	19.50	18.42	16.95	24.82	13.84
Zr/Hf	22.55	23.06	25.10	36.82	34.20	26.44	31.79

Note: values are in ppm.

Table 36 - LA-ICP-MS analyses of clinopyroxene of the sample 14JT50 (Milin - Tibet).

	Clinopyroxene				
Sc	96.27	93.57	90.14	97.99	93.41
Ti	2096.56	1958.62	2135.90	1902.09	1725.95
V	277.57	258.83	283.73	275.83	255.33
Cr	332.12	294.37	286.50	299.61	262.00
Co	40.91	38.26	41.51	42.77	43.83
Ni	96.38	89.78	91.33	96.39	92.62
Zn	62.66	61.80	51.17	53.07	54.80
Rb	0.22	0.22	0.04	0.05	0.11
Sr	42.72	43.46	44.60	47.78	45.83
Y	12.79	12.20	8.73	11.08	10.66
Zr	24.07	24.47	21.70	24.39	24.16
Nb	0.02	0.01	0.04	--	--
Cs	--	0.03	0.02	0.01	0.01
Ba	0.73	0.75	0.56	0.43	0.34
La	1.47	1.39	0.97	1.25	1.08
Ce	5.42	5.10	4.05	4.92	4.37
Pr	0.99	0.91	0.74	0.95	0.83
Nd	6.26	6.61	4.57	5.20	5.04
Sm	2.04	2.09	1.54	1.92	1.55
Eu	0.67	0.68	0.58	0.55	0.63
Gd	2.32	2.35	2.09	1.76	1.99
Tb	0.41	0.39	0.33	0.36	0.34
Dy	2.79	2.49	1.78	2.20	2.47
Ho	0.52	0.49	0.39	0.48	0.43
Er	1.30	1.37	0.92	1.25	1.23
Tm	0.19	0.14	0.13	0.17	0.14
Yb	1.38	1.33	0.82	1.36	0.99
Lu	0.16	0.14	0.09	0.15	0.11
Hf	1.06	1.08	1.15	1.09	1.04
Ta	--	--	--	--	--
Pb	0.17	0.15	0.18	0.18	0.18
Th	0.10	0.09	0.09	0.09	0.14
U	0.01	0.02	0.01	--	0.04

Note: values are in ppm.

Table 37 - LA-ICP-MS analyses of amphibole of the sample 14JT50 (Milin - Tibet).

	Amphibole					
Sc	62.30	63.32	65.93	63.98	65.32	73.82
Ti	9450.93	9670.68	10381.76	10084.61	10433.16	7540.72
V	504.56	517.94	544.43	532.14	537.20	422.00
Cr	464.06	521.66	444.82	462.61	455.41	693.58
Co	61.99	61.44	60.76	63.28	61.37	53.99
Ni	125.97	128.92	139.38	131.43	127.27	179.30
Zn	72.53	78.16	88.48	90.31	97.16	88.57
Rb	1.63	1.46	2.19	1.94	1.81	2.11
Sr	285.59	281.74	299.62	304.32	303.94	256.82
Y	16.18	17.17	17.95	17.43	17.47	17.88
Zr	16.79	16.17	17.87	17.36	16.96	18.85
Nb	1.05	0.88	1.14	1.06	1.12	0.91
Cs	--	0.01	--	--	--	0.02
Ba	56.65	56.78	64.29	62.71	62.02	56.88
La	1.58	1.73	1.95	1.81	1.68	1.81
Ce	5.93	5.98	6.83	6.50	6.22	6.60
Pr	1.19	1.26	1.41	1.30	1.15	1.25
Nd	8.31	7.52	8.86	8.73	8.80	9.28
Sm	3.07	2.86	3.24	3.31	3.04	3.07
Eu	1.06	1.11	1.06	1.12	1.17	1.02
Gd	3.14	3.13	3.57	3.10	3.24	3.50
Tb	0.54	0.57	0.56	0.63	0.58	0.61
Dy	3.58	3.49	3.64	3.66	3.35	3.82
Ho	0.69	0.80	0.70	0.69	0.68	0.77
Er	1.83	1.81	1.78	1.73	1.98	1.82
Tm	0.26	0.27	0.25	0.24	0.23	0.24
Yb	1.54	1.41	1.66	1.40	1.75	1.61
Lu	0.22	0.19	0.19	0.19	0.17	0.20
Hf	0.75	0.85	0.70	0.85	0.85	0.90
Ta	0.03	0.04	0.04	0.04	0.04	0.04
Pb	1.07	0.97	0.98	0.87	1.00	0.79
Th	0.07	0.06	0.10	0.06	0.07	0.07
U	0.03	0.02	0.02	0.01	0.03	0.02
Nb/Y	0.06	0.05	0.06	0.06	0.06	0.05
Nb/Ta	30.23	22.61	31.47	29.06	25.75	25.31
Zr/Hf	22.42	19.09	25.68	20.47	20.00	21.06

Note: values are in ppm.

Table 38 - LA-ICP-MS analyses of olivine, clinopyroxene and amphibole of the sample MAT15 (Adamello - Italy).
Data of olivine and clinopyroxene are from Tiepolo et al. (2011).

	Olivine				
Sc	5.07	5.57	4.72	4.68	6.79
Ti	76.10	51.70	42.00	44.50	80.30
V	2.21	2.29	1.13	0.64	6.14
Cr	10.00	19.20	16.50	8.53	98.30
Co	175.00	173.00	160.00	185.00	174.00
Ni	1061.00	1023.00	1581.00	832.00	1011.00
Zn	133.00	130.00	124.00	131.00	119.00
Sr	--	--	--	--	--
Y	--	--	--	--	--
Zr	--	--	--	--	--

	Clinopyroxene	
Sc	127.00	123.00
Ti	1197.00	948.00
V	179.00	181.00
Cr	944.00	976.00
Co	25.30	24.80
Ni		
Zn		
Rb	0.02	0.03
Sr	16.20	17.30
Y	3.17	3.11
Zr	9.47	10.52
Nb	0.01	0.01
Cs	--	--
Ba	0.75	0.10
La	2.51	2.44
Ce	5.42	5.02
Pr	0.58	0.53
Nd	2.08	1.94
Sm	0.42	0.63
Eu	0.16	0.14
Gd	0.75	0.68
Tb	0.10	0.11
Dy	0.66	0.57
Ho	0.14	0.14
Er	0.37	0.40
Tm	0.07	0.06
Yb	0.37	0.44
Lu	0.07	0.06
Hf	0.48	0.42
Ta	--	0.00
Pb	1.00	0.33
Th	0.08	0.05
U	0.04	0.01

	Amphibole	
Sc	132.44	99.00
Ti	10806.25	12470.56
V	484.93	498.96
Cr	2515.41	2067.93
Co	51.04	45.60
Ni	223.95	261.81
Zn	42.94	36.37
Rb	1.23	0.97
Sr	178.84	179.50
Y	15.25	17.90
Zr	20.99	20.11
Nb	3.17	2.26
Cs	0.01	--
Ba	54.55	45.24
La	3.03	1.98
Ce	13.10	7.65
Pr	2.18	1.58
Nd	10.76	8.61
Sm	2.79	2.47
Eu	1.15	0.91
Gd	2.89	2.79
Tb	0.53	0.46
Dy	3.31	3.52
Ho	0.71	0.70
Er	1.68	2.06
Tm	0.39	0.35
Yb	2.28	1.86
Lu	0.23	0.28
Hf	1.14	0.90
Ta	0.20	0.18
Pb	1.20	0.49
Th	0.17	0.07
U	0.16	0.07
Nb/Y	0.21	0.13
Nb/Ta	16.09	12.35
Zr/Hf	18.41	22.34

Note: values are in ppm.

Table 39 - LA-ICP-MS analyses of olivine, clinopyroxene and amphibole of the sample VS 9 (Adamello - Italy). Data from Tiepolo et al. (2002).

	Olivine	
Sc	2.92	2.40
Ti	33.10	46.23
V	0.19	0.26
Cr	3.56	3.14
Co	226.35	222.53
Ni	358.29	359.64
Zn	212.76	190.78
Sr	0.03	0.05
Y	0.02	--
Zr	0.04	--

	Clinopyroxene	
Sc	117.58	133.23
Ti	2204.36	2712.10
V	247.46	324.19
Cr	644.51	850.93
Co	28.44	30.52
Ni	45.56	55.56
Zn	35.74	38.34
Rb	0.20	0.13
Sr	18.16	17.56
Y	10.02	12.33
Zr	11.52	12.59
Nb	0.05	0.06
Cs	--	0.02
Ba	0.74	0.55
La	0.78	0.77
Ce	2.25	2.63
Pr	0.46	0.47
Nd	2.80	3.58
Sm	1.50	1.48
Eu	0.36	0.58
Gd	1.16	1.87
Tb	0.28	0.35
Dy	2.39	2.54
Ho	0.50	0.48
Er	0.64	1.38
Tm	0.12	0.15
Yb	0.97	1.49
Lu	0.08	0.14
Hf	0.32	0.48
Ta	0.02	0.01
Pb	0.12	0.17
Th	0.15	0.10
U	0.02	0.02

	Amphibole	
Sc	94.09	74.85
Ti	11684.52	10164.85
V	650.90	540.45
Cr	324.48	258.27
Co	58.81	54.57
Ni	127.14	120.85
Zn	83.92	57.38
Rb	2.64	2.52
Sr	120.96	109.67
Y	29.72	27.67
Zr	29.79	27.57
Nb	2.08	1.67
Cs	0.01	0.02
Ba	45.18	37.00
La	1.69	1.46
Ce	7.45	6.12
Pr	1.37	1.27
Nd	10.24	9.12
Sm	3.57	3.81
Eu	1.20	1.13
Gd	5.13	4.04
Tb	0.88	0.79
Dy	5.97	5.10
Ho	1.27	1.23
Er	3.26	2.95
Tm	0.39	0.49
Yb	3.32	2.52
Lu	0.34	0.33
Hf	1.31	1.01
Ta	0.13	0.09
Pb	0.38	0.78
Th	0.06	0.03
U	0.05	0.03
Nb/Y	0.07	0.06
Nb/Ta	16.25	19.15
Zr/Hf	22.74	27.30

Note: values are in ppm.

Table 40 - LA-ICP-MS analyses of brown amphibole of the sample SRD02305 (Batu Hijau - Indonesia).

	Amphibole						
Sc	118.19	96.29	102.01	117.84	107.45	127.87	133.17
Ti	7969.05	7676.50	7148.68	7358.56	6664.44	7984.62	8181.44
V	307.55	288.34	287.56	292.64	266.22	348.27	349.06
Cr	27.01	16.71	30.36	30.85	26.97	34.84	31.58
Co	65.03	62.79	62.83	63.20	61.95	62.55	64.21
Ni	59.90	49.79	58.87	58.67	55.59	71.27	77.73
Zn	170.63	174.98	199.77	194.17	191.56	178.48	183.57
Rb	0.40	0.35	0.34	0.23	0.30	0.39	0.33
Sr	60.78	56.16	43.97	52.36	44.70	56.05	56.68
Y	67.27	64.06	83.85	79.65	64.93	91.41	94.44
Zr	45.30	47.00	56.40	50.36	44.72	46.26	48.47
Nb	2.87	2.87	2.80	2.97	2.85	2.75	2.55
Cs	--	--	--	0.02	0.06	--	--
Ba	42.20	37.65	37.61	34.38	29.45	39.03	37.95
La	4.71	4.66	5.93	5.04	4.64	4.60	4.51
Ce	22.12	21.91	28.44	24.69	23.40	20.77	21.74
Pr	4.44	4.76	6.05	5.01	4.67	4.67	4.73
Nd	28.57	28.26	38.15	35.40	32.50	34.75	34.84
Sm	10.90	11.17	12.17	12.79	9.37	12.98	12.50
Eu	2.24	2.49	2.90	2.75	2.38	2.73	3.07
Gd	10.67	11.00	14.43	13.34	11.38	16.31	16.55
Tb	1.97	1.89	2.14	2.54	1.94	2.76	2.86
Dy	12.88	11.34	15.19	14.30	12.81	17.18	17.08
Ho	2.66	2.20	3.20	3.04	2.64	3.42	3.64
Er	6.79	6.34	7.57	7.51	6.44	8.82	9.84
Tm	0.97	0.97	1.30	1.14	0.91	1.22	1.19
Yb	6.67	6.22	7.33	7.67	5.53	8.17	8.86
Lu	0.95	0.83	1.26	1.10	0.89	1.14	0.96
Hf	1.83	1.96	2.26	2.57	2.71	2.21	1.99
Ta	0.10	0.07	0.08	0.10	0.05	0.02	0.05
Pb	0.48	0.24	0.22	0.35	0.30	0.37	0.31
Th	0.04	0.05	0.07	0.08	0.03	0.04	0.05
U	0.01	0.02	--	--	0.03	--	--
Nb/Y	0.04	0.04	0.03	0.04	0.04	0.03	0.03
Nb/Ta	27.86	41.00	33.73	29.41	53.77	114.58	50.00
Zr/Hf	24.75	23.98	24.96	19.60	16.50	20.93	24.36

Note: values are in ppm.

Table 41 - LA-ICP-MS analyses of brown amphibole of the sample MGT (Hoover Dam - United States of America).

	Amphibole									
Sc	42.32	43.36	44.68	42.53	46.99	47.83	47.37	45.89	48.65	47.61
Ti	31291.07	31255.04	31684.75	31483.65	31914.13	31825.35	31345.59	31475.57	30677.32	30356.28
V	449.00	449.20	451.76	452.95	520.63	521.38	521.07	515.17	525.86	519.71
Cr	6.13	3.77	6.80	5.74	311.73	537.18	371.13	302.48	745.21	739.28
Co	48.57	47.39	48.61	49.11	47.82	47.16	45.99	46.76	47.87	47.44
Ni	112.60	108.79	113.04	112.02	345.26	363.26	347.82	335.75	366.23	363.08
Zn	43.25	50.01	47.95	45.81	39.42	37.86	40.31	36.37	38.90	35.78
Rb	6.06	6.54	6.23	6.30	6.82	7.24	7.13	6.84	7.79	7.93
Sr	621.49	625.64	635.97	634.02	591.51	582.07	580.53	580.39	568.33	554.62
Y	21.07	22.13	21.52	21.96	20.37	20.23	19.34	18.85	20.35	19.86
Zr	71.40	72.21	71.75	72.59	57.71	57.04	55.88	54.86	54.49	55.36
Nb	25.33	25.31	26.71	25.74	23.00	22.70	22.83	22.78	22.85	21.58
Cs	--	--	--	0.04	0.02	--	--	--	0.06	0.07
Ba	268.52	268.70	273.52	272.86	281.15	294.25	281.40	276.23	287.04	279.57
La	7.93	7.89	8.06	7.60	6.87	6.78	6.79	6.94	6.94	6.60
Ce	25.02	25.16	25.21	24.32	21.10	21.31	21.26	20.66	21.28	20.25
Pr	3.97	4.07	4.13	4.10	3.55	3.31	3.52	3.39	3.71	3.42
Nd	22.05	23.09	22.52	23.69	19.62	18.68	18.64	18.61	19.62	17.33
Sm	6.89	6.33	7.55	6.15	5.53	5.62	5.45	5.51	5.10	5.91
Eu	2.29	2.07	2.19	2.19	1.80	1.87	1.95	1.89	2.07	1.96
Gd	5.70	6.37	6.24	5.59	5.65	5.11	5.48	5.14	5.86	4.88
Tb	0.93	0.91	0.87	0.92	0.89	0.85	0.72	0.81	0.86	0.89
Dy	4.65	4.73	4.67	5.51	4.58	3.87	4.08	4.17	4.38	4.10
Ho	0.89	0.96	0.87	1.01	0.90	0.84	0.82	0.90	0.85	0.93
Er	2.14	2.11	2.28	2.18	2.24	1.95	2.04	1.86	1.90	2.03
Tm	0.24	0.27	0.25	0.25	0.20	0.29	0.24	0.27	0.25	0.23
Yb	1.10	1.38	1.66	1.49	1.37	1.24	1.66	1.39	1.43	1.48
Lu	0.17	0.17	0.16	0.17	0.18	0.13	0.15	0.17	0.17	0.33
Hf	2.40	2.36	2.86	3.02	2.16	1.98	2.07	2.20	2.12	1.99
Ta	1.44	1.37	1.42	1.38	1.38	1.19	1.36	1.32	1.29	1.39
Pb	1.91	1.97	1.16	1.65	1.49	1.73	1.66	1.86	2.20	1.57
Th	0.10	0.05	--	0.11	0.05	0.07	0.08	0.06	0.16	0.16
U	0.03	--	0.01	0.06	0.01	0.02	--	0.02	0.06	0.12
Nb/Y	1.20	1.14	1.24	1.17	1.13	1.12	1.18	1.21	1.12	1.09
Nb/Ta	17.57	18.42	18.78	18.67	16.72	19.11	16.84	17.23	17.71	15.49
Zr/Hf	29.75	30.60	25.09	24.04	26.72	28.81	27.00	24.94	25.70	27.82

Note: values are in ppm.

Table 42 - LA-ICP-MS analyses of amphibole of the sample DH (Dish Hill - United States of America).

	Amphibole											
Sc	41.02	42.36	40.38	41.90	33.55	32.56	32.80	32.85	33.17	32.40	33.39	33.31
Ti	28152.67	28085.04	28056.06	28272.52	25942.82	25790.50	25738.71	25426.60	25201.69	25142.56	25804.56	25615.54
V	445.02	450.43	443.12	447.81	286.72	282.41	283.01	278.13	277.75	278.80	285.35	285.77
Cr	3.94	8.67	3.99	3.41	10.83	14.27	17.68	19.74	17.32	13.89	18.43	17.53
Co	57.46	58.64	57.22	58.51	42.02	42.13	42.80	41.16	41.78	42.01	43.50	42.65
Ni	5.65	6.43	7.26	6.25	10.20	11.77	11.44	9.27	8.63	10.89	10.48	9.48
Zn	74.89	73.47	76.31	71.47	107.28	93.07	95.09	97.47	91.04	83.56	86.45	86.31
Rb	10.21	10.15	9.63	10.19	10.94	10.97	11.05	10.84	10.81	10.79	11.39	10.76
Sr	484.97	486.58	490.74	492.09	540.78	531.70	537.05	533.83	533.03	529.30	545.25	538.64
Y	20.68	20.83	20.65	21.30	23.48	22.63	22.73	23.08	24.00	24.07	24.25	23.76
Zr	68.47	67.17	65.61	67.27	100.19	96.31	98.23	99.15	97.06	102.54	101.38	100.29
Nb	21.82	22.01	21.48	22.05	34.18	33.44	34.86	33.40	33.26	33.57	34.39	33.67
Cs	--	0.01	0.01	--	--	--	--	<0.0217	0.02	0.03	--	--
Ba	230.78	230.67	225.44	230.05	275.56	271.56	271.34	282.30	266.54	264.87	272.97	267.51
La	6.67	6.51	6.50	6.53	9.30	9.47	9.03	9.03	9.47	9.14	9.59	9.32
Ce	20.42	20.66	20.81	20.69	29.96	29.02	29.70	28.89	28.50	28.87	30.26	29.48
Pr	3.30	3.60	3.37	3.38	4.85	4.88	4.77	4.95	4.68	4.82	4.99	4.66
Nd	18.72	19.03	19.78	19.53	26.02	27.15	26.89	26.37	25.21	26.13	27.89	26.73
Sm	5.91	4.97	4.69	5.75	7.15	6.81	6.85	6.67	7.48	6.69	7.51	7.18
Eu	2.06	2.03	1.94	1.87	2.45	2.40	2.51	2.36	2.30	2.39	2.54	2.57
Gd	5.97	5.42	5.78	5.80	6.15	6.87	6.90	6.05	6.36	6.76	6.39	6.59
Tb	0.85	0.74	0.85	0.86	1.03	0.94	0.96	0.90	0.94	0.88	1.07	1.04
Dy	4.59	4.93	4.39	4.90	5.78	5.60	5.75	4.83	4.92	5.25	5.51	5.28
Ho	0.79	0.89	0.79	0.88	0.96	1.00	0.94	1.00	0.97	0.98	1.01	0.94
Er	2.09	2.17	1.94	2.31	2.45	2.35	2.42	2.12	2.41	2.62	2.50	2.59
Tm	0.24	0.25	0.21	0.28	0.28	0.26	0.32	0.30	0.31	0.29	0.31	0.27
Yb	1.59	1.48	1.62	1.78	1.59	1.56	1.65	1.55	1.89	1.51	1.83	1.78
Lu	0.17	0.19	0.22	0.20	0.23	0.24	0.25	0.23	0.31	0.26	0.29	0.26
Hf	2.79	2.85	2.67	2.97	3.43	3.09	3.58	3.71	3.61	3.87	4.23	3.89
Ta	1.21	1.34	1.21	1.31	1.72	1.72	1.72	1.66	1.67	1.59	1.61	1.70
Pb	0.34	0.51	0.36	0.42	0.74	0.69	0.54	0.56	0.58	0.91	0.75	0.67
Th	0.04	0.06	0.04	0.04	0.05	0.07	0.09	0.05	0.08	0.08	0.07	0.07
U	0.03	--	0.02	--	0.02	--	0.02	--	0.02	--	--	0.02
Nb/Y	1.06	1.06	1.04	1.04	1.46	1.48	1.53	1.45	1.39	1.39	1.42	1.42
Nb/Ta	18.09	16.49	17.69	16.88	19.83	19.42	20.29	20.07	19.95	21.09	21.36	19.76
Zr/Hf	24.54	23.57	24.57	22.65	29.21	31.17	27.44	26.73	26.89	26.50	23.97	25.78

Note: values are in ppm.

Table 43 - SIMS analysis for H_2O, F, Cl, Li and B contents in amphiboles fromAgnew-Wiluna greenstone belt (Western Australia).

	H_2O wt.%	Average	rsd	F ppm	Average	rsd	Cl ppm	Average	rsd	Li ppm	Average	rsd	B ppm	Average	rsd
	0.85	0.81	0.03	378	333.00	69.21	4128	3925.80	140.30	0.07	0.11	0.04	0.68	0.78	0.14
	0.80			313			4004			0.18			0.92		
Mt. Keith - sample MKD1	0.80			443			3725			0.10			0.76		
	0.83			278			3949			0.08					
	0.77			253			3823			0.12					
	0.63	0.72	0.07	885	437.00	188.58	4857	4494.00	286.85	2.70	2.14	0.35	5.20	4.96	0.96
	0.74			350			4230			2.17			4.69		
	0.68			349			4925			1.91			4.08		
Mt. Clifford - sample 85437	0.67			441			4016			2.28			6.70		
	0.70			377			4463			1.65			4.13		
	0.88			220			4473								

Table 44 - SIMS analysis for H_2O, F, Cl, Li and B contents in amphiboles from Abitibi greenstone belt (Canada).

	H_2O wt.%	Average	rsd	F ppm	Average	rsd	Cl ppm	Average	rsd	Li ppm	Average	rsd	B ppm	Average	rsd
	1.09	1.06	0.09	11669	10320.67	2258.86	2221	2435.33	250.03	0.40	0.40	0.14	1.96	2.67	1.69
	0.97			11216			2654			0.36			4.36		
Theo's Flow - sample T-2	1.11			8077			2431			0.41			1.69		
										0.64					
										0.19					
	1.04	1.13	0.15	182	228.75	65.98	1383	1434.00	87.12	0.03	0.11	0.09	0.43	0.57	0.19
	1.35			168			1557			0.05			0.75		
Boston Creek - sample B-5	1.09			309			1433			0.25			0.53		
	1.02			256			1363			0.20					
										0.04					
	1.01	1.06	0.16	1876	1929.8	51.0	3902	4021.20	73.49	0.81	1.22	0.29	13.68	12.73	2.93
	1.00			1999			4001			0.95			18.10		
Ghost Range - sample GR-1	1.32			1872			4075			1.51			10.83		
	0.84			1974			4010			1.53			10.47		
	1.13			1928			4118			1.28			10.58		
	0.74	0.98	0.49	4065	3851.20	381.63	3788	3527.80	277.91	0.78	0.79	0.08	2.66	1.81	0.88
	0.71			4162			3791			0.64			2.35		
Ghost Range - sample GR-2	0.75			3722			3441			0.81			0.77		
	0.73			4149			3580			0.89			0.70		
	1.95			3158			3039			0.83			2.56		

Table 45 - SIMS analysis for H_2O, F, Cl, Li and B contents in amphiboles from Pechenga complex (Russia).

	H_2O wt.%	Average	rsd	F ppm	Average	rsd	Cl ppm	Average	rsd	Li ppm	Average	rsd	B ppm	Average	rsd
Pilgüjarvi sill - sample Pilg 8 38	0.84	0.98	0.23	6205	4461.33	1748.50	863	937.33	198.61	0.11	0.39	0.55	0.48	1.10	0.79
	1.21			3477			1134			0.10			0.78		
	0.90			3702			815			0.13			0.51		
										0.11			1.13		
										1.49			2.61		
Pilgüjarvi sill - sample 106-44	1.12			3156			766			0.42	1.26	1.23	2.68	4.92	4.48
										0.49			7.16		
										1.09					
										3.04					
Pilgüjarvi sill - sample 116-6	0.93	1.25	0.84	2841	2316.33	782.70	1411	1391.67	158.22	0.65	1.93	1.17	42.49	59.08	16.82
	0.73			2557			1246			0.70			69.79		
	2.08			1551			1518			2.68			64.97		
										1.92					
										3.69					
Kammikivi sill - 57-HV-28	1.78	1.72	0.13	6990	5788.00	2404.00	626	858.00	464.00	0.17	0.20	0.11	36.56	36.09	23.37
	1.65			4586			1090			0.32			72.58		
										0.33			45.04		
										0.09			1.65		
										0.09			24.62		
Nyasyukka dike complex - sample N-2	0.94	0.90	0.03	897	872.60	17.51	1510	1566.00	60.38	5.45	6.02	0.30	0.57	0.80	0.25
	0.87			889			1619			6.19			1.29		
	0.88			866			1654			6.31			0.65		
	0.93			860			1545			6.08			0.80		
	0.86			851			1502			6.06			0.72		
Nyasyukka dike complex - sample N-3	0.82	0.77	0.04	1794	1646.00	116.67	902	1097.75	136.17	3.97	3.89	0.41	0.33	0.35	0.03
	0.74			1666			1136			3.91			0.38		
	0.75			1609			1135			4.14			0.33		
	0.75			1515			1218			4.31			0.40		
										3.13			0.31		

Table 46 - SIMS analysis for H_2O, F, Cl, Li and B contents in amphiboles from arc and collisional setting of Phanerozoic age.

	H_2O wt.%	Average	rsd	F ppm	Average	rsd	Cl ppm	Average	rsd	Li ppm	Average	rsd	B ppm	Average	rsd
Husky Ridge (Antarctica) - sample TT329	1.06	1.01	0.05	943	959.40	32.07	788	743.40	93.17	6.36	6.49	0.37	3.62	4.24	0.66
	1.07			962			708			5.83			4.96		
	0.95			929			619			6.65			5.13		
	0.95			1020			896			6.90			3.77		
	1.02			943			706			6.73			3.73		
Sanandaj Sirjan Zone (Iran) - sample AL89	0.66	0.67	0.02	563	530.00	52.75	700	686.20	34.79	5.65	5.42	0.37	1.11	1.24	0.36
	0.66			535			690			4.82			1.11		
	0.64			544			742			5.68			1.09		
	0.69			579			654			5.15			0.93		
	0.71			429			645			5.80			1.94		
Taku (Japan) - sample TK1B	1.08	1.11	0.06	542	521.00	15.53	703	696.60	45.02	2.50	1.91	0.42	1.21	1.98	0.58
	1.04			521			652			2.32			1.54		
	1.11			534			682			1.79			2.01		
	1.08			507			780			1.44			2.25		
	1.22			501			666			1.52			2.88		
Zenifudo (Japan) - sample ZN5	0.80	0.88	0.08	406	386.20	21.84	611	590.40	50.17	1.12	1.08	0.29	0.92	0.91	0.73
	0.86			392			672			1.63			2.31		
	0.98			399			531			0.97			0.46		
	0.81			390			592			0.87			0.45		
	0.97			344			546			0.82			0.39		
Hase no Yatsu (Japan) - sample HSY3B	0.82	0.83	0.02	792	804.20	48.69	321	359.00	43.11	2.06	2.05	0.42	4.13	3.97	0.19
	0.86			749			342			2.40			3.99		
	0.85			758			351			1.68			3.81		
	0.82			867			443								
	0.80			855			338								

Continued Table 46

	H_2O wt.%	Average	rsd	F ppm	Average	rsd	Cl ppm	Average	rsd	Li ppm	Average	rsd	B ppm	Average	rsd
Milin (Tibet) - sample 14JT50	0.99	0.97	0.02	999	1032.80	42.53	460	546.40	57.13	5.67	4.20	1.28	1.18	1.30	0.54
	0.94			1032			542			3.53			0.94		
	0.98			1020			607			5.74			1.41		
	0.98			1114			610			3.51			2.27		
	0.98			999			513			2.55			0.71		
Adamello (Italy) - sample MAT15	0.80	0.81	0.01	696	656.00	82.25	424	450.00	37.01	1.18	1.02	0.09	0.32	0.80	0.83
	0.82			708			481			0.95			0.44		
	0.79			696			449			1.06			1.62		
	0.80			688			397			0.94					
	0.82			492			499			0.96					
Batu Hijau (Indonesia) - sample SRD02305	1.18	1.21	0.05	1185	1236.40	140.28	1613	1467.00	120.93	0.87	2.14	1.20	1.06	3.08	3.47
	1.18			1221			1600			4.13			9.86		
	1.30			1137			1301			2.86			2.77		
	1.22			1130			1420			1.63			0.91		
	1.16			1509			1401			1.20			0.77		
Bregaglia (Italy-Swiss) - sample VS9										1.53	3.16	2.55	0.78	1.32	0.61
										0.40			1.65		
										3.77			1.90		
										2.33			0.39		
										7.75			1.86		

Table 47 - δD and $\delta^{18}O$ for amphiboles from Agnew-Wiluna greenstone belt (Western Australia).

	δD ‰	error	Average	rsd	$\delta^{18}O$ ‰	error	Average	rsd
Mt. Keith - sample MKD1	-103.7	0.000008	-115.6	6.7	5.4	0.09	5.0	0.3
	-120.5	0.000032			5.1	0.08		
	-113.6	0.000001			4.6	0.11		
	-117.6	0.000005			5.1	0.06		
	-122.7	0.000003			4.9	0.12		
Mt. Clifford - sample 85437	-135.1	0.000002	-129.6	9.9	2.5	0.09	2.5	0.3
	-134.2	0.000002			2.1	0.07		
	-134.5	0.000003			2.2	0.12		
	-114.7	0.000002			2.0	0.08		
					3.0	0.10		
					2.9	0.09		

Table 48 - δD and $\delta^{18}O$ for amphiboles from Abitibi greenstone belt (Canada).

	δD ‰	error	Average	rsd	$\delta^{18}O$ ‰	error	Average	rsd
Theo's Flow - sample T-2	-103.8	0.0000023	-101.5	10.0				
	-117.6	0.0000029						
	-104.3	0.0000060						
	-91.8	0.0000073						
	-90.1	0.0000026						
Boston Creek - sample B-5	-121.3	0.0000019	-115.8	12.8	3.1	0.11	3.7	0.7
	-111.6	0.0000018			3.2	0.16		
	-100.2	0.0000050			5.0	0.14		
	-130.0	0.0000048			3.4	0.08		
					3.8	0.12		
Ghost Range - sample GR-1	-189.5	0.0000027	-197.6	16.0	4.2	0.11	4.2	0.3
	-193.6	0.0000250			3.8	0.09		
	-177.4	0.0000096			4.5	0.11		
	-202.2	0.0000036			3.9	0.12		
	-225.3	0.0000034			4.6	0.12		
Ghost Range - sample GR-2	-219.5	0.0000034	-236.3	23.6	4.0	0.09	3.8	1.0
	-202.5	0.0000013			2.5	0.14		
	-210.3	0.0000020			3.8	0.12		
	-210.8	0.0000066			4.8	0.09		
	-245.8	0.0000018						
	-280.5	0.0000017						
	-230.6	0.0000029						
	-290.6	0.0000023						

Table 49 - δD and $\delta^{18}O$ for amphiboles from Pechenga complex (Russia).

	δD ‰	error	Average	rsd	$\delta^{18}O$ ‰	error	Average	rsd
Pilgüjarvi sill - sample Pilg 8 38	-116.39	0.000011	-121.2	4.5	4.3	0.12	4.5	1.3
	-125.03	0.000002			1.9	0.18		
	-118.38	0.000001			5.6	0.11		
	-125.14	0.000001			5.2	0.11		
					5.2	0.09		
Pilgüjarvi sill - sample 106-44	-124.03	0.000001	-129.8	6.8				
	-129.47	0.000002						
	-135.87	0.000002						
Pilgüjarvi sill - sample 116-6	-100.5	0.000002	-104.3	4.5	7.5	0.14	6.4	1.1
	-106.14	0.000001			6.1	0.10		
	-100.89	0.000002			5.6	0.13		
	-109.86	0.000002						
Kammikivi sill - 57-HV-28	-144.8	0.000002	-117.4	40.1	3.9	0.09	4.3	0.4
	-145.58	0.000002			4.5	0.11		
	-119.12	0.000007			4.9	0.10		
	-60.227	0.000004			4.0	0.09		
Nyasyukka dike complex - sample N-2	-97.478	0.000052	-99.5	4.3	3.9	0.12	3.0	1.0
	-103.63	0.000001			2.2	0.10		
	-92.107	0.000004			1.9	0.08		
	-102.92	0.000002			2.3	0.10		
	-101.43	0.000001			4.5	0.86		
Nyasyukka dike complex - sample N-3	-112.87	0.000001	-108.7	3.4	4.7	0.09	5.0	0.2
	-108.11	0.000001			5.2	0.14		
	-112.22	0.000001			5.2	0.13		
	-104.5	0.000002			5.1	0.11		
	-105.69	0.000001						

Table 50 - δD and $\delta^{18}O$ for amphiboles from acr and collisional setting of Phanerozoic age.

	δD ‰	error	Average	rsd	$\delta^{18}O$ ‰	error	Average	rsd
Husky Ridge (Antarctica) - sample TT329	-61.5	0.000001	-61.5	7.3	8.4	0.10	7.0	0.8
	-56.7	0.000004			6.9	0.12		
	-52.4	0.000002			8.0	0.12		
	-74.2	0.000001			6.4	0.10		
	-62.7	0.000002			6.4	0.12		
					6.1	0.12		
Sanandaj Sirjan Zone (Iran) - sample AL89	-109.7	0.000001	-104.6	5.7	6.9	0.15	6.2	0.4
	-94.0	0.000004			6.7	0.14		
	-109.5	0.000001			6.2	0.09		
	-103.8	0.000001			5.7	0.15		
	-106.0	0.000002			6.4	0.10		
					5.7	0.10		
Taku (Japan) - sample TK1B	-120.2	0.000001	-125.8	15.6	6.4	0.13	6.4	0.6
	-115.7	0.000002			5.4	0.14		
	-112.5	0.000002			6.0	0.16		
	-124.5	0.000002			6.2	0.12		
	-156.0	0.000006			7.2	0.10		
					7.2	0.13		
Zenifudo (Japan) - sample ZN5	-28.5	0.000001	-8.6	77.4	5.5	0.12	6.0	0.4
	-83.9	0.000005			5.6	0.10		
	123.8	0.000002			6.3	0.10		
	26.1	0.000012			6.3	0.11		
	-80.3	0.000002			6.7	0.14		
					5.8	0.14		
Hase no Yatsu (Japan) - sample HSY3B	13.1	0.000002	0.2	27.4	8.6	0.11	9.6	0.8
	7.2	0.000032			9.5	0.09		
	31.2	0.000001			10.9	0.12		
	0.3	0.000002			10.2	0.10		
	-50.7	0.000002			9.6	0.08		
					8.5	0.09		
					9.1	0.11		
Milin (Tibet) - sample 14JT50	-82.3	0.000002	-74.7	8.50	7.2	0.11	6.4	1.1
	-68.7	0.000001			7.1	0.10		
	-65.6	0.000002			6.7	0.09		
	-87.3	0.000001			5.3	0.11		
	-69.6	0.000001			7.9	0.13		
					4.2	0.23		

Continued Table 50

Adamello (Italy) - sample MAT15	-68.2	0.000005	-72.5	4.69	4.2	0.12	5.2	0.8
	-74.3	0.000001			4.3	0.09		
	-66.4	0.000004			6.4	0.26		
	-79.5	0.000001			6.4	0.12		
	-73.9	0.000004			5.1	0.09		
					4.6	0.11		
Batu Hijau (Indonesia) - sample SRD02305	-109.3	0.000016	-105.2	3.74	4.0	0.12	3.6	0.3
	-104.3	0.000009			3.4	0.09		
	-109.7	0.000006			3.6	0.11		
	-102.1	0.000003			3.1	0.11		
	-100.5	0.000007			3.8	0.09		
					3.9	0.11		
Bregaglia (Italy-Swiss) - sample VS9					4.1	0.09	4.8	0.6
					4.7	0.10		
					5.3	0.11		
					4.6	0.12		
					6.2	0.10		
					4.9	0.10		
					4.0	0.11		

Appendix C – Modelling and melts calculated

Table 1 - solid/liquid partition coefficients used in calculations

	$^{Amph/L}D$	$^{Cpx/L}D$	$^{Opx/L}D$	$^{Ol/L}D$
Li	0.14	0.14		
B	0.01	0.17		
Ba	0.37	0.00015		
Rb	0.09	0.00008		
Th	0.03	0.007		
U	0.03	0.006		
Nb	0.34	0.005		
Ta	0.32	0.021		
La	0.18	0.07	0.0006	0.0000088
Ce	0.3	0.12	0.0017	0.001
Sr	0.62	0.111		
Pb	0.12			
Nd	0.64	0.27	0.004	0.003
Zr	0.45	0.2		
Hf	0.76	0.42		
Sm	1.06	0.42	0.0011	0.002
Eu	0.96			
Gd	1.32	0.418	0.0546	0.0013
Ti	2.9	0.46		
Dy	1.42		0	0.0038
Y	1.39	0.51		
Yb	1.16	0.47	0.077	0.0267
Sc	3.47			
V	5.24			
F	1.84			
Cl	0.21			
H_2O	0.3			

Note: $^{Amph/L}D$ are from Tiepolo et al. (unpublished, 1999, 2007), $^{Cpx/L}D$, $^{Opx/L}D$ and $^{Ol/L}D$ are frome Adam and Green (2006).

Table 2 - Calculated composition of the clinopyroxene-equilibrium melt.

	Pilgüjarvi sill - sample Pilg 8 38	Pilgüjarvi sill - sample 106-44		Pilgüjarvi sill - sample 116-6		Kammikivi sill - 57-HV-28		Theo's Flow - sample T-2		Boston Creek - sample B-5		Ghost Range - sample GR-1		Ghost Range - sample GR-2	
		Average	rsd	Average	rsd	Average	rsd	Average	rsd	Average	rsd	Average	rsd	Average	rsd
Th	9.60	13.57	11.63	6.17	4.20	13.86		1.24	0.54			1.69			
U	1.93	2.00	2.77	1.63	0.62			0.82	0.17			1.98		2.79	1.00
Nb	129.80	130.80	110.68	24.07	13.40	73.93	45.90	4.91	2.89	7.08	4.15	5.28	2.48	7.00	
Ta	5.38	7.81	6.86	0.49	0.19	3.95				0.45	0.17	1.26	0.92		
La	123.00	126.00	104.89	37.32	5.62	70.38	25.12	3.34	1.41	11.26	3.89	2.80	1.17	4.21	0.70
Ce	288.67	278.25	235.92	82.03	10.52	156.83	64.32	9.53	3.18	22.69	9.14	7.29	1.59	6.19	4.71
Sr	742.61	898.65	814.25	474.92	17.30	662.04	83.40	118.73	16.39	487.43	60.29	71.35	3.77	62.13	34.56
Nd	157.00	150.78	125.60	42.86	2.95	83.85	42.84	6.67	3.15	10.29	3.71	5.04	0.64	5.18	2.72
Sm	33.50	31.86	25.85	9.23	1.04	18.64	7.34	2.40	0.99	2.09	1.01	1.35	0.45	1.41	0.71
Gd	35.00	30.05	28.12	9.97	0.19	19.44	5.80	2.61	1.52	2.31	1.21	2.25	0.57	2.24	1.52
Zr	657.80	791.35	705.36	171.10	10.57	390.82	176.71	23.15	15.22	21.14	11.53	20.81	4.34	18.29	7.50
Hf	14.83	18.24	15.63	4.03	0.81	9.80	3.23	0.75	0.67	0.52	0.21	0.59	0.30	0.67	0.16
Ti	23180.09	31278.22	33223.27	15928.99	690.84	25537.54	5828.17	4090.75	1338.34	4694.23	1206.37	2922.15	234.81	3254.88	188.76
Y	88.12	81.16	69.60	27.82	1.39	54.06	20.23	12.63	4.97	6.87	2.13	13.41	1.08	12.27	4.74
Yb	5.77	5.83	5.15	2.35	0.24	5.26	1.57	1.24	0.57	0.82	0.23	1.27	0.66	1.33	0.41

Note: values are in ppm

Table 3 - Calculated composition of the amphibole-equilibrium melt of Agnew-Wiluna and Abitibi greenstone belts.

	Agnew-Wiluna greenstone belt (Western Australia)				Abitibi greenstone belt (Canada)							
	Mt. Keith - sample MKD1		Mt. Clifford - sample 85437		Theo's Flow - sample T-2		Boston Creek - sample B-5		Ghost Range - sample GR-1		Ghost Range - sample GR-2	
	Average	rsd	Average	rsd	Average	rsd	Average	rsd	Average	rsd	Average	rsd
Li	0.78	0.32	16.19	2.34	2.86	1.15	0.81	0.72	8.68	2.33	4.72	2.39
B	151.31	197.61	516.79	111.95	182.77	337.72	57.27	16.45	1273.28	327.94	150.50	114.86
Ba	418.85	21.58	203.37	24.36	9.95	1.48	717.79	83.52	168.46	87.66	331.23	52.11
Rb	35.83	6.55	23.82	0.96	5.04	1.60	16.18	3.45	32.28	4.37	23.29	6.77
Th	14.04	5.87	69.50	37.73	8.66	4.53	10.61	3.77	69.63	43.33	39.07	20.66
U	3.67	2.70	5.11	1.65	3.38	2.20	1.88	0.61	8.08	5.04	1.99	1.36
Nb	47.77	7.37	96.63	58.10	78.61	23.10	208.76	28.66	103.46	39.09	121.09	11.99
Ta	2.91	0.52	4.73	2.59	3.46	1.02	12.05	1.70	6.10	1.90	8.19	3.12
La	95.64	15.32	146.50	48.75	52.40	18.21	241.05	54.48	148.96	23.49	151.95	22.12
Ce	195.57	23.64	297.68	155.20	120.87	44.13	438.19	80.60	314.40	53.87	287.06	18.58
Sr	79.21	11.93	21.98	2.24	23.34	11.72	1796.06	139.68	34.68	3.18	30.49	8.38
Pb	8.11	1.64	10.20	2.06	4.51	5.02	5.21	7.03	9.30	6.01	5.18	1.28
Nd	84.41	9.37	122.34	92.10	54.02	18.97	159.17	16.41	129.89	34.35	97.83	30.08
Zr	363.39	85.39	1393.41	324.18	588.61	291.58	510.48	105.24	1504.42	273.40	1611.11	277.65
Hf	8.69	1.65	21.40	5.69	8.23	5.30	9.21	2.04	29.21	6.51	31.56	10.68
Sm	15.98	3.06	24.05	18.46	10.06	3.80	21.99	2.75	23.66	8.11	17.40	6.26
Eu	3.50	0.51	3.81	1.11	3.01	0.48	7.49	0.67	4.07	0.59	4.21	1.84
Gd	15.19	3.65	21.21	14.74	9.49	2.98	15.64	1.83	20.75	6.95	14.09	5.50
Ti	8404.77	1253.80	7590.60	697.49	3991.27	370.03	7076.12	860.32	7962.44	1225.44	8213.39	159.92
Dy	14.77	3.73	22.10	14.19	10.14	2.60	13.26	1.40	22.18	8.28	14.23	4.84
Y	80.10	17.46	116.34	65.19	46.26	11.74	64.02	6.57	124.83	37.92	79.18	22.23
Yb	7.50	1.22	11.75	3.50	5.45	1.27	6.54	0.82	12.69	2.34	7.60	1.76
Sc	25.99		14.71		11.57		1.90		24.58		24.15	
V	129.89		154.49		76.96		44.35		153.07		143.55	
F	180.98		188.80		5609.06		124.32		1048.80		2187.23	
Cl	18694.29		21054.29		11596.83		6828.57		19148.57		17380.95	
H_2O	2.70		2.45		3.52		3.77		3.53		2.44	
$(Nb/Y)_{PM}$	1.02		1.30		2.69		5.24		1.34		2.60	

Note: values are in ppm. H_2O values are in wt.%

Table 4 - Calculated composition of the amphibole-equilibrium melt of Pechenga Complex.

	Pilgüjarvi sill - sample Pilg 8 38		Pilgüjarvi sill - sample 106-44		Pilgüjarvi sill - sample 116-6		Kammikivi sill - 57-HV-28		Nyasyukka dike complex - sample N-2		Nyasyukka dike complex - sample N-3	
	Average	rsd	Average	rsd	Average	rsd	Average	rsd	Average	rsd	Average	rsd
Li	0.80		4.74	2.64	4.81	9.32	1.42	0.86	43.00	2.37	3.89	0.46
B	72.39		267.77		4079.21	2728.84	164.88		80.46	28.24	0.35	0.04
Ba	1103.21	28.94	775.01	27.76	1028.97	99.67	1138.94	109.81	815.50	46.10	894.23	49.86
Rb	44.96	6.17	24.69	3.38	63.80	6.27	38.07	5.54	41.07	2.91	41.12	1.22
Th	8.78	1.45	6.09	2.56	32.93	24.58	10.78	3.61	6.85	1.36	8.44	1.08
U	2.22	0.81	1.13	0.66	6.51	5.14	2.71	0.14	1.02	0.62	1.27	0.52
Nb	245.15	27.45	154.31	8.34	77.05	8.34	231.57	37.02	162.78	14.61	168.23	3.88
Ta	11.82	1.30	8.43	0.45	3.57	0.45	10.57	1.31	8.08	0.73	9.41	0.63
La	238.07	42.80	113.01	19.66	225.60	24.20	243.47	69.19	157.02	14.86	175.70	20.46
Ce	475.53	69.59	244.44	36.10	362.28	78.24	469.73	123.50	316.98	18.63	332.61	18.66
Sr	643.12	100.73	1274.62	36.22	194.99	14.42	456.75	67.54	878.70	43.75	847.61	80.26
Pb	25.93	7.52	4.58	1.53	17.61	3.17	4.23	2.23	5.51	0.97		
Nd	193.63	20.02	115.29	8.27	100.53	35.82	186.50	54.72	124.74	7.67	116.75	11.96
Zr	762.41	97.07	433.06	48.34	416.26	31.18	705.17	152.54	501.40	35.27	560.03	43.77
Hf	16.64	1.33	9.68	0.83	7.87	0.75	15.38	2.90	10.83	0.69	11.37	0.88
Sm	30.53	2.90	20.63	1.54	13.91	5.56	30.48	10.25	19.06	2.23	15.32	2.42
Eu	9.80	1.25	7.58	0.23	4.72	1.04	9.72	2.16	6.13	0.50	4.96	0.81
Gd	22.62	3.70	15.41	1.20	10.35	3.59	21.62	7.76	12.37	1.85	10.28	1.85
Ti	10859.38	746.52	10768.36	342.53	10537.92	943.01	10834.02	657.78	9142.06	149.22		
Dy	17.36	3.05	10.97	0.91	8.12	2.52	16.94	5.48	9.13	1.32	7.79	1.40
Y	73.04	8.96	46.28	3.82	36.49	11.09	71.92	22.22	40.92	2.93	35.39	5.36
Yb	5.46	0.43	3.69	0.49	3.32	0.49	5.15	1.64	3.68	0.43	3.33	0.33
Sc	18.17		12.43		33.33		17.44		16.41		19.12	
V	98.59		89.05		159.45		103.89		102.02		107.29	
F	2424.64		1715.22		1258.88		3145.65		474.24		894.57	
Cl	4463.49		3647.62		6626.98		4085.71		7457.14		5227.38	
H_2O	3.28		3.73		4.17		5.72		2.99		2.57	
$(Nb/Y)_{PM}$	5.37		5.36		3.72		5.66		6.36		7.78	

Note: values are in ppm. H_2O values are in wt.%

Table 5 - Calculated composition of the amphibole-equilibrium melt of Agnew-Wiluna and Abitibi greenstone belts.

	Agnew-Wiluna greenstone belt (Western Australia)				Abitibi greenstone belt (Canada)							
	Mt. Keith - sample MKD1		Mt. Clifford - sample 85437		Theo's Flow - sample T-2		Boston Creek - sample B-5		Ghost Range - sample GR-1		Ghost Range - sample GR-2	
	Average	rsd	Average	rsd	Average	rsd	Average	rsd	Average	rsd	Average	rsd
Li	0.13	0.05	2.70	0.39	0.48	0.19	0.27	0.04	1.45	0.39	0.86	0.15
B	79.67	6.05	574.21	124.39	188.12	375.24	63.64	18.28	1414.76	364.38	173.16	123.96
Ba	51.08	2.63	24.80	2.97	1.21	0.18	87.54	10.18	20.54	10.69	42.61	2.47
Rb	49.08	8.98	32.63	1.31	6.91	2.20	22.16	4.73	44.22	5.98	22.72	4.03
Th	85.63	35.81	423.78	230.05	52.79	27.62	64.67	22.98	424.55	264.24	162.70	68.27
U	56.41	41.55	78.59	25.34	29.67	36.68	28.99	9.35	124.36	77.60	23.46	12.51
Nb	15.77	2.43	31.89	19.17	25.94	7.63	68.90	9.46	34.15	12.90	40.22	4.69
Ta	17.13	3.07	27.83	15.23	20.35	6.02	70.89	9.98	35.86	11.15	61.95	10.40
La	29.43	4.71	45.08	15.00	16.12	5.60	74.17	16.76	45.83	7.23	39.34	5.11
Ce	20.06	2.43	30.53	15.92	12.40	4.53	44.94	8.27	32.25	5.52	29.43	3.58
Sr	0.88	0.13	0.24	0.02	0.26	0.13	19.96	1.55	0.39	0.04	0.45	0.06
Pb	19.31	3.89	24.29	4.91	9.21	11.64	12.41	16.73	22.14	14.30	14.36	0.21
Nd	8.89	0.99	12.89	9.70	5.69	2.00	16.77	1.73	13.69	3.62	13.96	1.19
Zr	3.79	0.89	14.51	3.38	6.13	3.04	5.32	1.10	15.67	2.85	19.10	2.60
Hf	3.26	0.62	8.02	2.13	3.08	1.99	3.45	0.77	10.94	2.44	16.00	0.22
Sm	4.67	0.89	7.03	5.40	2.94	1.11	6.43	0.80	6.92	2.37	7.31	0.12
Eu	2.63	0.38	2.86	0.84	2.26	0.36	5.63	0.51	3.06	0.45	4.83	0.05
Gd	3.18	0.76	4.44	3.08	1.99	0.62	3.27	0.38	4.34	1.45	4.38	0.11
Ti	0.99	0.15	0.89	0.08	0.47	0.04	0.83	0.10	0.94	0.14	0.96	0.03
Dy	2.50	0.63	3.73	2.40	1.71	0.44	2.24	0.24	3.75	1.40	3.38	0.00
Y	2.18	0.47	3.16	1.77	1.26	0.32	1.74	0.18	3.39	1.03	2.86	0.09
Yb	1.89	0.31	2.96	0.88	1.37	0.32	1.65	0.21	3.20	0.59	2.37	0.09

Note: values are in ppm and normalised on MORB composition (McDonough and Sun, 1995).

Table 6 - Calculated composition of the melt$_{Amph}$/MORB of Pechenga Complex.

	Pilgüjarvi sill - sample Pilg 8 38		Pilgüjarvi sill - sample 106-44		Pilgüjarvi sill - sample 116-6		Kammikivi sill - 57-HV-28		Nyasyukka dike complex - sample N-2		Nyasyukka dike complex - sample N-3	
	Average	rsd	Average	rsd	Average	rsd	Average	rsd	Average	rsd	Average	rsd
Li	0.13		0.79	0.45	3.29	1.05	0.33	0.11	7.17	2.95	0.36	0.35
B	80.44		297.52		959.87		183.20		76.05	11.09	0.22	0.21
Ba	134.54	3.53	94.51	37.42	125.48	12.15	138.90	13.39	99.45	39.48	109.05	6.08
Rb	61.59	8.46	33.82	13.55	87.40	8.59	52.15	7.59	56.26	19.84	56.33	1.67
Th	53.52	8.86	37.15	18.22	200.77	149.89	65.75	22.01	41.75	15.34	51.49	6.60
U	28.44	17.82	17.39	8.54	100.12	79.10	15.64	21.62	12.55	9.93	19.51	7.95
Nb	80.91	9.06	50.93	18.95	25.43	2.75	76.42	12.22	53.72	18.74	55.52	1.28
Ta	69.55	7.67	49.56	17.40	20.97	2.67	62.16	7.69	47.54	16.72	55.37	3.71
La	73.25	13.17	34.77	17.50	69.42	7.45	74.91	21.29	48.31	14.92	54.06	6.30
Ce	48.77	7.14	25.07	11.00	37.16	8.02	48.18	12.67	32.51	10.50	34.11	1.91
Sr	7.15	1.12	14.16	5.64	2.17	0.16	5.08	0.75	9.76	3.56	9.42	0.89
Pb	61.74	17.92	10.90	3.52	41.92	7.54	8.80	6.07	13.12	2.85		
Nd	20.40	2.11	12.15	4.08	10.59	3.77	19.65	5.77	13.14	4.56	12.30	1.26
Zr	7.94	1.01	4.51	1.71	4.34	0.32	7.35	1.59	5.22	1.75	5.83	0.46
Hf	6.23	0.50	3.63	1.38	2.95	0.28	5.76	1.09	4.05	1.47	4.26	0.33
Sm	8.93	0.85	6.03	1.75	4.07	1.62	8.91	3.00	5.57	2.01	4.48	0.71
Eu	7.37	0.94	5.70	1.75	3.55	0.78	7.31	1.62	4.61	1.54	3.73	0.61
Gd	4.73	0.77	3.22	0.86	2.17	0.75	4.52	1.62	2.59	0.82	2.15	0.39
Ti	1.28	0.09	1.27	0.45	1.24	0.11	1.27	0.08	1.07	0.40		
Dy	2.93	0.51	1.85	0.57	1.37	0.43	2.86	0.92	1.54	0.46	1.32	0.24
Y	1.98	0.24	1.26	0.40	0.99	0.30	1.95	0.60	1.11	0.36	0.96	0.15
Yb	1.37	0.11	0.93	0.28	0.84	0.12	1.30	0.41	0.93	0.35	0.84	0.08

Note: values are in ppm and normalised on MORB composition (McDonough and Sun, 1995).

Table 7 - Model of fractional crystallisation for Canadian clinopyroxene-equilibrium melt with the amphibole as the only forming-mineral.

	Theo's Flow - sample T-2						
	La	Ce	Nd	Sm	Gd	Dy	Yb
1	14.23	15.80	14.74	16.32	13.28	13.27	7.63
0.9	15.80	17.54	16.35	18.07	14.69	14.68	8.45
0.8	17.77	19.71	18.35	20.25	16.45	16.43	9.46
0.7	20.29	22.50	20.92	23.04	18.70	18.67	10.77
0.6	23.65	26.21	24.33	26.75	21.68	21.64	12.49
0.5	28.36	31.40	29.10	31.92	25.83	25.76	14.90
0.4	35.40	39.17	36.22	39.62	32.01	31.90	18.48
0.3	47.13	52.10	48.02	52.34	42.19	42.01	24.39
0.2	70.54	77.86	71.47	77.51	62.28	61.94	36.08
0.1	140.55	154.75	141.06	151.63	121.19	120.28	70.43

	Boston Creek - sample B-5						
	La	Ce	Nd	Sm	Gd	Dy	Yb
1	47.98	37.62	22.75	14.21	11.75	8.12	5.05
0.9	53.21	41.66	25.10	15.61	12.87	8.88	5.54
0.8	59.73	46.71	28.03	17.34	14.26	9.83	6.15
0.7	68.10	53.17	31.76	19.54	16.01	11.02	6.92
0.6	79.23	61.74	36.69	22.43	18.31	12.58	7.93
0.5	94.76	73.68	43.52	26.40	21.44	14.71	9.31
0.4	117.98	91.49	53.62	32.23	26.03	17.82	11.34
0.3	156.49	120.94	70.20	41.69	33.41	22.80	14.63
0.2	233.03	179.21	102.60	59.90	47.50	32.29	20.93
0.1	460.28	351.05	196.29	111.31	86.70	58.53	38.63

	Ghost Range - sample GR-1						
	La	Ce	Nd	Sm	Gd	Dy	Yb
1	11.93	12.09	11.14	9.18	11.44	12.57	7.82
0.9	13.24	13.40	12.32	10.12	12.59	13.82	8.61
0.8	14.87	15.04	13.79	11.28	14.01	15.36	9.59
0.7	16.97	17.14	15.66	12.77	15.82	17.33	10.85
0.6	19.76	19.93	18.15	14.73	18.19	19.91	12.50
0.5	23.65	23.82	21.60	17.43	21.47	23.46	14.78
0.4	29.48	29.64	26.73	21.44	26.29	28.68	18.14
0.3	39.17	39.28	35.19	27.98	34.13	37.17	23.62
0.2	58.45	58.42	51.83	40.72	49.32	53.55	34.29
0.1	115.89	115.15	100.49	77.36	92.51	99.96	64.83

	Ghost Range - sample GR-2						
	La	Ce	Nd	Sm	Gd	Dy	Yb
1	17.94	10.26	11.45	9.59	11.39	9.44	8.18
0.9	19.90	11.38	12.66	10.57	12.54	10.37	9.02
0.8	22.36	12.77	14.17	11.78	13.95	11.54	10.05
0.7	25.51	14.55	16.10	13.34	15.75	13.01	11.36
0.6	29.70	16.92	18.65	15.38	18.11	14.95	13.09
0.5	35.56	20.23	22.20	18.21	21.37	17.61	15.47
0.4	44.33	25.17	27.47	22.39	26.17	21.54	18.99
0.3	58.89	33.35	36.16	29.22	33.98	27.90	24.74
0.2	87.89	49.60	53.27	42.53	49.10	40.20	35.91
0.1	174.25	97.78	103.28	80.80	92.10	75.05	67.89

Note: values are in ppm.

Table 8 - Model of fractional crystallisation for Russian clinopyroxene-equilibrium melt with the amphibole as the only forming-mineral.

	Pilgüjarvi sill - sample Pilg 8 38						
	La	Ce	Nd	Sm	Gd	Dy	Yb
1	524.07	478.56	271.88	227.74	178.03	109.52	35.51
0.9	581.20	531.90	302.50	250.23	195.08	119.88	38.97
0.8	652.47	598.33	340.48	278.02	216.07	132.63	43.25
0.7	743.88	683.42	388.90	313.27	242.63	148.73	48.67
0.6	865.46	796.36	452.83	359.55	277.36	169.76	55.77
0.5	1035.15	953.67	541.32	423.21	324.92	198.50	65.53
0.4	1288.75	1188.16	672.26	516.64	394.36	240.39	79.82
0.3	1709.46	1575.94	886.82	668.17	506.22	307.69	102.93
0.2	2545.54	2343.22	1306.12	960.09	719.76	435.71	147.30
0.1	5027.96	4605.47	2517.97	1784.15	1313.66	789.74	271.85

	Pilgüjarvi sill - sample 106-44						
	La	Ce	Nd	Sm	Gd	Dy	Yb
1	446.91	391.11	231.85	175.73	143.03	86.36	31.69
0.9	495.63	435.04	258.32	193.09	156.73	94.53	34.79
0.8	556.40	489.75	291.15	214.53	173.60	104.59	38.60
0.7	634.36	559.82	333.00	241.73	194.93	117.28	43.44
0.6	738.03	652.83	388.25	277.45	222.84	133.87	49.78
0.5	882.74	782.37	464.73	326.56	261.05	156.53	58.49
0.4	1099.00	975.47	577.89	398.66	316.84	189.56	71.24
0.3	1457.77	1294.78	763.28	515.59	406.72	242.63	91.87
0.2	2170.75	1926.58	1125.56	740.84	578.28	343.59	131.48
0.1	4287.67	3789.33	2172.52	1376.73	1055.44	622.76	242.64

	Pilgüjarvi sill - sample 116-6						
	La	Ce	Nd	Sm	Gd	Dy	Yb
1	159.01	135.99	94.74	62.75	50.71	32.30	14.46
0.9	176.58	150.96	105.05	69.49	56.11	35.73	16.01
0.8	198.53	169.65	117.92	77.88	62.83	40.00	17.94
0.7	226.72	193.65	134.42	88.63	71.43	45.45	20.40
0.6	264.29	225.61	156.36	102.89	82.83	52.68	23.68
0.5	316.83	270.29	186.97	122.76	98.68	62.73	28.23
0.4	395.57	337.19	232.72	152.36	122.26	77.67	35.02
0.3	526.60	448.42	308.58	201.30	161.17	102.29	46.23
0.2	788.18	670.18	459.28	298.08	237.90	150.81	68.37
0.1	1570.47	1332.02	906.42	583.16	462.93	292.85	133.48

	Kammikivi sill - 57-HV-28						
	La	Ce	Nd	Sm	Gd	Dy	Yb
1	299.87	260.00	185.34	126.72	98.88	59.74	32.37
0.9	332.88	288.43	205.25	140.01	109.11	65.89	35.75
0.8	374.09	323.91	230.03	156.53	121.79	73.51	39.94
0.7	427.02	369.44	261.77	177.63	137.97	83.22	45.29
0.6	497.49	430.02	303.90	205.55	159.34	96.03	52.37
0.5	596.01	514.61	362.56	244.29	188.92	113.75	62.19
0.4	743.52	641.12	449.97	301.77	232.70	139.95	76.73
0.3	988.80	851.14	594.47	396.28	304.43	182.83	100.62
0.2	1477.80	1268.98	880.20	581.78	444.58	266.47	147.42
0.1	2937.22	2511.70	1721.79	1121.59	849.40	507.34	283.23

Note: values are in ppm.

Table 9 - Model of fractional crystallisation for Canadian bulk-rock melt.

	Theo's Flow - sample T-2						
	La	Ce	Nd	Sm	Gd	Dy	Yb
1	14.23	15.80	14.74	16.32	8.70	8.08	7.45
0.9	15.77	17.47	16.30	18.04	9.50	8.81	8.10
0.8	17.68	19.54	18.23	20.18	10.48	9.71	8.90
0.7	20.13	22.19	20.70	22.91	11.72	10.84	9.91
0.6	23.39	25.70	23.97	26.54	13.34	12.31	11.21
0.5	27.93	30.58	28.51	31.57	15.53	14.31	12.97
0.4	34.70	37.82	35.26	39.04	18.72	17.21	15.51
0.3	45.91	49.75	46.36	51.34	23.82	21.83	19.53
0.2	68.10	73.21	68.18	75.53	33.44	30.51	27.02
0.1	133.66	141.69	131.86	146.12	59.71	54.07	47.08

	Boston Creek - sample B-5						
	La	Ce	Nd	Sm	Gd	Dy	Yb
1	47.98	37.62	22.75	14.21	19.79	13.76	10.09
0.9	53.21	41.66	25.19	15.73	21.74	15.11	11.17
0.8	59.74	46.70	28.23	17.64	24.16	16.77	12.51
0.7	68.11	53.15	32.12	20.07	27.22	18.88	14.23
0.6	79.25	61.72	37.29	23.30	31.25	21.65	16.50
0.5	94.79	73.65	44.49	27.80	36.78	25.44	19.67
0.4	118.03	91.43	55.21	34.51	44.91	31.01	24.38
0.3	156.59	120.83	72.93	45.60	58.09	40.02	32.15
0.2	233.22	179.00	107.97	67.53	83.49	57.33	47.50
0.1	460.81	350.45	211.18	132.14	155.20	106.01	92.57

	Ghost Range - sample GR-1						
	La	Ce	Nd	Sm	Gd	Dy	Yb
1	11.93	12.09	11.14	9.18	13.28	13.64	20.25
0.9	13.22	15.20	12.32	10.15	14.32	14.91	22.05
0.8	14.83	19.07	13.80	11.37	15.60	16.48	24.26
0.7	16.90	24.01	15.68	12.92	17.17	18.46	27.04
0.6	19.64	30.54	18.17	14.97	19.20	21.05	30.64
0.5	23.47	39.60	21.64	17.83	21.90	24.57	35.52
0.4	29.18	53.03	26.80	22.08	25.72	29.70	42.57
0.3	38.64	75.13	35.30	29.09	31.66	37.92	53.76
0.2	57.41	118.58	52.05	42.91	42.43	53.50	74.69
0.1	112.94	245.54	101.10	83.36	69.98	96.39	131.06

	Ghost Range - sample GR-2						
	La	Ce	Nd	Sm	Gd	Dy	Yb
1	17.94	10.26	11.45	9.59	13.28	13.64	20.25
0.9	19.88	13.19	12.67	10.61	14.53	14.93	22.08
0.8	22.31	16.83	14.19	11.88	16.07	16.52	24.32
0.7	25.42	21.47	16.13	13.51	18.01	18.54	27.15
0.6	29.56	27.61	18.71	15.66	20.55	21.16	30.81
0.5	35.33	36.13	22.29	18.66	24.02	24.76	35.80
0.4	43.95	48.78	27.62	23.13	29.06	30.00	43.01
0.3	58.23	69.60	36.41	30.49	37.17	38.42	54.48
0.2	86.56	110.58	53.75	45.03	52.58	54.45	76.04
0.1	170.51	230.55	104.63	87.67	95.11	98.85	134.44

Note: values are in ppm.

Table 10 - Model of fractional crystallisation for Russian bulk-rock melt.

	Pilgüjarvi sill - sample Pilg 8 38						
	La	Ce	Nd	Sm	Gd	Dy	Yb
1	524.07	478.56	347.04	227.74	31.79	19.86	10.34
0.9	581.34	532.02	384.41	252.28	34.97	21.83	11.34
0.8	652.79	598.63	430.97	282.86	38.90	24.26	12.56
0.7	744.48	683.96	490.61	322.04	43.90	27.35	14.12
0.6	866.45	797.27	569.80	374.07	50.47	31.41	16.15
0.5	1036.76	955.14	680.11	446.55	59.53	37.00	18.94
0.4	1291.40	1190.59	844.59	554.64	72.85	45.20	23.02
0.3	1714.08	1580.16	1116.66	733.47	94.51	58.52	29.60
0.2	2554.75	2351.63	1655.20	1087.54	136.40	84.21	42.17
0.1	5054.00	4629.12	3243.78	2132.47	255.41	156.89	77.27

	Pilgüjarvi sill - sample 106-44						
	La	Ce	Nd	Sm	Gd	Dy	Yb
1	446.91	391.11	277.63	175.73	31.79	19.86	10.34
0.9	496.11	435.68	307.91	194.91	35.12	21.93	11.39
0.8	557.55	491.29	345.68	218.84	39.27	24.50	12.69
0.7	636.45	562.64	394.13	249.55	44.56	27.78	14.34
0.6	741.53	657.55	458.57	290.39	51.56	32.12	16.52
0.5	888.41	790.06	548.52	347.40	61.27	38.14	19.53
0.4	1108.35	988.17	682.96	432.64	75.68	47.06	23.97
0.3	1474.08	1316.98	906.00	574.07	99.37	61.69	31.22
0.2	2203.28	1970.88	1349.33	855.28	145.86	90.37	45.29
0.1	4379.89	3914.60	2665.89	1690.82	281.13	173.54	85.57

	Pilgüjarvi sill - sample 116-6						
	La	Ce	Nd	Sm	Gd	Dy	Yb
1	157.73	135.99	94.74	62.75	31.79	19.86	10.34
0.9	174.94	152.45	104.91	69.49	34.80	21.72	11.32
0.8	196.40	172.94	117.57	77.88	38.50	24.00	12.53
0.7	223.93	199.18	133.79	88.64	43.18	26.89	14.06
0.6	260.55	234.00	155.32	102.91	49.29	30.65	16.06
0.5	311.66	282.48	185.29	122.78	57.64	35.78	18.80
0.4	388.06	354.71	229.95	152.40	69.80	43.24	22.79
0.3	514.81	474.11	303.77	201.37	89.36	55.21	29.20
0.2	766.76	710.24	449.74	298.22	126.56	77.91	41.43
0.1	1515.01	1405.96	879.59	583.56	229.45	140.36	75.32

	Kammikivi sill - 57-HV-28						
	La	Ce	Nd	Sm	Gd	Dy	Yb
1	299.87	260.00	185.34	126.72	31.79	19.86	10.34
0.9	332.65	288.05	205.31	140.38	34.97	21.83	11.34
0.8	373.54	323.01	230.19	157.40	38.91	24.27	12.57
0.7	426.02	367.81	262.05	179.21	43.92	27.37	14.12
0.6	495.83	427.30	304.37	208.17	50.50	31.43	16.16
0.5	593.31	510.20	363.31	248.52	59.57	37.03	18.96
0.4	739.07	633.85	451.21	308.70	72.92	45.25	23.04
0.3	981.02	838.49	596.62	408.28	94.64	58.61	29.64
0.2	1462.27	1243.81	884.46	605.45	136.66	84.38	42.26
0.1	2893.17	2440.75	1733.73	1187.44	256.09	157.33	77.49

Note: values are in ppm.

Table 11 - Calculated composition of the primary melt of Agnew-Wiluna and Abitibi greenstone belts.

	Agnew-Wiluna greenstone belt (Western Australia)		Abitibi greenstone belt (Canada)			
	Mt. Keith - sample MKD1	Mt. Clifford - sample 85437	Theo's Flow - sample T-2	Boston Creek - sample B-5	Ghost Range - sample GR-1	Ghost Range - sample GR-2
Sc	3.90	2.21	0.35	0.19	1.72	1.69
V	19.48	23.17	2.31	4.43	10.72	10.05
F	27.15	28.32	168.27	12.43	73.42	153.11
Cl	2804.14	3158.14	347.90	682.86	1340.40	1216.67
H_2O	0.41	0.37	0.11	0.38	0.25	0.17

Note: values are in ppm. H_2O values are in wt.%

Table 12 - Calculated composition of the primary melt of Pechenga Complex.

	Pilgüjarvi sill - sample Pilg 8 38	Pilgüjarvi sill - sample 106-44	Pilgüjarvi sill - sample 116-6	Kammikivi sill - 57-HV-28	Nyasyukka dike complex - sample N-2	Nyasyukka dike complex - sample N-3
Sc	1.82	1.24	1.00	0.87	5.75	6.69
V	9.86	8.90	4.78	5.19	35.71	37.55
F	242.46	171.52	37.77	157.28	165.98	313.10
Cl	446.35	364.76	198.81	204.29	2610.00	1829.58
H_2O	0.33	0.37	0.13	0.29	1.05	0.90

Note: values are in ppm. H_2O values are in wt.%

Table 13 - Calculated composition of the amphibole-equilibrium melt of the Phanerozoic samples.

	Husky Ridge (Antarctica) - sample TT329	Sanandaj Sirjan Zone (Iran) - sample AL89	Taku (Japan) - sample TK1B	Zenifudo (Japan) - sample ZN5	Hase no Yatsu (Japan) - sample HSY3B	Milin (Tibet) - sample 14JT50
Sc	18.17	19.38	21.07	18.49	22.41	18.96
V	92.08	79.29	93.80	72.48	85.10	97.27
F	521.41	288.04	283.15	209.89	437.07	561.30
Cl	3540.00	3267.62	3317.14	2811.43	1709.52	2601.90
H_2O	3.37	2.24	3.69	2.95	2.77	3.25
Nb/Y	2.33	11.77	4.41	7.69	12.25	1.58

Continued Table 13

	Adamello (Italy) - sample MAT15	Bregaglia (Italy-Swiss) - sample VS9	Batu Hijau (Indonesia) - sample SRD02305	Hoover Dam (USA) - sample MGT	Dish Hill (USA) - sample DH
Sc	33.35	24.34	33.05	13.18	10.32
V	93.88	113.68	58.33	94.02	64.32
F	356.52		671.96	673.91	869.57
Cl	2142.86		6985.71	952.38	476.19
H_2O	2.69		4.03	3.27	3.73
Nb/Y	4.38	1.74	0.96	31.02	35.25

Note: values are in ppm. H_2O values are in wt.%

Table 14 - Calculated composition of the primary melt of the Phanerozoic samples.

	Husky Ridge (Antarctica) - sample TT329	Sanandaj Sirjan Zone (Iran) - sample AL89	Taku (Japan) - sample TK1B	Zenifudo (Japan) - sample ZN5	Hase no Yatsu (Japan) - sample HSY3B	Milin (Tibet) - sample 14JT50
Sc	13.08	9.69	12.01	9.06	11.20	13.27
V	66.30	39.65	53.47	35.51	42.55	68.09
F	375.42	144.02	161.40	102.85	218.53	392.91
Cl	2548.80	1633.81	1890.77	1377.60	854.76	1821.33
H_2O	2.42	1.12	1.36	1.44	1.38	2.27

Continued Table 14

	Adamello (Italy) - sample MAT15	Bregaglia (Italy-Swiss) - sample VS9	Batu Hijau (Indonesia) - sample SRD02305	Hoover Dam (USA) · sample MGT	Dish Hill (USA) - sample DH
Sc	25.01	44.26	23.80	13.18	10.32
V	70.41	206.69	42.00	94.02	64.32
F	267.39		100.79	673.91	869.57
Cl	1607.14		1047.86	952.38	476.19
H_2O	2.02		0.60	3.27	3.73

Note: values are in ppm. H_2O values are in wt.%